ORGANIC-INORGANIC NANOCOMPOSITES FOR PHOTOVOLTAIC AND OTHER OPTOELECTRONIC APPLICATIONS

By

Yousaf Khan

School of Life, Sciences, Pharmacy and Chemistry

Kingston University London

2019

A thesis submitted for the degree of Doctor of Philosophy at Kingston University London, Kingston-Upon-Thames, United Kingdom

Abstract

Novel nanocomposite organic-inorganic compounds have been synthesised with several layered inorganic hosts (V_2O_5, MoO_3 and $ZnPS_3$). Three synthetic methods were used; direct intercalation taking advantage of any redox chemistry between the host and guest, an ion-exchange route in which pre-intercalated alkali metal cations were exchanged for organic guest cations and recrystallization of the dissolved host around the organic guest species. All methods afforded the intercalation of conducting polymers into the interlayer space of the inorganic hosts. Full characterisation of the composites was carried out as well as the determination of their (opto)electronic properties.

The direct method was used to intercalate polyaniline ($AnAn^+$) and 3,4-ethylenedioxythiophene (EDOT) into V_2O_5 2-amino-5-phenylpyridine (2A5PhPyr) used an acid-base direct intercalation method. $AnAn^+$ and 2A5PhPyr exhibited bilayer structures with $AnAn^+$ parallel to the inorganic layers. EDOT, however, produced a monolayer intercalate and all three products exhibited similar room temperature conductivities (~10^{-2} – 10^{-3} Sm^{-1}).

2A5PhPyr and 5-aminoquinoline (5AQ) were intercalated into V_2O_5 and MoO_3 using the ion-exchange method. A copolymer of 1,4-phenylenediamine and hydroquinone (1,4PDA-HQ) was also intercalated into V_2O_5 and 1,2-phenylenediamine (PDA) was intercalated into V_2O_5, MoO_3 and $ZnPS_3$ by this method. 2-Aminothiazole (2AmThia) was intercalated into MoO_3 using ion-exchange. PDA and 5AQ exhibited bilayer conformation upon intercalation while PDA was a monolayer intercalant in $ZnPS_3$. PDA intercalated V_2O_5 and MoO_3 exhibited the highest conductivities (~10^{-1} Sm^{-1}) whereas 2AmThia intercalated MoO_3 exhibited the lowest conductivity (~10^{-4} Sm^{-1}).

Aniline (An) was intercalated into MoO_3 via a novel recrystallization method resulting in room temperature conductivity similar to that of the 2AmThia intercalated MoO_3 (~10^{-4} Sm^{-1}).

The novel ion-exchange of $ZnPS_3$ with Mg^{2+} yielded $Mg_xZn_yPS_3$ which exhibited substantial interlayer expansion suspected to be due to hydration of intercalated Mg^{2+}. The Mg^{2+} cations were present in the interlayer spacing and did not occupy the vacant Zn^{2+} sites.

The intercalated materials exhibited p-type properties, unlike their n-type hosts. Using aluminium, copper, tin, zinc and $FePS_3$ as blocking contacts, Schottky devices of the composite materials exhibited improved semiconductor properties over their host materials.

Prototype photosensitive devices using $V_2O_5/AnAn^+$, V_2O_5/EDOT, V_2O_5/2A5PhPyr, MoO_3/PDA and $ZnPS_3$/PDA were constructed by spin coating the active material onto n-type silicon and p-type $FePS_3$ and are reported for the first time. The devices exhibited increased photocurrents under ambient light or an incandescent lamp illumination. Maximum efficiencies were 0.71% and 0.26% under ambient light and incandescent lamp respectively. The devices exhibited low charge mobilities of ~8 x 10^{-10} $m^2V^{-1}s^{-1}$ and ~3 x 10^{-11} $m^2V^{-1}s^{-1}$ under ambient sunlight and incandescent light respectively. It was noted that the polymer guests in their most conductive forms produced the best semiconducting and photoactive devices.

Overall, this work provided a proof-of-concept that the low-cost organic-inorganic nanocomposite materials synthesised exhibited promising novel optoelectronic properties when incorporated into junction devices.

Acknowledgements

I would firstly like to thank my supervisory team (Dr Richard Singer, Prof Peter Foot and Dr Roman Kresinski) for their support and guidance and in particular Dr Richard Singer for his invaluable insights in discussions. I could not have asked for a better supervisory team and first supervisor.

I would like to express my sincere gratitude towards the technical staff and Kingston University and in particular Wendy Brosnan, Dr Richard Giddens, Rizwan Merali, Dr Siamak Soltani and Paul Stovell. I am extremely grateful to Dr Peter Spearman and Dr Gemma Shearman who provided endless support and encouragement and to Dr Joseph Bear for having the patience and taking the time to carry out all XPS analysis at the University College London. I would like to express additional appreciation towards the Kingston University Doctoral School for giving me the opportunity carry out a PhD.

I would like to thank all my fellow colleagues Anis Daou, Federico Buonocore, Alex Fudger, Navid Shokri, Patrick Melia, Luke Bywaters, Samerah Malik and Mateo Zecchini.

And finally I would like to thank my family and friends for their support throughout my Phd studies, without them I would not have completed this thesis.

Contents

List of Figures

List of Tables

List of Acronyms

1,4PDA	1,4-Phenylenediamine
2A5PhPyr	2-amino-5-phenylpyridine
2AmThia	2-Aminothiazole
3-HPBIM	2-(3-pyridyl)-benzimidazolium
4-PBIM	2-(4-pyridyl)benzimidazole)
5AQ	5-Aminoquinoline
AB	Acid-Base Reaction
AEAE	2-(2-aminoethylamino) ethanol
AEE	2-(2-aminoethoxy) ethanol
An	Aniline
$AnAn^+$	Emeraldine
$AsPh_3$	triphenylarsine oxide
ATR-IR	Anntenutated total reflectance Infra-red spectroscopy
BDT	Benzothiophene
BEDT-TTF	bis(ethylenedithio)- tetrathiafulvalene
BET	Brunauer-Emmett-Teller
BJH	Baerret-Joyner-Halenda
bpy	bipyridine
DAMS	4-[2-(4-dimethyl-aminophenyl)ethenyl]-1-methylpyridinium
DEMS	4-[4-(diethylamino)-R-styryl]-1-methylpyridinium
DETA	Diethylenetriamine
diphos	1,2-bis(diphenylphosphino)ethane
DMPz	quinoxaline, dimethylpyrazine
DMSO	dimethyl sulphoxide
DSSC's	dye-sensitized solar cells
DTh	dimercaptothiophene
EDOT	3,4-ethylenedioxythiophene
EDS	Energy-dispervise X-ray Spectra
EDTA	Ethylenediaminetetraacetic acid
EELS	Electron energy loss spectroscopy
Eg	band-gap
EPR	Electron paramagnetic resonance
ESCA	Electron spectroscopy chemical analysis
ESR	Electron Spin Resonance
FT-IR	Furior transform Infrared spectroscopy
GPC	gel-permeation-chromatography
hmta	hexamethylenetetramine
HQ	Hydroquinone
ICP-AES	Inductively Coupled Plasma-Atomic Emission spectroscopy
ITO	Indium Tin Oxide
LPEI	linear poly(ethyleneimine)
MoO_3	Molybdenum trioxide
MPS_3	transition metal thiophosphates
n-BuLi	n-Butyllithium

NIR	Near Infra-red spectroscopy
OPBIM	2-(2-ol-3-pyridino)benzimidazole
OPV	organic photovoltaic devices
PAHCl	poly(allylamine hydrochloride
PAMAM	polyamidoamine
PANI	Polyaniline
PAPSA	poly(aniline-co-N-(-4-sulfophenyl)aniline)
PDA	Phenylene diamine
pdc	pyrrolidine dithiocarbamate
PDDACl	poly(diallymethylammonium chloride
PDMcT	poly(2,5-dimercapto-1,3,5-thiadiazole)
PEDOT	poly(3,4-ethylene dioxythiophene)
PEO	poly(ethylene Oxide)
PET	poly(ethylene terephthalate)
PNQA	poly(N-[5-(8-hydroxyquinoline)methyl]aniline)
pPDA	poly(para-phenylenediamine
PPP	poly(*p*-phenylene)
PPS	polystyrene sulfonate
PPV	poly(p-phenylene vinylene)
Ppy	Polypyrrole
PSA	pyridinesulfonic acid
PSPAN	poly(N-propane sulfonic acid aniline)
PTHNA	poly(5,6,7,8,-tetrahydro-1-naphthylamine)
PTMPD	poly(tetramethyl-*p*-phenylenediamine dihydrochloride)
PTOESA	poly(2-(3thienyloxy)ethanesulfonic acid)
PV	photovoltaic
PVP	poly(vinyl pyrrolidone)
py	pyridine
pyo	pyridine N-oxide
TGA	Thermogravimetric Analysis
TTF	Tetrathiafulvalene
UV-Vis	Ultra Violet - Visible absorption spectroscopy
V_2O_5	Vanadium pentoxide
XANES	X-ray Absorption Near edge Strcuture
XAS	X-ray absorption spectroscopy
XPS	X-ray Photoelectron Spectroscopy
XRD	X-ray Diffraction

1) Introduction

1.1) Photovoltaic Motivations

Major issues facing the 21st century include the energy crisis, depleting fossil fuel resources and their negative environmental effects (1). This is due to population growth combined with technological advancement (2)(3) and has given rise to the demand for reliable, cost-effective renewable energy sources. However, renewable energy sources still account for only 2.5% of all traded energy and around 6% of electricity produced (4,5). Solar energy is a free, limitless, long-term source of renewable energy for managing such energy and environmental problems (2,6) as it provides more than 10,000 times the energy that humans currently consume (7). A major benefit of the use of solar energy over other renewable energy resources lies in the ability to directly harvest sunlight into electricity with the use of photovoltaic (PV) solar cells (6,8). At the end of 2011, it was shown that the globally installed capacity of PV cells was 67.4 GW and growing. Furthermore, the installation of Si-PV cells showed a drop in cost from 4.05 USD/W to 2.21 USD/W in the two year period of 2008 to 2010 (9). Commercial PV cells have also shown a higher efficiency of 12% (10). There are two classes of semiconducting materials used in today's PV solar cells; inorganic and organic (11–13) and they fall into three generations *i)* First generation p-n junction crystalline silicon solar cells, *ii)* the second-generation thin-film solar cells made from amorphous silicon and other inorganic materials such as CdTe or CuInGaSe and finally *iii)* third generation solution-processed solar technologies which aim to lower overall cost of manufacturing while maintaining high solar conversion efficiencies. Examples of third-generation PV cells include dye-sensitized solar cells (DSSCs), organic photovoltaics and quantum dot solar cells(8,13,14). However, of the 6% of electricity generated from renewable energy sources less than 0.5% is generated using solar energy. The main drawback which has prevented widespread use of PV devices lies

in the high cost (but high efficiencies) of inorganic-based PV devices and the low efficiencies (but low cost) of organic/polymer PV devices (15).

1.1.1) Photovoltaic Fundamentals

When a semiconducting material absorbs a photon with at least the energy of its band-gap (E_g), an electron is promoted from the valence band to the conduction band forming an electron-hole pair.

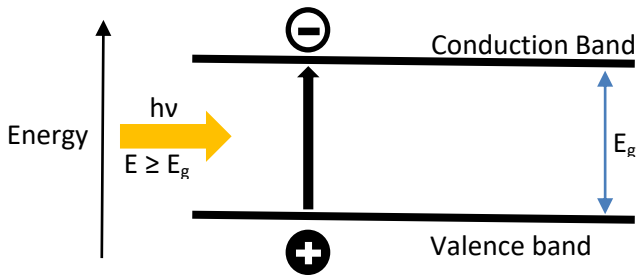

Figure 1.1 - Absorption of a photon (hv) resulting in the promotion of an electron from the valence band to the conduction band to produce an electron-hole pair

Upon creation of the electron-hole pair, charge separation is required in order to allow the promoted electron to undergo electrical work to power a device. In most cases, this charge separation is created by an electric field, which drives the electrons in one direction and the positive holes in the other direction (16) at a semiconductor junction.

There is a range of different junction types which take advantage of this effect including Ohmic, Schottky and P-N junctions.

1.1.1.1) Ohmic Junction

Ohmic junctions between semiconductors and metal contacts allow for charge carriers to flow from the semiconductor to the metal. For a p-type semiconductor, this contact is formed when the work function (Φ_m) of the metal is larger than the Fermi level of the semiconductor in question ($\Phi_m > \Phi_s$). Figure 1.2 shows the Ohmic junction for a p-type semiconductor.

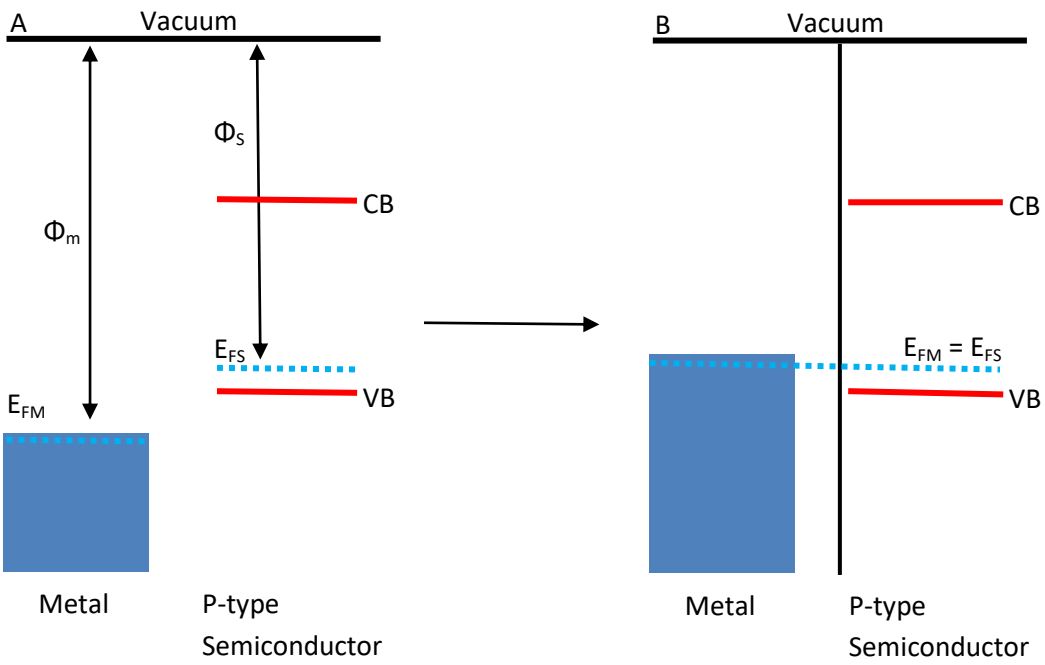

Figure 1.2 - Metal to p-doped semiconductor Ohmic junction. A) Pre-contact energy level alignment of the metals work-function (Φ_m) and the p-doped semiconductor work-function (Φ_S) and the metal and semiconductor fermi-level (E_{FM} and E_{FS}). The semiconductor valence and conduction band are also shown (CB and VB). B) The Ohmic contact between the metal and semiconductor.

After contact, E_{FM} and E_{FS} are now at the same energy and $E_{FM} = E_{FS}$ and no band bending is observed at the junction.

1.1.1.2) Schottky Junction

A Schottky junction inhibits the flow of charge carriers from the semiconductor to the metal contact (for a p-type material, the opposite is true for an n-type material). This is achieved by employing the inverse conditions compared to Ohmic junctions (i.e. the Φ_m would be smaller than the Φ_s of a p-type semiconductor i.e. $\Phi_s > \Phi_m$). Figure 1.3 shows the Schottky junction for a p-type semiconductor.

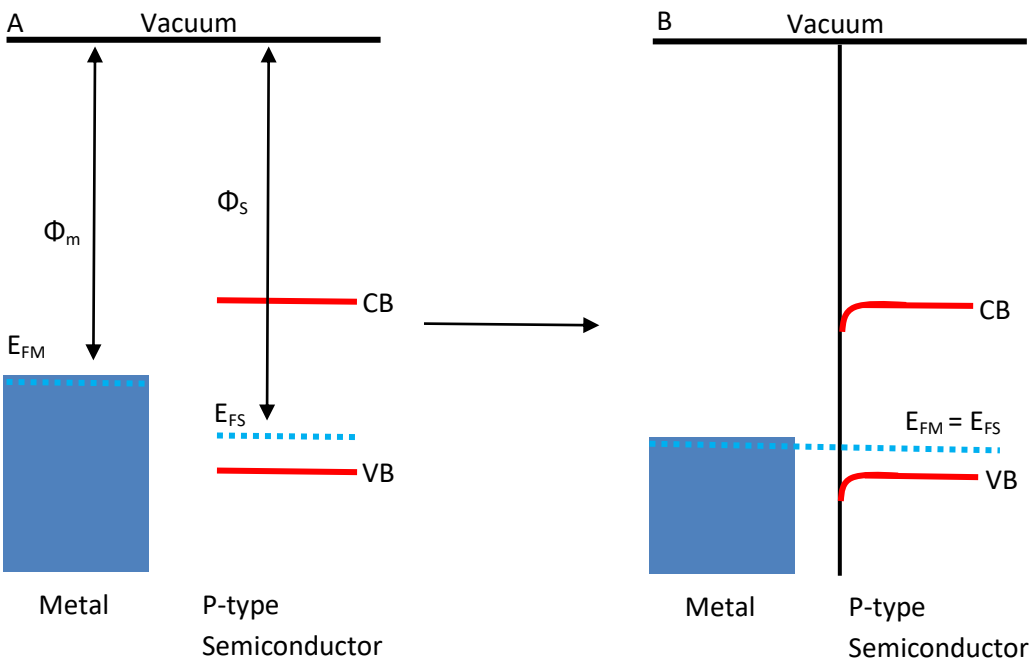

Figure 1.3 - Metal to p-type semiconductor Schottky junction. A) Pre-contact energy level alignment of the metal work-function (Φ_M) and the p-type semiconductor work-function (Φ_S) and the metal and semiconductor Fermi-levels (E_{FM} and E_{FS}). The semiconductor valence and conduction bands (VS and CB) are shown. B) The Schottky contact between the metal and semiconductor.

After contact, E_{FM} and E_{FS} are now at the same energy and $E_{FM} = E_{FS}$. The difference in energy between the now formed junction fermi-level and the p-type semiconductor VB is the barrier height of the junction.

1.1.1.3) P-N Junction

A P-N junction is formed when a p-type and n-type semiconductor are brought into contact with one another. Here, the charge carriers (holes in the p-type and electrons in the n-type) diffuse across the junction and recombine leaving a depletion region where no free charge carriers exist. In this depletion region, positive charges are built-up on the n-type side and negative charge is built-up on the p-type side. Upon illumination electrons are excited across the band-gap (as seen in Figure 1.4) and drift towards the n-type material (whose depletion region has built up a positive charge) which results in charge separation.

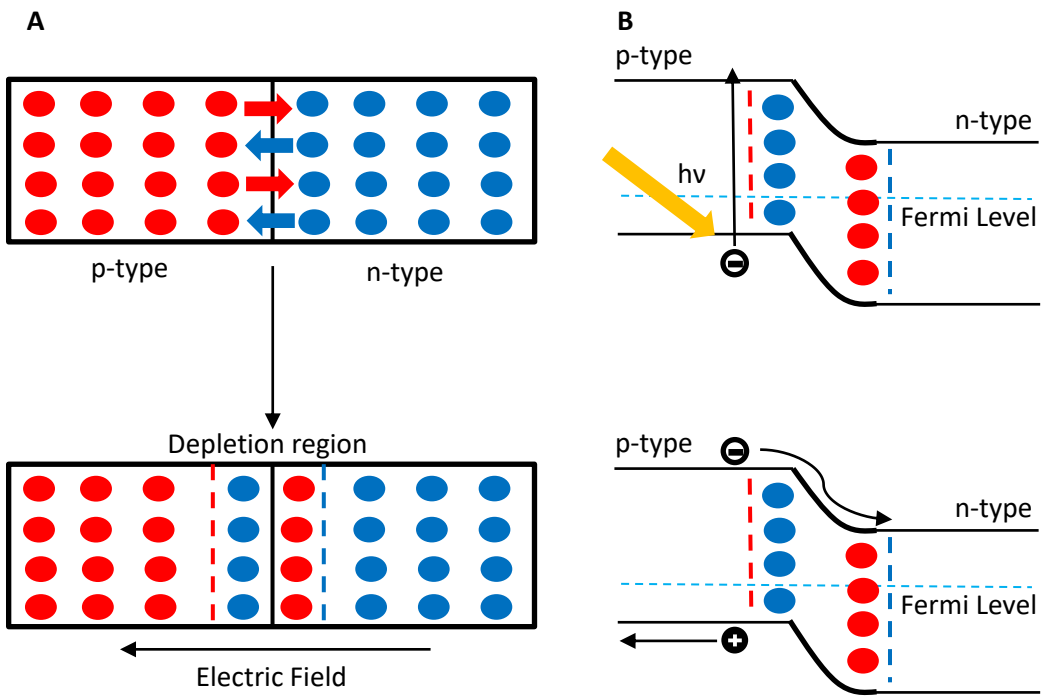

Figure 1.4 - A) The formation of the depletion region at the P-N junction when holes (red) and electrons (blue) migrate across the junction resulting in the formation of an electric field. B) The band structure of a P-N junction and its operation under illumination

1.1.1.4) Diode Equation

In solar cells, these junctions effectively behave as diodes, where under a reverse bias the barrier height at the metal-semiconductor junction increases and prevents the flow of charge carriers across the junction. Under a forward bias, the barrier height decreases, allowing charge carriers to travel more easily across the junction.

As the barrier height decreases, the number of charge carriers crossing the junction increases exponentially and as such can be modelled using the ideal-diode equation (Equation 1.1).

$$I = I_0(e^{\frac{qV}{kT}} - 1)$$

Equation 1.1

where:

- I is the net current measured through the diode.
- I_0 is the dark saturation current of the diode.
- q is the absolute value of the electron charge.
- V is the applied voltage across the diode.

However, under illumination, a photogenerated current (I_{ph}) needs to be taken into account and thus equation 1 is modified to give Equation 1.2:

$$\mathrm{I} = I_{ph} + \mathrm{I}_0(\mathrm{e}^{\frac{\mathrm{qV}}{\mathrm{kT}}} - 1)$$

Equation 1.2

1.1.1.5) Active Material Requirements

However, in order to fully take advantage of the junction types for photovoltaic applications, the material in question must be carefully selected to exploit the junction in use. Therefore the active material utilised must have some desirable properties that allow for its application in photovoltaics. There are several processes that contribute to the overall operation of a solar cell, but primarily for the active material these are photon absorption, charge separation and charge transport (17–19).

Photon Absorption

If the semiconductor active material used in a photovoltaic application exhibits poor photon absorption, therefore, produces a small concentration of charge carriers. This low concentration of charge carriers may not be sufficient enough for the device to exhibit a useful photogenerated current. The absorption spectrum and optical properties of a material help provide an understanding of its band-gap.

Charge Separation and Transport

Once a charge carrier has been produced from an adsorption of a photon if the charge carriers immediately recombine then not photogenerated current is observed. It is desired that once separated the charge carriers diffuse through the material before recombination occurs. There are two general types of recombination processes: unavoidable and avoidable recombination. Unavoidable recombination is also known as inter-band radiative recombination and can occur even in a perfect semiconductor single crystal. The radiative recombination process involves the emission of a photon upon recombination of the charge carriers. Avoidable recombination usually arises due to imperfections of various kinds in the material (such as crystal dislocations and defects). For example, once separated a charge carrier may become trapped by an edge-type dislocation. This would result in an

increase in the recombination lifetime, an increase large enough to exploit for the diffusion of charge carriers. Quantum yields and/or a measurement of the active material efficiency in the conversion the absorbed photons into current can provide useful information into the active materials charge separation properties.

Current-Voltage and electrical measurements can provide an insight into the charge transport properties of the overall device.

1.2) Inorganic Materials

The first silicon solar cell was reported in 1941 and was made using melt grown junctions. This early device showed less than 1% efficiency which has since been substantially improved upon, resulting in solar cell efficiencies of 25% (20). This, combined with silicon's abundance, general stability, non-toxic nature and the bandgap of 1.12eV, has resulted in silicon becoming the most popular commercial inorganic material used in solar cell devices accounting for roughly 90% of the market share (8). There are high manufacturing costs for producing silicon solar cells, however; silicon naturally occurs as silicon dioxide (SiO_2) in the earth's crust and requires large amounts of energy to extract and purify (10). In an attempt to reduce costs, technology in silicon solar cells evolved from bulk crystalline devices to thin-film amorphous silicon materials and nanostructures such as nanowires (7,21,22). Although efficiencies have reached upwards of 20%, silicon the commonly commercialised amorphous silicon devices still have several drawbacks if they aspire to challenge fossil fuel:

- The main recombination (of electron-hole pairs) centres in amorphous silicon are dangling silicon bonds which provide sites for charge carrier recombination, although most of these are removable by hydrogenation.
- Unlike typical p-n junctions of crystalline materials with high diffusion lengths for charge carriers (over 200µm), the disordered nature of amorphous silicon results in extremely small diffusion lengths (around 0.1µm) causing carrier collection to depend on diffusion alone
- There is still a relatively high production cost due to the requirement for thinner silicon wafers(7,21).

In an attempt to reduce manufacturing cost, other inorganic materials have become commercially available. These inorganic materials are usually alloys of which thin films can be formed from a solution or other low-energy methods. These include compounds such as $CuInSe_2$ (CIS), $Cu(In,Ga)Se_2$ (CIGS) (10,21), $CuInS_2$ (24) and $Cu(In,Ga)S_2$ (23,24) which have shown an upwards of 20% efficiency particularly for CIGS with a film length of 2.5-3.0µm (27) over an area of $0.4cm^2$. These CIS and CIGS compounds have the potential to challenge silicon for higher efficiencies, as well as commercial viability due to their non-toxicity and low overall synthetic cost. However, the major drawback in these materials comes from the cost of Indium (23) and the vapour-deposition of the material at high temperatures under selenium vapour is difficult and challenging to control over large substrate areas (10). Other Cu alloys have been proposed to avoid the use of In and Se include Cu_2ZnSnS_4 (25,26,28–30), Cu_2S (30), CuS_2 (24,28) and Cu_2O (26), of which the most efficient material (Cu_2ZnSnS_4) has achieved efficiencies of 5-8% (25,26).

Other commercially viable inorganic materials used are CdS and CdTe (8,17,24,25,26). Although they show promising efficiencies of 16.5% (33) and their low-temperature synthesis (10) when compared to the Cu alloys and silicon devices, the major concerns for these materials lie in the relative toxicity of cadmium(32,34,35) as well as the scarcity of Te(10,35).

1.3) Organic/Polymeric Materials

Organic materials provide some advantages over their inorganic counterparts, primarily their cheapness in synthesis, fabrication and processability along with their ease of tunability of the properties required (36). However, the early organic photovoltaic devices (OPV) had poor efficiencies of 10^{-3} to 10^{-2} % (26,30,31,32). Since these early devices, OPV's have been made more efficient reaching up to 10% (39) and in multi-junction devices 6% (39). One of the earliest polymer-based materials used was poly(p-phenylene vinylene) (PPV) and its derivatives, showing low efficiencies (40–42). The efficiencies were improved upon when more readily functionalised conjugated polymers were used, such as polyaniline (40,43), polythiophenes (which have a wide range of functionalised derivatives) (38,40,41,43–51) and pyrroles (34,37,44,46). The range of thiophene materials was further improved by the commercially utilised poly(3,4-ethylene dioxythiophene polystyrene sulfonate (PEDOT: PPS) (41,43,51,53–55) along with benzothiophene (BDT) (38,56), indacenodithiophene (56) and other fused ring thiophene-based polymers (45). Other common polymers used which show similar efficiencies to the thiophenes, anilines and pyrroles include carbazole-based polymers (and its derivatives) (38,40,41,55,57,58), fluorenes (38,41,51), azoles (42,43,46,53), acenes (46,59) and phenazine based ladder-type conjugated oligomers/polymers (43,46,49,52,55,60). Recently, more complex and larger systems have drawn attention, including porphyrins(40,46), perylene tetracarboxylic acids(42,46,49) and dendrimers(46) (such as thiophene-based dendrimers). Even with their advantages over their inorganic counterparts, OPV materials have drawbacks that have limited their efficiencies and widespread commercial applications. During the encapsulation of the OPV materials in the manufacturing of a commercial PV device, the presence of water and oxygen in the active organic layer can cause degradation under illumination(61). This is due to the excitation of oxygen to form singlet oxygen ($^1\Delta_g$) which causes degradation of the polymer and organic material and/or crosslinking (62). As

a result, this decreases charge carrier mobility and charge separation in the material, leading to significantly decreased efficiencies as well as overall productivity (63). An industrial level attempt used to prevent/limit the amount of oxygen and water present lies in the development of fast and more efficient encapsulation methods such as roll-to-roll processing(64). In their attempt to decrease the trace amounts of oxygen and water, the production cost of the OPV devices increased preventing widespread commercial use. Table 1.1 shows the structures of the commonly used OPV active materials an example of a derivative form.

Table 1.1 - Commonly used photovoltaic organic and polymers materials and an example of a derivative form

Polymer	Structure	Derivative example
Poly phenylene vinylene	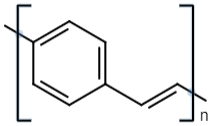	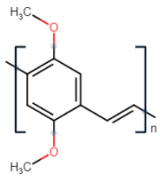
Polyaniline	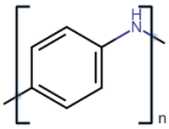	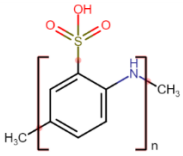
Polythiophene	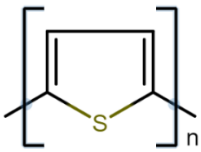	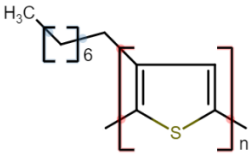
PEDOT	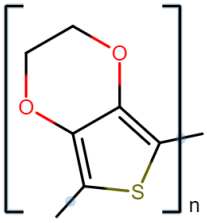	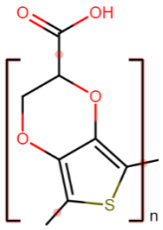

Polypyrroles	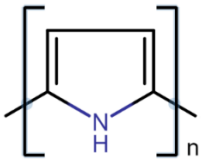	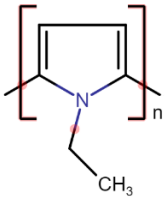
Carbazole based	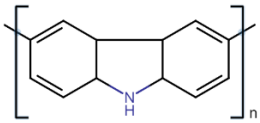	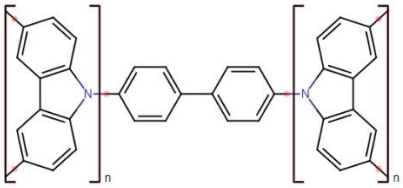
Fluorene	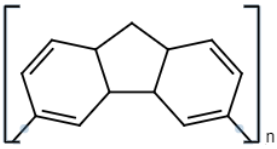	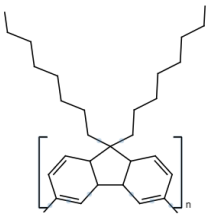
Azoles	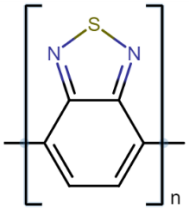	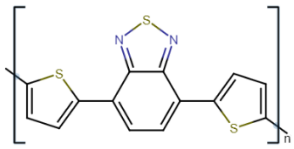
Acenes	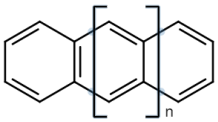	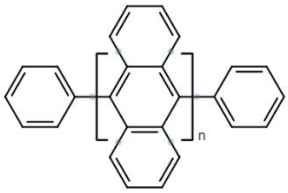
Ladder type	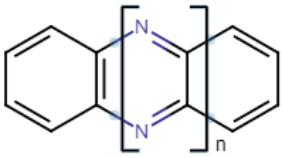	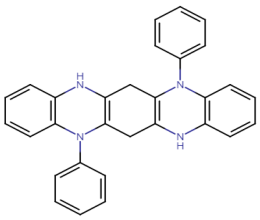

Polyporphyrins	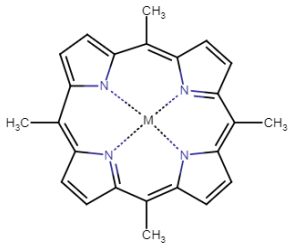	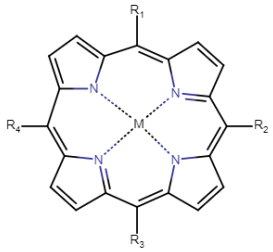
Perylene tetracarboxylic acids	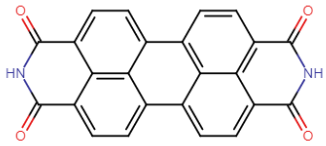	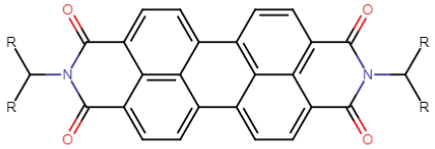 Where R = C_6H_{13}
Dendrimers	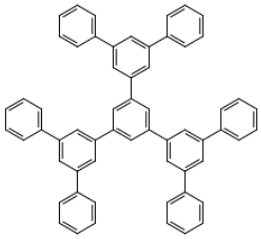	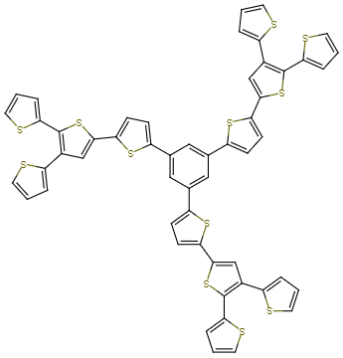

1.4) Intercalation Chemistry

In chemistry, intercalation refers to the reversible insertion of a guest species into a host structure while maintaining the overall structural features of the host. This intercalation can occur in lamellar inorganic materials or biochemical compounds (such as the complexation of planar molecules into the spirals of DNA). Lamellar structures have been shown as a promising family of materials which undergo intercalation chemistry. In these lamellar compounds, the layers are bound together by van der Waals forces and so the interlayer spacing between the layers can be increased to accommodate guest species. What makes intercalated materials an interesting field of study are the changes the guest and host undergo (to varying degrees from subtle to extreme) in geometry, chemical, electronic and optical properties. It is possible by adjusting the guest and host species as well as guest content to tune these properties for some desirable application, which could include tuning the conductivity of an insulator from insulating to semiconducting to metallic, or exfoliation to form 2-dimensional materials analogous to graphene. A typical intercalation reaction scheme is shown in Figure 1.5.

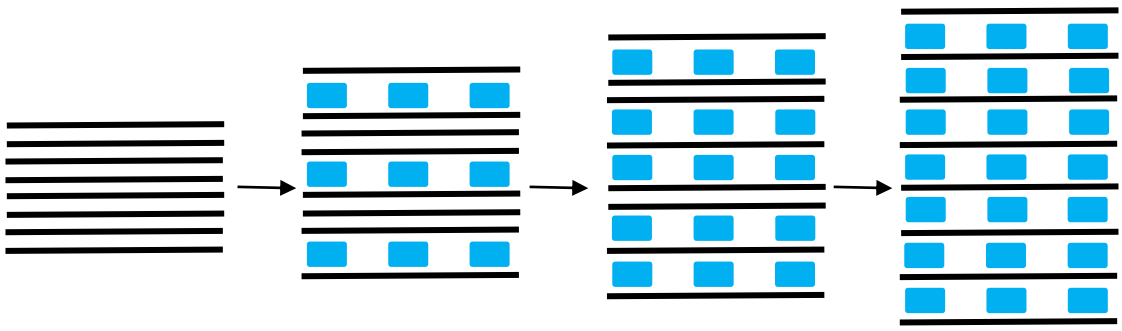

Figure 1.5 - A typical intercalation between a lamellar inorganic host (black) and organic guest (blue)

This research aimed to avoid the presence of oxygen and water during the polymerisation stage of commonly utilised organic and polymer active material in solar cell devices (thereby minimising levels during encapsulation without increase costs) and to take advantage of the properties of both inorganic and organic materials. This was

achieved by intercalating a range of organic monomers into the interlayer space of layered inorganic materials. The host materials selected were the metal oxides vanadium pentoxide (V_2O_5) and molybdenum trioxide (MoO_3) due to their wide-ranging intercalation chemistry and the transition metal thiophosphates (MPS_3) family due to their structural and chemical similarities to the transition metal dichalcogenides and their semiconducting properties.

1.5) Literature review

1.5.1) V_2O_5 composites

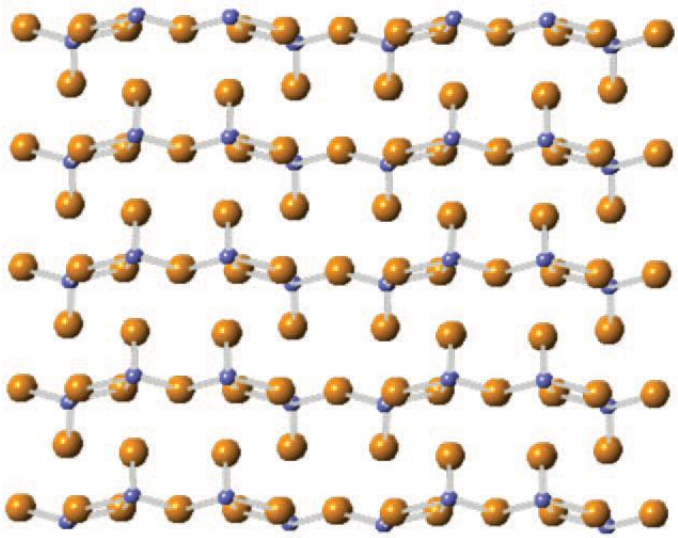

Figure 1.6 – Side view of V_2O_5 layers where the blue atoms are the V^{5+} and orange are the O^{2-} (65)

V_2O_5 has a layered structure (65), Figure 1.6, with the vanadium having a d^o electronic configuration. The basic building block of this oxide is the double chain of edge-sharing VO_6 octahedra. A chain of these octahedra alternates their apices up and down combining to produce the octahedral single-layer structure found in V_2O_5. One of the terminal bonds is a short vanadyl bond while the other V-O bond distance is much longer. The weak V-O bond provides the layered V_2O_5 character(66,67). Due to vanadium's variable oxidation states and its layered structure, V_2O_5 exhibits a range of intercalation chemistry which can be exploited to suit the desired application(68).

1.5.1.1) Small Cation Intercalation

A common intercalant is lithium cations (Li^+) which can be inserted within the interlayer spacing by reacting with Butyllithium (n-BuLi)(66). The vanadium ion is reduced from V^{5+} to V^{4+} allowing Li^+ to intercalate between the layers in order to maintain charge balance producing the lithiated vanadium pentaoxide ($Li_xV_2O_5$)(69). Up to 22 mol% has

been reported to successfully intercalate into V_2O_5(70) while the V^{4+}/V^{5+} ratio can vary between 1-20% while structural integrity is preserved(66). When studied with X-ray Absorption Spectroscopy (XAS), lithiated samples of V_2O_5 (specifically in this case for the xerogels) did not show any local environmental changes around the vanadium ion. It was only when $Li_xV_2O_5$ is heavily lithiated (x>2) did local changes around the vanadium ion environments occur (71,72). Spectroscopic optical analysis of this lithiated V_2O_5 showed two distinct regions appearing which corresponded to two separate phases being present. The two regions in the optical analysis appeared between 1.75V - 2.0eV (region 1) and 0.4V - 0.42eV (region 2) (70). Further analysis supported that region 1 suggested a direct forbidden transition and increased with increased lithium content corresponding to the lithiated phase of the intercalated material. Region 2, however, suggested and inter-band direct allowed transition which did not increase with lithium content corresponding to the unintercalated pristine phase of V_2O_5. In many cases, particularly with xerogels, the V_2O_5 is hydrated to form the $V_2O_5.nH_2O$ phase before lithium intercalation. Thermal treatment (annealing) can be used to remove water and it was shown that the electrochemical uptake of lithium into these xerogels shows better cycling performance of electrochemical Li^+ intercalation and deintercalation when the water content was reduced. It was shown that heating treatment at 250°C showed the most significant decrease in water(73).

Electrochemistry is another common intercalation method of Li^+ into V_2O_5, however, in order for best performance, the method required thin films of V_2O_5 xerogel(74). The intercalation of lithium electrochemically was examined after intercalation, between 3.3 and 2.8 volts, and deintercalation (at 3.4 and 3.8 volts) by XPS(74,75). It was shown that there was a reduction of the V^{5+} to V^{4+} during electrochemical insertion of lithium ions. During the intercalation, the concentration of V^{5+} ions was 73% and 65% at 3.3 volts and 2.8 volts respectively which was in agreement with 0.5 mol of Li^+ being intercalated per 1 mole of V_2O_5. The difference in the Li^+ between the

two intercalation steps is due to the quasi-reversible process of intercalation within this range. During intercalation the α-V_2O_5 phase changes to ε-phase in the first intercalation step and the γ-phases by the second intercalation step, both phases exhibiting a different Li^+ content intercalation due to their structural differences. The peak intensity of Li 1s core level was at its maximum after the second intercalation step. The vanadium 3d state is usually the lowest state in its valence band(76–78) and by XPS it was determined that the Li 2s electron is transferred into this 3d state causing the reduction of V^{5+}. Furthermore, Raman studies showed that structural integrity is maintained around the vanadium centres for $Li_xV_2O_5$ where $0<x<1$. However, the characteristic vanadyl stretching mode at 994cm^{-1} is the most sensitive to lithium intercalation(79). The results concluded that for $x<0.5$, all Raman bands shifted which is consistent with the interlayer spacing increasing (an increase of lattice parameter along the c-axis). This resulted in the peak at 994cm^{-1} shifting to 984cm^{-1}. For $0.5<x<1$, this band continues to shift from 984 to 975cm^{-1} as well as the appearance of a new vanadyl band appears at 957cm^{-1} corresponding to an increased interlayer spacing. From $x=0.7$ there was a single-phase exhibited which remains structurally ordered. An unfortunate side effect of electrochemical intercalation and deintercalation results in a build-up of surface contamination of Li-alkyl carbonates(75) and lithium oxides(74).

Other metal cations (mostly polyvalent) can also be intercalated which include K^+, Na^+, Mg^{2+}, Ca^{2+}, Cu^{2+}, Zn^{2+}, Ba^{2+} and Al^{3+}(66). It was shown that electrochemically 4, 3.33 and 2.5 equiv of Mg^{2+}, Al^{3+} and Zn^{2+} respectively were intercalated(80). It was further shown that Mg^{2+} can be intercalated electrochemically in two stages, one controlled thermodynamically and one controlled kinetically(81). The x-ray diffraction (XRD) pattern shows the (020) peak appearing at a lower 2θ position after intercalation of Mg^{2+} and returned upon de-intercalation. This demonstrated that the V_2O_5 structural integrity was not harmed by that the intercalation and deintercalation of Mg^{2+}.

Similarly, K^+ can also be intercalated to provide $K_xV_2O_5.nH_2O$ where $0 \leq x < 0.01$(82). This showed that a small amount of K^+ intercalates into V_2O_5. The optical measurements that had been carried out showed two optical gaps present in the material. These gaps correlate well with the optical study conducted on $Li_xV_2O_5$(70) where the first region was seen between 0.37-0.42 eV corresponding with the direct allowed transition for unintercalated $V_2O_5.nH_2O$. The second region was seen between 2.02-2.23 eV which corresponds to the intercalated phase of the material. However, unlike the lithium study, it is unknown whether the intensity of this transition increases with increasing K^+ content. Furthermore, unlike the lithium study, the width of localised states (band tail) was estimated to values within the range of 0.45-0.80 eV.

Other small cation systems can be intercalated into V_2O_5 systems. A useful example is the intercalation of NH_4^+ ions into V_2O_5 xerogel. The resulting intercalated material showed a stoichiometry of $(NH_4^+)_{0.5}V_2O_5.nH_2O$ and was synthesised using a surfactant-free hydrothermal method(83). From a pair distribution function analysis, it was shown that the intercalation of NH_4^+ shows interlayer spacing increasing due to the intercalation of the NH_4^+ and water molecules. In this case, the redox reaction with NH_4I was seen as a topotactic reaction(84).

1.5.1.2) Exfoliation – Restacking Intercalation

A major advantage of small cation intercalation is its application in the exfoliation and re-stacking method for the insertion organic molecules into the interlayer spacing of the host (65,85,86) (for full organic/polymer structures discussed see Table 1.4 and the end of section 1.5.1). Exfoliation and restacking is advantageous in intercalating organic intercalants in which intercalation may not occur by chemical methods (via ion-exchange or direct methods. Exfoliation can be achieved by agitating a host material which is

preintercalated with a small cation, the small cation assists in prying apart the layers. In particular, this method becomes extremely powerful or intercalating high molecular polymers. In this method, the layers are exfoliated and the exfoliated layers are restacked around a guest to achieve intercalation. This was shown to be successful when intercalating organic dyes (in this particular case methyl yellow)(87). Here the exfoliation method was used with the pre-intercalation of lithium using n-BuLi. Water was then added to the solution, it was purposed that the reduced V^{4+} provided an electron to water causing hydrogen evolution resulting in the layers exfoliating allowing for re-stacking to occur around the methyl yellow dye. It was shown that upon intercalation of lithium, all order was lost within the host material; this is somewhat contradictory to the previous study mentioned(70) which showed that lithiation via n-BuLi preserved the long-range structure of the V_2O_5. Thermogravimetric analysis (TGA) confirmed the intercalation of methyl yellow showing a 17% mass loss between ~250°C – 350°C. This temperature range for the TGA of unintercalated methyl yellow was shown to be between 150°C – 250°C and this increase in this temperature range was a result of the methyl yellow being intercalated in between the inorganic layers. In another study, lithiation was not required for the ultrasonication and restacking of organic material within the interlayer spacing of the V_2O_5(88). In this study, four different weight percentage of single-walled carbon nanotubes were intercalated simply stirring in 40mL of ethanol followed by ultrasonication for 60 minutes in the presence of V_2O_5. The orthorhombic V_2O_5 structure was unchanged upon intercalation of the nanotubes. The thermogravimetric analysis showed a mass loss after 450°C which signified the burning off of the carbon nanotubes. Similarly, it was also shown that the use of n-BuLi or the intercalation of metal cations is not necessary for the formation of composite materials and exfoliation may be achieved via a hydrothermal route. This process primarily involves dispersing or dissolving the inorganic material in a solvent which either has the organic material or the organic material is added afterwards.

4-aminopyridine was successfully intercalated via this method which utilises the exfoliation-reduction-restacking process(89). In this case, V_2O_5, 4-aminopyridine and an H_2O/MeOH (50:50) mixture were sealed in a thick-walled Pyrex tube. The mixture was heated to 110°C for eight days giving pure black, thin needles with a 92% yield. The V_2O_5 dissolved slightly in water producing a dispersed mixture. The methanol present readily reduces the dispersed layers to provide lamella anions which re-stack around the organic cations. It was suggested that the cation templating effect may be the reason the anion layers re-stack around the organic material. The FT-IR showed the pronated pyridine bands (3322 and 3172cm^{-1}) and stretching vibrations cause by the pyridinium ring (1667, 1600, 1543cm^{-1}). It was suggested that the NH_2 group remains unprotonated as the characteristic N-H bands remain (3497cm^{-1}). In conjunction with the FT-IR, electron spectroscopy chemical analysis (ESCA) shows two overlapping V2p$_{3/2}$ peaks suggesting mixed valence states of V^{5+} and V^4. The XRD suggests an interesting result, the 4-aminopyridine occupies the interlayer spacing with its C_2 axis perpendicular to the layers. The rings themselves are parallel to one another. A similar methodology was utilised for the intercalation of alkylviologen dications (90). Once again under hydrothermal conditions, the reaction underwent the exfoliation-reduction-restacking procedure to intercalate a range of alkylviologen iodide salts of differing alkyl chain lengths. The XRD showed an increase in their interlayer spacing with the characteristic (*001*) peaks being shifted from 5.7Å in V_2O_5 and steadily increasing dependent on the alkyl chain length with the dodecylviologen iodide composite showing the (*001*) peaks with a d-spacing of 24.9Å (90). The XRD did, however, show a broadening of peaks and fewer peaks the larger the alkyl chain became suggesting poorer long-range order. This exfoliation and restacking method in-fact shows difficulty in successfully reproducing the well-ordered material when dealing with larger organic molecules. Unlike the case of the 4-aminopyridine intercalated system, the FT-IR shed some light on the effect of organic materials and their interaction with the V_2O_5 host

material (90). As seen in the previous studies, the peaks that appear above 1000 cm^{-1} in the FT-IR correlate to the characteristic guest peaks, however as seen with the metal intercalation the bands appearing around and below 1000 cm^{-1} (V=O) and 810 and 560 cm^{-1} (in and out of plane V-O-V vibrations respectively) have been shifted lower (red-shift) compared to pure V_2O_5 (1020, 820 and 595 cm^{-1}). Two potential reasons, the first being the interaction between the organic material and the partially reduced vanadium leading to weaker V=O and V-O-V bonds and the second candidate being the organic guest decreasing the space for the V=O vibrations once intercalated (90). This is a common trend during the intercalation of organic guest species. The XPS indeed showed that reduction was caused with two peaks appearing for the $V2p_{3/2}$ corresponding to V^{5+} and V^{4+}. 1,1'-bis(4-carboxybenzyl)-4,4'-Bipyridine (carboxybenzylviologen) was also intercalated in a similar way(91) which showed similar results. Similarly, Polyaniline has also been shown to be successfully intercalated using this exfoliation method. In this case, it is named as an in-situ intercalation-polymerization-exfoliation mechanism(92). The XRD followed the trend mentioned previously with an increase in the interlayer spacing and broadening of the peaks. Energy-dispersive X-ray spectra (EDS) showed that the samples contained V, O, C and N. The FT-IR of the material showed O-H stretching peaks due to the aqueous nature of the synthetic route, water had either also intercalated into the interlayer spacing with polyaniline or else is loosely bound on the material surface. The expected shifting in the characteristic V_2O_5 peaks does not, however, occur in this material. This could either suggest that polyaniline does not decrease the vibrational space in the interlayer spacing upon intercalation or more likely is the presence of an unintercalated V_2O_5 phase. As seen previously the peaks above 1000 cm^{-1} correlate to the characteristic guest peaks. For this material, the C=C stretching mode of quinoid and benzenoid rings were seen in the IR spectrum (see Figure 4.3) suggesting the presence of an emeraldine phase which was further supported by the presence of peaks corresponding to C-N and C=N commonly seen

for emeraldine. In a recent study (93), aniline was intercalated into the V_2O_5 using the hydrothermal process by taking advantage of microwave-assisted synthesis', rapid volumetric heating and higher reaction rates which in turn resulted in shorter reaction time. Poly(diallymethylammonium chloride (PDDACl), poly(allylamine hydrochloride) (PAHCl)(94), poly(para-phenylenediamine) (pPDA)(95), 2-phenylethylamine(96) and 4-phenylbutylamine(97) were successfully intercalated into the V_2O_5 layers via hydrothermal synthesis. The intercalation of PDDACl, PAHCl and pPDA showed the expectant interlayer spacing increase along with broadening of other higher angle peaks (such as (*002*), (*101*) and (*110*). However, one difference in the XRD data for pPDA was the presence of a large amorphous peak in place of the peak corresponding to the interlayer expansion suggesting that the re-stacking of the layers occurred randomly giving no distinguishable long-range order. The 2-phenylethylamine and 4-phenylbutylamine however, showed an increase in the interlayer spacing but the peaks remained sharp and strong suggesting good long-range order and preservation of the V_2O_5 structure. As seen previously, the XPS further showed the presence of two vanadium environments.

Several methods have been developed in order to deal with the disadvantages caused by the exfoliation method in order to maintain the long-range order of the material. The most popular being ion exchange(98), direct insertion of the organic material into the swollen interlayer spacing and redox intercalation(99,100).

1.5.1.3) Ion-Exchange Intercalation

In the V_2O_5 system, ion-exchange occurs between a pre-intercalated small cation (as discussed previously in section 1 and the organic guest cation. This was shown to be successful in the intercalation of polymer electrolyte systems into V_2O_5 xerogel(101). Here a mixed polymer electrolyte system $(a\text{-}PEO)_{20}LiOTf$ where a-PEO = $(CH_2O)_{0.1}(CH_2CH_2O)_{0.9}$ and OTf = CF_3SO_3. As expected XRD showed that the interlayer

spacing increased, the peaks remained sharp suggesting good long-range order and structural integrity of the V_2O_5 host. After electrical measurements, films of this material showed an ionic conductivity in the order of magnitude of 10^{-5} Scm^{-1} at room temperature. It was observed that high electronic conductivity occurred parallel to the films while conduction pathways perpendicular to the film were closed.

Aniline hydrochloride was shown to exchange with NH_4^+ (102). Infra-red measurements showed a shift in the V_2O_5 host peaks associated with intercalation as well as peaks corresponding to the presence of emeraldine consistent with the previous study discussed. The TGA for this material showed the presence of polyaniline due to the continual loss in mass over a large temperature range consistent with differing polymeric chain lengths. This suggested that the aniline underwent a redox reaction once intercalated to produce oligomer and/or polymeric chains without the need of an external oxidant. The XPS once again showed two vanadium $2p_{3/2}$ peaks around 516.6 eV consistent with redox reaction after ion-exchange occurred leading to polymerization. The XPS also showed that in the composite material, the peaks for nitrogen shifted by 2 and 8.2eV which was concluded to be due to the strong interaction of the nitrogen with the oxygen atoms of the V_2O_5 material. The I-V characteristics of the composite material using silver and aluminium electrodes gave typical Schottky diode type behaviour with an increase in current when a positive bias was applied and a decrease in current when a negative bias was applied. As the organic content in the material decreases, the I-V curve becomes increasingly more non-linear. Furthermore, the hysteresis observed in the I-V characteristics clearly implied charge storage in the sample. It was concluded that the charge would be accumulated at the interface between the organic and inorganic components in the material.

1.3.1.4) Direct Intercalation

The direct insertion of polymer material is a very common technique used due to its one-pot nature and use of aqueous conditions. This method usually utilises the xerogels of V_2O_5 which is synthesised by mixing V_2O_5 with water allowing the water molecules to swell the interlayer spacing. This swelling allows for larger organic materials to be intercalated by directing entering the interlayer spacing or displacing the water. These larger molecules can be monomers which then undergo redox polymerisation once intercalated. Simple alkylamines (butyl, hexyl and octylamines) were shown to be easily intercalated within the interlayer spacing of V_2O_5(103) by adding dry V_2O_5 to a mixture of alkylamine in deionized water followed by stirring for 48 hours. The XRD showed that the structural integrity was maintained and the butyl, hexyl and octylamine intercalate showed an interlayer spacing increase to 13.8Å, 16.4Å and 19.6Å respectively. The FT-IR is consistent with the previously mentioned trend with the characteristic V_2O_5 peaks shifting and peaks above 1000 cm^{-1} corresponding to the characteristic peaks for the organic guests and in this case the characteristic peaks for N-H and C-H stretching and bending vibrations. The lack of an ESR signal showed that the vanadium centres were not reduced to V^{4+} in contrast to the previous studies discussed. However, this appears not to be a general trend with direct intercalation of V_2O_5. The intercalation of PEO into V_2O_5 gels(104). The EPR spectrum of the material showed a signal for a reduced V^{4+} (which was deemed to be in a small concentration) which could occur during the synthesis of the hydrogel itself but was concluded to not be a redox-based reaction between the PEO and the inorganic host during intercalation as this would lead to a stronger peak consistent with intercalation. This material showed a net interlayer distance increase of 4.5Å. Furthermore, V_2O_5 intercalated PEO reacted further with air in a photoreaction using a mercury lamp and LiI in acetonitrile(105). The interlayer spacing showed a net increase of 4Å (PEO

molar ratio of 1.1), a further 2Å (PEO molar ratio between 1.1 and 3) and no further increase for molar ratios above 3. It was shown that lithium ions also intercalated into the material without replacing the PEO in the interlayer spacing. The Li^+ coordinated to the PEO, therefore, an increase in the PEO content increased the Li^+ potential content in the material. The ESR only showed an increase in V^{4+} content during a photoreaction between the PEO and the V_2O_5. This increase was proportional to PEO content confirming a redox reaction was occurring. The redox reaction resulted in a conductivity increase from the un-irradiated to the irradiated material. The room temperature conductivity increased from 10^{-4} to 10^{-2} Scm^{-1}, 10^{-5} to 10^{-3} Scm^{-1} and 10^{-6} to $5x10^{-4}$ Scm^{-1} for PEO mole fractions of 0.5, 1 and 1.5 respectively. The significant drop in conductivity for a molar ratio of 1.5 was attributed to the increase in the insulating polymer content. A mix of 1:1 molar ratio of PEO and Aniline were intercalated into V_2O_5 (106). The aniline was further polymerized by an in-situ redox reaction with the host as has been seen previously. It was determined that direct insertion of conducting polymers allowed for control regarding the degree of reduction of the vanadium ions. Furthermore, the two polymer component system showed to have a larger charge capacity after five electrochemical cycles with approximately 1.2 times larger capacity for Li^+ than that of the polyaniline-V_2O_5 system and 1.5 times larger than the xerogel V_2O_5 parent material. Similarly, PEO was intercalated into V_2O_5 with graphene as a hybrid material via direct insertion(107). It was further shown that the material also exhibited multi-electrochromic behaviour. The change in transmittance (ΔT) of the graphene PEO material was 26.48% when compared to that of the gel which was shown to be 19.64%. Furthermore, the composite material was grown as a film and shown to demonstrate a transmittance variation of 30.28% showing good electrochromic and photoabsorbance properties. Other polymer electrolytes have also been shown to be intercalated directly in the same way as PEO. Poly(vinyl pyrrolidone) (PVP) is an example of such a polymer electrolyte in the use of lithium-ion battery applications(108). In this

case, the XRD showed a slight increase in the interlayer spacing as expected from intercalation. It was concluded this slight increase in the interlayer spacing occurred due to the PVP. The peaks seen were more closely related to that in section 1.5.1.2) where they were broad suggesting less long-range order. However, the intercalation of PVP did have a significant effect on the lithium content present which was quantified using XPS. The xerogel showed three lithium-ion states upon intercalation of lithium electrochemically. In the unmodified xerogel it was shown that uncoordinated lithium resided in the interlayer spacing (41.83% of total Li^+ content), coordinated to the bridging oxygens (in V-O-V with 38.67% of total Li^+ content) and those binding with the oxygen double bond in the V_2O_5 (19.50% of the total Li^+ content). However, with the PVP modification, the XPS data showed a much more intense signal with the lithium content now corresponding to 52.82% in the interlayer, 32.44% binding with the bridging oxygens and 15.04% binding with the oxygen double bonds. The increase in the interlayer spacing showed the presence of PVP within the interlayer spacing and thereby increased the reversibility of lithiation in the interlayer spacing. It was proposed (no experimental evidence was provided as support however) that the H-atoms in the PVP are hydrogen bonded to the oxygens in the V_2O_5 shielding the electrostatic interaction the lithium would otherwise experience resulting in more lithium being found being uncoordinated than binding to the vanadium oxygens.

Utilising the aqueous environment required to produce V_2O_5 gels the direct insertion of conducting polymers has been attempted using polymers such as poly(aniline-co-N-(-4-sulfophenyl)aniline) (PAPSA)(109) and poly(2-(3thienyloxy)ethanesulfonic acid) (PTOESA)(109,110). In both cases, the polymers were dissolved in water and added to the xerogels followed by mixing allowing the water-soluble polymers to easily enter the already swollen and hydrated interlayer space. Unlike previously discussed, in this case after intercalation of PAPSA, the d-spacing of the host material decreased from 13.8Å to 13.2Å, 11.6Å and 11.3Å for a polymer to V_2O_5 molar ratios of 0.05, 0.1 and 0.4

respectively. This trend was not seen for the PTOESA which showed an initial decrease at the lower molar ratio (0.07 molar ratio showed a decrease to 11.8 Å) and then an increase in the interlayer spacing for a higher molar ratio (for molar ratio of 0.1 an increase to 12.8 Å was shown). The TGA further showed the presence of polymer material as discussed with previous TGA data. Upon electrochemical oxidation, the colour of the PAPSA V_2O_5 compound changed between its initial dark green colour to yellow (similar colour to that of the host gel), brown and purple interchangeably showing reversible electrochromic properties. In respect to the PTOESA compound, it showed a significant increase in conductivity, yet was shown to be not as conductive as a pure conductive polymer. When molar ratios of 0.08 and 0.4 to 1 V_2O_5 where intercalated the conductivities exhibited were that of $2.9x10^{-6}$ and $2x10^{-6}$ Scm^{-1} respectively. The higher polymer content of 0.96 molar ratio exhibited a conductivity of $8.4x10^{-7}$ Scm^{-1} which could be due to a rougher surface and therefore higher particle contact resistance decreasing the conductivity.

Other conducting polymers of commercial interest which have been shown to be directly intercalated into the interlayer spacing of V_2O_5 include polyaniline(111) (as well as some of its derivatives) and polypyrroles(112) as well as larger organic molecules including oligomers and polymers of melanin(113,114), sulfunaylpyridine and dithiobispyridine(115). The polyaniline derivatives 4-Anilinoaniline and 4-Anilinoanilinium Iodide (111) was dissolved in an ethanolic solution and stirred with finely powdered $V_2O_5.nH_2O$. In-situ polymerization was further carried out by treatment of the intercalated compounds with $CuCl_2$. The IR spectra of the 4-Anilinoaniline intercalated compound showed bands at 1580, 1490, 1300 and $1160cm^{-1}$ which are characteristic of the poly(Anilinoaniline) suggesting in-situ polymerisation occurs once the monomer intercalates. In contrast, the IR spectra of the 4-Anilinianilinium Iodide intercalated material showed bands at 1600, 1490, 740 and $690cm^{-1}$ which are characteristic of the oligomer like Anilinoaniline as the bands at 740 and $690cm^{-1}$ are characteristic of the

terminal groups in the oligomer. Upon treatment of the 4-Anilinianilinium Iodide intercalated material with $CuCl_2$ showed that the oligomer peaks had disappeared and in their place, the polymer peaks had appeared signifying that the organic oligomers fully polymerised. In comparison, the intercalations of 2- and 4-sulfanylpyridine along with the 2,2'- and 4,4'-dithiobipyridine were intercalated into the V_2O_5 using the same method as for the polyaniline derivatives mentioned(115). The 2-sulfanylpyridine and 4-sulfanylpyridine showed an interlayer spacing increase of 3.6Å and 4.4Å respectively. However, the intercalated 2,2'- and 4,4'-dithiobipyridine are present mostly in their protonated form but not in their oligomeric or polymeric forms. The XPS further showed that the vanadium sites had been reduced upon intercalation as previously discussed. Using the PM3 method of calculation to optimize the structure of the organic guests within the interlayer spacing of V_2O_5(115), the protonated dithiobipyridine molecules were shown to lie parallel to the V_2O_5 layers which explained the increase in the interlayer spacing could occur due to bilayer like structures of the polymers occurring.

In a slightly different fashion, pre-intercalated small cations can be utilised also to directly insert molecules into the interlayer spacing of V_2O_5 as was seen with the Melanin like structure of 3,4-Dihydroxyphenylalanine(113,114) where the guest species chelates with these ions instead of exchanging with them. The XRD showed a slight increase in the interlayer spacing from the gel host from ≈11.8Å to ≈13.8Å. An interesting feature, however, is the broadening of the higher angle peaks, as discussed previously. This showed structural integrity in the direction of the *c-axis* but less longer-range order in the *a*- and *b*-axis. The TGA suggested a mass loss of approximately 2.5% between 280-350°C which was credited to the organic phase in the interlayer spacing, although suggesting there may not be much present. The conductivity of the intercalated material showed an increase from the room temperature conductivity of the gel host from $1.1\pm0.2\times10^{-4}$ to $5.2\pm1.0\times10^{-3}$ Scm^{-1}. The intercalated material displayed an EPR g-value increase from g=1.957 for the gel host

to g=1.969 corresponding to anisotropic behaviour which was suggested to show that the lamellar structure being preserved, which does not correspond to the findings from the XRD. It was suggested that the organic melanin like molecule had not been oxidised due to the absence of the intrinsic melanin radical peak which appears at g≈2.0037 in the ESR. The electrochemistry of this material showed that the hybrid material led to stabilisation of the electrochemical response for inserting of Li^+ electrochemically. This was concluded to be due to the enhanced Li^+ diffusion through the film owing to a decrease in steric and electrostatic effects because of the increased interlayer spacing. The presence of the organic material also allowed for the creation of channels between subsequent inorganic and organic layers facilitating the diffusion of the metal cation. This is particularly useful for the intercalation of organic molecules in which in-situ polymerisation may not be the direct goal or else for monomers that may not directly be intercalated via a redox method.

1.5.1.5) Redox Intercalation

Many studies have taken advantage of the redox chemistry of vanadium for the insertion and in-situ polymerisation of conducting polymers. Common conducting polymers grown within the interlayer spacing include polyanilines, polythiophenes and polypyrroles. In this case, the organic material is oxidised providing an electron to the V^{5+} centres reducing them to V^{4+}. This leaves a net negative charge on the inorganic layers which is balanced by the organic material intercalating within the interlayer spacing. This furthermore facilitates the polymerisation process in-situ via radical polymerisation.

Polyaniline was first intercalated using the redox method(116) in which the polyaniline was inserted and polymerised in the protonated form. It was subsequently shown(117) that the interlayer space increased by 5.2Å corresponding to a monolayer of polyaniline and the overall inorganic structure preserved, suggesting a topotactic process.

The IR spectra showed peaks in the regions of 1000-1600cm^{-1} corresponding to the emeraldine salt of polyaniline while the peaks below 1000cm^{-1} are characteristic to the V_2O_5 peaks. SEM and TEM images showed homogenous film formation. Furthermore, molecular oxygen appeared to play an important role in the polymerisation of the intercalated aniline as it was shown that oxygen indeed only participates in the intercalative polymerisation reaction and increases the reaction rate while allowing for the V_2O_5 structure to maintain its integrity. From gel-permeation-chromatography (GPC) is was shown that the number-average molecular weight for the intercalated polymer was 14,000 and the weight average molecular weight was 30,000 daltons. The conductivity of this material was shown to be that of 10^4 times higher than for pristine V_2O_5. In comparison, the intercalation of aniline into mesostructured porous V_2O_5(118) showed a conductivity for the host to be 6.4x10^{-7} Scm^{-1} while the polyaniline intercalated material showed initially of 3.2 x 10^{-4} Scm^{-1} but after being exposed to air and allowed to age for four months this increased to 3.0x10^{-2} Scm^{-1}. Furthermore, porosity measurements using nitrogen adsorption showed a decrease in the total pore volume from 0.21 cm^{3}g^{-1} in the host material to 0.09 cm^{3}g^{-1} in the intercalated material. In contrast, after intercalation the BET and Barret-Joyner-Halenda (BJH) average pore diameter (nm) increased from 3.12 to 10.70 and 4.73 to 13.99 respectively. The intercalation of V_2O_5 with PANI has led to the filling of small mesopores resulting in a total pore volume and a larger average pore diameter with the overall surface area reduced. However, structurally the mesostructured composite materials show wider and weaker peaks in the XRD indicating short-range order(119,120). The three-dimensional structure of the composite material was studied using atomic pair distribution functional analysis(121). It was shown that there are three potential conformations of the polymer within the interlayer spacing of V_2O_5 similar; bilayer structure, tri-layer structure or chain-like structures which are orientated perpendicular to the V_2O_5 layers and the distance between each polymer chain is ~3.4Å.

The polyaniline intercalated V_2O_5 composite material had several factors that affected its application in many devices; i) composition, ii) temperature used for intercalation and iii) the atmosphere used in intercalation(122). In an attempt to improve on this, substituted anilines have been shown to intercalate using the redox intercalation method. Poly-o-methoxyaniline is a polymer formed in such a manner with the V_2O_5 xerogel (123) where the role of the methoxy group is to allow for easier reduction of the aniline backbone. Upon successful intercalation, the interlayer spacing increase from the host material from 11.9 Å to 14.4 Å suggesting loss of water replaced by the poly-o-methoxyaniline. The EPR spectrum further showed signals that appeared from the polymer assigned to the free polarons as well as line broadening due to the presence of paramagnetic vanadium ions as seen in Figure 1.7.

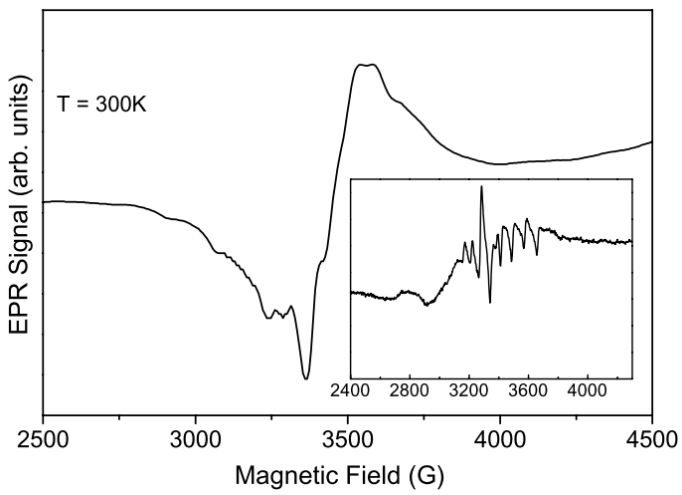

Figure 1.7 - EPR spectrum for V_2O_5 intercalated poly-o-methoxyaniline with the hydrated host, inset (123).

Similar to the polyaniline discussed previously in this section the conductivity showed an increase from1.4±0.3 x 10^{-4} Scm^{-1} in the pure host matrix to 2.1±0.4 x 10^{-1} Scm^{-1} in the polymer intercalated material. This trend is further shown in the intercalation of poly(N-propane sulfonic acid aniline) (PSPAN)(124) upon which the conductivity increased from the V_2O_5 xerogel (4.2x10^{-6} Scm^{-1}) to 5.9x10^{-4} Scm^{-1}. After allowing to age

in the presence of oxygen for 2 months, the conductivity increased further to $1.2x10^{-2}$ Scm^{-1}. The redox intercalation can be used for more complex polymer systems such as poly(N-[5-(8-hydroxyquinoline)methyl]aniline) (PNQA)(125) where the extracted polymer showed a number average polymer weight of 2800 and a weight average molecular weight of 7049. The conductivity of the material showed an increase upon PNQA intercalation $2x10^{-6}$ Scm^{-1} to $1.9x10^{-4}$ Scm^{-1}.

This method and the applications of the composite materials are also similar when dealing with the polypyrroles and polythiophenes. The intercalation of polypyrroles have shown calculated specific capacities for the electrochemical insertion of Li^{+} to be 279 Ah kg^{-1}(119) which is considerably higher than that for pristine V_2O_5. As with the composites in sections 1.5.1.1) – 1.5.1.3), it was concluded that the polymer prevents the trapping of the lithium ions due to the shielding the polymer provides against the interaction of lithium and the oxygen atoms in the inorganic chain. Polypyrrole intercalated bentonite/V_2O_5 as ternary composites exhibited a conductivity increase with increasing polypyrrole content(126). It was determined that the environment of intercalation affects the electrochemical properties of the hybrid material, for example, the acidic environment of the pyrrole solution upon intercalation was shown to have an effect on the overall conductivity exhibited(127). When intercalation was carried out in an HCl, H_2SO_4 or oxalic acid conditions no sharp or broadened peaks were seen in the XRD which either suggested complete exfoliation and/or the main component of the synthesised material was the polymer. However, in $HClO_4$ or acetic acid, the interlayer expansion increased from 11.39 Å in the host to 13.91 and 13.41 Å respectively. The specific capacity for $Lí^{+}$ electrochemical intercalation was further shown to be 98 $mAhg^{-1}$ for the pure polypyrrole intercalated material and this increased when the reaction occurred in $HClO_4$ to 135 but decreased to 60 $mAhg^{-1}$ with acetic acid.

In order to improve on the properties of polypyrrole intercalated V_2O_5 as a cathode material for Li-ion batteries the use of pyridinesulfonic acid (PSA) as an additive was investigated(128). Adding PSA (1:1 with Ppy) to the system showed the specific capacity rise to 160 $mAhg^{-1}$ from 89 $mAhg^{-1}$ for the pure Ppy intercalated material(128). It was concluded this occurred due to increased spacing between oxide layers due to the presence of the bulky PSA. The SO_3^- functional groups of the PSA favoured the polymerization of polypyrrole within the interlayer spacing of the oxide material.

Polythiophene, which is insoluble in water and unable to form protonated salts for ion-exchange has therefore been polymerised in-situ using the redox chemistry approach. Thiophene oligomers are preferred for this over thiophene itself due to the oligomers (e.g. bithiophene or terthiophene) having lower oxidation potentials. 2,2'-bithiophene has been shown to successfully intercalate and polymerise within the interlayer spacing of V_2O_5 xerogels(129). The intercalation occurs under reflux for 24 hours with 30mL of a 0.04mL acetonitrile solution of 2,2'-bithiophene. The XRD shows interlayer spacing of 14.70Å with the decrease in the xerogel interlayer spacing (as mentioned earlier ~19Å) is due to removal of water. It was concluded that the polythiophene is present in a bilayer structure in this material. At room temperature the conductivity was ~0.1 Scm^{-1} (4 orders of magnitude larger than that for pristine V_2O_5 gel). The EPR showed a broad signal at $g \approx 1.963$ arising from the V^{4+} centres confirming the redox mechanism of synthesis with no V or ^1H hyperfine being seen in the spectrum. The problem arising from the use of thiophenes is the limited solvent systems available and the use of the dimer or trimer. Therefore, substituted thiophenes are used such as 3,4-ethylenedioxythiophene (EDOT). EDOT has a lower oxidation potential than thiophene allowing for direct redox insertion of EDOT and better solubility in a wider range of solvents including aqueous conditions. Although the redox mechanism is used, two different experimental methods can be employed. The first is standard reflux intercalation(130) or the use of a microwave

reactor(131) in a similar fashion for hydrothermal synthesis. For the reflux method, EDOT was dissolved in distilled water and refluxed in the presence of V_2O_5 with molar ratios between 0.02 and 0.6. The XRD showed that at lower molar ratios (0.02-0.08) the interlayer spacing increases to 13.84 Å - 14.02Å similar to that seen for thiophene intercalation. However, due to the easier oxidation potential of EDOT driving the redox reaction, at higher molar ratios (0.4-0.6) of the intercalated EDOT polymer (PEDOT) we see that the interlayer spacing increases further to 17.8-19.04Å which suggests that the phase present within the interlayer spacing is twofold; i) monolayer PEDOT at lower molar ratios and ii) PEDOT bilayer at higher molar ratios. In contrast to this, the synthesis of the nanocomposite via microwave irradiation shows the intercalation of EDOT corresponds to a monolayer conformation the interlayer spacing increasing to 13.79Å - 14.15Å depending on the radiation time. The FTIR spectra showed polymerised EDOT (PEDOT) peaks appeared within the range of 1049-1600 cm^{-1} as well as the expected peaks shift of the characteristic V_2O_5 peaks below 1000 cm^{-1} typical for intercalation. These changes were concluded to be attributed to the presence of the V^{4+} centres due to the redox reaction occurring. The TGA showed an initial loss occurring around 100°C suggesting the presence of reversibly bound water. There was then a continuous weight loss up to ~420°C which is attributed to the organic material being broken down. This continuous mass loss is proposed that the oligomer/polymeric form of EDOT is present showing in-situ polymerisation had occurred. In terms of the conductivity of the materials, it was shown that the reflux intercalation produced a more conductive material at higher molar ratios due to the bilayer like structure. The conductivity before refluxing and microwave-assisted methods for pristine V_2O_5 was 8.78 x 10^{-5} Scm^{-1} and 6.78 x 10^{-5} Scm^{-1} respectively. However, the conductivity for the microwave-assisted material increases and after 8 minutes of irradiation to 4.46 x 10^{-3} Scm^{-1}. Comparing this with the refluxed method, we find that at molar fraction of 0.04 of EDOT the conductivity has increased to 6.97 x 10^{-3}

Scm^{-1} and after increasing to 0.4 molar ratio the conductivity has further increased to 9.82 x 10^{-2} Scm^{-2} and again increased further to 1.01 x 10^{-1} Scm^{-1} for the molar ratio of 0.6 when reacted with V_2O_5 under reflux (132–134). Similarly, the morphology was of great interest (with platinum nanoparticles dispersed on its surface)(135) for catalysis for methanol oxidation. The SEM and TEM showed porous morphology with good dispersion of the platinum nanoparticles on the PEDOT composite material surface showing an average platinum particle size of 2.3nm. Furthermore, it was shown that the platinum PEDOT/V_2O_5 material exhibited a high catalytic activity of 28 $mAcm^{-2}$ for methanol oxidation with a platinum loading of 10 μgcm^{-2}. This is due to the presence of the reduced vanadium sites which favour methanol oxidation showing that under certain conditions there may be a loss of reduced vanadium sites. Another modified thiophene which has shown to be intercalated in a similar method is 2,5-dimercaptothiophene (DTh) which is polymerised in situ (PDTh)(136). Upon intercalation, the interlayer spacing increased to 13.4Å suggesting that the PDTh is likely in a monolayer conformation as similarly seen for PEDOT intercalation. The discharge capacity for this material was shown to be ~260 $mAhg^{-1}$ which is lower than that of the PEDOT intercalated V_2O_5.

Other monomers can be used with either aniline or thiophenes to produce binary polymer structures intercalated into the interlayer spacing such as poly(2,5-dimercapto-1,3,5-thiadiazole) (PDMcT)(137). In this study, PDMcT was intercalated into the host material as well as being co-intercalated with polyaniline. The XANES spectral features suggested that during intercalation little change occurs in the chemical bonding and environment of the vanadium ions. The strong peak at 5471 eV is typical for the vanadium oxides due to the 1s to 3d transitions. Changes in the intensity and energy position are associated with any deviations from the octahedral symmetry and vanadium ion oxidation state. It was shown that after intercalation the peak shifts to lower energy signifying the

reduction of V^{5+} to V^{4+}. The redox intercalation method is useful for utilising a one-pot reaction provided that the organic material has a low oxidation potential.

1.5.1.5) Layer by Layer Intercalation

Another method used to synthesise nanocomposites is the layer-by-layer technique. In this technique, cationic and anionic species are assembled in a multi-layer architecture. This was shown in the intercalation of polyaniline into V_2O_5 xerogel(138–140). A typical experiment consists of dipping an inert substrate alternatively in a cationic solution of the organic material and an anionic solution of the V_2O_5. The anionic solution of V_2O_5 was obtained by hydrolysis of $VC_9H_{21}O_4$ in pure water. The FT-IR spectrum shows a broader band due to the hydrogen bonding between guest and host. The Raman spectrum for the material show peaks corresponding to emeraldine. The spectrum was found to change depending which material was the topmost layer. When V_2O_5 was the topmost layer the intensities for the peaks appearing at 1330cm^{-1} and 1486cm^{-1} decreased These peaks resemble those for oxidised PANI (pernigraniline) as the V_2O_5 contributes to the oxidation in-situ as seen in all the previous synthetic methods. Meanwhile, when the emeraldine material is the top layer, these peaks are characteristic of the emeraldine PANI form. This showed that there are strong interactions between the emeraldine and V_2O_5 and it was further seen that V_2O_5 can lead to over-oxidation of the emeraldine to the pernigraniline form. This means that there may be two forms present in the material, the more conducting V_2O_5/emeraldine phase and the insulating V_2O_5/pernigraniline phase. The electrochemical properties of the material measured by cyclic voltammetry showed V_2O_5 exhibiting the intervalence transition between V^{4+} to V^{5+} at a potential of -0.85 V. The prominence of this peak increased with increasing concentration of V^{4+} present. Whereas, the pure PANI shows redox peaks which correspond to the interconversion between the neutral and

emeraldine forms. It was shown that in the composite material the PANI reduction was incomplete which could be associated with the V_2O_5/pernigraniline phase due to its higher resistive path.

The major drawback of this method as compared to that of oxidative intercalation for V_2O_5 lies in the use of cationic organic materials and anionic inorganic materials which lead to the potential over-oxidation of the organic materials. This results in a material which has a resistive phase. Furthermore, it can be extremely challenging controlling the exact height of each layer.

Table 1.2 - The advantages and disadvantages of the different intercalation methods in V_2O_5 systems

Intercalation Method	Advantages	Disadvantages
Cation Intercalated Host Precursor		
Small Cation Intercalation	• Used as precursors for organic guest intercalation • Maintains high control of the host structural integrity • Intercalation is reversible with little effect on the host structural integrity.	• The resulting materials synthesised using the small cation precursors show a limited control over the structural integrity of the host material.
Precursor Based Intercalation		
Exfoliation – Restacking	• A wide range of guest species can be used - Small and large organic guests can be intercalated including polymers • In-situ polymerisation can occur for organic guests with low oxidation potentials. • One-pot synthesis	• There is very little control of the host structural integrity due cto the poor control over the restacking of the host layers.

Ion – Exchange	• A wide range of guest species can be used - Small and large organic guests can be intercalated including polymers • Monomers with low oxidations potentials are readily polymerised in-situ without the requirement of an external oxidant. • Produces materials with significantly higher conductivity than the host • Can be carried out in aqueous conditions.	• Medium control of the host structural integrity. • Requires guests to be present in a cationic form in solution.
Non-Precursor Based Intercalation		
Direct	• A wide range of guest species can be used - Small and large organic guests can be intercalated including polymers • Can be a one-pot synthesis	• Variable control over the host structural integrity • If host precursors used the metal ions can remain within the layers which may limit the materials applications • For non-precursor intercalation the hydrated xerogel is utilised

	• If a host precursor used polymer materials show chelation allowing for large guest species to be intercalated, useful for certain applications (i.e. battery) • Useful for non-cationic guest species • Useful for intercalating guests with a high oxidation potential • Can produce a more conducting material when compared to the host material	which affects control of the host structural integrity, hydrated xerogels are the most common precursor.
Redox	• One–pot synthesis • Polymerisation occurs within the interlayer spacing without the need of an external oxidant • Produces materials with a significantly higher	• Requires guest species to have a low oxidation potential • Medium control over the host structural integrity

	conductivity than the host • Useful for intercalating conducting polymers • Can be carried out in non-organic solvent/aqueous conditions • Can be carried out in an oxygen atmosphere	
Layer-by-Layer	• High structural control over the host structural integrity • Can produce materials with significantly higher conductivity than the host • Useful for producing thin-film intercalated materials. • Can be used to intercalate high molecular weight polymers	• Buildings layers of films as opposed to directly intercalating materials into the interlayer spacing of the host. • Requires organic guests to be in their polymeric form • Layer thicknesses are difficult to control • Requires solutions of the host and guest materials preferably in ionic form in a volatile solvent • Can cause over-oxidation of conductive polymers leading to a low conductive/highly resistive material.

Table 1.3 - Intercalation method summary

	Exfoliation – Restacking	Ion- Exchange	Direct	Redox	Layer-by-Layer
Precursor	✓	✓	✓		
Non-Precursor			✓	✓	✓
Small guest intercalation	✓	✓	✓	✓	✓
Large guest intercalation (e.g. polymers)	✓	✓	✓		✓
Intercalation of very high molecular weight polymers					✓
Polymerisation in-situ w/o external oxidant		✓	✓	✓	
One-pot synthesis			✓	✓	
Host structural integrity	Low	Medium	Variable	Medium	High
Aqueous conditions	✓	✓		✓	
High conductivity		✓		✓	
Low conductivity	✓		✓		✓
Guest species intercalated in cationic form		✓		✓	✓
Non-cationic guest intercalation	✓	✓	✓	✓	
Guests w/ high oxidation potentials	✓	✓	✓		✓
Guests w/ low oxidation potentials		✓		✓	
Synthesis carried out in air	✓			✓	✓
Produces thin films					✓

Table 1.4 - Polymer materials and their intercalation method/s in V_2O_5

Polymer	Structure	Intercalation Method/s
Multi-Method Intercalation		
Polyaniline	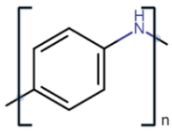	Exfoliation – Restacking, Ion-Exchange and Layer-by-Layer
Polypyrroles	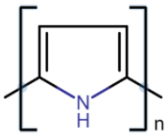	Direct and Redox
PEO	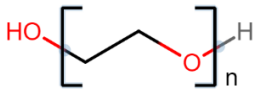	Ion-Exchange and Direct
Exfoliation – Restacking Intercalation		
Methyl Yellow	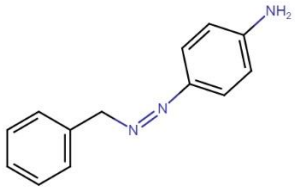	
Carbon Nanotubes	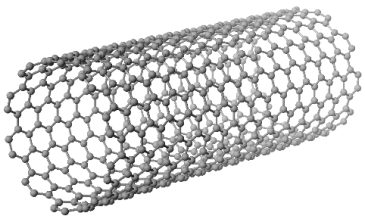	
4-Aminopyridine	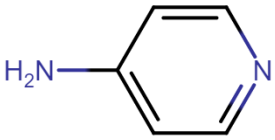	
PDDACl	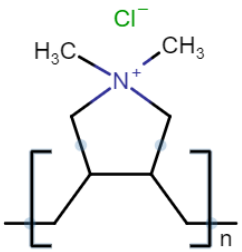	

a) Dodecylviologen b) Carboxybenzyl-viologen a) Dodecylviologen b) Carboxybenzyl-viologen	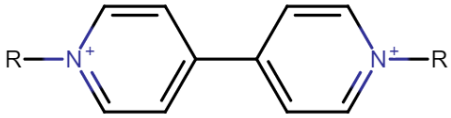 a) R = $C_{12}H_{25}$ b) R = 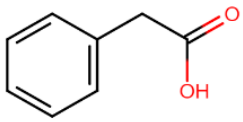
PAHCl	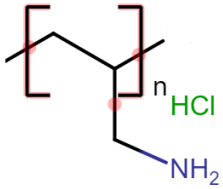
pPDA	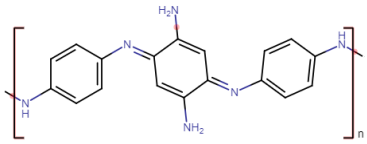
2-phenylethylamine	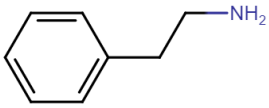
4-phenylbutylamine	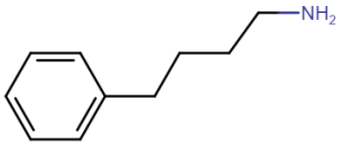
Direct Intercalation	
Butyl, Hexyl and Octylamine	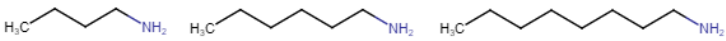
Graphene	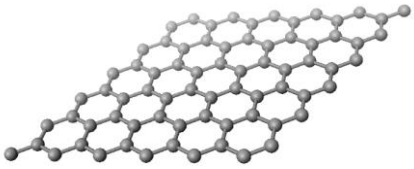

PVP	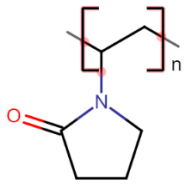
PAPSA	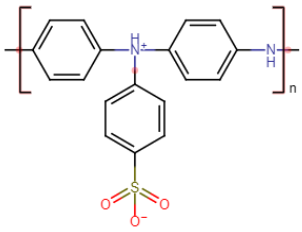
PTOESA	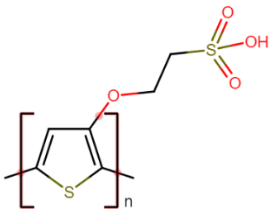
4-Anilinoaniline	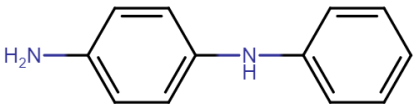
3-4 Dihydroxyphenylalanine	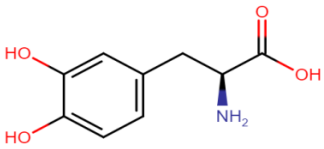
2- and 4- sulfanylpyridine	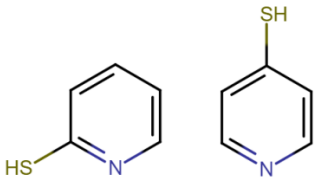
2,2'-dithiobispyridine and 4,4'-dithiobispyridine	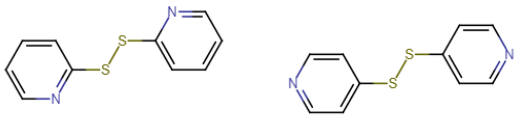

Redox Intercalation	
Poly-o-methoxyaniline	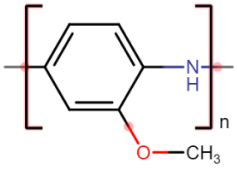
Poly(N-propane sulfonic acid aniline)	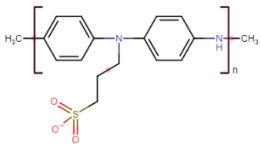
Poly(N-[5-(8-hydroxyquinoline)methyl]aniline] R = Poly(N-[5-(8-hydroxyquinoline)methyl]aniline] (cont)	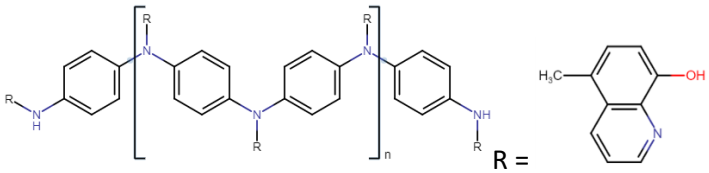
Polythiophene	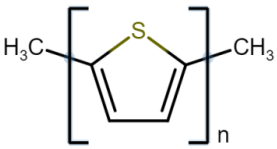
PEDOT	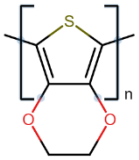
Poly(2,5-dimercaptothiophene)	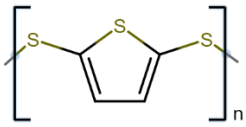
PDMcT	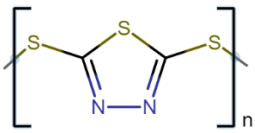

1.5.2) MoO_3 composites

Similar to V_2O_5, molybdenum trioxide (MoO_3) also contains metal ion centres exhibiting good redox chemistry and has shown a range of intercalation capabilities with Li^+ being very commonly utilised[59]. Unlike V_2O_5, however, the orthorhombic phase of MoO_3 (most commonly used phase for intercalation chemistry) has a layered structure which consists of double layered octahedral held together by covalent forces in the 100 and 001 direction and the interlayer spacing arises from the layers stacking by Van der Waals forces in the 010 direction (this structure is illustrated in Figure 1.8)(141).

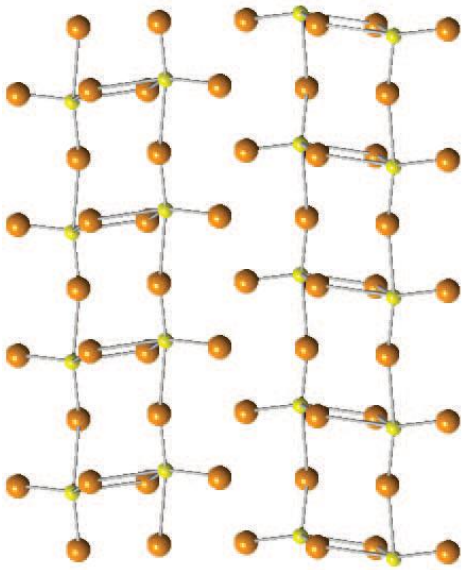

Figure 1.8 - Side view of MoO_3 layers where the yellow atoms are the Mo^{6+} and orange atoms are the O^{2-}

1.5.2.1) Small Cation Intercalation

Similarly to V_2O_5 metal cations have also been shown to successfully intercalate into the interlayer spacing of MoO_3 including Li^+, Mg^{2+}, Na^+ and K^+ as well as H^+. These intercalated metal cation composite materials have given rise to an interest in battery technologies as well as the possibility of ion-exchange or exfoliation of MoO_3 in the synthesis of organic-inorganic composites(65,142). There are two traditional methods for

the intercalation of these materials into MoO_3, *i)* electrochemical insertion and *ii)* redox chemistry.

Most common intercalation via electrochemical insertion is with Li^+. As was seen with the V_2O_5 materials, this Li^+ cations can be hydrated(143). Typically IR peaks for MoO_3 appear between 1000-400 cm^{-1} with the Mo=O stretching and bending mode of Mo-O-Mo appearing at 988 cm^{-1} and 584 cm^{-1} respectively. Upon intercalation of Li^+, the bands in the region of 1200-1080 cm^{-1} correspond to the stretching modes of the intercalated Li^+ vibrating against their nearest neighbouring oxygens of MoO_3(143). This intercalation leads to an increase in the interlayer spacing where an interlayer spacing of 1Å corresponds to a molar ratio of 1 Li^+ to one 1 MoO_3. The XRD showed the crystalline structural integrity of the host was maintained during the intercalation of lithium. Furthermore, this lithiated MoO_3 was shown to exhibit high ion mobility with a chemical diffusion coefficient for the Li^+ ions reaching a value of 3 x 10^{-9} cm^2 s^{-1}. The XPS study(144) showed that Mo^{6+} is reduced during intercalation to Mo^{5+} in a similar fashion to the reduction of the vanadium sites in V_2O_5. It was also shown that there was a reduction in the oxygen environment with two peaks appearing for the O1s core level confirming the interactions between the Li^+ and the oxygen in the MoO_3 upon intercalation.

Lithium intercalation can also be achieved by the reaction of MoO_3 and n-butyllithium (n-BuLi) in hexane solution under an inert atmosphere producing Li_xMoO_3(145). For this method typically, a molar ratio of $0<x<1.55$ is achieved(146). This method of intercalation is convenient due to the fact that the Fermi level of the MoO_3 is located below the conduction band (mostly dominated by the Mo d states) and has a band-gap of 3.1 eV(147–149). This is comparable to the decomposition potential of n-BuLi (-2.5 eV) resulting in spontaneous Li^+ intercalation. Furthermore, since n-BuLi serves as a good lithiating agent (at concentrations of greater than 0.4M exfoliation of the MoO3 layers occurs due to excessive Li^+ content) intercalation begins at the edges of the MoO_3 before

proceeding to the core allowing for the structural integrity and crystallinity of the host to be maintained(148).

Hydrogen ions (H^+) intercalate into uncommon sites in MoO_3(150) with three distinct phases present. Type 1 has molar ratios of 0.2-0.4 H^+ to MoO_3, type 2 molar ratios of 0.85-1.04 and type 3 having molar ratios of 1.55-1.72(151). The interlayer spacing between layers does not increase as the H^+ ions are found in the basal planes between neighbouring oxygen atoms rather than in the interlayer spacing itself (150–152).

In a similar manner, sodium dithionite ($Na_2S_2O_4$) is also a good reducing agent and is commonly used to intercalate Na^+ into the interlayer spacing of MoO_3 as it can be conveniently reacted under aqueous conditions. A typical method involves reacting a MoO_3 powder with $Na_2S_2O_4$ aqueous solution (1M). The interlayer spacing increases from 6.93Å to ~11.4Å due to hydrated Na^+ ions being present. The XRD showed that structural integrity and crystallinity is maintained upon intercalation(153,154).

Intercalation of K^+ was achieved by reaction of hydrated MoO_3 with KBH_4. The intercalation of K^+ does not change the structural integrity or crystallinity of the material(142). The lithium, sodium and potassium intercalated materials are commonly used as precursors for ion-exchange reactions.

Magnesium ions (Mg^{2+}) have been shown to intercalate into MoO_3 via the electrochemical route (81,155,156). It was shown that the molar ratio of Mg^{2+} could be varied between 0.05 and 0.4. The increase in the interlayer spacing correlated with the molar ratio (0.05 to 0.4) of Mg^{2+} intercalated. The IR spectrum of Mg_xMoO_3 shows the characteristic MoO_3 peaks (that appear below 1000 cm^{-1}) shifting as discussed above for Li^+ intercalation. However, the intensity for the peak at 806 cm^{-1} is shown to decrease during the same molar ratio range but is no longer present after the molar ratio increases above 0.2. The decrease in the peaks is due to the interaction of the magnesium ion with

the bridging oxygen (Mo-O-Mo) and with the M=O oxygen. The diffusivity was in the order of $10^{-17} – 10^{-18}$ cm^2s^{-1}(81,156).

In recent years it has been shown that zero-valent transition metals have been intercalated into the interlayer spacing of MoO_3. Cu(157), Sn and Co(158) have shown this phenomenon. In the case of Cu, it was shown that a molar ratio of 0.12 (3% atomic percentage) Cu to MoO_3 successfully intercalated into MoO_3 nanowires while preserving morphology. From the XRD the interlayer spacing showed a contraction from 2.322Å to 2.309Å while maintaining the MoO_3 overall crystallinity. This contraction was suspected to be due to the guest intercalant, in which the Cu exhibits some electron sharing with the MoO_3 layers due to its zero-valent state as was confirmed by XPS. For this material, the Mo $3d_{3/2}$ and $3d_{5/2}$ peaks are broadened upon intercalation. This is not seen in cation insertion as the interaction between the anionic layers and the cationic intercalant is mostly electrostatic. However, this is not the case in the intercalation of Sn and Co whereupon intercalation, there was an interlayer expansion. This expansion was shown to be reversible upon intercalation-deintercalation-re-intercalation of Sn and Co. The increase in the interlayer spacing is dependent on the molar ratio of Sn and Co. The Raman spectra further showed intercalation was successful for Cu as the vibrational peaks shifted to lower wavenumbers corresponding to less vibrational space available for the terminal oxygens. Electron energy loss spectroscopy (EELS) helped confirm that the Cu was in the zero-valent state as there were no additional peaks present in the Cu^0MoO_3 material while peaks appeared for Cu^+ and Cu^{2+} intercalation which could intercalate favouring a redox mechanism.

The intercalation of metal cations into the interlayer spacing of MoO_3 is used as a precursor to intercalate other cations (usually organic) into MoO_3.

1.5.2.2) Ion-Exchange Intercalation

Ion-exchange method of intercalation is a very common and reliable method which does not have an adverse effect of the overall crystalline structure of the MoO_3. This was shown in the intercalation of polyoxycations(159). The Na_xMoO_3 was synthesised using the redox method mentioned previously with $Na_2S_2O_4$. The sodium intercalated precursor showed an interlayer spacing of 11.5Å, which increased further upon ion-exchange with aluminium polyoxycations to 18.9Å. Interestingly this interlayer spacing increase was larger than the sum of the size of the two components of the composite (the MoO_3 interlayer spacing of 6.97Å and the Al polyoxycation ~9Å). This suggested that although the overall structure remained crystalline, the MoO_3 layers would have shifted due to the presence of the intercalant. In a similar fashion, Bi-polyoxycations were also intercalated in this fashion with an interlayer spacing increasing from 11.5Å to 13.8Å.

More interestingly, polymers can be intercalated in this fashion such as poly(p-phenylene vinylene) (PPV)(160) by intercalating the monomer precursors and polymerising in-situ. This was particularly convenient as PPV precursors cannot undergo a redox reaction and therefore not yield intercalation. Since most ion-exchange mechanisms require a water-soluble cation, PPV is insoluble in water and therefore direct insertion of the high molecular weight polymer is difficult. The interlayer spacing was shown to be 13.3Å with a net increase of ~6.4Å from that of the pure MoO_3 after ion-exchange. The IR spectrum further showed that in-situ polymerisation was successful due to the peaks appearing at 3024 and 964 cm^{-1} correspond to the conjugated form of PPV as well as the typical shifting of the host peaks as previously discussed. PEO is also a non-redox intercalative polymer which is intercalated in a manner similar to PPV(161,162). In this unusual situation, the intercalation of the polymer is in fact assisted by the insertion of the sodium or lithium ions. The polymer replaces the water molecules and “chelates” with the

metal cations in between the MoO_3 layers before exchanging with them. It was shown that there was two forms of PEO present, a monolayer and bi-layer structure with interlayer expansions to 12.9Å and 15Å respectively. Hydrogen bonding was shown to exist between the polymer and the oxygen atoms in the interstitial Mo=O bonds corresponding to PEO-MoO_3 interactions. Polystyrene was also intercalated as a polymer rather than through its monomer precursor(163). This was achieved by the use of surfactant due to the fact that styrene was unable to be charged. The surfactant (didodecyldimethyammonium) exchanged with the sodium ions, swelling the layers further, to allow the entire polymer to be incorporated into the interlayer spacing. This polymer intercalated material showed an interlayer spacing increase to ~30.5Å (varying between 29.5Å to 36.5Å when repeated). The dodecyltrimethylammonium compound itself can be intercalated with a bromide counter ion(164) ion exchanging with either the sodium or hydrogen intercalated MoO_3. A large increase to 22.9Å in the interlayer spacing was observed similar to the intercalation of polystyrene. This was due to the Keggin like cluster structure formed by the intercalant held together via hydrogen bonding with water.

This ion-exchange method can also be extended for producing conducting polymers in-situ (as many exhibits poor to very low solubility's) by intercalating the monomers which then undergo a redox reaction once intercalated with the MoO_3 layers. This is carried out by ion-exchanging the metal cation (for example Na^+ as previously discussed) with the protonated monomer precursor. This is followed by either the monomer's redox polymerising upon entering the interlayer spacing with MoO_3 or else the polymerisation is driven by the use of an external oxidising agent (such as ammonium persulphate) after the monomer as successfully intercalated. A simple common polymer intercalated in this manner is polypyrrole(165–167) whereupon pyrrole was ion-exchanged with the hydrated sodium ions, ferric chloride ($FeCl_3$) or ammonium persulphate was added to drive the polymerisation to completion. Upon ion-exchange, the interlayer spacing showed an

increase to 14.7Å (a net increase of 7.8Å when compared to MoO_3). This significant increase in the interlayer spacing corresponds to one of two cases; *i)* the polypyrrole chains aligning perpendicular to the plane of the MoO_3 layers or *ii)* bilayer formation of the polymer chains which are parallel to the MoO_3 plane. The overall crystallinity and integrity of the layered host structure were maintained during this reaction. The room temperature resistivity of this material was shown to be 258 Ω cm. With the MoO_3 being present as the major component in the composite, the transport properties were dominated by the MoO_3. The main challenge facing polypyrrole intercalation lies in the ease of polymerisation when protonating the pyrrole in acidic conditions before it has had a chance to be intercalated. In comparison, PANI is a widely used conducting polymer and has shown to successfully be intercalated, including substituted PANI's such as poly(o-anisidine), via ion-exchange(166,168–170). In both cases, the PANI and the poly(o-anisidine) were protonated to form their hydrochlorides before ion-exchanged with sodium ions. Ammonium persulphate was then used as the external oxidising agent. The interlayer spacing increased to ~13.6Å for both PANI and poly(o-anisidine) which corresponded to the polymer chains organising themselves perpendicular to the planes of the inorganic host (as confirmed by solid-state NMR(171)). This method was extended to more complex conducting polymer/organic semiconducting structures such as poly(5,6,7,8,-tetrahydro-1-naphthylamine) (PTHNA)(172,173) and 5,10,15,20-tetrakis(N-methyl-4-pyridino)porphyrin(166). The PTHNA composite showed an interlayer increase to 14.3Å (a net increase of 4.9Å compared to the $NaMoO_3$ and 7.4Å in relation to the MoO_3 host). The 5,10,15,20-tetrakis(N-methyl-4-pyridino)porphyrin meanwhile showed an interlayer spacing increase to 13.4Å corresponding to a net increase of 4.0Å with respect to the sodium precursor and 6.5Å with the host MoO_3. The PTHNA was also intercalated via ion-exchange in its hydrochloride form. It was shown that the interlayer spacing for this intercalant was larger than that for PANI (with an interlayer spacing for the PTHNA

intercalant of 14.3Å with a net increase of 4.9Å in respect to the sodium intercalant). From XPS analysis a reduction of Mo^{6+} to Mo^{5+} was shown due to the oxidative polymerization that the PTHNA precursor initially underwent immediately after being ion-exchanged and before the addition of ammonium peroxodisulfate as the external oxidant. The molar ratios of the Mo^{6+} and Mo^{5+} were calculated from the peak areas and shown to be between 91.8 - 87.1% for Mo^{6+} and 12.9 - 8.3% for Mo^{5+}. The lower Mo^{5+} content resulted in a more resistive material overall.

Another commonly utilised method of intercalation of the organic materials is direct intercalation of the polymer. These direct methods are analogous to the methods used in V_2O_5 (see section 1.3.1.3) and include direct insertion of the organic material via hydrothermal, exfoliation and sol-gel methods.

1.5.2.3) Direct Intercalation

The direct intercalation of organic materials was shown to work well for cubane clusters(174) and dimethyl sulphoxide (DMSO)(175). The Cubane clusters were intercalated by the treatment of the MoO_3 with cubane clusters in acetonitrile at 100°C. This resulted in the intercalation of the cluster into the interlayer spacing with a molar ratio of 0.15 to 1 MoO_3. The interlayer spacing increased from 6.9Å to between a maximum of 15.5Å (for $Fe(\eta\text{-}MeC_5H_4CH_2CH_2NH_2)\text{-}(\eta\text{-}C_5H_5)]^{2+}$ cubane cluster) and a minimum of 10.3Å for (for $Fe_4(\eta\text{-}C_5H_5Me)_4\text{-}(\mu^3\text{-}S)_4$ cubane cluster). DMSO was shown to intercalate into MoO_3 by simply dissolving the MoO_3 in hot DMSO and allowing for the MoO_3 to recrystallise out. The interlayer spacing showed an increase between 7.70Å-8.27Å. It was then shown that this material could be used in a very similar mechanism to the ion-exchange whereby the DMSO could be directly exchanged when the intercalated material was placed in a solution containing an excess of the desired organic intercalant. In this

case, these were solutions of pyridine (py), pyridine N-oxide (pyo) and triphenylarsine oxide ($AsPh_3$). The py, pyo and $AsPh_3$ intercalated MoO_3 showed interlayer expansions of 11.48Å, 9.51Å and 11.95Å respectively. In the case of the pyo intercalant, it was stated that the material showed poor crystallinity while maintaining crystallinity for the intercalation of py and $AsPh_3$. The infra-red specifically showed that the main change occurred for the Mo-O-Mo bridging region (800-720cm^{-1}). Butylamine, dodecylamine and hexadecylamine showed to intercalate into the MoO_3 layers in a similar manner to the pyridine compounds with interlayer spacings expanding to 15.13Å, 30.86Å and 38.74Å respectively(176). The expansion is dependent on the chain length. Upon intercalation, the peaks for the CH_2 and –NH vibrations appear at 2850 cm^{-1} and 2916 cm^{-1} for the CH_2 stretch and at 1628 cm^{-1} for the –NH (bending) while the characteristic MoO_3 peaks are shifted as seen previously. It was suggested from this data that the alkylamines adopt a double layer orientation where the chains are stacked on top of one another but are perpendicular to the inorganic plane. Nicotinamide also showed a similar interaction once intercalated with two possible coordinations taking place due to the orientation. The first was the hydrogen bonding between the oxygen in the inorganic layers and the N-H group while the other showed coordination between the metal and the oxygen in the C=O. When the N-H hydrogen bonded with the oxygen, the interlayer spacing increased to 13.2Å. Meanwhile, when the C=O was interacting with the layers the interlayer spacing increased to 11.2Å. It is suggested that the N in the aromatic ring showed interactions with the Lewis acid sites (the Mo^{6+} cations) in the oxide suggesting a degree of acid-base like reaction occurring in-situ. It seemed to be particularly the case when hexamethylenetetramine (hmta) was intercalated. Upon intercalation, the hmta showed an interlayer increase to 10.1Å. This supposed behaviour to show interaction with the Lewis acidic sites of the oxide layers was also proposed for 1,10-phenanthroline(177) and pyrrolidine dithiocarbamate (pdc)(178). 1-pyrrolidinecarbodithioic acid ammonium salt was used with

an increased interlayer spacing of 12Å. The orientation of the pdc anion in the interlayer spacing is perpendicular to the planes of the MoO_3 layers. Due to this orientation, the C-S^- group interacts with the Lewis acid sites of the inorganic oxide. Due to the perpendicular orientation of many of these intercalates, one would have expected the 1,10-phenanthroline to potentially intercalate perpendicular to the planes. However, due to this interaction with the Lewis acid sites, it was shown that there are three potential orientations this molecule can adopt. In the first, the nitrogen groups are interacting with the Lewis acid sites. The second is the ring system lying parallel to the planes of the MoO_3 leading to an interlayer spacing of 11.6Å in the first case and 7.7Å in terms of the second case. Diethylenetriamine (DETA), 2-(2-aminoethoxy) ethanol (AEE) and 2-(2-aminoethylamino) ethanol (AEAE)(179) were also intercalated in this manner. It was shown that the MoO_3 vibrational bands were shifted to lower wavenumbers due to the limited space for the Mo=O stretching. From the XRD patterns, the (*001*) peak shifts from the 6.9Å for MoO_3 to 10.56Å, 9.38Å and 8.38Å for DETA, AEE and AEAE intercalated composites respectively. The materials maintained a good crystalline structure and structural integrity.

Similar to that shown in V_2O_5 polyaniline(180) as well as the long chain poly(tetramethyl-*p*-phenylenediamine dihydrochloride)(181) were also intercalated using direct intercalation into MoO_3. With the inclusion of polyaniline, a 13.7Å interlayer spacing increase with a net increase of 6.7Å was seen corresponding to the polymer backbone being orientated roughly perpendicular to the planes of the MoO_3 layers. It was determined that there were two phases present; a major phase with a number average molecular weight (M_n) of the polymer was 4850 and average molecular weight (M_w) of 24200 while a minor phase showed a M_n of 280 and M_w 294 (corresponding to the trimer formation). For the minor phase the low average molecular weight was indicative of the amount of monomer available and the restrictive space in the interlayer spacing for polymerisation. However, the conductivity of the PANI as the intercalated material showed

three orders of magnitude increase in the room temperature conductivity compared to MoO_3, rising from $2x10^{-6}$ Scm^{-1} for pure MoO_3 to ~$3x10^{-3}$ Scm^{-1}. This is consistent with the presence of doped polyaniline in the emeraldine form. This room temperature conductivity is still, however, lower than that for bulk emeraldine. The Seebeck effect is measured by the Seebeck coefficient which is a measure of the induced thermoelectric voltage as a response to a temperature gradient across the material. In the polyaniline intercalated MoO_3, the Seebeck coefficient was shown to be relatively small, ~+8.6μVK^{-1} measured at 345K and this decreased linearly with decreasing temperature to ~+4.6μVK^{-1} at 235K and from the gradient, it was implied that the composite material is intrinsically p-type. The polyaniline derivative poly(tetramethyl-*p*-phenylenediamine dihydrochloride) (PTMPD) showed two potentially intercalated phases with interlayer spacings of 22.6Å and 11.3Å. The interlayer spacing of 22.6Å could correspond to a bilayer structure of the PTMPD while the 11.3Å is more consistent with a monolayer where the chains are in a fairly perpendicular orientation. The stoichiometry of this composite was determined as $PTMPD_{0.23}MoO_3(H_2O)_{0.31}$.

1.5.2.4) Exfoliation – Restacking Intercalation

Other common direct intercalation methods include exfoliation/re-stacking and hydrothermal methods. The exfoliation/re-stacking method is analogous to that used for the V_2O_5 with some minor alterations. In the case of the V_2O_5, we saw that it was advantageous to initially pre-intercalate with a metal cation or other small organic cations before carrying out the exfoliation (usually by ultrasound). In the case of the MoO_3, it was shown that in intercalating substituted pyridines (pyridine, 4-methylpyridine, 4-propylpyridine, 4-phenylpyridine, 4-benzylpyridine and 4-carboxypyridine) the MoO_3 could be directly exfoliated by ultrasound at room temperature for 5-150 hours in the

presence of the organic intercalant solutions(182). Upon re-stacking it was shown that the interlayer spacing expanded for pyridine, 4-methylpyridine and 4-propylpyridine to 10.6Å, 11.7Å and 13.7Å respectively with the increase dependant on the size of the substituted group. This suggested that the intercalated material was orientated perpendicular to the planes of the MoO_3 layers. The IR spectrum confirmed successful intercalation as the shifting of the characteristic MoO_3 peaks were seen as discussed previously. Meanwhile, the peaks appearing in the region of 1400cm^{-1} to 1700cm^{-1} are associated with the substituted pyridines. Due to the re-stacking nature, the XPS showed a singular Mo environment corresponding to Mo^{6+} suggesting the substituted pyridines did not undergo a redox reaction in-situ with the inorganic layers. This method was successful for the intercalation of the polymer linear poly(ethyleneimine) (LPEI), with weight average molecular weight of 40,000-60,000(183). In this case, the sodium or lithium intercalated precursor was used for the exfoliation. The interlayer expansion showed an increase in 11.6Å with a net increase of 4.7Å once the polymer was intercalated. In general, this is consistent with the intercalation of monolayer polymer structure within the interlayer spacing as previously discussed. The material retained its crystalline structure upon intercalation showing that the layers re-stacked in an ordered fashion. The interaction between the polymer and inorganic layers suggested that the protonated polymer was present as the polymer was intercalated in its hydrochloride form. By titration, they showed that there was indeed a low extent of protonation of the amine groups in the LPEI. This supported the conclusion that the LPEI was solvated within the interlayer spacing. The closely related structure of polyamidoamine (PAMAM) dendrimers further showed that for the smaller dendrimer structures an interlayer expansion of 11.8-12Å was observed while the larger structures showed an interlayer expansion between 13.4-15.1Å. Analogous to the LPEI the larger PAMAM structures adopt a bilayer conformation within the interlayer spacing while the smaller structures adopt a monolayer-like conformation as

seen with polyanilines. This was further shown with the TGA where the % organic mass present in the smaller structures was shown to be 12-14%, whereas for the bilayer larger structures this content doubled to 22-24%.

Another modification to the exfoliation and re-stacking method lies in stabilising the exfoliated layers and controlling the re-stacking with the use of a surfactant. This was used to intercalate poly(*p*-phenylene) (PPP) into MoO_3(184). The surfactant used in this case was dodecyltrimethylammonium hydroxide and the method involved intercalating the monomer followed by in-situ polymerisation. However, it must be noted that the surfactant is co-intercalated into the layers with the PPP. This showed that the interlayer expansion increased to 23Å for the co-intercalated PPP and surfactant. This suggested that the PPP monomer pre-polymerisation was stacked perpendicular to the planes of the MoO_3 layers. Upon polymerisation and the removal of the surfactant by heating, the interlayer spacing decreased to 11.96Å suggesting a monolayer structure of the PPP was present in the interlayer spacing. It was further shown that the para polymer was present and no crosslinking occurred as the IR bands show those for 806 cm^{-1} and 1482 cm^{-1} which corresponded to the C-H stretches for the para-substituted phenyl rings and the shifted characteristic MoO_3 peaks further suggested intercalation was successful.

The hydrothermal method is similar to that which was seen in the V_2O_5 and is similar to that of the exfoliation and re-stacking synthetic method where the inorganic layers are dissolved in a solution and regrown around an organic guest species. Bipyridine is a small conjugated molecule that has shown to successfully intercalate into the MoO_3 interlayer spacing. 2,2'-bipyridine(185,186) was intercalated at temperatures of 160-200°C where it was shown that the nitrogen in the 2,2-bipyridine chelates with the terminal oxygen groups of the MoO_3 which was seen in the IR spectrum as bands appeared for the chelated bipyridine and the inorganic oxygen N-O bonds. The 4,4'-bipyridine analogue and 1,2,4-triazole (187–189) was shown to show similar intercalation chemistry to the 2,2'-

bipyridine and showed an interlayer expansion between 11.22 Å - 11.37Å suggesting monolayers were formed which arranged perpendicular to the planes of the MoO_3 layers for the bipyridine while the triazole conformed to double layer stacked conformation. As with 2,2'-bipyridine, the nitrogens act as ligands chelating with the Mo metal centres in the case of both guest species. The triazole compound showed bidentate-bridging chemistry by coordinating through the 1,2 nitrogen sites. In both cases, the shifting of the characteristic MoO_3 peaks suggested successful intercalation had occurred as discussed previously. The peaks above 1000 cm^{-1} correspond to the organic guest species. XPS data showed that even during the hydrothermal method, due to the chelation of the nitrogen atoms some of the Mo^{6+} was reduced to the Mo^{5+}. However, intercalation of the bipyridine resulted in the lateral reduction of the overall unit cell dimensions and cracking in the lattice structure which was caused by the bipyridine chelating with the inorganic layers causing aggregation of the inorganic layers. The similar structure pyrazine (compared with pyridine) also intercalates in such a fashion in which the nitrogens chelate with the Mo(190). Pyrazine, which has structural similarities to pyridine, is small enough (molecular length 5.8Å compared to the MoO_3 interlayer spacing of 6.9Å to successfully intercalate without causing an increase in the interlayer spacing of the MoO_3 even though it intercalates perpendicular to the planes of the MoO_3 layers. In such a case it is clear that XRD may not provide sufficient details regarding successful intercalation but did show that the overall structural integrity of the material was maintained, which may suggest any pyrazine is surface based. Raman data, however, showed peaks for the symmetric stretching modes of the aromatic ring of pyrazine at 714 cm^{-1} and 932 cm^{-1}. As discussed, typically seen in IR and Raman there are shifts in the host peaks corresponding to a decrease in the vibrational space available due to intercalation. This was specifically shown for the terminal Mo=O and O-Mo-O where net shifts of 5 cm^{-1} and 3 cm^{-1} were seen. This is due to the chelating of the nitrogen to Mo as seen in the bipyridines.

Furthermore due to the chelating of the nitrogen to Mo, as seen with the bipyridines, the XPS showed the formation of the reduced Mo^{5+} ions being present. Although not discussed, the cause of Mo^{5+} centres may have been from the hydrothermal process and not due to any redox reactions caused by the guest hydrazine. From the photoluminescence spectrum, MoO_3 shows a single strong peak appearing at 332 nm. Upon intercalation, however, this single peak disappears and two new peaks are now present at 320 nm and 351 nm. This showed blue-shift with respect to the pure MoO_3 which is attributed to the presence of the pyrazine. This study was extended to other pyrazine based organic guests along with pyrazine and pyridines; the thiazole-based conjugated molecules; quinoxaline, dimethylpyrazine (DMPz), 2-(4-pyridyl)benzimidazole) (4-PBIM), 2-(2-ol-3-pyridino)benzimidazole (OPBIM), 2-(3-pyridyl)-benzimidazolium (3-HPBIM) which were co-intercalated with other metal cations such as Ag, Cu and Co. Here the oxide layers adopted a nearly perfect stochiometry after intercalation. For the intercalation of quinoxaline, DMPz, 4-PBIM, OPBIM and HPBIM the interlayer spacing increased to 12.32Å, 10.21Å, 13.54Å, 10.95Å and 10.13Å respectively. This suggested that the organic guest continued the trend for intercalants into MoO_3 where they orient themselves perpendicular to the planes of the MoO_3. This is facilitated by the fact that the nitrogen groups would chelate to Mo. The crystallinity in all cases was maintained and the lattice parameters only changed in the direction which corresponded to the increase in the interlayer spacing. Following on from the intercalation of complex single organic molecules, the direct intercalation of polymers via hydrothermal conditions was shown for the cases of poly(diallyldimethylammonium chloride) (PDDACl) (M_w 100,00-200.000) and poly(allylamine hydrochloride) (PAHCl) (M_w 15,000)(191). Two material compositions were obtained by this method showing a stoichiometry of $[PAHCl]_{0.18}[PAH]_{0.38}MoO_3$ and $[PDDACl]_{0.26}[PDDA]_{0.24}MoO_3$. Through elemental analysis, it was shown that there was partial intercalation of the chloride anions into the

interlayer spacing. The PAH shows an interlayer spacing increase of 22.4Å suggesting the formation of a bilayer like structure due to its linear backbone. Upon intercalation of the PDDACl, meanwhile, the interlayer spacing increased to 11.2Å suggesting monolayer formation. However, in the case for PAHCl, it was shown that the crystalline structure was maintained well during intercalation which was not the case in PDDACl in which the peaks broadened and became diffuse. Alternatively, the higher molecular weight of PDDA, with respect to PAH, caused by several different expanded peaks around the 11.2Å peak leading to the appearance of a single diffuse peak. The FTIR showed the presence of both NH_3^+ and NH_2 groups and therefore potential H-bonding to be occurring within the structure of PDDACl which may lead to regions of spiral-like conformations in the interlayer spacing which may lead to the appearance of the mentioned diffuse peak. Due to the guests being intercalated as the polymer there was no indication of chelation or Lewis acid like interactions between the polymers and the MoO_3 host which is consistent with that fact that it would be less energetically favourable to form these interactions rather than interactions within the polymer's own structure. The TGA further confirmed the presence of the polymers and mass loss only began to show after ~250°C and continued until ~550-600°C which corresponded to the polymer whereas the mass loss at ~750-800°C which is characteristic for MoO_3 sublimation. The UV-Vis diffuse reflectance spectrum(190) showed the characteristic band between the 200 nm and 360 nm region characteristic for MoO_3 while the shoulder appearing ~290 nm was associated with charge-transfer transitions for the structure where the polymer was present. This was further confirmed with the presence of additional bands between 300 nm and 400 nm usually associated with the presence of Mo^{6+} ions in a crystalline arrangement. This suggested that the crystalline structure of individual MoO_3 layers was still preserved and that the broad peaks shown in the XRD were attributed to the intercalation of the polymer. Meanwhile, the absorption bands at 600 and 930nm were associated with the Mo^{5+} to Mo^{6+} intervalence polaronic

charge transfer transitions while the bands occurring at 800 nm, 1440 nm, 1270 nm and 1500nm correspond to the d-d transitions of Mo^{5+} ions found in a distorted polyhedron environment in the MoO_3 solid. This sheds light on the mechanism of the intercalation slightly as even during hydrothermal conditions the method of intercalation causes some reduction of the MoO_3 material.

A widespread commercially applied polymer that has also been shown to be intercalated in such a manner as the PDDACl and PAH polymers is PEO which was applied for Li^+ electrochemical intercalation as seen previously for PEO intercalated V_2O_5(192). This PEO, in this case, was intercalated into MoO_3 nanobelts. In this case, the layers were first swelled in aqueous conditions before the addition of the PEO via exfoliation - restacking. The composite that formed showed no immediate change in the interlayer spacing which had expanded to 13.85Å. The crystallinity was shown to have been maintained throughout the reaction. There were, however, no peaks in the IR spectrum indicated to the presence of H_2O with signals between 3600 cm^{-1} and 1600 cm^{-1} corresponding to PEO suggesting that the swollen layers did not restack around water after exfoliation.

Table 1.5 - The advantages and disadvantages of the different intercalation methods for MoO_3 intercalation

Intercalation Method	Advantages	Disadvantages
Cation Intercalated Host Precursor		
Small Cation Intercalation	• Used as precursors for organic guest intercalation • Maintains high control of the host structural integrity • Intercalation is reversible with little effect on the host structural integrity.	• The resulting materials synthesised using the small cation precursors show a limited control over the structural integrity of the host material.
Precursor Based Intercalation		
Ion – Exchange	• A wide range of guest species can be used - Small and large organic guests can be intercalated including polymers • Monomers with low oxidations potentials are readily polymerised in-situ without the requirement of an	• Difficulty in controlling the degree of structural integrity of the host and the medium to high integrity is case by case. • Requires guests to be present in a cationic form in solution.

	external oxidant. • Produces materials with significantly higher conductivity than the host • Can be carried out in non-organic solvent/aqueous conditions. • Medium to high structural integrity of the host maintained.	
Exfoliation – Restacking	• A wide range of guest species can be used - Small and large organic guests can be intercalated including polymers (and very high molecular weight polymers) • In-situ polymerisation can occur for organic guests with low oxidation potentials. • Variable conductivity of resultant material when	• In cases where surfactant used, the surfactant can also be intercalated into the layers along with the desired guest species affecting properties (such as conductivity) • Very low to medium structural integrity of the host material and the degree of structural integrity is difficult to control

	compared to the host material • One-pot synthesis • Can show some medium control over host structural integrity.	
Non-Precursor Based Intercalation		
Direct	• A wide range of guest species can be used - Small and large organic guests can be intercalated including polymers (and very high molecular weight polymers) • Usually one-pot synthesis • If a host precursor used polymer materials show chelation allowing for large guest species to be intercalated, good for some applications (i.e. battery) • Useful for non-cationic guest species	• Overall, a variable host structural integrity from very low - medium with difficulty in controlling the degree of structural integrity, usually on a case by case basis. • If host precursors used the metal ions can remain within the layers which may limit the materials applications

	• Can produce a more conducting material when compared to the host material • Useful in the use of guests which are non-polar and insoluble in polar solvents (such as water) • Can result in high structural integrity of the host. • Does not require xerogel precursor	

Table 1.6 - Intercalation methods summary

	Ion-Exchange	Exfoliation - Restacking	Direct
Precursor	✓	✓	✓
Non-Precursor			✓
Small guest intercalation	✓	✓	✓
Large guest intercalation (e.g. polymers)	✓	✓	✓
Intercalation of very high molecular weight polymers		✓	✓
Polymerisation in-situ w/o external oxidant	✓		✓
One-pot synthesis		✓	✓
Host structural integrity	Medium to High	Very low to medium	Variable
Non-organic/aqueous conditions	✓		
Surfactant use, surfactant can remain intercalated		✓	
High conductivity	✓	✓	✓
Low conductivity		✓	
Guest species intercalated in cationic form	✓		
Non-cationic guest intercalation		✓	✓
Synthesis carried out in air		✓	

Table 1.7 – Polymer materials and their intercalation method/s in MoO_3

Polymer	Structure	Intercalation Method/s
Multi-Method Intercalation		
Polyaniline	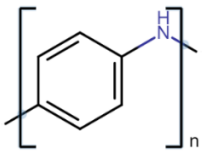	Ion-Exchange and Exfoliation - Restacking
Pyrroles	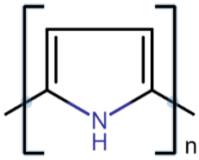	Direct and Exfoliation - Restacking
PEO	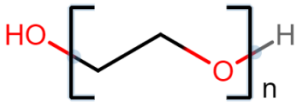	Direct and Exfoliation – Restacking
Ion-Exchange		
Polyoxycations and Bi-polyoxycations	$[AlO_4Al_{12}\text{-}(OH)_{24}(H_2O)_{12}]^{7+}$	
PPV	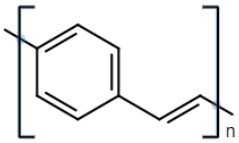	
Polystyrene	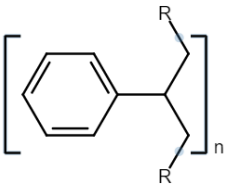	
Polypyrrole	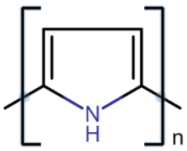	
Poly(o-anisidine)	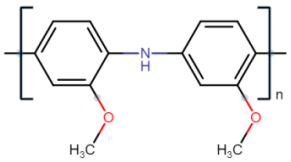	

PTHNA	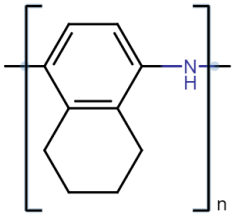
5,10,15,20-tetrakis(N-methyl-4-pyridino)porphrin	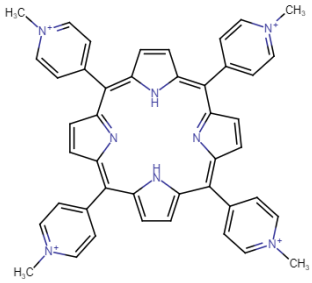
Direct Intercalation	
Cubane cluster	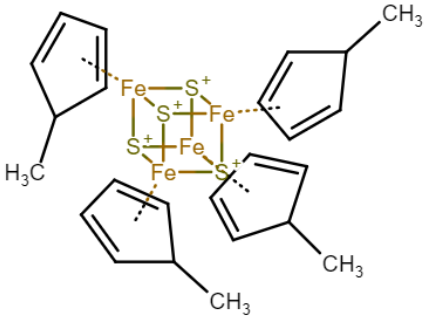
DMSO	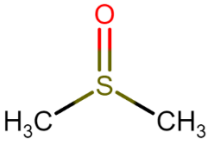
Pyridine N-oxide	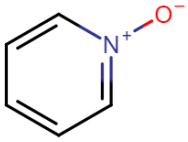
Triphenylarsine oxide	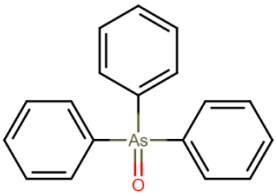

Butyl, dodecyl and hexadecylamine	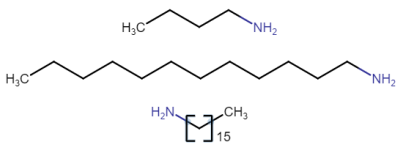
Nicotinamide	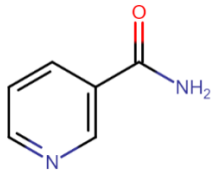
hexamethylenetetramine	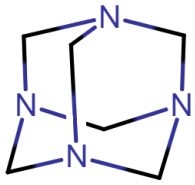
1,10-phenanthroline	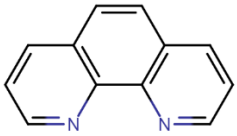
Pyrrolidine dithiocarbamate	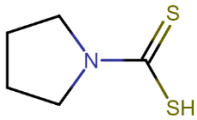
1-pyrrolidinecarbodithioic acid ammonium salt	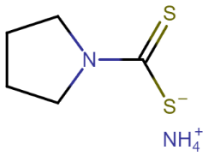
DETA	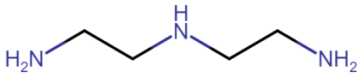
2-(2-aminoethoxy ethanol)	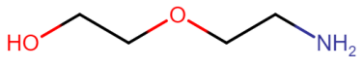
2-(2-aminoethylamino) ethanol	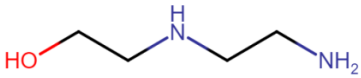

PTMPD	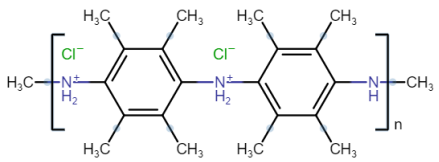
Exfoliation - Restacking	
4-methylpyridine, 4 propylpyridine, 4-phenylpyridine, 4-benzylpyridine and 4-carboxypyrdine	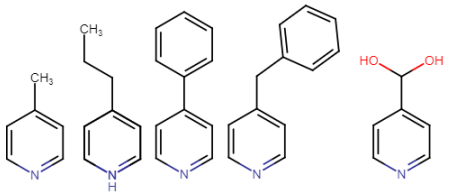
2,2' – Bipyridine and 4,4'-Bipyridine	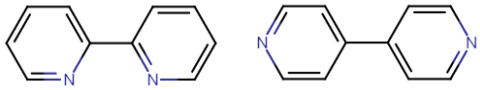
LPEI	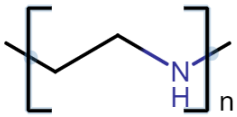
PAMAM	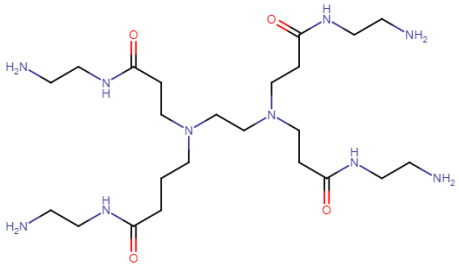
PPP	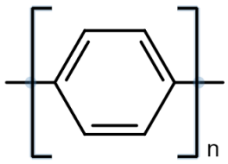
1,2,4 Triazole	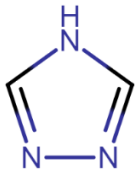

Pyrazine	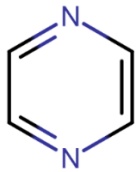
Quinoxaline	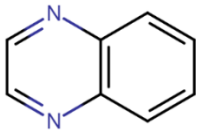
DMPz	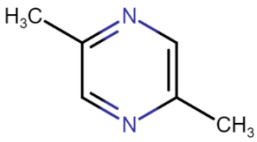
4-PBIM	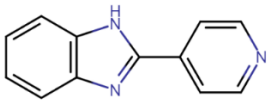
OPBIM	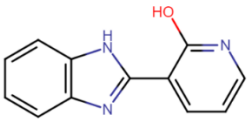
3-HPBIM	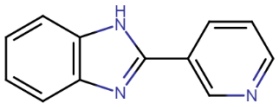
PDDACl	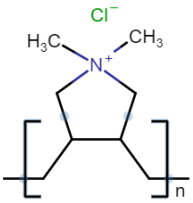
PAHCl	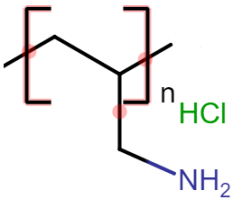

1.5.3) MPS_3 Intercalation

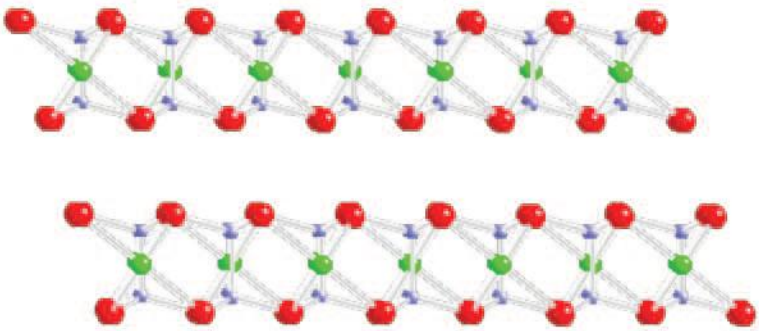

Figure 1.9 - $MnPS_3$ layers where the green atoms are the Mn^{2+}, the red atoms are S^{2-} and the blue atoms are the P^{4+}

The members of the family of MPS_3 (M = transition metal ion, usually first row) have drawn interest as functional materials due to their intermediate band-gaps which are between 1.3eV to 3.5eV(65,193). They all have the common defining structure feature in which $(P_2S_6)^{4-}$ sub-lattices appear within each layer. In fact, this family of materials are more accurately described as slightly distorted $CdCl_2$ and CdI_2 type structures with the ordered occupation of the octahedral holes by the metal cation and the P_2. Interestingly with increasing overall net change in electronegativity between different metal cations and the $(P_2S_6)^{4-}$, the structure changes from CdI_2 type to $CdCl_2$ type(194). The van der Waals gaps in these materials vary between 3.22-3.24Å and are much wider than the closely related MS_2 class of materials(193,194). The effect of intercalating these compounds with either metal cations or organic materials leads to the potential of fine-tuning this class of materials for various applications such as energy storage (electrochemical or otherwise), solid state electrolytes and catalysis(193,195).

1.5.3.1) Metal Cation Precursor Intercalation

As seen with the oxide materials, metal-cation intercalation can be used directly or as a precursor to the intercalation of organic or larger cation species(196). Commonly intercalated metal cations include lithium(197), potassium(198,199), sodium(198). N-BuLi was used to intercalate Li^+ into $FePS_3$ and $NiPS_3$ (197) as seen previously with V_2O_5 while potassium and sodium were intercalated into $CdPS_3$ by reactions with KCl and NaCl in the presence of a buffer solution of K or Na-EDTA (where EDTA is a chelating species for the Cd^{2+} cation in solution driving ion-exchange) (198,199). N-BuLi is a readily used reducing agent for the MPS_3 compounds with smaller bandgaps such as $FePS_3$ (1.5eV), $NiPS_3$ (1.6eV), $FePSe_3$ (1.3eV) and even potentially $MnPSe_3$ (2.5eV)(197,200–202) due to the small bandgap correlating well with the reduction potential of the n-BuLi(148). For the larger band gap compounds which include $MnPS_3$ (3.0eV)(200,203), $CdPS_3$ (3.5eV)(200,204) and $ZnPS_3$ (3.4eV)(197,200) ion-exchange is more favourable. In both cases, the intercalated metal-cations are used to ion-exchange with the organic cation desired.

Lithium content in the $FePS_3$ and $NiPS_3$ was shown to be variable between 0.2-0.5 molar concentration with respect MPS_3 while the interlayer spacing was shown to have a net increase of 5.8Å and it was suggested that this was consistent with the presence of bilayer water around the lithium ions (197). Under these conditions, it was shown that both materials underwent partial lithiation while the overall crystallinity of the material was maintained. The resistivity of both materials was also shown to decrease when the materials were reacted with n-BuLi for longer reaction times (i.e. higher Li^+ content). The $FePS_3$ showed an initial resistivity of 2.5×10^4 Ω cm and this decreased after a reaction time of 120 hours to 2.95×10^1 Ω cm. Meanwhile, the $NiPS_3$ showed an initial resistivity of 10^9 Ω cm and this decreased after 60 minutes reaction time to 1.84×10^1 Ω cm (197). In both cases, the trend suggested a higher conductive material with greater lithium content

and the room-temperature Seebeck measurements indicated that these intercalated materials show n-type conductivity. The K^+ and Na^+ intercalated materials further showed an increase in the interlayer spacing upon intercalation to 9.43Å (net increase of 2.63Å) and 12.10Å (net increase of 5.3Å) respectively into $MnPS_3$. From this, it can be seen that K^+ is likely to be present in the hydrated form coordinated to a monolayer of water (198,199) whereas the Na^+ possibly showed bilayer hydration. Na^+ was in a hydrated state when intercalated into $CdPS_3$ due to the increase in the interlayer spacing correlating to the hydrated radius of Na^+. The dc conductivity of the Na^+ intercalated compound was 10^{-6} Scm^{-1} at 300K and an Arrhenius activation energy of 65.27 $kJmol^{-1}$ for the dc ionic conductivity. Due to the insulating nature of the $CdPS_3$ layers, the conductivity was said to be due entirely to the interlamellar hydrated Na^+ being highly mobile. It was suggested that was only possible with the water molecules as they allowed for a more ionic conducting medium for the Na^+ (198).

It was further shown that non-alkali metal cations can also undergo intercalation. A range of paramagnetic transition metal ions underwent ion-exchange with Cd^{2+} in $CdPS_3$ (205). However, these transition metal ions are not located in the interlayer spacing (as seen with alkali metal cations) and occupy the vacant cation sites left upon removal of the Cd^{2+} ions. XRD did not show noticeable changes to in interlayer spacing and instead, EPR was utilised to monitor the presence of any cations. It was shown that Ni^{2+} underwent no exchange under aqueous conditions and showed slight signs of exchange when pyridine was used as a solvent. Co^{2+} showed no exchange in either aqueous or pyridine conditions. Mn^{2+}, however, showed rapid intercalation at room temperature in both solvent systems. This can be understood since the Mn^{2+} solvated complexes are less energetically stable than the exchanged Cd^{2+} solvated complexes and therefore Mn^{2+} is more readily exchanged for Cd^{2+}. Meanwhile, Co^{2+} complexes in aqueous medium show similar stability to Cd^{2+} solvated complex and therefore ion-exchange is less likely to occur as

both are energetically stable. However in pyridine, when Co^{2+} exchange was attempted it was deemed that the pyridine solvated Co^{2+} complexes are slightly less stable than the Cd^{2+} pyridine complexes (after the exchange in pyridine solution) and therefore we see the slight exchange occurring between the two cations. Furthermore, in both water and pyridine, it is more energetically favourable for Ni^{2+} to form solvated complexes than Cd^{2+} in the same solvated environments, therefore, no ion-exchange occurs between the two. However, when the $CdPS_3$ is pre-intercalated with K^+ there are some changes to this trend. The Co^{2+} now showed rapid exchange at room temperature in aqueous conditions replacing the K^+ ions before entering the Cd^{2+} vacancies. However, no ion-exchange was exhibited between Co^{2+} and K^+ when pyridine was used as a solvent. On the other hand, due to Mn^{2+} complex stability in an aqueous medium, the Mn^{2+} only enters the vacancies after heating to remove the solvent in both aqueous and pyridine solvent systems. It is therefore shown that solvent choice may play a role in the intercalation of metal cations into the interlayer spacing for the MPS_3 with larger bandgaps and that solvation energy may reverse the effect of crystal field stabilization in these systems.

1.5.3.2) Organic Cation Precursor Intercalation

As with the metal oxides, using the alkali-metal intercalated MPS_3 materials as precursors, larger complexes and organic materials can be further intercalated via the ion-exchange mechanism. The ion-exchange method is a widely used method for intercalating larger materials into the interlayer spacing. This was first shown with the intercalation of cationic metallocene ions. The commonly used metallocenes in these reactions are $Co(\eta^5\text{-}C_5H_5)_2^+$ ($CoCp_2$) and $Cr(\eta^5\text{-}C_6H_6)_2^+$ ($CrBz_2$) (see Table 1.10 for full structure) which were intercalated into $MnPS_3$ and $CdPS_3$ by exchanging with the potassium precursor (in $MnPS_3$) and sodium precursor (in $CdPS_3$)(206). For both inorganic materials, upon

intercalation of both metallocenes, the net increase in the interlayer spacing was 5.76Å for $CrBz_2$ and 5.32Å for $CoCp_2$. For vibrational studies, the key vibrational band in the infra-red appears at ~570cm^{-1} which is assigned to the $\nu_d(PX_3)$ vibrational motion. This peak splits upon intercalation of the metallocenes giving two new speaks found ~600cm^{-1} and 560cm^{-1} which is different from the shifting of peaks seen in the oxide materials. This is due to the fact that the metal ions do not coordinate to the sulfur as they did with the oxides. Instead, one peak is assigned to the sulfur for the intercalated phase of the material while the other is for the unintercalated phase of the material. It was shown that this peak is not related to any site distortion which is enhanced and larger in the intercalated material than in the unintercalated material due to the good resolution in the corresponding Raman spectrum (~570–560cm^{-1}). Furthermore the cationic forms of the $CrBz_2$ and $CoCp_2$ peaks appear after intercalation and are found between 3100-700cm^{-1} outside the range of the MPS_3 range (below 700cm^{-1}) and the peaks appearing correspond to that of the halide salts of $CrBz_2$ and $CoCp_2$ (for example the CH modes of the Cp ring would appear for neutral species at 778cm^{-1} and 828cm^{-1} whereas in the ionic form these are shifted to 860 and 893cm^{-1} respectively). It was further shown that the orientation of these guests show that the ring systems lie parallel to the inorganic layers(207). This is a common orientation for organometallic complexes and was also shown to be the case for nickel(II) cyclopolyamine complex in $MnPS_3$(208), manganese(III) macrocyclic complexes in $MnPS_3$ and $CdPS_3$(209) and crown ether complexes(210). The intercalation of these organometallic complexes is also shown to be extended to show intercalation for $Cr(en)_3$ (where en = 1,2-diaminoethane), $Ru(bpy)_3$ (where bpy = bipyridine) and Cp(diphos)COFe (where diphos = 1,2-bis(diphenylphosphino)ethane) into the potassium and sodium pre-intercalated $MnPS_3$(198). Unlike the case for $CrBz_2$ and $CoCp_2$ only partial exchange occurs for the organometallic compounds and the alkali metals in some reactions. Upon intercalation, the potassium pre-intercalated interlayer spacing (9.43Å) increases to 11.20Å for $Cr(en)_3$,

15.2Å for $Ru(bpy)_3$ and 17.8Å for Cp(diphos)COFe. However, only partial intercalation occurred in the cases of $Ru(bpy)_3$ and Cp(diphos)COFe where potassium content decreased from a molar ratio of 0.4 to 0.1 and 0.18 respectively. Full ion exchange occurred for $Cr(en)_3$. For the sodium pre-intercalated upon exchange with $Cr(en)_3$, $Ru(bpy)_3$ and Cp(diphos)COFe the interlayer spacing was shown to be 11.03Å, 15.2Å and 17.8Å. In each case, there was only partial exchange with the sodium ions with sodium ion content decreasing to between 0.5-0.1. The trend was similar to that of $CrBz_2$ and $CoCp_2$ as there was the characteristic peak splitting of the peak appearing at 570cm^{-1} as well as the peaks for the organometallic appearing above 700cm^{-1} shifted due to their presence in their ionic form. However, in the case of $NiPS_3$ phosphorus vacancies were instead seen upon intercalation of sodium and then further ion-exchange with $CrBz_2$ and $CoCp_2$(211) which appeared to occur in this isolated case. However, it has also been shown that the pre-intercalation with alkali-metal is not required prior to introducing organic guests into the interlayer space. Direct intercalation of PyH^+ has been demonstrated into $FePS_3$ with a stoichiometry showing $Fe_{0.88}PS_3(pyH^+ + py)_{0.36}$. The intercalation was confirmed by an increase in the interlayer spacing (to 9.725Å), which suggested the rings were orientated perpendicular to the inorganic layers, as well as the splitting of the peak at 570cm^{-1} in the infra-red spectrum(212). It was further elaborated that the pyridine molecules underwent condensation reactions to form the 4,4'-bipyridyl molecules and protons. These protons then protonated the remaining neutral pyridines allowing for the ion-exchange mechanism to occur. Furthermore, ESR studies showed that for pure $MnPS_3$ the intercalation of pyridine caused no change in the oxidation state of the Mn^{2+} and there was no crystal field effect felt by the ion(213) suggesting no direct interactions between the pyridine and inorganic layers exist (which is contrary to what occurred in the metal oxides). Overall upon intercalation, the crystal structure remains unchanged with only increases occurring in the *c*-axis direction. However, three distinct phases appear each owing its presence due

to the angle at the which pyridine in orientated within the interlayer spacing(214). This was extended to show that bipyridine could also be intercalated into $MnPS_3$ when protonated exchanging with the Mn^{2+} and intercalating into the interlayer spacing either in the planar or perpendicular orientation(215) with similar results as to the intercalation of the singular pyridinium ions. This two-phase appearance of either a planar or perpendicular orientated pyridine based molecule is further shown in substituted pyridines such as 4-aminopyridine which also undergoes ion-exchange when protonated (in this case with acetic acid)(216) where the planar orientation shows a net interlayer increase of 3.4Å while the 6.0Å for the perpendicular orientation.

In the case of both alkali-metal ions or pyridine, these intercalated materials are more often than not utilised as precursors for intercalation of more complex organic structures due to their potential conductive or chelating effects as was seen with the metal oxides.

1.5.3.3) Precursor Ion-Exchange Intercalation

The more complex substituted structure of stilbazolium based derivates, e.g. 4-[2-(4-dimethyl-aminophenyl)ethenyl]-1-methylpyridinium cation ($DAMS^+$), have been shown to intercalate in this fashion in aqueous conditions. $DAMS^+I^-$ is utilised with the $DAMS^+$ substituting for the precursor cation. $DAMS^+$ was exchanging for K^+(217,218) with the interlayer spacing increasing to 12.51Å suggesting that the rings were aligned perpendicular to the inorganic layers in a similar fashion as was seen with the oxide materials. The lattice parameters only changed in the direction associated with the interlayer spacing. This was further shown to also be the case when pyridinium ions were exchanged with the $DAMS^+$(219). This intercalation was confirmed with the IR which showed the characteristic peaks for $DAMS^+$ above 1000cm^{-1} and for the characteristic $CdPS_3$ the peak to split as mentioned previously confirming intercalation meanwhile for

the intercalation into $MnPS_3$ the peak splitting was shown to be three which appeared at 608cm^{-1}, 588cm^{-1} and 555cm^{-1}. The splitting of this peak corresponds to the presence of the interlamellar metal vacancies due to the ion-exchange that occurred. The UV-Visible spectra for both Mn and $CdPS_3$ intercalated $DAMS^+$ showed peaks at 585nm with a shoulder appearing at 540nm(217) and was further shown to be a broad band which may be contributing from the organic material(220). Furthermore, a range of substituted N-methylstilbazolium cations into $FePS_3$ showed an increase in the interlayer spacing to between 12-21Å further giving support to the perpendicular orientation of the aromatic rings as the interlayer spacing increased when larger groups were substituted on the aromatic rings(221). It was suggested here that the dipolar interactions between guest molecules due to the substituted groups allowed for the rings to lie parallel to one another while being perpendicular to the inorganic layers. However, when $MnPS_3$ has intercalated with 4-[4-(diethylamino)-R-styryl]-1-methylpyridinium (DEMS) cations, the absorption spectrum showed an intense charge-transfer band at 488nm which was concluded to be between the organic and inorganic components and appeared red-shifted in the solid state(222). The charge-transfer peaks in the absorption spectra of the DAMS (and their derivatives) was only occurring for the Mn and $CdPS_3$ intercalated compounds whereupon further deconvolution of the spectrum the first peak usually found ~500nm corresponded to pure MPS_3 phases whereas the red-shifted and narrower peaks was deemed to be due to the interacting molecular dipoles between the inorganic and organic components. This was shown to be contrary to $ZnPS_3$ intercalated materials were the UV-absorption spectra for the organic region correspond closely to the solution based spectra for the organic material showing no dipole-dipole interactions within the system(223–226). This extends beyond the DAMS based materials to other conjugated guests species such as triarylpyrylium cations(227), N-methylated pyridospiropyran (228) and 1-(N-methylpyridinio-4-yl)-2- (N-methylpyrrol-2-yl)ethane cations(229) intercalated under similar conditions.

Building on the intercalation of conjugated systems, conductive conjugated molecules and/or polymers have been shown to successfully be intercalated into the MPS_3 systems analogous to the metal oxide systems. Tetrathiafulvalene (TTF) salts have shown to successfully intercalate into the MPS_3 systems by exchange with K^+ or tetraethylammonium cations in $CdPS_3$, $MnPS_3$ and $FePS_3$ respectively(230,231). This produced an increased interlayer spacing of 12.15Å in the $CdPS_3$ and $MnPS_3$ composites (molar ratio of 0.42 TTF to 1 MPS_3) and 12.02Å in the $FePS_3$ (molar ratio of 0.18 TTF to 1 MPS_3) composite materials. Upon insertion of the organic cations, the conductivity of the composite materials increased. The $MnPS_3$-TTF composite showed a room temperature conductivity of 2.3 x 10^{-3} $\Omega^{-1}cm^{-1}$ increasing from $3x10^{-9}$ $\Omega^{-1}cm^{-1}$ for the $MnPS_3$ and $1x10^{-8}$ $\Omega^{-1}cm^{-1}$ for the $KMnPS_3$. Meanwhile, for the $FePS_3$ composite, the room temperature conductivity was reported to be ≈3 $\Omega^{-1}cm^{-1}$ and the conductivity was reported to increase with decreasing temperature indicating a metallic behaviour. It was concluded this increase in conductivity was due to the charge-transfer that would result in the mixed valency between the organic and inorganic species. Building on this the modified TTF, bis(ethylenedithio)- tetrathiafulvalene (BEDT-TTF) salts were shown to be more conducting than that for TTF alone (232,233). The room temperature conductivity of BEDT-TTF salt single crystals can reach up to 200 Scm^{-1}(234) allowing for the synthesis of potentially more conductive composite materials. BEDT-TTF can be intercalated into $MnPS_3$ by exchange with bpy and yields an expanded interlayer spacing of ~10.5Å with the overall conductivity being 10^5 times greater than that for pure $MnPS_3$ being in the same order of magnitude to that for the TTF composites(235,236). From EPR experiments it was in-fact deemed that the protonated form did intercalate between the layers and the synthesised composite's magnetic properties were neither similar to its intercalant nor similar to the pure $MnPS_3$(237). Furthermore, it was shown that the BEDT-TTF cations exchanged for 1,10-phenanthroline in $FePS_3$ with a net increase in the interlayer spacing of

4.0Å and was oriented parallel to the inorganic layers. However, the conductivity of the compressed pellet of the BEDT-TTF $FePS_3$ compound was shown to be ~10^{-7} Scm^{-1} which is in the same order of magnitude of the pristine $FePS_3$ (238). In this case, the parallel orientation of the organic intercalant may in fact not produce the dipole-dipole interaction required for sufficient charge transfer to occur.

Building upon this work a range of polymeric materials were shown to intercalate into the MPS_3 compounds which include the polyethylene oxide (PEO) and polyethylene glycol (PEG). It was shown that these, in fact, undergo partial exchange with K^+ and Na^+ in $MnPS_3$ and K^+ in $CdPS_3$(239). From a 2 molar ratio of the metal cations with the MPS_3 phase, upon intercalation of PEG the potassium and sodium content decreased to molar ratios of 0.21 and 0.38 respectively and for PEO decreased to 0.2 and 0.35 respectively in $MnPS_3$. For intercalation in $CdPS_3$, PEO and PEG intercalation resulted in a decrease of K^+ content to 0.27 for both PEO and PEG (from the initial 2 molar ratio of metal cations) while the interlayer spacing for both systems showed an increase to ~15Å. Furthermore, $NiPS_3$ shows similarities when intercalated with PEG as the interlayer spacing increases from 6.45Å to 14.98Å. The sodium content also decreased to approximately 0.3-0.5 in a molar ratio to the MPS_3(240). It could be suggested that complete exchange may not occur due to PEO and PEG polymers chelating and coordinating with the metal cations as was similarly seen in V_2O_5 and MoO_3. In the lithiated MPS_3 systems in which Li^+ are exchanged with PEO (and other polymer systems such as polypropylene oxide), it was shown that little lithium is lost but PEO is still intercalated into the system suggesting the same chelating effect as mentioned previously(241,242). Here it was shown that the interlayer spacing for the PEO intercalated material increased to 14.4-15.09Å and the ionic conductivity was that of $1.3x10^{-7}$ Scm^{-1} while the dc electronic conductivity is that $1x10^{-7}$ Scm^{-1} (determined from Nyquist diagrams). The overall electronic conductivity may be several orders of magnitude greater than the measured value due to the preferential

alignment of the layers to be perpendicular to that of the current path. These materials showed ohmic behaviour from the current-voltage measurements sweeping between the ranges of -1 to +1V. It was assumed that the electronic mobilities were higher than ionic mobilities and the electrodes are ohmic and therefore ionic contribution is blocked and the dominating contribution arrives from the electronic transport. The conductivities of these materials can be further improved when conductive polymers are introduced into the interlayer spacing. PANI was shown to intercalate and partially exchange with potassium in both $MnPS_3$ and $CdPS_3$(243,244). Upon intercalation, two conformations of PANI were found. In PANI intercalated $MnPS_3$ the interlayer spacing increased from 6.8Å to 14.42Å which corresponds to the helical chain conformation. Meanwhile, the $CdPS_3$ intercalated material showed an increase of 3.6Å to a spacing of 10.15Å which corresponds with the PANI chains orientated such that the phenyl rings are lying parallel to the inorganic sheets. In its neutral form, the conductivity was shown to be in the order of magnitude of 10^{-7} Scm^{-1} for both the Mn and Cd compounds. In its conductive emeraldine form, it is shown that this conductivity increases to between $2x10^{-5}$ and $6x10^{-5}$ Scm^{-1}. Furthermore, these materials showed photoconductive properties when the materials were pressed into cylindrical disks of 13mm diameter and 0.3mm thickness under 10^{-3} torr and were illuminated using a halogen lamp of 50 mW/cm^{-2}. In the case of the $MnPS_3$ intercalated material, under illumination, the current increased from ~$6.0x10^{-7}$ to ~$6.4x10^{-7}$ Scm^{-1}. Upon removal of the light source (after 180s) decay in the conductivity was observed with the current returning to its original conductivity after a further 200s. The same effect was seen for the $CdPS_3$ intercalated material. Here the conductivity increased under illumination from ~$8.8x10^{-7}$ to ~$10.4x10^{-7}$ Scm^{-1} and after removal of the light source (after 80s) the decay in the conductivity was observed and the conductivity returned to its initial value. This was attributed to the MPS_3 phase of the material the illumination causes the generation of free holes in the P-S hybrid valence band and the electrons in the metal 3d e_g

states. The $P3p_z$ band then acts as the recombination level for the holes and electrons. In comparison, the conductivity of the emeraldine intercalated MPS_3 showed greater conductivity than that of pure MPS_3 but lower than that of the pure bulk emeraldine polymer. It is considered that the shorter chain lengths and the intercalation of the polymer (into the insulating or poor semiconducting inorganic phase) contributes to an overall decrease in the conductivity of the material. However, the intercalation of the polymer material further caused metallic vacancies to form in the host lattice which may improve the conductivity of the overall material considering the layers tendencies to lie perpendicular to the dc current flow. The main drawback of the ion-exchange method, in general, is the multiple steps that are required to intercalate the more interesting organic guests, these steps can cause greater defects in the overall crystalline structure (i.e. step defects) which are not as easily seen in the XRD data that may cause decreased or hinder conductive and/or other properties such as providing sites for current leakages (series or shunt resistance sites). However, from a photovoltaic perspective, these defects may allow for extended lifetimes of excitons being formed at a device junction enhancing the photoconductive properties of the composite material.

1.5.3.4) Direct Intercalation

One simple method for overcoming such problems is to directly intercalate organic materials into the interlayer spacing in a number of ways. This method does not change the overall stoichiometry of the inorganic layers and allows for organic materials to be directly inserted into the layers. One simple way is to simply immerse the inorganic crystals in a solution of the organic materials that contain a high excess of the desired guest species. This was shown to work well for alkylamines(245) where $MgPS_3$, $ZnPS_3$ and $MnPS_3$ crystals were placed in 10M alkylamine solutions. The interlayer spacing increase was independent on the alkylamine chains and increased for all three to ~10.5Å and it was

proposed that there was a double layer structure forming where two chains lined up parallel to each other but perpendicular to the inorganic layers such that the amine groups appeared closest to the sulphide layer. This was further shown to be the case for metallocenes where only cobaltocene complexes showed intercalation into $MnPS_3$, $ZnPS_3$, $FePS_3$ and $NiPS_3$ with a net increase in the interlayer spacing of 5.32-5.96Å. These were achieved in a similar fashion to the alkylamines where excess cobaltocene was dissolved in toluene and then reacted with the inorganic host(246). After the intercalation of cobaltocene into $CdPS_3$ the overall bandgap of the material was smaller than that of pure $CdPS_3$ while ESR measurements showed that two phases of cobaltocene were present, neutral and cationic(247). It was suggested that the direct intercalation causes the oxidation of the neutral cobaltocene complexes for example in the $CdPS_3$ powder as the oxidation can be catalysed by surface states generated by the formation of steps and/or other surface defects. Common methods for the intercalation of conjugated organic species directly can involve vapour intercalation as seen with the intercalation of pyridine into $CdPS_3$(248). Here, $CdPS_3$ and a stoichiometric amount of pyridine were placed in an evacuated ampoule and heated to the boiling point of pyridine. It was seen that the crystal size affects the kinetics (and thermodynamics) of intercalation. The flexibility of smaller crystals and the rigidity as crystals become larger leads to easier interlayer expansion in smaller crystals as they a less hindered by the bulk crystal. These expansions in smaller crystals result is less crystal strain throughout bulk material and intercalation and intercalant permeation (through diffusion) occurring more efficiently. It was further shown that when pyridine was intercalated into $CdPS_3$, the changes to the photoluminescence and emission peaks of $CdPS_3$ were dependant on the water content present during the intercalation process(201). The maximum of the excitation peak shifts by ~0.5eV to lower energy while the original photoluminescence bands of the host are no longer present in the spectrum. This shows that the intercalated guest had some electronic or charge transfer based interaction with the

inorganic host. Pyridine further also intercalates into $MnPS_3$ using the vapour based intercalation method(249). Expanding on this the pyridine dimer, 2,2'-bipyridine (bpy) molecules also undergo vapour intercalation. It was shown that in $NiPS_3$ the interlayer expanded to 9.83Å(250) while in $MnPS_3$ the interlayer expansion was that of 15.769Å and in both cases the crystalline structure of the material was shown to be well maintained. This was due to the bpy being intercalated such that it lies approximately perpendicular to the inorganic planes. The conductivity of the $NiPS_3$ bpy compound was shown to be that of $4.5x10^{-13}$ Scm^{-1}. As with the ion-exchange mechanism, by intercalating larger (or more conjugated organic) species and polymers into the interlayer spacing may improve the desired properties of the composite materials such as increased conductivity. 1,10-phenanthroline which orientated itself in a similar manner to the bpy molecule when intercalated with an expanded interlayer spacing of ~15.12Å in $MnPS_3$ (net increase of ~8.6Å). The $DAMS^+$ cations also intercalated in such a manner in which the interlayer spacing increases to 12.75Å where it was shown that unlike the bpy and the 1,10-phenanthroline the $DAMS^+$ molecules form bilayer like structures lying parallel to one another and to the inorganic sheets.

1.5.3.5) Exfoliation – Restacking Intercalation

Another useful method of intercalation is the exfoliation and re-stacking (analogous to that of V_2O_5 and MoO_3) of the MPS_3 phase around larger more complex organic materials such as dye like porphyrin-based salt, meso-tetrakis(N-methylpyridinium-4-yl)porphyrin (H_2T_4) intercalated into $MnPS_3$(251). The re-stacking proved to yield a highly ordered crystalline phase with an expanded interlayer spacing of 12.1Å. This increase in size is smaller than that of the H_2T_4 length dimension (17.5Å, with H_2T_4 molecular dimensions being 17.5Å x 17.5Å x 4Å) and hence it is not expected that the H_2T_4 lies perpendicular to the $MnPS_3$

layers. The XPS data showed a strong interaction between the H_2T_4 material and the inorganic layers which caused the H_2T_4 to adopt the flattened orientation between the layers. The exfoliation and re-stacking are particularly useful when intercalating high molecular weight polymer materials such as LPEI and PEO(183,252) into $MnPS_3$ and $CdPS_3$. The LPEI intercalated increasing the interlayer spacing to that of ~10.5Å suggesting a helical-like structure. Whereas the PEO intercalated via the same method showing an increase to between 15.2-15.9Å. The TGA showed that the polymer material degraded between 241-377°C in $MnPS_3$ and 221-377°C in $CdPS_3$ with the overall material showing a gradual mass loss over these ranges corresponded into a 17% and 13% mass loss respectively.

Melt intercalation of the high molecular weight of PEO into Mn and $CdPS_3$ further shows similar results(253). PEO, LPEI and polyvinylpyrrolidone (PVP) can also be directly intercalated using the template preparation in $NiPS_3$(254). Although there was a similar expanded interlayer peak in the XRD data as seen in previous cases corresponding to successful intercalation, the broadening of all peaks showed random stacking of the inorganic layers in all axial directions around the polymer chains similar to the restacking synthesis in V_2O_5 and MoO_3. The intercalation of spiropyran on the other hand in $MnPS_3$ instead took advantage of the photochromic properties of the organic guest(255). This was synthesised using a direct solution based method where a surfactant was used to maintain small micelle-like structures of the layered $MnPS_3$ before the guest was introduced and the surfactant removed allowing for the layers to re-stack around the organic guest species. However, unlike previous methods, this produced a very broad peak around 14Å and strong crystalline phases corresponding to the pure $MnPS_3$. This suggests that the re-stacking is disordered along the direction of the interlayer spacing and/or there is a mix of amorphous poorly ordered material and highly crystalline pure host. The produced nanoparticles were around 10-20nm in size and agglomerated in hyperbranched structures.

This composite material further showed photochromic activities showing that the guest species induces photoactivity in the material. Prior to any irradiation, the material was pale yellow and no band above 350nm was shown in its spectrum suggesting that the organic guest was in its closed non-photochromic form. However, upon irradiation at 365nm for 10 minutes the material rapidly turned violet and a new peak appearing around 560nm grew and was observed corresponding to the organic open form. When irradiated once again at 550nm this colouration disappeared and the peak at 550nm showed rapid decay hence the open form returned to the closed form. This further showed that under irradiation these organic-inorganic composites can be air stable.

Overall, the most commonly used method for intercalation into V_2O_5 includes direct (hydrothermal and redox methods) while the preferred methodology for intercalation organic materials into MoO_3 either hydrothermal or ion-exchange methods. For both oxide materials, these methods yield the composite materials with the most structural integrity as well as a wider variety of organic guests. Due to the redox intercalation of lithium or sodium into the metal oxides, the layers exhibit a significant increase in the conductivity of the layers as well as the highly well-maintained crystallinity and this increased conductivity is further shown upon exchange with organic species particularly polymer and organic semiconductors. For MPS_3 it was shown that the ion-exchange method yields the best control of the overall structural integrity of the nanocomposite materials while direct intercalation yields poor conductivity and less crystalline structure along the *c*-axis.

Table 1.8 - The advantages and disadvantages of the different intercalation methods for MPS_3 intercalation

Intercalation Method	Advantages	Disadvantages
Host Precursor		
Small Cation Intercalation	• Used as precursors for organic guest intercalation • Maintains high control of the host structural integrity • Intercalation is reversible with little effect on the host structural integrity. • Organic precursors can be used which are intercalated as cations	• Affects stoichiometry of host due to the ion-exchange mechanism. The degree of change in the host stoichiometry can have an effect on the desired property of the final material.
Precursor Based Intercalation		
Ion – Exchange	• A wide range of guest species can be used - Small and large organic guests can be intercalated including polymers (including high molecular weight polymers). • Can produce materials with significantly higher	• Overall, there is a range of conductivities present which is dependent on the nature of the guest material. • Ion-exchange can cause further effects on the host's stoichiometry

	conductivity than the host • Can be carried out in non-organic solvent/aqueous conditions. • Medium to high structural integrity of the host maintained. • In some cases, initial ion-exchange can lead to chelation of the polymer with remaining ions, good for certain applications. • The host can be prepared as a single crystal for intercalation	• Can cause crystal defects such as step defects which are difficult to see in XRD which can lead to a negative effect on the conductivity.
Exfoliation – Restacking	• A wide range of guest species can be used - Small and large organic guests can be intercalated including polymers (and very high molecular weight polymers) • Can show high control of the host structural integrity	• Although high structural integrity of the host can be achieved, overall, however, the degree of control is difficult and a range of structural integrities can be possible from very low to high. This occurs on a case to case basis. • This method usually exhibits little to no change in conductivity from the host material.

Non-Precursor Based Intercalation		
Direct	• A wide range of guest species can be used - Small and large organic guests can be intercalated including polymers (and very high molecular weight polymers) • One-pot synthesis • Good for intercalating single crystals • Useful in the use of guests which are non-polar and insoluble in polar solvents (such as water) • Medium to high structural integrity of the host. • Maintains host stoichiometry	• Requires a high excess of guest species in respect to the host material • Crystal size can have an effect on the intercalation energetics • Efficiency of intercalation is dependent on the specific MPS_3 host in question • Electrical and photoinduced properties are dependent on the nature of the organic.

Table 1.9 - Intercalation method summary

	Ion-Exchange	Exfoliation - Restacking	Direct
Precursor	✓	✓	
Non-Precursor			✓
Small guest intercalation	✓	✓	✓
Large guest intercalation (e.g. polymers)	✓	✓	✓
Intercalation of very high molecular weight polymers	✓	✓	✓
One-pot synthesis			✓
Host structural integrity	Medium to High	Very low to High	Medium to high
Aqueous conditions	✓		
Single Crystal Intercalation	✓		✓
Single Crystal Defects Present	✓		✓
High conductivity	✓		✓
Low conductivity		✓	
Properties dependant on guest	✓	✓	✓
Affects host stoichiometry	✓		✓
Synthesis carried out in air		✓	

Table 1.10 – Polymer materials and their intercalation method/s in MPS_3

Polymer	Structure	Intercalation Method/s
Multi-Method Intercalation		
PEO	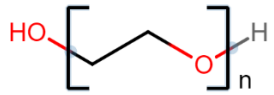	Ion-exchange and Exfoliation-restacking
Organic Cation Precursors		
Bis(cyclopentadienyl)cobalt(II) (Cobaltocene)	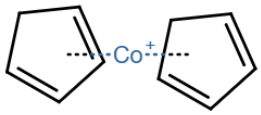	
Nickel (II) cyclopolyamine	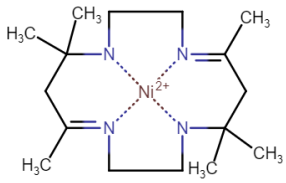	
$Cr(en)_3$	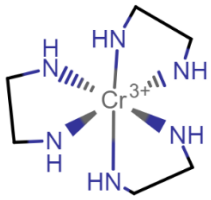	
$Ru(bpy)_3$	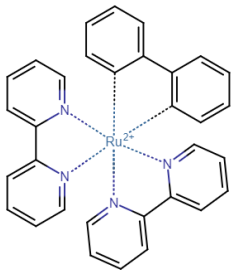	
Cp(disphos)COFe	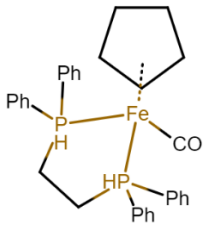	

4,4'-bipyridine	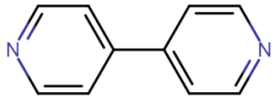
Ion-Exchange	
DAMS$^+$	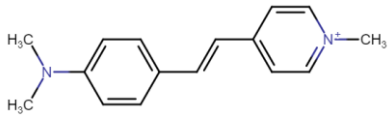
Substituted N-methylstilbazolium	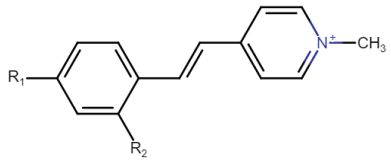
DEMS$^+$	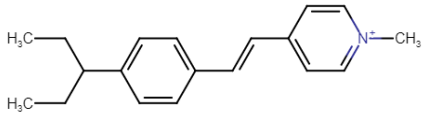
N-methylated pyrisdospiropyran	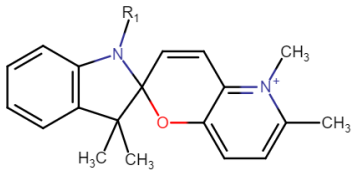
1-(N-methylpyridino-4-yl)2-(N-methylpyrrol-2-yl)ethane	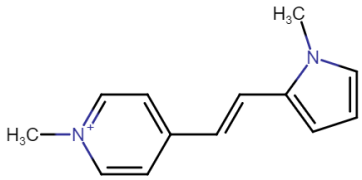
TTF	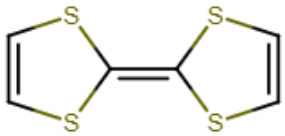
BEDT-TTF	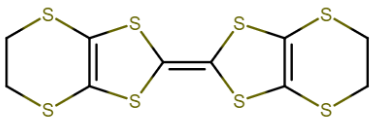

PEO	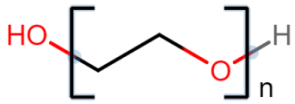
PEG	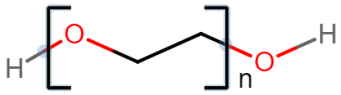
PPO	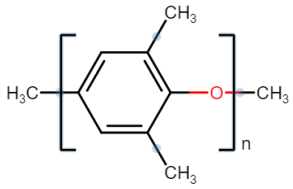
Polyaniline	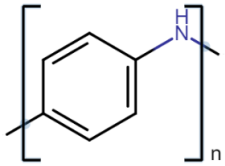
Direct Intercalation	
Alkylamines	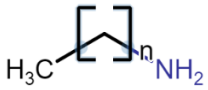
Pyridine	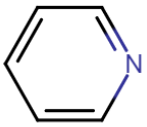
2,2'-Bipyridine	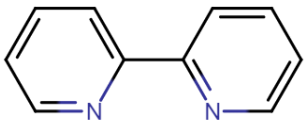
Exfoliation - Restacking	
H_2T_2	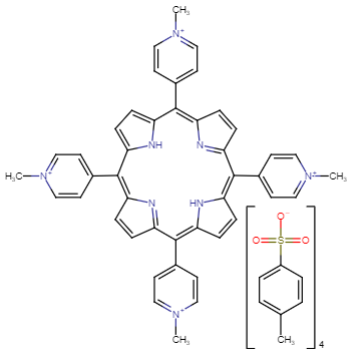

LPEI	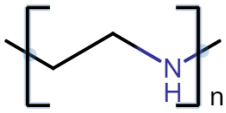
PEO	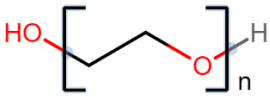
PVP	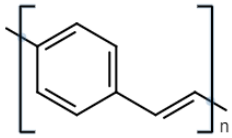

1.5.4) Summary

The application of intercalation chemistry has yielded the synthesis of a wide range of organic-inorganic nanocomposite materials by taking advantage of a variety of synthetic techniques. It is apparent that the major focus of the application of these materials is directed towards battery (e.g. as lithium-ion battery cathode materials) and sensor-based applications (such as the applications in VOC sensors). The applications of organic-inorganic nanocomposites for the application in photovoltaic and/or optoelectronic systems is an area of little research and development for the application of these materials has yet to be fully realised due to the range of host and guest combinations possible. This thesis examines the feasibility of these nanocomposite systems for photoconductive and photovoltaic applications and presents a proof-of-concept that these materials provide a worthwhile area of research in photovoltaic and optoelectronic technologies.

For all three host inorganic materials, the most common intercalation syntheses are Exfoliation – Restacking, Ion-exchange and Direct methods. Exfoliation – Restacking and Ion-exchange yield minimal control over the long-range structural integrity of the host after intercalation (primarily in the direction perpendicular to the host layers, the c-axial direction) whereas Direct methods provide a better degree of control. The use of a precursor in Ion-exchange intercalation requires the use of the monomer salt. For V_2O_5, redox and layer-by-layer intercalation have shown to be successful in the intercalation of organic guest species. Redox intercalation only provides control over the structural integrity on a case-by-case basis whereas layer-by-layer intercalation is limited by the solubility of the bulk polymer.

Based on this, as well as the ease of lithium intercalation into V_2O_5 and MoO_3, Ion-exchange intercalation was the method chosen to synthesise the nanocomposite materials. Although for many applications structural integrity is required, in a photovoltaic or optoelectronic application any defects in the c-axial direction may allow for

recombination lifetimes of excitons to be extended allowing charge carriers to diffuse throughout the material and be collected at the device electrodes. Furthermore, the choice of intercalants ranged from previously synthesised materials (such as EDOT intercalation into V_2O_5) to the novel organic intercalants: aminoquinoline, amino phenylpyridine, aminothiazole, diaminopyridines into both oxide hosts. A strategy for the redox intercalation of emeraldine into the interlayer of V_2O_5 by utilising a mix of neutral and salt aniline forms is also explored in this thesis. $ZnPS_3$ was selected as the MPS_3 material of choice due to its wide band-gap and novelty of organic intercalation into the $ZnPS_3$ systems where ion-exchange with a metal cation was also the choice of method for the same reasons as described for the metal oxide hosts.

2. Aims

The aims of this research are to;

1) Seek improvements in the performance of existing conducting polymers as electronic device materials by:
    a. Selecting inorganic materials as favourable host cavities in which to grow or contain conjugated polymers to produce semiconducting nanocomposites
    b. Using chemically modified organic monomers to improve the molecular organisation and energy-conversion efficiency of the semiconducting components
2) To assess the effectiveness of the nanocomposites in the interconversion of optical and electrical energy as electronic device materials.

3) Methodology

The synthesis and analytical measurements described in this chapter were performed by the author at Kingston University with only the XPS experiments conducted by Dr Joe Bear at University College London (UCL).

3.1) Nanocomposite Synthesis

3.1.1) V_2O_5 nanocomposites synthesis

3.1.1.1) Emeraldine V_2O_5 (V_2O_5/AnAn$^+$)

In a typical reaction, to a solution of Aniline (Sigma-Aldrich) (0.0256g, 2.7491x10^{-4} moles) and Aniline Sulfate (Sigma-Aldrich) (0.03908g, 1.375x10^{-4} moles) in distilled water (100mL), V_2O_5 (Sigma-Aldrich) (0.5g, 2.7491x10^{-3} moles). This yielded a molar ratio of 1:0.2 between V_2O_5 and total aniline content (aniline and aniline sulfate combined). The reaction was refluxed for 24hours with the reaction mixture turning green upon completion. The reaction was then centrifuged to obtain the dark green/black solid. This was followed by washing with copious amounts of distilled water until the supernatant liquid turned colourless. This resulting solid was then dried under vacuum at 60°C for 12hours with a yield of 0.47g with a calculated empirical formula AnAn$^+_{0.22}V_2O_5$ (see section 4.1.1.3).

3.1.1.2) 2-amino-5-Phenylpyridine (2A5PhPyr) V_2O_5 (V_2O_5/2A5PhPyr) – Acid-Base reaction

In a typical reaction, to a solution of 2A5PhPyr (Fluorochem) (2.340g, 0.0137 moles) dissolved in distilled water (100mL) V_2O_5 fine power (Sigma-Aldrich) (0.5g, 0.002749 moles) was added This yielded a molar ratio of 1:5 between V_2O_5 and 2A5PhPyr. The

reaction was refluxed for 24hours with the reaction mixture turning a very pale red colour and was centrifuged in order to collect the dark red solid. This was followed by washing with copious amounts of water until the supernatant liquid was colourless. The solid was dried for 12hours at 60°C under vacuum with a yield of 0.47g with a calculated empirical formula 2A5PhPyr$_{0.18}$V$_2$O$_5$ (see section 4.1.1.3)

3.1.1.3) 3,4-ethylenedioxythiophene (EDOT) V_2O_5 (V_2O_5/EDOT)

In a typical reaction, to a solution of EDOT (Sigma-Aldrich) (0.0782g, 5.498x10^{-4} moles) dissolved in distilled water (100mL) V_2O_5 fine power (Sigma-Aldrich) (0.5g, 0.002749 moles) was added. The reaction was refluxed for 24hours with the reaction mixture turning a very pale yellow colour and was centrifuged in order to collect the dark red solid. This was followed by washing with copious amounts of water until the supernatant liquid was colourless. The solid was dried for 12hours at 60°C under vacuum with a yield of 0.48g with a calculated empirical formula EDOT$_{0.23}$V$_2$O$_5$ (see section 4.1.1.3)

3.1.1.4) N-BuLi V_2O_5 ($Li_xV_2O_5$)

In a typical reaction, V_2O_5 fine power (0.5g, 0.002749 moles) was placed in dry hexane (18ml). The mixture was then evacuated and purged with dry nitrogen several times. To this mixture, 1.6M n-BuLi in hexane (6mL, 9.6 x 10^{-3} moles) was then added to the mixture. The reaction was carried out under a nitrogen atmosphere and stirred for 2hours at room temperature. Upon addition of the n-BuLi, the reaction mixture immediately turned black. After 2hours the reaction was quenched with methanol and centrifuged to obtain a black solid. The solid was washed three times with dry hexane and dried in a vacuum oven with to obtain a yield of 0.48g.

3.1.1.5) O-phenylenediamine hydrochloride V_2O_5 (V_2O_5/PDA)

In a typical reaction, PDA (Sigma-Aldirch) (5.6442g, 0.05219 moles) was added to a 150mL HCl solution (0.2M). The solution was purged with nitrogen for 20min before $Li_xV_2O_5$ precursor (0.48g) was added. The reaction was carried out under a nitrogen atmosphere and left for 24hours at room temperature. The reaction mixture turned deep red and was centrifuged in order to collect the black solid. This was followed by washing with copious amounts of water until the supernatant liquid was no longer red. The solid was dried for 12hours at 60°C under vacuum with a yield of 0.41g with a calculated empirical formula $PDA_{0.26}V_2O_5$ (see section 4.1.1.3)

3.1.1.6) 2-amino-5-phenylpyridine V_2O_5 (LiV_2O_5/2A5PhPyr) Ion-Exchange

In a typical reaction, 2A5PhPyr (Fluorochem) (5.1063g, 0.030 moles) was added to a 150mL HCl solution (0.2M). The solution was purged with nitrogen for 20min before $Li_xV_2O_5$ precursor (0.48g) was added. The reaction was carried out under a nitrogen atmosphere and left for 24hours at room temperature. The reaction mixture turned a pale red and was centrifuged in order to collect the black solid. This was followed by washing with copious amounts of water until the supernatant liquid was colourless. The solid was dried for 12hours at 60°C under vacuum with a yield of 0.41g with a calculated empirical formula $2A5PhPyr_{0.23}V_2O_5$ (see section 4.1.1.3)

3.1.1.7) 5-aminoquinoline (5AQ) V_2O_5 (V_2O_5/5AQ)

In a typical reaction, 5AQ (Fluorochem) (4.3251g, 0.030moles) was added to a 150mL HCl solution (0.2M). The solution was purged with nitrogen for 20min before $Li_xV_2O_5$ precursor (0.48g) was added. The reaction was carried out under a nitrogen atmosphere and left for 24hours at room temperature. The reaction mixture turned a very deep red colour and was centrifuged in order to collect the black solid. This was followed by

washing with copious amounts of water until the supernatant liquid was colourless. The solid was dried for 12hours at 60°C under vacuum with a yield of 0.43g with a calculated empirical formula $5AQ_{0.26}V_2O_5$ (see section 4.1.1.3)

3.1.1.8) Phenylene-1,4-diamine (1,4PDA)/hydroquinone (HQ) V_2O_5 (V_2O_5/1,4PDA-HQ)

In a typical reaction, to a solution of phenylene-1,4-diamine (Sigma-Aldrich) (2.7282g, 0.015 moles) and hydroquinone (Sigma-Aldrich) (1.65165g, 0.015 moles) in a 150mL solution of HCl (0.2M). The solution was purged with dry nitrogen for 20min before $Li_xV_2O_5$ precursor (0.48g) was added. The reaction was carried out under a nitrogen atmosphere and left for 24hours at room temperature. The reaction mixture turned a very pale red colour and was centrifuged in order to collect the black solid. This was followed by washing with copious amounts of water until the supernatant liquid was colourless. The solid was dried for 12hours at 60°C under vacuum with a yield of 0.42g with a calculated empirical formula $(1,4PDA\text{-}HQ)_{0.19}V_2O_5$ (see section 4.1.1.3).

3.1.2) MoO_3 nanocomposites synthesis

3.1.2.1) Aniline MoO_3 recrystallisation (MoO_3/An)

In a typical reaction, to a solution of MoO_3 (Sigma-Aldrich) (0.2g, 1.3895×10^{-3} moles) dissolved in 500mL of water (4 weeks) aniline (Sigma-Aldrich) (0.0259g, 2.7789×10^{-4} moles) was added. The solution was purged with nitrogen for 30mins before the water was removed under reduced pressure at 70°C. The resulting solid was very pale pink in colour and washed with copious amounts of water to remove any excess aniline from the surface of the solid. The resulting solid was then added to a solution of ammonium persulfate (Sigma-Alrich) (0.6341g, 2.7789×10^{-3} moles) dissolved in 100mL of distilled water for 12 hours. The resulting red solid was washed with copious amounts of water before being dried for a further 12 hours at 60°C under vacuum with a yield of 0.15g with a calculated empirical formula $An_{0.19}MoO_3$ (see section 4.1.2.3).

3.1.2.2) N-BuLi MoO_3 (Li_xMoO_3)

In a typical reaction, MoO_3 (Sigma-Aldrich) fine power (0.5g, 3.4737×10^{-3} moles) was placed in dry hexane (Sigma-Aldrich) (21ml). The mixture was then evacuated and purged with dry nitrogen several times. To this mixture, 1.6M n-BuLi (Sigma-Aldrich) in hexane (3mL) was then added to the mixture. The reaction was carried out under a nitrogen atmosphere and stirred for 2 hours at room temperature. Upon addition of the n-BuLi, the reaction mixture immediately turned a deep dark blue/black colour. After 2 hours the reaction was quenched with methanol and centrifuged to obtain a deep dark blue/black solid. The solid was washed three times with dry hexane and dried in a vacuum oven to obtain a yield of 0.49g.

3.1.2.3) PDA MoO_3 (MoO_3/PDA)

In a typical reaction, PDA (Sigma-Aldrich) (3.6813g, 0.03404moles) was added to a 150mL HCl solution (0.2M). The solution was purged with nitrogen for 20min before Li_xMoO_3 precursor (0.49g) was added. The reaction was carried out under a nitrogen atmosphere and left for 24 hours at room temperature. The reaction mixture turned deep red and was centrifuged in order to collect the black solid. This was followed by washing with copious amounts of water until the supernatant liquid was no longer red. The solid was dried for 12hours at 60°C under vacuum with a yield of 0.44g with a calculated empirical formula $PDA_{0.2}MoO_3$ (see section 4.1.2.3).

3.1.2.4) 2A5PhPyr MoO_3 (MoO_3/2A5PhPyr)

In a typical reaction, 2A5PhPyr (Fluorochem) (5.1063g, 0.030moles) was added to a 150mL HCl solution (0.2M). The solution was purged with nitrogen for 20min before Li_xMoO_3 precursor (0.49g) was added. The reaction was carried out under a nitrogen atmosphere and left for 24 hours at room temperature. The reaction mixture a pale red colour and was centrifuged in order to collect the black solid. This was followed by washing with copious amounts of water until the supernatant liquid was no longer pale red. The solid was dried for 12 hours at 60°C under vacuum with a yield of 0.45g with a calculated empirical formula $2A5PhPyr_{0.18}MoO_3$ (see section 4.1.2.3).

3.1.2.5) 2-Aminothiazole (2AmThia) MoO_3 (MoO_3/2AmThia)

In a typical reaction, 2AmThia (Fluorochem) (3.0042g, 0.030moles) was added to a 150mL HCl solution (0.2M). The solution was purged with nitrogen for 20min before Li_xMoO_3 precursor (0.49g) was added. The reaction was carried out under a nitrogen atmosphere and left for 24 hours at room temperature. The reaction mixture turned a very pale yellow colour and was centrifuged in order to collect the black solid. This was

followed by washing with copious amounts of water until the supernatant liquid was colourless. The solid was dried for 12 hours at 60°C under vacuum with a yield of 0.46g with a calculated empirical formula $2AmThia_{0.23}MoO_3$ (see section 4.1.2.3).

3.1.2.6) 5AQ MoO_3 (MoO_3/5AQ)

In a typical reaction, 5AQ (Fluorochem) (4.3251g, 0.030moles) was added to a 150mL HCl solution (0.2M). The solution was purged with nitrogen for 20min before Li_xMoO_3 precursor (0.48g) was added. The reaction was carried out under a nitrogen atmosphere and left for 24 hours at room temperature. The reaction mixture turned a very deep red colour and was centrifuged in order to collect the black solid. This was followed by washing with copious amounts of water until the supernatant liquid was colourless. The solid was dried for 12 hours at 60°C under vacuum with a yield of 0.43g with a calculated empirical formula $5AQ_{0.17}MoO_3$ (see section 4.1.2.3).

3.1.3) MPS_3 nanocomposites synthesis

3.1.3.1) $ZnPS_3$

Crystalline $ZnPS_3$ was synthesised in an evacuated ampoule at high temperature (450-490^oC temperature gradient was used) by a literature method(256) from stoichiometric amounts of Zinc sulphide (ZnS) (Sigma-Aldrich), red phosphorus (Sigma-Aldrich) and sulphur (Sigma-Aldrich) for 1 week. The resulting grey-white crystalline material was then washed with 0.1M HCl, water and finally acetone before being dried under vacuum at 60^oC for three hours. The dried product was then washed with copious amounts of xylene before being dried once again at 100^oC under vacuum for 12 hours.

3.1.3.2) Magnesium $ZnPS_3$ (Mg_xZnPS_3)

$ZnPS_3$ (200mg, 1.04mmol) was added to a 10:1 molar ratio of aqueous magnesium chloride solution in distilled water (60mL). The mixture was purged with nitrogen and left stirring for 4 weeks under a nitrogen atmosphere. The temperature was maintained between 80-100^oC during the reaction period. The resulting grey-white product was washed with distilled water before being collected by centrifugation and dried under vacuum at 60^oC for 12 hours. The colour of the material remained grey-white throughout. A yield of 192 mg was obtained with a calculated empirical formula $Mg_{0.18}Zn_{0.66}P_1S_{2.65}$ (see section 4.1.3.3).

3.1.3.3) PDA $ZnPS_3$ ($ZnPS_3$/PDA)

PDA (Sigma-Aldrich) (1.6368g, 15.14mmol) was added to a 0.2M HCl solution (90mL). The solution turned a pale red colour and was purged with nitrogen for 30mins. The magnesium precursor, $MgZnPS_3$, (0.1155g) was then added to the mixture and the reaction was left stirring for 3 days under a nitrogen atmosphere at room temperature. The grey-

white solid turned pale red/pink immediately upon addition with the PDA solution turning red. The pale red/pink product was washed with copious distilled water until the supernatant liquid was colourless and the product was then collected by centrifugation and dried under vacuum at 60°C overnight. The colour of the resultant dried material was pale red/pink. The dried product was then reacted with a 1:1 molar ratio of ammonium persulfate solution (60mL) for 1 day. The product remained pale red/pink in colour was washed with copious amounts of distilled water before being collected centrifugation. The resulting pellet was then dried under vacuum at 60°C for 12 hours $PDA_{0.1}Zn_{0.53}P_1S_{2.24}$ (see section 4.1.3.3).

3.2) Nanocomposite Characterisation

3.2.1) X-Ray Diffraction

X-ray Diffraction was carried on a Bruker-AXS D8 Advance instrument with Cu Kα radiation (λ = 1.504Å) and all samples were ground using pestle and mortar beforehand. For the $ZnPS_3$, $MgZnPS_3$ and $ZnPS_3$/PDA compounds, the samples were mounted on double-sided adhesive tape due to insufficient amount of material to occupy the complete area of the sample holder.

3.2.2) ATR-IR and Raman Spectroscopy

ATR-IR was carried out on all samples which had been pre-ground using pestle and mortar using a Nicolet iS5 spectrometer with an ID1 transmission attachment with 16 scans over the range of 650 cm^{-1} to 4000 cm^{-1}.

Raman Spectroscopy was carried out on a Renishaw InVia Raman Microscope with WiRE 3.3 software and Renishaw MS20 encoded mechanical stage. An argon 514 nm laser was used and it was found the optimum laser power for the experiment to be 1%.

3.2.3) Thermogravimetric Analysis (TGA) and Inductively Coupled Plasma-Atomic Emission spectroscopy (ICP-AES)

TGA experiments were carried out on a Mettler Toledo at a rate of 12 $^{o}Cmin^{-1}$ between the temperatures of 25°C – 600°C under a nitrogen atmosphere.

For ICP-AES (ULTIMA 2C, Jobin Yvon Horiba) the vanadium, molybdenum and zinc content were quantified in triplicate. For determination of the V_2O_5 and MoO_3 nanocomposite stoichiometries, 0.001g of sample were added to 10 mL of ≥69% HNO_3. Digestion took place at room temperature and after digestion the digested solutions were diluted to 7% HNO_3. From the ICP-AES the stoichiometry was calculated by determining the total vanadium content in the digested nanocomposite sample (assuming the stoichiometry of the vanadium host to be V_2O_5) and comparing this to the theoretical maximum vanadium content if no organic intercalant was present (which was the total vanadium content measured in the digested pristine V_2O_5 sample). It is assumed that there may be undigested sample and the theoretical maximum vanadium content is the vanadium content detected in the pristine host. This is, therefore, the maximum vanadium content possible for detection in all samples. The difference in vanadium content was concluded to arise due to the presence of the organic guest. For determination of the $ZnPS_3$ nanocomposite stoichiometries, 0.001g of sample were added to 10 mL of neat aqua regia. After digestion the digested solutions were further diluted 10 fold. The stoichiometry was calculated as described for the V_2O_5 and MoO_3 samples where the total zinc content for the pristine host was taken as the maximum zinc content possible for detection in all digested samples.

3.2.4) Optical Spectroscopy

UV-Visible reflectance spectroscopy (Agilent Technologies Cary 7000, Cary series UV-Vis-NIR spectrophotometer using the integrating sphere attachment) was carried out on all samples which were pre-ground using a pestle and mortar. The samples were deposited (spun-coated) onto a glass slide and placed in the beam path.

3.2.5) X-ray Photoelectron Spectroscopy (XPS)

XPS measurements were carried on a Thermo Scientific Kα spectrometer using monochromated Al Kα radiation. The instrument was calibrated using carbon (C1s) binding energy, 284.8 eV. Survey scans were collected in the binding energy range of 100 eV to 1500 eV. High-resolution peaks were used for the principal peaks of V(2p), O(1s) and Li(1s). The high-resolution peaks were fitted using CASA XPS software with Shirley backgrounds.

3.2.6) Electron Spin Resonance (ESR)

ESR spectroscopy (Bruker active spectrum micro ESR) was carried out on all samples which were pre-ground using pestle and mortar. The spectrometer was calibrated using a DPPH standard with a calibration error of the DPPH g-factor value of ±0.0002 for all samples. ~0.07g of sample was placed in a melting point tube (which was pre-scanned to ensure no peaks were present), the melting point tube was then placed in the main ESR tube and inserted into the ESR spectrometer cavity.

3.3) Electrical and Device Measurements

3.3.1) Room Temperature Conductivity

Room temperature conductivity was carried out using the four-probe method Van der Pauw method (257). The polycrystalline and powdered materials were pressed into disks (13mm diameter). The disks were placed in a PTFE cell and four copper electrodes were spring-loaded and placed around the perimeter of the sample to make the four-probe measurements. A digital micrometre was used to determine the sample thickness and a Keithley 195 current source and Keithley 197 electrometer were used to make the electrical measurements.

3.3.2) Seebeck Coefficient

All Seebeck coefficient measurements were measured using an in house built apparatus. For samples with sufficient enough material, thin pellets were pressed for the determination of the Seebeck coefficient. Two copper electrodes were placed across from one another on the pellet surface. A wire connected to an external power source was wrapped around one of the copper electrodes and a thermocouple. A voltage was passed through the wire coil and the temperature measured using the thermocouple after the temperature of the electrode and sample had equilibrated. Figure 3.1 diagrammatically shows the Seebeck coefficient set-up.

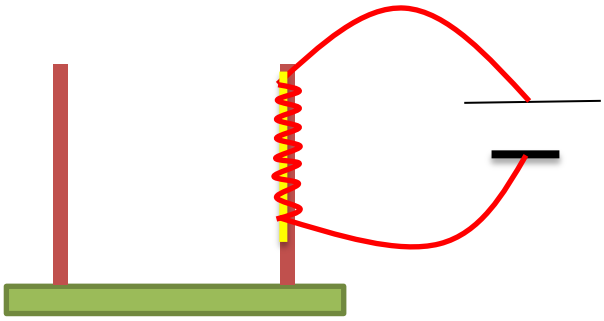

Figure 3.1 – The schematics of the experimental setup to measure the Seebeck coefficient where the copper electrodes (dark red) are placed on the sample (green) pellet surface. One copper electrode is attached to a thermocouple (yellow) to measure the temperature when a voltage is applied through a wire (red).

3.3.3) Dielectric Constant

All dielectric constant measurements were carried out using the Leader LCR-745G capacitance bridge, which was zeroed with only the connecting leads attached. For samples with sufficient enough material, a known amount of material was pressed into sufficiently thin pellets of known dimensions. The pellet was placed between two identical copper electrodes and the capacitance was measured. The pellet was removed and the two electrodes (separated by an air gap equal to the pellet thickness) and the capacitance of the air was measured. The ratio of the two capacitance measurements resulted in the determination of the nanocomposite material dielectric constant. Equation 3.1 to Equation 3.3 were used to determine the dielectric constant of the air and the material and Figure 3.2 shows the experimental setup.

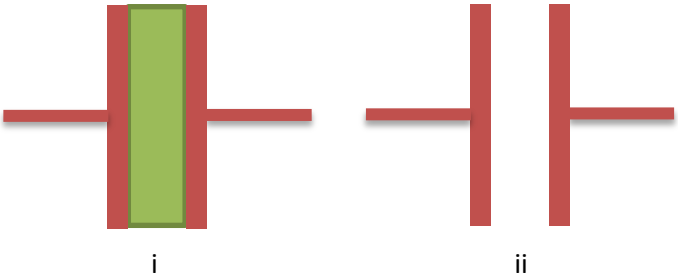

Figure 3.2 – The schematics of the experimental setup to measure i) the capacitance of the nanomaterials (green) and ii) the capacitance of air.

$$C_{sample} = \frac{\varepsilon_{sample} A}{d}$$

Equation 3.1

where:

- C_{sample} is the capacitance of the sample
- ε_{sample} is the dielectric constant measured for the sample.
- A is the sample surface area
- d is the distance between the electrodes (for all purposes this is the length of the pellet)

$$C_{air} = \frac{\varepsilon_{air} A}{d}$$

Equation 3.2

Where:

- C_{air} is the capacitance of air
- ε_{air} is the dielectric constant measured for air.
- A is the sample surface area
- d is the distance between the electrodes (for all purposes this is the length of the pellet)

from which the material dielectric constant is determined from

$$\varepsilon_r = \frac{\varepsilon_{sample}}{\varepsilon_{air}}$$

Equation 3.3

3.3.4) Schottky Diode Device current-voltage (I-V) and capacitance-voltage (C-V Measurements)

The Schottky devices were constructed using two different methods; pressed pellet devices and evaporated devices (see Figure 3.3 for the Schottky device architecture)

1) Pressed Pellet Devices

The nanocomposite material was placed onto the metal electrode foil and pressed together under 10 tons of pressure between two metal dies. An indium tin oxide (ITO) coated on PET (Sigma-Aldrich) was then pressed onto top nanocomposite material for the I-V and C-V measurements.

2) Evaporated Metal Contact Devices

For the materials with sufficient amount of material, the metal electrode foil was evaporated under vacuum onto the nanocomposite pellet. The metal contact was limited to a surface area of 0.78 mm^2 (i.e. 1mm diameter). The pellet face without the metal contact was then placed onto a copper foil when conducting the I-V and C-V measurements.

I-V measurements were carried out using a Keithly multi-meter between a minimum of -30 V and a maximum of 30 V with a 2 mA current limit at 0.05 V intervals. C-V measurements were carried out on a Leader LCR-745G at 1 kHz.

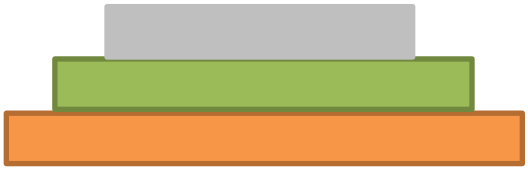

Figure 3.3 – A typical Schottky pressed and evaporated device architecture showing the copper electrode (orange), nanocomposite material (green) and ITO coated on PET (grey)

3.3.5) Photosensitive Device Construction and I-V Measurements

The photosensitive devices were constructed using two p-type silicon wafers (the largest had a surface area of ~4.4 x 10^{-3} m^2 and the smallest had a surface area of ~1.26 x 10^{-3} m^2) and a $FePS_3$ substrate. The nanocomposites were dispersed into 50 ml of isopropanol. This mixture was then centrifuged to remove the larger more coarse particles and leaving a dispersion of the finer material in solution. This solution was then deposited onto the p-type silicon wafers by spin coating.

For $V_2O_5/AnAn^+$ coated on $FePS_3$, on a $FePS_3$ single crystal the nanocomposite material was cast from the solution of finely dispersed nanocomposite material in isopropanol.

After spin coating or casting the photosensitive devices were constructed by placing the nanocomposite covered substrate with the uncovered side of the substrate in contact with a copper electrode and the nanocomposite covered substrate in contact with an ITO coated on PET strip of equal surface area of the substrate, a clear plastic plate was then sandwiched upon this device with a dual purpose: *i)* to reflect and minimise heating of the device sample under illuminated conditions and *ii)* to keep the ITO coated PET in as intimate contact with the nanocomposite material as possible.

For the $FePS_3$ coated with $V_2O_5/AnAn^+$, the device was placed under a magnetic field of 0.3T. The device was placed parallel (Para Mag) and perpendicular (Perp Mag) to the magnetic field.

Figure 3.4 – A typical photosensitive device architecture showing the copper electrode (orange), silicon/$FePS_3$ substrate (black), nanocomposite material (green) ITO coated on PET (grey) and the plastic plate (white)

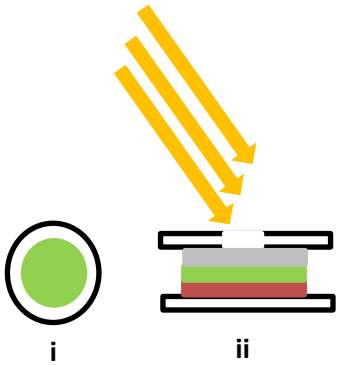

Figure 3.5 – i) Top view of the $V_2O_5/AnAn^+$ $FePS_3$ device where the green component in the composite material and the white component in the plastic encasing, ii) side view of the $V_2O_5/AnAn^+$ $FePS_3$ device where the red component is the copper electrode, green component is the composite material and the grey component is the transparent ITO electrode and the white components are the plastic encasing

Figure 3.6 – i) The parallel set up of the device and magnetic (Para Mag) and ii) the perpendicular set up of the device and magnetic (Perp Mag)

1) 1-V Measurements

I-V measurements were performed using a Keithley multimeter (as previously used for the Schottky Device I-V measurements in Section 3.3.4) for all devices. The device I-V character was determined between the ranges of -8 V and 8 V (to prevent heating of the device the voltage was limited to within this range) at intervals of 0.05 V with a 2 mA current limit. It was also observed that under illuminated conditions some of the devices exceeded the current limit above 8 V and therefore this voltage range was restricted for all devices. For all devices, the I-V measurement in dark conditions (Dark) were carried out in a black box. For determining the change in the I-V character under ambient light (A.Light), the device was placed out of the box to allow the A.Light to illuminate the device. The devices were further illuminated using a tungsten incandescent lamp (Lamp). The incandescent lamp was placed 30 cm away from the device.

3.3.6) Device Modelling

Graphpad was used to model the Schottky device I-V plots with the diode equations. There were no restrictions applied on I_0 and the n value was restricted to between $0<n<5$.

4) Results and Discussion

4.1) Characterisation

4.1.1) V_2O_5 Intercalation

4.1.1.1) X-ray Diffraction (XRD)

Table 4.1 - Table to show the interlayer spacing and change in interlayer spacing of the V_2O_5 composite materials

Method	Interlayer spacing/(Å)	Interlayer spacing change/(ΔÅ)	2θ (°)	Intensity/peak shape
Direct Intercalation				
V_2O_5	4.373	/	20.9	
V_2O_5/$AnAn^+$	12.80	8.43	6.8	Strong sharp peak with a broad shoulder
V_2O_5/2A5PhPyr	12.16	7.79	9.8	Medium intensity and broad
V_2O_5/EDOT	9.02	4.65	7.0	Strong sharp peak with a broad shoulder
Ion-exchange				
LiV_2O_5	12.62	8.25	6.8	Strong sharp peak
V_2O_5/PDA	9.02	4.65	9.6	Strong broad peak
LiV_2O_5/ 2A5PhPyr	12.27	7.90	7.0	Strong broad peak
V_2O_5/5AQ	13.38	9.01	6.6	Medium peak with broad shoulders
V_2O_5/1,4PDA-HQ	9.60	5.23	8.6	Strong broad peak

From Table 4.1, Figure 4.1 and Figure 4.2, we can see that both direct and ion-exchange methods yield an increase in the interlayer spacing suggesting intercalation has occurred. When directly intercalated with $AnAn^+$, 2A5PhPyr and EDOT the interlayer spacing increases by 8.43, 7.79 and 4.65Å respectively. For V_2O_5/$AnAn^+$ and V_2O_5/2A5PhPyr, this degree of increase has previously been seen(115,121,130) and therefore could correspond to one of two cases; *i)* the polymer backbone is orientated perpendicular to the V_2O_5 plane or *ii)* the polymer intercalants are parallel to the V_2O_5 plane are but are stacked to form a bilayer. Since the EDOT intercalation showed approximately half the increase in the

interlayer spacing, when compared to that of $AnAn^+$ and 2A5PhPyr, it suggests that the EDOT polymer exists as a monolayer in the interlayer spacing and parallel to the inorganic layers. V_2O_5/$AnAn^+$ and V_2O_5/EDOT further showed large disperse shoulders (between 2θ values of 6.6 – 14.6^o and 6.6 – 15.6^o respectively) in the XRD which presumably correspond to the presence of amorphous material. However, the higher angle peaks present are weaker compared to the interlayer spacing peak but are still sharp peaks. This suggests that the overall structural integrity of the crystalline host has been maintained. The disperse shoulders could, therefore, arise from the changes in the (*001)* plane along the *c*-axis. The intercalation of the guest species could result in effects that could cause this shoulder to arise in the diffractogram such as any shearing or screw dislocations of the layers during intercalation (which would produce a similar effect to random re-stacking of layers). Another possibility is incomplete intercalation producing a distribution in the interlayer spacings. From these possibilities, the latter appears to be more likely for the EDOT material as characteristic (*001*) peaks for V_2O_5 (~2θ = 20°) remains present in the diffractogram. This is not the case, however, for the intercalation of 2A5PhPyr. In this case, we would expect an acid-base reaction between the V_2O_5 acidic oxide and the basic 2A5PhPyr. The peak corresponding to the interlayer expansion is sharp with no broad shoulder suggesting regular structure along the *c*-axis. On the other hand, the peaks appearing at higher 2θ values have now either disappeared or broadened. This suggests that the short-range order along the other axes may have been compromised during the reaction. This is particularly prominent for the (*020*) peaks (~2θ = 16°) where it has disappeared in $AnAn^+$ and EDOT materials, it is now a large broad peak for 2A5PhPyr. The characteristic (*001*) peak, however, is still present. A possible explanation is presence skew dislocations of various degrees of skewing such that consecutive layers are no longer parallel. This effect would allow for an unaltered *001* plane but potential alterations in the other planes.

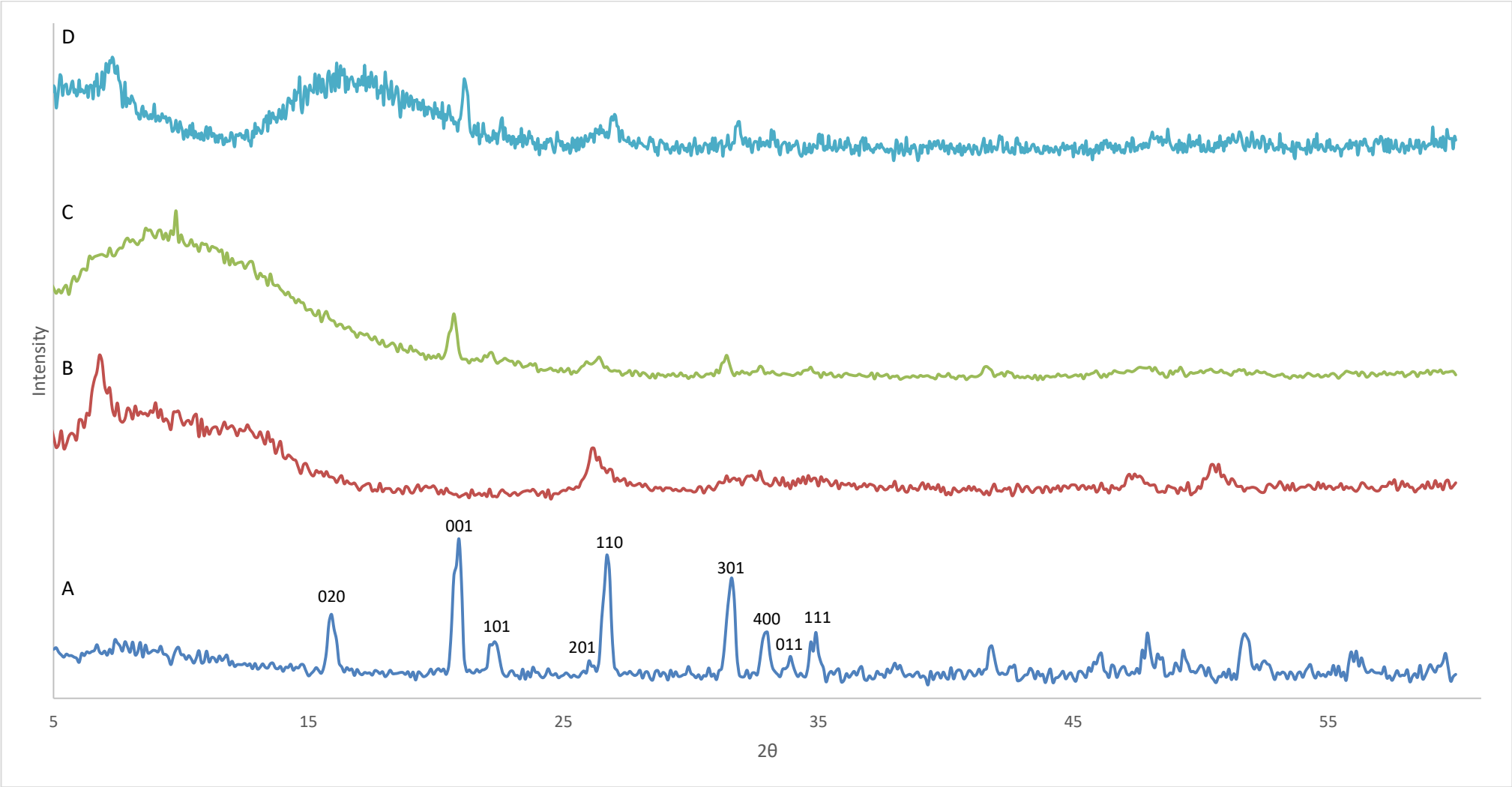

Figure 4.1 - X-ray Diffractograms for A) V_2O_5 host, B) V_2O_5/AnAn$^+$, C) V_2O_5/EDOT and D) V_2O_5/2A5PhPyr synthesised via direct intercalation

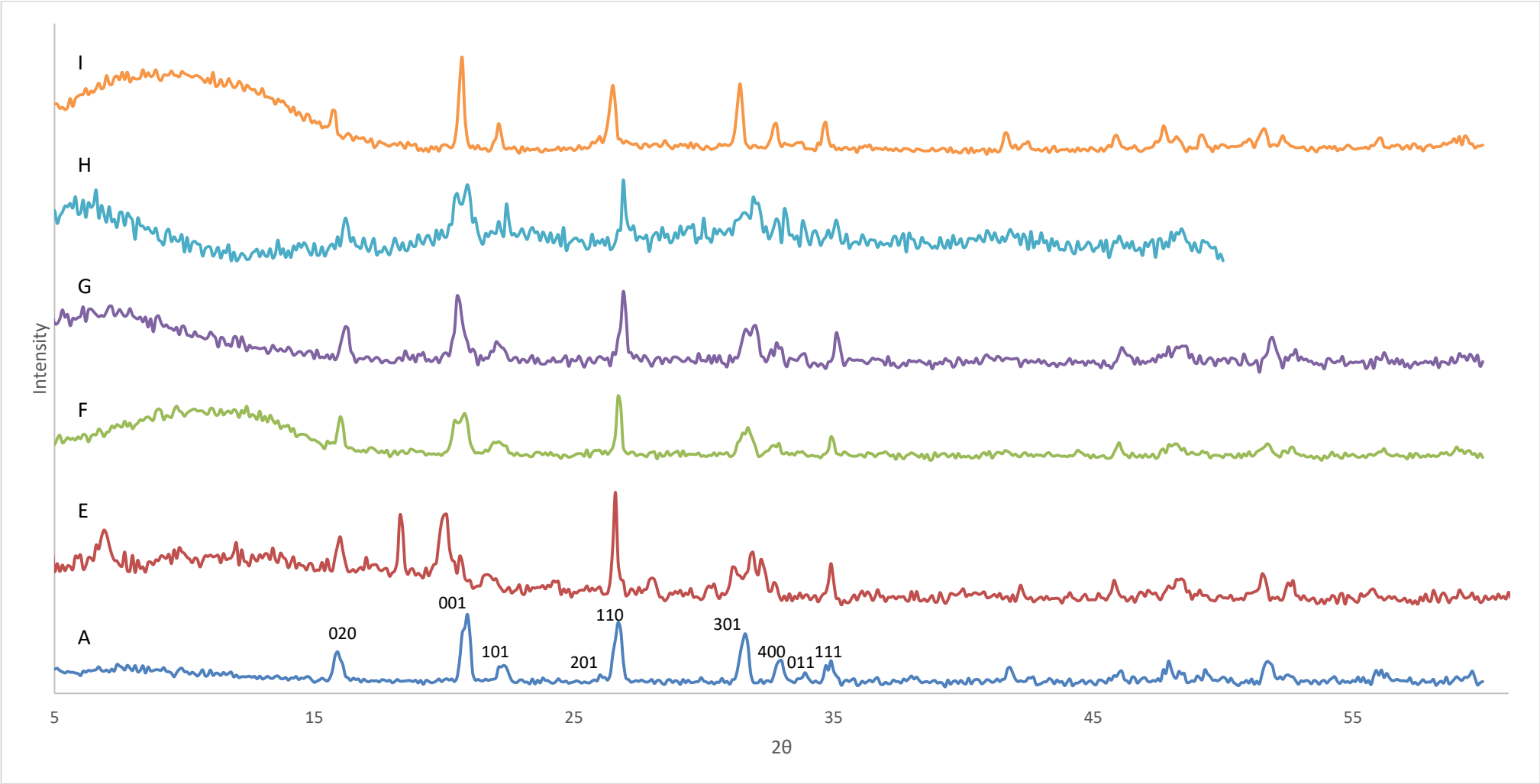

Figure 4.2 - X-ray Diffractograms for E) LiV_2O_5, F) V_2O_5/PDA, G) LiV_2O_5/2A5PhPyr, H) V_2O_5/5AQ and I) V_2O_5/1,4PDA-HQ synthesised via ion-exchange

In the case of the ion-exchanged intercalants (Figure 4.2), the lithiated V_2O_5 showed partial intercalation (the presence of two phases; an un-intercalated phase and an intercalated phase) of the lithium ions as the *001* V_2O_5 peak is still present (as is many of the peaks appearing at higher angles). Due to the presence of sharp strong peaks in the diffractogram, the structural integrity of the overall inorganic material was well maintained.

Here we can compare the two V_2O_5/2A5PhPyr materials synthesised by direct intercalation and by ion-exchange. A broad strong peak appears in the XRD ($2\theta = \sim5\text{-}12^o$) for the intercalation via ion-exchange compared to the sharper peak ($2\theta = 7.05^o$) exhibited via direct intercalation. Partial intercalation could lead to such a peak being shown in the diffractogram where only the Li^+ preintercalated phase exhibits intercalation to varying degrees via ion-exchange. The appearance of a medium-strong diffuse peak (usually found between $2\theta = \sim7 – 10^o$) along with peaks which correspond well with pure V_2O_5 appears to be a common phenomenon during the ion-exchange reactions. For the intercalation of PDA, 5AQ and HQ-PDA there is a strong broad peak (peaking at $2\theta = 9.8^o$) corresponding to partial intercalation with strong sharp peaks appearing at higher angles. In both 2A5PhPyr and PDA cases, the higher angle peaks correspond well with that of pure V_2O_5 which also suggests that there are two phases present; the partially intercalated V_2O_5 and pure V_2O_5.

Overall the X-ray diffraction data show that there has been a successful interlayer expansion which corresponds to the organic guest species being present. However, it is clear that the ion-exchange method is more prone to give rise to incomplete intercalation. On the other hand, the direct intercalation methods are prone to partial intercalation occurring where the material appears to lose its short range order due to the rise of defects such as skewing dislocations.

4.1.1.2) Infra-red and Raman Spectroscopy

The Infra-red and Raman vibrational transitions for V_2O_5 intercalation via direct and ion-exchange methods are shown in Table 4.2, Table 4.3 and Table 4.4 respectively (see Appendix A.1 and A.2 for full spectra). Peaks appearing below, or very close to, 1000cm^{-1} correspond to the V_2O_5 phase of the material. When intercalated, the host material peaks are shifted to higher wavenumbers along with the appearance of organic guest peaks which can provide some insight into the presence of organic materials in the interlayer spacing. In the direct intercalated materials, for $AnAn^+$ the peaks appearing between 3300-2800cm^{-1} correspond to C-H stretching and O-H stretching of the guest molecules. The O-H stretching vibration is present due to the aqueous nature of the reaction and corresponds to any loosely bound water molecules still present on the surface or in the interlayer spacing. The peak appearing at 1466cm^{-1} corresponds to C=C stretching mode of the quinoid ring.

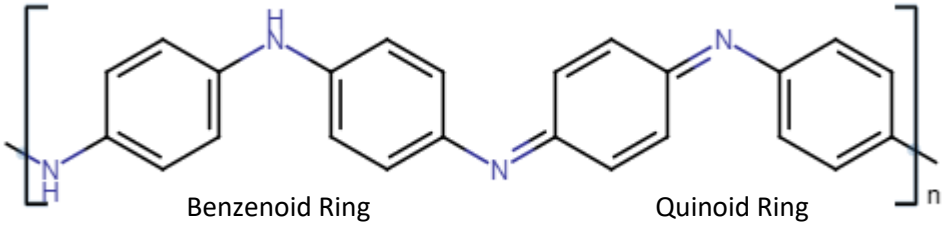

Figure 4.3 – Benzenoid and Quinoid ring systems present in polyaniline.

The peaks appearing between 1400-1300cm^{-1} are assigned to the stretching from the C-N and C=N bonds. The 1107cm^{-1} peak is associated with the V=O stretching mode shifted from 991cm^{-1} in the pure host. Finally, the 816 and 597 cm^{-1} features correspond to the V-O-V stretching modes. Overall, some peaks have shown to shift and some characteristic V_2O_5 peaks remain unshifted. This suggests that there is still unreacted V_2O_5 present. Furthermore, the Raman peaks have also been shown to shift which is consistent with the presence of intercalated material in the interlayer spacing constricting space for the inorganic vibrations. The appearance of both shifted and un-shifted peaks are seen for the

direct intercalation of 2A5Ph2Pyr and EDOT. For the 2A5Ph2Pyr, it is seen that the peaks appearing at 1346 and 1660 cm^{-1} correspond well to NH_2 stretching modes whereas the closely related peaks of 1619 and 1621 cm^{-1} correspond to the presence of NH_3^+. This suggests that there are two forms of the amine group present, protonated and neutral forms. The shifting of the peaks as seen in the $AnAn^+$ corresponds to the intercalation has occurred. The vibrations found at 1518 and 1338 cm^{-1} can be associated with the EDOT ethylenedioxy group. Both nanocomposites show a mix of the original V_2O_5 peaks and new shifted peaks in the region below 1100 cm^{-1}. This shows that there is partial intercalation of the organic monomers with two phases, the first being unreacted V_2O_5 while the other involves the composite material.

This was further seen in the Raman data where there is a mix of peaks corresponding to the presence of the characteristic un-shifted V_2O_5 peaks as well as new peaks corresponding to the intercalated shifted peaks. This shows the presence of the two phases. This was also seen in the XRD data (Table 4.1, Figure 4.2 and Figure 4.3) and confirms that these changes in the IR and Raman data are indicative of intercalated organic guest in the interlayer spacing. This may further suggest that the material is present in its oligomeric or polymeric forms as the peaks corresponding to the quinoid ring system are only present upon polymerisation with the oligomer or polymer being present in its protonated (p-type) form. However, the IR and Raman data alone cannot confirm this. The IR and Raman spectra become slightly more complex in the case of the ion-exchanged V_2O_5 composite materials. Upon intercalation of $Li^{+,}$ we immediately see changes in both the IR and Raman data. The peak appearing at 991 cm^{-1} appears to split into two different peaks in the lithiated V_2O_5 (995 and 970 cm^{-1}). This is consistent with intercalation as this peak corresponds to the V=O stretching mode. This stretching mode has less vibrational space upon intercalation of Li^+ which interacts with oxygen in the inorganic layers.

Furthermore, the peak normally at ~600 cm^{-1} shifts to ~590 cm^{-1} upon Li^+ intercalation corresponding to red-shift of the V-O-V vibrations.

Table 4.2 - Infra-red and Raman wavenumbers (cm^{-1}) for V_2O_5 intercalated compounds via direct intercalation

		Direct Intercalation						
V_2O_5		**V_2O_5/AnAn$^+$**		**V_2O_5/ 2A5PhPyr**		**V_2O_5/EDOT**		**Assignment**
IR	*Raman*	*IR*	*Raman*	*IR*	*Raman*	*IR*	*Raman*	*Organic Guest*
		3331.3						C-H, O-H and NH_2, =NH stretching
		2969.4						
		2930.8						
		2882.6						
				1660.1				NH_3^+ stretching
				1619.8				
				1557.0				
						1517.7		Ethylenedioxy group
		1466.7						Quinoid and benzene C=C stretching
		1407.4						
		1378.4						C-N, C=N and NH_2 stretching
		1340.1		1346.8		1338.8		
		1306.0						
				1276.6		1244.7		C=C quinoid stretching
		1159.7		1154.8		1217.9		
				1140.1				
		1127.9						
								Inorganic Host
								V=O stretching
		1107.1		1002.9		1106.0		
991.1	997	950.4	993	918	995	979.6	992	
		816.3				922.6		
781.0	705		693	734.4	698	766.2	698	V-O-V stretching and bending
665.8	532	627.6	409	597.6	525	697.4	410	
630.5	488	608.6	283	556.4	483	694.0	286	
599.9	408	597.3	195		406	546.1	198	
565.2	307	587.9	142		294		140	
548.4	285	576.3			285			
	202	560.2			197			
	146	544.4			145			
		537.3						

Table 4.3 - Infra-red and Raman wavenumbers (cm^{-1}) for V_2O_5 intercalated compounds via ion-exchange intercalation

				Ion-exchange								
V_2O_5		**LiV_2O_5**		**V_2O_5/PDA**		**LiV_2O_5/2A5PhPyr**		**V_2O_5/5AQ**		**V_2O_5/1,4PDA-HQ**		**Assignment**
IR	*Raman*	*IR*	*Raman*	*IR*	*Raman*	*IR*	*Raman*	*IR*	*Raman*	*IR*	*Raman*	*Organic Guest*
				3333.42		3305.55		3300		3209.59		NH_2, =NH
				2969.39		3079.19		3080				NH_3^+, NH_2^+ and NH^+
				2931.19								
				2882.75								
												N-H bending and N=C=S stretching
						1666.3					1651	NH_2 , >NH, NH_3^+ bending and Benzene C-C
						1621.15		1638.77				
							1608			1613.57	1605	
						1550.69				1564.05		
									1546		1537	
				1466.2		1475.25				1488.85		Benzenoid C=C stretching
				1407.51		1444.64				1423.28		
				1378.32				1362.89	1370	1360.94	1364	Quinoid C=C stretching
				1344.11		1348.01					1321	
				1306.1								
				1159.68		1275.22				1290.11	1268	
				1127.87		1156.15				1175.3	1176	

Table 4.4 - Infra-red and Raman wavenumbers (cm^{-1}) for V_2O_5 intercalated compounds via ion-exchange intercalation

				Ion-exchange								
V_2O_5		**LiV_2O_5**		**V_2O_5/PDA**		**LiV_2O_5/2A5PhPyr**		**V_2O_5/5AQ**		**V_2O_5/1,4PDA-HQ**		**Assignment**
												Inorganic Host
				1107.97		1018.58					997	V=O stretching
991.11	997	995.37	982	950.48	993	957.94	998	966.29	980	981.86		
		970.03					995					
781.01	705	780.54	698	816.33	689		861					V-O-V stretching and bending
665.8	532	591.87	544	632.74	407	797.66	710	781.66		765.29	710	
630.53	488	565.32	477	608.21	286	760.16	530	599.09	682	630.95	583	
599.91	408	545.61	430	573.55	189	718.36	484	570.09	524	598.04	513	
565.16	307		288	558.77	140	694.41	411	565.45	417	555.94	411	
548.43	285		157	545.54		642.04	307	549.68	284		286	
	202			537.05		596.37	288		145		148	
	146					570.33						

The observation of both shifted and unshifted vibrational modes of LiV_2O_5 compared to the pure host corroborates with the XRD data in suggesting a mixture of two phases. When the Li^+ is exchanged for $PDACl_2$ we find the IR spectrum changes accordingly. The peak new appearing at 3333 cm^{-1} corresponds to the NH stretching mode from either NH_2 or =NH groups. The peaks at 2969 and 2931 cm^{-1} confirms to the presence of an NH_3^+ group while the peak at 2882 cm^{-1} corresponding to the NH stretching mode in either NH_2^+ or NH^+ groups. This suggests that PDA was present with both neutral with protonated amine groups. Meanwhile, the peaks appearing at 1407 and 1466 cm^{-1} correspond to the C=C benzenoid ring system while those appearing at 1378, 1340 and 1306 cm^{-1} correspond to the C=C quinoid ring system suggesting a polymerised system which is partially protonated giving rise to an intercalated doped polymer. However, the doped organic guest appears to have produced the ladder-like oligomer phase due to the presence of a mix of NH_3^+ and NH groups in which NH is formed due to the polymerisation whereas NH_3^+ groups correspond to protonated NH_2 groups in unpolymerised precursors. These potential coupled forms of the PDA in the interlayer spacing in Figure 4.4 are shown. The peaks below 1156 cm^{-1} correspond to the V_2O_5 peaks and as seen before, the peak at 1018 cm^{-1} corresponds to V=O stretching while the rest of the peaks can be seen to undergo red-shift corresponding to the limited V-O-V and V=O stretching phases. In the Raman spectrum, we see a mix of shifted and unshifted peaks which is indicative of a mixed phase of unintercalated and intercalated V_2O_5. The other composite materials followed this trend, peaks appearing from 3000 cm^{-1} and higher corresponded to NH_2 or =NH stretches while peaks appearing between ~1700-1200 cm^{-1} correspond to the benzenoid and quinoid ring systems. Peaks appearing below 1100 cm^{-1} are a mix of shifted and un-shifted peaks suggesting that in all nanocomposite materials there is a mix between two phases which include the intercalated phase and the

unintercalated phase. Furthermore, unlike in the PDA case, the 2A5PhPyr, 5AQ and 1,4PDA-HQ Raman shows peaks appearing between 1000 cm^{-1} – 1700 cm^{-1}.

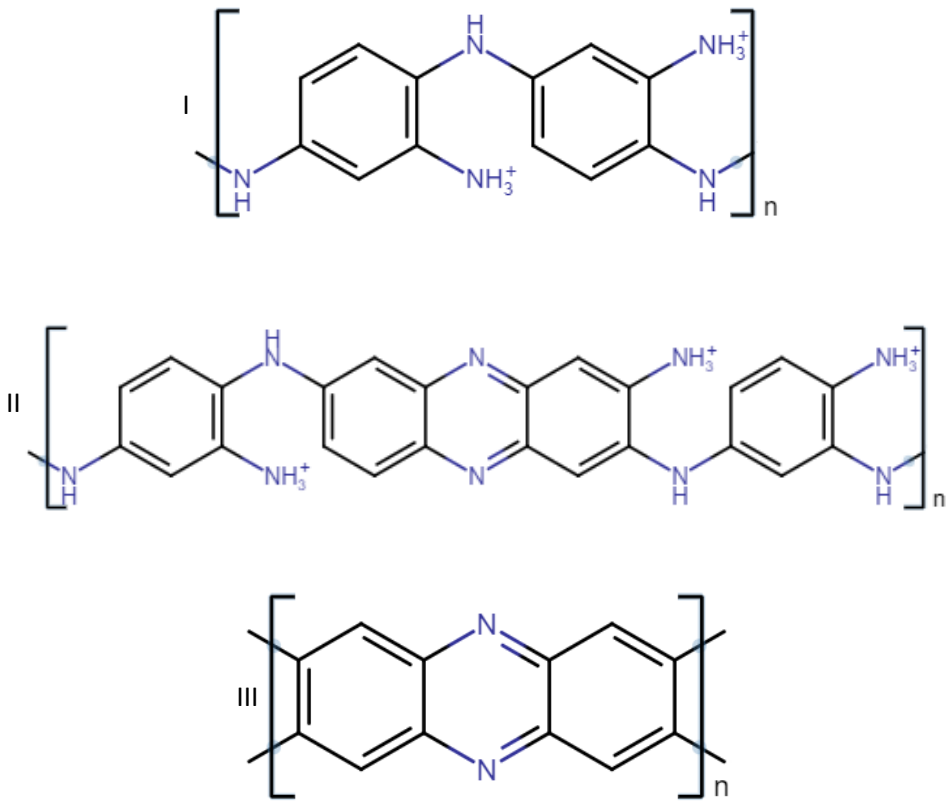

Figure 4.4 – I) Polymerised PDA to produce a substituted polyaniline form, II) Polymerised PDA with two phases present; a non-ladder phase and a ladder oligomer phase and III) Fully polymerised PDA producing the Ladder like polymer

These peaks are correlated to the presence of the organic guest. The red-shift is associated with the presence of an intercalated guest, however, there are some instances where a blue shift is observed. This may occur when the layers expand due to the intercalation (or any layer based defects such as a skew defect) but no the organic material was unable to penetrate far enough in between the layers producing essentially an expanded interlayer spacing with no guest species. This would result in a blue shift due to the V=O peaks now having more space to vibrate.

When comparing the IR and Raman data for both direct and ion-exchange intercalation with the XRD data presented we can determine that the cause of the interlayer

expansion is due to the presence of an organic guest species which is suspected to be in its oligomeric or polymeric form.

4.1.1.3) TGA and ICP-AES

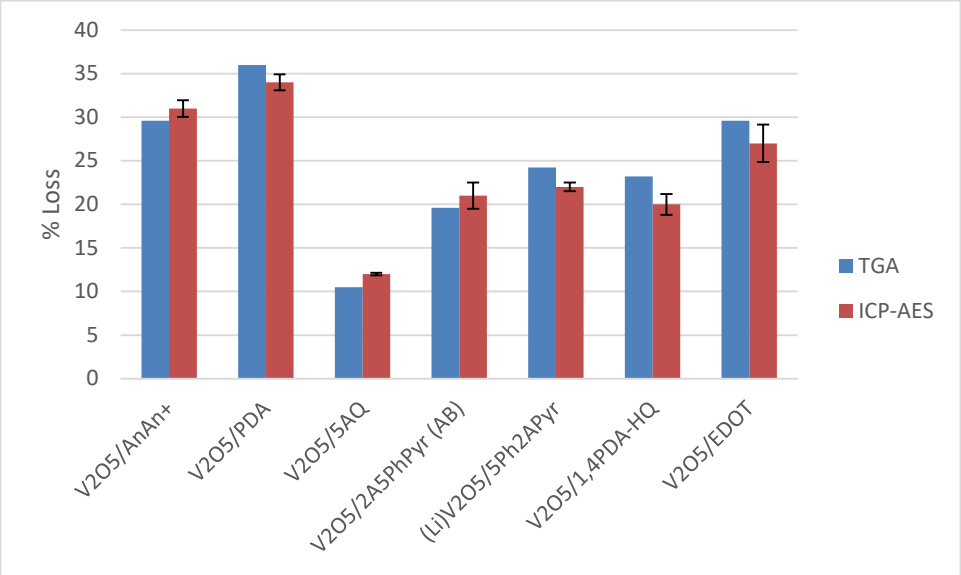

Figure 4.5 - % Weight Loss via TGA and ICP-AES for V_2O_5 intercalated materials after the initial mass loss due to water. The error bars in the ICP-AES where obtained in-situ via three consecutive measurements as described in section 3.1.4).

Figure 4.5 shows the total percentage loss in mass determined by TGA and ICP-AES independently (for full TGA data see Appendix A.3). Shown here is the % by mass of the guest species in the composite material. From the ICP-AES the stoichiometry was calculated by determining the total vanadium content in the digested sample (assuming the stoichiometry of the vanadium host to be V_2O_5) and comparing this to the theoretical vanadium content if no organic intercalant was present (which is the total vanadium content in the digested pristine V_2O_5 sample). The difference in vanadium content was concluded to arise from the presence of the organic guest. Thus, the stoichiometry was determined to be $Li_{0.21}V_2O_5$, $AnAn_{0.22}V_2O_5$, $PDA_{0.26}V_2O_5$, $5AQ_{0.15}V_2O_5$, $2A5PhPyr_{0.18}V_2O_5$ (Acid-Base reaction) $2A5PhPyr_{0.23}V_2O_5$ (ion-exchange), $(1,4PDA\text{-}HQ)_{0.19}V_2O_5$ and $EDOT_{0.23}V_2O_5$

We can initially see that for both TGA and ICP-AES analysis the V_2O_5/PDA composite showed the largest guest content followed by the V_2O_5/AnAn$^+$ and V_2O_5/EDOT. The initial loss in all samples in the TGA around 100°C is related to any loosely bound water on the surface or in the interlayer spacing due to the aqueous nature of the reactions. However, the continuous loss shown in all the samples suggests that the materials are oligomeric/polymeric (as suspected from the IR and Raman data) as there is a gradual loss in mass over the measured temperature range. If the organic guests remained in the monomer form one would expect all the guest species to be removed around a single temperature and not over a large range. The presence of the oligomeric or polymeric form could explain the diffuse peaks seen in the XRD data. These diffuse peaks may be caused by defects in the inorganic host but alternatively may arise due to the morphology of the oligomeric or polymeric chains for example if the chains were in a helical orientation in some regions of the material or lying parallel to the inorganic layers. This would lead to the material exhibiting a distribution in the overall expanded interlayer spacing caused by intercalation.

4.1.1.4) Optical Spectroscopy

Table 4.5 - Optical band-gaps determined from UV-Visible spectroscopy tauc plots

	Optical band-gap (eV)		
Compound	**Composite material**	**Host Tauc Plot Region**	**Literature V_2O_5** (258)
V_2O_5	N/A	2.33	2.3-2.38
V_2O_5/AnAn$^+$	3.69	2.35	
V_2O_5/2A5PhPyr (AB)	3.70	2.46	
V_2O_5/EDOT	3.70	2.37	
V_2O_5/PDA	3.72	2.36	
(Li) V_2O_5/2A5PhPyr	3.71	2.42	
V_2O_5/5AQ	3.69	2.37	
V_2O_5/1,4PDA-HQ	3.64	Not present	

The calculated optical band-gaps for the composite materials are shown in Table 4.5 (see Appendix A.4 for full UV-Visible reflectance spectra and their associated Tauc plots) with

Figure 4.6 and Figure 4.7 showing an example of the V_2O_5 and V_2O_5/2A5PhPyr tauc plots where the optical band length is determined by extrapolation of the linear part/s of the plot. Overall it is shown that the intercalated materials have a larger band-gap than that for pure V_2O_5 host (which shows good correlation with the literature band-gap range). This could be due to two possibilities. The most plausible explanation lies in the fact that as the organic material is intercalated into the interlayer spacing, it is disrupting the band-structure of the bulk inorganic. Thereby there is less band overlap between inorganic layers leading to a larger band-gap.

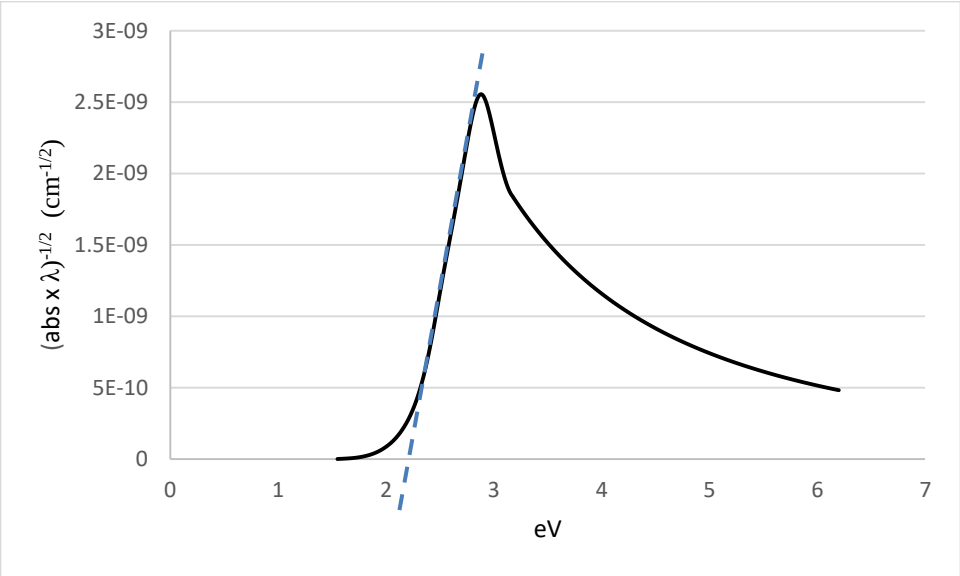

Figure 4.6 - Tauc plot for V_2O_5

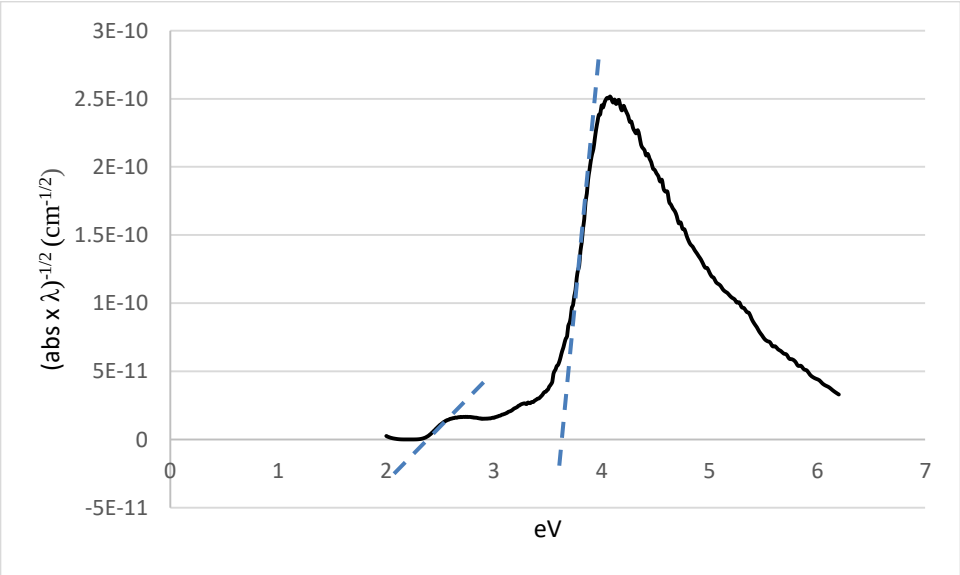

Figure 4.7 - Tauc plot for V_2O_5/2A5PhPyr showing two regions present

The second possibility lies in that the increase in the band-gap is due to poor conduction – valence band overlap occurring between the organic guests (which are understood to be in their protonated phases demonstrated from the IR and Raman data, therefore may be present in the interlayer spacing as conductive oligomeric or polymeric guests) and the inorganic host materials. If the material is determined to be semiconducting then this would result in the material exhibiting indirect semiconductor properties as illustrated in Figure 4.8.

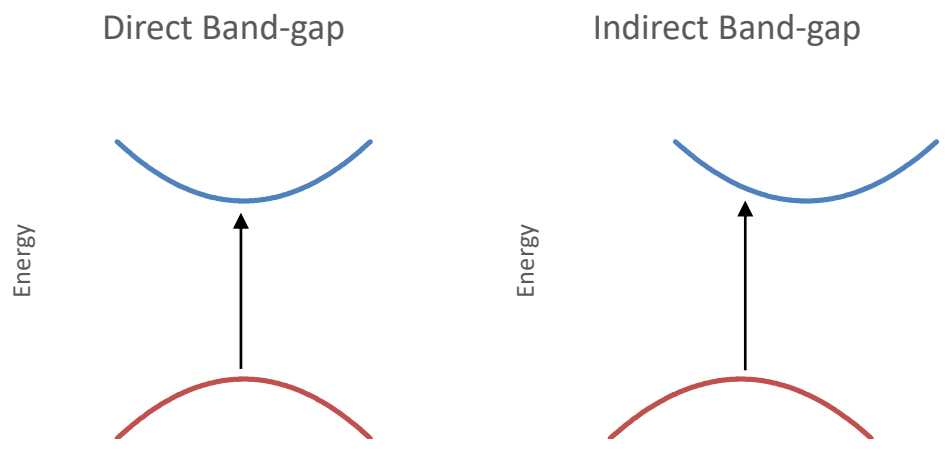

Figure 4.8 - The direct and indirect semiconductor band-gaps

The band-gap of the intercalated materials, in general, is found to be between 3.64-3.71 eV. In all but the 1,4PDA-HQ intercalated material, there was a remnant peak in the region characteristic of the host material. In some cases, this peak is extremely small in the tauc plot when compared to the peak of the composite material. From the tauc plots, we can determine that any changes in the overall properties of the material are caused by the presence of the intercalant. In the case of the V_2O_5/1,4PDA-HQ, the lack of the V_2O_5 peak could suggest that in this material the partial intercalation phase seen in the X-ray diffractogram may be a major phase.

From the UV-Visible spectra, we can further see shoulders to the main absorption edge of the composite material appearing between 350-390nm in all the intercalated

materials. This shoulder corresponds to charge transfer occurring between the organic guest and the inorganic host material. This change in the bandgap signifies that the organic guest that had been intercalated (as concluded from the previous characterisations techniques) has an effect on the overall band structure of the material with the new intercalated material and not treated as two separate phases.

4.1.1.5) X-ray Photoelectron Spectroscopy

XPS is a surface sensitive spectroscopic technique which provides information regarding the potential reduction of the vanadium nuclei as well as information regarding any intercalates.

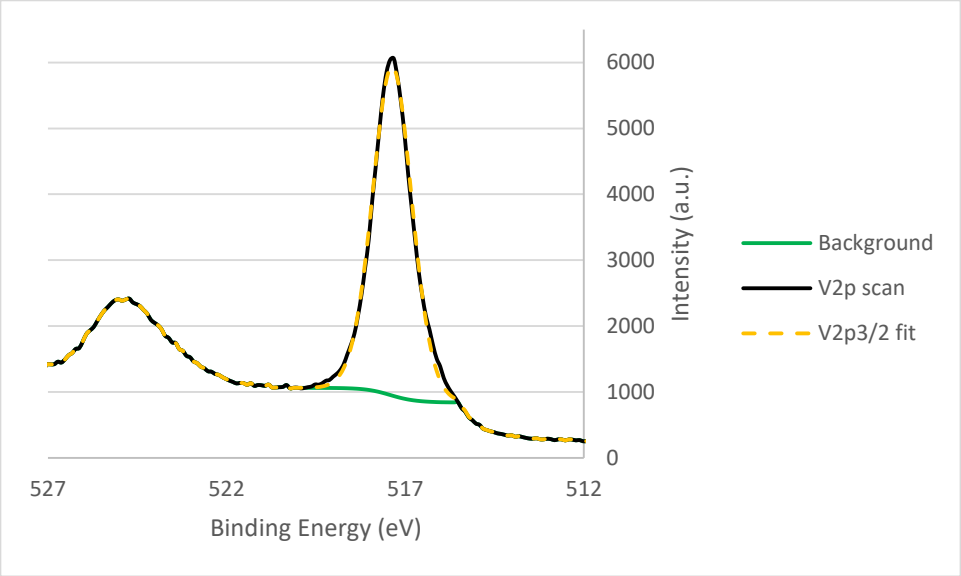

Figure 4.9 - The XPS scan for V_2O_5 host showing $V2p_{3/2}$ environment (black) fitted with a single environment (517.42 eV) corresponding to V^{5+} (orange). The peak at 525 corresponds to the $V2p_{3/2}$

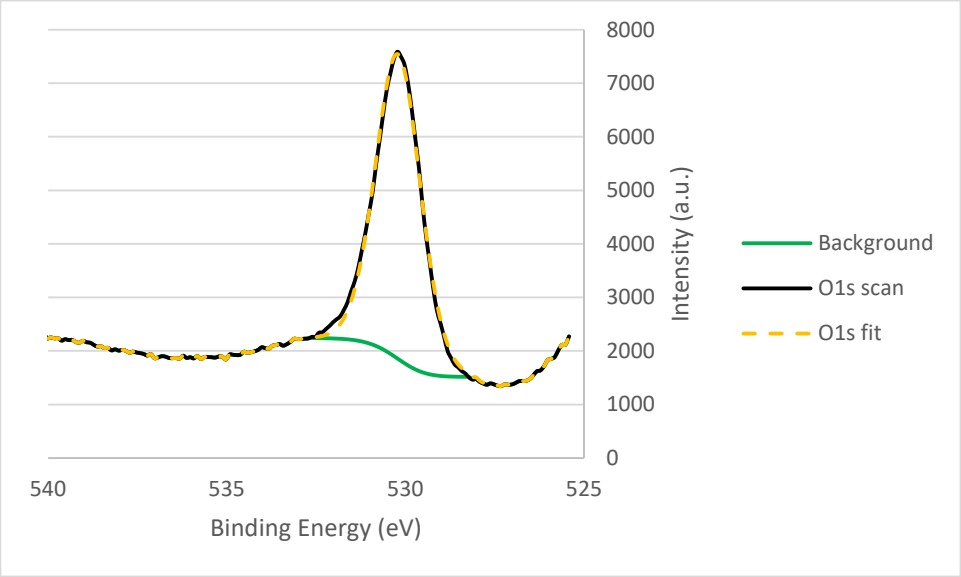

Figure 4.10 - The XPS scan for V_2O_5 host showing O1s environment (black) fitted with a single environment (530.22 eV) corresponding to O^{2-} (orange)

Figure 4.9 and Figure 4.10 show the XPS scans for the vanadium and oxygen environments in the pure host V_2O_5. In Figure 4.9 the vanadium peak appearing at ~517.4 eV corresponds to $V2p_{3/2}$ for V^{5+} which matches literature values (259,260) and has been fitted for a single environment. Figure 4.10 shows that the O1s peak appears ~530.2 eV which also matches literature value 517.40eV (261,262) and shows a single environment.

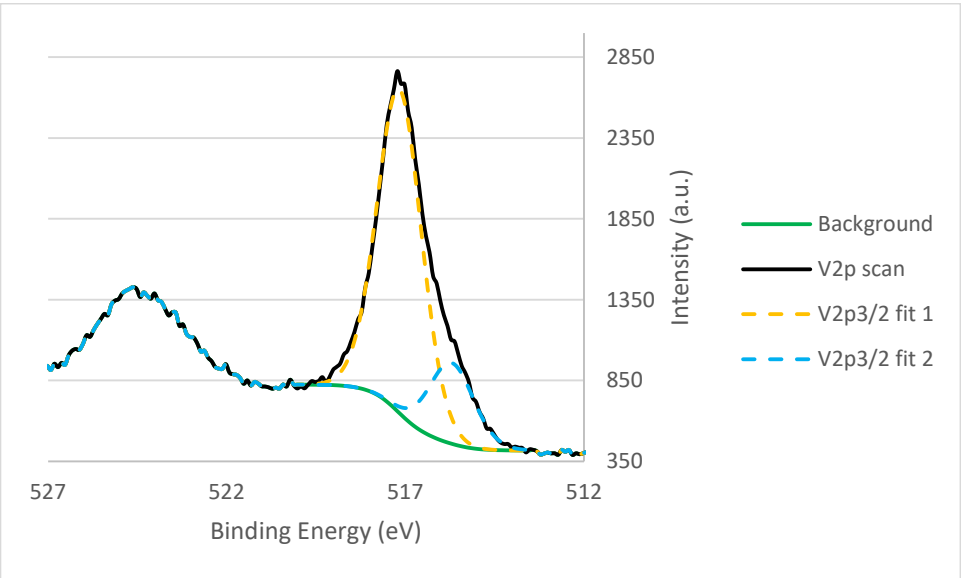

Figure 4.11 - XPS scan for V_2O_5/AnAn$^+$ synthesised via direct intercalation showing the $V2p_{3/2}$ environment (black) fitted with two environments (orange; 517.22 eV and blue; 515.82 eV)

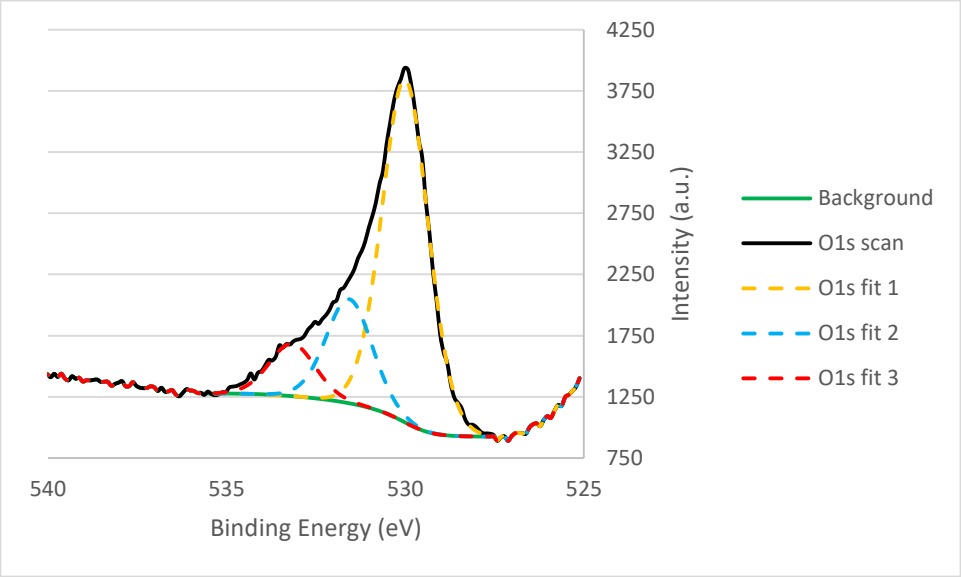

Figure 4.12 - XPS scan for V_2O_5/AnAn$^+$ synthesised via direct intercalation showing the O1s environment (black) fitted with three potential environments (orange; 530.12 eV, blue; 531.72 eV and red; 533.32 eV)

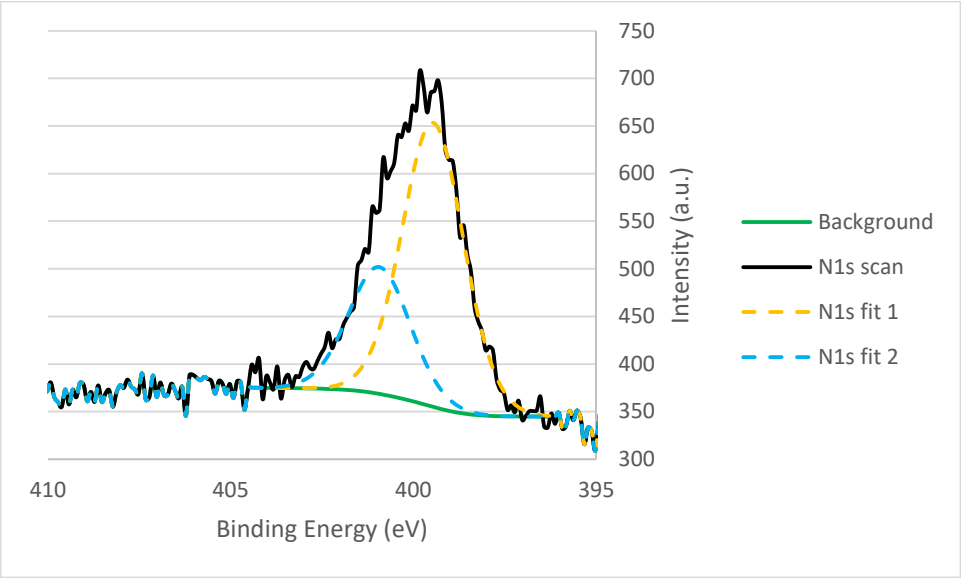

Figure 4.13 - XPS scan for V_2O_5/AnAn$^+$ synthesised via direct intercalation showing the N1s environment (black) fitted with two potential environments (orange; 399.62 eV and blue; 401.12 eV)

Figure 4.11, Figure 4.12 and Figure 4.13 show the XPS scan V2p$_{3/2}$, O1s and N1s environments respectively in the V_2O_5/AnAn$^+$ material. Compared with pure V_2O_5 (Figure 4.9 and Figure 4.10) there are noticeable changes. In Figure 4.11, the major V2p$_{3/2}$ peak appears at ~517.4 eV as was seen in Figure 4.9 matching well with the literature value. However, the minor peak (V2p$_{3/2}$ fit 2) appears at ~516 eV which corresponds well to literature value for V^{4+} (263) showing that there was indeed a redox reaction occurring between the inorganic host and the organic guest in which the V^{5+} was reduced to V^{4+}. In

relation to this, we now have a peak appearing for the N1s (Figure 4.13) at ~400 eV which would arise from the organic guest. This corresponds well with both neutral and protonated forms of polyaniline (401.0 eV in the neutral form 399.50 eV in the protonated form) (264,265). Due to the noise-to-peak-ratio, two environments were fitted but it has been shown for emeraldine that four environments can be potentially seen appearing at 398.5, 399.5, 400.8 and 402.2 eV for a highly resolved N1s signal corresponding to the presence of the bipolaron, polaron and neutral amine and non-emeraldine phases(265). When combining the evidence gathered from previous techniques Figure 4.13 tells us that the aniline-based guest that is present in the interlayer spacing is indeed in the emeraldine form which was seen in the IR and Raman which showed presence of the quinoid rings which may give rise to the signal seen in the ESR (Figure 4.41) whereas the TGA and ICP-AES showed the guest being present the oligomeric/polymeric form. This is further corroborated by the ESR for this material (Figure 4.41, pg. 158) in which the single symmetric peak was concluded to arise from the inorganic phase of this material and would be likely to be formed from any redox chemistry between the inorganic phase and the organic phase giving rise to delocalised polarons or bipolarons present in the emeraldine material. Figure 4.12, on the other hand, shows the O1s signal can be fitted with three potential environments. The main peak (O1s fit 1) appears at ~530.2 eV which corroborated well with the literature values mentioned in Figure 4.10. However, the two minor environments appear at ~531 (O1s fit 2) and ~533 (O1s fit 3) eV respectively. Fit 3 corresponds closely with the O1s of water (533.10 eV) (266) and as seen in the TGA this may either be due to loosely bound water molecules on the surface or in the interlayer spacing. Fit 2, however, may be due to any interactions of hydrogen bonding that is occurring from the V=O oxygen and the N-H hydrogen from the emeraldine guest which was demonstrated to exist for certain orientations of organic guests containing amine groups (in section 1.5.1) limiting the V=O vibrational space. This sheds a little more light on the nature of the

intercalation discussed in the XRD data where it was observed that there was a broadening of the interlayer expansion peak, the oligomeric or polymeric guest species may not lie ideally parallel to the inorganic layers in the interlayer spacing. The guest oligomer or polymer backbone may be twisted (such as a helical orientation of the backbone) giving rise to various different d-spacings throughout the material.

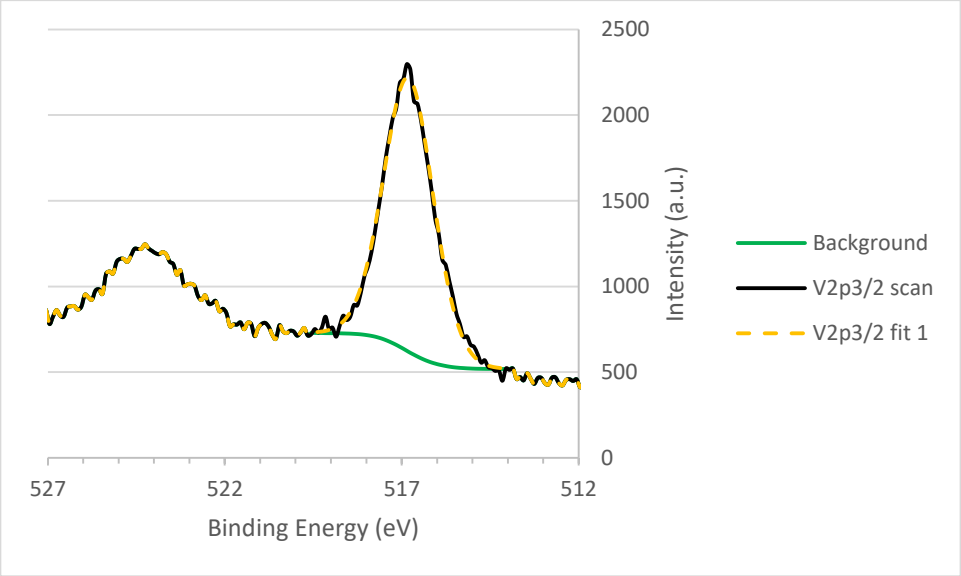

Figure 4.14 - XPS scan for V_2O_5/2A5PhPyr synthesised via direct intercalation showing the $V2p_{3/2}$ environment (black) fitted a single environment (orange; 517.42 eV)

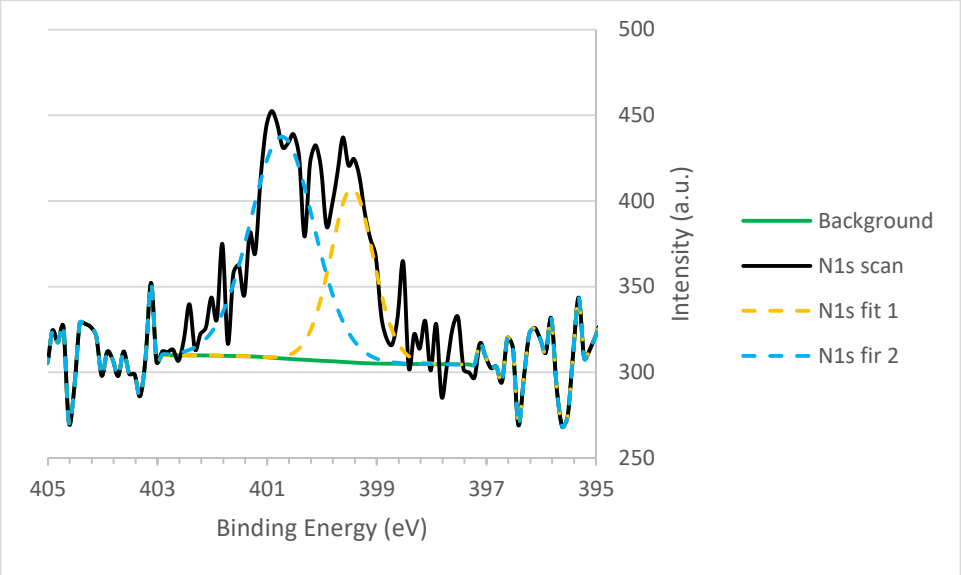

Figure 4.15 - XPS scan for V_2O_5/2A5PhPyr synthesised via direct intercalation showing the N1s environment (black) fitted with two potential environments (orange; 399.52 eV and blue; 401.92 eV)

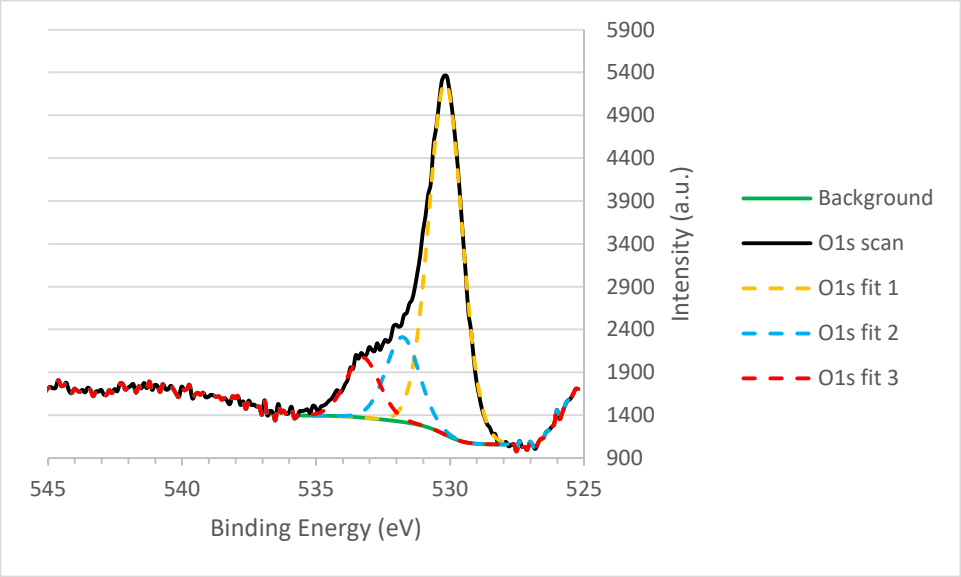

Figure 4.16 - XPS scan for V_2O_5/2A5PhPyr synthesised via direct intercalation showing the O1s environment (black) fitted with three potential environments (orange; 530.22 eV and blue; 531.92 eV and red; 533.42 eV)

Figure 4.14, Figure 4.15 and Figure 4.16 show the XPS scans for the $V2p_{3/2}$, N1s and O1s environments respectively for the V_2O_5/2A5PhPyr material. Figure 4.14 appears to show that the best fit for the signal resides with a single fit. In comparison to the $V_2O_5/AnAn^+$ material (Figure 4.11) which showed two environments (V^5 and V^{4+}) this does not appear to be the case in this material, therefore, it may be possible that the direct intercalation that was shown in the XRD data did not occur via a redox reaction based solely XPS data presented (a surface specific technique). However, in the intercalated material, there are at least two nitrogen environments which would be expected from the nitrogen of the amine group and the nitrogen in the aromatic ring. From the IR, TGA and ICP-AES it was concluded that the material was indeed in its oligomer or polymeric form. Figure 4.16 suggests that there may be an interaction between the guest and the oxygen of the V=O or V-O-V as these peaks appear to match that for the $V_2O_5/AnAn^+$ material (Figure 4.12). This suggests that fit 1 seen in Figure 4.16 corresponds to that of V_2O_5 oxygen while fit 3 arises from any surface bound water molecules. Fit 2 is possibly the interacting hydrogen bond between the hydrogen of the amine group and the oxygen from V=O. As stated above with the $V_2O_5/AnAn^+$ material, the fact that the organic intercalant would have to twist its conformation in order for this hydrogen bonding to occur and appear in the signal could

lead to the broadening of the shifted interlayer spacing (*001*) peak in the XRD data. However, the IR, Raman, ESR (Figure 4.42), TGA and ICP-AES data was concluded to suggest that the organic material was in fact polymerised within the interlayer spacing of V_2O_5. From this XPS it is conclusive of the fact that any polymerisation did not occur via the redox mechanism seen for V_2O_5/AnAn$^+$. The mechanism may, therefore, have undergone an acid-base like mechanism whereby the 2A5PhPyr (acting as a base when solvated) could have chelated with the V_2O_5 (which may show some acid oxide characteristics in the aqueous conditions) which would further facilitate redox chemistry with the V^{5+} centres. However, it is noticeable in Figure 4.14 only V^{5+} is present. It must be noted that XPS is a surface specific technique and therefore it is possible that any V^{4+} present in the surface layers may have been quenched and oxidised most likely during the washing and cleaning process.

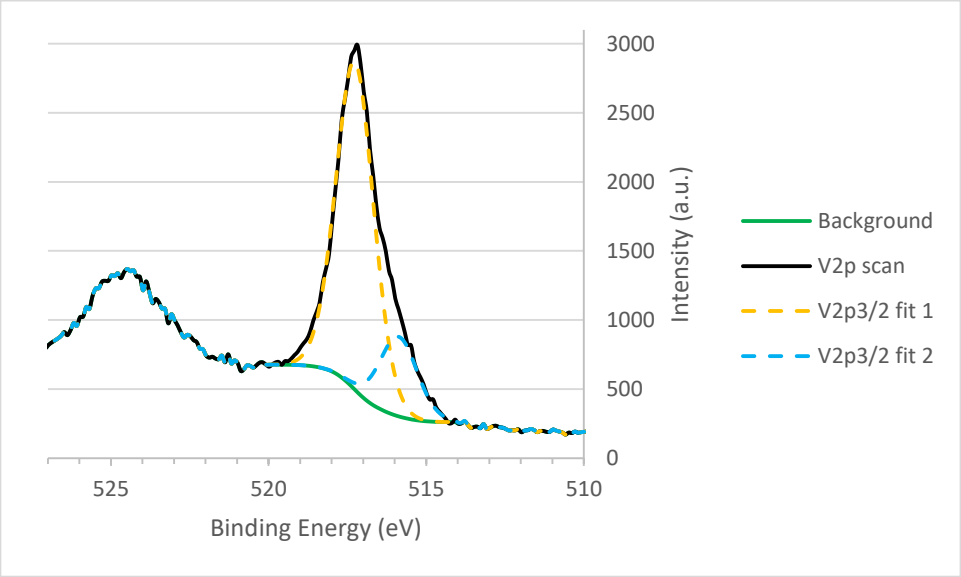

Figure 4.17 - XPS scan for V_2O_5/EDOT synthesised via direct intercalation showing the V2p$_{3/2}$ environment (black) fitted with two environments corresponding to V^{5+} (orange; 516.18 eV) and V^{4+} (blue; 517.38 eV)

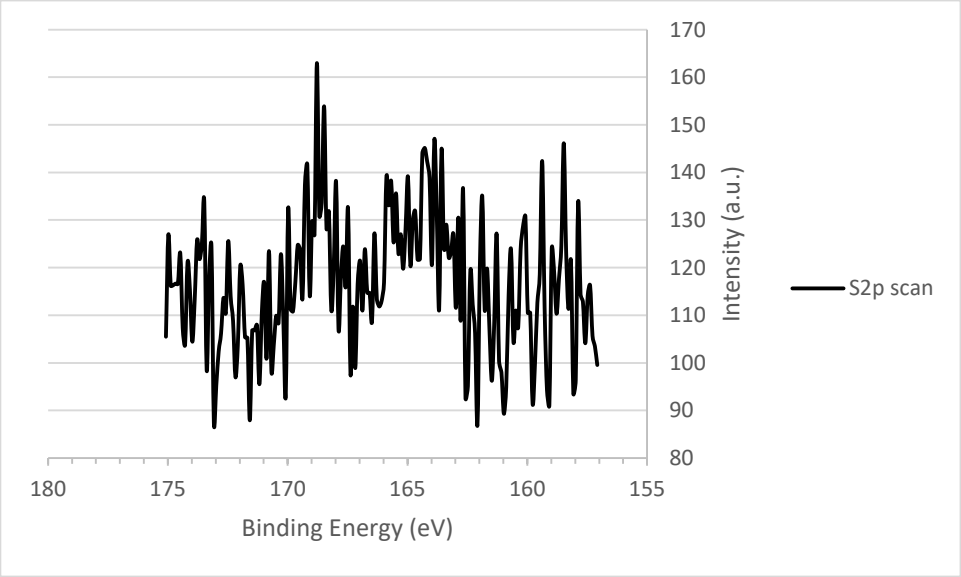

Figure 4.18 - XPS scan for V_2O_5/EDOT synthesised via direct intercalation showing the S1p environment (black)

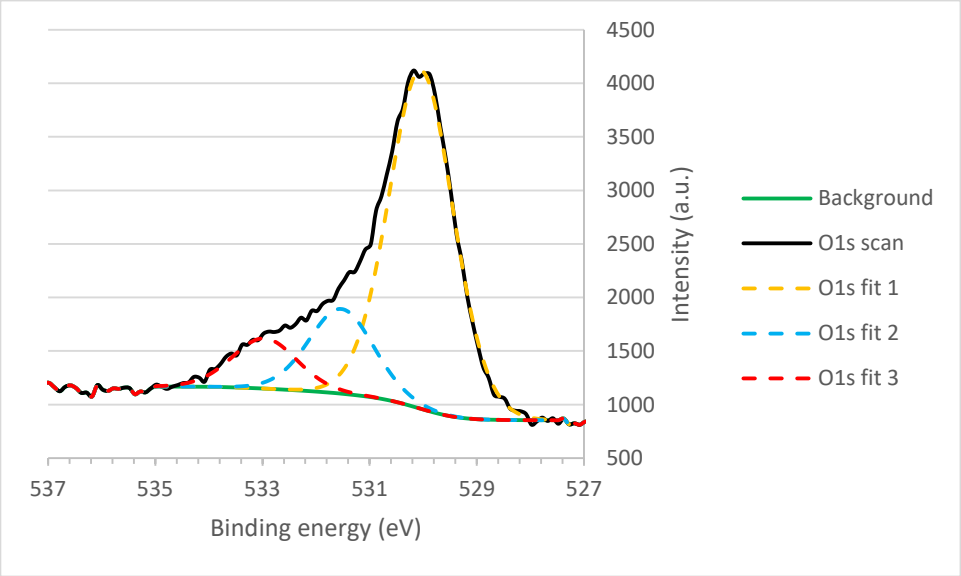

Figure 4.19 - XPS scan for V_2O_5/EDOT synthesised via direct intercalation showing the O1s environment (black) fitted with three environments (orange; 530.18 eV, blue; 531.68 eV and 533.18 eV)

Figure 4.17, Figure 4.18 and Figure 4.19 show the V2p$_{3/2}$, S2p and O1s environments for the V_2O_5/EDOT material. Figure 4.17 matches the V2p$_{3/2}$ environments seen for V_2O_5/AnAn$^+$ (Figure 4.11) confirming intercalation occurred through the direct redox intercalation method which is in contrast to that seen for V_2O_5/2A5PhPyr (Figure 4.14). Figure 4.18 suggests that there is no S content in the material, however, due to XPS being a surface sensitive technique this could be explained by suggesting that there is very little organic material intercalated near the surface of the V_2O_5 material. As such, the varying degree intercalation that may be occurring could lead to the diffuse shifted (*001*) peak

exhibited in the XRD for this material. Furthermore, Figure 4.19 at first glance appears to be the same as for the previous materials discussed with fits 1 and 3 corresponding to the oxygen from the oxide and surface-bound water respectively. However, in this particular case, we do not expect to see any hydrogen bonding occurring from the organic intercalant and the oxygen from the host. Therefore fit 2 does not correlate with the conclusions drawn from the previous material and is, in fact, corresponding to the oxygen present in the organic guest species(267).

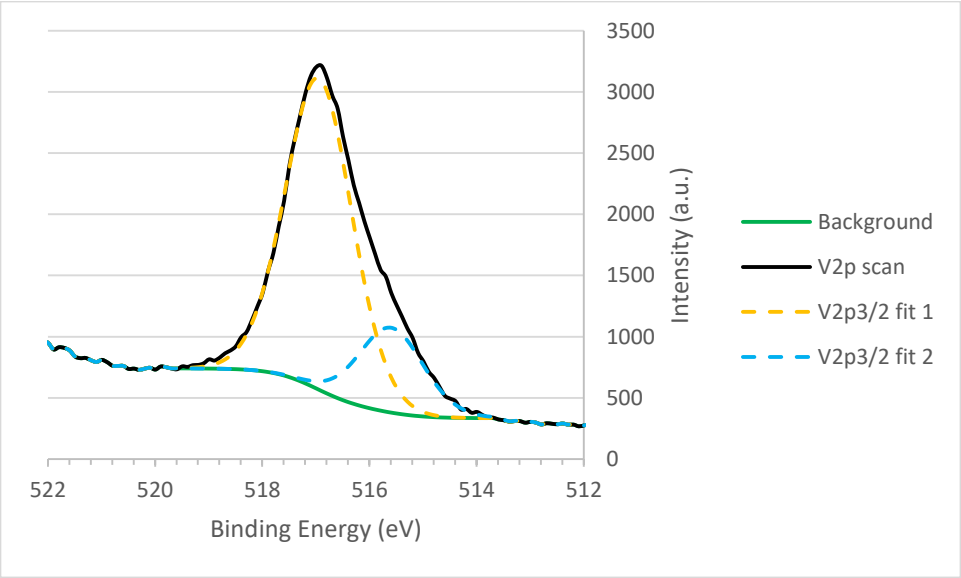

Figure 4.20 - XPS scan for LiV_2O_5 showing the $V2p_{3/2}$ environment (black) fitted to two environments (orange; 517.09 eV and blue; 515.69 eV)

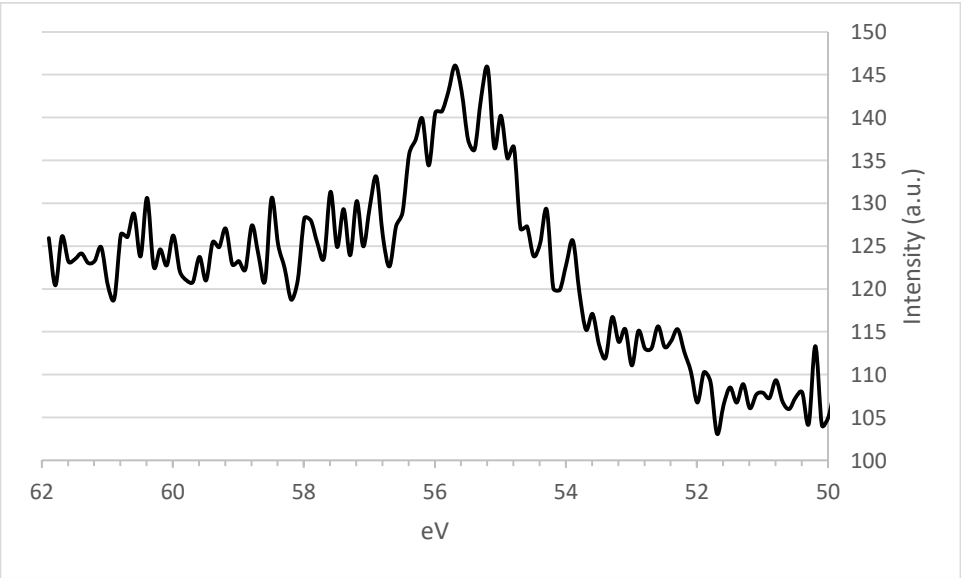

Figure 4.21 - XPS scan for LiV_2O_5 showing the Li1s environment

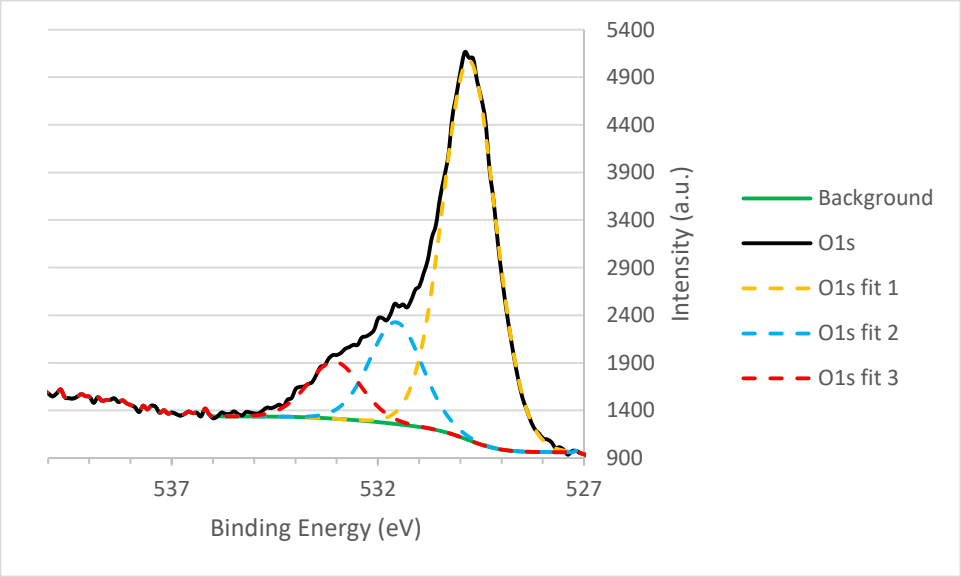

Figure 4.22 - XPS scan for LiV_2O_5 showing the O1s environment (Black) with a possible three environments fitted (orange; 529.79 eV, blue; 531.59 eV and red; 533.19 eV)

Figure 4.20, Figure 4.21 and Figure 4.22 show the XPS scan for LiV_2O_5 showing the $V2p_{3/2}$, Li1s and O1s environments respectively. In Figure 4.20 we see that there are two $V2p_{3/2}$ environments appearing in the same peak positions as that seen in Figure 4.11 suggesting that there is indeed a redox reaction with n-BuLi reducing V^{5+} to V^{4+}. Due to the low atomic mass of lithium, it is difficult to detect in the XPS hence the difficulty in fitting the data in Figure 4.21, however, a real peak appears to be present (noisy nonetheless) suggesting the successful insertion of Li^+ into V_2O_5. However, as seen in Figure 4.12, the O1s environments in Figure 4.22 can be potentially fitted into three environments. However, unlike in Figure 4.12 in which the material was synthesised under aqueous conditions, the peak that would usually be associated with the presence of H_2O (O1s fit 3) could in fact arise due to the small Li^+ being able to interact with the bridging oxygen (V-O-V) in V_2O_5 as well as the V=O (O1s fit 2).

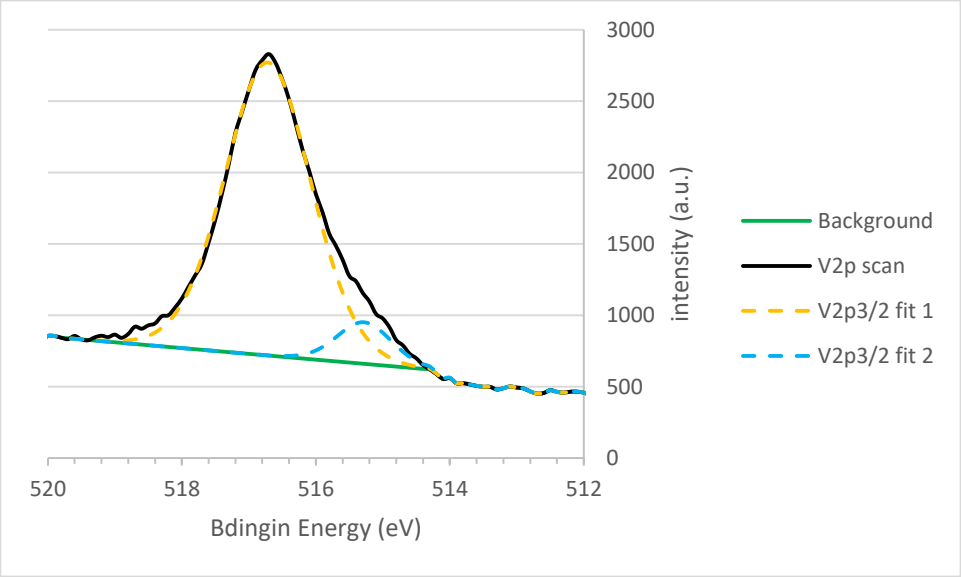

Figure 4.23 - XPS scan for V_2O_5/PDA synthesised via ion-exchange showing the V2p$_{3/2}$ environment (black) and the two fitted environments (orange; 516.70 eV and blue; 515.30 eV)

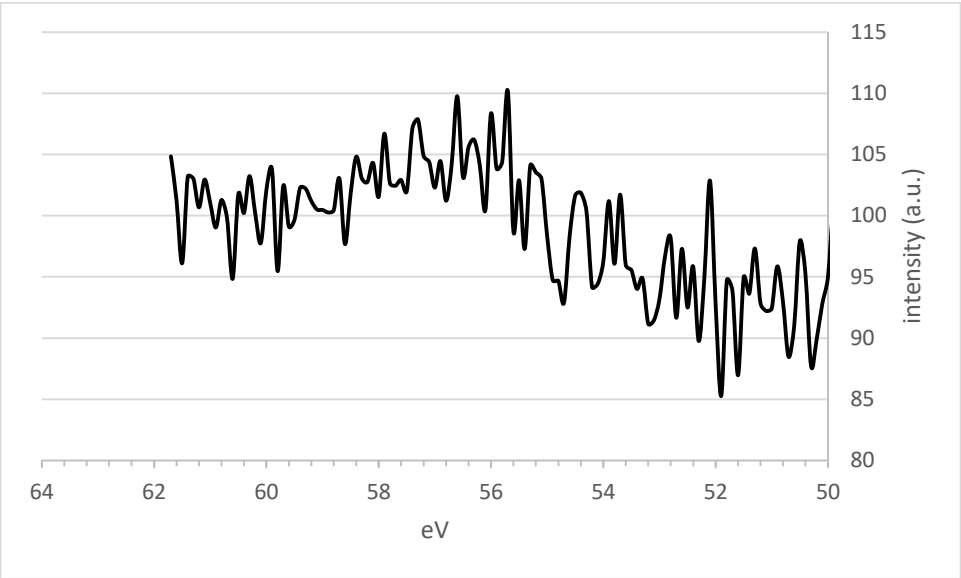

Figure 4.24 - XPS scan for V_2O_5/PDA synthesised via ion-exchange showing the Li1s environment

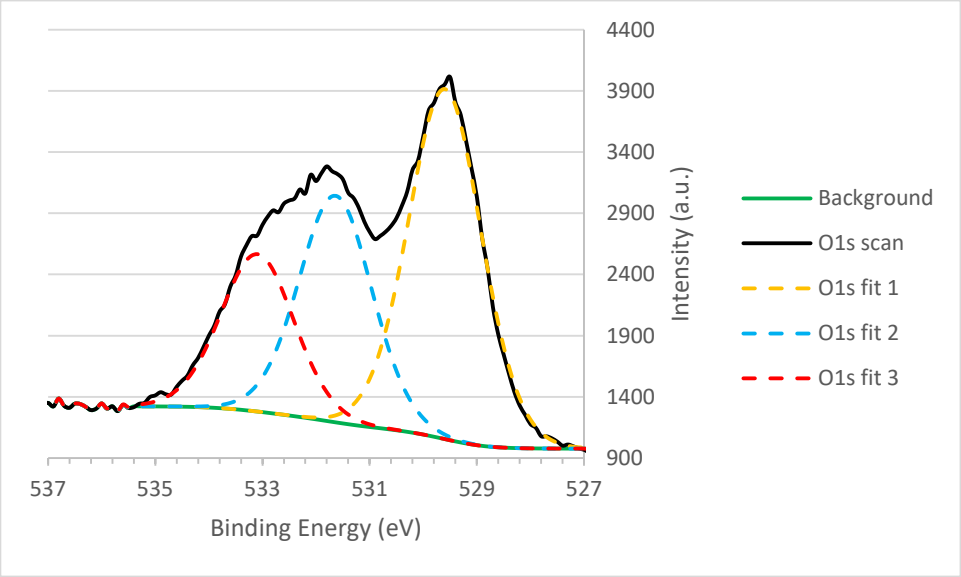

Figure 4.25 - XPS scan for V_2O_5/PDA synthesised via ion-exchange showing the O1s environment (black) with three potential environments fitted (orange; 529.7 eV, blue; 531.8 eV and red; 533.2 eV)

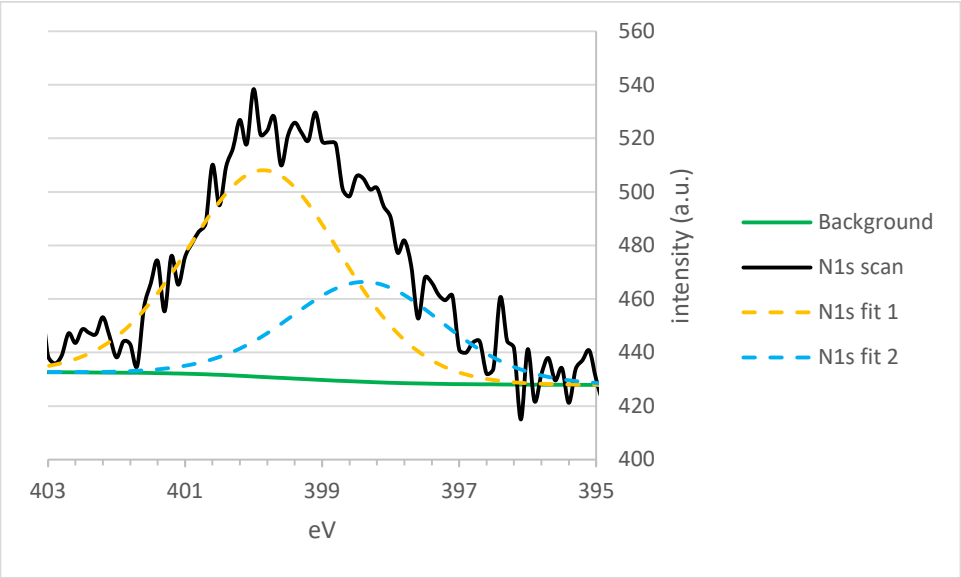

Figure 4.26 - XPS scan for V_2O_5/PDA synthesised via ion-exchange showing the N1s environment (black) and the two fitted environments (orange; 399.9 eV and blue; 398.4 eV)

Figure 4.23, Figure 4.24, Figure 4.25 and Figure 4.26 show the XPS scans for the $V2p_{3/2}$, Li1s, O1s and N1s environments respectively. Immediately it is clear from Figure 4.24 that there is no Li^+ remaining in the sample unlike in the case of LiV_2O_5 (Figure 4.21) suggesting ion-exchange had successfully removed the Li^+ ions. From Figure 4.26 we can see that there are two potential N1s environments as was seen in V_2O_5/AnAn$^+$ (Figure 4.13) with the peak positions corresponding well with the literature described in Figure 4.13 for an oligomeric or polymeric form of emeraldine suggesting successful intercalation of the organic cation exchanging with the Li^+ and polymerisation to form a conductive

phase (Figure 4.4). This further supports the conclusions drawn from the TGA and IR data where the TGA suggested oligomeric or polymeric organic intercalant present and the IR strongly suggested this material to be present in a conductive form, however from the XPS due to the potential at least more than one environment we can suggest that when combined with the IR data that the PDA polymerised with some phases resembling emeraldine while others resemble the ladder form. Interestingly, Figure 4.23 shows two $V2p_{3/2}$ environments that were seen in $V_2O_5/AnAn^+$ (Figure 4.11) and LiV_2O_5 (Figure 4.20) corresponding to V^{5+} (main component $V2p_{3/2}$ fit 1) and V^{4+} (minor component $V2p_{3/2}$ fit 2). When compared to the $V_2O_5/AnAn^+$ and LiV_2O_5 scans, the O1s environment has shown some changes. Figure 4.25 also shows three O1s environments but the two minor environments (O1s fits 1 and 2) are more pronounced than in the previous samples but the signals appear in the same positions suggesting that these signals are caused by the same mechanism with the signal appearing at 529.7 eV corresponding to the oxygen in the inorganic layers. The signal appearing at 533.2 eV can correspond to oxygen from any surface bound H_2O molecules while the signal at 531.8 eV appears to correlate to hydrogen bonded oxygen in the inorganic layers and the hydrogen from the amine groups of the organic guest. Unlike in the previous samples, the intensities of the peaks are much stronger, the intensity could be indicative of the amount present this particular sample was more hydrated on the surface than the previous samples) in the sample. By that logic, in this particular sample, we may be seeing far more hydrogen bonding occurring because of the presence of the polymerised protonated amine groups on PDA as well as this sample having more surface hydration than the previous samples.

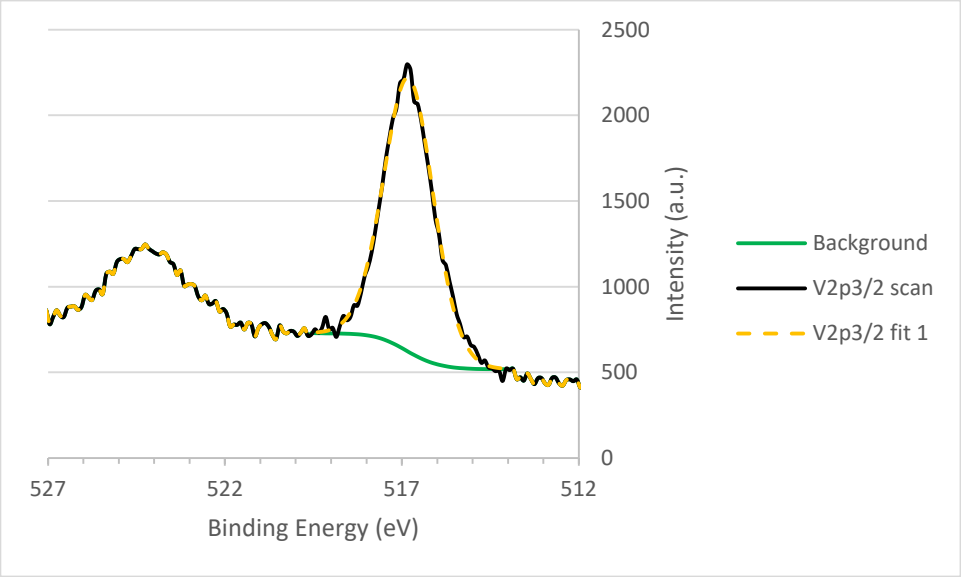

Figure 4.27 - XPS scan for LiV_2O_5/2A5PhPyr synthesised via ion-exchange showing the $V2p_{3/2}$ environment fitted to one environment (orange; 517.05 eV)

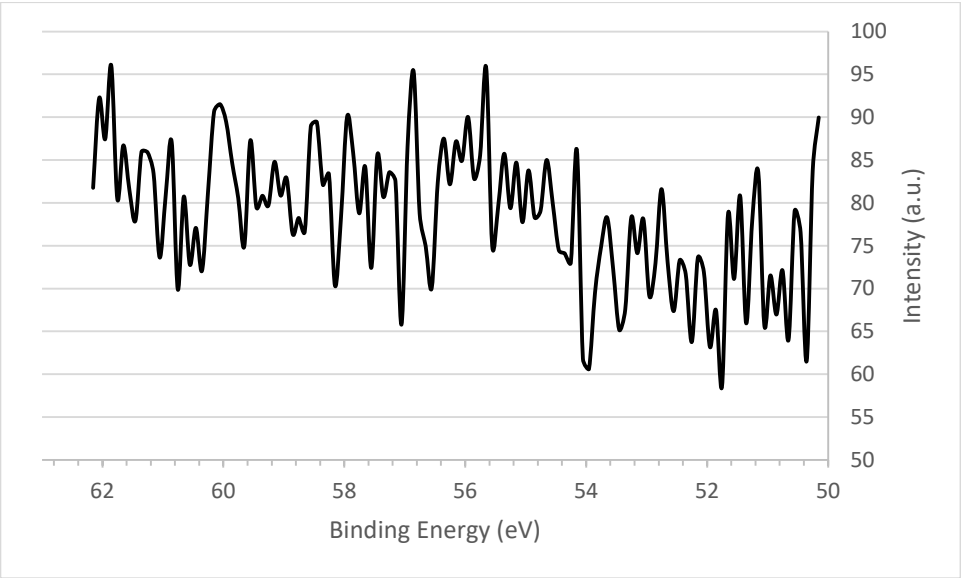

Figure 4.28 - XPS scan for LiV_2O_5/2A5PhPyr synthesised via ion-exchange showing the Li1s environment

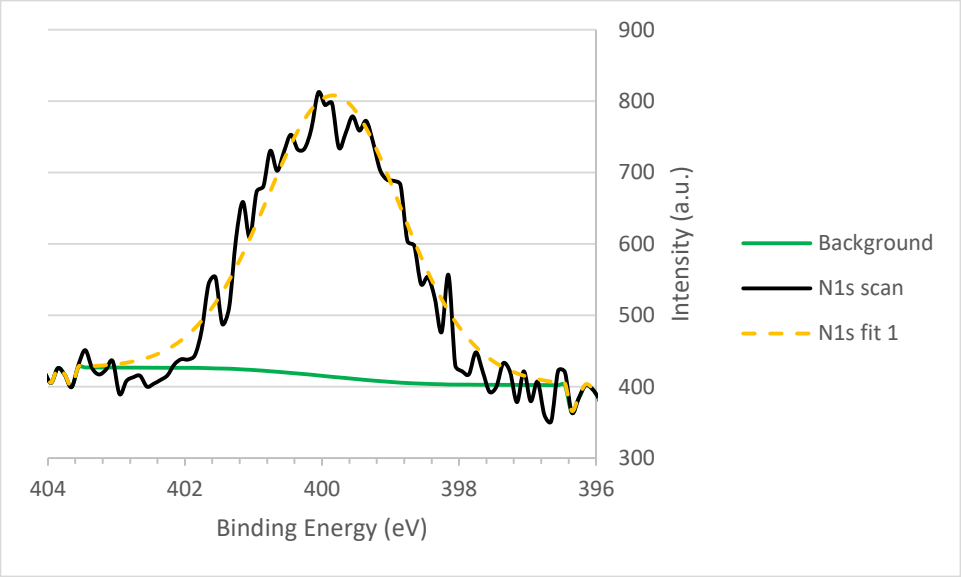

Figure 4.29 XPS scan for V_2O_5/2A5PhPyr synthesised via ion-exchange showing the N1s environment (black) with one fitted environment (orange; 399.84 eV)

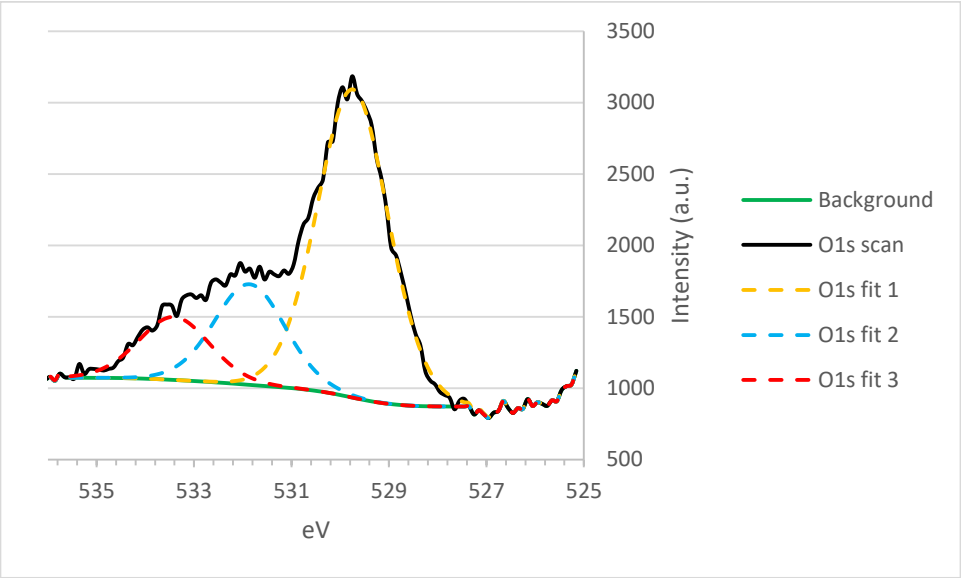

Figure 4.30 - XPS scan for V_2O_5/2A5PhPyr synthesised via ion-exchange showing O1s environment (black) with three fitted environments (orange; 529.85 eV, blue; 532.05 eV and red; 533.45 eV)

Figure 4.27, Figure 4.28, Figure 4.29 and Figure 4.30 show the XPS scans for the LiV_2O_5 /2A5PhPyr $V2p_{3/2}$, Li1s, N1s and O1s environments respectively. In Figure 4.11, interestingly, there is a single vanadium environment in the same position as for V_2O_5 (Figure 4.9) and V_2O_5/2A5PhPyr synthesised via an acid-base reaction (Figure 4.14) unlike in the previous figures in which two V environments are present (corresponding to V^{4+} and V^{5+}). As mentioned previously for V_2O_5/2A5PhPyr, XPS is a surface specific technique and therefore since no V^{4+} is present this suggests that any V^{4+} that was formed from lithiation was subsequently oxidised back to V^{5+} likely during the washing procedure

where this electron was quenched or by a redox reaction with the organic guest species. In Figure 4.28, it is clear that no Li^+ remains in the material and from Figure 4.29, the strong presence of Nitrogen suggests successful intercalation of the organic guests. However, although a single environment appears to show the best fit, it is likely more than one peak which is masked due to the noise of the signal as one could expect two separate signals from the N in the aromatic system and the polymerised amine group (reminiscent of a polyaniline like structure). From the IR and TGA, we know that the organic intercalant in this material is in its oligomeric or polymeric form. As such, it is possible that a redox reaction may have occurred between the inorganic and organic materials in which the electron that would then be present in the inorganic layer was removed returning it back to its neutral form due to the variable oxidation states of V. Figure 4.30 shows the same three O1s environments as discussed the previous materials.

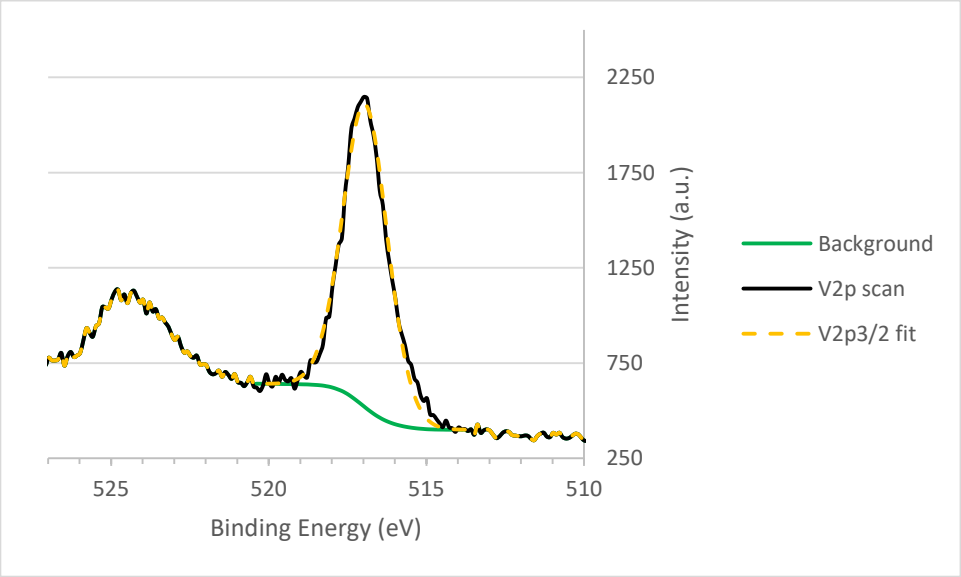

Figure 4.31 - XPS scan for V_2O_5/5AQ synthesised via ion-exchange showing V2p$_{3/2}$ environment (black) with fitted with a single environment corresponding to V^{5+} (orange; 517.08 eV)

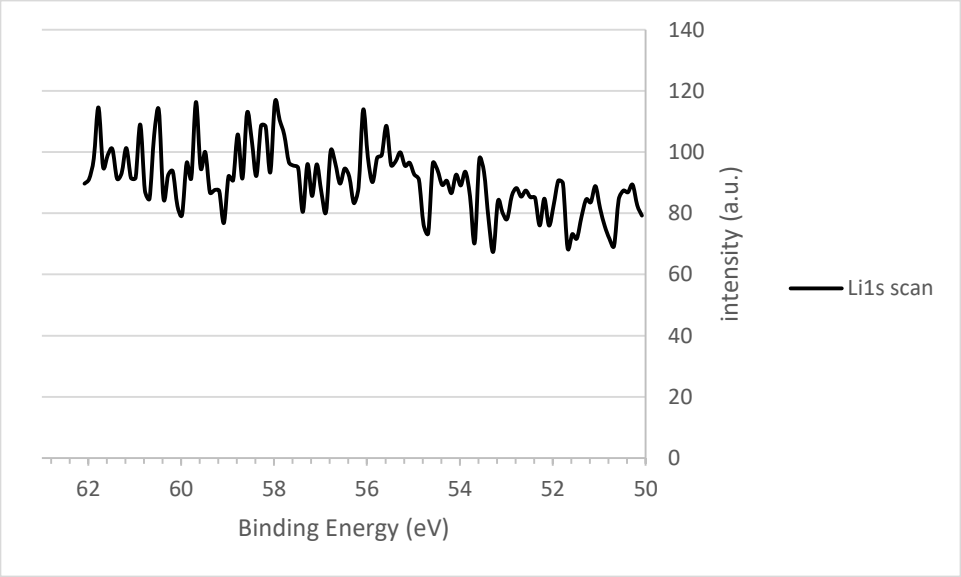

Figure 4.32 - XPS scan for V_2O_5/5AQ synthesised via ion-exchange showing Li1s environment (black)

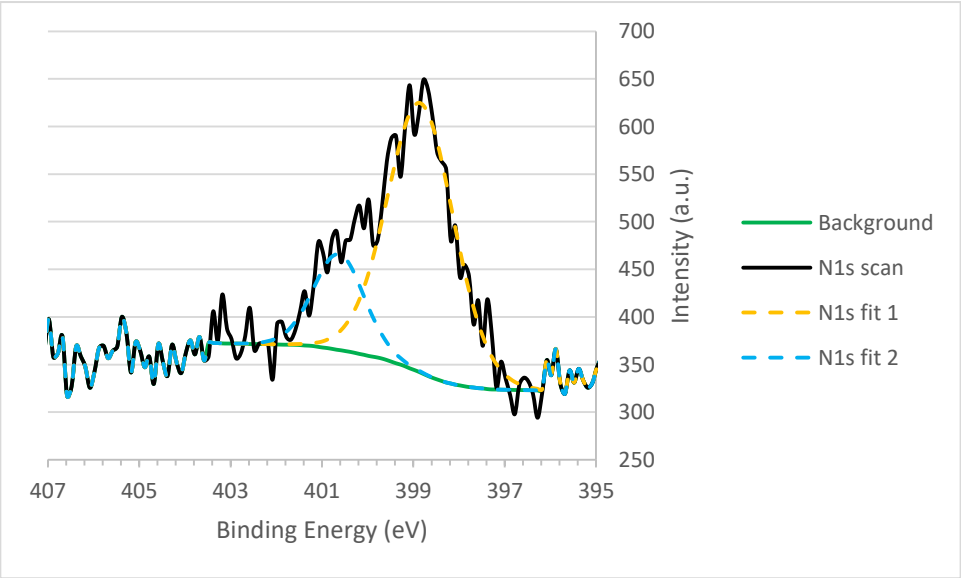

Figure 4.33 - XPS scan for V_2O_5/5AQ synthesised via ion-exchange showing the N1s environment (black) and the two fitted environments (orange; 399.98 eV and blue; 400.78 eV)

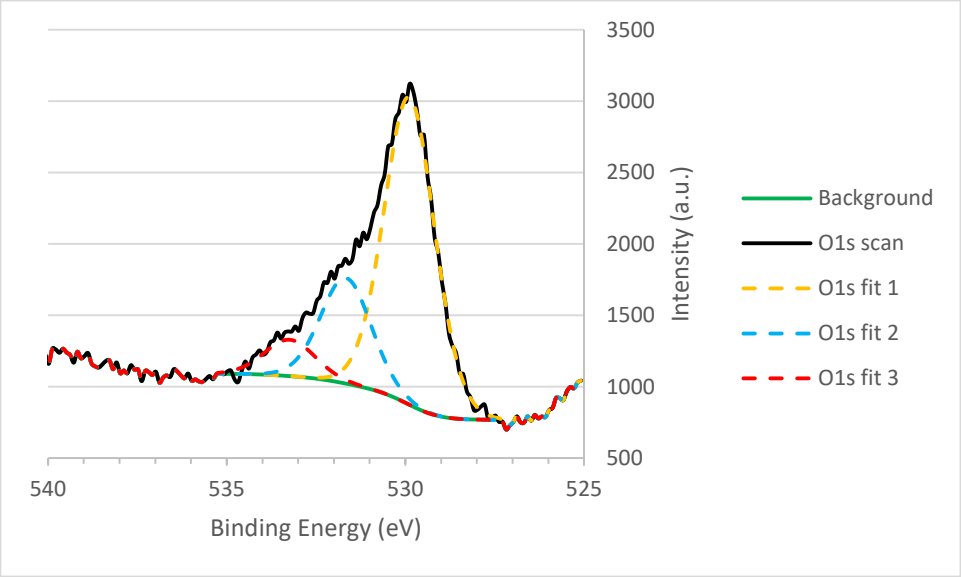

Figure 4.34 - XPS scan for V_2O_5/5AQ synthesised via ion-exchange showing O1s environment (black) with three fitted environments (orange; 529.98 eV, blue; 531.88 eV and red; 533.38 eV)

Figure 4.31, Figure 4.32, Figure 4.33 and Figure 4.34 shows the XPS scans for the V_2O_5/5AQ material. It can be seen that successful ion-exchange has occurred as there is no lithium present. However, Figure 4.31 shows a single vanadium environment. The lack of the V^{4+} peak is similar to that for V_2O_5/2A5PhPyr and LiV_2O_5/2A5PhPyr and therefore is likely due to the surface specific nature of XPS and concluded that any V^{4+} in the surface layers may have been quenched during the washing process. The presence of the organic was confirmed in the previously discussed techniques and as seen in the previous samples two nitrogen environments are seen in Figure 4.33. These peaks closely resemble that for V_2O_5/AnAn$^+$ (Figure 4.13) in respect to peak positions suggesting that the intercalated material may contain protonated amide groups similar to that in structure with V_2O_5/AnAn$^+$ in its oligomeric or polymeric form (as concluded from the IR, TGA and ICP-AES). The oxygen environments Figure 4.34 are as discussed for the previous samples confirms that the interlayer expansion seen in the XRD for this material is a result of successfully intercalating the guest into the interlayer spacing.

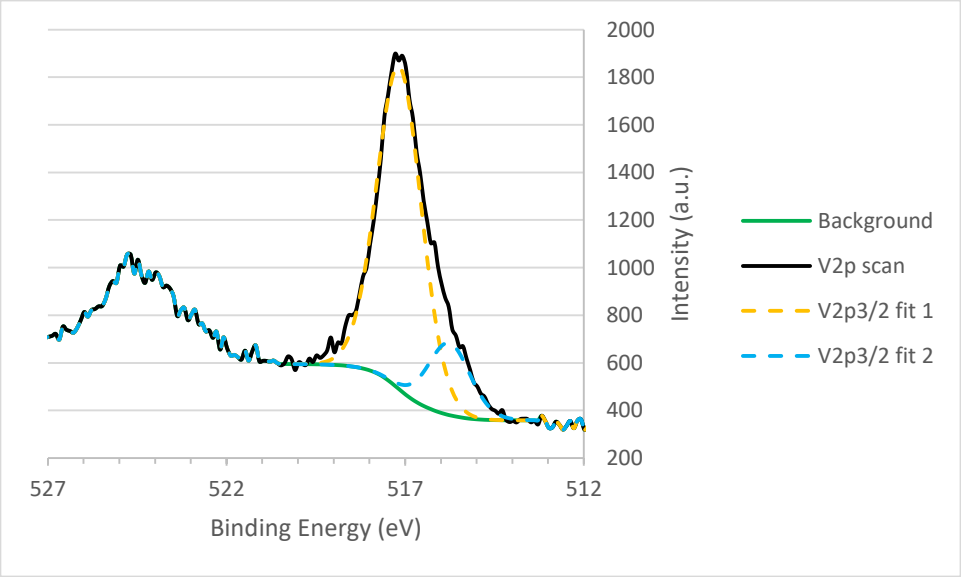

Figure 4.35 - XPS scan for V_2O_5/1,4PDA-HQ synthesised via ion-exchange showing V2p$_{3/2}$ environment (black) with two fitted environments (orange; 517.18 eV and blue; 515.88 eV)

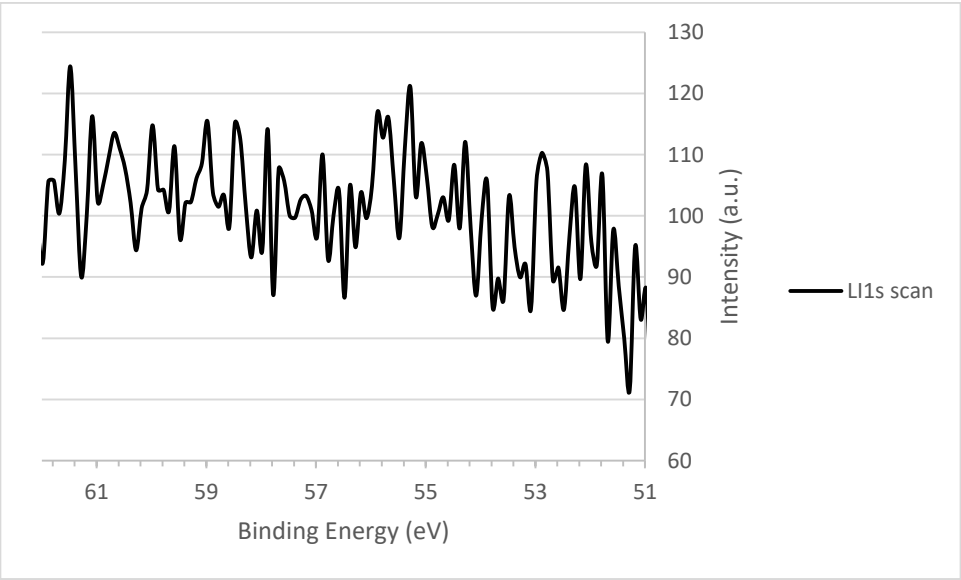

Figure 4.36 - XPS scan for V_2O_5/1,4PDA-HQ synthesised via ion-exchange showing Li1s environment (black)

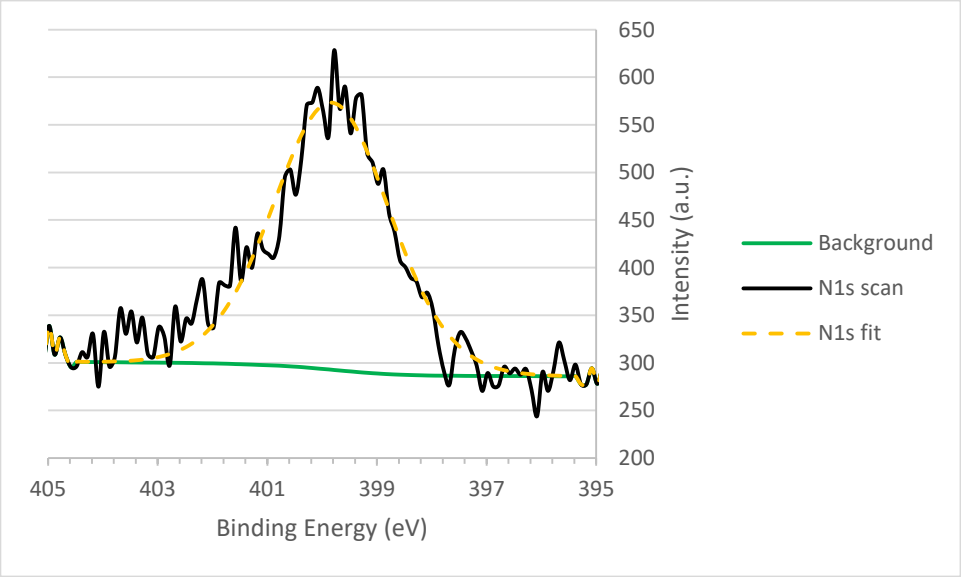

Figure 4.37 - XPS scan for V_2O_5/1,4PDA-HQ synthesised via ion-exchange showing N1s environment (black) with a single environment (orange; 399.78 eV)

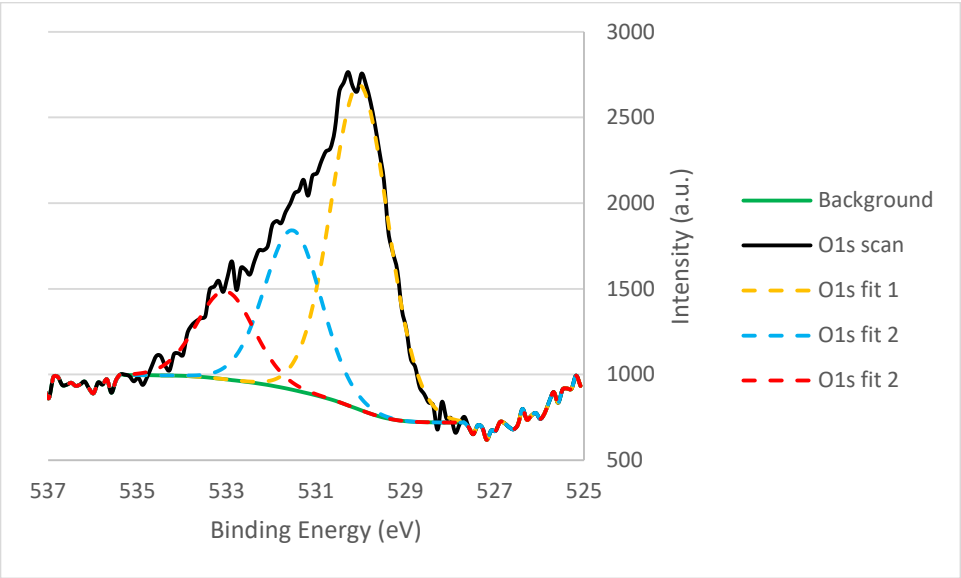

Figure 4.38 - XPS scan for V_2O_5/1,4PDA-HQ synthesised via ion-exchange showing O1s environment (black) with three fitted environments (orange; 530.18 eV, blue; 531.68 eV and red; 533.18 eV)

Figure 4.35, Figure 4.36, Figure 4.37 and Figure 4.38 show the XPS scans for the V_2O_5/1,4PDA-HQ material. As with the general case seen in the previous materials, Figure 4.35 shows two peaks for the $V2p_{3/2}$ environments corresponding with V^{5+} and V^{4+}. From the XRD, IR and Raman data we have seen that the organic material was intercalated into the interlayer spacing and from Figure 4.36 we see no Li^+ ions remaining when compared to the corresponding region in LiV_2O_5 (Figure 4.21) showing a successful exchange between the organic cation and the Li^+. Figure 4.37 shows a singular environment for N1s

fitted, it should be noted a singular environment was the best fit due to the noisy signal obtained. As seen in previous materials it is possible that there exist two or more environments in this signal. More telling is Figure 4.38 which on first inspection is identical to the O1s environments seen throughout the XPS data, however, due to the potential copolymer nature of this material (in the IR data the carbonyl C=O peak persists confirming its presence in the organic guests species and the oligomeric/polymeric nature of the material confirmed in the TGA and ICP-AES) the O1s peaks appearing at 531.68 eV and 533.18 eV can, in fact, be attributed to the ketone carbonyl O1s seen in a variety of polymer materials (268). The fact that these peaks are seen in polymer-based materials further lends evidence to the TGA for suggesting that a copolymer between 1,4PDA and HQ occurred within the interlayer spacing of V_2O_5.

4.1.1.6) Electron Spin Resonance Spectroscopy (ESR)

The pure V_2O_5 host showed no ESR peak present.

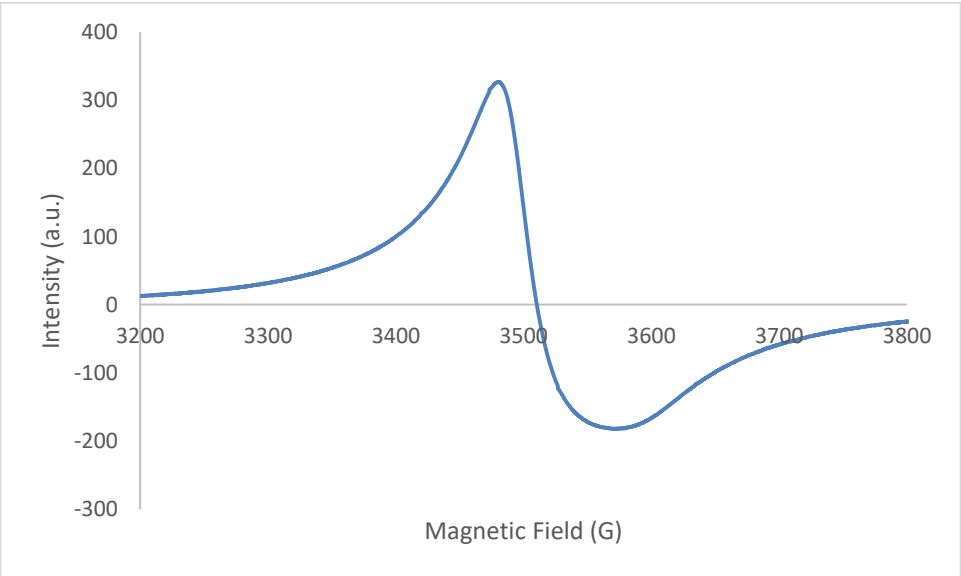

Figure 4.39 - LiV_2O_5 ESR spectrum

Figure 4.39 shows that ESR spectrum for the lithiated V_2O_5 precursor material. The spectrum centred at a g value of 1.974 with a peak-to-peak width of 90 Gauss and resembles that of the γ-phase of the material(269). When compared to the host material

there is a strong singlet signal suggesting that the suspected mechanism of electron-exchange between the n-BuLi and the inorganic host has occurred resulting in the formation of the V^{4+} centres. The low g-factor compared to that for the free electron (g-factor = 2.00232) suggests the signal is arising from the reduced V^{4+} centres. Furthermore, there is no hyperfine splitting present and as such the electron is undergoing no coupling with any vanadium nuclei. The sharpness of the peak suggests that there is a degree of localisation occurring in this system, which is supported by the lack of hyperfine structure present. Any asymmetry and enhanced broadening exhibited in the spectrum could could arise from any structural defects caused by the intercalation process (i.e. any stacking defects in the *c*-axial direction or screw defects in the bulk and/or surface based) or due to the presence of the V^{4+} centres which may be insufficient enough concentration to be considered as impurities leading to the material being treated as an inhomogeneous material. It is less likely that other vanadium oxides have formed (such as the VO_x family) contributing to the asymmetry or enhanced broadening as these systems were not present in the UV-Vis or XRD data.

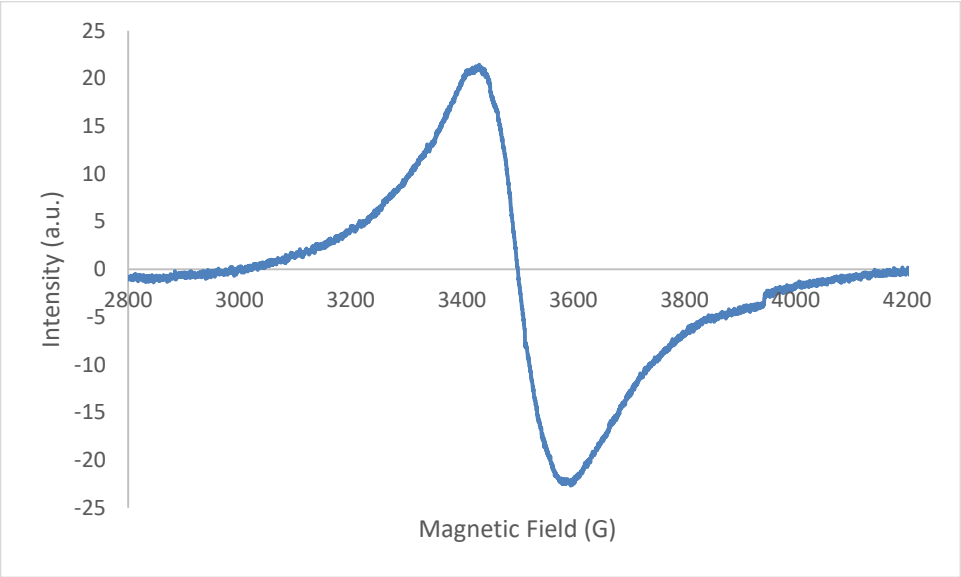

Figure 4.40 - V_2O_5/EDOT ESR Spectra

In Figure 4.40, it is shown that the spectra for direct intercalated EDOT into V_2O_5 interlayer spacing resulting in a singlet single (i.e. no hyperfine splitting) which, similar to the case in Figure 4.39, the signal arises from the inorganic phase for a localised electron. The signal is centred with a g value of 1.971 and a peak to peak width of 168 Gauss which is broader than that shown to the lithium intercalation (Figure 4.39). This peak to peak width corresponds to the presence of the δ-V_2O_5 phase (269). However, as for Figure 4.39, the g-factor values below that for the free electron is suggestive that the peak arising from the V^{4+} reduced centres. The broadening of the peak could further be enhanced due to stacking defects or irregular interlayer spacing in the *c*-axial direction (and/or on the surface) as well as the homogenous broadening similarly exhibited in the LiV_2O_5 material due to the mix of V^{5+} and V^{4+} centres. This is supported in the XRD data where the peak corresponding to the interlayer expansion is diffuse which could be explained as a range stacking orientations, skewing defects or other *c*-axial defects. The single peak suggests that the electron present is not undergoing interaction with vanadium nuclei and therefore no hyperfine structure is present and is likely to be localised.

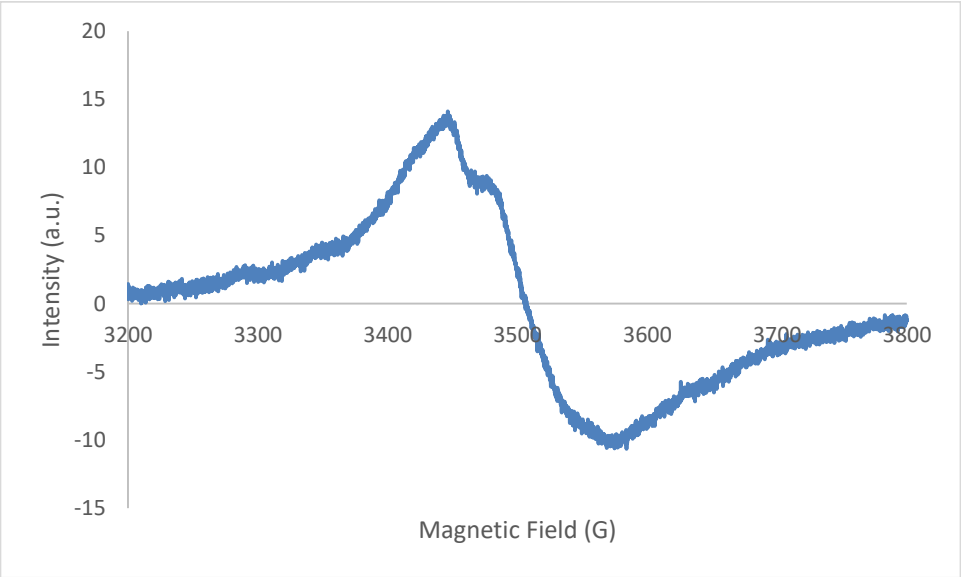

Figure 4.41 - V_2O_5/AnAn$^+$ ESR spectrum

Figure 4.41 shows the spectra of the AnAn$^+$ intercalated V_2O_5 via the direct intercalation. The signal is centred at a g value of 1.974 with a peak to peak width of 129 Gauss. There is

also the presence of a shoulder located at a g value of 1.997 (3474 Gauss). The peak to peak width suggests the presence of the δ-V_2O_5 phase (269). Some asymmetry is evident in the amplitude of the spectra as well as broadening. As seen in the previous ESR spectra the asymmetry and broadening are likely to be attributed to any stacking defects that may be present in the *c*-axial direction. Once again the presence of the single peak (i.e. no hyperfine splitting) the electron is not exhibiting any interactions with the vanadium nuclei but due to the low g value as seen previously suggests that the electron is localised on the inorganic phase of the material. On the other hand, the spectra could be a combination of two different signals (i.e. a combination of a narrow and broad peak) that could arise from two different phases of the inorganic material, as seen previously (269). The XRD data supports this as the diffuse peak correlating to interlayer expansion could be diffuse due to the differing inorganic phases in the bulk material. Furthermore, compared to the previous spectra this spectrum exhibits a weaker signal such that one could conclude that the concentration of the unpaired electrons present is small. This could be explained by the fact that a small concentration of the monomer reacts via a redox reaction with the V_2O_5 upon which once the layers are swelled, the remaining monomers (protonated and neutral) in solution are able to intercalate and react with the intercalated monomers previously oxidised rather than undergoing further redox reactions the V_2O_5.

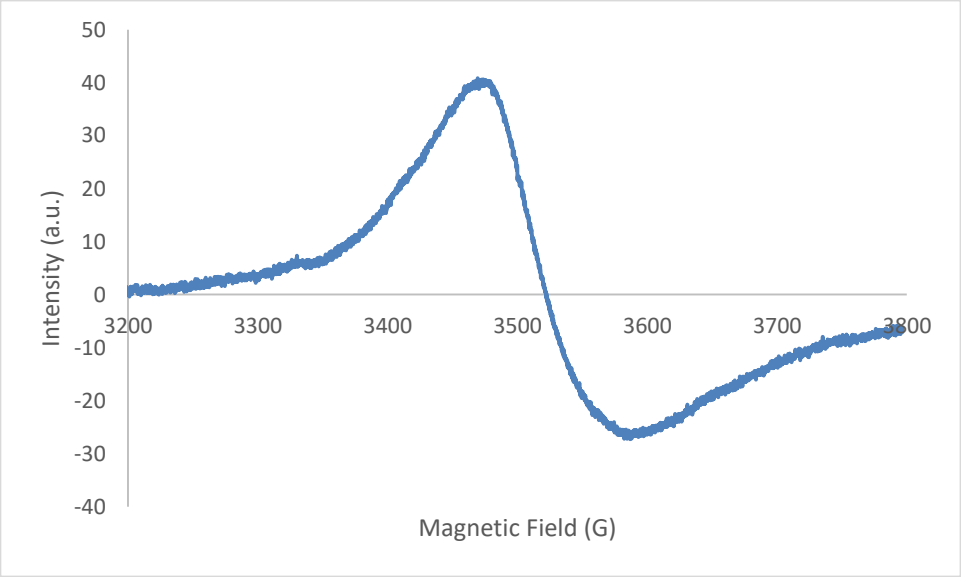

Figure 4.42 -V_2O_5/2A5PhPyr (AB) ESR Spectrum

Figure 4.42 shows the ESR spectrum for the V_2O_5/2A5PhPyr synthesised via acid-base direct intercalation and is centred at a g value of 1.966 with a peak-to-peak width of 118 Gauss, as seen previously this peak to peak width is closely related to the presence of the δ-V_2O_5 phase (269). As with the previous spectra, this material also exhibits a broadened and asymmetric peak. This broadening could be due to any defects (on the surface or bulk along the c-axial plane) that may have occurred during the intercalation process. This was seen in the XRD where the peak appearing for the characteristic (*001*) has broadened along with the peak corresponding for the interlayer spacing expansion. The asymmetry is reminiscent to that for the LiV_2O_5 material (Figure 4.39) and due to its g-factor value being lower than that for the free electron it is likely that this peak is attributed to a localised electron in the inorganic phase of the material. Although the XPS suggested that no V^{4+} is present, this ESR signal is representative of the property of the bulk material and not surface specific (as with XPS) suggesting that the V^{4+} in the surface layers have been quenched (oxidised) to the V^{5+} likely to occur from the washing process in the synthesis. The V^{4+} given rise to this peak in the ESR may, therefore, be found at a depth in the material beyond that of the detectable by XPS.

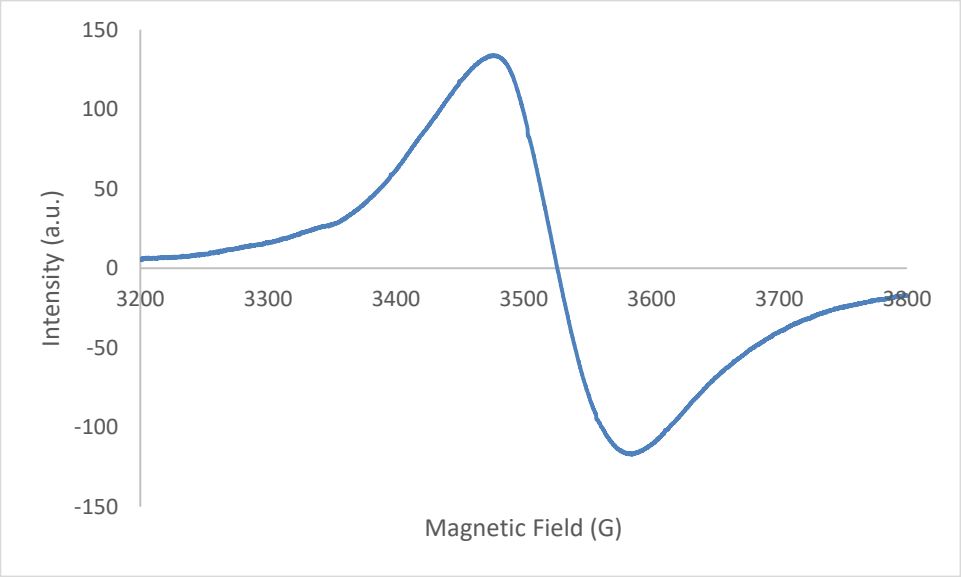

Figure 4.43 - V_2O_5/PDA ESR spectrum

Figure 4.43 shows the ESR spectrum of the V_2O_5/PDA material synthesised via ion-exchange. The spectrum is centred at a g-factor value of 1.9648 with a peak-to-peak width 108 Gauss. This peak to peak width is representative of the δ-phase, as seen previously (269). The low g-factor value, when compared to that of the free electron, suggests that the localised electron is present in the inorganic phase of the material and any redox chemistry caused by the organic guests during intercalation post-ion-exchange may increase the concentration of unpaired electrons. The lack of any hyperfine further suggests this localised electron is not interacting with any vanadium nuclei. As with the previous spectra, we observe peak broadening with a slight asymmetry present. This suggests that the unpaired electrons reside in the inorganic host. The major component to the asymmetry and broadening, as seen in the previous spectra, arises from any defects occurring from the intercalation reaction (in the c-axial direction and/or surface based). These defects are seen in the XRD data for this material where the expanded interlayer spacing peak is a large diffuse peak with some small sharp peaks.

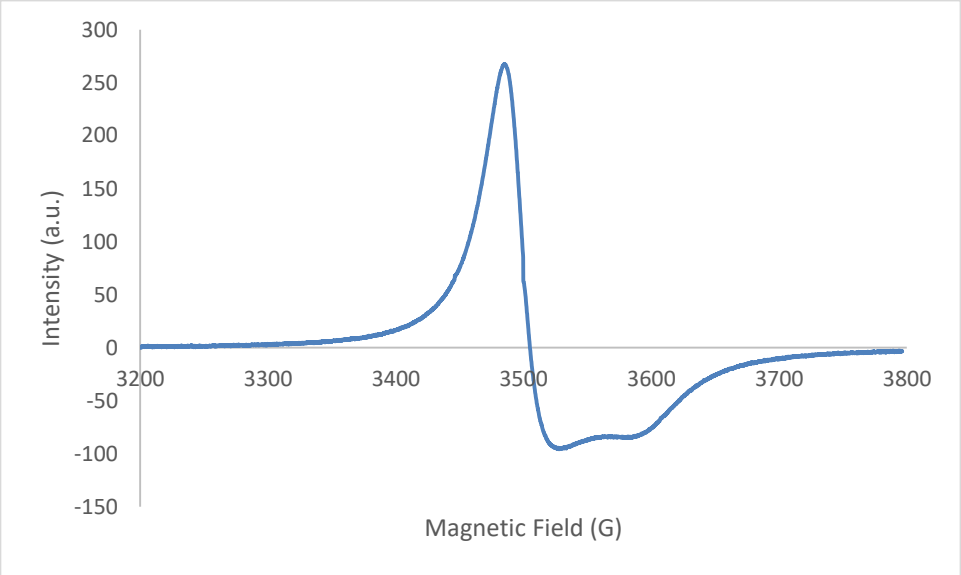

Figure 4.44 – LiV_2O_5/2A5PhPyr ESR Spectrum

Figure 4.44 shows the ESR spectrum for the LiV_2O_5/2A5PhPyr synthesised via ion-exchange. The spectrum is centred at a g value of 1.9756 with a peak-to-peak width of 38 Gauss with a shoulder appearing in the negative region at a g-factor value of 1.9282 (3594 Gauss). This spectra resembles that for the LiV_2O_5 (Figure 4.39) and as such the narrowness of this peak is closely related to that for the γ-phase for V_2O_5, as seen previously (269). The g-factor value lower than that for the free electron suggests that this electron is localised and present on the inorganic phase of the material. The full spectrum peak to peak width (including the shoulder is 108 Gauss). This shoulder appears to be more defined than that seen in Figure 4.41 and appears in the negative region as opposed to the positive region seen in Figure 4.41. The spectrum exhibits an asymmetric nature (minimum peak intensity of ~-93 and a maximum intensity of~261) as well as peak broadening. As seen in the previous spectra, this asymmetry is likely due to any c-axial defects and/or other defects (such as screw defects) on the surface. Again, as with the previous spectra, the XRD gives some insights as the expanded interlayer spacing peak is broad and diffuse suggesting that there is the presence of c-axial defects in this material. The appearance of the shoulder could be the overlapping of two different signals, with different line shapes and hence the signal appearing is a result of a combination of the two different signals

which could result in the enhanced asymmetry as compared to the previous spectra. From XRD, IR and Raman data it was concluded that there are two phases present in this material; the intercalated phase and the pure phase. It may be conceivable that the two peaks arise as a combination of peaks from the γ-phase from the intercalated V_2O_5 phase of the material pure host material which may also have some V^{4+} centres remaining from the Li^+ intercalation. As with V_2O_5/2A5PhPyr (Figure 4.42) although the XPS suggested that no V^{4+} is present, this ESR signal is representative of the property of the bulk material and not surface specific (as with XPS) suggesting that the V^{4+} in the surface layers have been quenched (oxidised) to the V^{5+} likely to occur from the washing process in the synthesis. The V^{4+} given rise to this peak in the ESR may, therefore, be found at a depth in the material beyond that of the detectable by XPS.

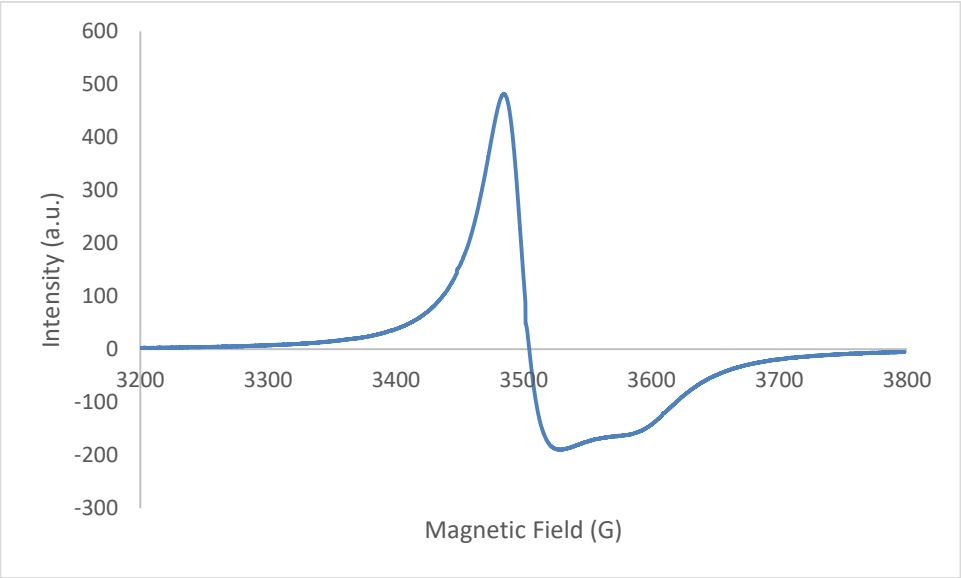

Figure 4.45 - V_2O_5/5AQ ESR spectrum

Figure 4.45 shows the ESR spectrum for the V_2O_5/5AQ material also synthesised via ion-exchange. The spectrum is centred at a g value of 1.976 and a peak-to-peak width 43 Gauss with a shoulder appearing located with a g-factor value of 1.931 (3586 Gauss) with full peak-to-peak width (including shoulder) of 100 Gauss. Compared to the previous composite material ESR spectra, the spectrum in Figure 4.45 is the narrowest and the 43

Gauss peak width corresponds to that for the γ-phase for the V_2O_5 as seen previously (269). The g-factor value. The narrow peak is similar to that in both LiV_2O_5/2A5PhPyr (Figure 4.44) and LiV_2O_5 (Figure 4.39) and more enhanced when compared to the other spectra. As such this asymmetry is associated with any c-axial defects (such as screw defects) and/or surface based defects (such as dislocations). The shoulder appearing in this spectrum appears to be found in the same region as that seen in Figure 4.44 and as such allows us to determine that this shoulder is not related to the main peak in the negative region and could indeed be arising from a different signal. Hence, as with the case in Figure 4.44, this signal may be a combination of two separate signals with differing line shapes. As with that in Figure 4.44, the XRD, IR and Raman data showed that there are two phases in this material, though still subjected to the effects of some defects (some of the characteristic V_2O_5 peaks in the XRD appear broad). It may be conceivable that the two peaks arise as a combination of peaks from the γ-phase from the intercalated V_2O_5 phase of the material pure host material which may also have some V^{4+} centres remaining from the Li^+ intercalation. As with V_2O_5/2A5PhPyr (Figure 4.42) although the XPS suggested that no V^{4+} was present, this ESR signal is representative of the property of the bulk material and not surface specific (as with XPS) suggesting that the V^{4+} in the surface layers have been quenched (oxidised) to the V^{5+} likely to occur from the washing process in the synthesis. The V^{4+} given rise to this peak in the ESR may, therefore, be found at a depth in the material beyond that of the detectable by XPS.

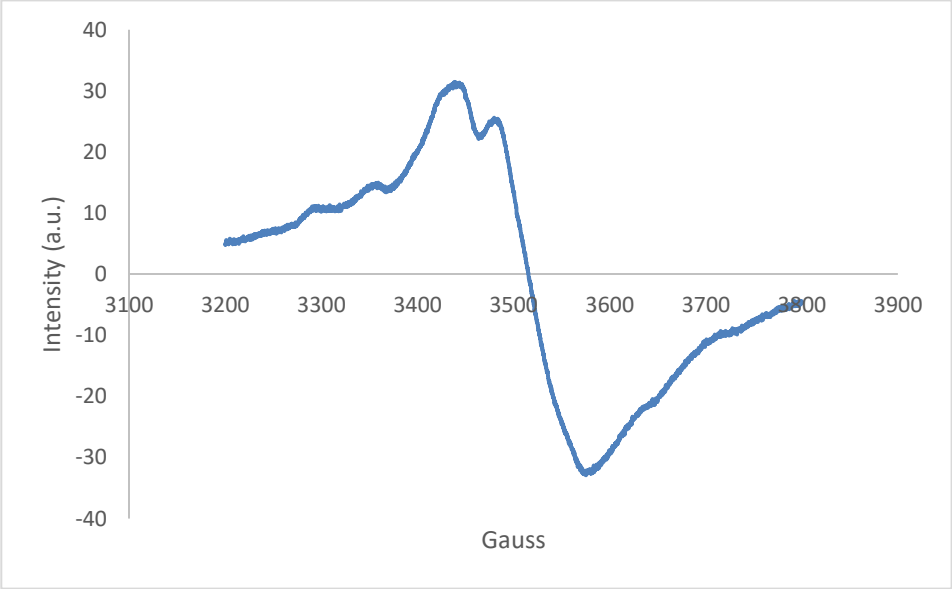

Figure 4.46 - V_2O_5/1,4PDA-HQ ESR spectrum

Figure 4.46 shows the ESR spectrum of the V_2O_5/1,4PDA-HQ synthesised via ion-exchange. The spectrum is centred with a g value of 1.971 with a peak-to-peak width of 98 Gauss with three shoulder peaks appearing in the positive region with g value maximum values of 2.064 (3440 Gauss), 2.104 (3356 Gauss) and 2.146 (3294 Gauss) with a full peak-to-peak width of 286 Gauss. The spectrum as a whole (including the shoulder peaks) appears to be symmetric suggesting that similar to Figure 4.39 the unpaired electrons are found in the organic guest species. The narrowness of the initial peak-to-peak region (the narrowest of all V_2O_5 composite spectra) is closely related to that of the δ-phase for V_2O_5 and the low g-factor value suggests that we are seeing a signal arising from a localised electron on the inorganic host material. However, the shoulders in this could arise from due to the copolymer formation between the p-phenylenediamine and hydroquinone(270) the symmetry of the OH on the hydroquinone part of the oligomer or polymer (as determined from the TGA and ICP-AES) may not be magnetically symmetric. As such these peaks could arise due to ^{1}H hyperfine coupling. This would suggest that there are two signals being exhibited in this material, the first that of the inorganic phase and the second that for the organic phase, which is unlike that for the previous spectra. Another possibility for the rise of these peaks could be due to a combination of various defects leading to several

differing phases in the inorganic leading to this peak being a combination of several peaks. As with V_2O_5/2A5PhPyr (Figure 4.42) although the XPS suggested that no V^{4+} is present, this ESR signal is representative of the property of the bulk material and not a surface based analysis as seen with the XPS.

Summary

Overall it has been shown that intercalation of the organic guest species into the interlayer spacing of V_2O_5 was successfully carried out. A full characterisation of the literature synthesised material V_2O_5/EDOT has been presented in this chapter as well as a novel method for synthesising emeraldine intercalated V_2O_5 (V_2O_5/$AnAn^+$) utilising a one-pot synthesis method which has previously not been reported by literature (section 1 where the common method for emeraldine growth involves substituted aniline monomers and doping after intercalation (and in some cases followed by the ageing process in the presence of oxygen) which may take several days to weeks to achieve. The novel compounds V_2O_5/2A5PhPyr, V_2O_5/PDA, LiV_2O_5/2A5PhPyr, V_2O_5/5AQ and V_2O_5/1,4PDA-HQ have been synthesised and fully characterised confirming the successful intercalation of the organic monomers within the V_2O_5 interlayer spacing. The increase in the interlayer spacing in the XRD data (Figure 4.1) corresponds to the presence of the intercalated organic guest species which is further corroborated with the XPS data. In the case of both direct intercalation and ion-exchange methods, the materials exhibit defects in the *c*-axial direction and a medium degree of control over the structural integrity of the host material during the intercalation process. This is further supported in the infra-red and Raman data (Table 4.2 - Table 4.4) in which the presence of the organic peaks and the shifted host peaks are typical for intercalated V_2O_5 (as previously discussed in section 1. Furthermore, the optical band-gap for the materials also change and in the case of these materials increases which have been concluded due to poor band overlap between the

organic and inorganic leading to the possible formation of indirect semiconducting material. The UV-visible data (Table 4.5) further show that the host region persists suggesting incomplete intercalation occurs in these materials which are also seen in the XRD where the characteristic host peaks remain along with the expanded *001* peaks. The organic intercalant has been shown to be fully polymerised within the interlayer spacing of the host confirmed with the TGA and ICP-AES independently. Along with these physical changes, chemical changes are shown to have occurred. The ESR and XPS data suggest that upon intercalation (for both methods in the general case) a redox mechanism is present at some point in the synthesis between the organic guest and inorganic host leading to a conducting material. The XPS shows that the V^{5+} ions are reduced to V^{4+} ions and that upon intercalation there are three oxygen O1s environments. From the characterisation carried out, any electrical/photovoltaic properties these materials exhibited (see Section 4.2.1) is likely to arise due to the nature of the organic material within the interlayer spacing. From the presented data the following reaction schemes are proposed;

Scheme 1 - Direct Intercalation

$$(V^{5+})_2O_5 + Monomer \rightarrow (V^{5+})_{2-x}(V^{4+})_xO_5(Monomer^+)_x$$

Scheme 2 - Direct Intercalation

i) $$(V^{5+})_2O_5 + nBuLi \rightarrow (V^{5+})_{2-x}(V^{4+})_xO_5(Li^+)_x + C_4H_{10}$$

ii) $$(V^{5+})_{2-x}(V^{4+})_xO_5(Li^+)_x + (Monomer^+)_{aq\ (excess)} \rightarrow$$

$$(V^{5+})_{2-x}(V^{4+})_xO_5(Monomer^+)_x + x(Li^+)_{aq} + (Monomer^+)_{aq\ (excess)}$$

4.1.2) MoO_3 Intercalation

4.1.2.1) X-ray Diffraction

Table 4.6 - Table to shows the interlayer spacing and change in interlayer spacing for the MoO3 intercalated compounds

Method	Interlayer spacing (Å)	Interlayer spacing change (ΔÅ)	2θ (°)	Intensity
Ion-exchange				
MoO_3	6.75	/	13.1	Strong sharp peak
$LiMoO_3$	9.20	2.45	9.6	Strong sharp peak
MoO_3/PDA	13.18	6.43	6.6	Strong sharp peak
MoO_3/2A5PhPyr	12.98	6.23	7.2	Strong sharp peak
MoO_3/5AQ	12.80	6.05	6.7	Strong sharp peak with a diffuse shoulder
MoO_3/2AmThia	13.38	6.63	6.6	Strong sharp peak
Recrystallization				
MoO_3/An	12.27	5.52	7.1	Strong Sharp peak with a diffuse shoulder

From Table 4.6 and Figure 4.47 we can see that in all cases intercalation increases the interlayer spacing of the host MoO_3. Upon reaction with n-BuLi, the new intercalated material Li_xMoO_3 not only showed an increase in the interlayer spacing when compared with the host but also maintained its crystalline ordered structure due to the sharpness of the peaks present. Upon ion-exchange with the organic guest monomers, it was shown that the crystalline ordered structure was maintained overall.

There is an increase in the interlayer spacing during ion-exchange for the synthesis of MoO_3/PDA composite with an overall interlayer spacing change 6.43Å (*020* peak appearing at 2θ ≈ 6.7Å). This suggests that the guest species is oriented planar and parallel to the host inorganic layers. Overall the MoO_3/PDA material shows good structural integrity upon ion-exchange. This maintaining of the structural integrity is further shown for the MoO_3/2A5PhPyr and MoO_3/2AmThia materials with interlayer spacings of 12.98Å (a change of 6.23Å with the *020* peak appearing at 2θ ≈ 6.8Å) and 13.38Å (a change of 6.63Å with the *020* peak appearing at 2θ ≈ 6.9Å) respectively. It had been mentioned in a

previous study (170) that this increase in interlayer spacing is characteristic of the oligomer or polymer backbone lying perpendicular to the plane of the inorganic layers. The peaks in the XRD that corresponds an increased interlayer spacing are, overall, sharp and strong as opposed to broad and diffuse (which could arise as a result of varying interlayer spacings which can occur if the intercalant is in a double layer conformation). The absence of a broad and diffuse peak for the expanded (*020*) would suggest a monolayer conformation of the intercalant. Furthermore, the sharp and well resolved expanded (*020*) peaks suggest good long structural order.

For MoO_3/5AQ the shifted (*020*) peak corresponds to the interlayer spacing of 12.80Å (a change of 6.05Å with the *020* peak appearing at 2θ = 6.8Å). In the case of MoO_3/5AQ, the (*020*) exhibits a slightly broadened or diffuse character that does not further show other discerning peaks. This may be due to structural defects in the *c*-axial direction (such as screw defects or step defects) due to intercalation. Some of the characteristic MoO_3/5AQ peaks at higher 2θ angles are still sharp but weaker which may suggest that there may be a small unintercalated phase present in this material. In MoO_3/An the shifted (*020*) peak corresponds to the interlayer spacing of 12.27Å (a change of 5.52Å with the *020* peak appearing at 2θ = 7.1Å). The expanded (*020*) peak in MoO3/An is weaker than the previous MoO_3 materials but also sharp which may suggest a minor amorphous phase could exist in the MoO3/An material.

Overall the X-ray diffraction data shows that there has been successful interlayer expansion which corresponds to the organic guest species being present. The sharp characteristic (*020*) suggests that there is little to no defects arising from the intercalation reaction, except a small degree occurring for that in MoO_3/5AQ.

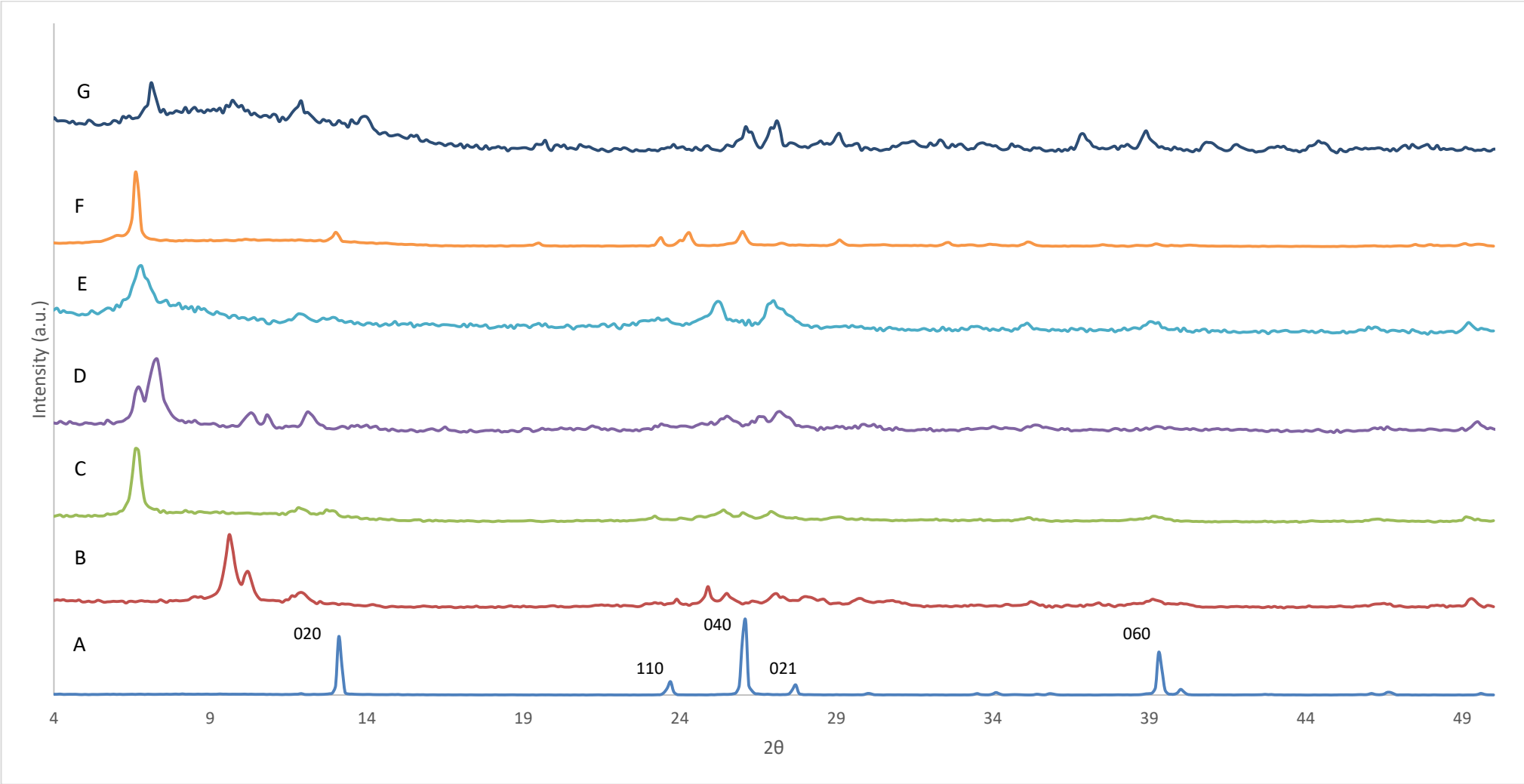

Figure 4.47 - XRD diffractograms for the MoO_3 intercalated materials for A) MoO_3, B) Li_xMoO3, C) MoO_3/PDA, D) MoO_3/2A5PhPyr, E) MoO_3/5AQ, F) MoO3/2AmThia and G) MoO_3/An

Table 4.7 - Infra-red and Raman wavenumbers (cm^{-1}) for MoO_3 intercalated materials

MoO_3		$LiMoO_3$		MoO_3/PDA		MoO_3/2A5PhPyr		MoO_3/5AQ		MoO_3/2AmThia		MoO_3/An		Assignment
IR	*Raman*	*IR*	*Raman*	*IR*	*Raman*	*IR*	*Raman*	*IR*	*Raman*	*IR*	*Raman*	*IR*	*Raman*	*Organic Guest*
					2884	3376		3367		3109		3566		C-H, O-H and NH_2, =NH stretching
					2796	3301		3240				3037		
					2659	3182						2943		
				2119						2119				
				1991	1992									NH_2, >NH, NH_3^+ bending and benzene C-C and N=C stretching
						1667								
								1635	1635					
						1622				1621				
				1613								1615		
						1598	1595		1591			1590		
								1589		1582			1585	
												1576		
				1557		1550		1564		1550				
								1517						
				1489	1498	1498		1471	1464	1489		1487		Benzenoid C=C stretching
				1457		1437		1431						
				1417	1403							1417		

Table 4.7 (cont) - Infra-red and Raman wavenumbers (cm^{-1}) for MoO_3 intercalated materials

MoO_3		**$LiMoO_3$**		**MoO_3/PDA**		**MoO_3/2A5PhPyr**		**MoO_3/5AQ**		**MoO_3/2AmThia**		**MoO_3/An**		**Assignment**
IR	*Raman*	*IR*	*Raman*	*IR*	*Raman*	*IR*	*Raman*	*IR*	*Raman*	*IR*	*Raman*	*IR*	*Raman*	*Organic Guest*
				1370		1339	1351	1362	1362			1324		Quinoid C=C stretching
								1306					1317	
					1254	1275		1249	1221	1270				
						1246								
						1221		1219						
					1162	1154								
														Inorganic Host
												1096		M=O stretching
					1030							1031		
		1000		1006		1006		1005		1005				
971	997		977				995				993		993	Mo-O-Mo bending

Table 4.7 (cont) - Infra-red and Raman wavenumbers (cm^{-1}) for MoO_3 intercalated materials

MoO_3		$LiMoO_3$		MoO_3/PDA		MoO_3/2A5PhPyr		MoO_3/5AQ		MoO_3/2AmThia		MoO_3/An		Assignment
IR	*Raman*	*IR*	*Raman*	*IR*	*Raman*	*IR*	*Raman*	*IR*	*Raman*	*IR*	*Raman*	*IR*	*Raman*	*Inorganic Host and Organic Guest*
				955	972	971	968	943		952		945		M=O stretching
		915			924	943						922		
				900		933		901						
						913								
808	820	816				898	822			804	820	884	819	
						838						841		
						830								
				729	798	761		783				735		
					777			700				704		
					736									
										677	667		667	C-S stretching
646	668	667		667	654	667						661		M=O stretching
		630				644								
597		600		601	605	603		600		596		617		Mo-O-Mo bending

Table 4.7 (cont) - Infra-red and Raman wavenumbers (cm^{-1}) for MoO_3 intercalated materials

MoO_3		Li_xMoO_3		MoO_3/PDA		MoO_3/2A5PhPyr		MoO_3/5AQ		MoO_3/2AmThia		MoO_3/An		Assignment
IR	*Raman*	*IR*	*Raman*	*IR*	*Raman*	*IR*	*Raman*	*IR*	*Raman*	*IR*	*Raman*	*IR*	*Raman*	*Organic Guest*
				579	587							577		Mo-O-Mo Bending
				572		569		546				557		Mo=O stretching
		561		568										
		557		561										
		552		554	555	553			485					
548		547		548										
				542	275									
				534										
				531										
				528										
	476										474		468	
	380		456				337				378		379	
	368		360				292				338		338	
	339		348				250				283		286	
	285		319				155				237		240	
	248		264				127				215		216	
	220		228								197		197	
	201		200								148		149	
	158		181								125		124	
	130		139								112		114	
	118													

4.1.2.2) Infra-red and Raman Spectroscopy

The infra-red and Raman vibrational transitions for the MoO_3 intercalated materials are shown in Table 4.7 (see Appendix B.1 and B.2 for full spectra). Peaks appearing within the region 1000-400 cm^{-1} correspond to the MoO_3 phase of the material where majority of the peaks correlate to the Mo=O stretching modes with peaks around 600 cm^{-1} corresponds to the Mo-O-Mo bending modes. Upon intercalation of Li^+, we see these peaks shifting wavelengths consistent with the presence of an intercalated phase (as previously discussed in section 1.5.2) for V_2O_5). The new peaks appearing below 1100 cm^{-1} correspond to the new intercalated phase Mo=O vibrational transitions whereas other peaks have shown to be directly shifted (e.g. 971 cm^{-1} shifts to 1000 cm^{-1}). This occurs due to the interaction between the Li^+ ions and the Mo=O oxygen leading to reduced vibrational space for this stretching mode. Some peaks in the IR correlate to the pristine host MoO_3 which suggests that there are two phase present in this material which difficult to determine from the XRD due to a loss in the MoO_3 characteristic peaks at higher 2θ angles. However, for Li_xMoO_3, more noticeably, the Raman data shows a more significant shift which is indicative of the intercalated phase. The trend in the shifting of the peaks in the IR and Raman are also consistent when Li^+ are exchanged for the organic cations.

The IR spectrum of MoO_3/PDA shows a new peak appearing at 1457 cm^{-1} corresponding to the benzenoid ring system while the peaks appearing at 1417 cm^{-1} and 1370 cm^{-1} correspond to the quinoid ring system. This would suggest that the organic intercalant is in an oligomeric or polymeric form with some regions in their protonated phase (seen previously in Figure 4.4).

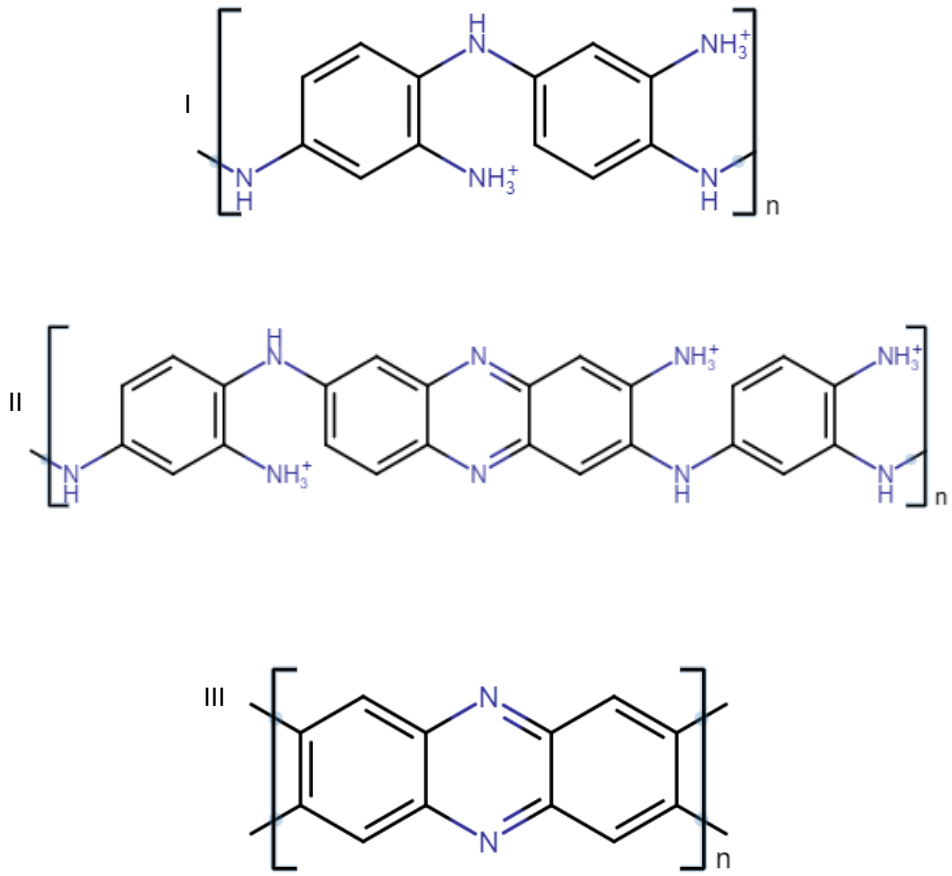

Figure 4.4 – I) Polymerised PDA to produce a substituted polyaniline form, II) Polymerised PDA with two phases present; a non-ladder phase and a ladder oligomer phase and III) Fully polymerised PDA producing the Ladder like polymer

Furthermore, the presence of the secondary amine, >NH, bending modes appearing at 1557 cm^{-1} and 1489 cm^{-1} along with $-NH_3^+$ or $–NH_2$ suggesting the presence of the non-ladder-like oligomeric or polymeric structure (a similar structure to that seen in Figure 4.4 with terminal NH_3^+ or $–NH_2$ groups on the benzene ring).

However, there is still the presence of non-shifted peaks which further suggests that a MoO_3 phase may still be present in MoO_3/PDA. This is similarly shown in the MoO_3/PDA Raman spectrum where peaks appearing above 1000cm^{-1} correspond to the presence of the polymer in the material and the shifting to lower wavenumbers corresponds to the presence of the polymer in the interlayer spacing restricting the Mo=O and Mo-O-Mo stretching and bending modes.

This trend is further seen in the other MoO_3 intercalants (including the intercalation of polyaniline via recrystallization). For the intercalation of 2A5PhPyr, 5AQ, 2AmThia and An the presence of a secondary amine, >NH, and the possible $–NH_3$ or $–NH_2$ groups confirms that the structure of these oligomer or polymer materials is analogous to that of image I in Figure 4.4 with some regions of the oligomer or polymer being protonated and the polymerisation occurring through the primary amine.

For MoO_3/AmThia the presence of the C-S stretching mode (appearing at 677 cm^{-1} in the IR) and C=N (appearing at 1621 cm^{-1}) confirms the presence of the AmThia in the material.

In some cases (e,g. MoO_3/2A5PhPyr) extra peaks are observed in the spectrum which could arise from a mix of blue and red-shifted peaks with respect to the MoO_3 host peaks. The blue-shifted peaks can arise where the Li^+ has been removed but the layer (through step defects for example) may remain expanded leading to an increase in vibrational space for the Mo=O bonds.

Similarly, for MoO_3/An the presence of the organic peaks are analogous to that seen in MoO_3/PDA and confirms that once dissolved in water, the MoO_3 layers restack around the organic guest species leading to the increased interlayer spacing observed in the XRD data. However, unlike the case for the ion-exchange mechanism, this method results in a random stacking of the inorganic layers leading to the broader diffuse peaks compared to that for the materials synthesised via ion-exchange.

The interlayer expansion observed from the XRD is caused by the presence of the organic guest species which in these systems are also suspected to be its oligomeric or polymeric forms.

4.1.2.3) TGA and ICP-AES

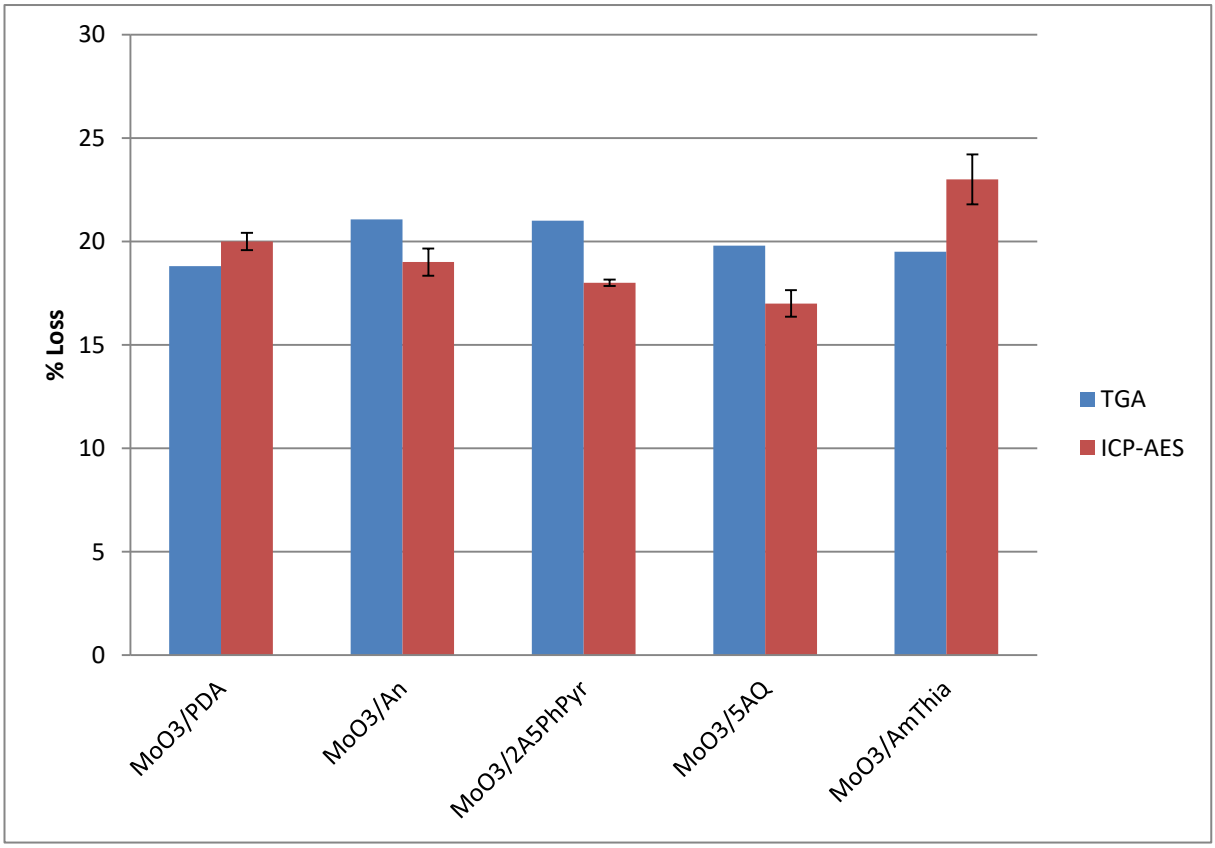

Figure 4.48 - % Weight Loss via TGA and ICP-AES for MoO_3 intercalated materials after the initial mass loss due to water. The error bars in the ICP-AES where obtained in-situ via three consecutive measurements as described in section 3.1.4).

Figure 4.48 shows the total percentage loss in mass determined by TGA and ICP-AES independently (for full TGA data see Appendix B.3). From the ICP-AES the stoichiometry was calculated using the same method as that for V_2O_5 materials. From the ICP-AES the stoichiometry was calculated by determining the total Mo content in the digested sample (assuming the stoichiometry of the Mo host to be MoO_3) and comparing this to the theoretical Mo content of the host (which is the total Mo content in the digested pristine MoO_3 host). The difference in Mo content between the host and the composite material was concluded to arise from the presence of the organic guest. The stoichiometries were then determined to be $PDA_{0.2}MoO_3$, $An_{0.19}MoO_3$, $2A5PhPyr_{0.18}MoO_3$, $5AQ_{0.17}MoO_3$ and $AmThia_{0.23}MoO_3$. We initially see that for both TGA and ICP-AES analysis that the guest content is consistent in all materials. The initial loss in mass for all samples around 100°C in the TGA is related to either loosely bound water on the material surface or in the

interlayer spacing due to the aqueous nature of the reactions. As in the V_2O_5 systems, the continuous gradual loss in mass over the remaining temperature range thereafter reflects the guest species oligomeric or polymeric nature (as previously concluded from the IR and Raman data). If the guest species were not oligomeric or polymeric in form one would expect the guest species to be removed around a single temperature and not over a large range. As discussed previously (section 1.5.2) the stoichiometry's determined here are consistent with that related to either a non-planer polymer backbone (i.e. a helical like structure in the interlayer spacing) or a double layer like conformation. This would explain the large increase in the interlayer spacing observed in the XRD data.

4.1.2.4) Optical Spectroscopy

Table 4.8 - Optical band-gaps determined from UV-Visible spectroscopy tauc plots for the MoO_3 composite materials

	Optical band-gap (eV)	
Compound	**Calculated Optical Band-gap**	**Lit** (271,272)
MoO_3	3.16	3.05 - 3.2
MoO_3/PDA	3.45	
MoO_3/2A5PhPyr	3.57	
MoO_3/AmThia	3.68	
MoO_3/5AQ	3.66	
MoO_3/An	3.78	

The calculated optical band-gaps for the MoO_3 composite materials are shown in Table 4.8 (see Appendix B.4 for full UV-Visible reflectance spectra and their associated tauc plots) with (Figure 4.50, Figure 4.51 and Figure 4.51) showing an example of the absorption spectrum of MoO_3/PDA and the tauc plots of MoO_3 and MoO_3/PDA respectively where the optical band-gap is determined by extrapolation of the linear part of the tauc plots. Overall it is shown that the intercalated materials exhibit a larger band-gap than that for the pure MoO_3 host (which shows good correlation with the literature band-gap range). The most plausible explanation lies in the fact that as the organic material is intercalated into

the interlayer spacing, it is disrupting the band-structure of the bulk inorganic. The resulting decrease in the band overlap between inorganic layers leads to a larger band-gap.

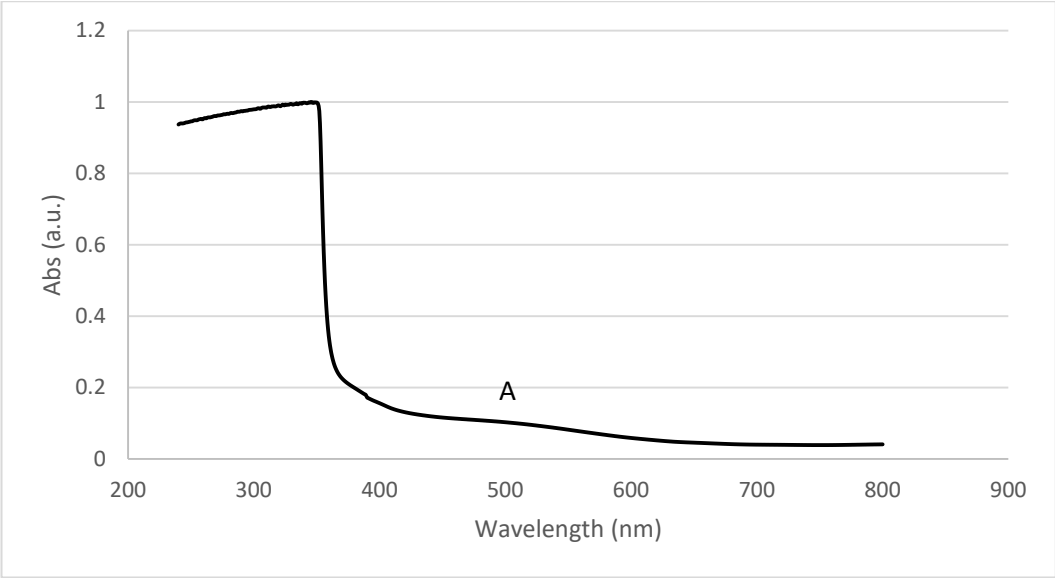

Figure 4.49 – UV-Vis Absorption spectrum for MoO_3/PDA

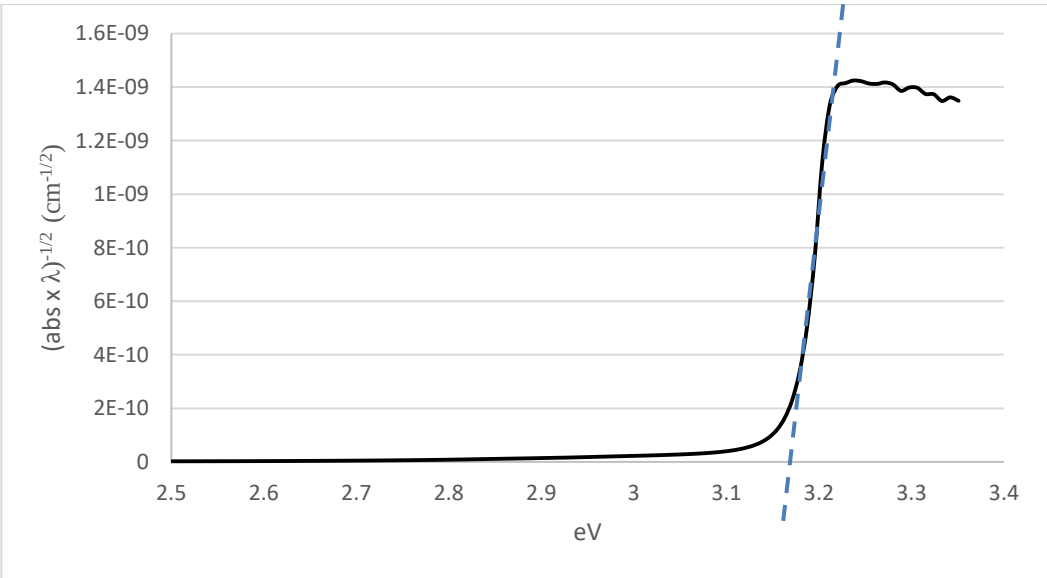

Figure 4.50 - Tauc plot for MoO_3

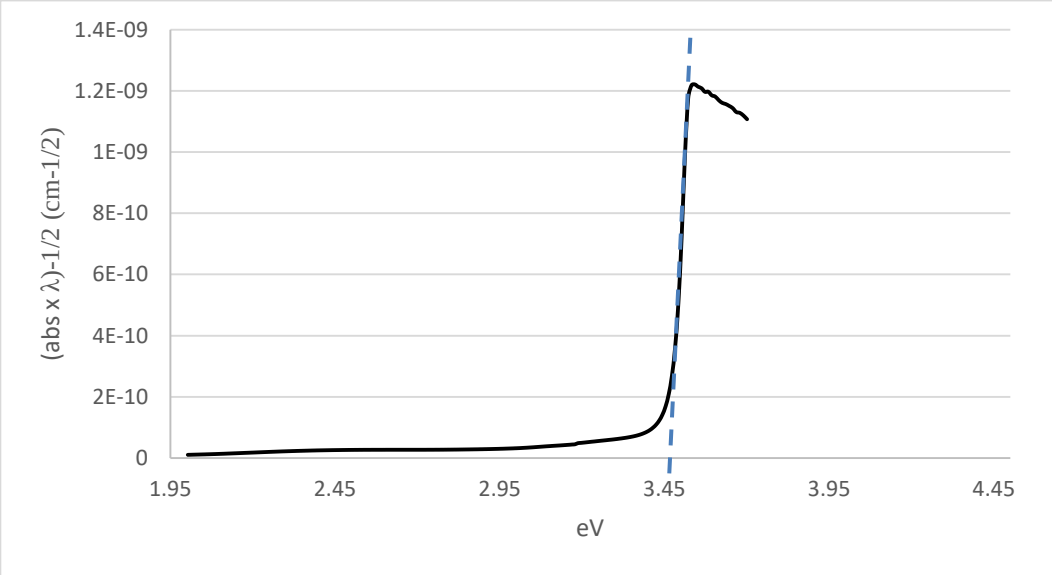

Figure 4.51 - Tauc plot for MoO_3/PDA

For the MoO_3 composite materials, a small peak or shoulder approximately around ~ 470 nm to 530 nm (region A in Figure 4.49) which does not persist in the tauc plots is present in the UV-Visible spectra. In the MoO_3 composite this peak or shoulder appears with an energy between ~ 2.25 eV to 2.76 eV which is not associated with the MoO_3 host material. It is more likely to be a charge-transfer analogous to that of the V_2O_5 systems occurring between the inorganic host and the organic guest species. However, in the MoO_3 systems this charge-transfer peak is more prevalent than in the V_2O_5 systems which may suggest that there is a better band overlap between host and guest in the MoO_3 systems. This is further demonstrated in the increase in the band-gap of these MoO_3 materials, which exhibits a band-gap increase to a much lesser extent to that of the V_2O_5 systems. The band-gap of the MoO_3 intercalated materials is found to be within the range of 3.45 eV – 3.78 eV with no remnant peak in the region characteristic of the host material with the amount of band-gap increase dependant on the specific organic guest present. The lack of unintercalated host material was previously seen in the XRD data. As with the V_2O_5 systems, from the tauc plots it can be determined that any changes in the overall properties of the material are caused by intercalation.

4.1.2.5) X-ray Photoelectron Spectroscopy (XPS)

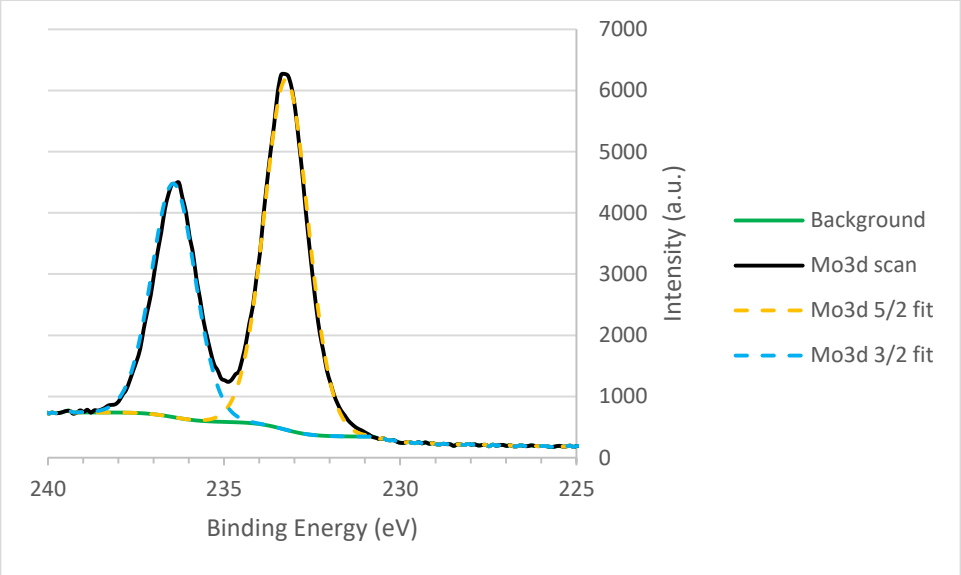

Figure 4.52 – XPS scan for the MoO_3 host showing the Mo3d environments (black) with $Mo3d_{5/2}$ (orange) and $Mo3d_{3/2}$ (blue) environments fitted with a single environment respectively (orange; 233.18 eV and blue; 236.28 eV)

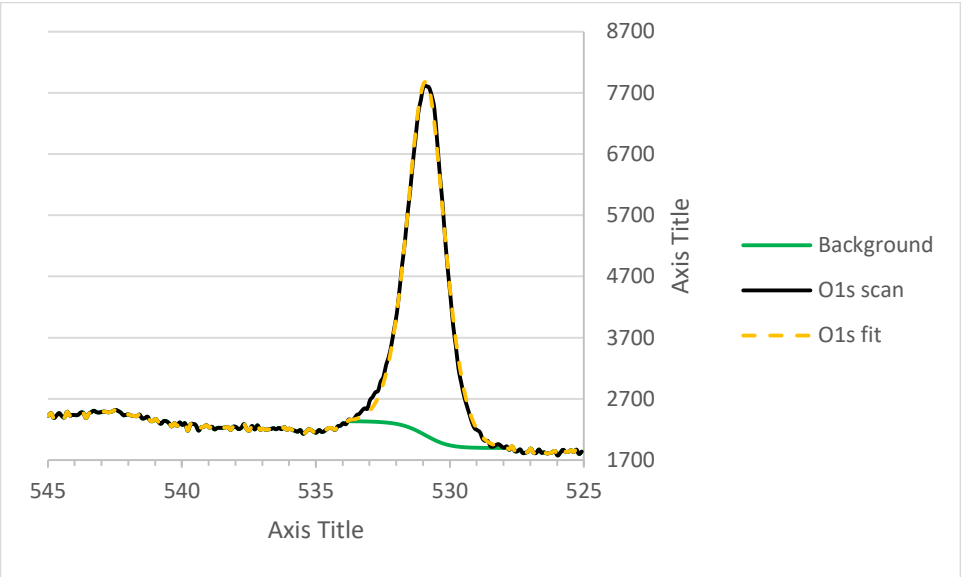

Figure 4.53 – XPS scan for the MoO_3 host showing the O1s environment (black) fitted with a single environment (orange; 530.78 eV)

Figure 4.52 and Figure 4.53 show the XPS scans for the molybdenum and oxygen environments in the pure host MoO_3. In Figure 4.52 the $Mo3d_{5/2}$ peak appears at 233.18 eV and $Mo3d_{3/2}$ peak 236.28 eV is consistent with the literature values (233.1 eV and 236.3 eV respectively) (273,274) with both fitted for a singular environment correlating to Mo^{6+} present. Figure 4.53 shows that the O1s peak appears 530.78 eV consistent with the

literature value for this oxygen environment in the host (275) and is fitted to a singular environment.

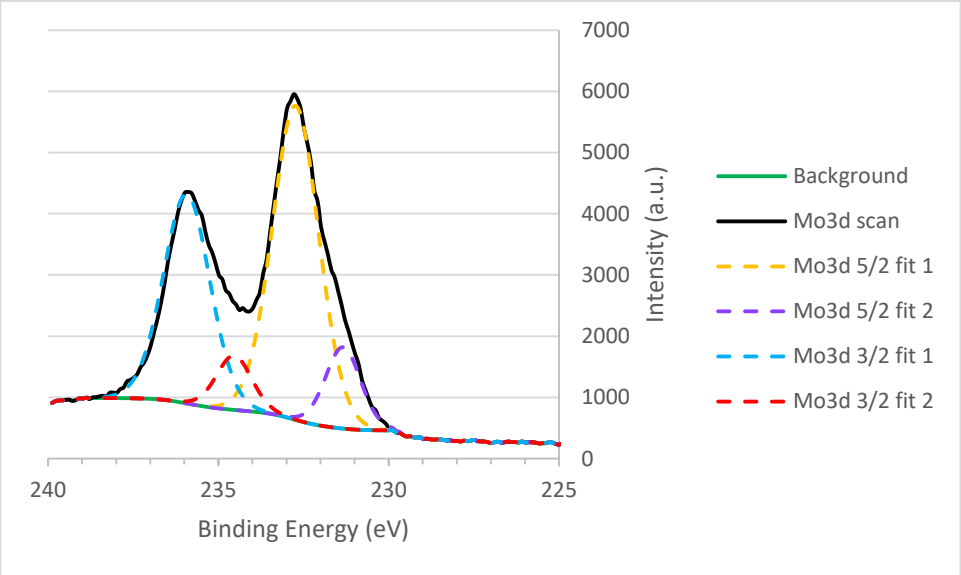

Figure 4.54 – XPS scan for $LiMoO_3$ host showing the Mo3d environments (black) with $Mo3d_{5/2}$ (orange and purple) and $Mo3d_{3/2}$ (blue and red) environments fitted with a two environments respectively (orange; 233.18 eV, purple; 231.18 eV, blue; 235.78 eV and red; 234.28 eV)

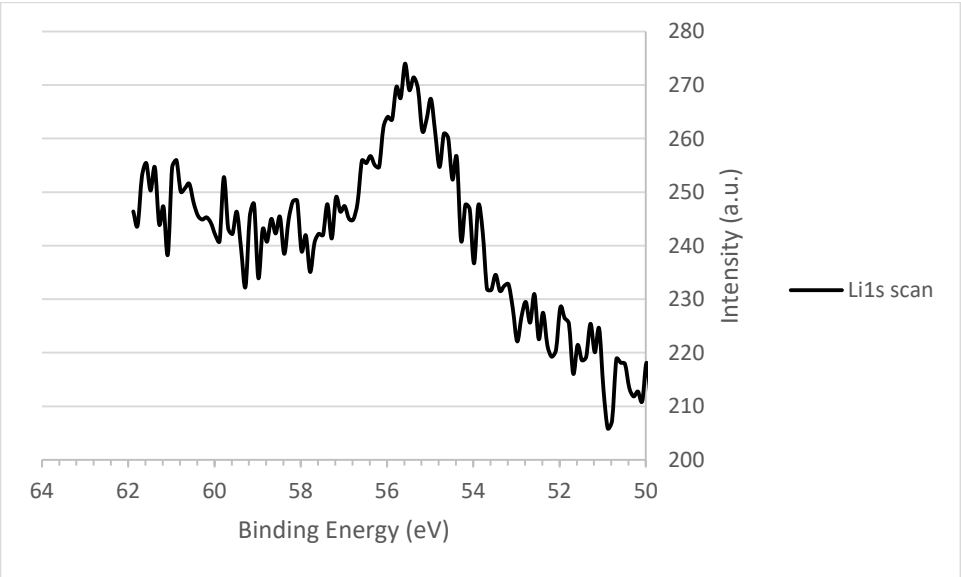

Figure 4.55 - XPS scan for $LiMoO_3$ showing the Li1s environment

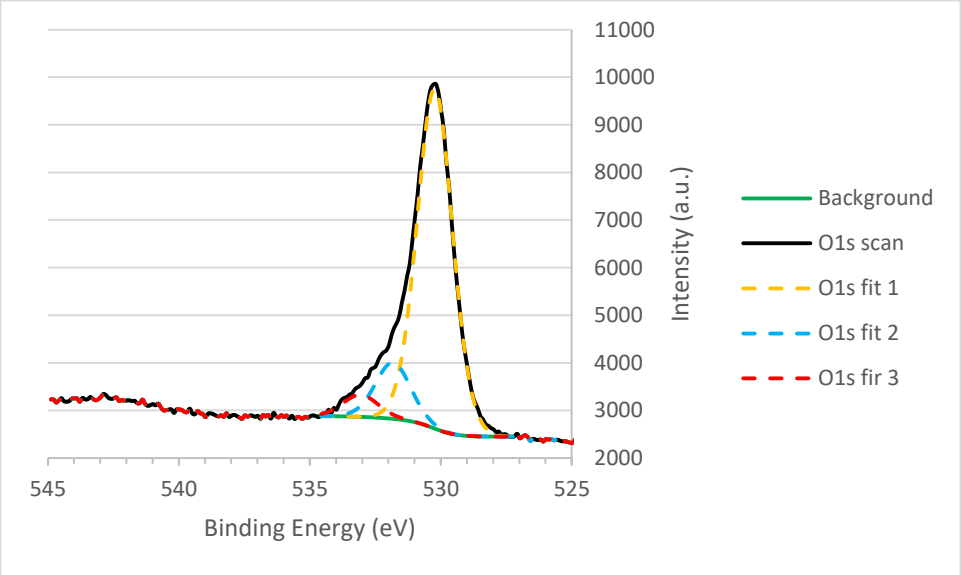

Figure 4.56 – XPS scan for $LiMoO_3$ host showing the O1s environment (black) fitted with three environments (orange; 530.78 eV, blue; 531.78 eV and red; 533.08 eV)

Figure 4.54, Figure 4.55 and Figure 4.56 show the XPS scan for $LiMoO_3$ showing the Mo3d, Li1s and O1s environments respectively. In a similar fashion to LiV_2O_5 (Figure 4.20), the Mo3d peaks in Figure 4.54 both show two environments present. The main environments (orange and blue) correspond to the presence of Mo^{6+} (orange and blue fitted peaks appearing at 233.18 eV and 235.78 eV respectively which relate closely with the peaks seen in the pure host material in Figure 4.52). The new environments (purple and red fits) correspond to the presence of reduced Mo^{5+} appearing at 231.18 eV ($Mo3d_{5/2}$) and 234.28 eV ($Mo3d_{3/2}$) which correlates well with the literature value for these two peaks (231.1 eV and 234.2 eV respectively)(276). This suggests (as in the case of LiV_2O_5) that the reaction with n-BuLi follows a redox reaction resulting in the reduction of Mo^{6+} to Mo^{5+} which further supports the fact that the signal appearing in the ESR for this material (Figure 4.76) arises from a localised electron in the inorganic layers. Due to the low atomic mass of lithium, it is difficult to detect in the XPS hence the difficulty in fitting the data in Figure 4.55, however, a real peak appears to be present (noisy nonetheless) suggesting the successful insertion of Li^+ into MoO_3. There are similarities in the peaks arising for the O1s environment in this material and that seen for LiV_2O_5 (Figure 4.22) where the peak appearing for fit 3 is close to that for the O1s peak for water molecules (533.10 eV) (266)

which from the TGA could be from any loosely bound water molecules on the sample surface.

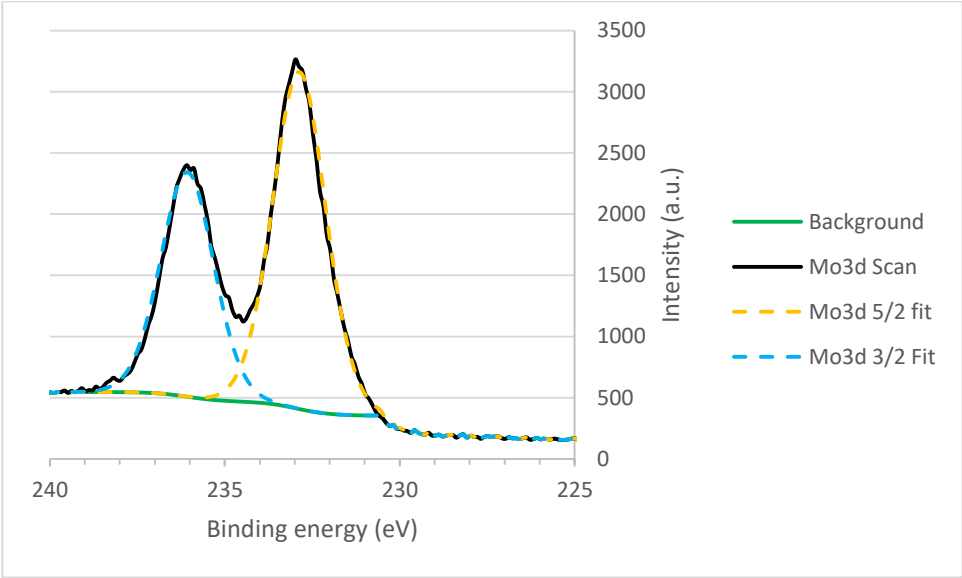

Figure 4.57 – XPS scan for the MoO_3/PDA showing the Mo3d environments (black) with $Mo3d_{5/2}$ (orange) and $Mo3d_{3/2}$ (blue) environments fitted with a single environment respectively (orange; 233.08 eV and blue; 236.28 eV)

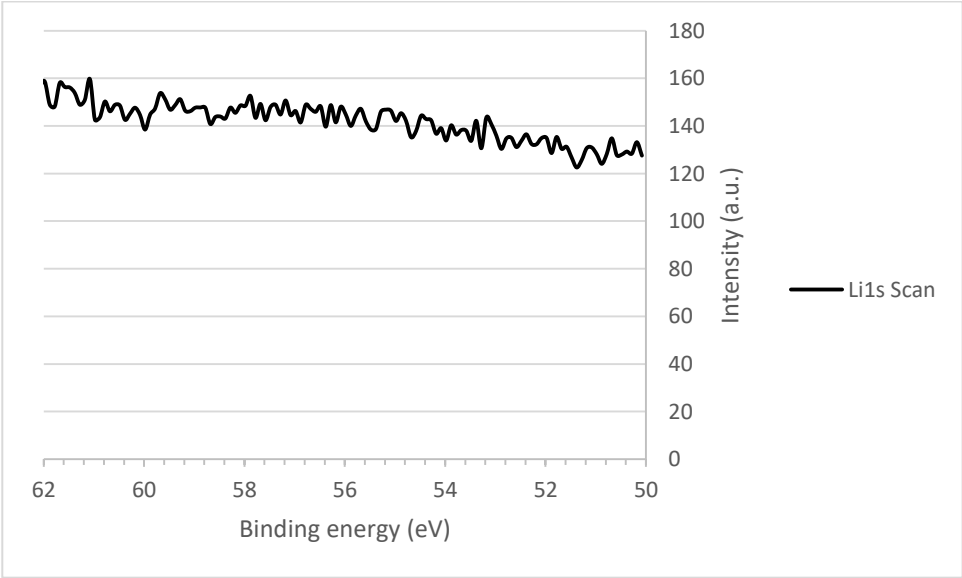

Figure 4.58 - XPS scan for MoO_3/PDA showing the Li1s environment

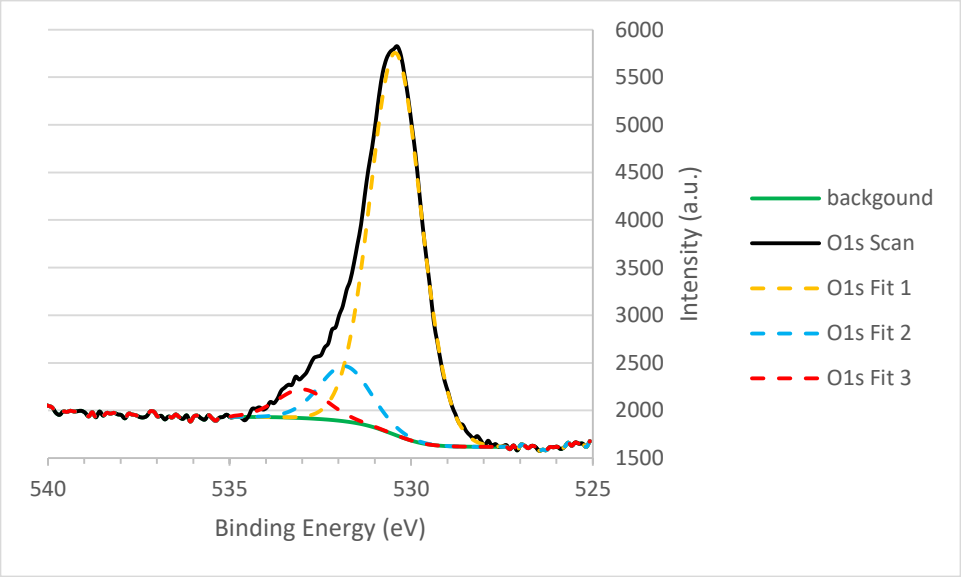

Figure 4.59 – XPS scan for MoO_3/PDA showing the O1s environment (black) fitted with three environments (orange; 530.58 eV, blue; 532.18 eV and red; 533.48 eV)

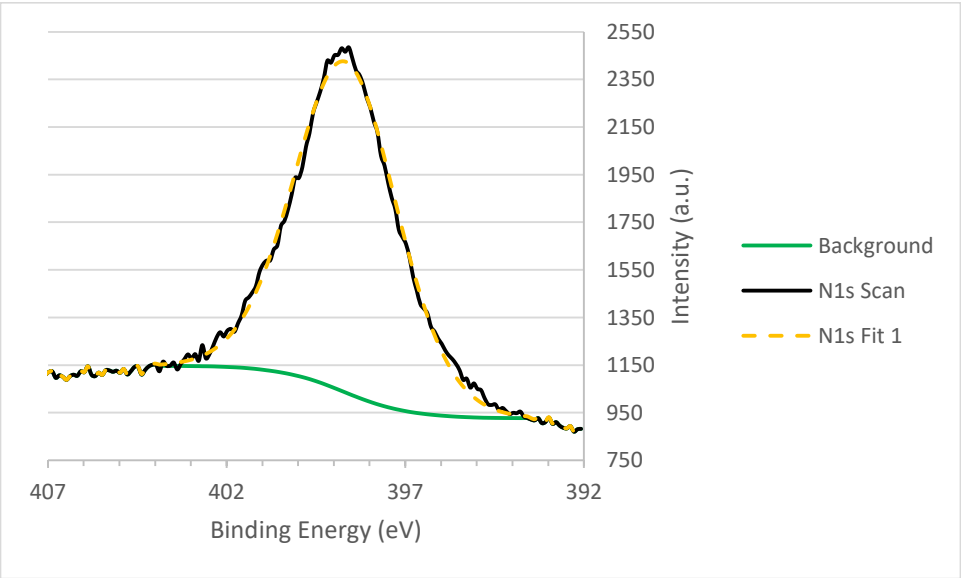

Figure 4.60 – XPS scan for MoO_3/PDA host showing the N1s environment (black) and fitted with a single environment (orange; 399.08 eV)

Figure 4.57, Figure 4.58, Figure 4.59 and Figure 4.60 shows the XPS scan for MoO_3/PDA showing the Mo3d, Li1s, O1s and N1s environments respectively. Figure 4.58 shows no presence of Li^+ indicating complete exchange, and an N1s signal (Figure 4.60) is now present from the organic intercalant. However, the Mo environments (Figure 4.57) appear to correlate well for those for Mo^{6+} host material (Figure 4.52) and are unlike those seen for the reduced Mo^{5+} peaks seen in $LiMoO_3$. It must be noted that due to XPS being a

surface specific technique, the Mo^{5+} centres may not be found within the detection depth of this technique. Figure 4.59 shows three O1s environments which match closely to those seen in $LiMoO_3$ and are analogous to that for the MoO_3/PDA's V_2O_5 counterpart. The main peak (fit 1) appearing ~530 eV corresponds well to that for the host O1s environment (Figure 4.53) whereas the two minor environments correspond well to those seen for $LiMoO_3$ (Figure 4.56). Fit 2, appearing ~532 eV, appears to correspond to a small change in the O1s environment due to interaction with the intercalated organic material. Fit 3, appearing ~533 eV, corresponds to O1s appearing from any loosely bound water molecules which may cause the initial mass loss appearing at ~100°C in the TGA. the N1s environment (Figure 4.60) seen for MoO_3/PDA does not appear to be as noisy as its V_2O_5 composite counterparts. The single environment (appearing at ~ 399 eV) corresponds well to neutral polyaniline the like structure (264,265).

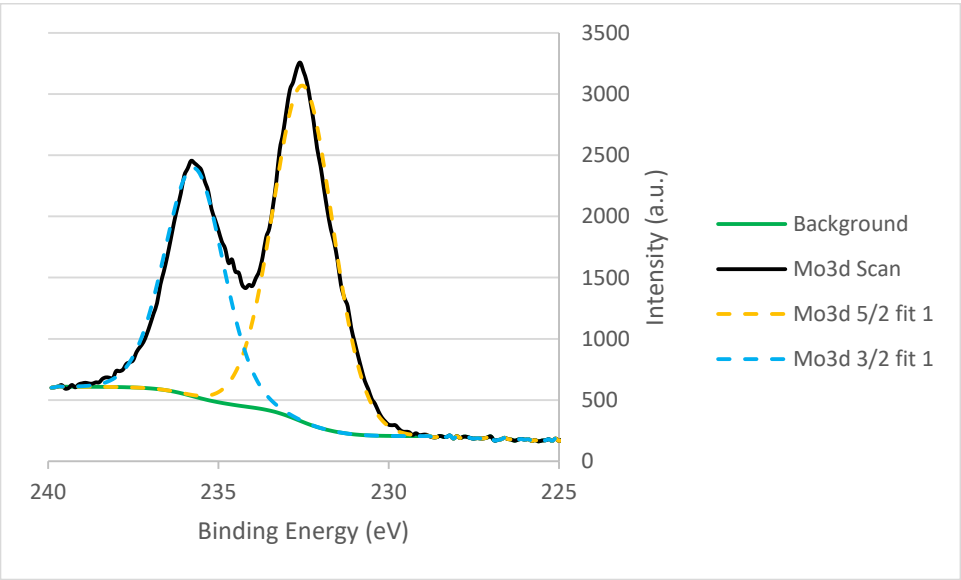

Figure 4.61 – XPS scan for MoO_3/2A5PhPyr showing the Mo3d environments (black) with $Mo3d_{5/2}$ (orange) and $Mo3d_{3/2}$ (blue) environments fitted with a single environment respectively (orange; 232.8 eV and blue; 236 eV)

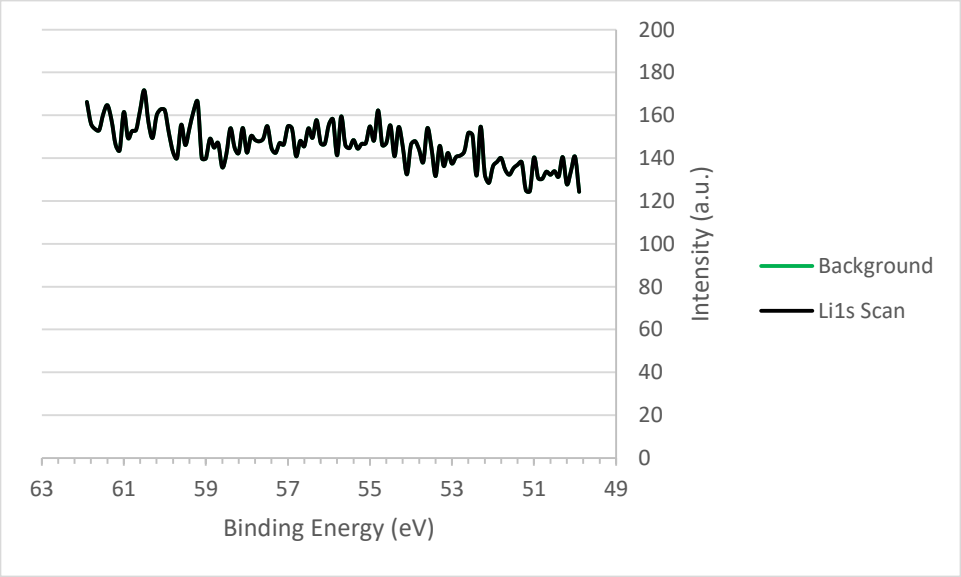

Figure 4.62 - XPS scan for MoO_3/2A5PhPyr showing the Li1s environment

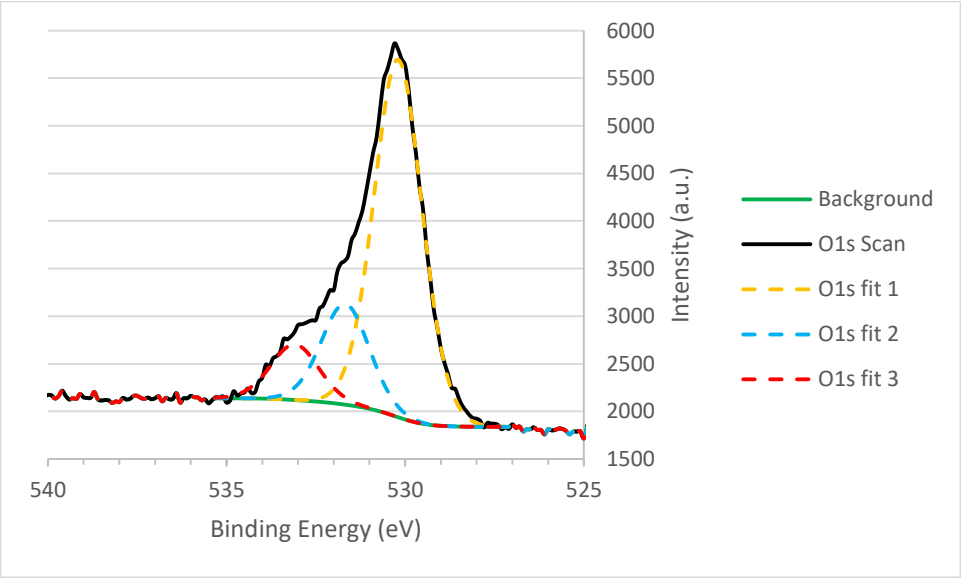

Figure 4.63 – XPS scan for MoO_3/2A5PhPyr showing the O1s environment (black) fitted with three environments (orange; 530.4 eV, blue; 532.1 eV and red; 533.4 eV)

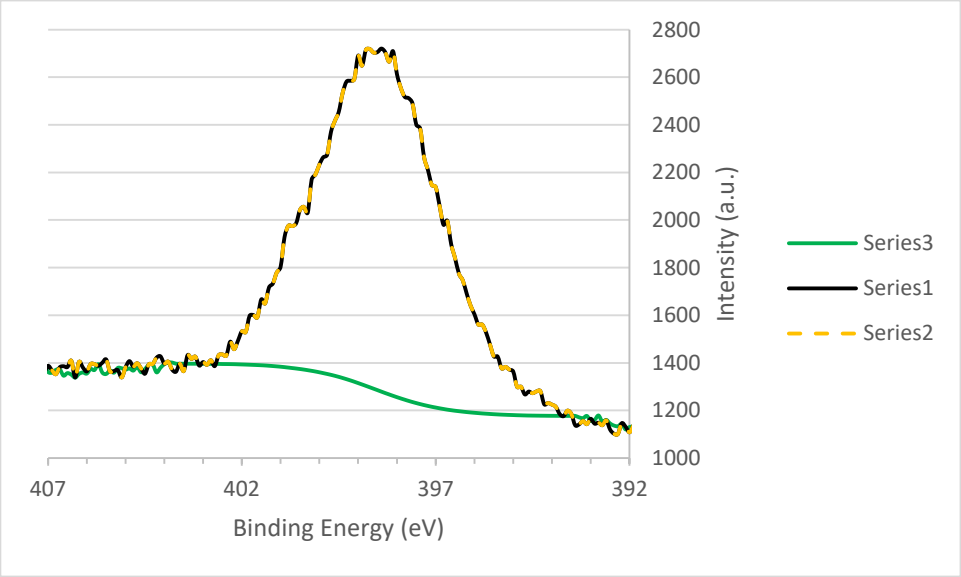

Figure 4.64 – XPS scan for MoO_3/2A5PhPyr host showing the N1s environment (black) and fitted with a single environment (orange; 399 eV)

Figure 4.61, Figure 4.62, Figure 4.63 and Figure 4.64 shows the XPS scan for MoO_3/2A5PhPyr showing the Mo3d, Li1s, O1s and N1s environments respectively. As previously seen for MoO_3/PDA (Figure 4.57), MoO_3/2A5PhPyr exhibits a singular Mo^{6+} environment (Figure 4.61 where $Mo3d_{5/2}$ appears ~ 232.8 eV and $Mo3d_{3/2}$ appears ~ 236 eV). These peaks correspond well with the literature values for the host Mo^{6+} environments (Figure 4.52) suggesting no reduced Mo^{5+} present. The ESR, on the other hand, for this material suggested there was a small presence of reduced Mo^{5+} in the bulk material (similar to that seen for V_2O_5/2A5PhPyr). It would appear, therefore, that due to the surface specific nature of XPS, this XPS spectrum is suggesting potential oxidation of the surface of this material. This most likely to have occurred during the washing stages of this material and any Mo^{5+} present in the material is further than the detection depth for this XPS analysis. The Li1s environment is also similar to that seen for MoO_3/PDA (Figure 4.58) where the XPS spectrum shows no presence of the Li^+ and therefore suggests that the Li^+ were successfully exchanged for organic intercalant. The O1s environment (Figure 4.63) is also similar to that seen for MoO_3/PDA where three environments are now seen in contrast to the host MoO_3 O1s environment (Figure 4.56). The MoO_3/2A5PhPyr O1s fit (appearing ~ 530.4 eV) appears to correspond well with the literature value seen previously

for the MoO_3 O1s environment. Fit 2 (appearing at ~ 532 eV) and fit 3 (appearing at ~ 533 eV) further correspond well to the environments seen previously where fit 2 corresponds to an intercalant interacting with the MoO_3 oxygen and fit 3 corresponds to that for loosely bound water molecules on the material surface (or intercalated). Furthermore, similar to MoO_3/PDA (Figure 4.60) once again the N1s environment for MoO_3/2A5PhPyr exhibits a singular fit. However, there is a small shoulder appearing ~ 400 eV which may correspond to another N1s environment. Two environments are expected in this material, one for the pyridine nitrogen and one for the amine group. The two environments may appear to be very close and as such the broad peak being exhibited in this spectrum could be a result of a combination of the two expected environments.

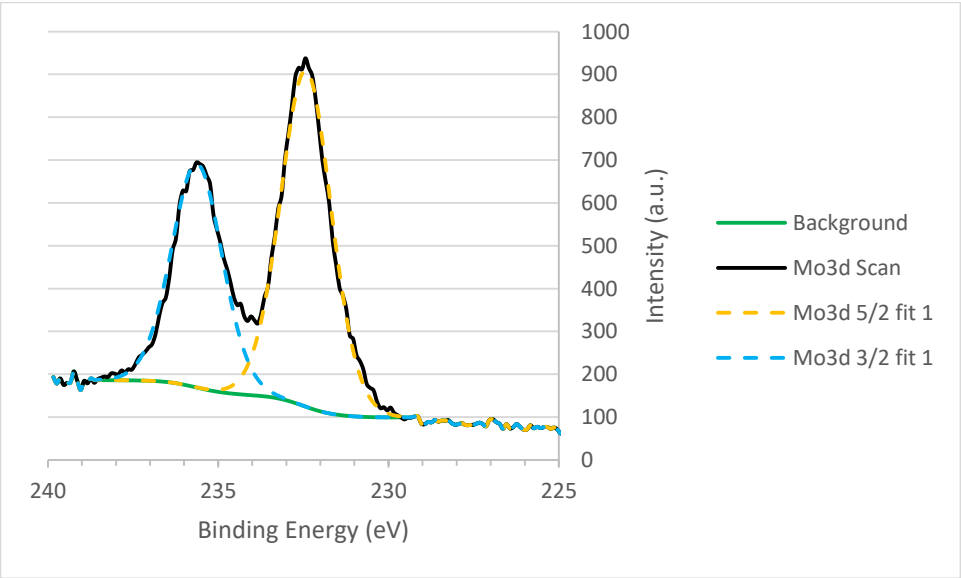

Figure 4.65 – XPS scan for MoO_3/5AQ showing the Mo3d environments (black) with $Mo3d_{5/2}$ (orange) and $Mo3d_{3/2}$ (blue) environments fitted with a single environment respectively (orange; 232.63 eV and blue; 235.84 eV)

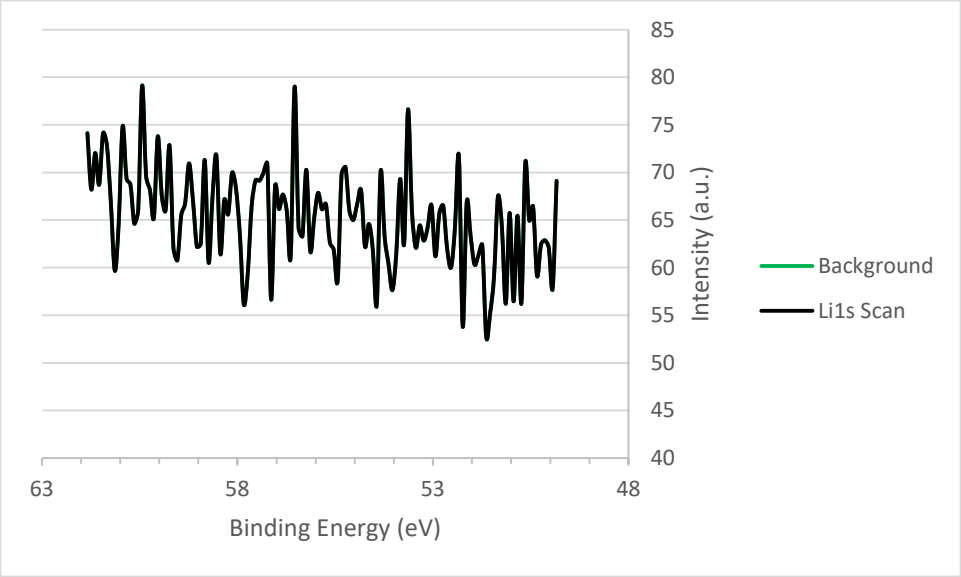

Figure 4.66 - XPS scan for MoO_3/5AQ showing the Li1s environment

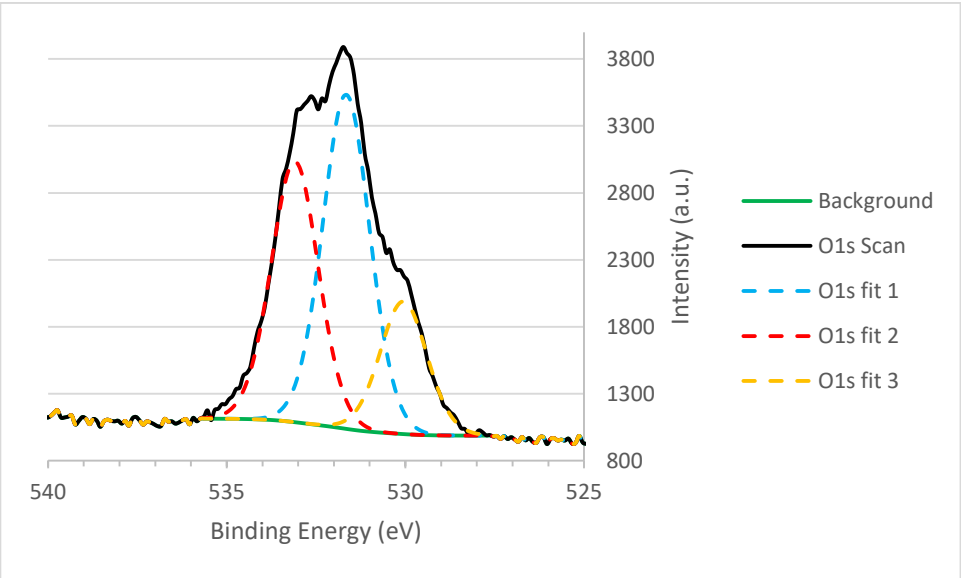

Figure 4.67 – XPS scan for MoO_3/5AQ showing the O1s environment (black) fitted with three environments (orange; 530.24 eV, blue; 531.81 eV and red; 533.24 eV)

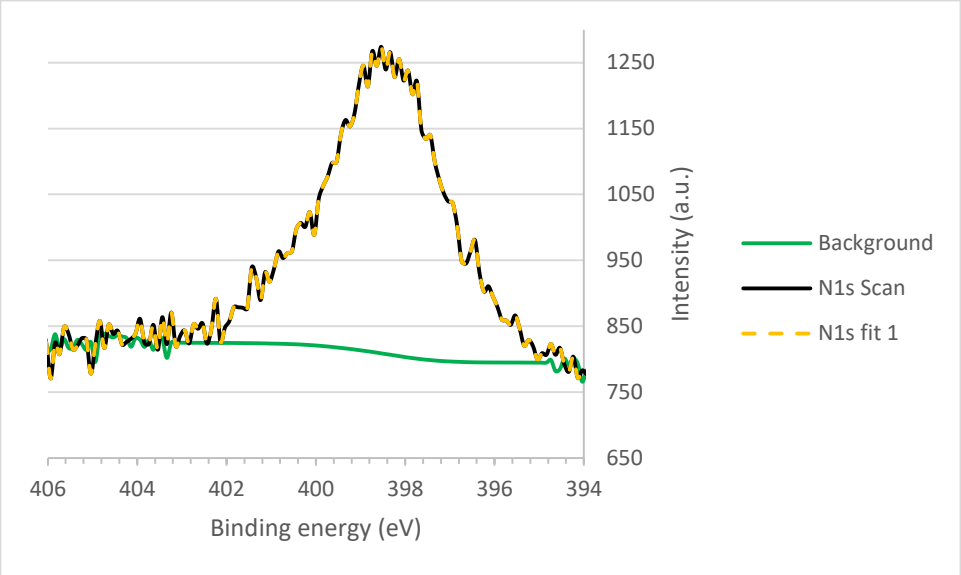

Figure 4.68 – XPS scan for MoO_3/5AQ host showing the N1s environment (black) and fitted with a single environment (orange; 398.74 eV)

Figure 4.65, Figure 4.66, Figure 4.67 and Figure 4.68 shows the XPS scan for MoO_3/5AQ showing the Mo3d, Li1s, O1s and N1s environments respectively. As seen in the previous spectra, the Mo3d environment is fitted for a single environment for both $Mo3d_{5/2}$ and $Mo3d_{3/2}$ (peaks appearing at ~ 233 eV and 236 eV respectively). These peaks match closely with those for the host MoO_3 and literature values for Mo^{6+} environments (Figure 4.52). This spectrum suggests that there is no reduced Mo^{5+} present in the material (specifically no Mo^{5+} is present within the detection depth for the XPS technique). Furthermore, as seen with all composite materials synthesised by ion-exchange (including the V_2O_5 materials) Figure 4.66 shows no Li^+ present in the material as expected. Combined with the previous characterisation techniques, this is indicative of a successful ion-exchange mechanism between the Li^+ ions and the 5AQ cations. The O1s environments (Figure 4.67) however, are slightly different from those seen in the previous spectra. The three environments (fit 1, 2 and 3) appear in the same positions as those of the previous spectra suggesting that the main peak (fit 1) corresponds to the MoO_3 oxygen environment while fit 2 corresponds to any oxygen interacting with the organic intercalant causing a small change in the oxygen environment and fit 3 corresponds to loosely bound water on the surface or in the interlayer spacing of the material. The difference between

this spectrum and that for the previous MoO_3 composite materials lies in the intensities of these environment fits. It must be noted that the dip at the apex of the scanned peak makes fitting the data more complex than for the previous spectra. It is shown that there appears to be a large amount of interaction occurring between the 5AQ intercalant and the MoO_3 oxygen and that this sample could be the most hydrated of the samples thus far. Once again, the N1s environment (peak appearing at ~ 398 eV) corresponds to a single neutral N environment and appears in the same position as the previous N1s XPS spectra. As with its V_2O_5/5AQ counterpart, the noise-to-signal ratio makes fitting more than one fitting difficult. There could, therefore, be more than a single N environment present in the material corresponding to the organic phase of the composite.

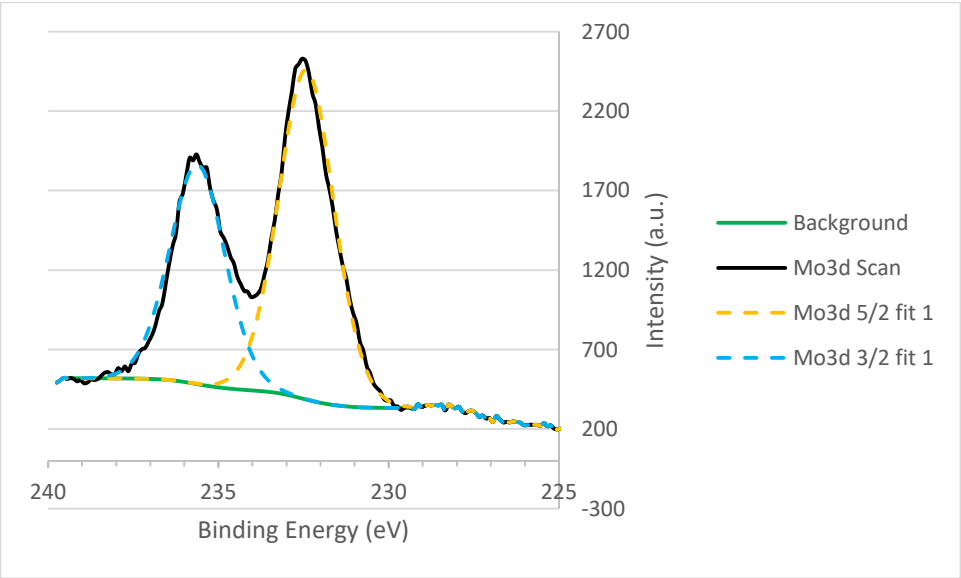

Figure 4.69 – XPS scan for MoO_3/AmThia showing the Mo3d environments (black) with $Mo3d_{5/2}$ (orange) and $Mo3d_{3/2}$ (blue) environments fitted with a single environment respectively (orange; 232.64 eV and blue; 235.74 eV)

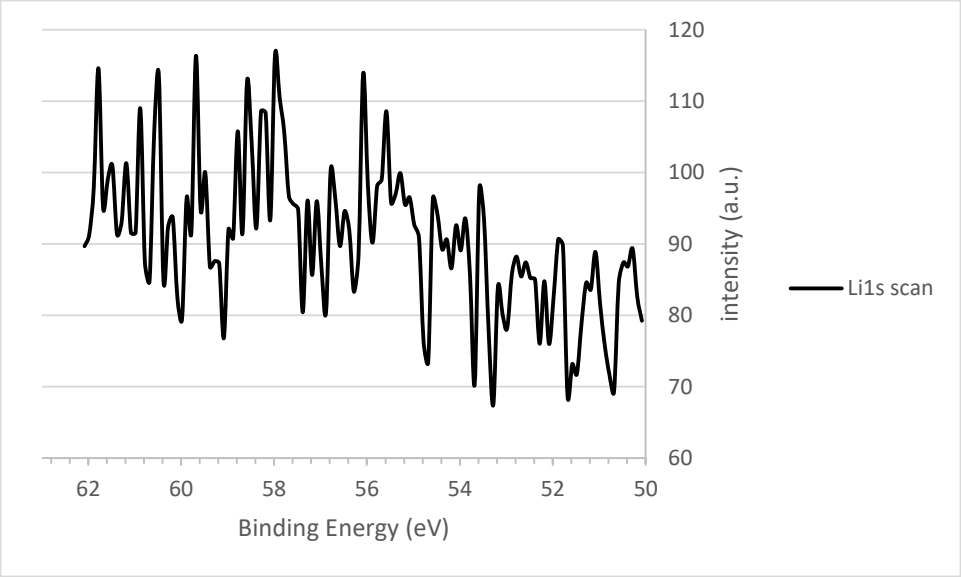

Figure 4.70 - XPS scan for MoO_3/AmThia showing the Li1s environment

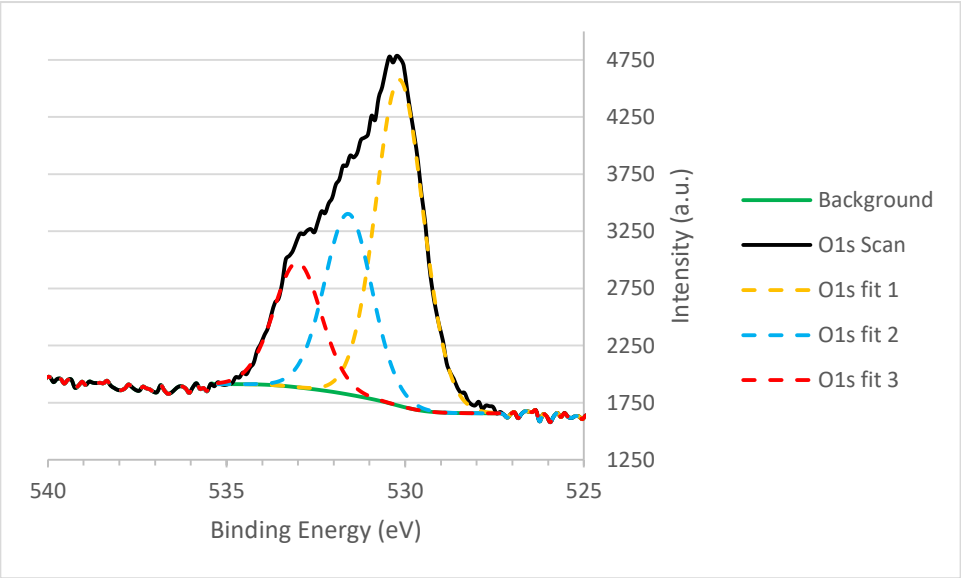

Figure 4.71 – XPS scan for MoO_3/2AmThia showing the O1s environment (black) fitted with three environments (orange; 530.32 eV, blue; 531.84 eV and red; 533.24 eV)

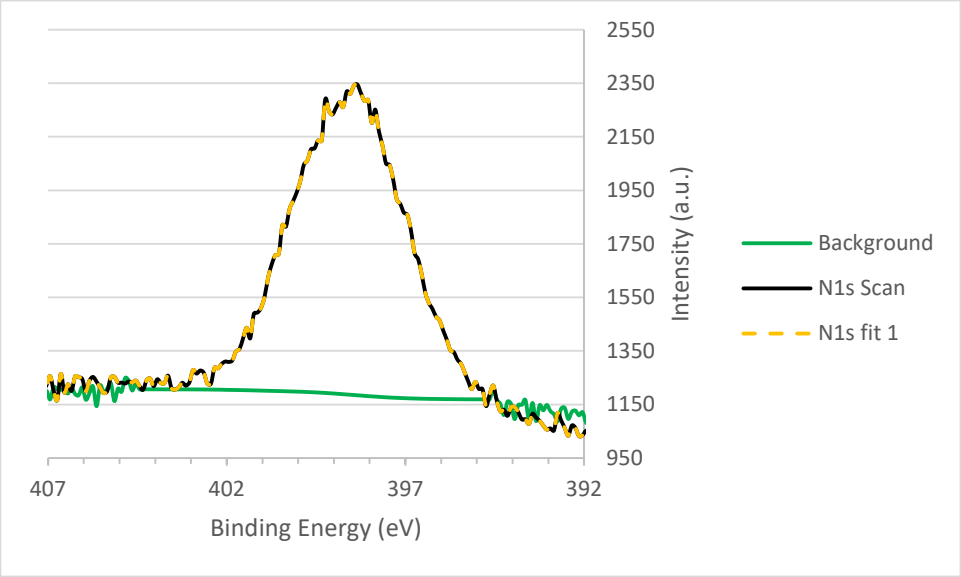

Figure 4.72 – XPS scan for MoO_3/2AmThia host showing the N1s environment (black) and fitted with a single environment (orange; 398.62 eV)

Figure 4.69, Figure 4.71 and Figure 4.72 shows the XPS scan for MoO_3/2AmThia showing the Mo3d, Li1s, O1s and N1s environments respectively. Once again it is shown that there is a single environment for the Mo environment ($Mo3d_{5/2}$ peak appearing ~ 232 eV and $Mo3d_{3/2}$ peak appearing at ~ 235 eV) and correspond well to the environments found for the pure host MoO_3 and literature values (Figure 4.52). Once again this suggests that there was limited to no redox chemistry between the organic intercalant and the inorganic host material. Furthermore, there appears to be no Mo^{5+} centres present in this material (or at least within the detection depth for this analysis). The reduced Mo^{5+} was likely re-oxidised during the washing procedure. The oxygen environments are once again similar to those seen in the previous spectra with three environments now present upon intercalation. The three environments corresponding to the MoO_3 oxygen environment (fit 1 ~ 530 eV) MoO_3 oxygen interacting with the organic intercalant (fit 2 ~ 531 eV) and any oxygen from any loosely bound water molecules on the surface or in the interlayer spacing of the material (fit 3 ~ 533 eV). The N1s environment also shows a single fitted environment (Figure 4.72) but due to the signal-to-noise ratio compared to the other spectra it is possible that more than one fitted environment is present corresponding to the protonated phase of the organic intercalant (as seen in the IR and Raman data).

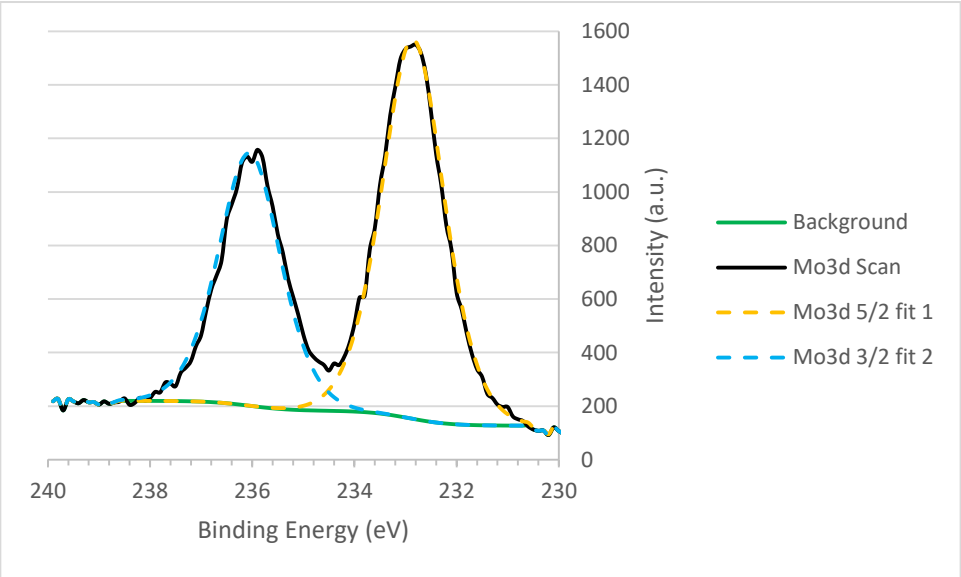

Figure 4.73 – XPS scan for MoO_3/An showing the Mo3d environments (black) with $Mo3d_{5/2}$ (orange) and $Mo3d_{3/2}$ (blue) environments fitted with a single environment respectively (orange; 233 eV and blue; 236.2 eV)

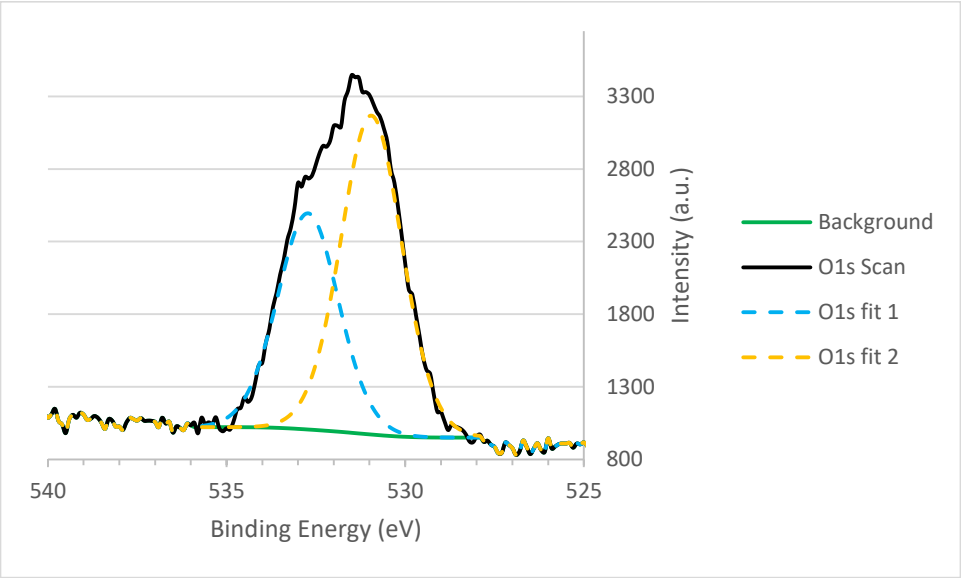

Figure 4.74 – XPS scan for MoO_3/An showing the O1s environment (black) fitted with two environments (orange; 531.2 eV and blue; 533 eV)

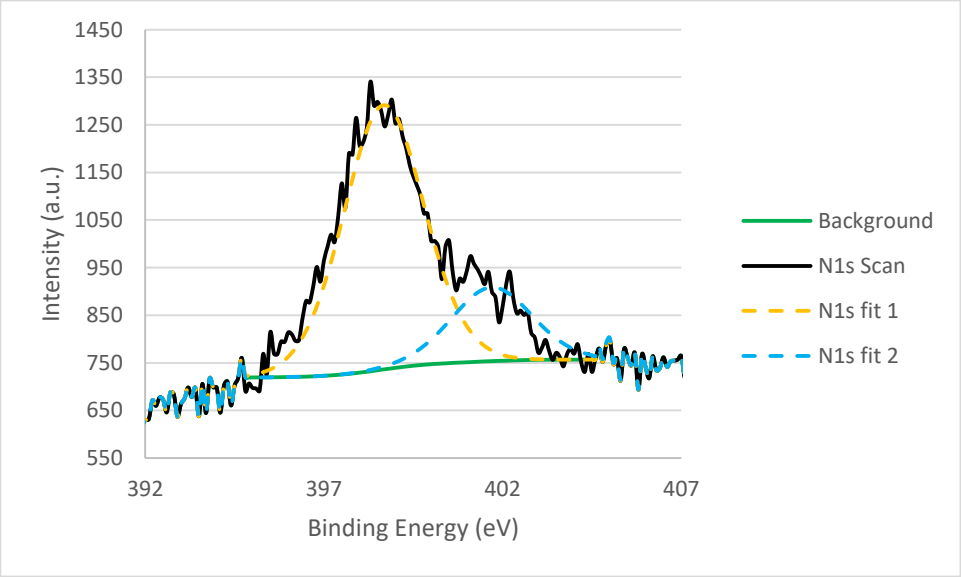

Figure 4.75 – XPS scan for MoO_3/An host showing the N1s environment (black) and fitted with two environments (orange; 399 eV and blue: 402.4 eV)

Figure 4.73, Figure 4.74 and Figure 4.75 show the Mo3d, O1s and N1s environments respectively for MoO_3/An synthesised via recrystallization. In Figure 4.73 we see that once recrystallized within the MoO_3 structure there appears to be no redox chemistry with the inorganic layers as no Mo^{5+} was detected via XPS (or within the detection depth of the technique). The peaks appearing in Figure 4.73 are close to those for the host MoO_3 environments relating to Mo^{6+} (Figure 4.52). Since we know that polyaniline is present in the interlayer spacing (determined previously from IR, Raman, TGA and ICP-AES analysis) it likely that polymerisation occurred while the aniline monomer was in solution with the inorganic layer growing around the oligomeric or polymeric form of aniline in solution resulting in the synthesised material. This, however, does not immediately rule out the possibility of the polyaniline not being present in its doped emeraldine form. From Figure 4.75 it can be seen that there are at least two nitrogen environments which are dissimilar to the previous spectra of the MoO_3 composite materials. The peaks of the two environments (appearing at ~ 399 eV and 402 eV) which corresponds closely to that for the emeraldine form of polyaniline (264,265) as previously seen in V_2O_5/AnAn$^+$. It is likely that due to the noise-to-signal ratio that more than two environments could be fitted which may correspond to further polaron features of emeraldine. The IR and Raman

spectra showed the presence of the benzenoid and quinoid ring systems along with the presence of NH_3^+ and $>NH^+$ further suggesting that the oligomeric or polymeric polyaniline is present in its emeraldine form. The O1s Figure 4.75 is further different from that from the previous spectra. Here, it is seen that there a minimum of two oxygen environments present. The two environments (appearing at ~ 531 eV and 533 eV) correspond to the oxygen in the MoO_3 interacting with any organic intercalant and that for the present MoO_3 oxygen environment respectively as seen in previous spectra. It must be noted that the broad shoulder that appears after the apex between ~ 532 eV and 533 eV could contain another oxygen environment similar to that seen for the previous spectra.

4.1.2.6) Electron Spin Resonance Spectroscopy (ESR)

The ESR spectrum of the pure host MoO_3 showed no peaks.

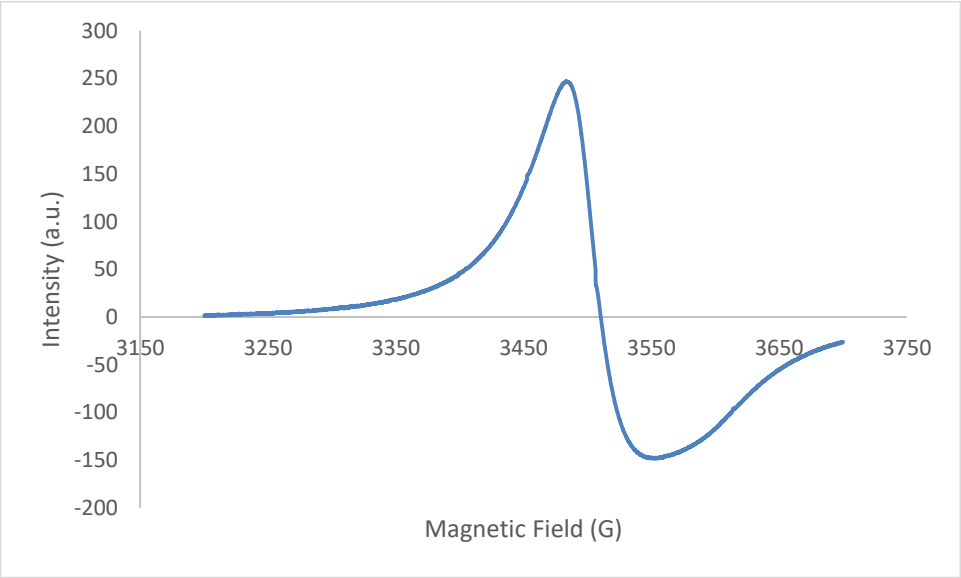

Figure 4.76 - $LiMoO_3$ ESR spectrum

In Figure 4.76, the ESR spectrum of Li_xMoO_3 shows a single asymmetric peak centred at a g-factor value of 1.9727 with a peak-to-peak width of 69 Gauss. The spectrum is similar to that seen for the $Li_xV_2O_5$ material (Figure 4.39). The spectrum also exhibits a similar asymmetry to that for $Li_xV_2O_5$ suggesting successful redox reaction with n-BuLi. The sharpness and low g-factor value compared to that for the free electron (g-factor =

2.00232) suggests that the signal arises from a localised electron in the inorganic host and as such the formation of the reduced Mo^{5+} centres. The fact that the peak does not exhibit any hyperfine structure suggests that the electron transfer has reduced the Mo^{6+} to Mo^{5+} is not experiencing any nuclear interaction with Mo ions. This further supports the presence of a localised electron in the inorganic layers from the redox reaction. The asymmetry and any enhanced broadening exhibited in the spectrum could arise from any structural defects caused by the intercalation process such any stacking, screw or dislocation defects in the bulk and/or surface of the material. Furthermore the concentration of Mo^{5+} centres may be enough to be considered as impurities leading to the material being treated as an inhomogeneous material. It is unlikely that other Mo oxides may have been formed contributing to the asymmetry as the presence of these systems were not present in the UV-Vis or XRD data.

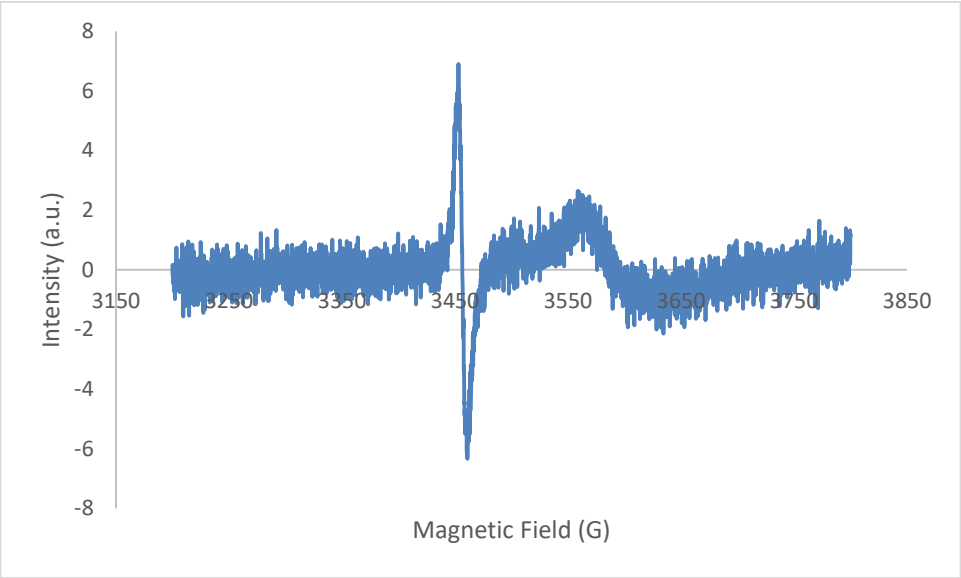

Figure 4.77 - MoO_3/PDA ESR spectrum

Figure 4.77 shows the ESR spectrum MoO_3/PDA in which we can see two distinct features. The first is a weak but sharp peak centred at a g-factor value of 2.00383 with a peak-to-peak width of 7.91 Gauss. The second feature is a broader weaker asymmetric signal centred at a g-factor value of 1.929 (3558 Gauss). The second feature appears to be a much weaker signal (in respect to the sharper first feature). This broad peak is possible to

be part of a hyperfine structure, however, it is possible that the hyperfine structure is weak and not be discernible from the background. Due to this the broad peak is treated as not relating to any hyperfine structure. However due to the high g-factor value of the sharp peak compared to that for the free electron (g-factor = 2.00232) suggests that this peak arises from a localised electron on the organic material. The XPS for this material Figure 4.57 showed no presence of the Mo^{5+} analogous to some of the V_2O_5 systems which also did not exhibit a reduced V^{4+} peak. The peak in Figure 4.77 is arising from an unpaired electron in the organic, it is possible that the reduced Mo^{5+} was oxidised back to Mo^{6+} by donating its electron to the organic guest. This would thus make the organic guest an anion (n-type). However, it will be demonstrated (in section 4.2.2) that the MoO_3 composites exhibit p-type behaviour. As such, a neutral MoO_3 and n-type organic intercalant should exhibit n-type behaviour in the bulk material overall. A more likely scenario is the oxidation of these Mo^{5+} centres during the washing process or from being in the presence of air of a long period of time resulting in the reformation of the Mo^{6+} and the organic intercalant remaining in its p-type phase.

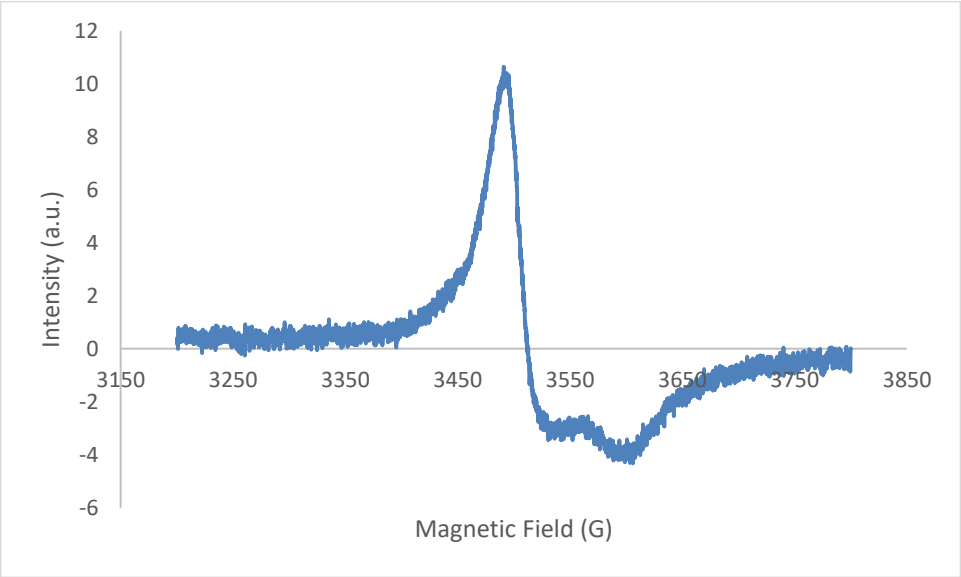

Figure 4.78 - MoO_3/2A5PhPyr ESR spectrum

An asymmetric peak with a shoulder is seen in Figure 4.78 for MoO_3/2A5PhPyr. The spectrum is centred with a g-factor value of 1.97545 with a peak-to-peak width of 47.82 Gauss. The shoulder appearing in the negative region appears at a g-factor value of 1.93085 (3598.84 Gauss). The spectrum appears to be very similar to that seen for LiV_2O_5/2A5PhPyr (Figure 4.44) except for this peak is significantly weaker than that for its V_2O_5 counterpart. As seen previously for $Li_xV_2O_5$ the low value for the g-factor when compared to that for the free electron (g-factor = 2.00232) and the sharpness of this peak suggests that the signal arises from a localised electron on the inorganic phase of the material. The presence of no hyperfine structure further suggests that the electron resulting in the formation of the Mo^{5+} centres is not interacting with any Mo nuclei including its own nucleus. The intensity of this peak is similar to that for V_2O_5/$AnAn^+$ (Figure 4.41) and as such a similar conclusion can be drawn that the concentration of unpaired electrons in this material could be small. Due to the UV-Vis data showing a single phase of MoO_3 it is unlikely that other reduced Mo oxide phases are present and unlikely that this shoulder in the ESR arises due to the presence of a different MoO_x phase. The appearance of the shoulder could be resultant either from a different MoO_3 phase present in the material arising as a consequence of the intercalation reaction or an axial system. As seen with the analogous V_2O_5 systems, the broadness and asymmetry exhibited in the spectrum could be due to any defects in the c-axial direction (stacking defects for example) or from other defects (such as screw, dislocations or step defects). As seen for MoO_3/PDA, the XPS of this material (Figure 4.61) also exhibited no Mo^{5+} environments and therefore the same conclusions can be drawn as was for MoO_3/PDA that due to the XPS being a surface specific technique showed no Mo^{5+} on the surface whereas the ESR signal is representative of the bulk material which may contain Mo^{5+} centres. It is unlikely that the Mo^{5+} is oxidised back to Mo^{6+} by donation of its electron to the organic intercalant as the signal in this spectrum arises from the inorganic phase. It is more likely that this oxidation occurring

during the washing process or due to the material being in contact with air for a prolonged period of time. However, in this case, it may have only occurred in the surface layers and thus the Mo^{5+} giving rise to this signal may lie deeper in the bulk material than possible for detection via XPS.

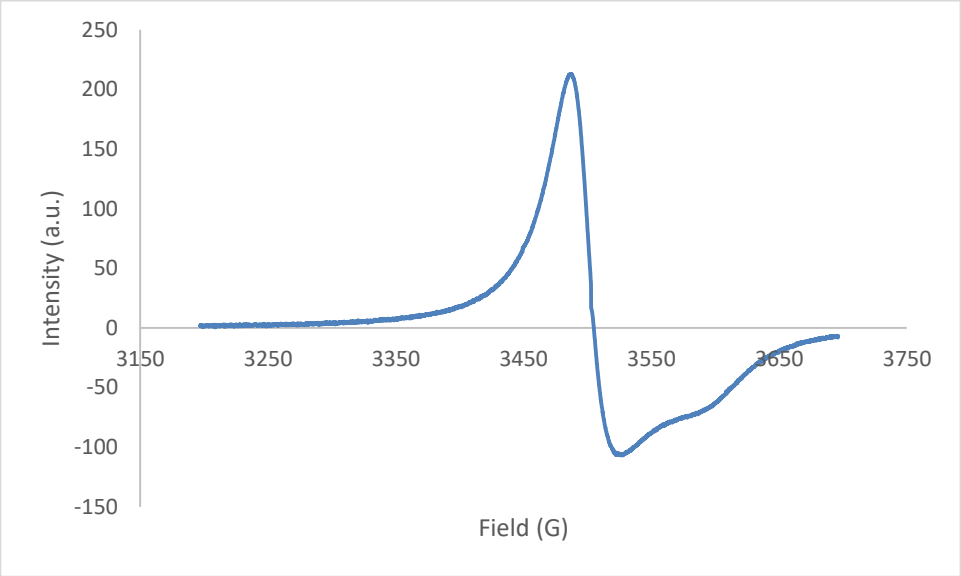

Figure 4.79 - MoO_3/5AQ ESR spectrum

In Figure 4.79 we see the ESR spectrum for the MoO_3/5AQ material. The spectrum is centred with a g-factor value of 1.97614 and is asymmetric with a shoulder appearing in the negative region which is less pronounced than that seen in Figure 4.78. The peak-to-peak width of the signal is 40.52 Gauss. The same conclusions are drawn from this spectrum as with Figure 4.78 due to the similarities between the two. Furthermore, it is noticeable that this spectrum is analogous to its V_2O_5 counterpart (V_2O_5/5AQ, Figure 4.45). As such, due to the low value for the g-factor when compared to that for the free electron (g-factor = 2.00232) and sharpness of the peak and its analogous structure to V_2O_5/5AQ, it is likely that the signal arises from a localised electron in the inorganic phase. The lack of any hyperfine structure further suggests that this electron is not interacting with any nuclei in the inorganic phase. The shoulder in the negative region could arise from the presence of a different MoO_3 phase that is exhibited due to the

changes in the c-axial direction from the intercalation reaction. The asymmetry and broadening of the peak are once again attributed to any structural defects in the c-axial direction (stacking defects for example) or from other defects (such as screw, dislocations or step defects). As seen previously for MoO_3/2A5PhPyr, the XRD and UV-Vis for this data shows no evidence for the presence of any other MoO_x phases present and therefore it is unlikely that this shoulder arises due to the presence of these other oxide impurities. Again, the absence of the Mo^{5+} in the XPS of MoO_3/5AQ suggests that the ESR signals must originate from a paramagnetic species below the detection limits of the XPS or from regions deeper than the escape depth of the photo-electrons. It is unlikely that the Mo^{5+} is oxidised back to Mo^{6+} by donation of its electron to the organic intercalant as the signal in this spectrum arises from the inorganic phase. It is more likely that this oxidation occurring during the washing process or due to the material being in contact with air for a prolonged period of time. However, in this case, it may have only occurred in the surface layers and thus the Mo^{5+} giving rise to this signal may lie deeper in the bulk material than possible for detection via XPS.

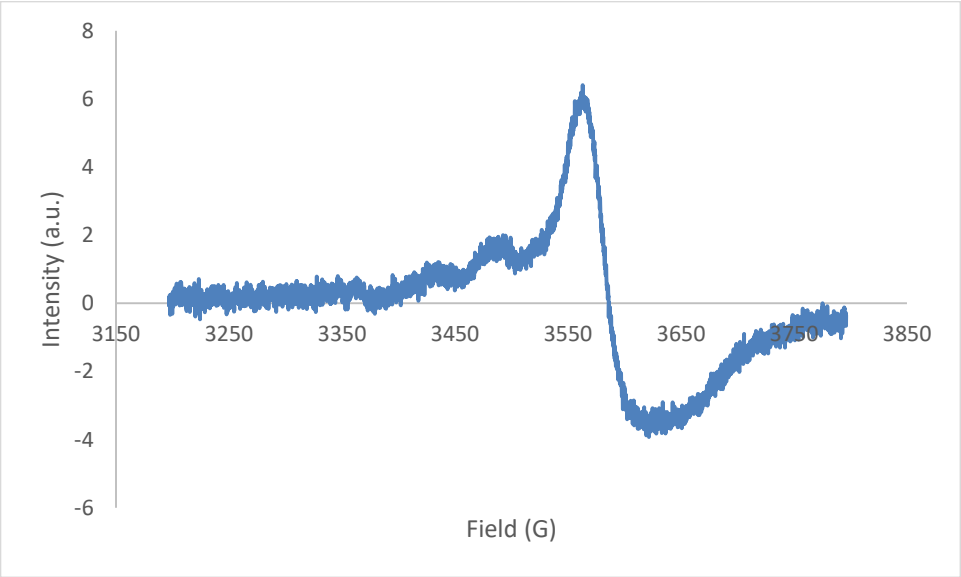

Figure 4.80 - MoO_3/AmThia ESR spectrum

The ESR spectrum for MoO_3/AmThia (Figure 4.80) is asymmetric with two shoulders appearing at lower field strength (3496.58 Gauss) that do not appear to be related to the main feature in the spectrum. It is possible that these peaks are related to a hyperfine structure however it may be that some of the hyperfine structure is not discernible from the background. As such it is difficult to determine whether these shoulders are related to a hyperfine structure. The main feature is centred at a g-factor value of 1.93246 with a peak-to-peak width of 73.35 Gauss. The spectrum appears to be similar to that seen in the previous samples in relation to the asymmetry of the main peak. Due to the low value for the g-factor when compared to that for the free electron (g-factor = 2.00232) and sharpness of the peak suggests that the main feature is related to that of a localised unpaired electron in the inorganic phase. Once again this spectrum exhibits a weak peak suggesting a low concentration of the unpaired electron present in the inorganic phase which may suggest that there was limited redox chemistry between the organic intercalant and the MoO_3 host. The shoulders are analogous to the shoulders seen for the V_2O_5/1,4PDA-HQ system (Figure 4.46) which were attributed potential ^1H hyperfine structure. It is possible for such a structure to exist in this material if an unpaired electron was found in the organic phase. It was previously confirmed that the AmThia in this system is in an oligomeric or polymeric form (from the TGA and ICP-AES) as well as the IR and Raman data confirming the presence of a protonated (p-type) phase of the organic guest species. As per the previous spectra, the asymmetry and any enhanced broadening of the main peak could be attributed to any c-axial defects or other defects (such as screw or dislocations). However, when comparing such a conclusion with that of the XRD data, the sharpness of the XRD peaks are such that such defects are less likely to be present in this material (unlike in the V_2O_5 systems). As seen from the previous ESR spectra, the XPS of this material (Figure 4.69) also exhibited no Mo^{5+} environments and therefore the same conclusions can be drawn as was for the previous ESR spectra. It is unlikely that the Mo^{5+}

is oxidised back to Mo^{6+} by donation of its electron to the organic intercalant as the signal in this spectrum arises from the inorganic phase. Therefore if this mechanism does occur, the hyperfine ^{1}H structure would arise from the organic guest. It is more likely that this oxidation is occurring during the washing process or due to the material being in contact with air for a prolonged period of time. However, in this case, it may have only occurred in the surface layers and thus the Mo^{5+} giving rise to this signal may lie deeper in the bulk material than possible for detection via XPS.

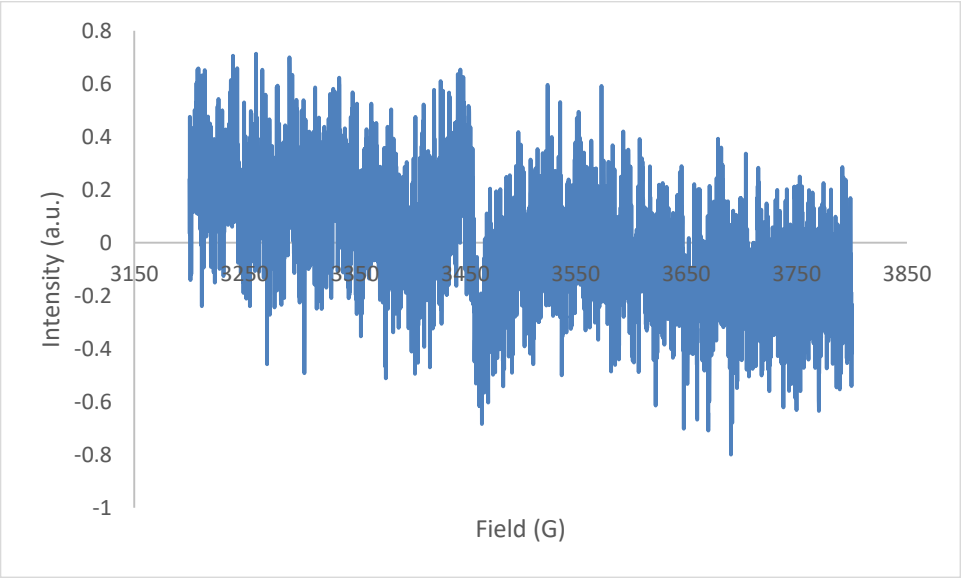

Figure 4.81 - MoO_3/An ESR spectrum

However, unlike the previous spectra, when aniline was intercalated via the recrystallization method to form MoO_3/An the ESR spectrum (Figure 4.81) appears to show no signal on first glance. On further inspection, it could be suggested that there is an extremely weak peak centred at a g-factor value of 2.00299 with a peak-to-peak width of 16.84 Gauss. However, it is likely that there is no peak present in this spectrum and that under the conditions for recrystallization from an aqueous solvent, there appeared to be no redox chemistry between the intercalated aniline and the MoO_3 material.

Summary

Overall it has been demonstrated that intercalation of the organic guest species into the interlayer spacing of MoO_3 was successfully carried out. A full characterisation of the literature synthesised material MoO_3/An has been presented using a novel intercalation method (via recrystallization from an aqueous solvent medium) not previously reported. The novel composite materials MoO_3/PDA, MoO_3/2A5PhPyr, MoO_3/5AQ and MoO_3/AmThia have been synthesised and fully characterised confirming the successful intercalation of the organic monomers within the MoO_3 interlayer space. The increase in the interlayer spacing in the XRD data (Figure 4.47) corresponded to the presence of the intercalated organic guest species. The sharpness of the expanded (*020*) peak (unlike those seen in the analogous V_2O_5) suggested that the overall structural integrity was maintained throughout the composite materials upon intercalation. The ESR data suggested that there may have been some c-axial defects being exhibited in the materials which were not seen in the XRD and therefore it is likely that any defects were minimised during the synthesis and are only seen in the ESR due to the sensitivity of the technique. Furthermore the IR and Raman data (Table 4.7) supports the presence of the organic material within the interlayer spacing as the shifted host peaks are typical for intercalated MoO_3 (seen previously seen in section 1.5.2)). The organic peaks present suggest that the organic intercalants are in their protonated (p-type) phases and due to the presence of the benzenoid and quinoid ring systems are oligomeric or polymeric in form. The calculated optical band-gaps for these materials also change upon intercalation and follow the trend seen in their analogous V_2O_5 systems where intercalation causes an increase in the optical band-gap. This was concluded to be due to poor band overlap between the organic and inorganic leading to the possible formation of an indirect semiconducting material. Furthermore, the expansion of the interlayer spacing could also result in the inorganic material exhibiting a band structure more similar to that seen for a single or multi-layer

system. In some cases the host region persists suggesting incomplete intercalation has occurred in these materials (which was seen in the IR and Raman data with a mix of shifted and unshifted host vibrational modes). The TGA and ICP-AES further confirmed independently that the organic intercalant was in its oligomeric or polymeric form within the interlayer spacing of the host material.

Along with these changes, the ESR and XPS data showed some changes in the chemical environment of these materials. Upon ion-exchange the XPS showed no Mo^{5+} present, however, the ESR showed that a small concentration of these reduced Mo centres could exist beyond detection limit of XPS (due to XPS being a surface specific technique). The re-oxidation of any reduced Mo^{5+} centres on the surface layers of the material is determined to be likely to occur during the washing stages of the synthesis. Though the changes in the ESR and XPS generally showed a similar trend suggesting that any electrical and/or photoconductive properties of these materials (see section 4.2.2) is likely to arise due to the changes in the nature of the organic material within the interlayer spacing and not due to the inorganic host (as concluded for the V_2O_5 systems).

From the characterisation, ion-exchange and recrystallization mechanisms are proposed;

Scheme 1 – Ion-exchange mechanism

i) $$(Mo^{6+})O_3 + nBuLi \rightarrow (Mo^{6+})_{1-x}(Mo^{5+})_x O_3(Li^+)_x + C_4H_{10}$$

ii) $$(Mo^{6+})_{1-x}(Mo^{5+})_x O_3(Li^+)_x + (Monomer^+)_{aq\ (excess)} \rightarrow$$
$$(Mo^{6+})_{1-x}(Mo^{5+})^*_x O_3(Monomer^+) + x(Li^+)_{aq}$$

* It is during this step re-oxidation of this reduced Mo^{5+} could occur on the material surface.

Scheme 2 – Recrystallization mechanism

i) $MoO_{3\,(s)} \xrightarrow{Water} MoO_{3\,(aq)}$

ii) $MoO_{3\,(aq)} + Aniline_{(aq)} \xrightarrow[-H_2O]{} MoO_3(Aniline)_{(s)}$

4.1.3) $ZnPS_3$ Intercalation

4.1.3.1) X-ray Diffraction

Table 4.9 - Table to show the interlayer spacing and change in interlayer spacing for the ZnPS3 intercalated compounds

	Interlayer Spacing (Å)	Interlayer spacing change (ΔÅ)	2θ (°)	Intensity/Morphology
$ZnPS_3$	6.32	/	14.0	Strong sharp peak
Mg_xZnPS3	10.39	4.07	8.4	Strong peak with a diffuse shoulder
$ZnPS_3$/PDA	8.02	1.70	8.7	Strong sharp peak

From Table 4.9 and Figure 4.82 we can see that the ion-exchange between the Mg^{2+} ions from solution and Zn^{2+} ions of the host inorganic layers yield successful intercalation of the Mg^{2+} into $ZnPS_3$. It is suspected that the Mg^{2+} ions are located within the interlayer spacing rather than occupying the vacant Zn^{2+} sites. This has been concluded as the expanded (*001*) peak appearing for Mg_xZnPS_3 at $2\theta = 8.5^o$ corresponds to a change in interlayer spacing of 4.07 Å. The minimum diameter of a hexa-hydrated Mg^{2+} has been reported to be approximately 5.72Å(277). Therefore partially hydrated Mg^{2+} (present due to the aqueous nature of the reaction) could be present in the interlayer spacing leading to the expansion seen (the presence of a hydrated Na^+ has been previously reported to be intercalated into the MPS_3 compounds(199)). A weak peak appears ≈ 6Å (at $2\theta \approx 14^o$) correlating strongly to the initial *001* of the pristine host material. The Mg_xZnPS_3 material, therefore, exhibits two phases, the first is the Mg^{2+} intercalated phase while the second corresponds to the pristine $ZnPS_3$ host. The broad shoulder that appears around the expanded (*001*) peak suggests that there may be some *c*-axial defects (such as screw defects) that have occurred during the ion-exchange process. Since it has been suspected that the intercalated cation is partially hydrated, the diffuse broad peak could correspond to phases in the material where there are differing degrees of hydration leading to the material exhibiting a range of interlayer spacing. Although less likely to be observed, the lack of occupation of the vacant Zn^{2+} sites could further lead to the appearance of some expanded

(*001*) as the (*001*) peak corresponds to the distance between Zn^{2+} in adjacent layers. Therefore with vacancies present, some of the (*001*) peaks would appear to be shifted due to a greater difference in distance between Zn^{2+} ions situated further apart when vacancies are present compared to $ZnPS_3$ with no Zn^{2+} vacancies.

When the Mg_xZnPS_3 material was further reacted with PDA, once again structural changes are observed. Noticeably the characteristic (*001*) peak of $ZnPS_3$ has returned showing that one phase of this material is the pristine $ZnPS_3$ host. Furthermore, a new strong peak appears at 8.02 Å ($2\theta = 10.9^o$) not corresponding to the expansion associated with Mg^{2+} intercalation and it is concluded this peak corresponds to an interlayer expansion due to the organic intercalant. The organic cation appears to exchange with the Mg^{2+} and also displace any water molecules located in the interlayer spacing. A weak peak appears at $2\theta = 8.09^o$ in a similar position to the expanded *001* peak seen for Mg^{2+}. This may suggest that not all of the Mg^{2+} have been exchanged.

The change in the interlayer spacing shown in $ZnPS_3$/PDA (1.70 Å) correlates well with the Van der Waals radius of carbon which is approx. 1.4Å(278). It can be concluded therefore that once exchanged with Mg^{2+}, the organic intercalant is orientated parallel to the inorganic host layers rather than perpendicular or in a bilayer fashion as previously seen for intercalation in the oxides (see sections 4.1.1) and 4.1.2).

Overall it has been shown from the XRD data that Mg^{2+} successfully intercalate into $ZnPS_3$ and that the organic PDA cations exchange with Mg^{2+}.

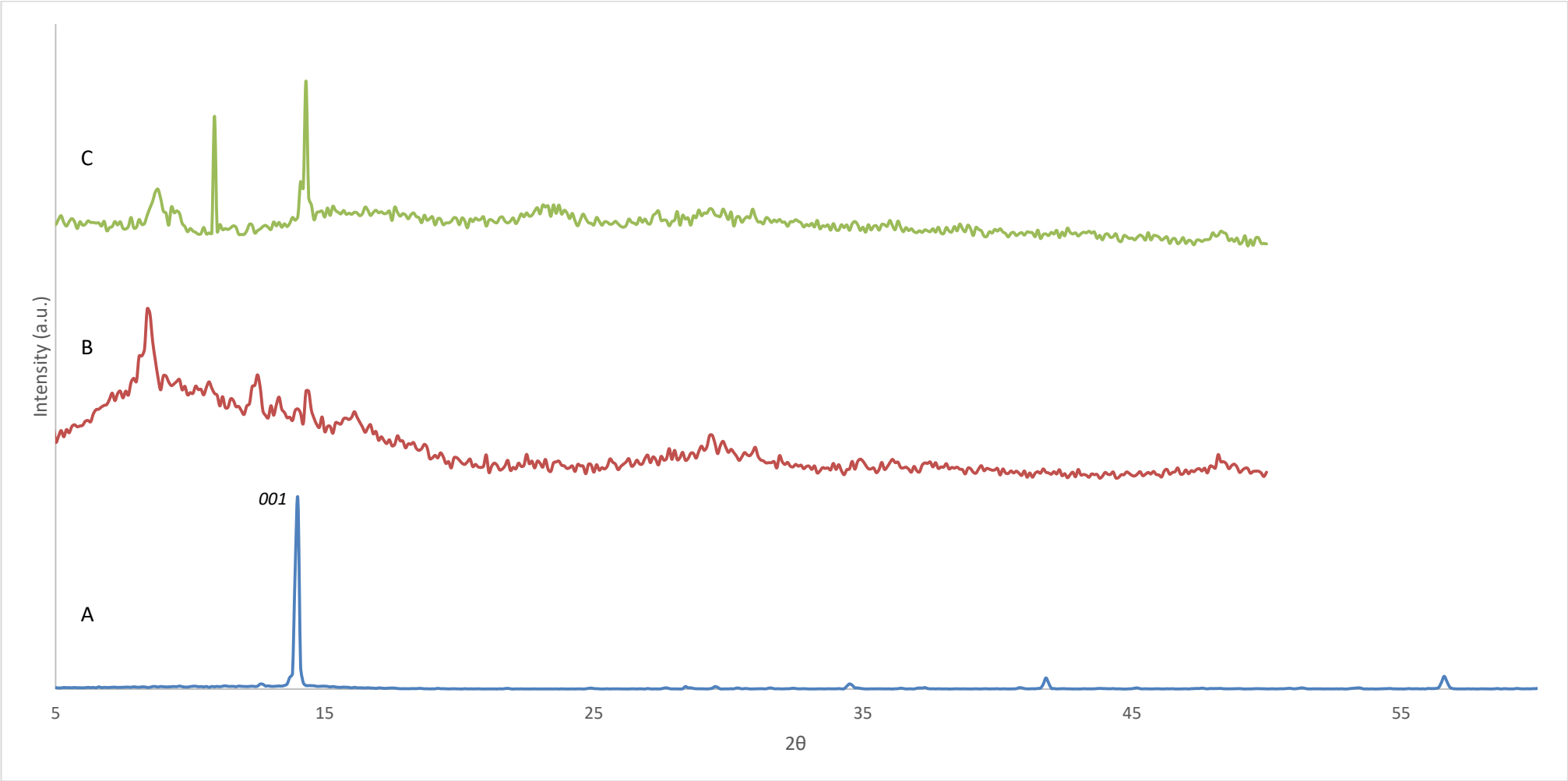

Figure 4.82 – X-ray diffractograms for A) $ZnPS_3$ host, B) Mg_xZnPS_3 and C) $ZnPS_3$/PDA

4.1.3.2) Infra-red and Raman Spectroscopy

Table 4.10 - IR and Raman wavenumbers (cm^{-1}) for $ZnPS_3$ intercalated compounds where v_d = asymmetric stretching mode, v_s = symmetric stretching mode, δ_s = symmetric bending mode, δ_d = asymmetric bending mode, $T'_{z\ or\ xy}$ = Translational mode in z or xy plane and $R'_{z\ or\ xy}$ = rotational mode in the z or xy plane.

$ZnPS_3$		**$MgZnPS_3$**		**$ZnPS_3$/PDA**		**Lit ($ZnPS_3$)** (206)		**Assignment**
IR	Raman	IR	Raman	IR	Raman	IR	Raman	
		3387						O-H stretch
				2924				
		1634		1621				NH_2, >NH, NH_3^+ bending
					1573			
				1495	1475			
					1374			Benzenoid C=C and Quinoid C=C stretching
					1257			
					1160			
				1032				
710				784				C-H aromatic bending
		616		620	602			v_d (PS_3)
595	577	586	563	595	585	571	577	
		569		580				
562								
		555						
545						510		
							568	
		514					525	
		495						
452		454				451		T'z (PS_3) and v_d (P-P)
	386		377				387	v_s (PS_3)
						312	310	δ_s (PS_3)
	277		273			274	277	δ_d (PS_3)
	256					259	257	T'_{xy} (PS_3)
			233					R'_{xy} (PS_3)
	225						225	
						199	200	T'_{xy} (PS_3)
						182		
						140	150	R'_{xy} (PS_3)
						120	130	T' (M)
							79	R'_z (PS_3)
						75	55	T' (M)

The vibrational frequencies for the $ZnPS_3$ compounds are shown in Table 4.10. In general, peaks appearing below 600 cm^{-1} in the IR and Raman corresponds to the inorganic host material whereas those above 600 cm^{-1} are modes of the organic intercalant. It was seen that the intercalation of Mg^{2+} ions resulted in the appearances of new peaks in both the IR and Raman spectra (see Appendix C.1 and C.2 for full spectra). The peaks below 600 cm^{-1} correspond to the $ZnPS_3$ vibrational modes whose corresponding peaks have either split (as discussed previously in section 1.5.3) typically indicating intercalation into the MPS_3 host compounds. Furthermore, it was concluded from the XRD that the Mg^{2+} ions are suspected to be present in the interlayer and not occupying the vacant Zn^{2+} sites. The splitting of peaks would only occur where the Mg^{2+} ions are located within the interlayer spacing rather than being located in the Zn^{2+} vacancies due to the increase in the interlayer spacing. For example, in Mg_xZnPS_3 the initial $ZnPS_3$ peak appearing at 595 cm^{-1} appears to have split into two peaks appearing at 616 cm^{-1} and 586 cm^{-1} which remains in $ZnPS_3$/PDA where the two peaks appear at 620 cm^{-1} and 580 cm^{-1}. The peaks appearing centred at 3387 cm^{-1} and 2924 cm^{-1} for Mg_xZnPS_3 and $ZnPS_3$/PDA respectively are associated with the O-H stretching peaks either arising from any residual moisture physically bound to the surface of the material or else the water molecules found within the interlayer spacing. This also seen in the Raman spectra of $ZnPS_3$ and Mg_xZnPS_3 where shifts in the Raman peaks (e.g. 577 has been shifted to 563 and 386 shifts to 377) suggest Mg^{2+} is located in the interlayer spacing rather than within the vacant Zn^{2+} sites. Shifting in the Raman peaks is typically seen in intercalated MPS_3 compounds (as discussed previously in section 1.5.3). Upon ion-exchange between Mg^{2+} and PDA cations we further see changes in the infra-red spectra. The peaks appearing between 1700 cm^{-1} and 1500 cm^{-1} corresponds a mix of >NH, NH_2 and NH_3^+ which (as seen previously for V_2O_5 and MoO_3) may suggest that the polymerised PDA could have a mix between several forms within the interlayer spacing (shown previously in 4.1.1). The peaks between 1500 cm^{-1} and 1000 cm^{-1}

correspond to a mix of benzenoid and quinoid structures. From this, it can be concluded that there was successful polymerisation of PDA using an external oxidant (ammonium persulphate in this case) and is in a conductive form with some phases of the polymer being in the ladder-type form while others being a polyaniline like structure with NH_3^+ groups remaining as previously seen in Figure 4.4.

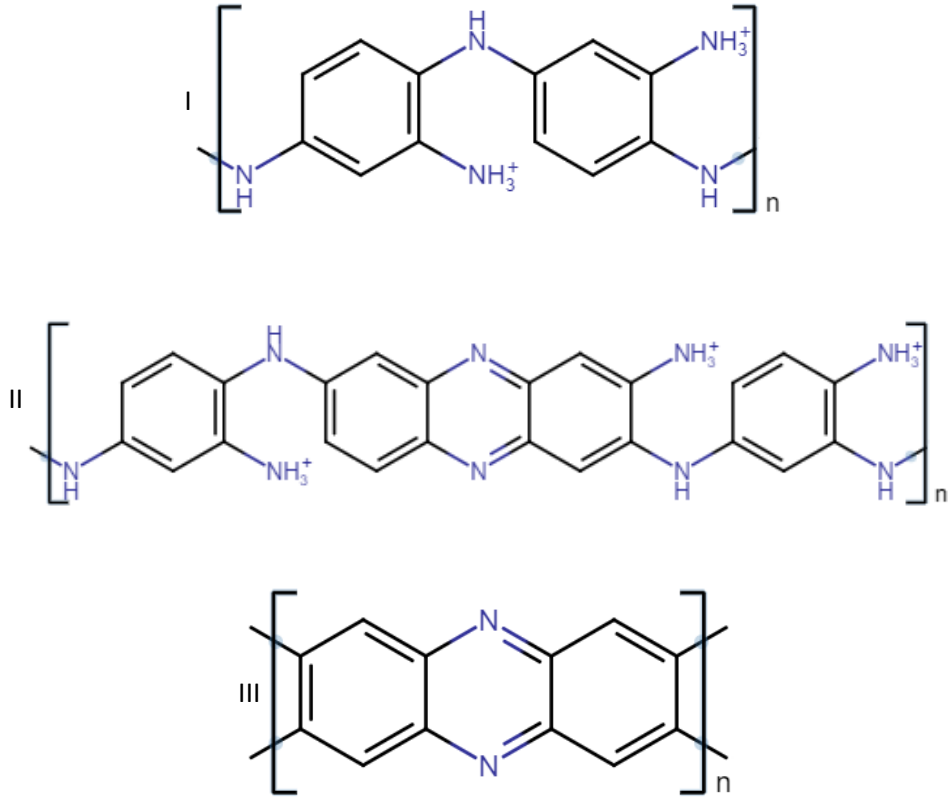

Figure 4.4 – I) Polymerised PDA to produce a substituted polyaniline form, II) Polymerised PDA with two phases present; a non-ladder phase and a ladder oligomer phase and III) Fully polymerised PDA producing the Ladder like polymer

Furthermore, noticeable changes are observed in the Raman spectra compared to both $ZnPS_3$ and $MgZnPS_3$. We can see peaks appearing at higher wavenumbers (above 1000 cm^{-1}) which have only appeared due to the presence of the organic guest in the interlayer spacing. Interestingly, however, the Raman spectroscopy confirms for the $ZnPS_3$/PDA material two phases are present; the $ZnPS3_3$/PDA material and the pure pristine host $ZnPS_3$ which is also evident in the XRD data. However, it is difficult to determine whether any Mg^{2+} is still present in this material as suspected from the XRD

4.1.3.3) TGA and ICP-AES

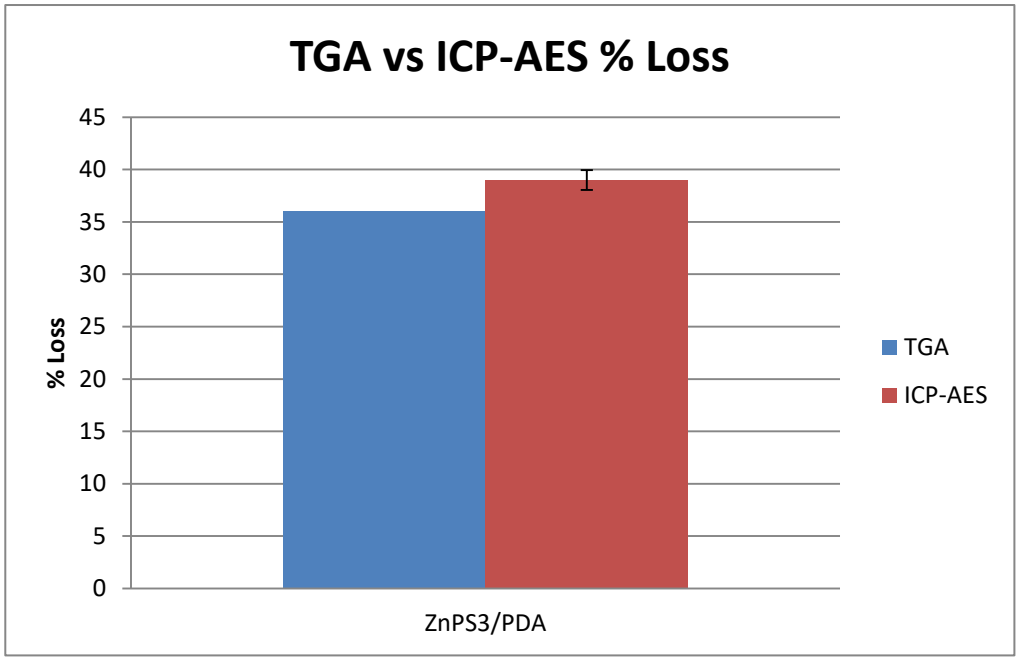

Figure 4.83 - % weight loss via TGA and ICP-AES for the $ZnPS_3$/PDA composite after the initial mass loss due to water. The error bars in the ICP-AES were obtained in-situ via three consecutive measurements as described in section 3.1.4.

Figure 4.83 shows the total percentage loss in mass determined by TGA and ICP-AES independently (for full TGA data see Appendix C.3). Shown here is the % by mass of the guest species in the composite material. From the ICP-AES data the stoichiometry was calculated by determining the total Zn content in the digested sample (assuming stoichiometry to be $ZnPS_3$) and comparing this to the theoretical Zn content if no organic intercalant was present. The difference in the zinc content was concluded to arise from the presence of the organic guest.

The stoichiometry of the host from the Zn, P and S concentrations was calculated by to be $Zn_{0.93}P_1S_{2.7}$. This shows a near stoichiometry of the host material where the small differences to the ideal $ZnPS_3$ stoichiometry may arise due to incomplete digestion and therefore this is was taken as the maximum zinc content detectable. Similarly, the composite material stoichiometry were calculated to be $Mg_{0.18}Zn_{0.66}P_1S_{2.65}$ and $PDA_{0.1}Zn_{0.53}P_1S_{2.24}$. It is clear that there is a deviation from the ideal $ZnPS_3$ stoichiometry in both intercalated materials due to the ion-exchange mechanism being utilised. From this we can propose accompanying any non-intercalated pristine $ZnPS_3$ host, the loss in Zn^{2+}

ions and the lack of occupation of these sites from the exchanged cations leads to some non-stoichiometric inorganic host being present with an overall combined (of pristine and intercalated phases) potential stoichiometry being $Mg_{0.54}Zn_{1.98}P_2S_{7.95}$ (with rounding to give integers for the host $Zn_2P_2S_8$) in the Mg^{2+} intercalated material and $Mg_{0.4}Zn_{2.12}P_4S_{8.96}$ (with rounding to give integers for the host $Zn_2P_4S_9$). The non-stoichiometry of the materials could arise from different phases of the $ZnPS_3$ being present. In the Mg_xZnPS_3 material, this non-stoichiometry could explain the broad shoulder that appears around the expanded (*001*) peak in the XRD as being potentially related to interlayer spacing of different inorganic host phases. In the TGA for both materials, the initial loss around 100°C is associated with any loosely bound water on the surface due to the aqueous nature of the reactions. The continuous loss of mass in several steps seen in the TGA for the $MgZnPS_3$ could be associated with the loss of water that is coordinated with the Mg^{2+} ions located in the interlayer spacing. As these water molecules are being lost, the remaining water molecules are bound stronger to the Mg^{2+} ion and would require more energy to remove. For the $ZnPS_3$/PDA material the continuous loss in mass over the remaining temperature range relating to that of the presence of oligomeric or polymeric intercalant. This is supported also by the IR and Raman evidence showing the presence of the polymer or oligomers. If the organic guest remained in its protonated monomer form, one would expect all the guest species to be removed around a narrow range of temperatures and not as a continual loss over a wide range. The oligomeric or polymeric guest species is likely to be found in a monolayer conformation lying parallel to the inorganic layers. This is due to the interlayer spacing increase of 1.70Å which correlates to the van der Waals radius of carbon. If certain regions of the guest were to be found in, for example, a helical conformation than this would lead to a range of interlayer spacing being exhibited by the material which can be interpreted as a broad or diffuse peak (as previously seen in the oxide materials).

4.1.3.4) Optical Spectroscopy

Table 4.11 - Optical band-gaps determined from for the $ZnPS_3$ compounds

	Band gap (eV)	Tauc plot r-value
$ZnPS_3$	3.30	1/2 (direct allowed transition)
$MgZnPS_3$ (I)	3.81	1/2 (direct allowed transition)
$MgZnPS_3$ (II)	3.50	1/2 (direct allowed transition)
$ZnPS_3$/PDA (III)	2.41	2 (indirect allowed transition)
$ZnPS_3$/PDA (IV)	1.96	2 (indirect allowed transition)

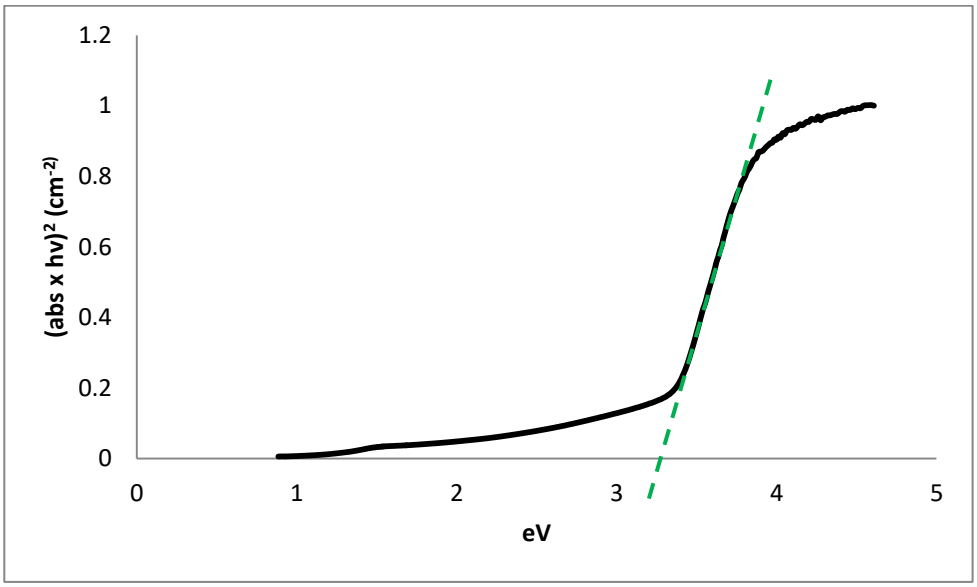

Figure 4.84 – Tauc plot for $ZnPS_3$ host

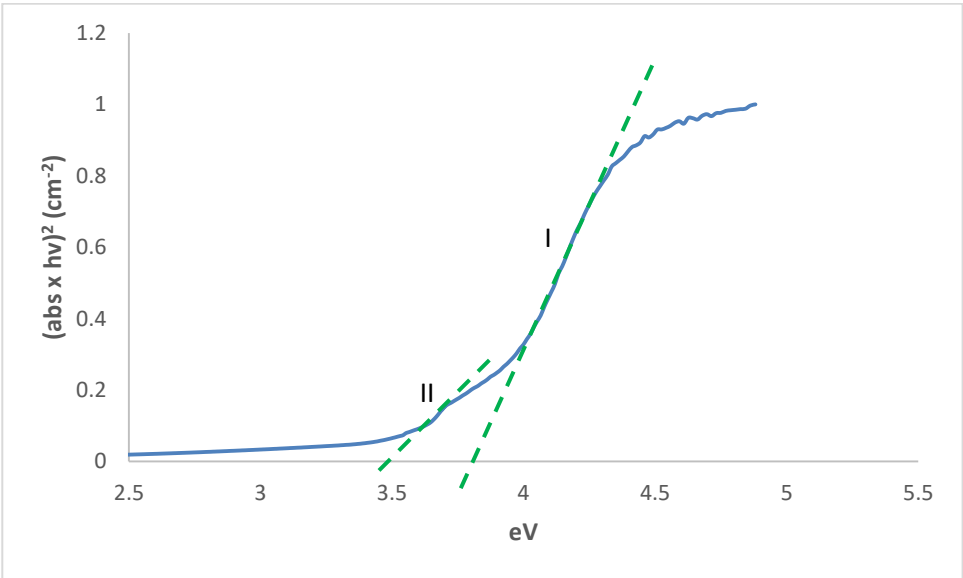

Figure 4.85 – Tauc plot for Mg_xZnPS_3

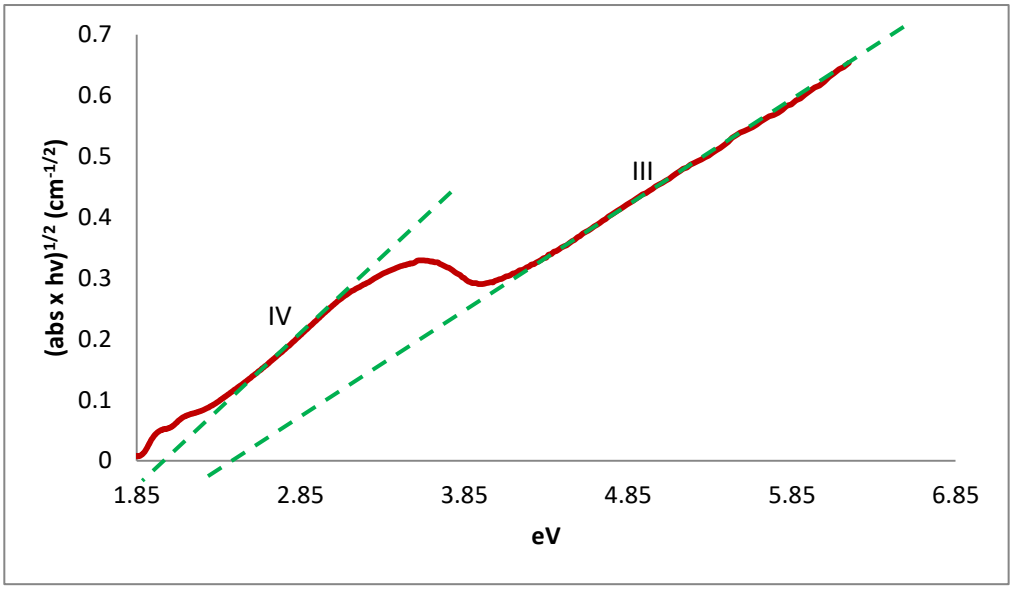

Figure 4.86 – Tauc plot for $ZnPS_3$/PDA

The calculated optical band-gaps and their associated tauc plots are shown in Table 4.11 and Figure 4.84, Figure 4.85 and Figure 4.86 where the optical band-gaps were determined by extrapolation of the linear part/s of the plot. The optical band-gap for $ZnPS_3$ has been shown to correspond well with the literature values(197,200,279). Upon intercalation of the Mg^{2+} ion two regions can be seen in the UV-Vis spectrum (regions I and II in Figure 4.85). The major phase (region I) corresponds to a band-gap of 3.8eV while the minor phase (region II) corresponds to a band-gap of 3.5eV. It is concluded that the intercalated $MgZnPS_3$ material is the major phase (at least the phase in this material which exhibits an increase in the interlayer spacing) while the minor phase is that of pure pristine $ZnPS_3$. This increase in the interlayer spacing is attributed to the fact that the layers would have weaker electronic interactions and therefore are exhibiting a band-gap more closely associated with a single layer (monolayer) $ZnPS_3$. It was therefore determined that no interactions occur between the Mg^{2+} and the $ZnPS_3$ layers, specifically there is no interaction between the Mg^{2+} and the PS_3^{2-} cluster. This was also suggested by IR, Raman and XRD data where it was concluded that Mg^{2+} does not occupy the Zn^{2+} vacancies. If Mg^{2+} occupied the vacant Zn^{2+} sites there would be ionic interactions between the Mg^{2+}

and PS_3^{2-} clusters that would yield a decrease in the overall band-gap (as seen in systems such as $MgPS_3$ due to the more ionic nature between the Mg^{2+} and the PS_3 cluster) and not an overall increase. Substitution of the Mg^{2+} for PDA causes a further change in the band-gap. Once more there are two regions present and in contrast to the precursor materials where the tauc plot corresponds to a direct-allowed transition, $ZnPS_3$/PDA has a band gap that corresponds to an indirect allowed transition (r-value of 2). The two regions (III and IV) corresponds to band-gaps of 2.41 eV and 1.96 eV respectively. Furthermore, the overall shape of the spectra is noticeably different to pristine host and Mg intercalated material which correlates to the noticeable changes in the XRD, IR and Raman data. This change in the spectrum could arise from two likely possibilities. The first is the presence of the polymer (as concluded from the TGA-ICP) which is in a conducting form (as seen in the IR and Raman data). In contrast to the oxide composites, the $ZnPS_3$/PDA may show better band overlap between the inorganic and organic species. Also, as previously discussed from the TGA and ICP-AES analysis, if the $ZnPS_3$ host is now present in a non-stoichiometric form this could also lead to changes in the spectrum resulting from a different band-gap. For $ZnPS_3$/PDA it is quite possible that the change in the spectrum arises from a combination of these two likely possibilities.

Overall it is shown that there are chemical and physical (optical spectroscopic) changes occurring during intercalation from the pure pristine host, to the intercalation of Mg^{2+} and finally exchange between the metal cation and the organic guest cations.

4.1.3.5) Electron Spin Resonance Spectroscopy (ESR)

The ESR of pure $ZnPS_3$ shows no peak present.

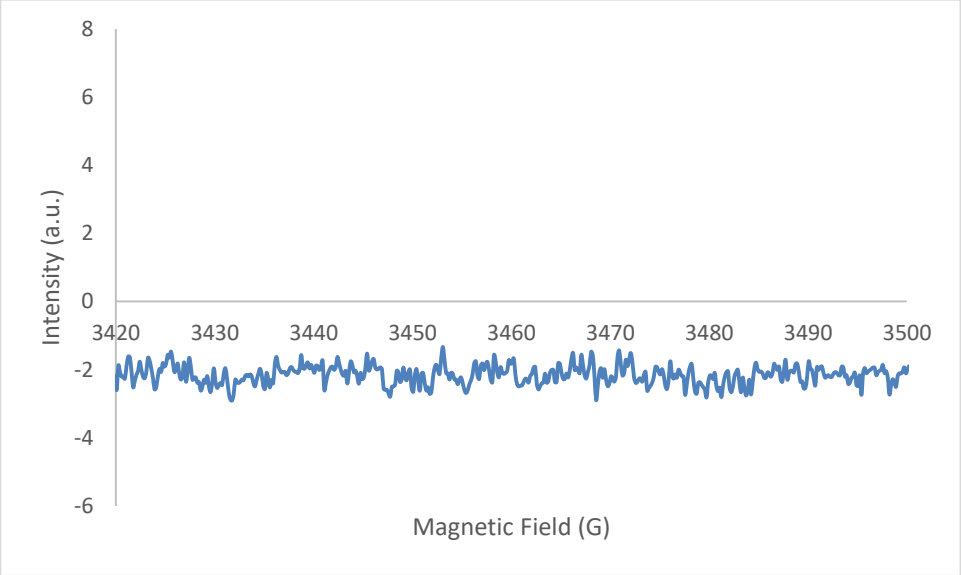

Figure 4.87 - ESR spectrum of $MgZnPS_3$ material

The ESR spectrum of Mg_xZnPS3 (Figure 4.87) also shows no signal which may indicate that the intercalation of Mg^{2+} maintains the neutral charge of the overall material. It is difficult to conclude from this whether the vacant Zn^{2+} sites result in any possible rearrangement to a non-stoichiometric structure as potentially discussed in the TGA and ICP-AES results from this spectrum

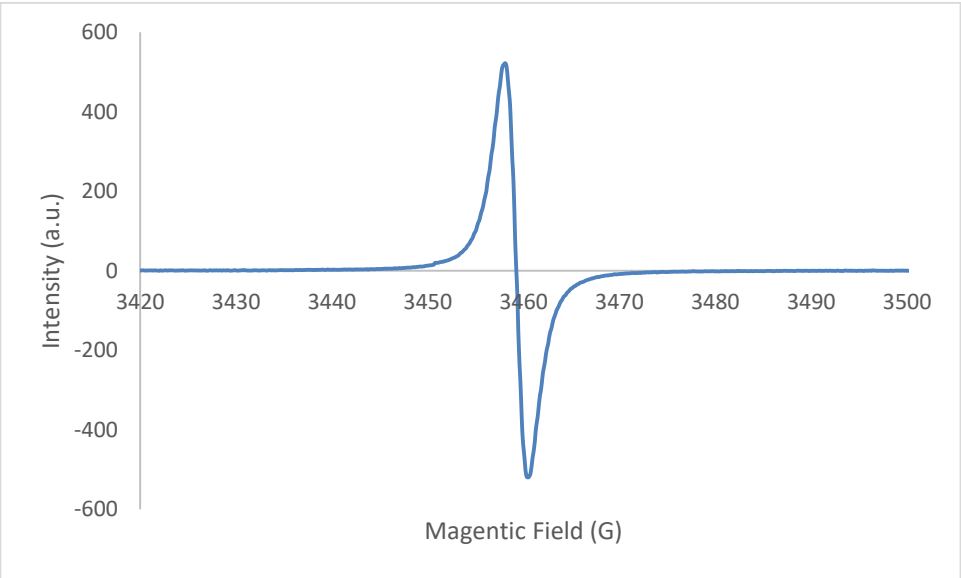

Figure 4.88 - ESR spectrum for the $ZnPS_3$/PDA composite material

However, when the exchange of Mg^{2+} with the organic guest changes the spectrum and a strong symmetric singlet centred at a g-factor value of 2.003477 with a peak-to-peak width of 2.34 Gauss is now present. The symmetric, narrow nature and g-factor value close to free-electron value suggest a localised electron (or an unpaired electron resulting from a positive hole). The absence of a hyperfine structure suggests that the electron from which this signal results from is not interacting with any magnetic nuclei. There are two potential possibilities for the rise of the signal, the first is the presence of this electron in the organic polymer due to the use of an external oxidant (in this case APS) and since it has been previously concluded from the IR data that this polymer is in a conductive phase. This is in contrast to that of the oxide ESR spectra, the asymmetry, broadness and low g-factor values which are attributed to the electron present in the inorganic phase. In the case of the $ZnPS_3$/PDA if the electron is present on the organic guest it could suggest the conductive phase of the organic guest where no hyperfine is exhibited due to the conductive electron results in the hyperfine being averaged to zero. If this signal arises from the inorganic phase of the material it could be from any non-stoichiometry present in the inorganic phase where the vacant Zn^{2+} sites can be treated as electron deficient (i.e. the inorganic being deemed to be a p-type material) and therefore any unpaired electrons arise due to the combination of the non-stoichiometry and vacant Zn^{2+} sites. This non-stoichiometry has been discussed previously in the ICP-AES data and could further explain the unusual nature of the UV-Vis spectrum. This is more likely due to the spectrum suggesting that this electron is non-conducting (as we have seen with the V_2O_5 and MoO_3), would not show any hyperfine structure and would be constrained to the vacancy due to the poor conductive (and lack of redox chemistry of d^{10} Zn) of the inorganic material.

From the characterisation, ion-exchange mechanisms are proposed;

Scheme 1 – Mg^{2+} ion intercalation

i) $$ZnPS_3 + Mg^{2+}_{excess} \rightarrow (Zn)_{1-x}Mg_yPS_3 + Zn^{2+}_x$$

Scheme 2 – Metal cation and monomer intercalation

ii) $$(Zn)_{1-x}Mg_yPS_3 + (Monomer^+)_{aq\ (excess)} \rightarrow (Zn)_{1-x}PS_3(Monomer^+) + Mg^{2+}_y$$

Scheme 3 – Monomer polymerisation

iii) $$(Zn)_{1-x}Mg_yPS_3 + (Monomer^+)_{aq\ (excess)} + APS \rightarrow (Zn)_{1-x}PS_3(Polymer)$$

4.2) Electrical and Photoelectric Measurements

4.2.1) V_2O_5 Nanocomposite Materials

4.2.1.1) Room Temperature Conductivity

Table 4.12 - Room temperature electrical conductivity for V_2O_5 composite materials

Material	Conductivity, σ (Sm^{-1})
V_2O_5	2.8×10^{-5}
Direct	
$V_2O_5/AnAn^+$	9.8×10^{-2}
V_2O_5/2A5PhPyr	5.6×10^{-3}
V_2O_5/EDOT	3.4×10^{-2}
ion-exchange	
V_2O_5/PDA	1.5×10^{-1}
LiV_2O_5/2A5PhPyr	1.3×10^{-3}
V_2O_5/5AQ	4.0×10^{-2}
V_2O_5/1,4PDA-HQ	6.5×10^{-4}

The room temperature conductivities were measured at room temperature (293K average) (temperature measured at the time of the experiment) and are shown in Table 4.12. It is clear that the host V_2O_5 has a low conductivity (corresponding to a poor semiconductor) which increases upon insertion of the organic intercalant. This increase is between one and four orders of magnitude. The increase in the conductivity is attributed to a combination of two factors, namely the formation of the V^{5+}/V^{4+} pairs in the inorganic layers and the presence of conductive organic intercalants (as concluded from the characterisation of these materials in Section 4.1.1). The most conductive material was shown to be V_2O_5/PDA, which was synthesised via ion-exchange. This was followed by $V_2O_5/AnAn^+$, V_2O_5/EDOT and V_2O_5/5AQ. The least conducting material was V_2O_5/1,4PDA-HQ which may have been due to the possibility of co-polymer formation(270) which in this particular case leads to limited chain lengths of the intercalated conducting polymer, and as a result, the material could exhibit a lower conductivity than the other composite materials.

4.2.1.2) Seebeck Coefficient

Table 4.13 - Seebeck Coefficients for some V_2O_5 composite materials and their doping type

Material	Seebeck Coefficient (μVK^{-1})	Material type
V_2O_5	-385 to -436(280)	n-type
V_2O_5/AnAn$^+$	268	p-type
V_2O_5/2A5PhPyr (AB)	148	p-type
V_2O_5/EDOT	73	p-type
V_2O_5/1,4PDA-HQ	119	p-type

In general, the V_2O_5 composite materials show positive Seebeck coefficients (see Appendix A.5) in contrast to the pristine host V_2O_5. The materials are therefore designated as p-type semiconductor materials, with V_2O_5/AnAn$^+$ exhibiting the largest value and V_2O_5/EDOT the lowest. In general, the increase in the Seebeck coefficient could be due to the presence of the polymers in the interlayer spacing of the inorganic material. In a similar trend to that seen for their conductivities (Table 4.12), the intercalated polymers appear to dominate in contributing to the observed positive Seebeck coefficients of the composite materials. The p-type nature of these materials appears to follow that of the intercalated polymer materials in which (from section 4.1.1) these polymers are concluded to be in their protonated forms, in contrast to the host V_2O_5. Overall it appears that the intercalation of p-type conducting polymers leads to an increase in both Seebeck coefficient and room temperature conductivity.

4.2.1.3) Schottky Device I-V Curves

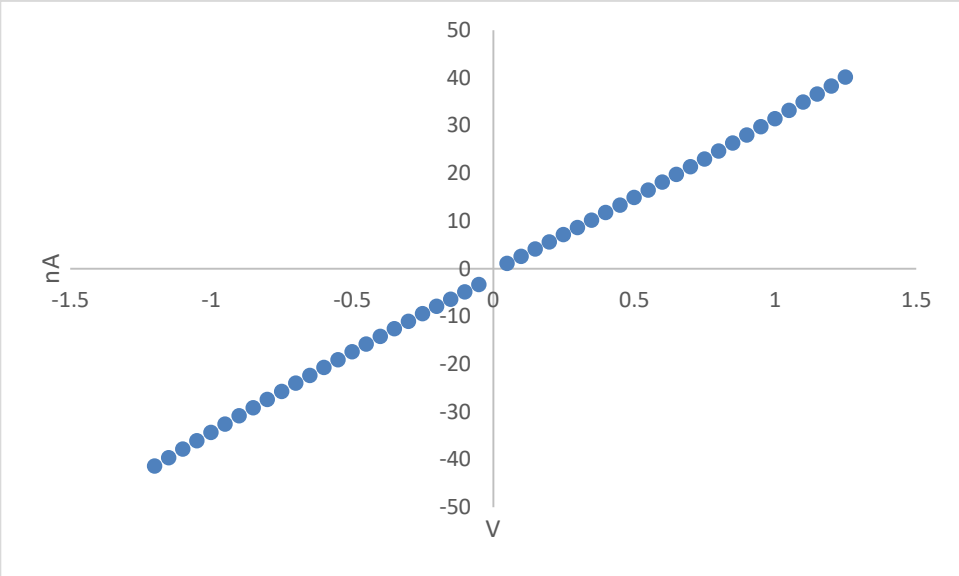

Figure 4.89 - I-V graph for V_2O_5 with Al contact

Pristine V_2O_5 exhibits ohmic properties with no rectification.

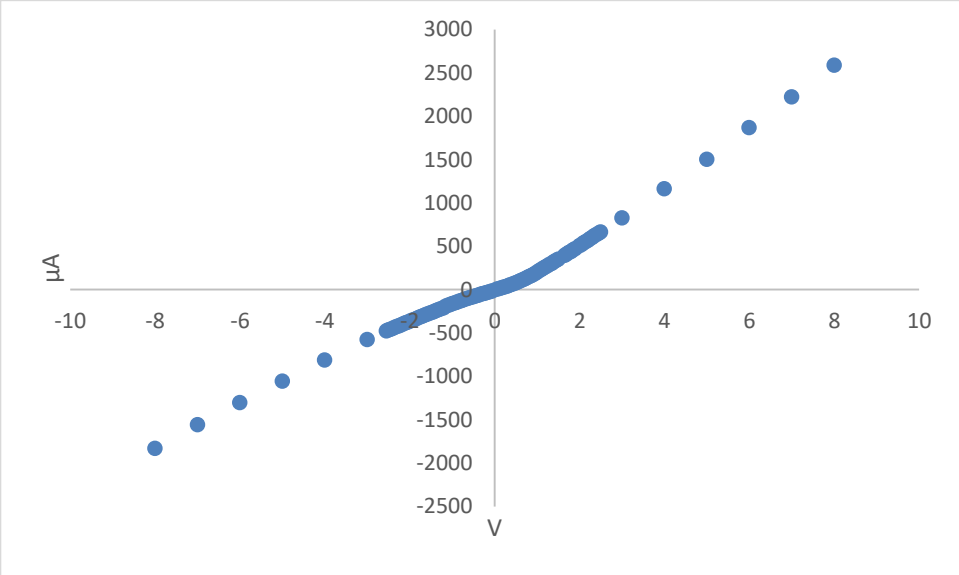

Figure 4.90 - I-V graph for V_2O_5/AnAn$^+$ with Zn contact

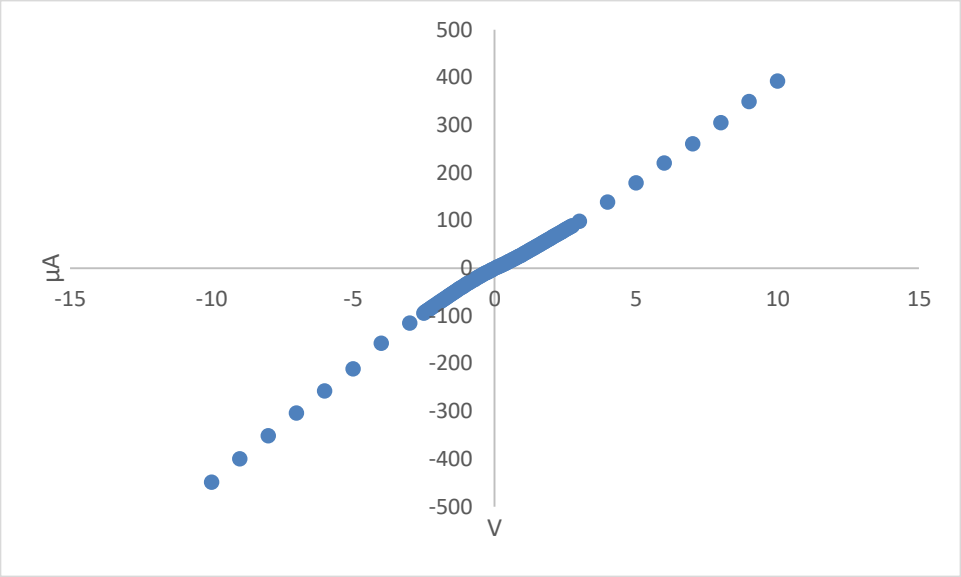

Figure 4.91 - I-V graph for V_2O_5/AnAn$^+$ with Al contact

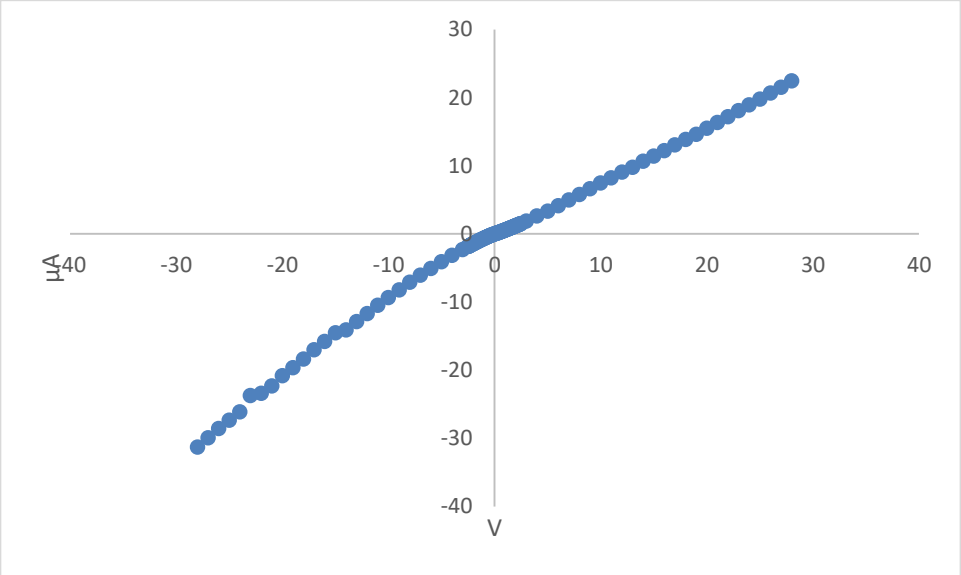

Figure 4.92 - I-V graph for V_2O_5/AnAn$^+$ with Cu contact

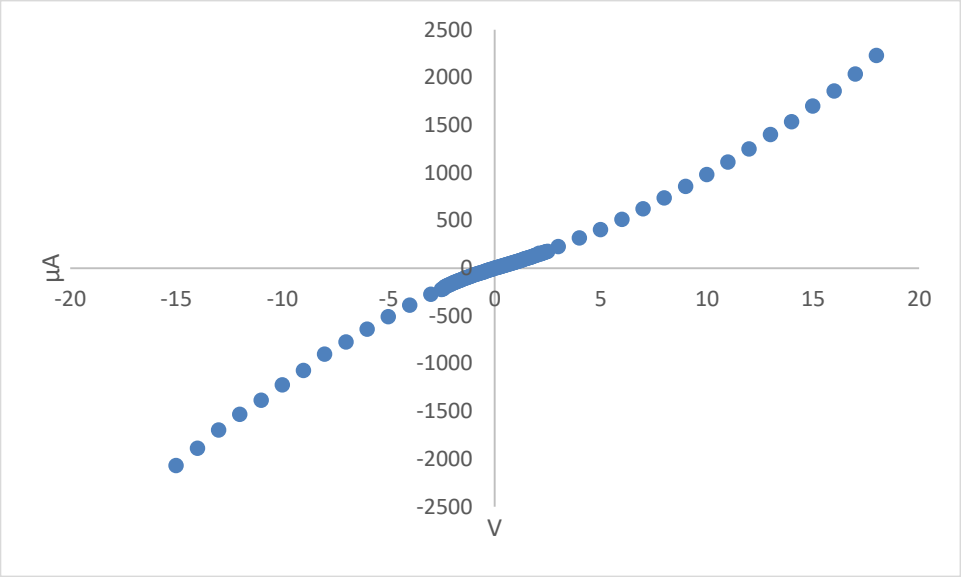

Figure 4.93 - I-V graph for V_2O_5/AnAn$^+$ with Sn contact

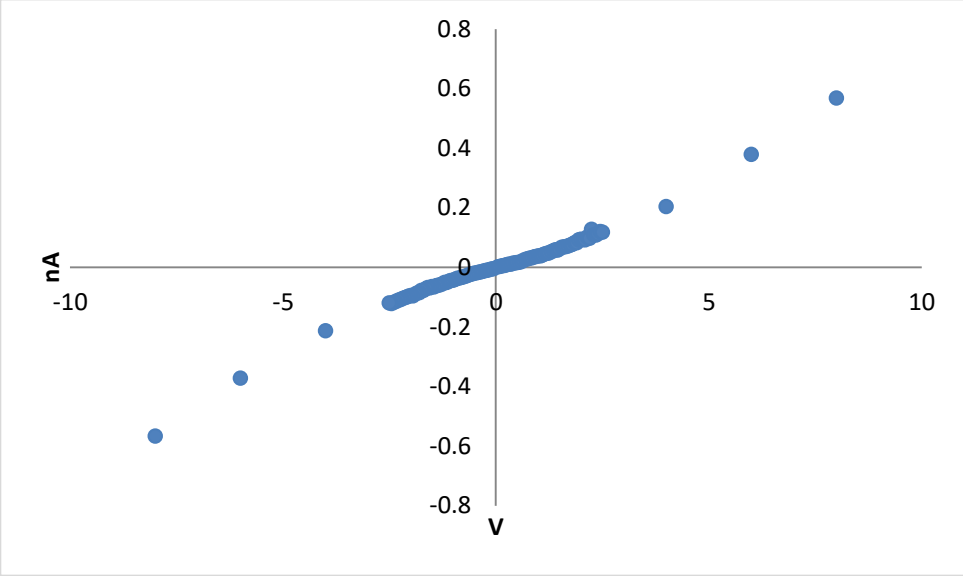

Figure 4.94 - I-V graph for V_2O_5/AnAn$^+$ with $FePS_3$ contact

Figure 4.90 - Figure 4.94 show the I-V graphs for the V_2O_5/AnAn$^+$ composite material diodes with various metallic contacts. For all I-V graphs, it is shown that within a small potential difference range (from -2.5 to 2.5V) the graphs exhibit rectifying behaviour. This is different from the V_2O_5 host material's behaviour. As concluded (in section 4.1.1) the polymer materials were successfully intercalated into the interlayer space of V_2O_5; therefore the changes in the I-V graphs are a result of the presence of the particular polymer intercalant. In the case of V_2O_5/AnAn$^+$, any changes to the I-V character of the host material would be caused by the presence of AnAn$^+$. The least rectifying device was

shown to be that with the Cu contact and the most rectifying was with the Sn contact. The two most conducting devices had Zn and Sn contacts. The rectification ratios between the maximum and minimum measured voltage for Figure 4.90 - Figure 4.94 are 1.02, 1.41, 1.14, 1.39, 1.07 and 1.00 respectively.

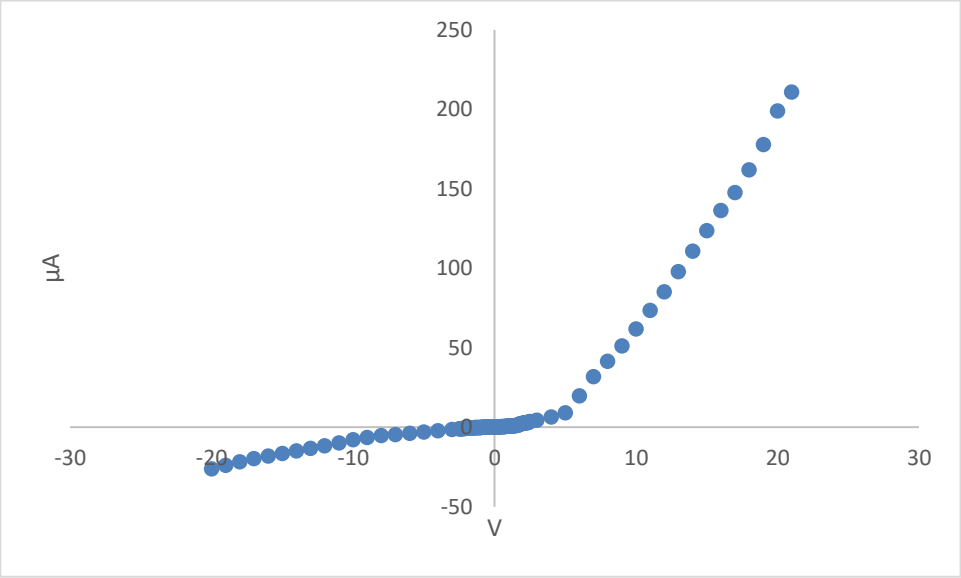

Figure 4.95 - I-V graph for V_2O_5/2A5PhPyr with Zn contact

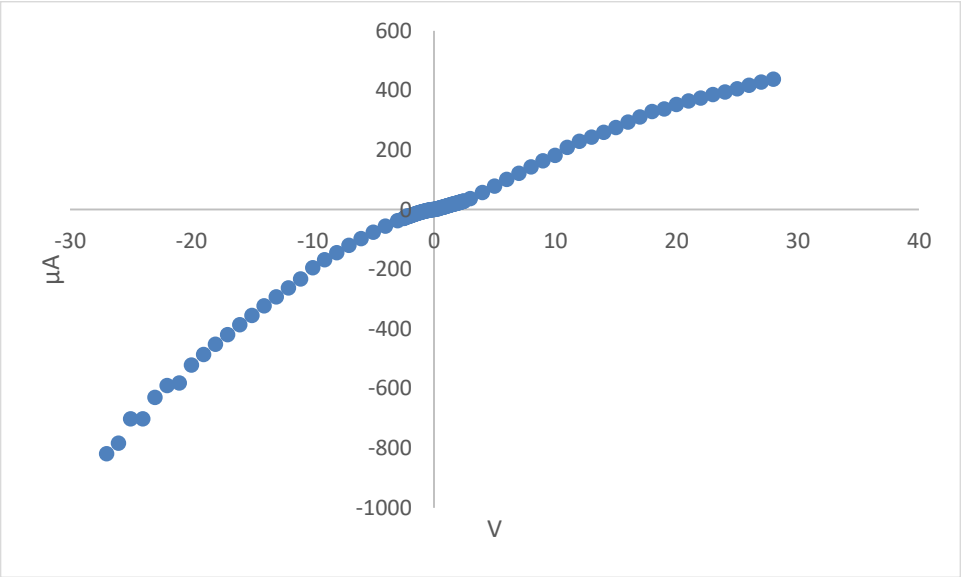

Figure 4.96 - I-V graph for V_2O_5/2A5PhPyr with Al contact

Figure 4.95 and Figure 4.96 show I-V graphs for the V_2O_5/2A5PhPyr composite (synthesised via direct intercalation) and it is clear that with a Zn contact (Figure 4.95), the diode exhibits rectifying properties. With an Al contact, however, there is again a non-linear relationship within a small potential difference range (-2.5V to 2.5V), after which we reach a saturation point where the material exhibits a linear I-V relationship. In the reverse bias region, the relationship remains non-linear. As with the V_2O_5/AnAn$^+$, the deviation from the V_2O_5 I-V character is associated with the presence of the polymer intercalant 2A5PhPyr.

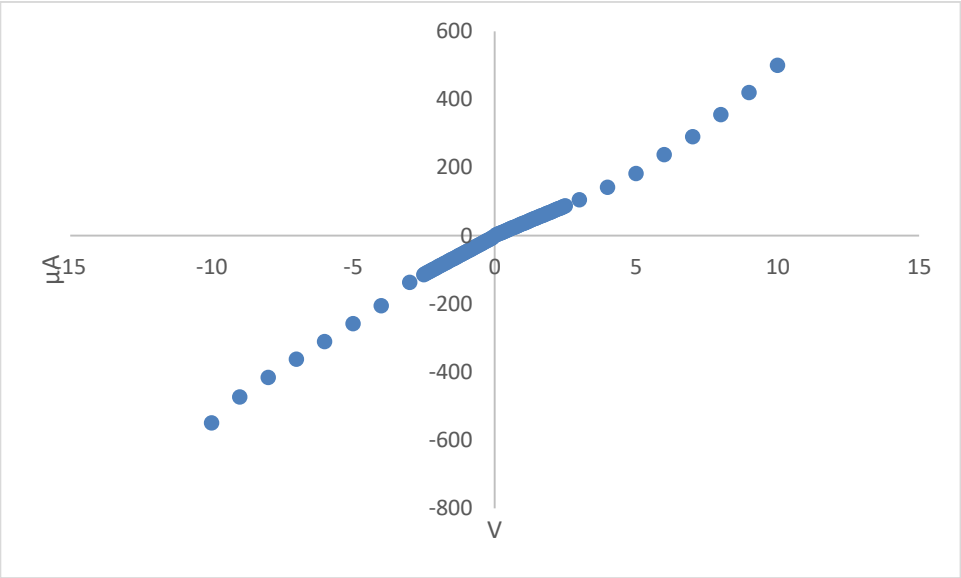

Figure 4.97 - I-V graph for V_2O_5/EDOT with Zn contact

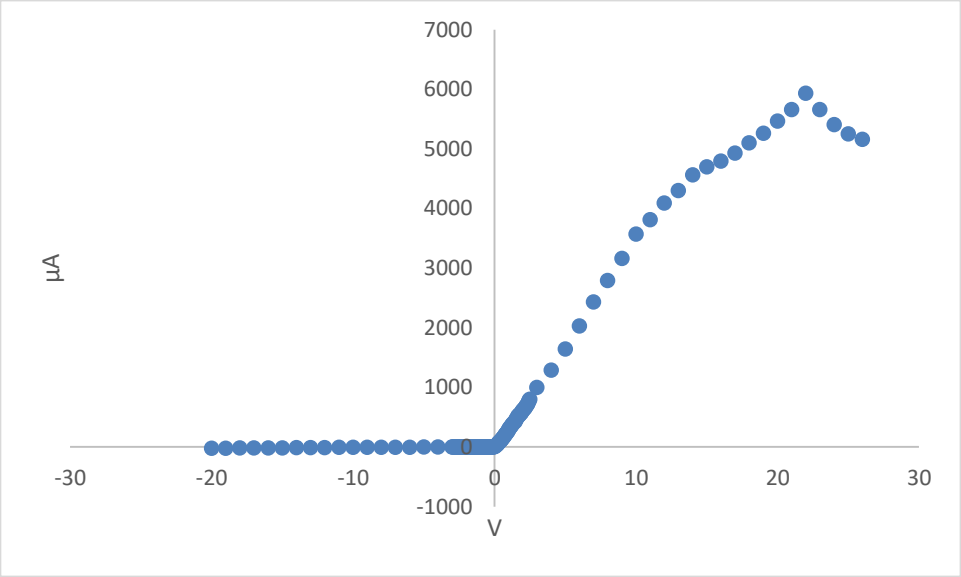

Figure 4.98 - I-V graph for V_2O_5/EDOT with Al contact

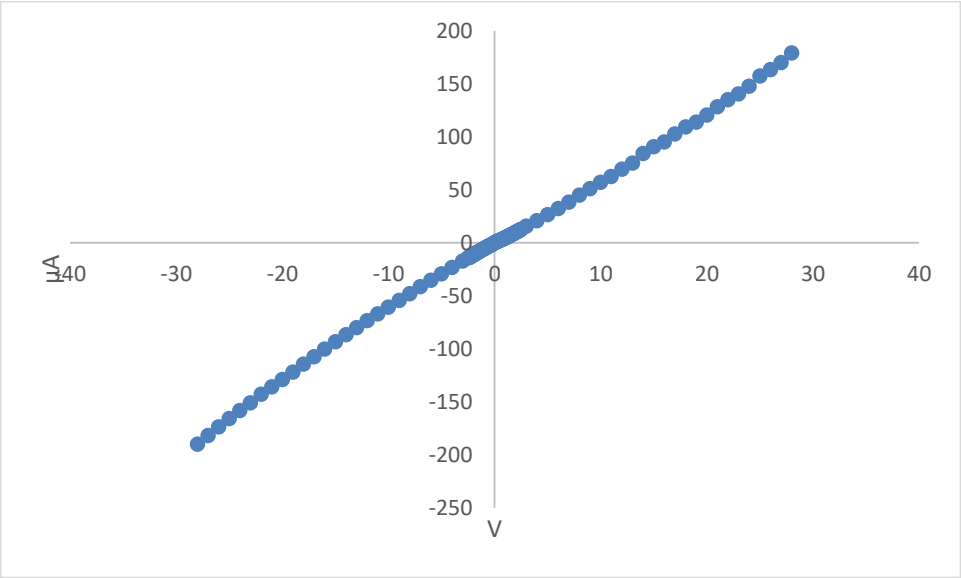

Figure 4.99 - I-V graph for V_2O_5/EDOT with Cu contact

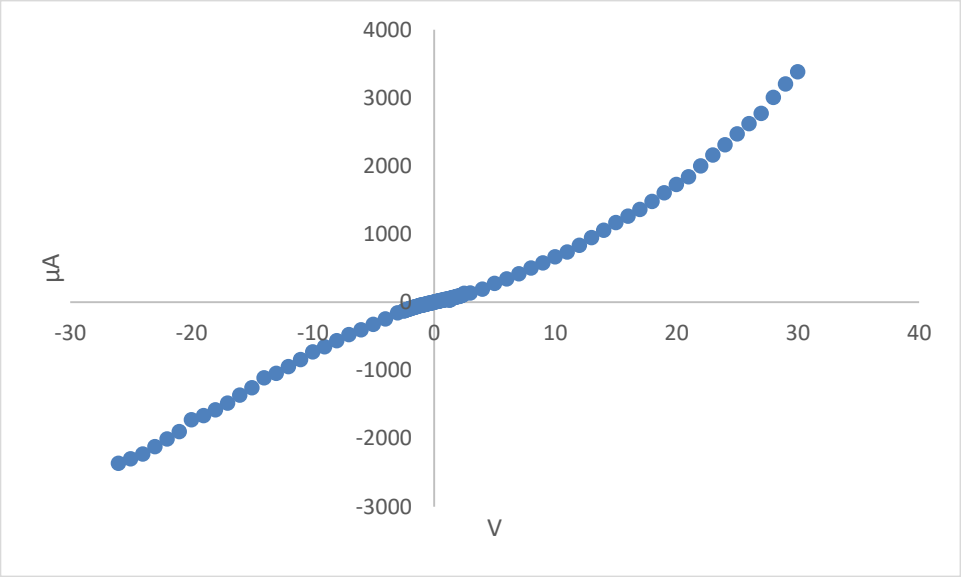

Figure 4.100 - I-V graph for V_2O_5/EDOT with Sn contact

Figure 4.97 to Figure 4.100 show the I-V graphs for the V_2O_5/EDOT composite material. With a Cu contact (Figure 4.99), the I-V graph was shown to exhibit ohmic behaviour while with an Al contact (Figure 4.98) the material exhibited rectifying behaviour. Meanwhile, the Zn (Figure 4.97) and Sn (Figure 4.100) contacts showed the most rectifying behaviour with rectification ratios of 1.1 and 1.43 respectively.

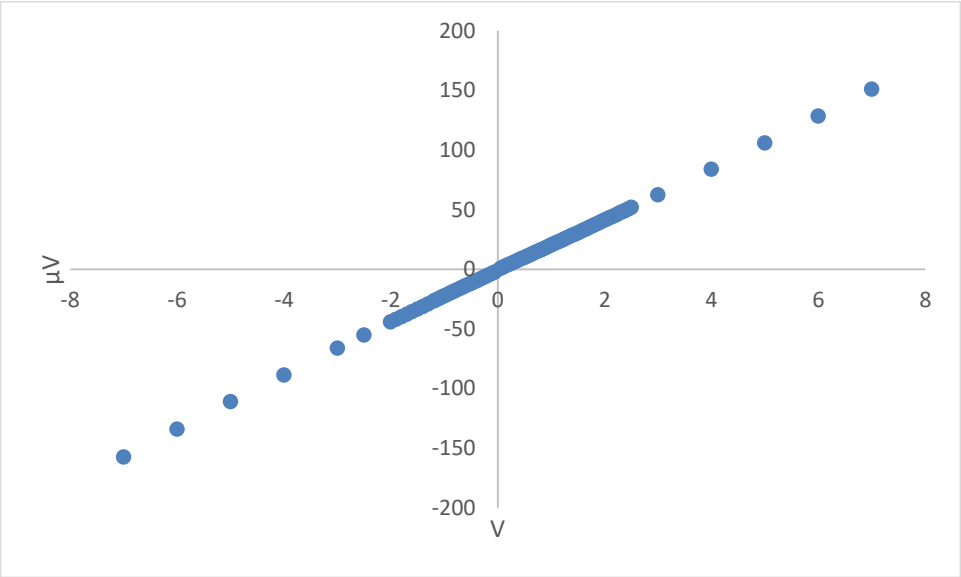

Figure 4.101 - I-V graph for V_2O_5/PDA with Zn contact

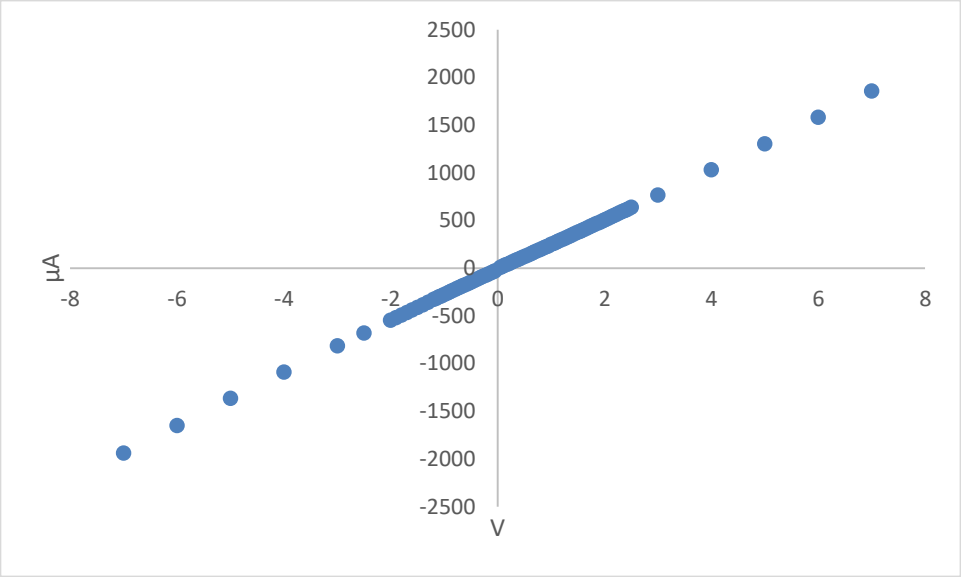

Figure 4.102 - I-V graph for V_2O_5/PDA with Al contact

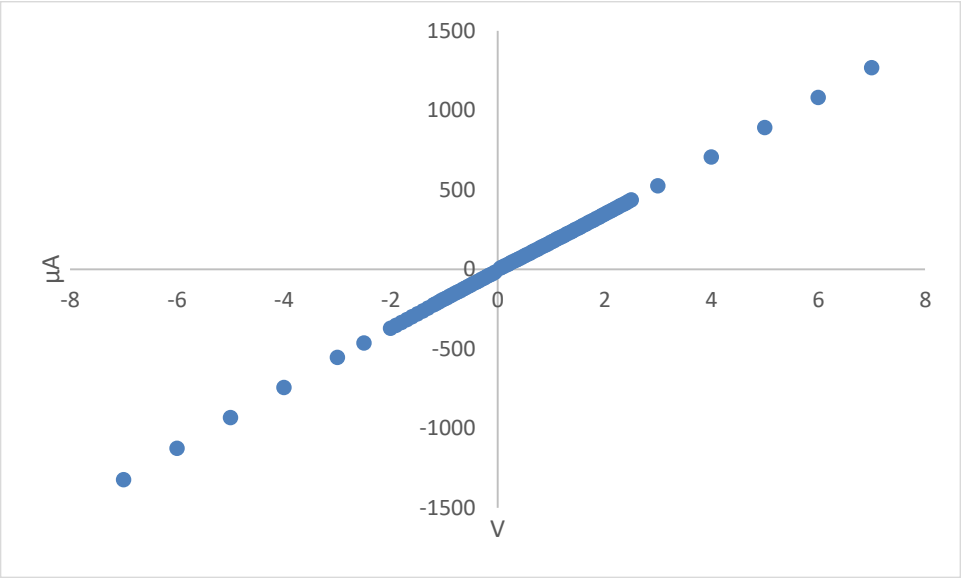

Figure 4.103 - I-V graph for V_2O_5/PDA with Cu contact

Figure 4.101 to Figure 4.103 shows the I-V graphs for V_2O_5/PDA and all three cases exhibit ohmic properties, unlike those for the previous diodes.

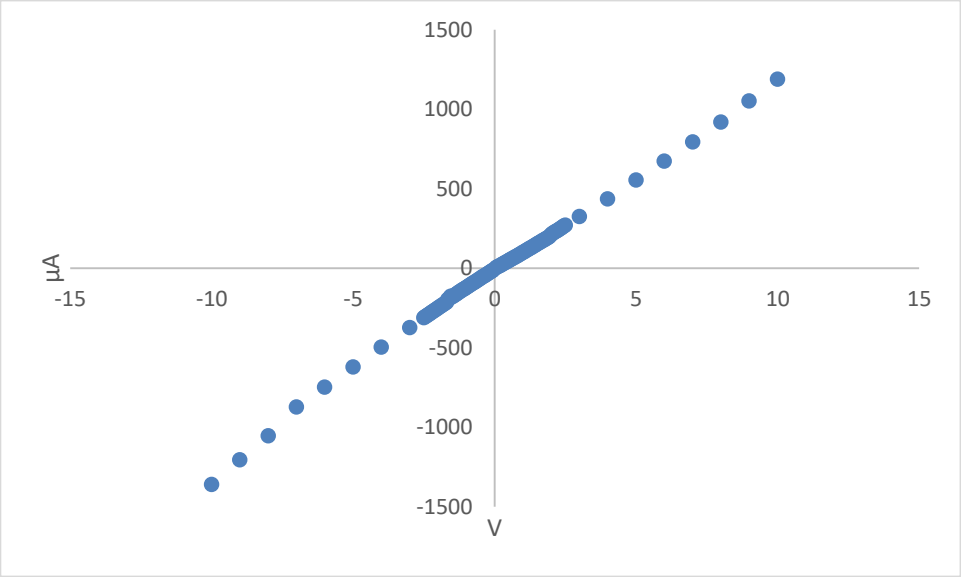

Figure 4.104 - I-V graph for V_2O_5/Li2A5PhPyr with Zn contact

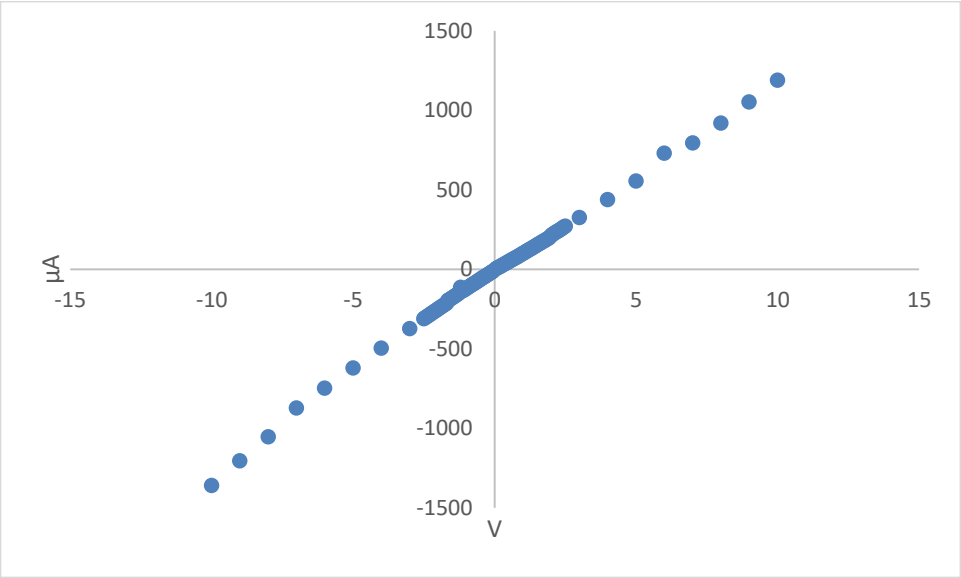

Figure 4.105 - I-V graph for V_2O_5/Li2A5PhPyr with Al contact

From Figure 4.104 it can be seen that LiV_2O_5/2A5PhPyr also exhibits close to ohmic behaviour, as observed for the V_2O_5/PDA composite material. However, with the Al contact in Figure 4.105, the material appears to have a slight rectifying behaviour and (as will be discussed) also provides informative capacitance measurements.

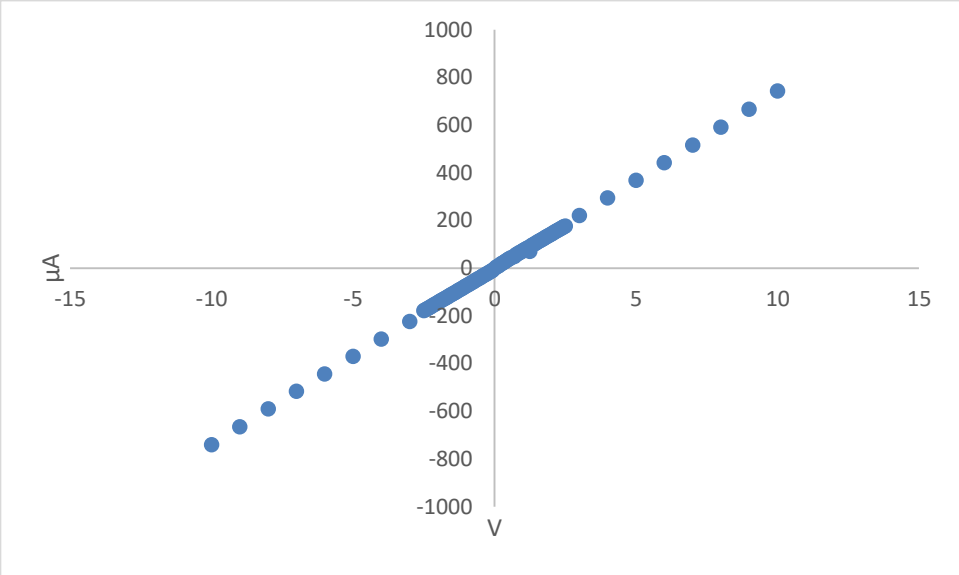

Figure 4.106 - I-V graph for V_2O_5/5AQ with Zn contact

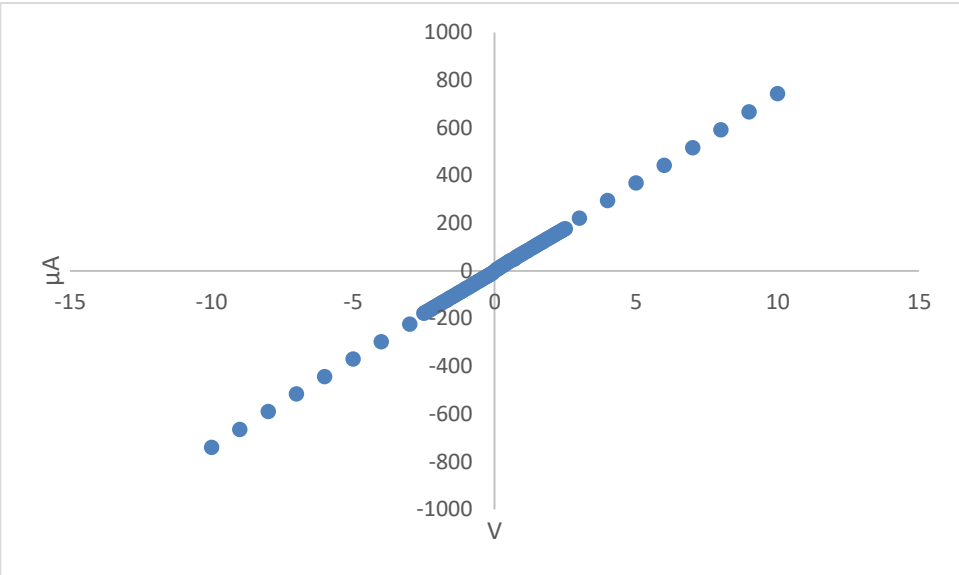

Figure 4.107 - I-V graph for V2O5/5AQ with Al contact

In Figure 4.106 and Figure 4.107, we can see that V_2O_5/5AQ exhibits ohmic characteristics with both Zn and Al contacts.

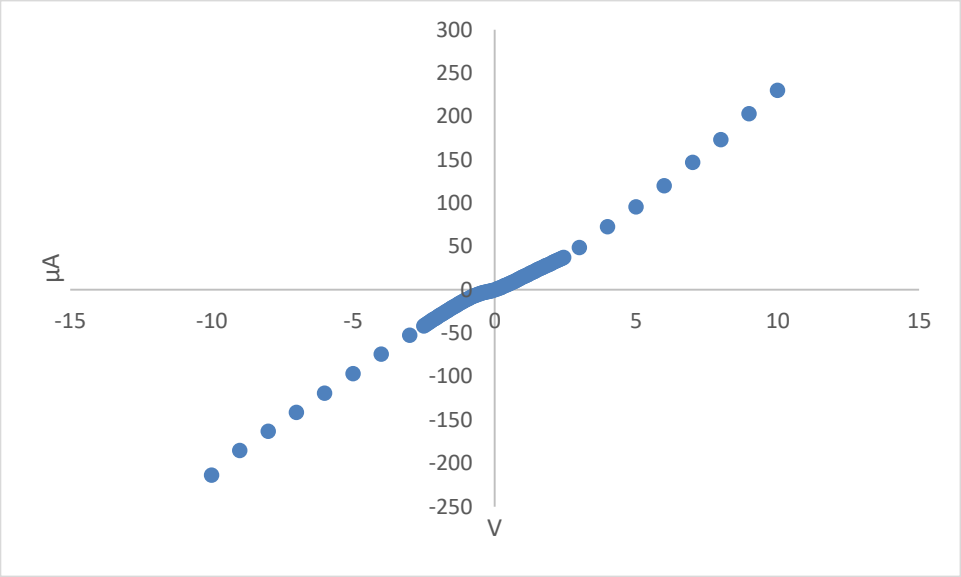

Figure 4.108 - I-V graph for V_2O_5/1,4PDA-HQ with Zn contact

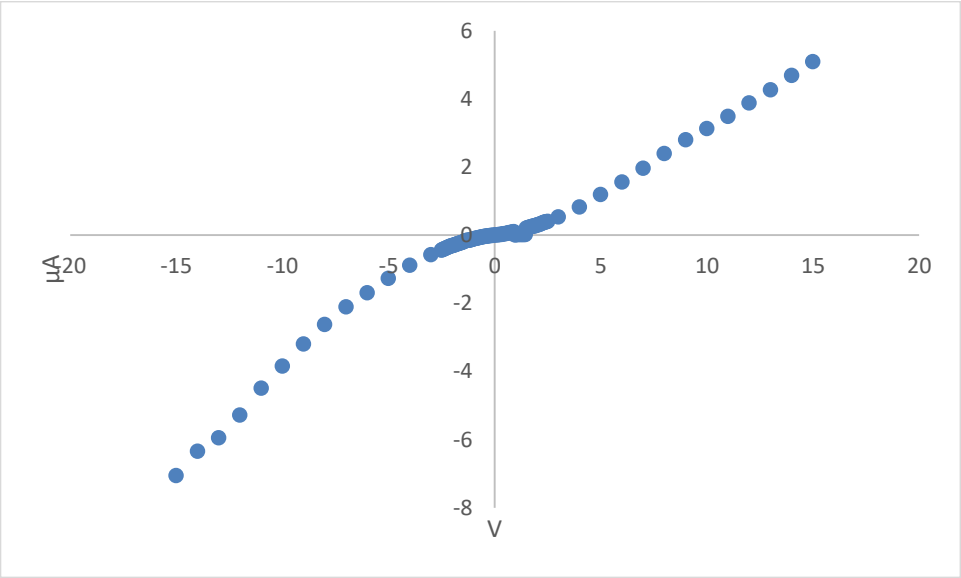

Figure 4.109 - I-V graph for V_2O_5/1,4PDA-HQ with Al contact

Figure 4.108 and Figure 4.109 show the I-V graphs for V_2O_5/1,4PDA-HQ composite material devices. In Figure 4.108 it is clear that the diode device exhibits non-linear properties under a forward and reverse bias. However, in Figure 4.109, the forward bias appears to show non-linear behaviour below 4 V and becomes linear >4 V. Under reverse bias, appears to reach its breakdown voltage at -2.5 V.

The I-V curves can be further modelled using a modified version of the ideal diode equation which will henceforth be called the non-ideal diode equation (Equation 4.1);

$$I = I_0\left(e^{\frac{qV-IR_s}{nkT}} - 1\right)$$

Equation 4.1

where:

- I is the net current measured through the diode.
- I_0 is the dark saturation current of the diode.
- q is the absolute value of the electron charge.
- V is the applied voltage across the diode.
- k is the Boltzmann constant.
- T is the temperature (in Kelvin)
- n is the ideality factor (which is usually between 1 and 2).
- R_s is the series resistance estimated from the gradient of the linear most part of the I-V plot.

Similarly, Equation 4.1 can be rearranged to give:

$$V = \frac{1}{q}[\mathrm{nkTln}\left(\frac{I}{I_0} - 1\right) + IR_s]$$

Equation 4.2

When Equation 4.2 is fitted (using Graphpad) against a V vs I plot of the I-V curve, n and I_0 can be extracted from the model. In general, n is 1 for indirect gap semiconductors and 2 for direct gap semiconductors.

Thus, once I_0 has been determined, one can calculate the Schottky barrier height (Φ) for the diode junction using Equation 4.3:

$$I_0 = AA^*T^2 e^{\frac{-\Phi}{kT}}$$

Equation 4.3

where:

- I_0 is the dark saturation current of the diode.
- A is the diode junction area.
- A^* is the Richardson's constant (1.20173 x 10^6 $Am^{-2}K^{-2}$)
- k is the Boltzmann constant.
- T is the temperature (in Kelvin)
- Φ is the diode junction barrier height.

Furthermore, rearranging Equation 4.3 yields the following expression for calculating Φ:

$$\Phi = -\ln\left(\frac{I_0}{AA^*T^2}\right)kT$$

Equation 4.4

The calculated values of I_0 and n are reported in Table 4.14 and Φ in Figure 4.110;

Table 4.14 - I_0 and n values for the non-ohmic Schottky devices

Zn Contact	**I_0 (μA)**	**n**
V_2O_5/EDOT	18.61	1.53
V_2O_5/AnAn$^+$	85.76	1.14
V_2O_5/2A5PhPyr	0.186	0.82
Al Contact	**I_0 (μA)**	**n**
V_2O_5/EDOT	157.75	1.49
V_2O_5/AnAn$^+$	16.55	1.52
V_2O_5/2A5PhPyr	5.64	1.47
V_2O_5/AmThia	1.84	1.34
Cu Contact	**I_0 (μA)**	**n**
V_2O_5/EDOT	2.43	1.47
V_2O_5/AnAn$^+$	0.3	1.49
Sn Contact	**I_0 (μA)**	**n**
V_2O_5/EDOT	17.49	1.27
V_2O_5/AnAn$^+$	35.9	1.51
$FePS_3$ Contact	**I_0 (μA)**	**n**
V_2O_5/AnAn$^+$	0.0175	0.81

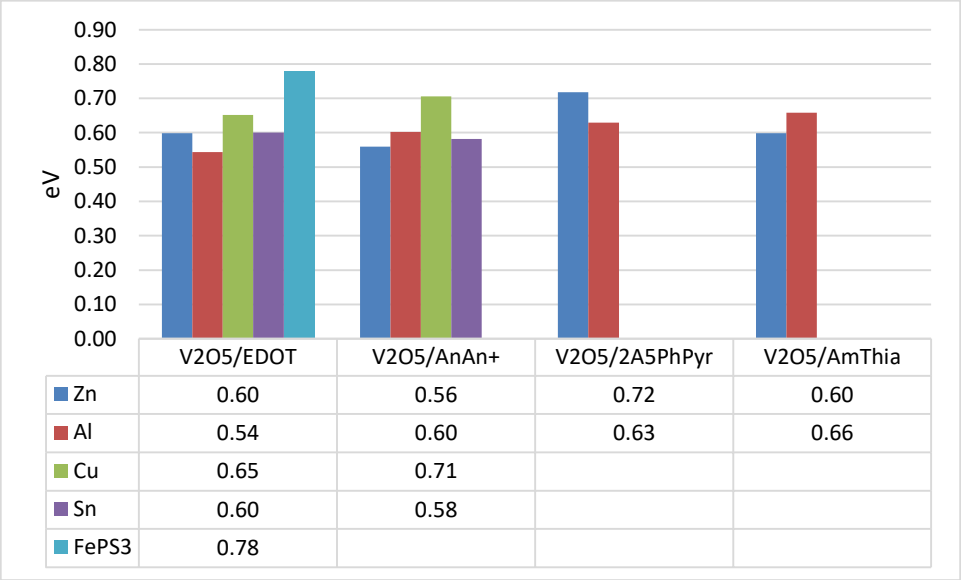

Figure 4.110 - Calculated barrier heights, Φ, for the non-ohmic Schottky diode junctions

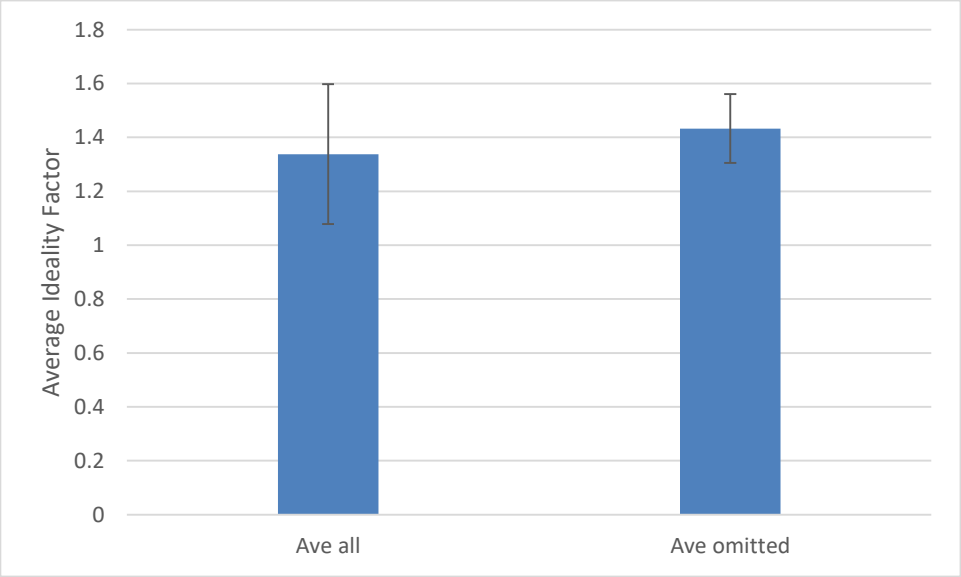

Figure 4.111 - Average ideality factor, n, for all V_2O_5 Schottky devices (Ave all) and for devices omitting n<1 (Ave omitted)

From Table 4.14 it is observed that utilising the non-ideal diode equation, calculating n yields an average value of 1.34 when including the two devices which showed a slight deviation with n<1 (V_2O_5/2A5PhPyr with a Zn contact and V_2O_5/AnAn$^+$ with a $FePS_3$ contact). As there are only two cases of devices with n<1 these n values could be considered as outliers and are either due to a modelling error or a problem in the construction of the device. Upon omitting the n value for n<1 the average value is 1.43 (Figure 4.111) with a maximum value of 1.53 (V_2O_5/EDOT and V_2O_5/AmThia devices with an Al contact) and a minimum of 1.14 (V_2O_5/AnAn$^+$ device with an Al contact). The ideality factor indicates likely asymmetry between electronic bands for excitation and/or recombination. This band asymmetry for the general case was previously shown in Figure 4.8. This would suggest that for the V_2O_5 devices (including those with values of n<1) the organic and inorganic components exhibit poor band overlap in the composite materials, as was concluded from the optical spectroscopy data for the V_2O_5 materials (Table 4.5). The average Φ was shown to be 0.63eV, with the lowest being 0.54eV (V_2O_5/EDOT with an Al contact) and the highest being that for V_2O_5/AnAn$^+$ with $FePS_3$ (0.78eV).

The calculated dielectric constants (ε_r) shown in Table 4.15 were used in the calculation for the dopant densities. Due to the limited amounts of material available to

make sufficiently stable pellets, an average ε_r was used in the calculation of the dopant densities for the non-ohmic Schottky devices where ε_r could not be calculated.

Table 4.15 - Dielectric constants for composite materials

Material	ε_r
V_2O_5/AnAn$^+$	13.47
V_2O_5/EDOT	10.52
MoO_3/PDA	5.52
Average	9.836

Starting with Equation 4.5:

$$\frac{d(\frac{1}{C^2})}{dV} = \frac{2}{\varepsilon_r \varepsilon_0 A^2 e N_d}$$

Equation 4.5

where:

- ε_r is the dielectric constant of the composite material.
- ε_0 is the vacuum permittivity (8.854 x 10^{-12} Fm^{-1}).
- A is the depletion region area (m^2).
- *e* is the electron charge (C).
- N_d is the dopant density (m^{-3}).
- C is the capacitance (F^{-2}).
- V is the voltage (Volts).

Equation 4.5 can be rearranged to yield an expression for N_d shown in Equation 4.6:

$$N_d = \frac{2}{\varepsilon_r \varepsilon_0 A^2 e \frac{d(\frac{1}{C^2})}{dV}}$$

Equation 4.6

Table 4.16 shows a comparison of the dopant densities calculated from the capacitance-voltage measurements (see Appendix A.6) between the pressed pellet Schottky devices and the evaporated contact Schottky devices (those with non-ohmic properties).

Table 4.16 - Dopant density comparison between the pressed Schottky devices and the evaporated metal contacts Schottky devices

Dopant Densities (N_d) (m^{-3})			
Material	**Pressed**	**Evap**	**Ratio**
Al Contact			
$AlV_2O_5/AnAn^+$	2.62E+14	1.58E+14	1.656
AlV_2O_5/EDOT	1.68E+15	1.77E+15	0.947
AlV_2O_5/2A5PhPyr	1.79E+13	1.01E+13	1.776
Cu Contact			
$CuV_2O_5/AnAn^+$	1.37E+14	1.42E+14	0.967
CuV_2O_5/EDOT	4.5E+14	3.57E+14	1.259

Figure 4.112 and Figure 4.113 graphically represent the data shown in Table 4.16. It can be seen that N_d values for the evaporated metal contacts and the pressed contacts are within the same order of magnitude with a small overall difference. The material with the largest dopant density was shown to be V_2O_5/EDOT, while the smallest dopant density belonged to V_2O_5/2A5PhPyr.

The Schottky devices made using Cu and Al contacts showed an average N_d of 3.86 x 10^{14} m^{-3}. On closer inspection V_2O_5/2A5PhPyr with an Al contact displayed the lowest N_d of 5.12 x 10^{11} m^{-3} followed by V_2O_5/AmThia also with an Al contact (N_d of 5.12 x 10^{12} m^{-3}). The devices with the highest N_d using both Cu and Al contacts were those for $V_2O_5/AnAn^+$ and V_2O_5/EDOT. This could be due to $AnAn^+$ and EDOT being the most conductive guest species in the V_2O_5 interlayer space and being intercalated via a direct redox reaction with the host. These two materials were also pressed onto Cu and Sn contacts to make device structures that both exhibited N_d in the order of 10^{14} m^{-3} (comparable with the overall N_d average). Therefore it is suggested that the dopant density

is not affected by the method of polymer insertion into V_2O_5 as both direct and ion-exchange methods cause reduction of V^{5+} (as seen from the XPS data in Section 4.1.1). Therefore it appears that the N_d is proportional to the concentration of reduced V^{5+} sites. However, it must be noted that within the three materials synthesised via direct intercalation, $AnAn^+$ and EDOT showed a significantly larger N_d than that for 2A5PhPyr which was synthesised via acid-base mechanism. Therefore it can be proposed that redox intercalation produces the highest concentration of the reduced V^{4+} centres which may contribute to the larger N_d exhibited.

Table 4.17 - Dopant densities for all Schottky device contacts

Contact	Dopant Density (m^{-3})
Zn	
$V_2O_5/AnAn^+$	3.32E+14
V_2O_5/2A5PhPyr	2.76E+14
V_2O_5/EDOT	3.63E+14
Al	
$V_2O_5/AnAn^+$	2.62E+14
V_2O_5/2A5PhPyr	5.12E+11
V_2O_5/EDOT	1.68E+15
Cu	
$V_2O_5/AnAn^+$	1.37E+14
V_2O_5/EDOT	4.50E+14
Sn	
$V_2O_5/AnAn^+$	6.68E+14
V_2O_5/EDOT	3.28E+14
$FePS_3$	
$V_2O_5/AnAn^+$	1.30E+14

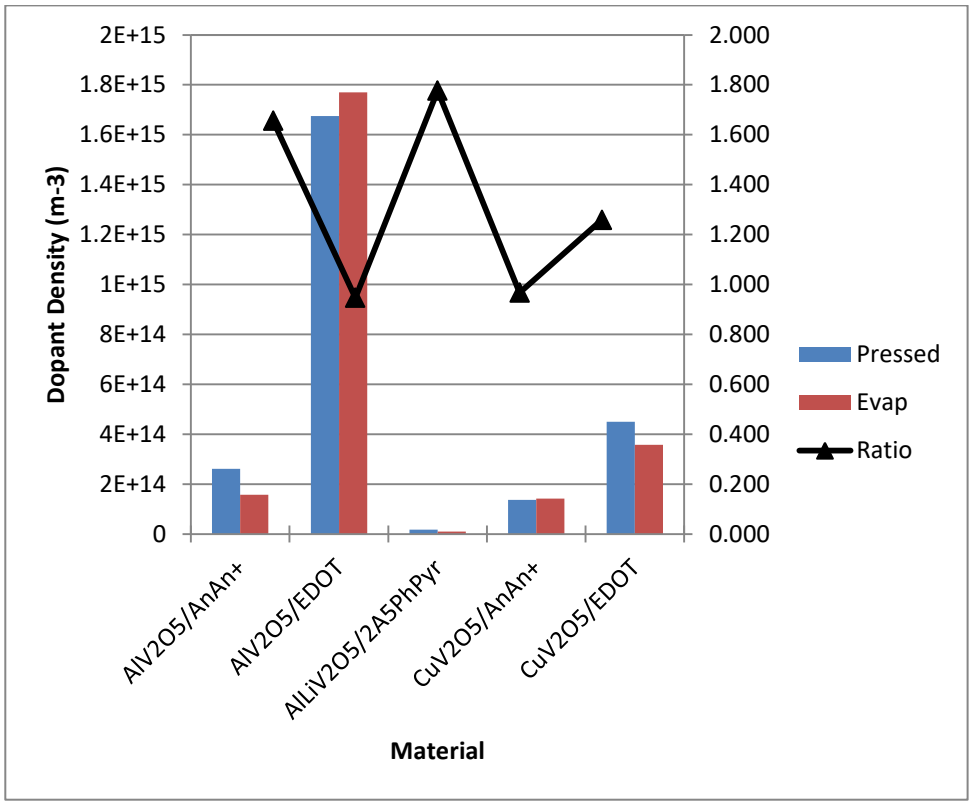

Figure 4.112 - Comparison of dopant densities between the pressed pellet devices and the evaporated pellet devices

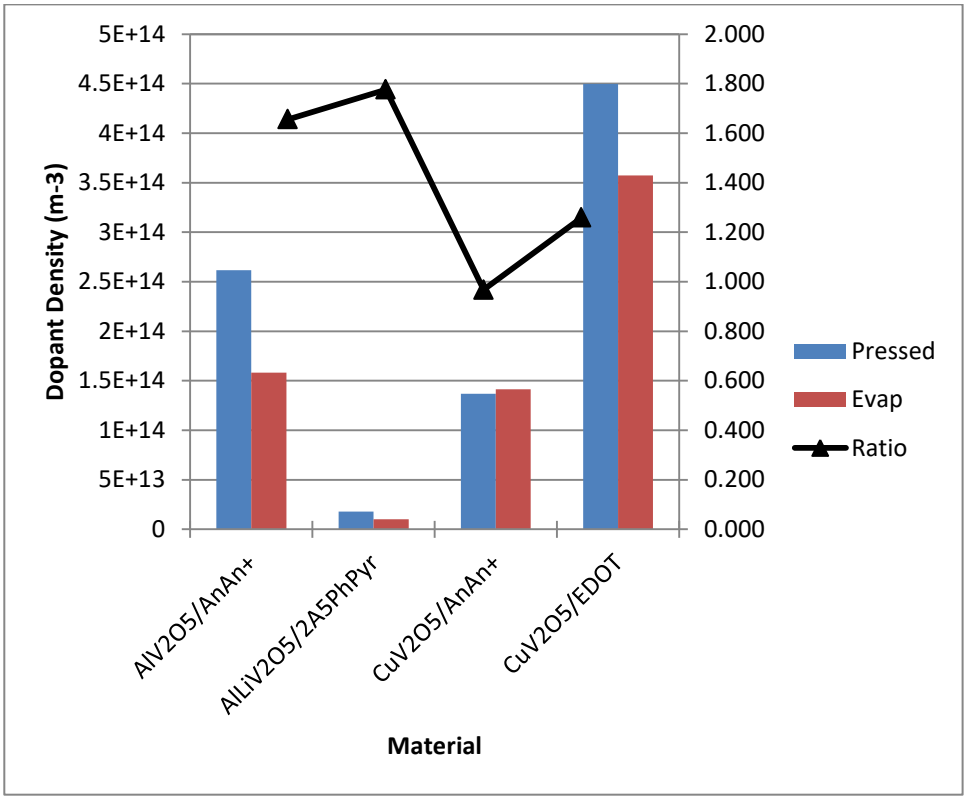

Figure 4.113 - Comparison of dopant densities for the pressed pellet devices and the evaporated pellet devices (omitting AlV_2O_5/EDOT)

4.2.1.4) Photosensitive devices

The prototype photosensitive devices were made by spin-coating the photoactive composite material onto n-type silicon and an ITO counter electrode. The most conductive materials, with the highest dopant density, were evaluated for their optoelectronic properties. These materials were V_2O_5/AnAn$^+$, V_2O_5/2A5PhPyr, V_2O_5/EDOT as well as V_2O_5/AnAn$^+$ which had been cast onto $FePS_3$. The devices were illuminated under ambient light (A.Light) and also under an incandescent lamp (Lamp).

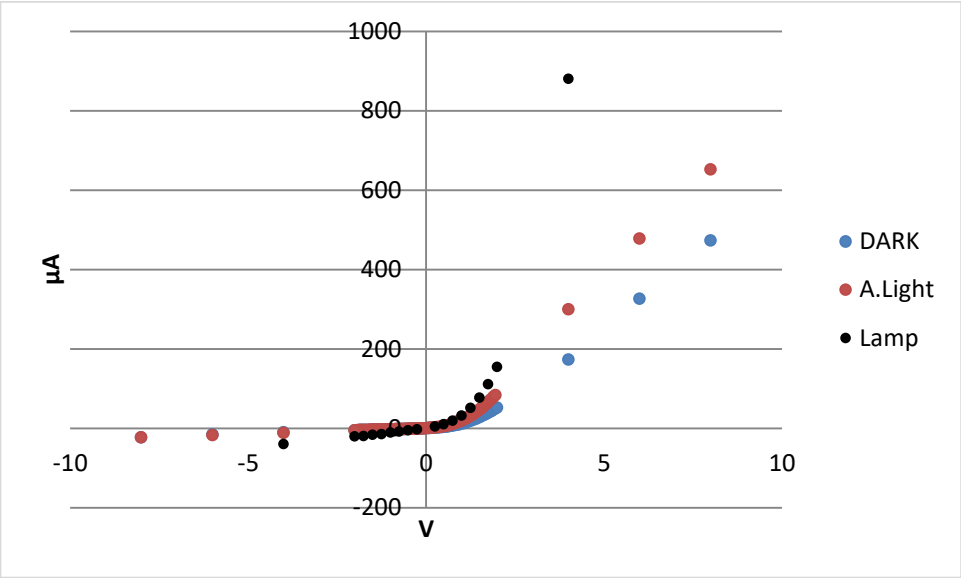

Figure 4.114 - I-V graph for V_2O_5/AnAn$^+$ photovoltaic device under dark, A.Light and Lamp illumination

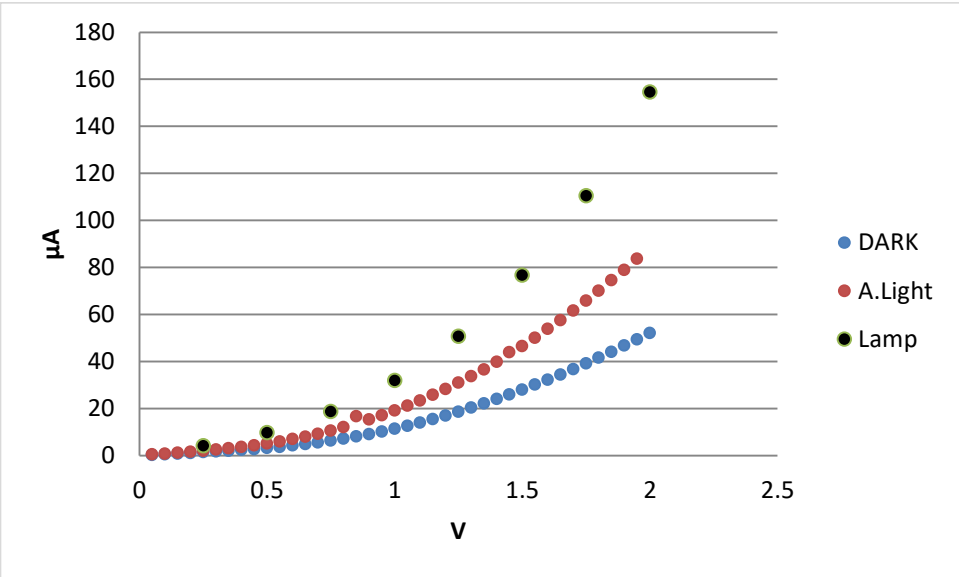

Figure 4.115 - ExpandedI-V graph for V_2O_5/AnAn$^+$ photovoltaic device under dark, A.Light and Lamp illumination between 0-2V

Figure 4.114 and Figure 4.115 show the changes in the I-V graph for the device using V_2O_5/AnAn$^+$ as the photoactive material. It is noticeable that in dark conditions the I-V graph for the device exhibits rectifying properties. When illuminated under A.Light there is little change under reverse bias. However, under forward bias, there is a noticeable increase in the current. A significant change in the rectifying behaviour is observed when the device is illuminated under Lamp conditions, with a significant increase in the forward current compared to that for illumination under A.Light.

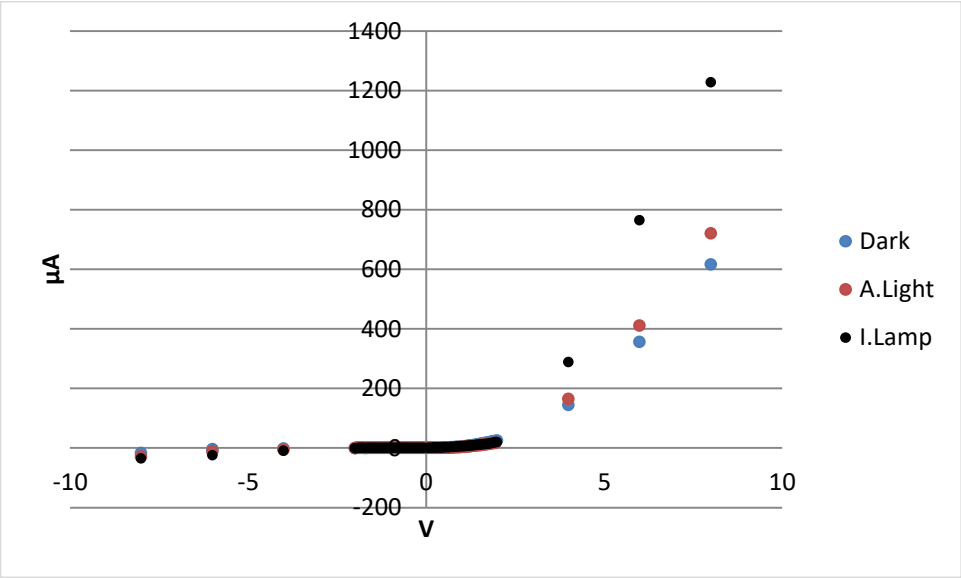

Figure 4.116 - I-V graph for V_2O_5/EDOT photovoltaic device under dark, A.Light and Lamp illumination

The increase in current when illuminated is also seen when the V_2O_5/EDOT material is used as the active material (Figure 4.116), and rectifying behaviour is again observed. Interestingly there appears to be little or no change under either A.Light or Lamp conditions up to 2V. After this, the current increases under illuminated conditions.

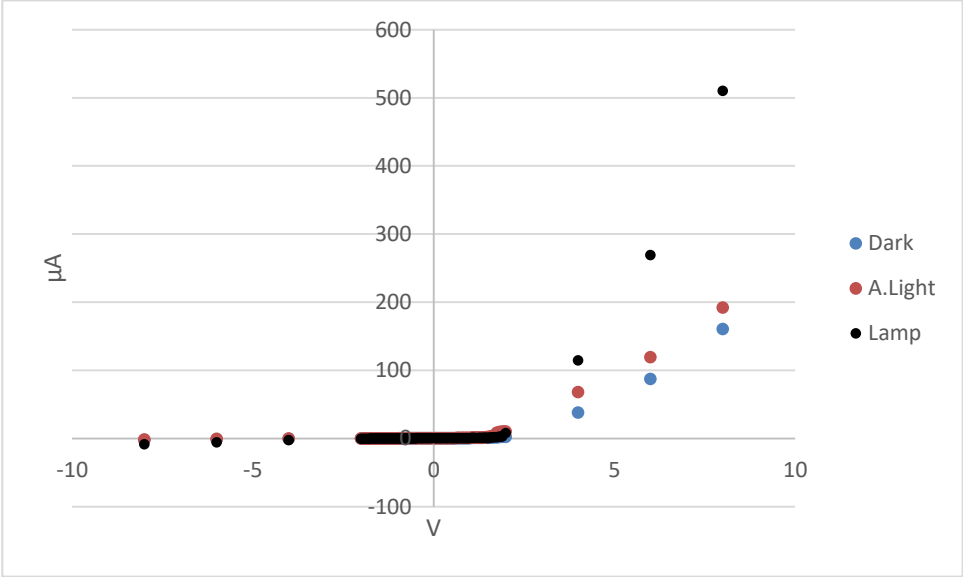

Figure 4.117 - I-V graph for V_2O_5/2A5PhPyr photovoltaic device under dark, A.Light and Lamp illumination

Figure 4.117 shows the same trend for V_2O_5/2A5PhPyr. The I-V graph for the material once again exhibits rectifying behaviour and at low voltages and there appears to be no significant change under positive bias up until 2V. At this point, a trend similar to that seen in Figure 4.116 is exhibited where under A.Light illumination there is a small increase in the current showing some photoconductive properties; however, under Lamp conditions we again see a much larger increase in the current.

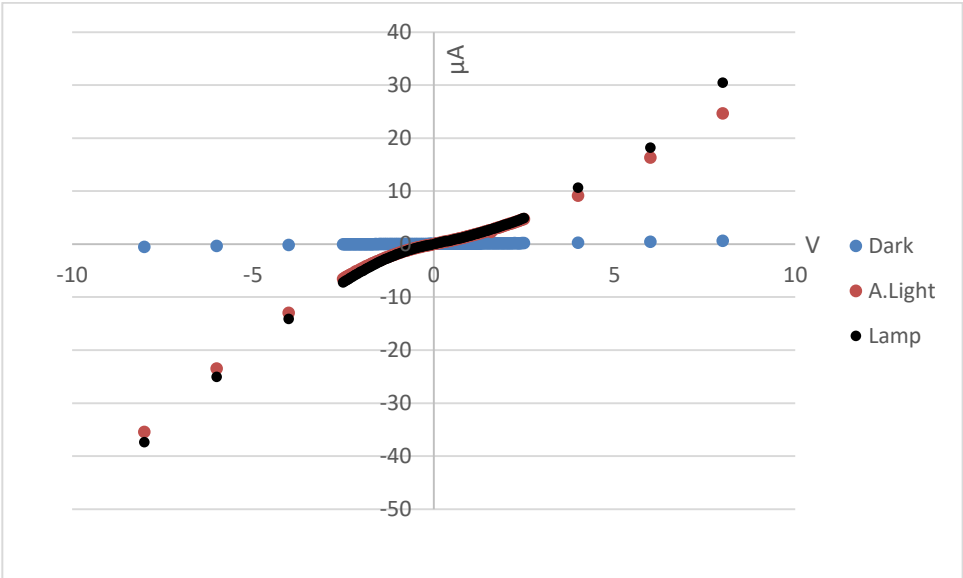

Figure 4.118 - I-V graph for $FePS_3$ V_2O_5/$AnAn^+$ photovoltaic device under Dark, A.Light and Lamp conditions

The I-V curve for $V_2O_5/AnAn^+$ cast onto $FePS_3$ (a p-type semiconductor) follows a similar trend, shown in Figure 4.118. However, in this case, it can be seen that there is little or no current under Dark conditions and there is a significant increase in the current when under both A.Light and Lamp conditions. Under illumination, there also appears to be a non-linear nature to the I-V curve.

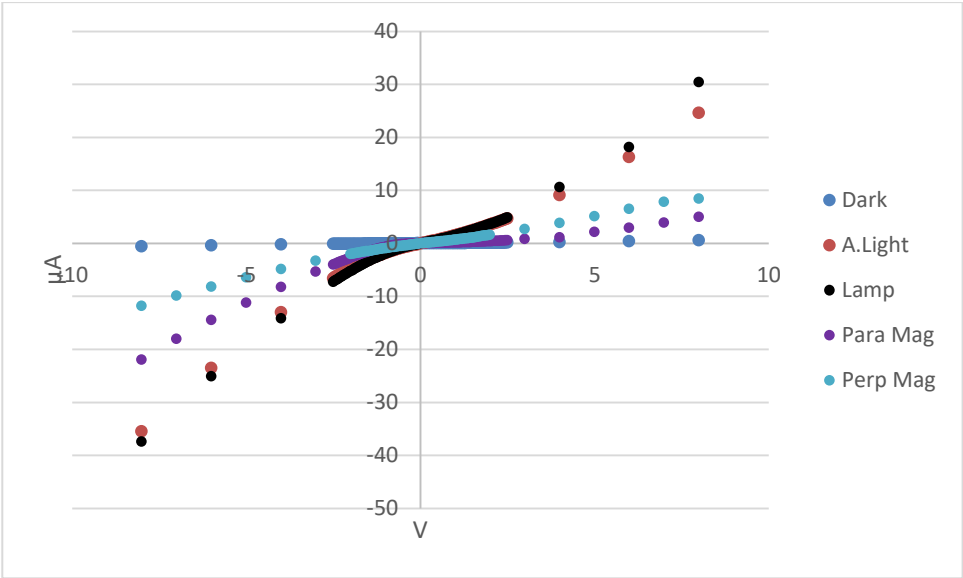

Figure 4.119 - I-V graph for $FePS_3$ $V_2O_5/AnAn^+$ device under Dark, A.Light and Lamp conditions and applied parallel (Para Mag) and perpendicular magnetic (Perp Mag) fields.

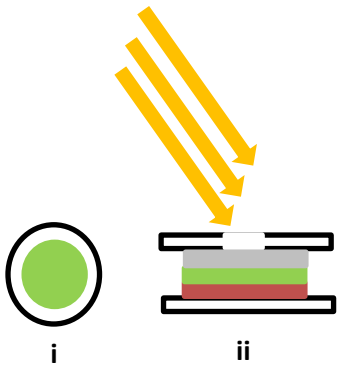

Figure 3.5 – i) Top view of the $V_2O_5/AnAn^+$ $FePS_3$ device in the plastic encasing, ii) side view of the $V_2O_5/AnAn^+$ $FePS_3$ device architecture shows the copper electrode (red) composite material (green), the transparent ITO electrode (grey) and the plastic encasing (white).

Figure 3.6 – i) The parallel set up of the device and magnetic (Para Mag) and ii) the perpendicular set up of the device and magnetic (Perp Mag)

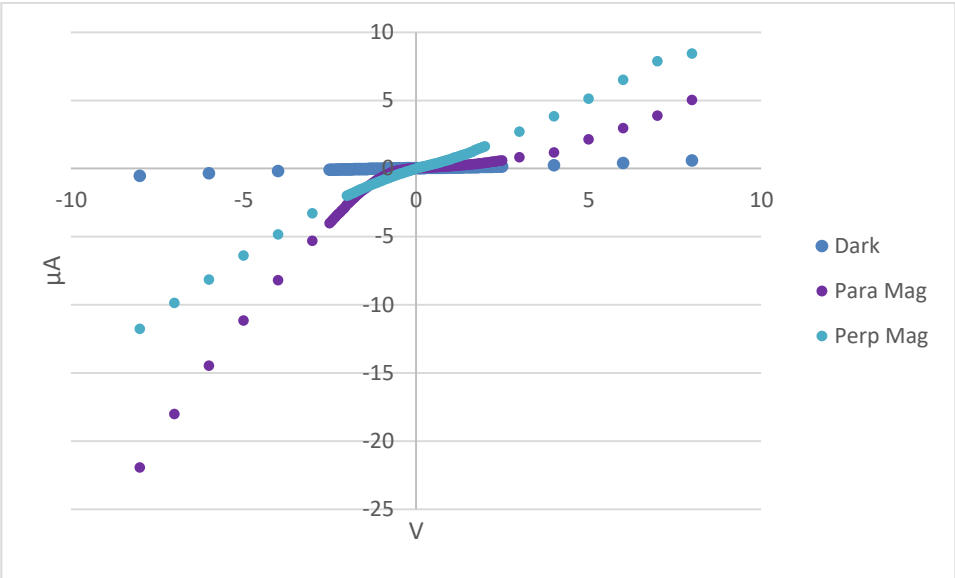

Figure 4.120 - I-V graph for $FePS_3$ V_2O_5/$AnAn^+$ device under Dark, applied parallel (Para Mag) and perpendicular Magnetic (Perp Mag) fields

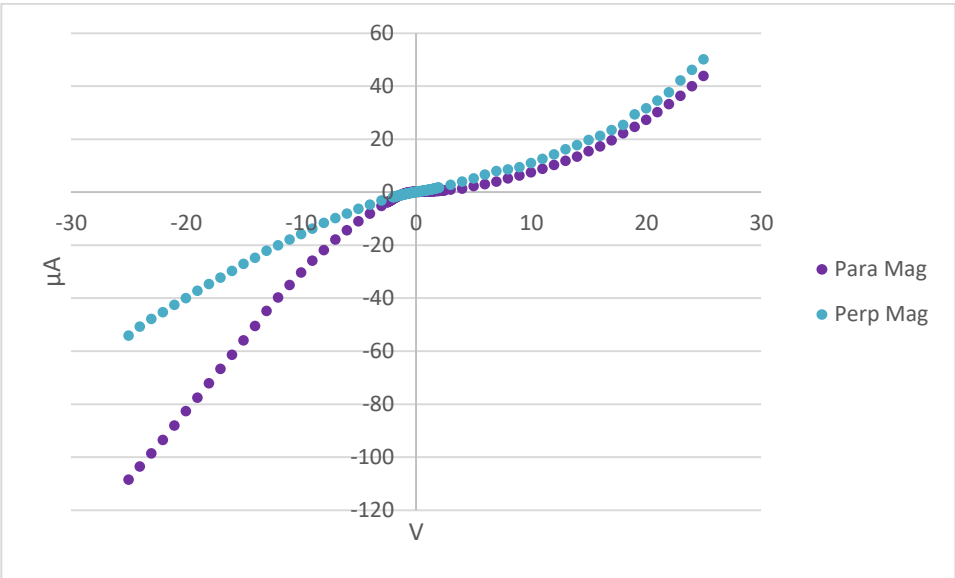

Figure 4.121 - I-V graph for $FePS_3$ V_2O_5/$AnAn^+$ photovoltaic device under applied parallel (Para Mag) and perpendicular magnetic (Perp Mag) fields

Interestingly, Figure 4.119 - Figure 4.121 show the effects of placing the device under dark conditions in a magnetic field (see Figure 3.5 and Figure 3.6) for device structure and magnet orientation. Within a small voltage range, placing the device parallel or perpendicular to the magnetic field results in an increase in current, though not quite as much as when the device is illuminated. Here it is possible that the presence of the magnetic field assists in charge separation after the creation of electron-hole pairs which, placed under a bias, could lead to the increase in current observed. Furthermore, when the material is placed under Para Mag conditions, the device appears to exhibit a greater rectification than when placed under Perp Mag conditions. Over a much larger voltage range, we can see that the Perp Mag configuration consistently exhibits a larger current than that for the Para Mag conditions. Para Mag configuration continues to exhibit a larger rectification ratio, however. Perp Mag is shown to exhibit non-ohmic properties under higher voltages.

Table 4.18 - Table 4.22 show the change in photocurrent current (ΔI) caused by illumination under forward bias.

Table 4.18 - ΔI for Silicon V_2O_5/AnAn$^+$ photosensitive device between A.light - Dark and Lamp - Dark conditions

V_2O_5/AnAn$^+$								
Voltage (V)	**0.25**	**0.5**	**0.75**	**1**	**1.25**	**1.5**	**1.75**	**4**
ΔI (μA) A.Light - Dark	0.661	1.948	4.216	7.79	12.354	18.45	26.57	126
ΔI (μA) Lamp - Dark	2.722	6.574	12.35	20.51	32.044	48.64	71.26	706.5

Table 4.19 - ΔI for Silicon V_2O_5/EDOT photosensitive device between A.Light - Dark and Lamp - Dark conditions

V_2O_5/EDOT				
Voltage (V)	**1**	**4**	**6**	**8**
ΔI (μA) A.Light - Dark	1.917	20.39	54.1	104.6
ΔI (μA) Lamp - Dark	0.575	144.22	407.9	611.6

Table 4.20 - ΔI for Silicon V_2O_5/2A5PhPyr photosensitive device between A.Light - Dark and Lamp - Dark conditions

V_2O_5/2A5PhPyr				
Voltage (V)	**2**	**4**	**6**	**8**
ΔI (μA) A.Light - Dark	7.781	29.85	31.77	31.2
ΔI (μA) Lamp - Dark	5.551	76.6	181.81	349.56

Table 4.21 - ΔI for $FePS_3$ V_2O_5/$AnAn^+$ photosensitive device between A.Light - Dark and Lamp - Dark conditions

V_2O_5/$AnAn^+$								
Voltage (V)	**0.05**	**0.5**	**1**	**1.5**	**2**	**4**	**6**	**8**
ΔI (μA) A.Light - Dark	0.04255	0.6334	1.4371	2.373	3.412	8.854	15.91	21.04
ΔI (μA) Lamp - Dark	0.0033	0.653	1.487	2.456	3.524	10.38	17.74	29.85

Table 4.22 - ΔI for $FePS_3$/$AnAn^+$ photosensitive device under magnetic conditions

V_2O_5/$AnAn^+$								
Voltage (V)	**0.1**	**0.5**	**1**	**1.5**	**2**	**4**	**6**	**8**
ΔI (μA) Perp Mag - Dark	0.04452	0.2798	0.6214	1.015	1.500	3.601	6.105	7.845
ΔI (μA) Para Mag - Dark	0.005191	0.04526	0.1028	0.1849	0.2967	0.9357	2.555	4.431

Voltage (V)	**0.1**	**0.5**	**1**	**1.5**	**2**	**4**	**6**	**8**
ΔI (μA) Para Mag – Perp Mag	0.03961	0.2345	0.5186	0.8298	1.203	2.666	3.55	3.414

From Table 4.18 - Table 4.22 the power generated when the device is illuminated (P_{out}, as a function of voltage) can be calculated by multiplying ΔI by the voltage. Figure 4.122 shows the power vs voltage plot for V_2O_5/$AnAn^+$ (see Appendix A.7 for full power vs voltage plots).

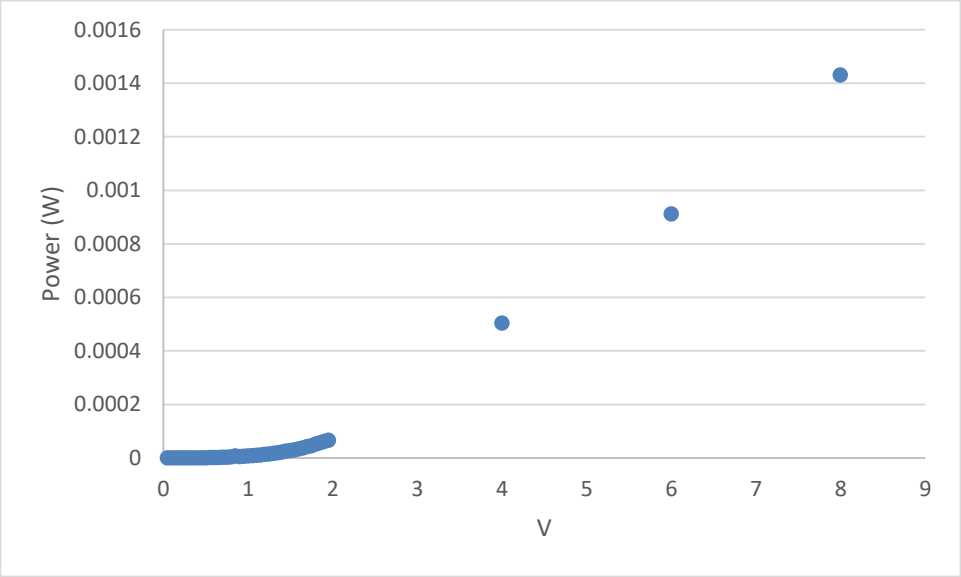

Figure 4.122 - The power vs voltage plot for V_2O_5/AnAn$^+$ Si device under A.Light illumination

From the P_{out} vs V plots, a device efficiency (Eff) at the maximum P_{out} observed can be determined. For all devices, the maximum P_{out} was observed at the maximum voltage applied to the device. The Eff was calculated using Equation 4.7:

$$Eff\ (\%) = \frac{P_{out}}{P_{in}} \times 100$$

Equation 4.7

where P_{in} is the total power being input into the device from the illuminating radiation. P_{in} was calculated by converting the average measured lux value of the illumination source to Power (W) using Equation 4.8:

$$P_{in} = \frac{Lux\ \times\ A}{\eta}$$

Equation 4.8

where:

- Lux is the measured illuminance (lm/m^2)
- A is the surface area of the photosensitive device
- η is the luminous efficacy (lm/w)

The intensities in Lux for A.Light and Lamp illumination conditions were measured to be 3540 lm/m^2 and 5982 lm/m^2 respectively. The Si and $FePS_3$ device surface areas for the large Si device, small Si device and for the $FePS_3$ device were 4.418 x 10^{-3} m^2, 1.257 x 10^{-3} m^2 and 6.23 x 10^{-4} m^2 respectively. The average η for A.Light and Lamp was taken to be 105 lm/m^2 (281) and 16 lm/m^2 (282) respectively. Table 4.23 shows the calculated P_{in} for each device surface area.

Table 4.23 – Calculated P_{in} for the three device surface areas

Large Si Device Surface Area	
Illumination	**P_{in} (W)**
A.Light P(W)	0.15
Lamp P(W)	1.65

Small Si Device Surface Area	
Illumination	**P_{in} (W)**
A.Light P(W)	0.042
Lamp P(W)	0.47

FePS3 Device Surface Area	
Illumination	**P_{in} (W)**
A.Light P(W)	0.021
Lamp P(W)	0.24

Using the results obtained in Table 4.23 and applying Equation 4.7, Table 4.24 and Figure 4.123 show the calculated maximum efficiencies. It must be noted that these are the efficiencies observed at the maximum voltage and may not represent the practical Eff value of the device in question which is expected to be lower than this value.

Table 4.24 – Calculated device Eff (%) for the Si and $FePS_3$ photosensitive devices

	Large Si Device		Small Si Device	$FePS_3$ device
Material	**V_2O_5/AnAn$^+$**	**V_2O_5/EDOT**	**V_2O_5/2A5PhPyr**	**V_2O_5/AnAn$^+$**
A.Light Illumination				
Max Power Volt	8	8	8	8
Max Power (W)	1.430E-03	8.368E-04	2.496E-04	1.923E-04
Eff (%)	0.96	0.56	0.59	0.92
Lamp Illumination				
Max Power Volt	4	8	8	8
Max Power (W)	2.826E-03	4.893E-03	2.796E-03	2.388E-04
Eff (%)	0.17	0.30	0.59	0.10

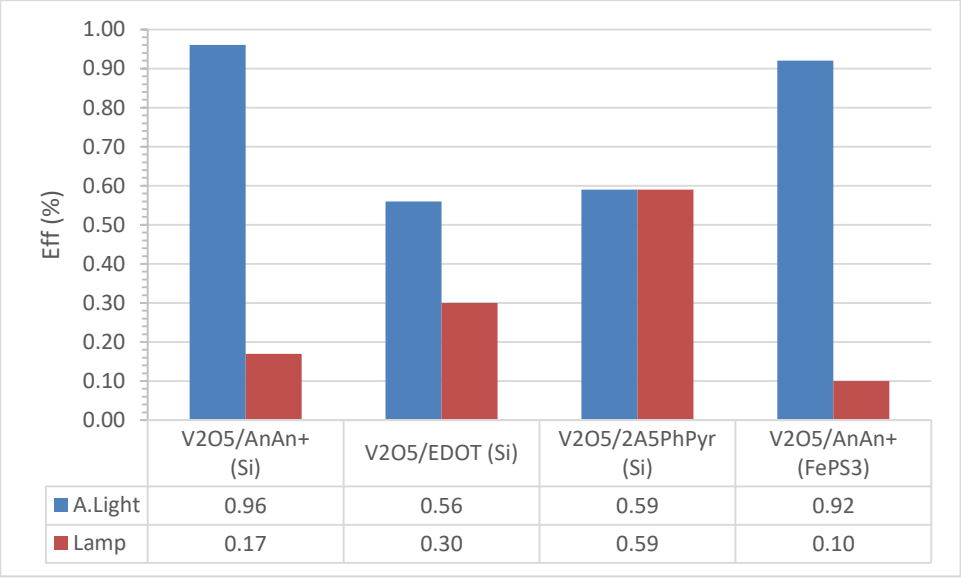

Figure 4.123 – Calculated device Eff (%) for the Si and $FePS_3$ photosensitive devices (the device type is stated in the parentheses)

A general trend is noticeable where the devices exhibit a greater Eff under A.Light illumination than for the Lamp illuminated conditions. This is consistent with the absorption edges and optical band-gaps determined in Section 4.1.1 where the absorption edges for the V_2O_5 composites were observed to occur within the range of 350nm to 390nm which would lie within the near UV to the blue region of the electromagnetic spectrum. The maximum solar spectral irradiance at the Earth's surface is between 350 nm to 600 nm (centred at ~500 nm) (281) whereas the spectrum of Lamp peaks at ~800 nm, with most of its emission occurring in the near infra-red and infra-red region (283).

Therefore it is likely that the formation of charge carriers from photon absorption is occurring from the absorption of light in the blue and near UV regions of the spectrum resulting in the difference in Eff between that seen under A.Light and Lamp illuminated conditions. A notable exception is that for V_2O_5/2A5PhPyr Si device (where the active material is coated onto the smaller device surface area), the material displays similar device Eff under both A.Light and Lamp conditions. The $V_2O_5/AnAn^+$ exhibited the highest Eff in both the Si and the $FePS_3$ device when illuminated under A.Light. Of the three active materials ($V_2O_5/AnAn^+$, V_2O_5/EDOT and V_2O_5/2A5PhPyr) it appears that $V_2O_5/AnAn^+$ is the most efficient material under all conditions. Considering the non-optimised nature device architecture and construction, it is assumed here that there is a uniform film of the active materials of which all are in intimate contact with the Si or $FePS_3$ substrate. It may be that the $V_2O_5/AnAn^+$ films produce the most intimate contact and therefore exhibit higher device Eff. It is also possible, though less likely, that $V_2O_5/AnAn^+$ may absorb a wider wavelength range and therefore allow for a greater generation of charge carriers.

Further analysis of the device ΔI vs V plots can provide information regarding the photoconductivity and charge carrier mobility (CCM) of these devices. The ΔI vs V plots were modelled with a second-order polynomial (Equation 4.9) and an exponential function (Equation 4.10) of the form of:

$$y = Ax^2 + Bx + C$$

Equation 4.9

where the parameters A, B, and C are constants and;

$$y = Ae^{kx}$$

Equation 4.10

where the parameters A and k are constants.

ΔI vs V plots showing a better fit to Equation 4.9 are favoured over Equation 4.10 as an exponential increase in the ΔI with increasing voltage may be caused by charge carriers not produced as a result of photon absorption. It is possible that any charge carriers which are generated when the device is under Dark conditions may become trapped, due to a layer-based defect in the inorganic such as step or screw defects or example. These trapped charge carriers would not be able to recombine at any interfaces and may also not be able to travel through the material (between active material particles) leading to either Shockley-Read-Hall, trap-assisted recombination or surface recombination (which are possible in organic-inorganic systems) (284). Upon illumination, these trapped charge carriers may become free and therefore contribute to the ΔI observed (however small or large that may be) but this contributed current is, in principle, not the primary photocurrent.

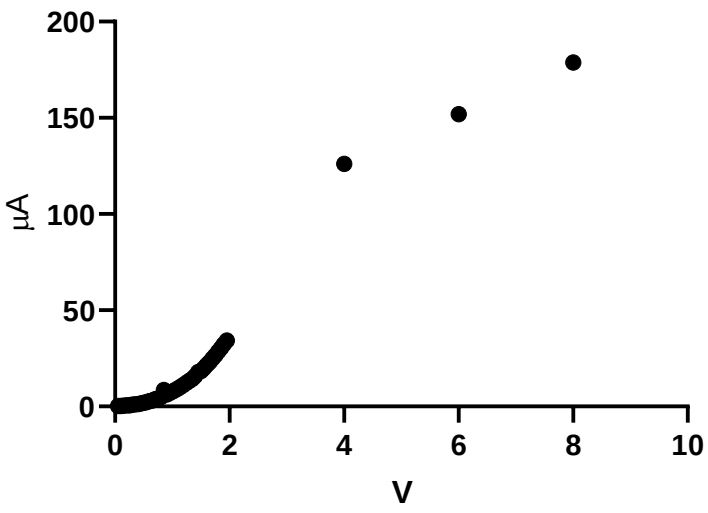

Figure 4.124 – Full ΔI vs V plot for V_2O_5/AnAn$^+$ Si Device under A.Light illumination

In Figure 4.124 we can see two distinct regions for V_2O_5/AnAn$^+$ Si device, the first being 0 V to 4 V where there appears to be a non-linear relationship between ΔI and V. The second region appears between 4 V to 8 V exhibiting a linear relationship between ΔI and V. This

is assumed to be due to the device resistance limiting the current (ohmic region). The modelling was therefore restricted to the first region.

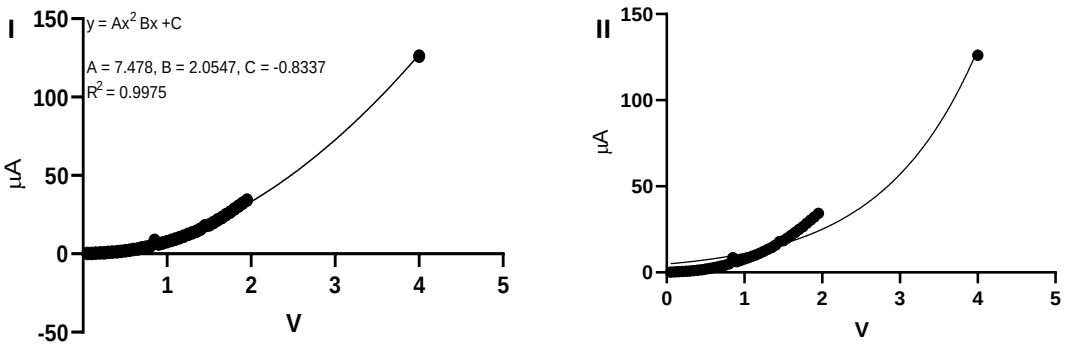

Figure 4.125 – ΔI vs V plot for V_2O_5/AnAn$^+$ Si Device under A.Light illumination between 0V to 4V where I) shows the second-order polynomial fit II) shows the attempted fit for an exponential curve

Figure 4.125.I and .II shows the ΔI for the device illuminated under A.Light; the best fit occurs for the second-order polynomial function (R^2 = 0.9975) in Figure 4.125.I whereas it becomes difficult to obtain a good fit for a purely exponential function (Figure 4.125.II).

For the device illuminated under Lamp, the full range of 0 V to 4 V was used.

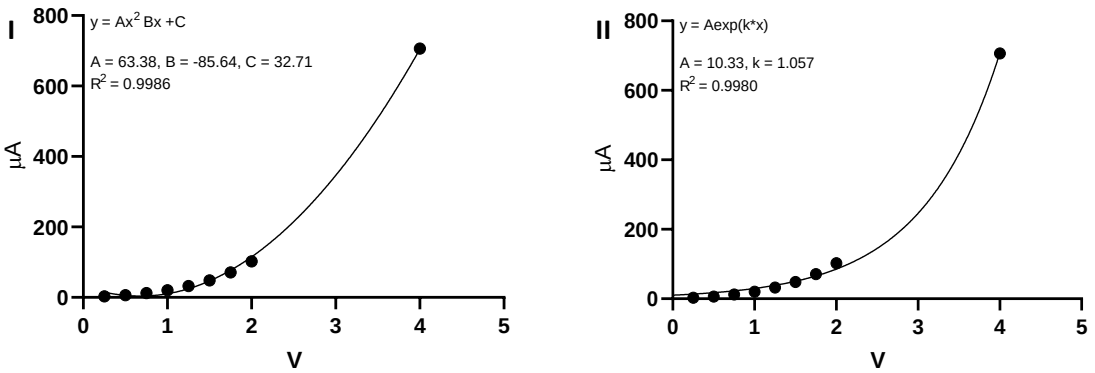

Figure 4.126 - ΔI vs V plot for V_2O_5/AnAn$^+$ Si Device under Lamp illumination between 0V to 4V where I) shows the second-order polynomial fit II) shows the fit for an exponential curve

Figure 4.126.I and .II shows ΔI for the V_2O_5/AnAn$^+$ Si device under Lamp illumination for both polynomial and exponential functions. Unlike Figure 4.125, both functions show an

excellent fit to the data (R^2 values of 0.9986 and 0.9980 respectively) with the polynomial function exhibiting a better fit.

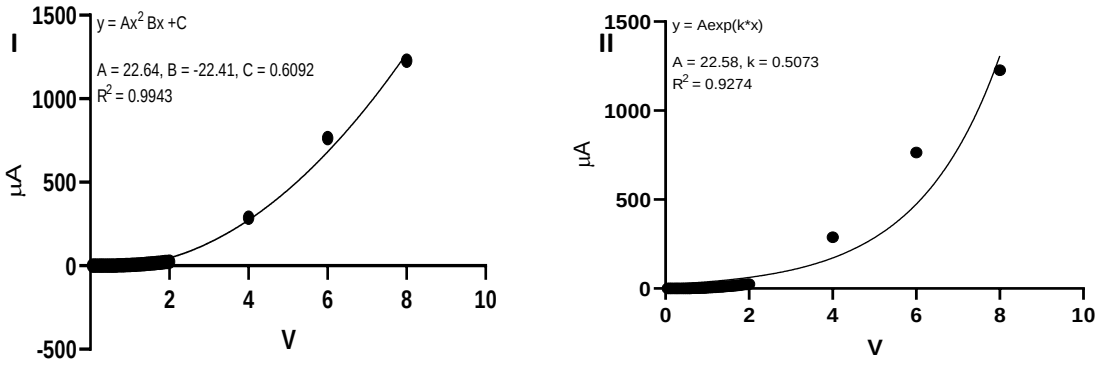

Figure 4.127 – ΔI vs V plot for V_2O_5/EDOT Si Device under A.Light illumination where I) shows the second-order polynomial fit II) shows the fit for an exponential curve

Figure 4.127.I and .II shows ΔI for the V_2O_5/EDOT Si device under A.Light illumination and the second-order polynomial shows the best fit to the data (R^2 = 0.9943) whereas the exponential function is less well fitted (R^2 = 0.9274).

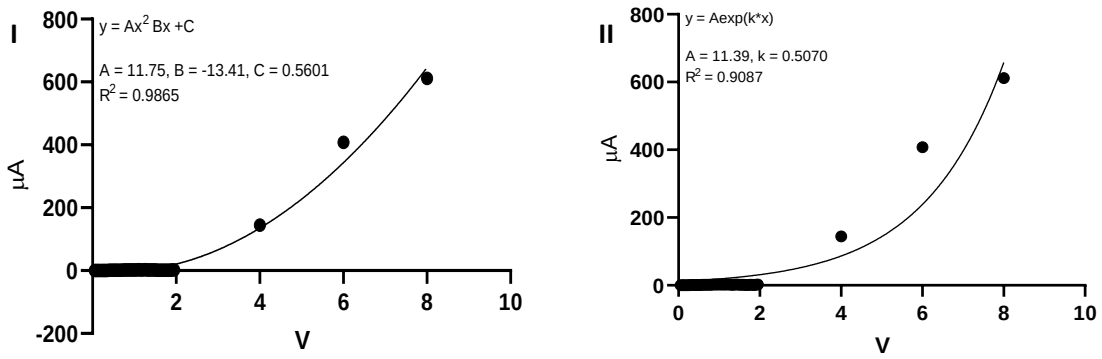

Figure 4.128 - ΔI vs V plot for V_2O_5/EDOT Si Device under Lamp illumination where I) shows the second-order polynomial fit II) shows the fit for an exponential curve

Figure 4.128.I and .II shows ΔI for the V_2O_5/EDOT Si device under Lamp illumination, where the best fit is that for the polynomial (R^2 = 0.9865), while the exponential fit has R^2 = 0.9087.

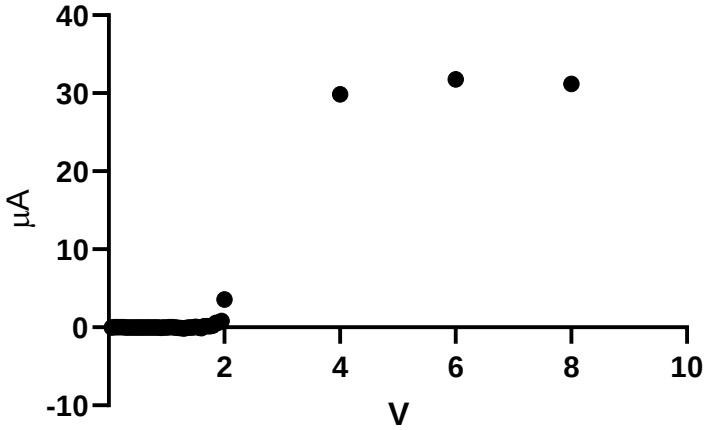

Figure 4.129 - Full range for V_2O_5/2A5PhPyr for the ΔI for the device under A.Light illumination

As seen previously in Figure 4.124, Figure 4.129 shows the full range of ΔI for the V_2O_5/2A5PhPyr Si device under A.Light illumination where two distinct regions are present. The first region occurs between 0 V to 4 V where a nonlinear relation between ΔI and V exists. The second occurs between 4 V to 8 V and appears to show that ΔI exhibits little change with increased positive potential. For modelling, both the polynomial and exponential functions were fitted to the first region.

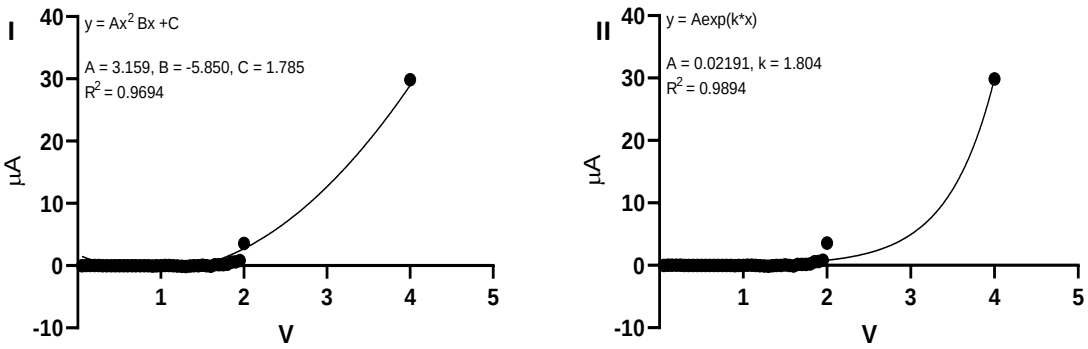

Figure 4.130 - ΔI vs V plot for V_2O_5/2A5PhPyr Si Device under A.Light illumination between 0V to 4V where I) shows the second-order polynomial fit II) shows the fit for an exponential curve.

Figure 4.130.I and .II shows the ΔI for the V_2O_5/2A5PhPyr Si device under A.Light illumination between 0 V to 4 V. The exponential function exhibits the best fit (R^2 = 0.9894) while that for the polynomial fit is R^2 = 0.9694.

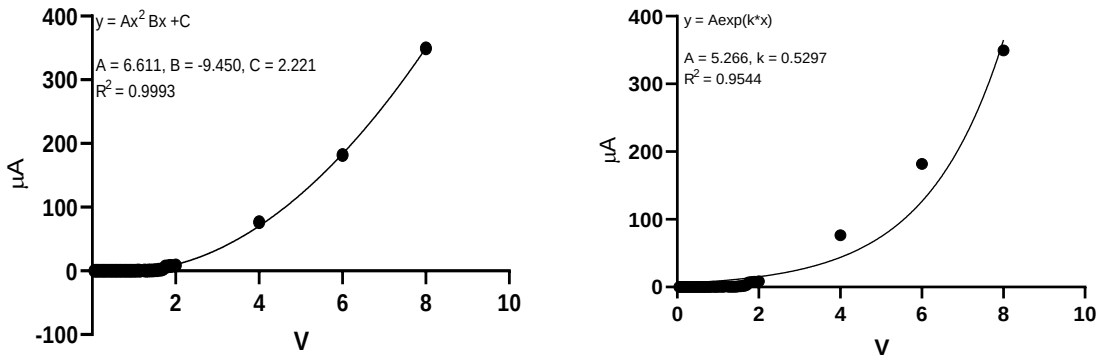

Figure 4.131 – ΔI vs V plot for V_2O_5/2A5PhPyr Si Device under Lamp illumination between 0V to 4V where I) shows the second-order polynomial fit II) shows the fit for an exponential curve.

Figure 4.131.I and .II shows the ΔI for the V_2O_5/2A5PhPyr Si device under Lamp illumination between 0 V to 4 V. Here the best fit is the polynomial (R^2 = 0.9993) with the exponential function exhibiting a poorer fit.

Overall, under A.Light illumination, the V_2O_5/AnAn$^+$ and V_2O_5/EDOT Si devices can be modelled well using a second-order polynomial fit whereas under Lamp conditions the V_2O_5/AnAn$^+$, V_2O_5/EDOT and V_2O_5/2A5PhPyr devices can be modelled well using the second-order polynomial. From the fitted second-order polynomials, an estimated photoconductivity can be calculated using Equation 4.11:

$$\Delta\sigma = \frac{dI}{dV}\left(\frac{L}{A}\right)$$

Equation 4.11

where:

- Δσ is the photoconductivity in Sm^{-1}
- dI/dV is the gradient at the linear most part of the ΔI vs V plot
- L is the device height
- A is the device surface area

Table 4.25 shows the estimated photoconductivities of the devices which were fitted well to the second-order polynomial. It is immediately obvious that the photosensitive devices exhibit low photoconductivities. However, it is shown that the photoconductivities under A.Light illumination are of 1 order of magnitude greater than that exhibited when the devices are under Lamp illumination.

Table 4.25 – Photoconductivities of the Si Devices modelled using the second-order polynomials where σ_{obvs} is the calculated photocurrent from the I – V plot of the respective material's photosensitive device.

Si Device		
Material	**Δσ (Sm^{-1})**	**$\Delta\sigma/\sigma_{obvs}$**
A.Light Illumination		
V_2O_5/AnAn$^+$	2.76E-11	0.43
V_2O_5/EDOT	1.45E-10	2.237
Lamp illumination		
V_2O_5/AnAn$^+$	8.01E-12	0.036
V_2O_5/EDOT	7.23E-11	0.50
V_2O_5/2A5PhPyr	1.20E-11	0.69

When comparing this with the Eff (%) in Table 4.24 and Figure 4.123 it is evident that the devices with a higher photoconductivity also exhibit a higher estimated maximum Eff. As the true Eff are expected to be lower than the estimated maxima, is it clear that in these un-optimised devices the highest photoconductivities and Eff will be exhibited under A.Light conditions. The major factor limiting the photoactivity of the active material and the overall device Eff may be the recombination of the excitons being produced. The active material film coated on the Si substrate is made up of individual particles of the composite material and not a continuous uniform film. Therefore the mobility of the charge carriers that are being conducted through the composite material to the electrodes is dependent on how efficiently these charge carriers are able to move between the composite particles. If the charge carrier mobility (CCM) is therefore poor in the material recombination could

occur. From the photoconductivity an estimated CCM can be calculated using Equation 4.12:

$$\Delta\sigma = \frac{dI}{dV}\left(\frac{L}{A}\right) = \mu(n+p).e$$

Equation 4.12

where:

- σ is the photoconductivity in Sm^{-1}
- dI/dV is the gradient at the most linear part of the ΔI vs V plot
- L is the device height (measured between the copper-substrate interface to the top of the ITO contact) (m)
- A is the device surface area (m^2)
- μ is the CCM ($m^2V^{-1}s^{-1}$)
- (n+p) is the total number of charge carriers created when the device is under illuminated conditions
- e is the electron charge value (C)

Equation 4.12 can be rearranged to provide an expression for determining the CCM:

$$\mu = \frac{\Delta\sigma}{(n+p).e}$$

Equation 4.13

(n+p) can be determined under two assumptions;

- all the composite materials form a uniform film and the entire surface area of the film is in intimate contact with the entire surface area of the substrate.

- All the photons are absorbed and produce an exciton (a single charge carrier) when the device is under illuminated conditions.

From these assumptions one can convert the P_{in} (Table 4.23) into the total number of photons by utilising the following equation;

$$(n + p) = \frac{P_{in} \times \lambda}{hc}$$

Equation 4.14

where:

- (n+p) is the total number of charge carriers created when the device is under illuminated conditions
- P_{in} is the absorbed power in watts (Table 4.23)
- λ is taken to be the wavelength at the maximum intensity of the illuminating light (for A.Light this is taken to be ~500 nm and for Lamp ~800 nm)
- h is the Planck constant
- c is the speed of light (ms^{-1})

Figure 4.132 shows the calculated estimated CCM's for the V_2O_5 composite material devices.

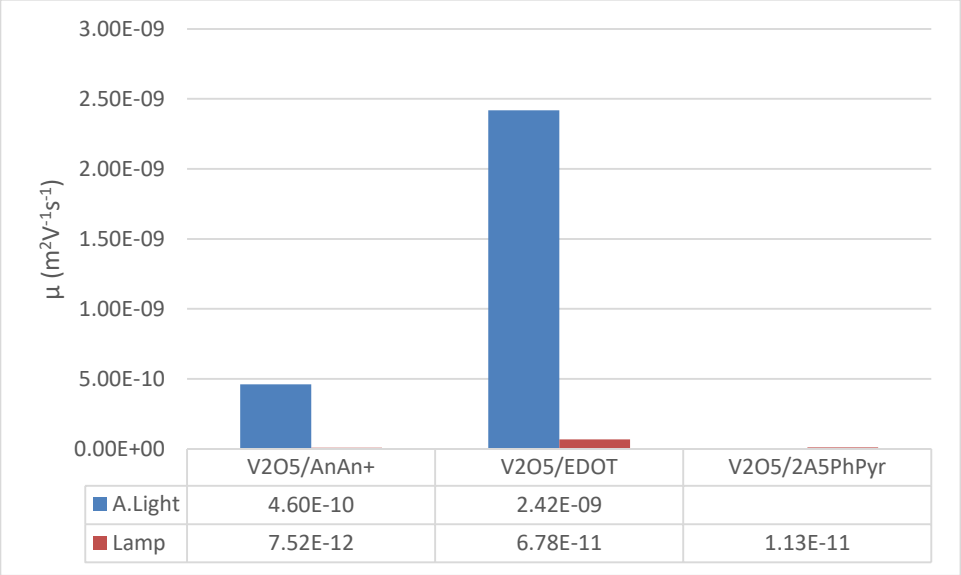

Figure 4.132 – Calculated CCM's for the V_2O_5 composite Si devices under A.Light and Lamp illumination

It is immediately clear that the V_2O_5 devices exhibit small CCMs but the calculated values help to begin in building a picture of the charge separation occurring in the device. It should be stated here that the CCM are the minimum values under the assumptions explained earlier, so it is expected that the true values will be higher than those calculated in Figure 4.132. However, these estimated CCM provide some picture regarding the creation of excitons and charge separation occurring in the device itself. We can conclude that the very low values of the CCM (which are several orders of magnitude lower than that of optimised organic devices (285)) are due to recombination of the charge carriers being a dominant mechanism in these devices. This suggests that upon formation of the charge carriers (via photon absorption) and due to the un-optimised nature of the photosensitive devices, most of these charge carriers are recombined and not efficiently separated to be collected at the electrodes. This is expected to be due to the device construction where the active composite material is spin-coated. The spin coating of the active composite material results in the deposition of a film made up of individual particles as opposed to a continuous uniform film of the material, which means that any charge

carriers that are formed need to migrate between particles in order to be separated effectively. As such, the particles could be treated as defects within the spin-coated film which could result in charge carriers being trapped; recombination is then likely to follow a Shockley–Read–Hall, trap assisted or surface recombination mechanism. Is it most probable that surface recombination is occurring in these devices due to the small CCM values resulting in charge carriers travelling a small distance away from the depletion region before recombining.

However, as seen earlier, the devices which exhibit an exponential increase in ΔI as a function of V could also undergo an Auger recombination like mechanism where a small proportion of any trapped charge carriers produced under dark conditions gain enough energy from a recombining charge carrier to be freed and collected at the electrode. In practice, this mechanism may only contribute a small increase in the ΔI.

Summary

Overall, it has been shown that upon successful intercalation of the polymer materials (as concluded from Section 4.1.1), the electrical and optoelectronic properties of the new materials differ from those of the inorganic host V_2O_5. The previously synthesised composite materials and novel composite materials showed an increase in their electrical conductivities compared to the inorganic host, with all composite materials exhibiting p-type semiconductor properties. It was also shown that all composite materials exhibited novel photosensitive effects, with an increase in current when illuminated under A.Light and Lamp conditions. It has been demonstrated that intercalation of the polymers increased the room temperature conductivities by a minimum of one order of magnitude for V_2O_5/1,4PDA-HQ (synthesised via ion-exchange) and two orders of magnitude for V_2O_5/2A5PhPyr (synthesised via direct intercalation) and LiV_2O_5/2A5PhPyr (synthesised by ion-exchange). This could be due to these intercalated polymers having fewer

conductive phases present and therefore limiting the overall material conductivity. The most conductive materials, V_2O_5/AnAn$^+$ and V_2O_5/EDOT, were synthesised by direct intercalation exploiting V redox chemistry and exhibited increases of 3 orders of magnitude in the room temperature conductivity compared to V_2O_5. It is expected that AnAn$^+$ and EDOT are present in a more conductive phase than 1,4PDA-HQ and 2A5PhPyr due to the nature of the redox reaction with V_2O_5. Furthermore, the presence of the An$^+$ cations in the AnAn$^+$ was shown to increase the conductivity. V_2O_5/5AQ (synthesised via ion-exchange) also shows a similar conductivity to V_2O_5/AnAn$^+$ and V_2O_5/EDOT which could be due to the increased conjugation due to the presence of its fused ring system. Furthermore, the presence of the fused rings could improve its redox chemistry with V leading to a more conductive polymer. Therefore, it can be deduced that the conductive properties of these materials are independent of the intercalation method in V_2O_5 and that *i)* the electrical properties are dependent on the nature of the intercalated polymer (the degree to which it is in its conductive phase) and *ii)* the nature of polymer intercalant is dominant in determining the electrical properties of the overall composite material. This was further demonstrated by the Seebeck coefficient measurements in which the n-type property of V_2O_5 changes upon intercalation and a positive Seebeck coefficient is seen relating to an overall p-type nature of the composite materials (as it was demonstrated in Section 4.1.1) that the intercalated polymers are in their p-type doped form. Though the polymer would be found within the layers of the inorganic host, the inorganic host would exhibit n-type nature due to the electron transfer in the intercalation reactions).

The I-V behaviour of V_2O_5 devices not only appears to be dependent on the intercalant present but also on the type of metal-semiconductor contact used. For example, for V_2O_5/AnAn$^+$ there appears to be a largely ohmic relationship when using a Zn, Al and Cu contacts but the material showed rectifying behaviour when an Sn or $FePS_3$ contact were used. Meanwhile, V_2O_5/2A5PhPyr (synthesised via direct intercalation) exhibited a

rectifying I-V relationship with a Zn contact, but mostly ohmic with Al. Furthermore, V_2O_5/PDA was shown to have the highest room temperature conductivity but exhibited ohmic properties with all metal contacts used, whereas V_2O_5/EDOT was shown to exhibit the most non-ohmic properties and exhibited a similar conductivity to $V_2O_5/AnAn^+$ and V_2O_5/5AQ.

The non-ohmic materials were generally modelled well using the non-ideal diode equation (Equation 4.1) determined from the calculated I_o and n values, but V_2O_5/2A5PhPyr with a Zn contact and $V_2O_5/AnAn^+$ with a $FePS_3$ contact exhibited n values lower than 1.

Interestingly, for both the evaporated and pressed Schottky devices the dopant densities were shown to be within the same order of magnitude, showing that there was good intimate contact between the semiconducting material and the metal electrode. V_2O_5/2A5PhPyr (synthesised via direct intercalation) had the lowest dopant density and this could be due to the lack of redox chemistry present in the acid-base reaction used for the synthesis. It could be suggested that the dopant densities are dependent on both the nature of the intercalated polymer and the inorganic host material. From the XPS data, V_2O_5/2A5PhPyr showed a single V^{5+} environment unlike many of the other materials; hence the dopant densities could be solely dependent on the nature of the intercalated polymer material. Thus overall it appears that the limiting factor in all cases is the poorly semiconducting inorganic V_2O_5 host.

In terms of devices for the prototype photosensitive devices for the highest dopant density non-ohmic Schottky materials, all the devices exhibited rectifying behaviour. In all cases, it was shown that the current measured in dark conditions increased when illuminated under A.Light conditions and further increased when illuminated under Lamp conditions. This showed that all the materials exhibited a photosensitive response. $V_2O_5/AnAn^+$ and V_2O_5/EDOT exhibited the largest responses (which were shown from the

ΔI values in Table 4.18 to Table 4.22). This could be due to the fact that the intercalated polymers in both materials are in their most conductive phases (as demonstrated in section Section 4.1.1) and again although V_2O_5 appears to be the limiting factor for the electrical and photosensitive properties, so the specific polymer and its degree of doping affects the overall photosensitivity of these materials.

An interesting phenomenon shown here for $V_2O_5/AnAn^+$ was the increase in the dark current when the device is placed within a magnetic field with using a $FePS_3$ contact. Although the increase in the current from that measured under dark conditions to that under the magnetic field was not seen to the same extent under illuminated conditions, the magnetic field still caused a significant deviation of the I-V character from the dark current. When the device orientation was perpendicular, the increase in current was shown to be greater than that when the device was orientated parallel. This effect could simply be that the magnetic field assisted the charge separation or more likely prevented recombination occurring at the interface that occurs in dark conditions leading to a greater observed current when a potential difference was applied.

From the ΔI vs V plots for the devices under A.Light and Lamp conditions the estimated maximum device Eff were calculated (Table 4.24 and Figure 4.123) where the photosensitive devices exhibited Eff up to ~1% with the $V_2O_5/AnAn^+$ material exhibiting Eff ~0.90% when used as the active material. Although this is an estimation of the maximum Eff the device could exhibit, it does provide a good indication of the true Eff as it would be expected to be much lower than this calculated value. It is possible that a fully optimised device may operate with an efficiency similar to the calculated Eff for these un-optimised devices. It was evident that there was a significantly lower Eff under Lamp illumination which suggested that the material operated poorly around ~800nm and above operating better within the blue visible light and near-UV regions of the electromagnetic spectrum.

However, unlike in the case for the room temperature conductivities of the composite materials, the photosensitive devices exhibit poor photoconductivities in the range of 10^{-10} to 10^{-12} Sm^{-1}. It is suspected that the low photoconductivities are due to the device not being optimised for the best performance. The poor photoconductivities are therefore related to the fact that the composite materials were spin-coated onto the Si or $FePS_3$ and thus the film obtained was made up of discrete particles of the material forcing the photogenerated current to be conducted between particles. In relation to the entire film, its non-uniformity could be treated as defects caused by these particles. Thus, any conductive charge carriers produced by illumination may become trapped while moving between these particles. This trapping may be sufficient enough to result in a form of Shockley-Read-Hall, trap assisted or surface recombination mechanisms. This is further seen in the calculated device CCM of which for all devices are found in the order of magnitude of 10^{-12} to 10^{-9} $m^2V^{-1}s^{-1}$. These low mobilities suggest that there a large number of the charge carriers recombining as opposed to being collected at the electrodes. It is therefore likely that the low mobilities are due to the charge carriers not effectively migrating between the particles that are making the composite material film and could be trapped leading to recombination. The low mobilities suggest that the likeliest mechanism of recombination will be that of surface recombination between the substrate and the composite material. This further provides evidence that the increased current observed when the V_2O_5/$AnAn^+$ $FePS_3$ device was placed within a magnetic field is probably due to the magnetic field preventing some recombination occurring leading to more effective charge separation. These effects are likely to be minimised if a suitable method for the deposition of a uniform film leading to a more optimised device architecture.

4.2.2) MoO_3 Nanocomposite Materials

4.2.2.1) Room Temperature Conductivity

Table 4.26 - Room temperature conductivities for the MoO_3 nanocomposite materials

Material	Conductivity, σ (Sm^{-1})
MoO_3	4.3×10^{-5}
Direct	
MoO_3/PDA	8.1×10^{-1}
MoO_3/2A5PhPyr	3.8×10^{-3}
MoO_3/5AQ	2.7×10^{-2}
MoO_3/2AmThia	7.8×10^{-4}
Recrystallisation	
MoO_3/An	4.5×10^{-4}

The room temperature conductivities at ~293K (measured at the time of the experiment) are shown in Table 4.26. The host MoO_3 exhibits the lowest conductivity (corresponding to the host being a wide-gap semiconductor) and increases upon insertion of the organic intercalants. This increase in conductivity is between one and four orders of magnitude. The increase is attributed to two main contributions; the first being the formation of the Mo^{6+}/Mo^{5+} pairs in the inorganic host layer and the second being the presence of the organic intercalants (as concluded from the characterisation of these materials in Section 4.1.2). The most conducting material was shown to be MoO_3/PDA (synthesised by ion-exchange). This was followed by MoO_3/5AQ and MoO_3/2A5PhPyr, and the least conducting materials were MoO_3/AmThia and MoO_3/An. The low conductivities of the MoO_3/AmThia and MoO_3/An may be due to the materials being present in their least conductive phase.

4.2.2.2) Seebeck Coefficient

Table 4.27 - Seebeck Coefficients for some MoO_3 composite materials and their doping type.

Material	Seebeck Coefficient (μVK^{-1})	Material type
MoO_3	-200 (286)	n-type
MoO_3/PDA	125	P-type
MoO_3/2A5PhPyr	98.14	P-type
MoO_3/AmThia	80.93	P-type

In general, the MoO_3 composite materials show positive Seebeck coefficients (see Appendix B.5) in contrast to the pristine host MoO_3. The materials are therefore designated as p-type semiconductors, with MoO_3/PDA exhibiting the highest Seebeck coefficient and MoO_3/AnThia the lowest. The increase in the Seebeck Coefficient could be due to the presence of the polymers in the interlayer spacing of the inorganic material. As shown by the conductivities (Table 4.26), the intercalated polymers appear to dominate in contributing to the observed positive Seebeck coefficients of the composite materials. The p-type nature of these materials appears to follow that of the intercalated polymer materials (as concluded in Section 4.1.2) these intercalated polymers are in their protonated forms, leading to the conclusion that the intercalation of the p-type conducting polymers leads to an increase in both the Seebeck coefficient and room temperature conductivity.

4.2.2.3) Schottky Device I-V Curves

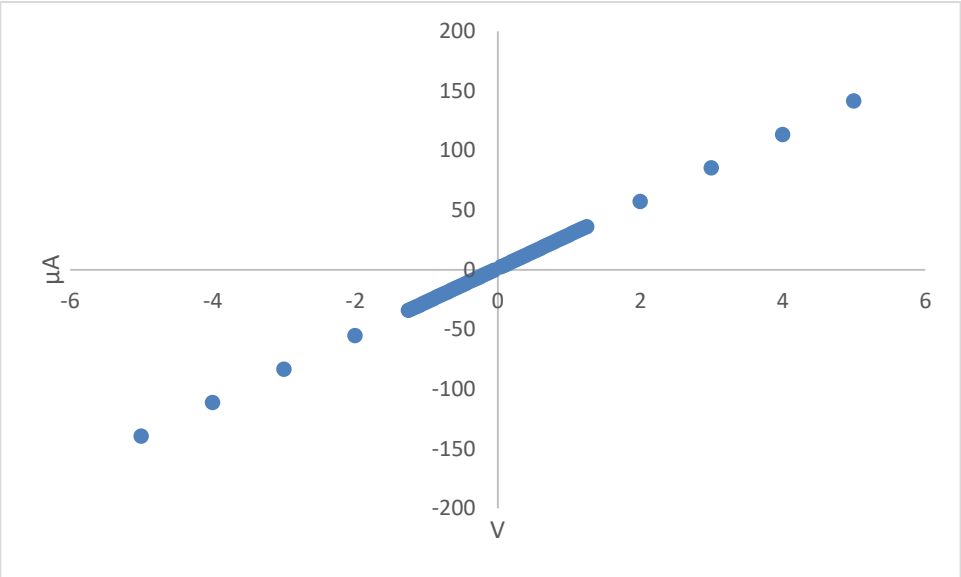

Figure 4.133 – I-V graph for MoO_3 with Zn contact

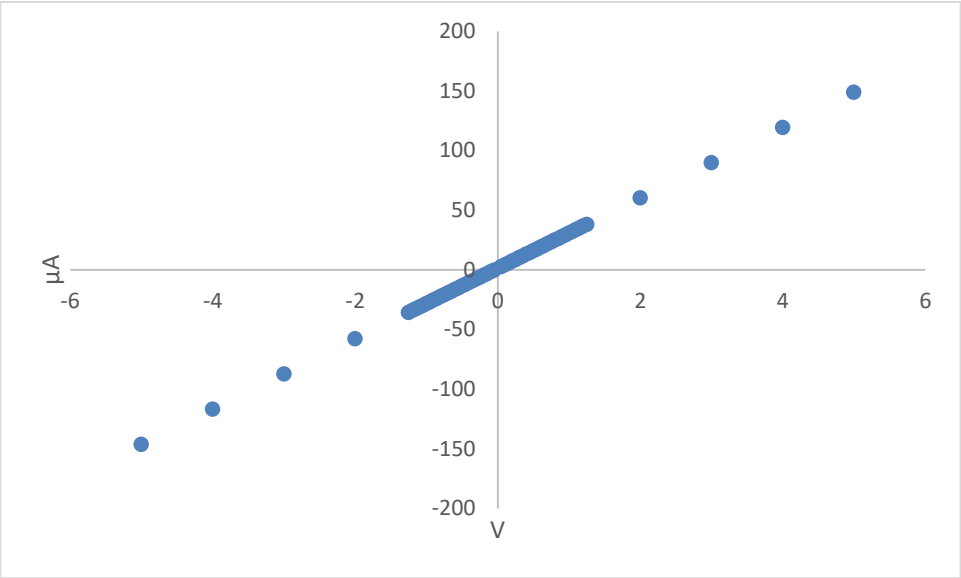

Figure 4.134 - I-V graph for MoO_3 with an Al contact

Figure 4.133 and Figure 4.134 show that the host MoO_3 exhibits ohmic properties with no rectification using both Zn and Al contacts.

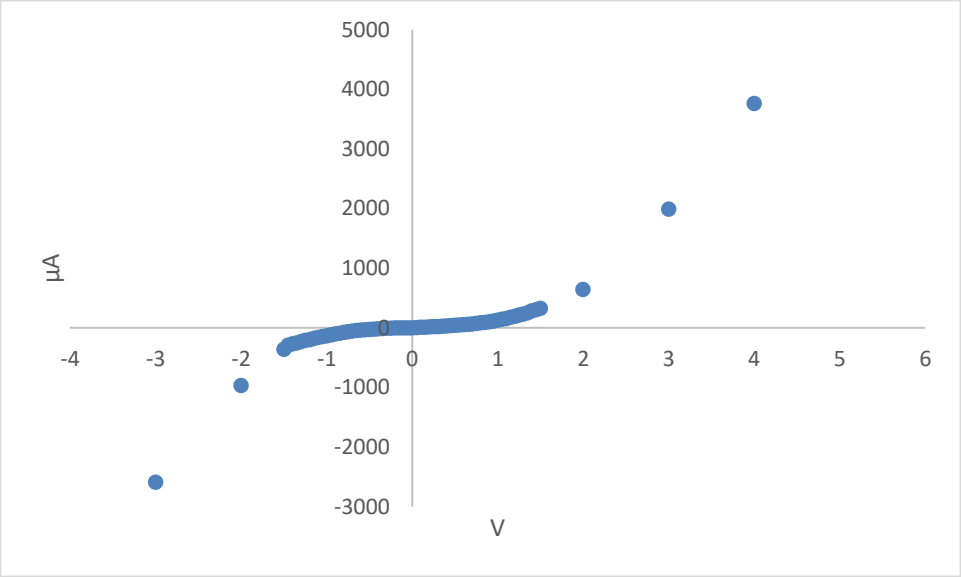

Figure 4.135 - I-V graph of MoO_3/PDA with Zn contact

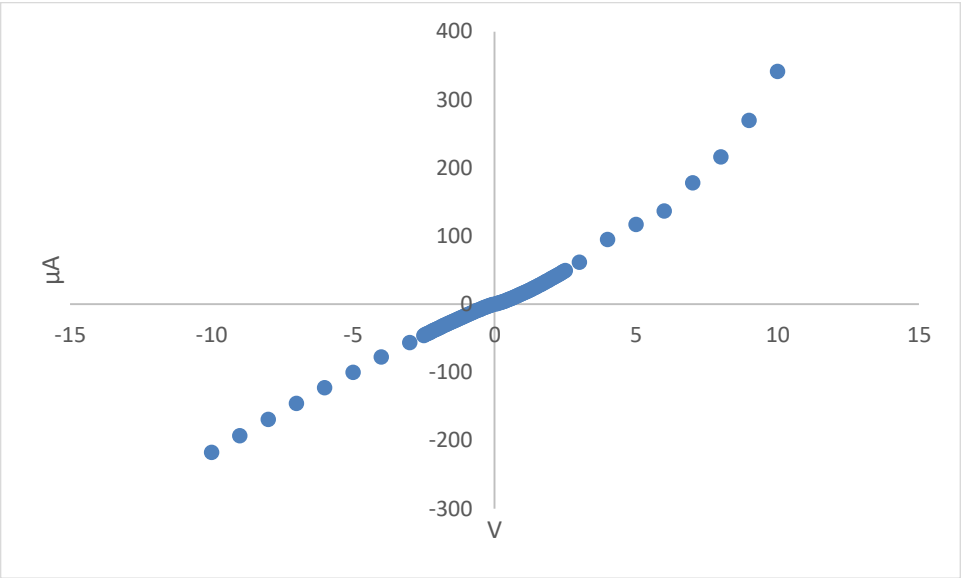

Figure 4.136 - I-V graph of MoO_3/PDA with Al contact

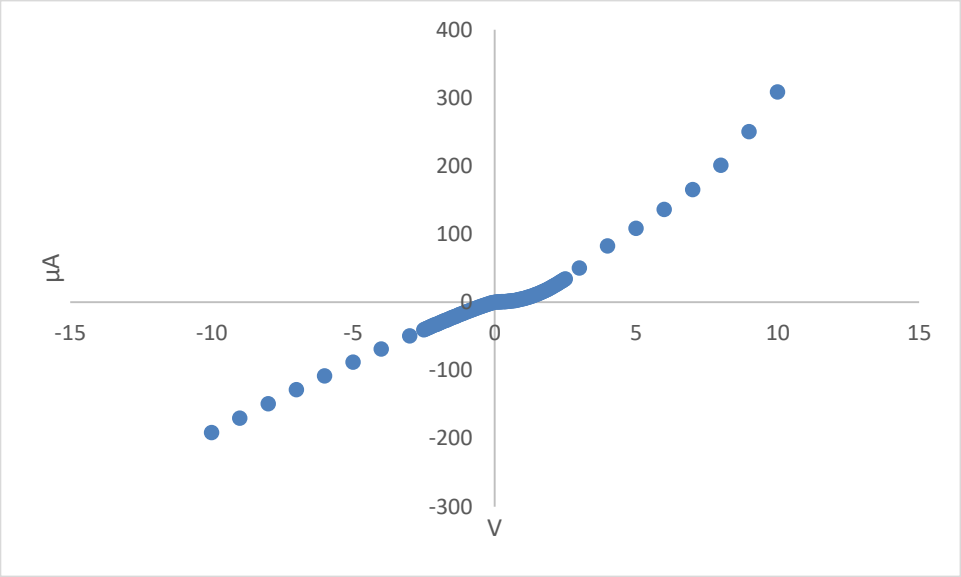

Figure 4.137 - I-V graph of MoO_3/PDA with Cu contact

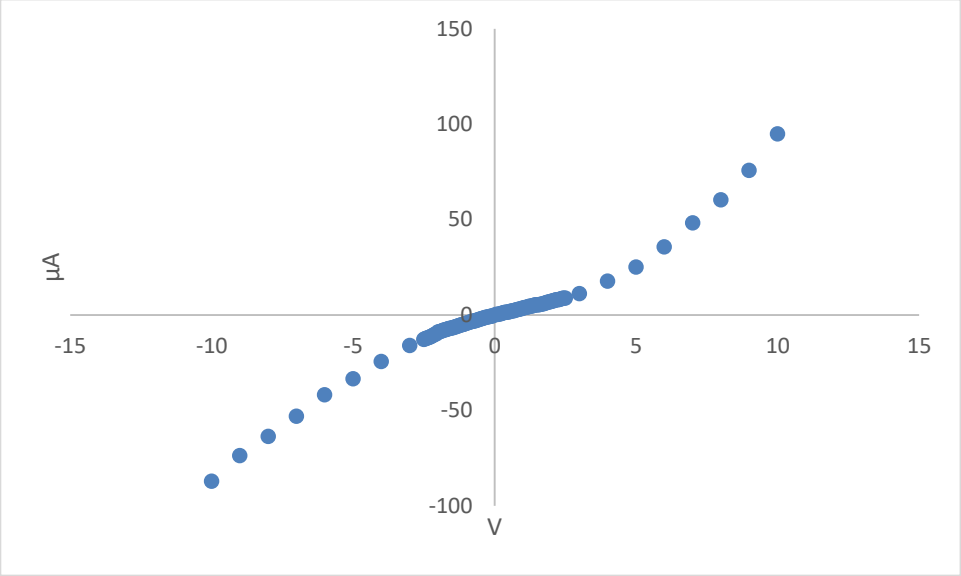

Figure 4.138 - I-V graph of MoO_3/PDA with a Ni contact

Figure 4.135 - Figure 4.138 show the I-V curves for the MoO_3/PDA composite material diodes with various metallic contacts. Unlike MoO_3, all the devices are shown to exhibit non-ohmic properties. As concluded (in Section 4.1.2) the polymer materials were successfully intercalated into the interlayer space of MoO_3; therefore the changes in the I-V graphs are a result of the presence of the particular polymer intercalant. In the case of MoO_3/PDA, any changes in the I-V character of the host material are caused by the presence of PDA. For Figure 4.135 - Figure 4.138 the rectification ratios between the maximum and minimum voltages are 1.45, 1.57, 1.61 and 1.09 respectively.

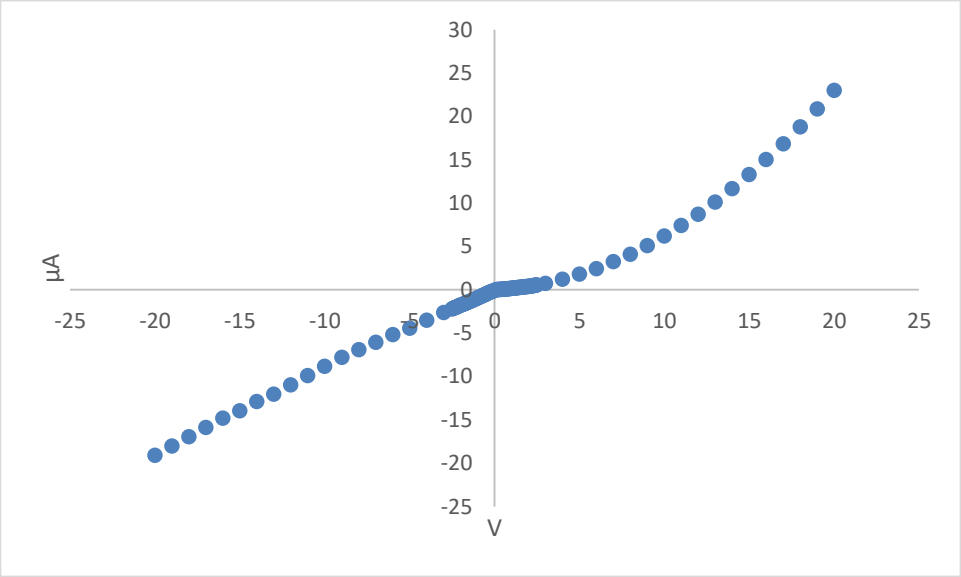

Figure 4.139 - I-V graph for MoO_3/2A5PhPyr device with Zn contact

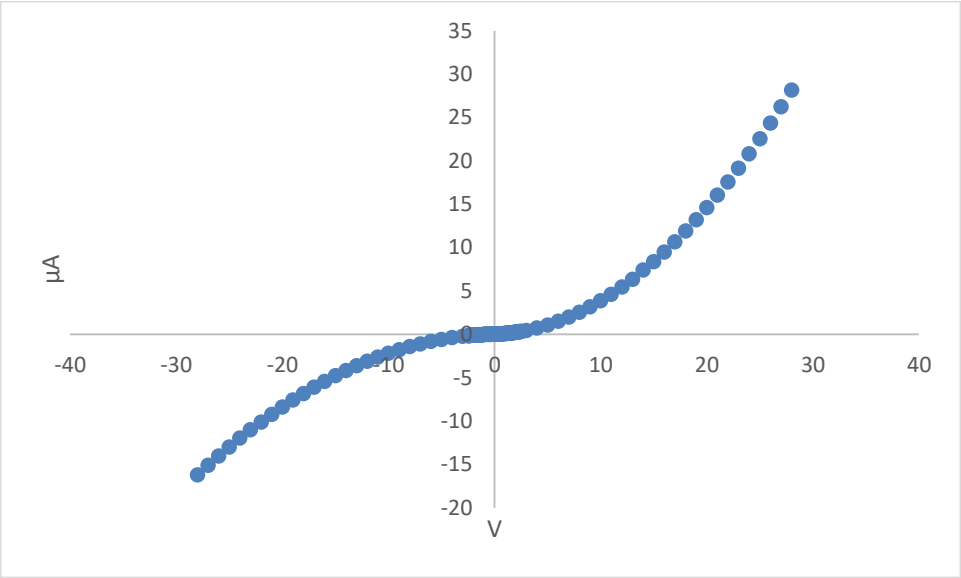

Figure 4.140 - I-V graph for MoO_3/2A5PhPyr device with Al contact

Figure 4.139 and Figure 4.140 show the I-V graphs for the MoO_3/2A5PhPyr composite material. In both cases, rectifying behaviour is seen. Under reverse bias, the Zn device shows non-ohmic behaviour until -3 V. Below -3 V a linear I-V relationship is observed as the device reaches a saturation point. The rectification ratios for the Zn and Al devices were 1.21 and 1.73 respectively.

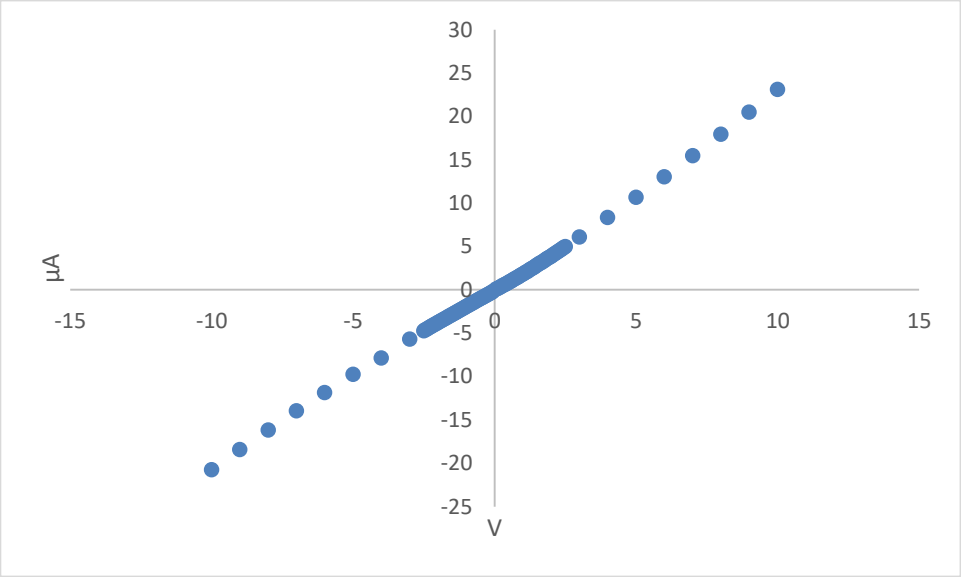

Figure 4.141 - I-V graph for MoO_3/5AQ device with Zn contact

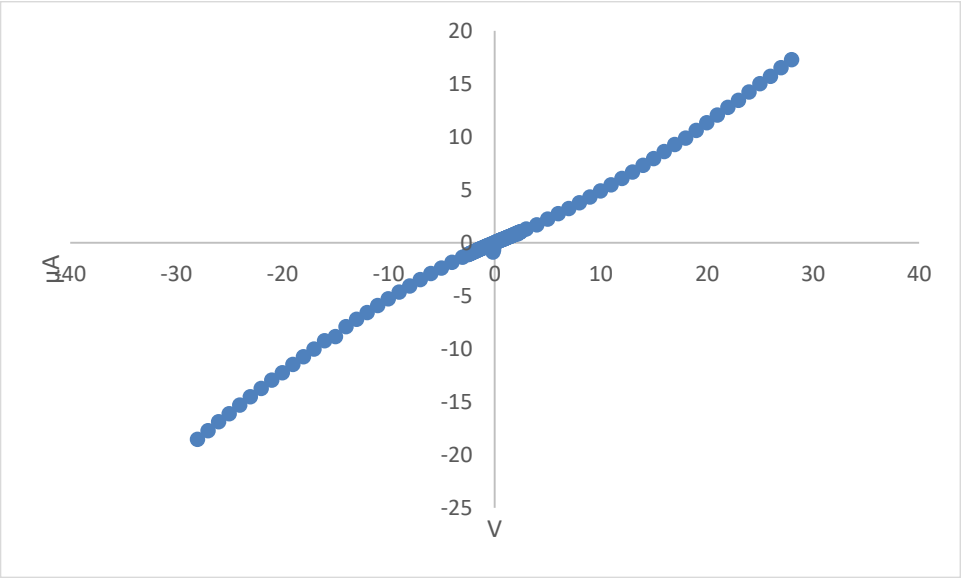

Figure 4.142 - I-V graph for MoO_3/5AQ device with Al contact

Figure 4.141 and Figure 4.142 show the I-V graphs for the MoO_3/5AQ Schottky devices with Zn and Al contact respectively. With the Zn contact, the device shows a small rectifying property while the Al contact exhibits a rectifying property. The rectification ratios were 1.18 and 0.93 for the Zn and Al devices respectively.

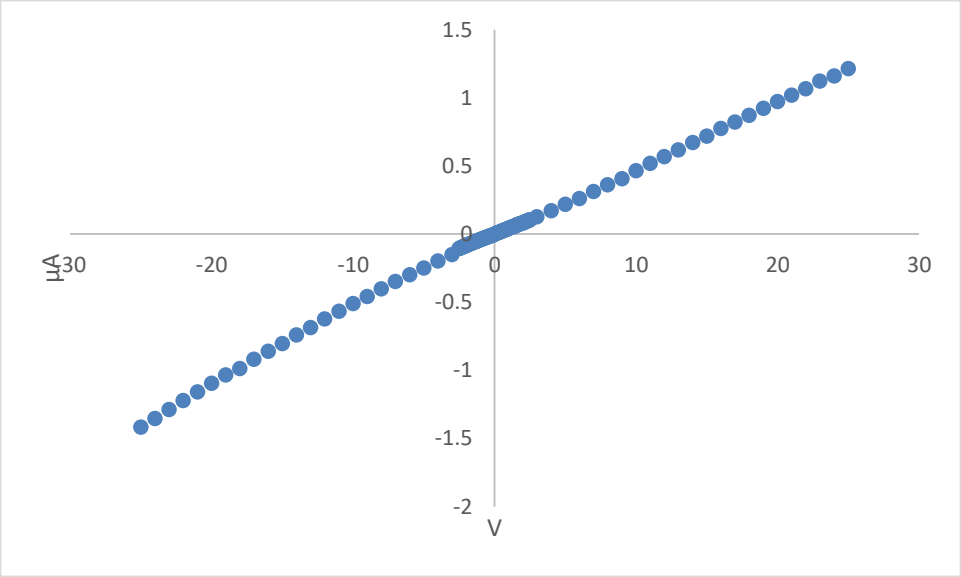

Figure 4.143 - I-V graph for MoO_3/AmThia device with Zn contact

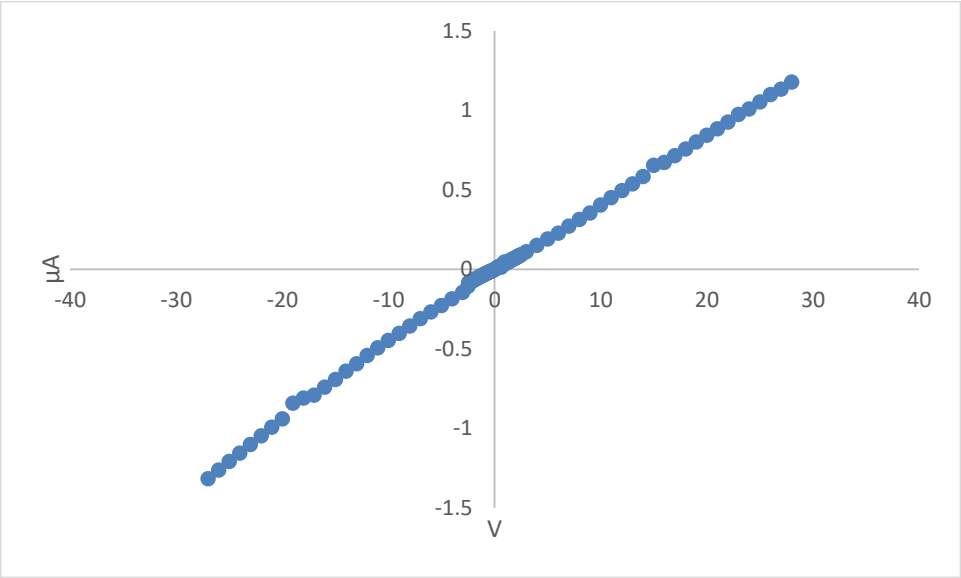

Figure 4.144 - I-V graph for MoO_3/AmThia device with Al contact

Figure 4.143 and Figure 4.144 show the I-V graphs for the MoO_3/AmThia Schottky devices and show a linear (ohmic) relationship when both Zn and Al contacts are used. This may be due to a lack of protonation on the polymer intercalant.

MoO_3/An showed poor contact with all metal contacts, resulting in no current measurements being possible.

Modelling the I-V curves using the non-ideal diode equation (Equation 4.1 and Equation 4.2), I_0 and n can be extracted from the model and are reported in Table 4.28. Using Equation 4.4, Φ can be calculated and is shown in Figure 4.145.

Table 4.28 - I_0 and n values for the non-ohmic MoO_3 composite material Schottky devices

Zn Contact	**I_0 (μA)**	**n (V)**
MoO_3/PDA	13.19	1.45
MoO_3/2A5PhPyr	0.087	1.33
MoO_3/5AQ	1.073	1.58
Al Contact	**I_0 (μA)**	**n (V)**
MoO_3/PDA	0.001	1.71
MoO_3/2A5PhPyr	0.037	1.15
MoO_3/5AQ	0.24	1.67
Cu Contact	**I_0 (μA)**	**n (V)**
MoO_3/PDA	0.58	1.65
Ni Contact	**I_0 (μA)**	**n (V)**
MoO_3/PDA	1.94	1.54

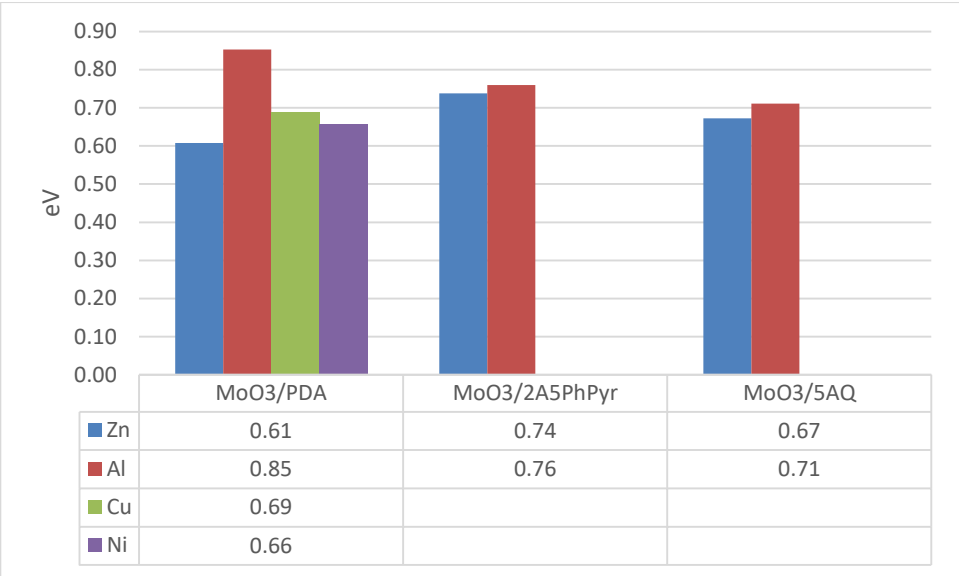

Figure 4.145 - calculated barrier heights, Φ, for the non-ohmic Schottky diode junctions

From Table 4.28 we can see that utilising the non-ideal diode equation and calculating n values yields an average value overall of 1.51 with no values n<1. The maximum ideality factor was shown to be for MoO_3/PDA with the Al contact of 1.71 and the lowest

MoO_3/2A5PhPyr with the Al contact. Notice that the average ideality factor suggests these devices show likely asymmetry between the bands required for excitation and/or recombination. This asymmetry (previously shown in Figure 4.8) suggests there may be poor band overlap in the composite materials between the organic and inorganic components as was previously concluded from the optical spectroscopy data for the MoO_3 materials (Figure 4.49).

The average Φ was shown to be 0.71 eV, with the highest barrier height being exhibited by MoO_3/PDA (0.85 eV) with an Al contact and the lowest being MoO_3/PDA with a Zn contact (0.61 eV).

From the voltage-capacitance relationship (see Appendix B.6) for the MoO_3 Schottky devices and using the average dielectric constant measured (Table 4.15) the dopant densities (N_d) calculated using Equation 4.6 are shown in Table 4.29. A comparison of the evaporated and pressed pellet N_d are shown in Table 4.30.

Table 4.29 - Dopant densities for all MoO_3 Schottky device contacts

Device Contact	Dopant Density (N_d) (cm^{-3})
Zn	
MoO_3/PDA	2.07E+14
MoO_3/2A5PhPyr	6.61E+13
MoO_3/5AQ	3.54E+13
Al	
MoO_3/PDA	9.12E+14
MoO_3/2A5PhPyr	7.17E+13
MoO_3/5AQ	3.58E+12
Cu	
MoO_3/PDA	2.41E+14
Ni	
MoO_3/PDA	1.06E+15

Table 4.30 - Dopant density comparison between the MoO_3 pressed Schottky devices and the evaporated metal contact Schottky devices

Dopant Densities (cm^{-3}) (N_d) Collated			
Device	**Pressed**	**Evap**	**Ratio**
Al contact			
MoO_3PDA	9.12E+14	3.7E+14	2.467
MoO_3/2A5PhPyr	7.17E+13	4.37E+13	1.639
Cu contact			
MoO_3/PDA	2.41E+14	1.65E+14	1.46198

Pressed pellet contacts and evaporated contacts show comparable dopant densities for the Schottky devices. Figure 4.146 shows a graphical representation of Table 4.30.

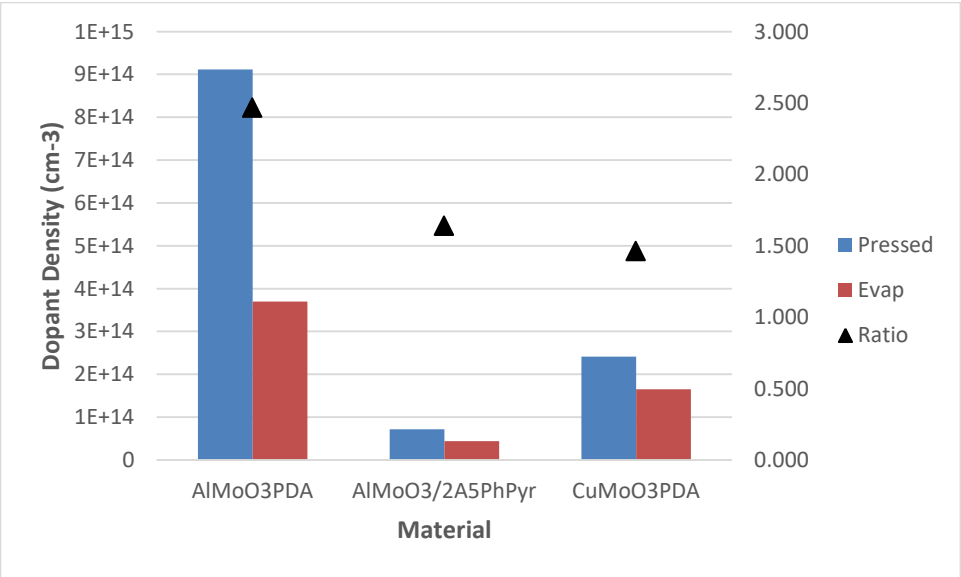

Figure 4.146 - Comparison of dopant densities between the pressed pellet (Pressed) MoO_3 devices and evaporated pellet (Evap) MoO_3 devices

It can be seen that N_d values for the evaporated metal contacts and pressed contacts are within the same order of magnitude with a small overall difference. The material with the largest N_d was shown to be MoO_3/PDA (for both Al and Cu evaporated contacts), while the smallest was for MoO_3/2A5PhPyr. On closer inspection, it is clear that for both the pressed and evaporated pellets, MoO_3/PDA exhibits the largest N_d and MoO_3/2A5PhPyr exhibits the smallest. For the pressed pellet devices, MoO_3/5AQ with the Al contact has the

smallest N_d (3.58 x 10^{12} cm^{-3}) while MoO_3/PDA with a Ni contact has the largest N_d (1.06 x 10^{15} cm^{-3}). MoO_3/PDA exhibited the largest N_d irrespective of the metal contact used with N_d values ~10^{14}.

From this, the same conclusions can be made as was the case for V_2O_5 where N_d is proportional to the concentration of Mo^{6+}/Mo^{5+} pairs. Since all the materials were synthesised via ion-exchange mechanism it is possible that PDA exhibited better redox chemistry with the MoO_3 host material upon intercalation which may increase the Mo^{6+}/Mo^{5+} pair concentration compared to that for the other materials. The extent of redox chemistry between the organic intercalant and the inorganic host would then have an effect on the material's N_d.

4.2.2.4) Photosensitive Devices

The prototype photovoltaic devices were made by spin-coating the photoactive composite material onto n-type silicon and using an ITO counter electrode. The MoO_3/PDA material was shown to be the most conductive and most promising for photosensitive/conductive applications (4.2.2.3) and was therefore selected for photovoltaic analysis.

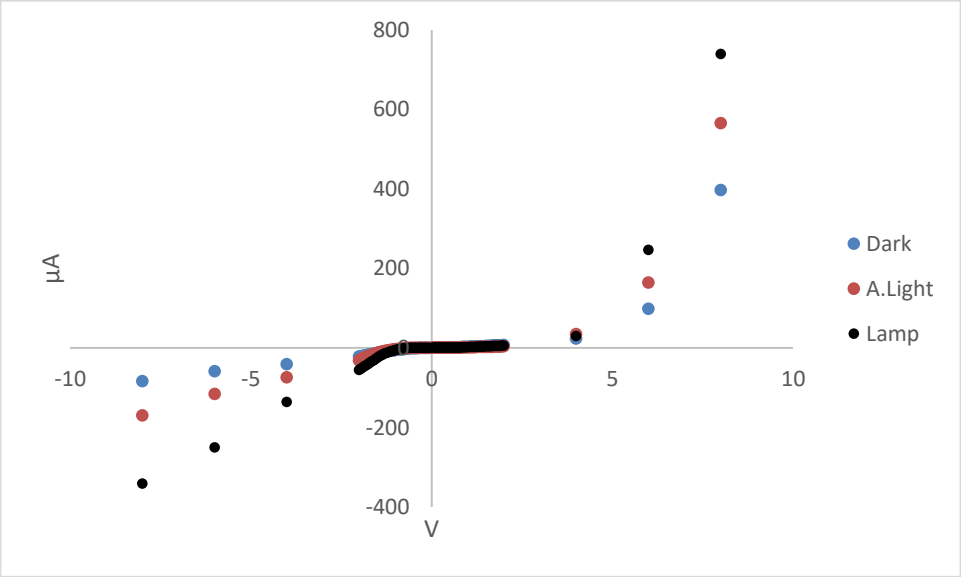

Figure 4.147 - I-V graph for MoO_3/PDA photovoltaic device under Dark, A.Light and Lamp conditions

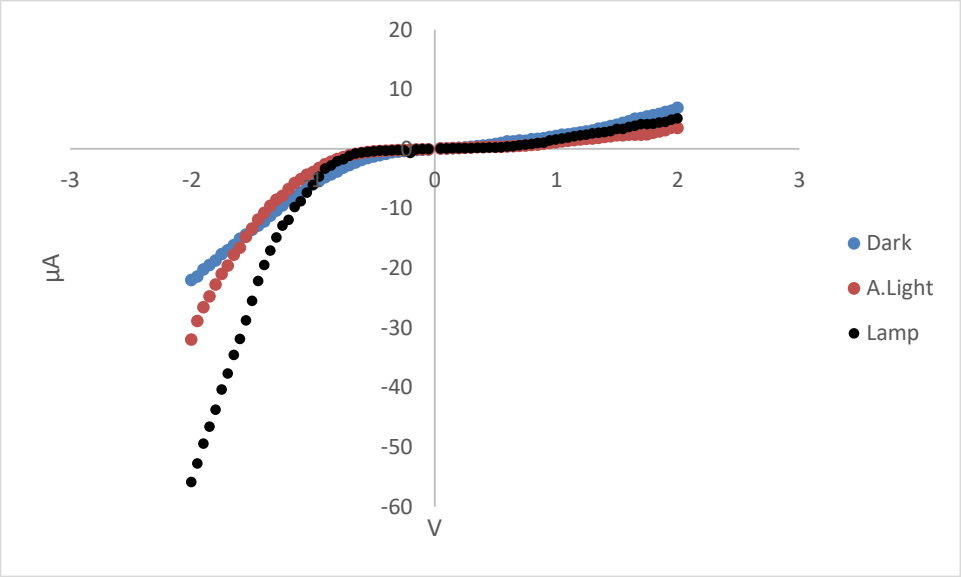

Figure 4.148 - I-V graph for MoO_3/PDA photovoltaic device under dark, A.Light and Lamp conditions between -2 and 2 V

Figure 4.147 and Figure 4.148 show the I-V curves for the MoO_3/PDA silicon photovoltaic device. Overall, under Dark and illuminated conditions there is a nonlinear relationship between current and voltage. Between 0 V and 4 V, there is little change in current occurring between Dark, A.Light and Lamp conditions. Then after 4 V, there is a noticeable deviation from the Dark current when the device is illuminated. Under reverse bias, this deviation from the Dark current when the device illuminated is more noticeable. Table 4.31 and Table 4.32 show the overall change in current (ΔI) for selected voltages.

Table 4.31 - Change in the current (ΔI) for Silicon MoO_3/PDA photovoltaic device between A.Light - Dark and Lamp - Dark conditions under forward bias

MoO_3/PDA									
Voltage (V)	**0.05**	**0.25**	**0.5**	**1**	**1.5**	**2**	**4**	**6**	**8**
ΔI (µA) A.Light - Dark	-0.00068	-0.06873	-0.4856	-1.043	-1.779	-3.401	11.39	66.21	168.7
ΔI (µA) Lamp - Dark	-0.00078	-0.08737	-0.5847	-0.585	-0.705	-1.793	6.37	148.31	342.7

Table 4.32 - Change in the current (ΔI) for Silicon MoO_3/PDA photovoltaic device between A.Light – Dark and Lamp – Dark conditions under reverse bias

MoO3/PDA									
Voltage (V)	**-0.05**	**-0.25**	**-0.5**	**-1**	**-1.5**	**-2**	**-4**	**-6**	**-8**
ΔI (µA) A.Light - Dark	0.018	0.1611	0.8103	2.023	0.213	-9.97	-32.81	-57.7	-85.5
ΔI (µA) Lamp - Dark	0.0493	0.1331	0.843	-0.084	-11.92	-33.87	-94.54	-192.12	-257.52

As shown in Table 4.31 Table 4.32, under forward bias the photo-effect is most prominent ≤ 4 V whereas under reverse bias, the deviation begins to occur earlier and it appears that the device reaches its breakdown voltage under illuminated conditions.

As previously seen for the V_2O_5 composite materials (Section 4.2.1.4), the power generated when the device is illuminated (P_{out}, as a function of voltage) can be calculated by multiplying ΔI by the voltage. Figure 4.149 and Figure 4.150 shows the power vs voltage plots for MoO_3/PDA.

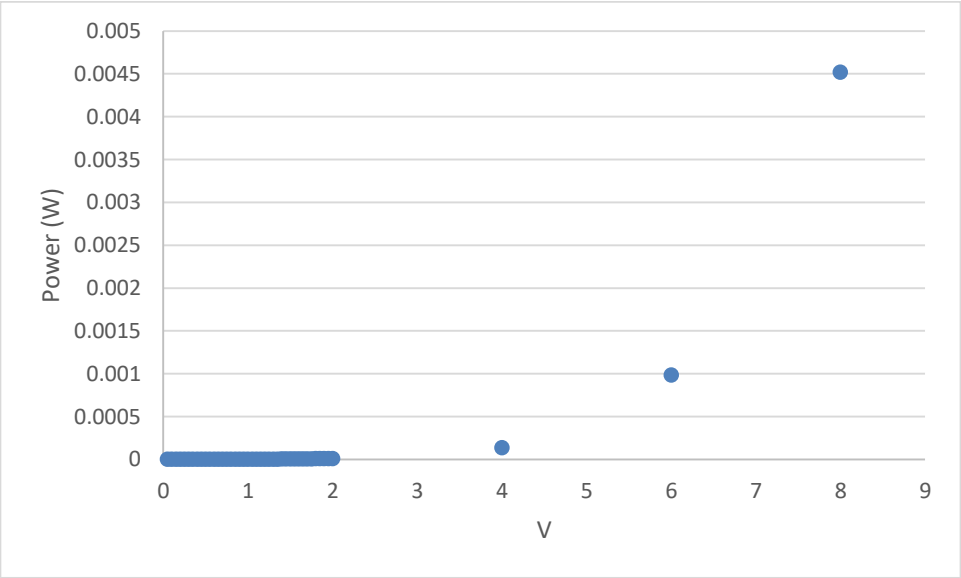

Figure 4.149 – The power vs voltage plot for MoO_3/PDA Si device under A.Light illumination

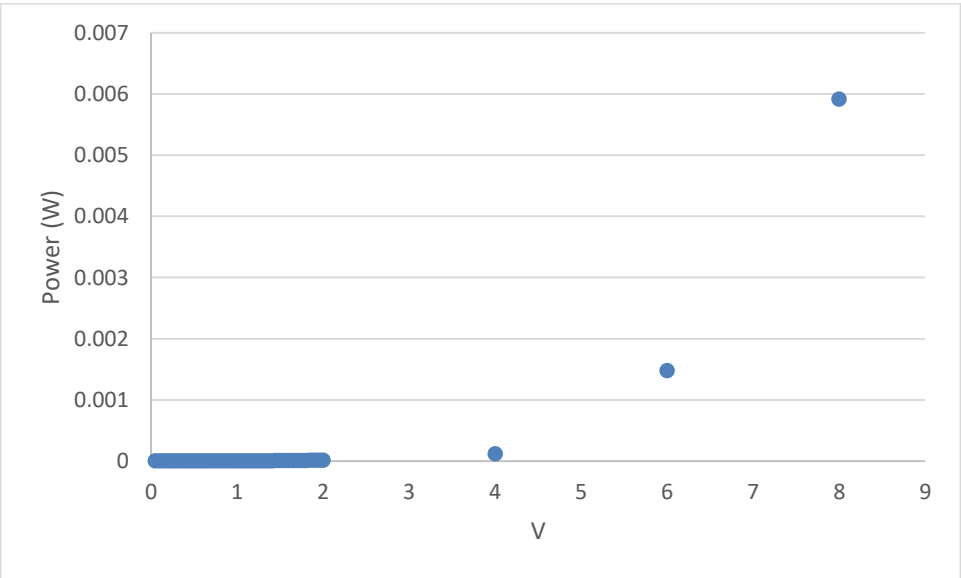

Figure 4.150 – The power vs voltage plot for MoO_3/PDA Si device under Lamp illumination

From the P_{out} vs V plots, the device efficiency (Eff) as the maximum P_{out} can be determined. The Eff is calculated using Equation 4.7 where the total power being input into the large silicon device is 0.15 W and 1.65 W for A.Light and Lamp illuminated conditions respectively (previously shown in Table 4.23). Table 4.33 and Figure 4.151 show the calculated maximum efficiencies. It must be noted that these are the efficiencies observed at the maximum voltage and may not represent the practical device Eff vawhich is expected to be lower than this value.

Table 4.33 – Calculated device Eff(%) for the Si MoO_3/PDA photosensitive device

Material	MoO3/PDA
A.Light Illumination	
Max Power Volt	8
Max Power (W)	0.00452
Eff (%)	0.91
Lamp Illumination	
Max Power Volt	8
Max Power (W)	0.00591
Eff (%)	0.17

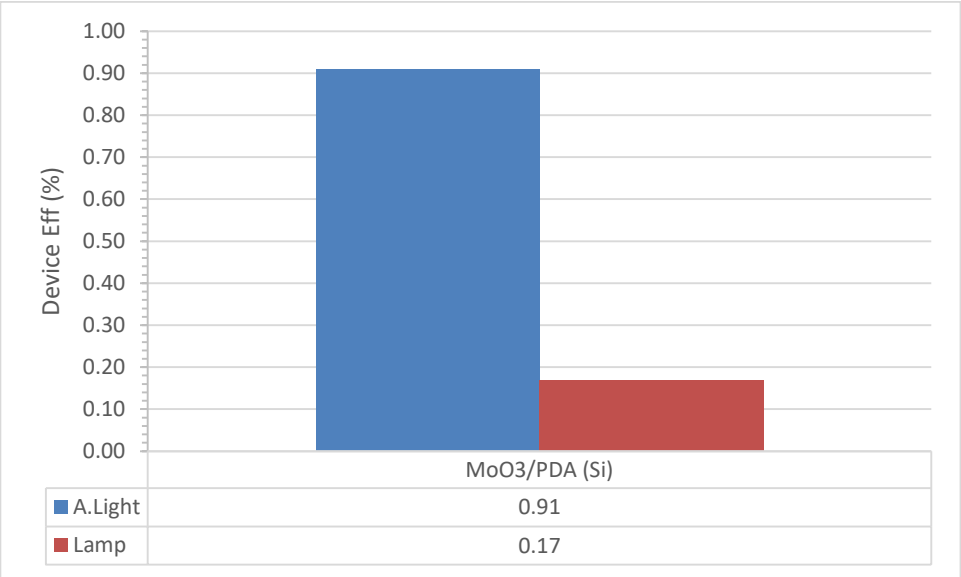

Figure 4.151 – Calculated device Eff (%) for the Si MoO_3/PDA photosensitive device

As seen for the V_2O_5 composite materials (Section 4.2.1.4), the MoO_3/PDA device exhibits a greater Eff under A.Light illumination than for the Lamp illuminated conditions. This is consistent with the absorption edges and optical band-gaps for the MoO_3 composite materials (Section 4.1.2.4) which were observed to occur within the range of ~3.4 to ~3.8 eV. The same conclusions apply for the V_2O_5 photosensitive devices (Section 4.2.1.4) where is it likely that the formation of charge carriers from photon absorption is occurring from the absorption of light in the blue and near UV regions. This corresponds well with the maximum solar spectral irradiance at the Earth's surface (centred at ~500nm) (281) compared to that for the spectrum of Lamp (peaks at ~800nm). This results in the difference observed in the Eff between A.Light and Lamp illuminated conditions.

Further analysis of the device ΔI vs V plots can provide information regarding the photoconductivities and charge carrier mobility (CCM) of this device. The ΔI vs V plots were modelled using a second-order polynomial (Equation 4.9 from Section 4.2.1.4) and an exponential function (Equation 4.10 from Section 4.2.1.4). The plots show a better fit to the second-order polynomial than over the exponential function (as previously described in Section 4.2.1.4) for modelling the V_2O_5 composite material ΔI vs V photosensitive device plots.

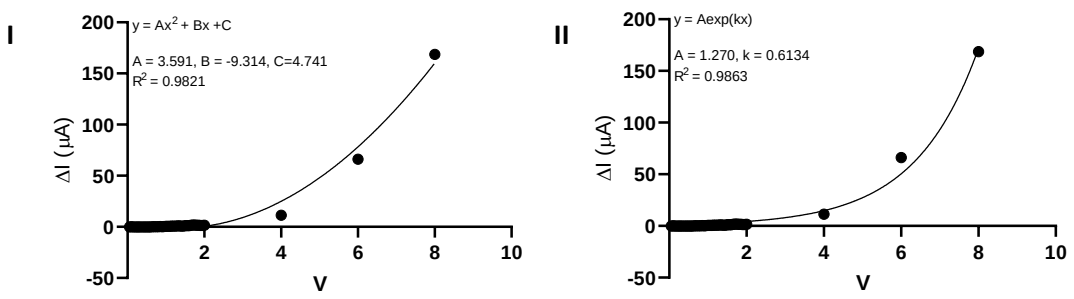

Figure 4.152 – ΔI vs V plot for MoO_3/PDA Si device under A.Light illumination where I) shows the second-order polynomial fit II) shows exponential fit

Figure 4.152.I and .II show the ΔI for the device illuminated under A.Light: both functions show a good and very similar fit to the plot R^2 = 0.9821 and R^2 = 0.9863 for the second-order polynomial and exponential function respectively.

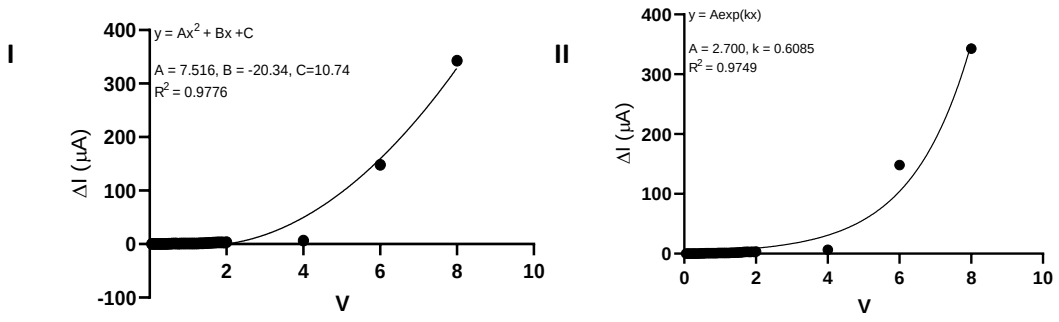

Figure 4.153 – ΔI vs V plot for MoO_3/PDA Si device under Lamp illumination where I) shows the second order polynomial fit II) shows exponential fit

As similarly seen in Figure 4.152.I and .II, Figure 4.153.I and .II show a good and similar fit to both polynomial (R^2 = 0.9776) and exponential functions (R^2 = 0.9749).

Overall, both Figure 4.152 and Figure 4.153 are well fitted by both second-order polynomial and exponential functions, with little to differentiate the two models. It is therefore assumed that both Figure 4.152 and Figure 4.153 exhibit a good fit for the polynomial function and these are carried forward for calculating the photoconductivities and CCM for this device. From the fitted second-order polynomials the estimated photoconductivity (Δσ) can be calculated using Equation 4.11 (see Section 4.2.1.4). Table 4.34 shows the estimated photoconductivities and the relative changes in conductivity for the MoO_3/PDA device fitted to the second-order polynomial.

Table 4.34 – Photoconductivities of the Si Devices modelled well with the second-order polynomials where σ_{obvs} is the calculated photocurrent from the I – V plot of the respective material's photosensitive device

Material	Δσ (Sm^{-1})	$\Delta\sigma/\sigma_{obvs}$
A.Light Illumination		
MoO_3/PDA	2.43E-11	0.30
Lamp illumination		
MoO_3/PDA	5.20E-11	0.47

Table 4.34 shows that under both illumination conditions the photoconductivity of the device is of the same order of magnitude (10^{-11} Sm^{-1}). However, since the Eff (seen in Table 4.33 and Figure 4.151) shows a clear difference between A.Light and Lamp illumination, it is likely that in the case of the MoO_3/PDA the Eff of the device is more closely related to the CCM, which is a function of the total number of charge carriers (n+p) created when the device is under illumination.

Equation 4.13 is used to determine the CCM (see Section 4.2.1.4) and Figure 4.154 shows the estimated CCM valuess for the MoO_3/PDA Si device.

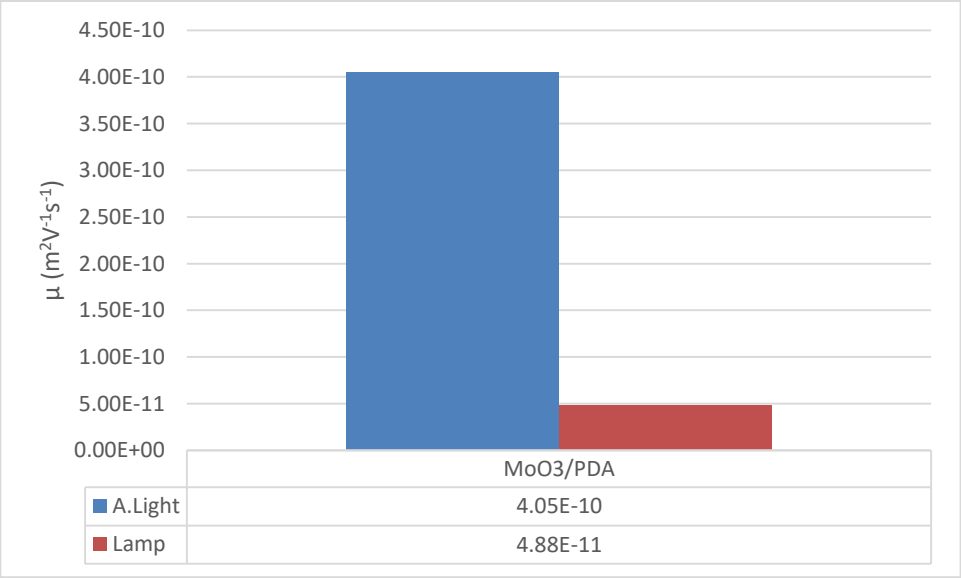

Figure 4.154 – Calculated CCM values for the MoO_3/PDA Si device under A.Light and Lamp illumination

It is immediately clear that the MoO_3/PDA Si device exhibits small CCM compared to those for optimised organic devices (285). On closer inspection, it is shown that illumination under ambient light produces a calculated CCM of approximately one order of magnitude greater than that under Lamp illumination. This correlation is similar to that when comparing the calculated device Eff under the two illumination conditions. Therefore the CCM values help begin to build a better picture of the charge separation occurring in the device. It is apparent that the Eff calculated is related to the mechanism of exciton creation and charge separation occurring in the device itself.

The calculated estimated CCM values are the minimum values under the assumptions explained earlier when describing Equation 4.13. It is expected that the true value will be higher than those calculated in Figure 4.154. However, the very low CCM values suggest that upon formation of the charge carriers, and due to the un-optimised nature of the photosensitive devices, most of these charge carriers recombine and are not efficiently separated. This is expected to be due to the device construction when the active composite material is spin-coated. The spin-coating of the active composite material results in the deposition of a film comprising individual particles as opposed to a continuous uniform film of the material. This means that any charge carriers that are formed need to migrate between particles in order for efficient separation to occur. Therefore, the particles could be treated as defects within the spin-coated film and result in the charge carriers being trapped; recombination is then likely to follow a Shockley-Read-Hall, trap-assisted or surface recombination mechanism. Due to the nature of the composite material film, it is probable that surface recombination is occurring in these devices due to the small CCM values resulting in charge carriers travelling a small distance from the depletion region before recombining.

However, if the ΔI vs V plots are to be modelled with an exponential function as opposed to the second-order polynomial equation, the MoO_3/PDA device could undergo an Auger recombination like mechanism where a small proportion of any trapped charge carriers (produced under dark conditions) gain enough energy from a recombining charge carrier to be freed and collected at the electrode. In practice, this mechanism may only contribute to a small increase in ΔI.

Summary

Overall, it has been shown that upon successful intercalation of the polymer materials (as concluded in Section 4.1.2), the electrical and optoelectronic properties of the

new materials differ from those of the inorganic host MoO_3. The previously synthesised composite materials and the novel ones showed an increase in the room temperature electrical conductivity compared to the inorganic host with all the composite materials exhibiting p-type semiconductor properties. The intercalation of the polymers increases the room temperature conductivity by a minimum of one order of magnitude (MoO_3/2AmThia and MoO_3/An) and a maximum of four orders of magnitude (MoO_3/PDA). PDA was intercalated in its most conductive phase by design compared to the other intercalated polymers, and therefore it is likely that the extent of increased electrical and semiconducting properties (compared to the inorganic host) of the materials is due to the extent that the polymer is present in its conductive form. MoO_3/5AQ showed an increase of 3 orders of magnitude in its room temperature conductivity compared to the inorganic host. This increase could be due to the increased conjugation due to the presence of its fused ring system. The presence of the fused rings could further improve its redox chemistry with Mo leading to a more conductive polymer being present in the interlayer spacing. The lowest conductivity was that for MoO_3/An synthesised via recrystallization. It is suspected that the polyaniline intercalant is not in its most conductive form. Therefore, since all the composite materials (except MoO_3/An) were synthesised via ion-exchange it can be deduced that their conductive properties are dependent on the nature of the intercalated polymer (the degree to which it is in its conductive phase) which is dominant in determining the electrical and semiconducting properties of the overall composite material. This was further demonstrated by the Seebeck coefficient measurements in which the n-type property of MoO_3 changes upon intercalation and a positive Seebeck coefficient is seen relating to an overall p-type nature of the composite materials.

However, MoO_3/PDA not only showed the highest conductivity (~10^{-1} Sm^{-1}) but also exhibited the best semiconducting properties. MoO_3/PDA exhibited the highest N_d (~10^{14} cm^{-3} for Zn, Al and Cu contacts and ~10^{15} cm^{-3} with a Ni contact) irrespective of the

metal contact used for the Schottky device. As seen previously for the V_2O_5 composite materials, the evaporated and pressed Schottky device N_d values were shown to be within the same order of magnitude, showing that there was good intimate contact between the semiconducting material and the metal electrode. Due to ion-exchange and recrystallization synthesis utilised, the N_d values for these composite materials may be solely dependent on the amount of reduced Mo^{5+} present in the material formed from the Li^+, and more importantly formed from any redox chemistry between the organic intercalant and Mo^{n+}. Furthermore MoO_3/PDA and MoO_3/2A5PhPyr showed the most non-ohmic behaviour while the remaining composite materials showed a small deviation from the linear nature of the host's I-V plot (but were still noticeably non-ohmic). MoO_3/2A5PhPyr, however, did not show the large N_d (~10^{13} cm^{-3}) compared with MoO_3/PDA. The non-ohmic materials were generally modelled well using the non-ideal diode equation (Equation 4.1) determined from the calculated I_0 and n values with all n values being between 1 and 2.

In terms of prototype photosensitive devices, due to MoO_3/PDA exhibiting the most desirable conductive and semiconducting properties, it was selected for use in the prototype photosensitive device. The MoO_3/PDA Si device exhibited novel photosensitive effects, with an increase in current when illuminated under A.Light and Lamp conditions. It is clear that although the MoO_3 host is the limiting factor in terms of the material's overall electrical and semiconductor properties, the inclusion of a conducting polymer and partical doping is the cause for the photosensitivity in the MoO_3/PDA Si device.

From the ΔI vs V plots for the photosensitive device under A.light and Lamp conditions the estimated maximum device Eff was calculated (Table 4.33 and Figure 4.151). the photosensitive device exhibited an Eff up to ~1% under A.Light illumination and ~0.1% under Lamp illumination. Although this is an estimation of the maximum Eff the device could exhibit, it does provide a good indication of the true Eff as it the true

practical Eff of this un-optimised device would be expected to be much lower than the calculated value. It is possible that for a fully optimised device, the Eff may be similar to the calculated maximum Eff for the un-optimised device. It is, however, evident that there was a significant difference between the calculated device Eff values under A.Light and Lamp illumination. This suggested that the MoO_3/PDA composite material operated poorly around ~800nm and above and operating better within the blue visible light and near-UV regions of the electromagnetic spectrum.

In contrast to the room temperature conductivity and due to the un-optimised design of the photosensitive device, the MoO_3/PDA Si device showed poor photoconductivity ~10^{-11} Sm^{-1} (Table 4.34), related to the fact that the composite material was spin-coated onto the Si and thus the film obtained was comprised of discrete particles. This forced the photogenerated current to be conducted between particles. In relation to the entire film, its non-uniformity could be treated as defects caused by these particles and the unknown geometry. Thus, any conductive charge carriers produced by illumination may become trapped at the particle edges while attempting to move between these particles. This trapping may be sufficient to result in Shockley-Read-Hall, trap-assisted or surface recombination mechanisms. This was further seen in the calculated device CCM where the device exhibited a CCM of ~10^{-10} and ~10^{-11} $m^2V^{-1}s^{-1}$ under A.Light and Lamp illumination respectively. These low mobilities suggest that a large number of photogenerated charge carriers are recombined instead of being separated and collected at the electrodes. It is likely that the low mobilities are due to the charge carriers not effectively migrating between the discrete particles of the MoO_3/PDA spin-coated film leading to recombination. The mechanism of recombination, in this case, would likely be surface recombination between the substrate and the composite material.

4.2.3) $ZnPS_3$ Nanocomposite Materials

4.2.3.1) Room temperature electrical conductivity

Room temperature electrical conductivity

Table 4.35 - Room temperature conductivities for $ZnPS_3$ nanocomposite materials

Material	Conductivity, σ (Sm^{-1})
$ZnPS_3$	4.1×10^{-8}
$ZnPS_3$/PDA	3.5×10^{-3}

The room temperature conductivities measured at a temperature of ~293K shown in Table 4.35. The low $ZnPS_3$ conductivity corresponds to that of a wide-gap semiconductor. The $ZnPS_3$/PDA showed an increase in conductivity by five orders of magnitude compared to the $ZnPS_3$ host, which is mainly attributed to the presence of the polymer material. Unlike the cases of V_2O_5 and MoO_3 (where reduced Mo and V ions are present), $ZnPS_3$/PDA was synthesised using ion-exchange between Zn^{2+} ions in the host material and the organic guest cations. This loss of Zn^{2+} cations in the inorganic layers leaves behind positively-charged, immobile, localised vacancies. These vacancies are therefore unlikely to give rise to the increase in conductivity observed in the composite material. It is concluded that the major component contributing to the increase in the composite conductivity is the presence of the intercalated conducting polymer (as concluded in Section 4.1.3).

4.2.3.2) Schottky Device I-V curves

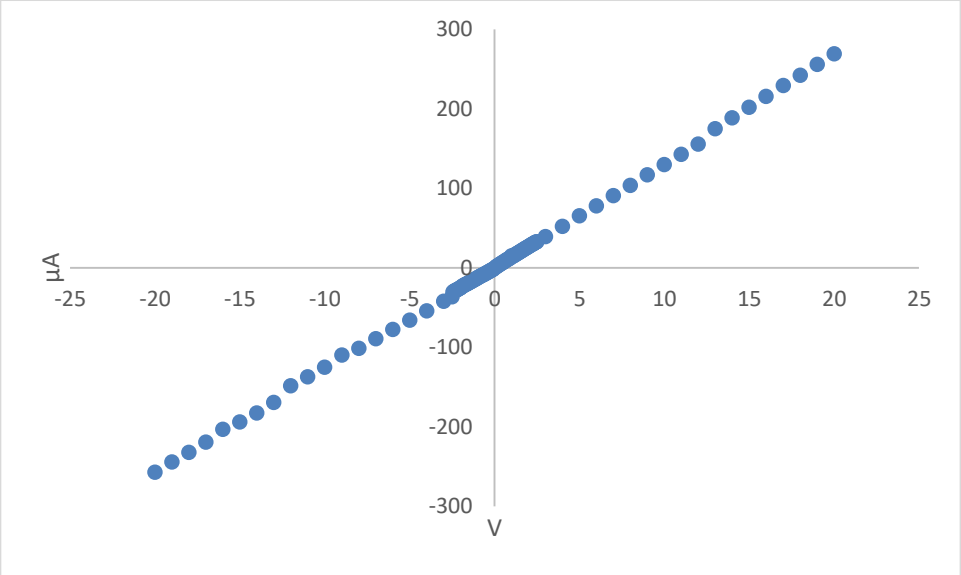

Figure 4.155 - I-V graph for $ZnPS_3$ with a Zn contact

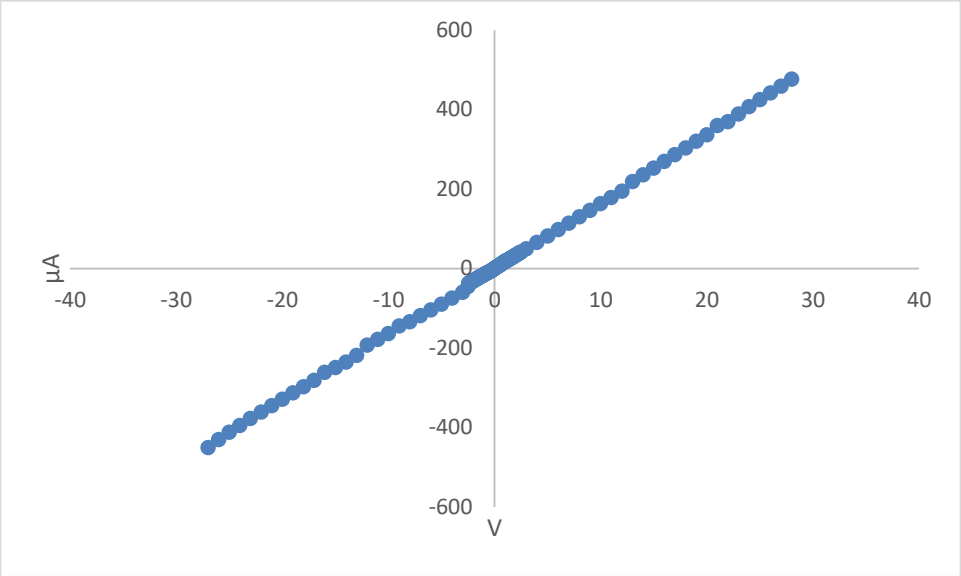

Figure 4.156 - I-V graph of $ZnPS_3$/PDA with Zn contact

Figure 4.155 and Figure 4.156 show the I-V plot for $ZnPS_3$ and the $ZnPS_3$/PDA composite with a Zn contact. Both devices exhibit ohmic behaviour.

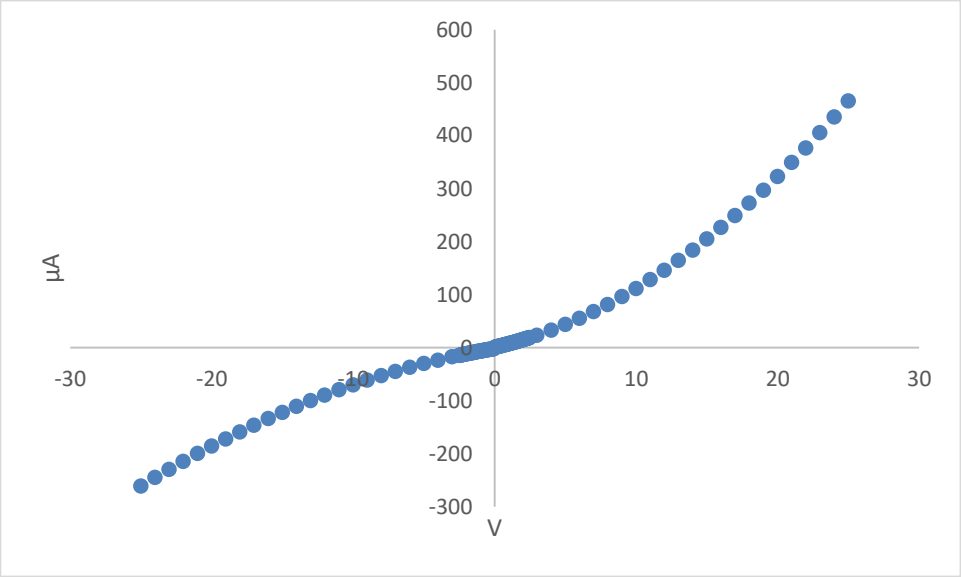

Figure 4.157 - I-V graph of $ZnPS_3$/PDA with a Cu contact

Figure 4.157 shows that the $ZnPS_3$/PDA device with a Cu contact exhibits rectifying behaviour with a rectification ratio of 1.78. This behaviour is different from that of the host $ZnPS_3$, which is probably due to the successful intercalation of the polymer into the interlayer space of $ZnPS_3$: therefore any changes in the I-V graphs are a result of the presence of the PDA polymer.

Using non-ideal diode equation (Equation 4.2) and the Schottky barrier height equation (Equation 4.3) to model the non-ohmic $ZnPS_3$/PDA device with a Cu contact, the I_0, n and Φ can be calculated and are shown in Table 4.36.

Table 4.36 - I_0, n and Φ values for the non-ohmic $ZnPS_3$/PDA Schottky device

Cu Contact	I_0 (µA)	n	Φ
$ZnPS_3$/PDA	4.4	1.66	0.64

Table 4.36 shows that the $ZnPS_3$/PDA device with a Cu contact is modelled well using the non-ideal diode equation. The ideality factor of 1.66 suggests there may be asymmetry between the electronic bands for excitation and/or recombination. It is therefore possible that the organic guest and inorganic host exhibit poor band overlap in the composite material, as suggested by the optical spectroscopy data (Table 4.11). The changes in the I-V plot from ohmic behaviour between the use of the Zn contact (Figure 4.156) and the Cu

contact (Figure 4.157) could be explained by suggesting that the Cu contact produces a Φ sufficiently large for a depletion region to be formed, allowing the $ZnPS_3$/PDA deivce to behave as a Schottky diode.

Furthermore, from the voltage-capacitance relationship (see Appendix C.4) for this device (using the average dielectric constant measured in Table 4.15) the dopant density for this device was calculated using Equation 4.6 and is shown in Table 4.37.

Table 4.37 - Dopant Density for the $ZnPS_3$/PDA Schottky device

Material	Contact	Dopant Density (N_d) (cm^{-3})
$ZnPS_3$/PDA	Cu	7.44E+14

Overall, the dopant density for this material is similar (in magnitude) to that for both the V_2O_5 and MoO_3 composite material devices. Since there is no reduction of the Zn^{2+} ions in the inorganic host, the Zn^{2+} vacancies and the presence of the conducting polymer intercalant (concluded to be in its protonated form in Section 4.1.3.2) are likely to be the contributing factors for the measured N_d.

However, the Zn^{2+} vacancies are expected to be immobile and the host material to exhibit non-stochiometry as a result of the synthetic method (as concluded from the ICP-AES and TGA data in Section 4.1.3.3). As a result, it is concluded that the Zn^{2+} vacancies and any non-stoichiometry would be small contributors to the electrical properties that $ZnPS_3$/PDA exhibits. The major contributing factor is expected to be the presence of the conducting polymer intercalant in the interlayer spacing.

4.2.3.3) Photosensitive devices

The prototype photovoltaic device was made by spin-coating the photoactive composite material onto n-type silicon with an ITO counter electrode. The constructed photosensitive device was illuminated under ambient light (A.Light) and under an incandescent lamp (Lamp)

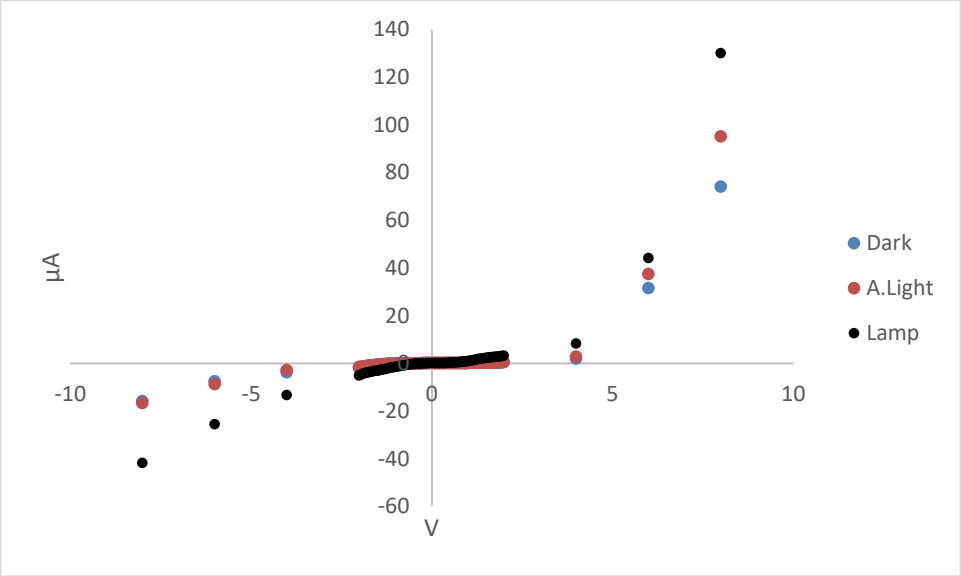

Figure 4.158 - I-V graph for $ZnPS_3$/PDA photovoltaic device under Dark, A.Light and Lamp conditions

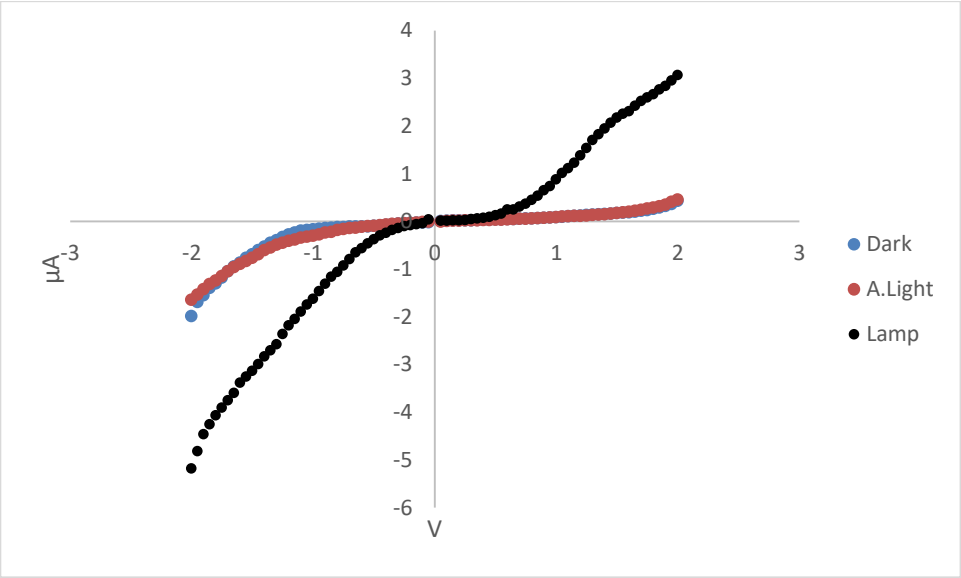

Figure 4.159 - I-V graph for $ZnPS_3$/PDA photovoltaic device under Dark, A.Light and Lamp conditions between -2V to 2V

Figure 4.158 and Figure 4.159 show the I-V curves for the $ZnPS_3$/PDA silicon photosensitive device. It is clear that the device exhibits rectifying behaviour. Between -2

V and 2 V (Figure 4.159) there is little no change between the dark and A.Light illuminated current. However, under Lamp conditions there is a significant increase in current where the device deviates from the behaviour seen under Dark and A.Light conditions. Below -2 V, the dark and A.Light currents appear to show little difference, while the current under Lamp conditions continues to decrease. Above 2 V however, both A.Light and Lamp conditions cause deviations from the dark current. Table 4.38 and Table 4.39 show the overall changes in current (ΔI).

Table 4.38 - Change in the current (ΔI) for Silicon $ZnPS_3$/PDA photovoltaic device between A.Light - Dark and Lamp - Dark conditions under forward bias

$ZnPS_3$/PDA									
Voltage (V)	**0.05**	**0.25**	**0.5**	**1**	**1.5**	**2**	**4**	**6**	**8**
ΔI (μA) A.Light - Dark	-0.01398	-0.0031	-0.00587	0.00223	0.0023	0.023	0.919	5.95	21.01
ΔI (μA) Lamp - Dark	0.000654	0.00327	0.08687	0.79334	2.0003	2.637	6.37	12.56	55.92

Table 4.39 - Change in the current (ΔI) for Silicon $ZnPS_3$/PDA photovoltaic device between A.Light - Dark and Lamp - Dark conditions under reverse bias

$ZnPS_3$/PDA									
Voltage (V)	**-0.05**	**-0.25**	**-0.5**	**-1**	**-1.5**	**-2**	**-4**	**-6**	**-8**
ΔI (μA) A.Light - Dark	0.0119	0.00394	0.0012	-0.133	-0.072	0.34	0.839	-1.243	-0.877
ΔI (μA) Lamp - Dark	0.06201	-0.0615	-0.2801	-1.455	-2.442	-3.19	-9.602	-17.95	-25.95

From Table 4.38 and Table 4.39, the power generated when the device is illuminated (P_{out}) as a function of voltage) can be calculated by multiplying ΔI by the voltage. Figure 4.160 and Figure 4.161 shows the power vs voltage plot for the $ZnPS_3$/PDA Si device. As previously seen for the V_2O_5 and MoO_3 composite materials (Sections 4.2.1.4) and 4.2.2.4) the device efficiency (Eff) at the maximum P_{out} can be determined from the P_{out} vs V plots.

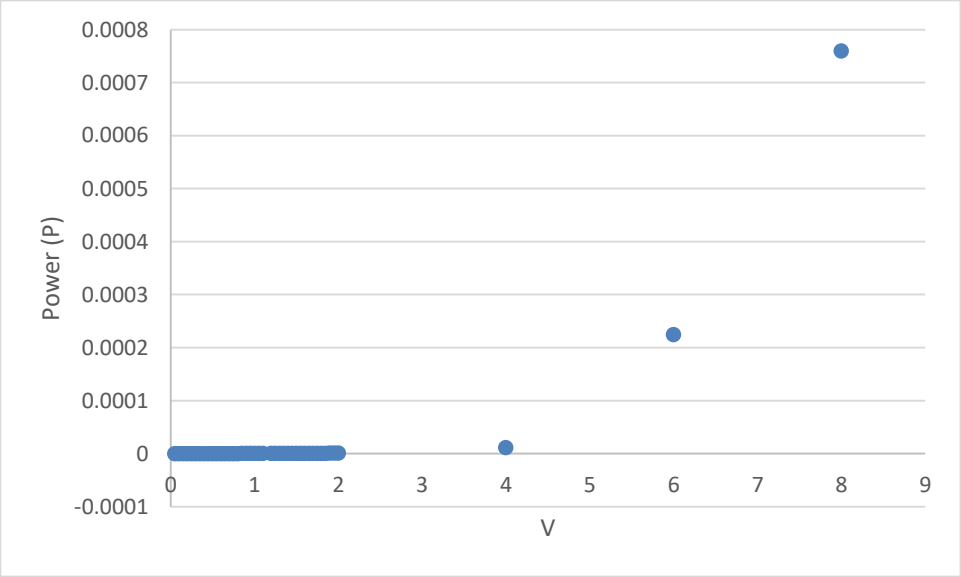

Figure 4.160 – The power vs voltage plot for $ZnPS_3$/PDA Si device under A.Light illumination

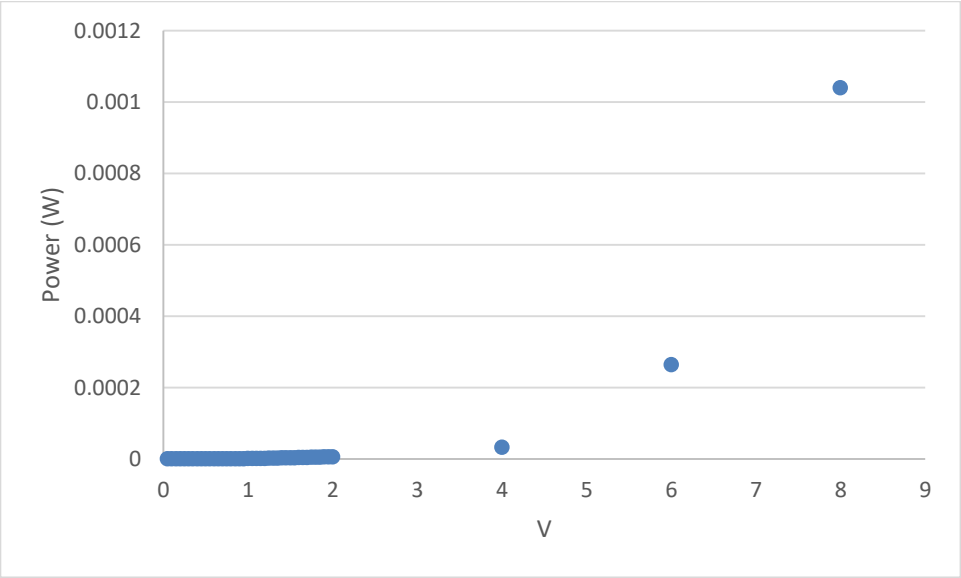

Figure 4.161 – The power vs voltage plot for $ZnPS_3$/PDA Si device under Lamp illumination

The Eff is calculated using Equation 4.7 where the total luminous power being input into the large silicon device is 0.15 W and 1.65 W for A.Light and Lamp illuminated conditions respectively (Table 4.23). Table 4.40 shows the calculated maximum efficiencies. It is noted that these are the efficiencies observed at the maximum voltage and may not represent the practical efficiencies of the device, which are expected to be lower than these value.

Table 4.40 – Calculated device Eff (%) for the $ZnPS_3$/PDA Si photosensitive device

Material	$ZnPS_3$/PDA
A.Light Illumination	
Max Power Volt	8
Max Power (W)	0.00076
Eff (%)	0.34
Lamp Illumination	
Max Power Volt	8
Max Power (W)	0.00104
Eff (%)	0.22

Unlike the cases for the V_2O_5 and MoO_3 composite materials (where there was a significant difference in Eff (%) between A.Light and Lamp conditions) the $ZnPS_3$/PDA device exhibits low Eff (%) under both A.Light and Lamp illumination. It is suspected that in the case for $ZnPS_3$/PDA, the poorly-conducting host material could be a limiting factor in transporting any charge carriers formed from photon absorption. It is also assumed that there is a uniform film of the active material in intimate contact with the Si substrate. Considering the non-optimised device architecture and construction (via spin-coating) and the insulating inorganic host, it is likely that any charge carriers formed may be recombined before being collected. Calculating the charge carrier mobility may provide a better picture.

Further analysis of the device ΔI vs V plots can provide information regarding the photoconductivities and CCM of the device. The ΔI vs V plots were modelled with a second-order polynomial (Equation 4.9) and an exponential function (Equation 4.10) seen previously in Section 4.2.1.4). As discussed in Section 4.2.1.4) and 4.2.2.4), the ΔI vs V plots showing a better fit to the second-order polynomial are favoured over the exponential equation. A ΔI vs V plot which fits an exponential function may be caused by a non-primary photocurrent caused by the release of trapped charge carriers.

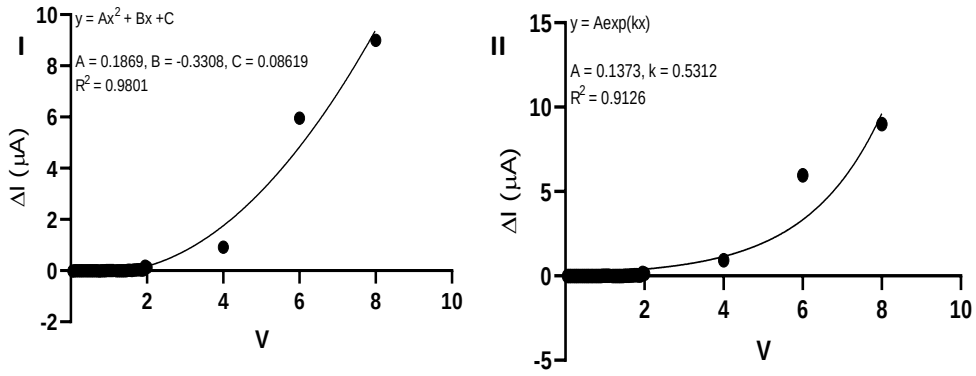

Figure 4.162 – ΔI vs V plot for $ZnPS_3$/PDA Si device under A.Light illumination where I) shows the second-order polynomial fit and II) shows the fit for an exponential curve

Figure 4.162.I and .II show the ΔI for the device illuminated under A.Light; the best fit occurs for the second-order polynomial function (R^2 = 0.9801) in Figure 4.162.I compared to the exponential fit (R^2 = 0.9126).

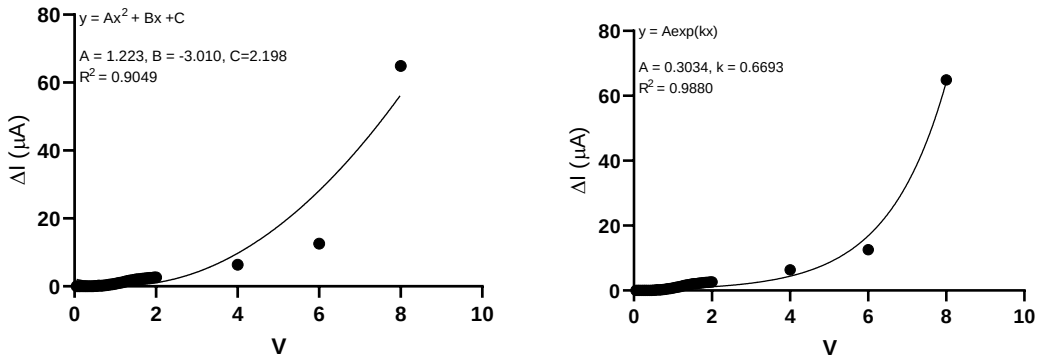

Figure 4.163 – ΔI vs V plot for $ZnPS_3$/PDA Si device under Lamp illumination where I) shows the second-order polynomial fit and II) shows the fit for an exponential curve

Figure 4.163.I and .II show ΔI for the device illuminated under Lamp illumination for both polynomial and exponential functions. Unlike Figure 4.162, the ΔI vs V plot shows a significantly better fit for the exponential function (R^2 = 0.9880) than for the second-order polynomial (R^2 = 0.9049).

From the fitted second-order polynomial (Figure 4.162) an estimated photoconductivity can be calculated using Equation 4.11. Table 4.41 shows the estimated

photoconductivity calculated for the $ZnPS_3$ device modelled using the second-order polynomial.

Table 4.41 – Photoconductivity of the $ZnPS_3$/PDA Si photosensitive device modelled using the second-order polynomial where σ_{obvs} is the calculated photocurrent from the I – V plot of the respective material's photosensitive device

Material	Δσ (Sm^{-1})	$\Delta\sigma/\sigma_{obvs}$
A.Light Illumination		
$ZnPS_3$/PDA	2.08E-11	0.087

The un-optimised device exhibits poor photoconductivity which may have an impact on the exhibited low Eff (Table 4.40). It is clear from the calculated photoconductivity and Eff that the factor limiting the photoactivity of the active material and the overall device Eff is likely to be recombination of the excitons being produced. The active material film coated on the Si substrate is made up of individual particles of the composite material and not a continuous uniform film. Therefore the mobility of the charge carriers that are being conducted through the composite material to the electrode is dependent on how efficiently the charge carriers are able to move between the composite particles. Therefore if the CCM is poor in the material, recombination is likely to occur. From the photoconductivity an estimated CCM can be calculated using Equation 4.13 (as previously described in Section 4.2.1.4). Table 4.42 shows the calculated CCM for the $ZnPS_3$/PDA Si photosensitive device.

Table 4.42 – The calculated CCM for the $ZnPS_3$/PDA Si photosensitive

Material	μ
A.Light Illumination	
$ZnPS_3$/PDA	2.07788E-11

It should be stated here that the calculated CCM is the minimum value calculated. The true practical value is expected to be higher than this. However, the estimated CCM provides

some indication regarding the active material and the creation of excitons and charge separation in the device. As discussed previously (in Sections 4.2.1.4) and 4.2.2.4), in comparison to optimised organic devices (285) the estimated CCM is concluded to be very low. When comparing the CCM with the Eff and photoconductivity of the $ZnPS_3$/PDA Si device, the calculated values suggest that recombination of charge carriers is dominant in this device. This is likely to be due to the un-optimised nature of the photosensitive device in which the photoactive material is spin-coated onto Si. The deposited film would be made up of individual particles as opposed to a continuous uniform film of the material. Any charge carriers formed by photoabsorption are required to migrate between the individual particles in order to be separated effectively, so that the particles could be treated as defects within the spin-coated film, which may result in the charge carriers becoming trapped at the particle edges. Recombination of the charge carriers is then likely to follow a Schockley-Read-Hall, trap-assisted or surface recombination mechanism. It is, more probable that the the small CCM value indicates that the charge carriers only travel a small distance away from the depletion region before recombining.

It was observed earlier that the ΔI vs V plot for the device under Lamp illumination fitted the exponential function better than the second-order polynomial. In this case, it is possible that Auger recombination mechanism is occurring where a small proportion of any trapped charge carriers, produced under dark conditions, gain enough energy from recombining charge carriers to be freed and collect at the electrode. In practice, this mechanism may only contribute to a small increase in the ΔI seen.

Summary

Overall, it has been shown that upon successful intercalation of the polymer material (as concluded in Section 4.1.3), the electrical and optoelectronic properties of $ZnPS_3$/PDA differ from those of the inorganic host $ZnPS_3$. $ZnPS_3$/PDA showed an increase

of 5 orders of magnitude in its room temperature conductivity compared to the inorganic host. Although the $ZnPS_3$/PDA is expected to contain vacant Zn^{2+} sites (due to the ion-exchange mechanism) leaving behind positive holes in the inorganic layers, these vacant sites would be immobile and unlikely to contribute to the increase in the conductivity. Therefore is it more likely that the increase in electrical conductivity is due to the presence of the PDA polymer that was intercalated in its conductive phase (as concluded in Section 4.1.3). The intercalated material had a N_d of ~7 x 10^{14} cm^{-3} which is of the same order of magnitude as for V_2O_5/PDA and MoO_3/PDA materials.

The presence of the intercalated polymer also affected the composite materials' semiconducting properties. The $ZnPS_3$ Schottky device exhibited ohmic properties, as did the $ZnPS_3$/PDA Schottky device using a Zn contact but it showed non-ohmic properties when a Cu contact was utilised. It may be that when the Cu contact was utilised, a sufficiently large barrier height was established which led to the formation of a depletion region between the composite material and the metal contact. The non-ohmic $ZnPS_3$/PDA Schottky device (with a Cu contact) was modelled well using Equation 4.1 (as described in Section 4.2.1.4) determined from the calculated I_0 and n values with the n value being between 1 and 2.

In terms of the prototype photosensitive device, the $ZnPS_3$/PDA Si device exhibited novel photosensitive effects with an increase in current (a generated photocurrent) when the device was illuminated under A.Light and Lamp conditions. It is clear that the inclusion of a conducting polymer (and the degree of its doping) are major factors for the observed photosensitivity in the device. From the ΔI vs V plots for the photosensitive device under A.light and Lamp conditions the estimated maximum device Eff was calculated (Table 4.40). The photosensitive device exhibited an Eff of 0.34% and 0.22% under A.Light and Lamp illumination respectively. These values are estimates of the maximum Eff of the device. For a fully optimised device, the Eff may well be closer in

value to the estimated maximum Eff for this un-optimised device. However, it is evident that unlike for the V_2O_5 and MoO_3 materials, $ZnPS_3$/PDA Si device exhibits a low Eff under both A.Light and Lamp illumination. This suggests that the device operates poorly around both the blue visible light and near UV regions (A.Light) and around ~800nm and above (Lamp) of the electromagnetic spectrum, and it may operate best at an intermediate wavelength.

The poor Eff is likely to be related to the photoconductivity and charge mobility of charge carriers in the device itself. In contrast to the room temperature conductivity, the $ZnPS_3$/PDA Si device showed a poor photoconductivity ~10^{-11} Sm^{-1} under A.Light illumination. It is expected that the major contributor to the poor photoconductivity is the non-optimised design of the photosensitive device. The composite material was spun-coat onto Si and thus the film obtained would be made up of discrete particles and as discussed earlier and lead to recombination. The CCM for the device was only ~10^{-11} $m^2V^{-1}s^{-1}$ under A.Light illumination, which suggests that a large number of photogenerated charge carriers are recombined as opposed to being separated and collected at the electrodes

5) Conclusion and Future Work

5.1) Conclusion

Overall, this work presents several novel inorganic-organic nanocomposites, new synthetic methods for previously synthesised materials and their novel applications in photosensitive devices.

This thesis reports the synthesis and complete characterisation of a range of novel organic-inorganic nanocomposite materials via intercalation chemistry. The nanocomposite materials were synthesised by inserting organic monomer compounds into a layered inorganic host via direct redox and ion-exchange mechanisms using an aqueous medium. Other green solvents can be explored where the intercalation mechanisms are unfavourable in the aqueous medium (e.g. if the organic guest species exhibits poor solubility in water). Alternative green solvents could include ketones (e.g. acetone and methyl ethyl ketone for redox reactions), alcohols (e.g. ethanol and isopropanol or both redox and ion-exchange reactions) and ethyl acetate (for redox reactions) (287). The guest monomer species were polymerised in-situ to afford the organic-inorganic nanocomposite materials. The results obtained in this thesis demonstrate a novel proof-of-concept for the potential of organic-inorganic nanocomposites as low-cost active materials in photosensitive devices.

The direct intercalation method obtained the previously synthesised V_2O_5/AnAn$^+$ (redox reaction using a novel method), V_2O_5/EDOT (redox reaction) and MoO_3/An (recrystallization using a novel method) nanocomposite materials and the novel V_2O_5/2A5PhPyr (acid-base reaction) material. The novel method of intercalating both neutral aniline and the cationic aniline sulphate was demonstrated to be successful and afforded results comparable to that of earlier work (see Section 1.5.1) for intercalating emeraldine into V_2O_5. However c-axial defects were found to be prevalent in all

nanocomposites synthesised via direct intercalation. Upon intercalation, a redox reaction facilitated the polymerisation of the organic monomer guest species. A novel acid-base reaction between V_2O_5 and 2A5PhPyr was shown to successfully intercalate and polymerise the monomer guest species within the interlayer space of V_2O_5. A novel method for aniline intercalation into MoO_3 was further demonstrated in which an aqueous solution of MoO_3 was shown to regrow around the aniline guest species. This intercalation allowed for in-situ polymerisation to occur.

The ion-exchange of $Li_XV_2O_5$, Li_xMoO_3 and Mg_xZnPS_3 with various organic cations afforded the novel nanocomposite materials: V_2O_5/PDA, V_2O_5/2A5PhPyr, V_2O_5/5AQ, V_2O_5/1,4PDA-HQ, MoO_3/PDA, MoO_3/2A5PhPyr, MoO_3/5AQ, MoO_3/2AmThia and $ZnPS_3$/PDA. The ion-exchange method was found to result in fewer c-axial defects when compared to direct intercalation methods. Upon intercalation of the organic guests into V_2O_5 and MoO_3 host materials, in-situ polymerisation via a redox reaction occurred between the organic guest and inorganic host. An external oxidant (APS) was required to facilitate the polymerisation of PDA in $ZnPS_3$ to afford the polymerised guest.

The general trend was that upon intercalation of the polymer into the inorganic host layers there were striking improvements in electrical properties (e.g. room temperature conductivity, semiconductor property, Schottky device I-V character and photosensitive device properties) compared to the host material. The nanocomposites were shown to exhibit p-type semiconductor properties compared to the n-type properties of their inorganic parent compounds. It was concluded that the presence of the polymer in the inorganic host leads to these observed changes. The specific polymer (and whether the polymer was designed to be present in its protonated or conductive form) and the degree of doping, in the nanocomposite material as a whole, appeared to correlate with the extent of improvement of the electrical and device properties. This was shown particularly for

$AnAn^+$ and PDA (which were designed to be in their most conductive forms upon intercalation) where the nanocomposites of these polymers produced the most conductive materials and exhibited the best device properties irrespective of the inorganic host.

From the synthesised nanocomposite materials, $V_2O_5/AnAn^+$, V_2O_5/EDOT, V_2O_5/2A5PhPyr, MoO_3/PDA and $ZnPS_3$/PDA showed the best semiconducting properties and were selected for the investigation of their applications in photosensitive devices. The non-optimised silicon and $FePS_3$ devices exhibited an increase in the illuminated current under both ambient light and an incandescent lamp. The average estimated maximum device efficiencies were 0.71% and 0.26% under daylight and the incandescent lamp respectively. The devices were shown to perform more efficiently under ambient light and it was concluded that these devices absorbed light from mostly the blue to the near-UV region of the solar spectrum. As a consequence, they exhibited poor efficiencies under higher wavelength visible light to IR regions of the solar spectrum. The estimated minimum charge mobility's for the devices were shown to be 8.26×10^{-10} $m^2V^{-1}s^{-1}$ and 3.38×10^{-11} $m^2V^{-1}s^{-1}$ under ambient light and the incandescent lamp respectively. The devices exhibited poor charge mobilities with the excitons produced presumed to more likely be recombined than separated and collected at the electrodes. However, due to the non-optimised nature of the devices, it is difficult to determine the amount of nanocomposite in intimate contact with the silicon or $FePS_3$ contacts utilised in the photosensitive devices as well as the geometry of the nanocomposites (at the interface with the silicon or $FePS_3$). Furthermore, it was assumed in these calculations that all of the photons are being absorbed by the device and creating an exciton, in a more realistic model it may be likely that only a small fraction of the photons are absorbed by the device. Taking this into account, the true device efficiencies are expected to be lower than the estimated values calculated but the photoconductive properties and charge mobilities of the

nanocomposite materials in the device structure are likely to be significantly larger than the estimated values calculated.

The methods used for the synthesis of the nanocomposite materials can be extended to other host structures. For example, the ion-exchange mechanism could be useful if the inorganic host does not undergo the desirable redox chemistry. The ion-exchange mechanism can be extended to other members of the metal oxides, MPX_3 and MX_2 families with varying band-gap and band structures allowing for the tunability of the nanocomposite properties. The nanocomposite materials showed promising novel photosensitive and photoconductive properties in the non-optimised photosensitive devices. This has opened the door and much ground is still left for greater exploration in the development of low-cost organic-inorganic nanocomposites as photovoltaic materials.

5.2) Future Work

This study has demonstrated that there is a bright future for the use of organic-inorganic nanocomposites in photovoltaic and other optoelectronic applications, however, their full potential is yet to be realised. Although the work presented in this thesis has provided a proof-of-concept, showing that these nanocomposite materials may indeed overcome the drawbacks of both the organic and inorganic materials alone, there is still much ground left to explore. Future work based on that presented in this thesis has been grouped under two categories; material optimisation and device optimisation.

5.1.1) Material Optimisation

It is clear that the choice of the inorganic host material plays an important role in the physical and electrical properties of the material. In particular, the choice of inorganic host material can limit the overall electrical and device properties of the nanocomposite. The

use of insulating/poorly semiconducting host materials may have been a limiting factor in the nanocomposites electrical and device properties and therefore not completely ideal as host materials. These materials exhibited an increase in the band-gap of the overall material as such, photon absorption occurred in the higher energy regions of the visible light spectrum. This limited the materials efficiencies and photoconductivity when constructed as part of a device.

A possible strategy to overcome this would be to investigate nanocomposite materials which utilise a layered inorganic host that is an excellent semiconducting material with a low band-gap (such as $NiPS_3$). Such inorganic hosts may exhibit better electronic interaction with their organic guest species leading to a lowering of the band-gap, allowing for the material to access a wider range of wavelengths for photon absorption. On the other hand, if the band-gap increases upon intercalation as a general trend, the resulting increased band-gaps may still be small enough to maximise the absorption of the solar spectrum at the Earth's surface.

A further study into the particular mechanism of the interactions within the nanocomposite materials is also required to build a more fundamental understanding of energy transfer, the production and mobilities of excitons created from photon absorption. It is unclear whether the organic guest is solely responsible for the production of excitons or whether there is an interplay between the guest and host species. Such fundamental understanding would allow for a better selection of the host and guest species in order to tune the resulting nanocomposites materials for photovoltaic applications.

5.1.2) Device Optimisation

A clear unknown factor in the work presented lies in the relationship between the silicon/$FePS_3$ substrate and the active material due to the spin coating method utilised for

nanocomposite deposition. As such the geometry of the nanocomposite materials, the true surface coverage and total photon absorption are unknown. Poor geometry of the nanocomposite materials at the interface between the nanocomposites and the substrates maximises any avoidable exciton recombination.

It is, therefore, important to develop a method to optimise device construction such that the nanocomposites are a single uniform film of known thickness on the selected substrate. This may be achieved via molecular beam deposition or vacuum deposition of each component (inorganic and organic alternatively) separately. The presence of an as-close-to-perfect single uniform film of the nanocomposite would help to minimise avoidable exciton recombination occurring by limiting recombination sites and more importantly minimising defects which would result in exciton trapping and recombination. Furthermore, it would allow for sufficient probing into the particular exciton recombination mechanism present in these heterojunction like devices.

It is also clear that the devices are required to be illuminated under known wavelengths to be certain of the exact absorption wavelength range and the degree of light which is reflected back to build a model to determine the facte of charge carriers and their mobilities through the material.

Bibliography

1. Goetzberger A, Hebling C, Schock H-W. Photovoltaic materials, history, status and outlook. Mater Sci Eng R Reports [Internet]. 2003;40(1):1–46. Available from: http://linkinghub.elsevier.com/retrieve/pii/S0927796X0200092X
2. Kannan N, Vakeesan D. Solar energy for future world: - A review. Renew Sustain Energy Rev. 2016;62:1092–105.
3. Pandey J. Solar Cell Harvesting: Green Renewable Technology of Future. Int J Adv Res Eng Appl Sci. 2015;4(11):93–103.
4. Jenkins N, Ekanayake J. Renewable Energy Engineering. 1st ed. Cambridge University Press; 2017. 2-7 p.
5. Donovan CW. Renewable Energy finance: Powering The Future. Imperial College Press; 2015. 17-47 p.
6. Sharma S, Jain KK, Sharma A. Solar Cells: In Research and Applications—A Review. Mater Sci Appl [Internet]. 2015;06(12):1145–55. Available from: http://www.scirp.org/journal/doi.aspx?DOI=10.4236/msa.2015.612113
7. De Wolf S, Descoeudres A, Holman ZC, Ballif C. High-efficiency Silicon Heterojunction Solar Cells: A Review. Green [Internet]. 2012;2(1):7–24. Available from: https://www.degruyter.com/view/j/green.2012.2.issue-1/green-2011-0018/green-2011-0018.xml
8. Sampaio PGV, Gonzalez MOA. Photovoltaic solar energy: Conceptual framework. Renew Sustain Energy Rev. 2017;74(June 2016):590–601.
9. Kim J, Rivera JL, Meng TY, Laratte B, Chen S. Review of life cycle assessment of nanomaterials in photovoltaics. Sol Energy [Internet]. 2016;133:249–58. Available from: http://dx.doi.org/10.1016/j.solener.2016.03.060
10. Stolle CJ, Harvey TB, Korgel BA. Nanocrystal photovoltaics: A review of recent progress. Curr Opin Chem Eng [Internet]. 2013;2(2):160–7. Available from:

http://dx.doi.org/10.1016/j.coche.2013.03.001

11. Coakley KM, McGehee MD. Conjugated polymer photovoltaic cells. Chem Mater. 2004;16(23):4533–42.

12. Spanggaard H, Krebs FC. A brief history of the development of organic and polymeric photovoltaics. Sol Energy Mater Sol Cells. 2004;83(2–3):125–46.

13. Green MA, Bremner SP. Energy conversion approaches and materials for high-efficiency photovoltaics. Nat Mater [Internet]. 2016;16(1):23–34. Available from: http://dx.doi.org/10.1038/nmat4676

14. Chen G, Seo J, Yang C, Prasad PN. Nanochemistry and nanomaterials for photovoltaics. Chem Soc Rev. 2013;42(21):8304–38.

15. Letcher TM, Fthenakis VM. A comprehensive Guide to Solar energy Systems: With special Focus On Photovoltaic Systems. 1st ed. Academic Press; 2018.

16. Wenham SR. Applied Photovoltaics. Earthscan; 2007. 35-36 p.

17. K. Schroder D. Semicondcutor Material and Device Characterization. 3rd ed. John Wiley & Sons; 2015. 390-411 p.

18. Landsberg PT. A review of recombination mechanisms in semiconductors. Inst Electr Eng. 1959;908–14.

19. Aspnes DE. Recombination at semiconductor surfaces and interfaces. Surf Sci. 1983;132(1–3):406–21.

20. Green MA. The Path to 25% Silicon Solar Cell Efficiency: History of Silicon Cell Evolution. J Optoelectron Res Appl. 2009;17:183–9.

21. Shah A V., Schade H, Vanecek M, Meier J, Vallat-Sauvain E, Wyrsch N, et al. Thin-film silicon solar cell technology. Prog Photovoltaics Res Appl [Internet]. 2004;12(23):113–42. Available from: http://doi.wiley.com/10.1002/pip.533

22. Garnett E, Yang P. Light trapping in silicon nanowire solar cells. Nano Lett. 2010;10(3):1082–7.

23. Meng T. Inorganic Photovoltaic Solar Cells: Silicon and Beyond. Electrochem Soc Interface

[Internet]. 2008;17(c):30–5. Available from: http://scholar.google.com/scholar?hl=en&btnG=Search&q=intitle:Inorganic+Photovoltaic+Solar+Cells:+Silicon+and+Beyond#0

24. Kolny-Olesiak J, Weller H. Synthesis and application of colloidal CuInS2 semiconductor nanocrystals. ACS Appl Mater Interfaces. 2013;5(23):12221–37.

25. Aldakov D, Lefrançois A, Reiss P. Ternary and quaternary metal chalcogenide nanocrystals: Synthesis, properties and applications. J Mater Chem C. 2013;1(24):3756–76.

26. Habas SE, Platt HAS, Hest MFAM Van, Ginley DS. Low-Cost Inorganic Solar Cells : From Ink To Printed Device. Chem Rev. 2010;110:6571–94.

27. Jackson P, Harikos D, Lotter E, Paetel S, Wuerz R, Menner R, et al. New world record efficiency for Cu(In,Ga)Se2 thin film solar cells beyond 20%. J Optoelectron Adv Mater. 2011;19:894–7.

28. Singh A, Geaney H, Laffir F, Ryan KM. Colloidal Synthesis of Wurtzite Cu_2ZnSnS_4 Nanorods and Their Perpendicular Assembly. J Am Chem Soc [Internet]. 2012;134(6):2910–3. Available from: http://pubs.acs.org/doi/10.1021/ja2112146

29. Woo K, Kim Y, Moon J. A non-toxic, solution-processed, earth abundant absorbing layer for thin-film solar cells. Energy Environ Sci. 2012;5(1):5340–5.

30. Guo Q, Hillhouse HW, Agrawal R. Synthesis of Cu 2 ZnSnS 4 Nanocrystal Ink and Its Use for Solar Cells. J Am Chem Soc [Internet]. 2009;131(33):11672–3. Available from: http://www.ncbi.nlm.nih.gov/pubmed/19722591%5Cnhttp://pubs.acs.org/doi/abs/10.1021/ja904981r

31. Green MA. Third generation photovoltaics: Solar cells for 2020 and beyond. Phys E Low-Dimensional Syst Nanostructures. 2002;14(1–2):65–70.

32. Hoppe H, Sariciftci NS. Organic solar cells: An overview. J Mater Res. 2004;19(7):1924–45.

33. Miles RW, Zoppi G, Forbes I. Inorganic photovoltaic cells. Mater Today [Internet]. 2007;10(11):20–7. Available from: http://dx.doi.org/10.1016/S1369-7021(07)70275-4

34. Green M a. Thin-film solar cells: Review of materials, technologies and commercial status. J

Mater Sci Mater Electron. 2007;18(SUPPL. 1):15–9.

35. Ki W, Hillhouse HW. Earth-abundant element photovoltaics directly from soluble precursors with high yield using a non-toxic solvent. Adv Energy Mater. 2011;1(5):732–5.

36. Wohrle D, Meissner D, Liman C. Organic Solar Cells. Adv Mater. 1991;3(3):36420367.

37. Kippelen B, Brédas J-L. Organic photovoltaics. Energy Environ Sci. 2009;2(3):251.

38. Zhan X, Zhu D. Conjugated polymers for high-efficiency organic photovoltaics. Polym Chem. 2010;1(4):409–19.

39. Po R, Bianchi G, Carbonera C, Pellegrino A. “all that glisters is not gold”: An analysis of the synthetic complexity of efficient polymer donors for polymer solar cells. Macromolecules. 2015;48(3):453–61.

40. Cheng YJ, Yang SH, Hsu CS. Synthesis of Conjugated Polymers for Organic Solar Cell Applications. Chem Rev. 2009;109(11):5868–923.

41. Zhou H, Yang L, You W. Rational design of high performance conjugated polymers for organic solar cells. Macromolecules. 2012;45(2):607–32.

42. Facchetti A. Polymer donor-polymer acceptor (all-polymer) solar cells. Mater Today [Internet]. 2013;16(4):123–32. Available from: http://dx.doi.org/10.1016/j.mattod.2013.04.005

43. Bundgaard E, Krebs FC. Low band gap polymers for organic photovoltaics. Sol Energy Mater Sol Cells. 2007;91(11):954–85.

44. Sun B, Hong W, Yan Z, Aziz H, Li Y. Record High Electron Mobility of 6.3 $cm^2 V^{-1} s^{-1}$ Achieved for Polymer Semiconductors Using a New Building Block. Adv Mater [Internet]. 2014;26(17):2636–42. Available from: http://doi.wiley.com/10.1002/adma.201305981

45. Holliday S, Donaghey JE, McCulloch I. Advances in charge carrier mobilities of semiconducting polymers used in organic transistors. Chem Mater. 2014;26(1):647–63.

46. Segawa Y, Maekawa T, Itami K. Synthesis of extended π-systems through C-H activation. Angew Chemie - Int Ed. 2015;54(1):66–81.

47. Fitzner R, Mena-Osteritz E, Mishra A, Schulz G, Reinold E, Weil M, et al. Correlation of π-

conjugated oligomer structure with film morphology and organic solar cell performance. J Am Chem Soc. 2012;134(27):11064–7.

48. Li Y. Molecular design of photovoltaic materials for polymer solar cells: Toward suitable electronic energy levels and broad absorption. Acc Chem Res. 2012;45(5):723–33.

49. Mishra A, Bäuerle P. Small molecule organic semiconductors on the move: Promises for future solar energy technology. Angew Chemie - Int Ed. 2012;51(9):2020–67.

50. Kim BG, Ma X, Chen C, Ie Y, Coir EW, Hashemi H, et al. Energy level modulation of HOMO, LUMO, and band-gap in conjugated polymers for organic photovoltaic applications. Adv Funct Mater. 2013;23(4):439–45.

51. Ameri T, Khoram P, Min J, Brabec CJ. Organic ternary solar cells: A review. Adv Mater. 2013;25(31):4245–66.

52. Guo X, Facchetti A, Marks TJ. Imide- and amide-functionalized polymer semiconductors. Chem Rev. 2014;114(18):8943–9012.

53. Journal I. Review Article Review of Polymer , Dye- Sensitized , and Hybrid Solar Cells. Int J Photoenergy. 2014;2014(August 2016).

54. Mayer AC, Scully SR, Hardin BE, Rowell MW, McGehee MD. Polymer-based solar cells. Mater Today [Internet]. 2007;10(11):28–33. Available from: http://dx.doi.org/10.1016/S1369-7021(07)70276-6

55. Helgesen M, Søndergaard R, Krebs FC. Advanced materials and processes for polymer solar cell devices. J Mater Chem. 2010;20(1):36–60.

56. Lin Y, Zhan X. Oligomer Molecules for Efficient Organic Photovoltaics. Acc Chem Res. 2016;49(2):175–83.

57. Sathiyan G, Sivakumar EKT, Ganesamoorthy R, Thangamuthu R, Sakthivel P. Review of carbazole based conjugated molecules for highly efficient organic solar cell application. Tetrahedron Lett [Internet]. 2016;57(3):243–52. Available from: http://dx.doi.org/10.1016/j.tetlet.2015.12.057

58. Facchetti A. π-Conjugated polymers for organic electronics and photovoltaic cell

applications. Chem Mater. 2011;23(3):733–58.

59. Takimiya K, Shinamura S, Osaka I, Miyazaki E. Thienoacene-based organic semiconductors. Adv Mater. 2011;23(38):4347–70.

60. Hains AW, Liang Z, Woodhouse MA, Gregg BA. Molecular semiconductors in organic photovoltaic cells. Chem Rev. 2010;110(11):6689–735.

61. Kawano K, Pacios R, Poplavskyy D, Nelson J, Bradley DDC, Durrant JR. Degradation of organic solar cells due to air exposure. Sol Energy Mater Sol Cells. 2006;90(20):3520–30.

62. Jørgensen M, Norrman K, Krebs FC. Stability/degradation of polymer solar cells. Sol Energy Mater Sol Cells. 2008;92(7):686–714.

63. Lizin S, Van Passel S, De Schepper E, Maes W, Lutsen L, Manca J, et al. Life cycle analyses of organic photovoltaics: A review. Energy Environ Sci. 2013;6(11):3136–49.

64. Jørgensen M, Norrman K, Gevorgyan SA, Tromholt T, Andreasen B, Krebs FC. Stability of polymer solar cells. Adv Mater. 2012;24(5):580–612.

65. Nicolosi V, Chhowalla M, Kanatzidis MG, Strano MS, Coleman JN. Liquid exfoliation of layered materials. Science (80-). 2013;340(6139).

66. Chernova NA, Roppolo M, Dillon AC, Whittingham MS. Layered vanadium and molybdenum oxides: Batteries and electrochromics. J Mater Chem. 2009;19(17):2526–52.

67. Nazri GA, Thackeray M, Ohzuku T. Intercalation compounds for battery materials. 2000. 23-26 p.

68. Zaghib K, Julien CM, Prakash J. New Trends in Intercalation Compounds for Energy Storage and Conversion. 2003. 505-506 p.

69. El-Desoky MM, Ibrahim FA. Synthesis, structural and transport properties of Li-doped molybdenum and vanadium oxide nanocrystalline films. J Sol-Gel Sci Technol. 2011;59(3):629–34.

70. Al-assiri MS, El-desoky MM, Alyamani A, Al-hajry A, Al-mogeeth A, Bahgat AA. Spectroscopic study of nanocrystalline V2O5.nH2O films doped with Li ions. Opt Laser Technol [Internet]. 2010;42(6):994–1003. Available from:

http://dx.doi.org/10.1016/j.optlastec.2010.01.020

71. Passerhi S, Smyrl WH, Berrettonib M, Tossicib R, Rosolenb M, Marassib R, et al. XAS and electrochemical characterization of lithium intercalated. Solid State Ionics. 1996;90:5–14.

72. Rocquefelte X, Boucher F, Gressier P, Ouvrard G. First-principle study of the intercalation process in the LixV2O5 system. Chem Mater. 2003;15(9):1812–9.

73. Wang Y, Shang H, Chou T, Cao G. Effects of thermal annealing on the Li(+) intercalation properties of V(2)O(5) x nH(2)O xerogel films. J Phys Chem B. 2005;109(22):11361–6.

74. Ibris N, Salvi AM, Liberalore M, Decker F, Surca A. XPS study of the Li intercalation process in sol-gel-produced v 2O5 thin film: Influence of substrate and film synthesis modification. Surf Interface Anal. 2005;37(12):1092–104.

75. Światowska-Mrowiecka J, Maurice V, Zanna S, Klein L, Marcus P. XPS study of Li ion intercalation in V2O5thin films prepared by thermal oxidation of vanadium metal. Electrochim Acta. 2007;52(18):5644–53.

76. He C, Su DS, Zandbergen HW, Tiemeijer PC, Kothleitner G, Ha M, et al. High resolution EELS using monochromator and high performance spectrometer : comparison of V 2 O 5 ELNES with NEXAFS and band structure calculations. Micron. 2003;34:235–8.

77. Khyzhun OY, Strunskus T, Gr W, Ch W. Valence band electronic structure of V 2 O 5 as determined by resonant soft X-ray emission spectroscopy. J Electron Spectros Relat Phenomena. 2005;149:45–50.

78. Wu Q. Resonant photoemission spectroscopy study of electronic structure of V 2 O 5. Chem Phys Lett. 2006;430:309–13.

79. Baddour-Hadjean R, Pereira-Ramos JP, Navone C, Smirnov M. Raman Microspectrometry Study of Electrochemical Lithium Intercalation into Sputtered Crystalline V 2 O 5 Thin Films. Chem Mater [Internet]. 2008;20(5):1916–23. Available from: http://pubs.acs.org/doi/abs/10.1021/cm702979k

80. Le DB, Passerini S, Coustier F, Guo J, Soderstrom T, Owens BB, et al. Intercalation of Polyvalent Cations into V 2 O 5 Aerogels. Chem Mater [Internet]. 1998;10(3):682–4.

Available from: http://pubs.acs.org/doi/abs/10.1021/cm9705101

81. Gershinsky G, Yoo HD, Gofer Y, Aurbach D. Electrochemical and spectroscopic analysis of Mg2+intercalation into thin film electrodes of layered oxides: V2O5 and MoO3. Langmuir [Internet]. 2013;29(34):10964–72. Available from: http://pubs.acs.org/doi/10.1021/la402391f

82. Mady HA, Negm SE, Moghny ASA, Abd-Rabo AS, Bahgat AA. Study of optical properties of highly oriented nanocrystalline V2O5·nH2O films doped with K ions. J Sol-Gel Sci Technol [Internet]. 2012;62(1):18–23. Available from: http://link.springer.com/10.1007/s10971-012-2675-0

83. Chandrappa GT, Chithaiah P, Ashoka S, Livage J. Morphological evolution of (NH4)0.5V 2O 5.mH2O fibers into belts, triangles, and rings. Inorg Chem. 2011;50(16):7421–8.

84. Trikalitis PN, Petkov V, Kanatzidis MG. Structure of redox intercalated (NH4)0.5V2o5·mH2O xerogel using the pair distribution function technique. Chem Mater. 2003;15(17):3337–42.

85. Oriakhi CO. Polymer Nanocomposition Approach to Advanced Materials. J Chem Educ [Internet]. 2000;77(9):1138. Available from: http://pubs.acs.org/doi/abs/10.1021/ed077p1138

86. Hagrman PJ, Finn RC, Zubieta J. Molecular manipulation of solid state structure: Influences of organic components on vanadium oxide architectures. Vol. 3, Solid State Sciences. 2001. p. 745–74.

87. Kuawahara T, Tagaya H, Kadokawa J. Intercalation of organic dyes in the layered host lattice V2O5. Inorg Chem Commun [Internet]. 2001;4(3):63–5. Available from: https://apps.webofknowledge.com/full_record.do?product=UA&search_mode=GeneralSearch&qid=120&SID=W24cjizKNnZuYToKOrY&page=1&doc=1

88. Liu P, Wang B, Sun X, Gentle I, Zhao XS. A comparative study of V2O5 modified with multi-walled carbon nanotubes and poly(3,4-ethylenedioxythiophene) for lithium-ion batteries. Electrochim Acta [Internet]. 2016;213:557–64. Available from: http://dx.doi.org/10.1016/j.electacta.2016.07.132

89. Shan Y, Huang RH, Huang SD. A New Route to Organic Intercalates Consist- ing of Vanadium Pentoxide and Pyridines: (4-H2 N-C5 H5NH)V2O5. Angew Chemie - Int Ed. 1999;12(38):1751–4.

90. Lai K, Kong A, Yang F, Chen B, Ding H, Shan Y, et al. Intercalation of alkylviologen dications into the layered vanadium pentoxide. Inorganica Chim Acta. 2006;359(4):1050–4.

91. De Oliveira RS, Alves WA, Ponzio EA. Spectroelectrochemical study of the hybrid between vanadium oxide and carboxybenzylviologen for application in electrochromic electrodes. ECS Trans [Internet]. 2012;43(1):363–9. Available from: http://dx.doi.org/http://dx.doi.org/10.1149/1.4704979

92. Chen Y, Yang G, Zhang Z, Yang X, Hou W, Zhu JJ. Polyaniline-intercalated layered vanadium oxide nanocomposites - One-pot hydrothermal synthesis and application in lithium battery. Nanoscale. 2010;2(10):2131–8.

93. Jagtap MA, Kulkarni M V, Apte SK, Naik SD, Kale BB. Microwave-assisted hydrothermal synthesis and characterization of tremella-like polyaniline – vanadium oxide nanocomposite nanosheets. Mater Sci Eng B [Internet]. 2010;168(1–3):199–203. Available from: http://dx.doi.org/10.1016/j.mseb.2010.01.016

94. Quites FJ, Bisio C, Cássia R De, Vinhas G, Landers R, Marchese L, et al. Vanadium oxide intercalated with polyelectrolytes: Novel layered hybrids with anion exchange properties. J Colloid Interface Sci [Internet]. 2012;368(1):462–9. Available from: http://dx.doi.org/10.1016/j.jcis.2011.11.013

95. Soltane L, Sediri F. Hydrothermal synthesis, characterization and electrical investigation of poly (para-phenylenediamine)/ vanadium oxide nanocomposite nanosheets. Mater Sci Eng B [Internet]. 2013;178(8):502–10. Available from: http://dx.doi.org/10.1016/j.mseb.2013.02.005

96. Soltane L, Sediri F. Hydrothermal synthesis and characterization of mesoporous rod-like hybrid organic-inorganic nanocrystalline based vanadium oxide. Ceram Int [Internet]. 2014;40(1):1531–8. Available from: http://dx.doi.org/10.1016/j.ceramint.2013.07.039

97. Nefzi H, Sediri F. Vanadium oxide nanourchins : Hydrothermal synthesis , characterization , frequency dependent electrical properties. Ceram Int [Internet]. 2015;41(1):1391–9. Available from: http://dx.doi.org/10.1016/j.ceramint.2014.09.072

98. Rojas-Cervantes ML, Casal B, Aranda P, Savirón M, Galvaán JC, Ruiz-Hitzky E. Hybrid materials based on vanadium pentoxide intercalation complexes. Colloid Polym Sci. 2001;279(10):990–1004.

99. Sengodu P, Deshmukh AD. Conducting polymers and their inorganic composites for advanced Li-ion batteries: A review. RSC Adv. 2015;5(52):42109–30.

100. Livage J. Vanadium Pentoxide Gels. Vol. 3, Chemistry of Materials. 1991. p. 578–93.

101. Kloster GM, Thomas JA, Brazis PW, Kannewurf CR, Shriver DF. Synthesis, Characterization, and Transport Properties of New Mixed Ionic-Electronic Conducting V2O5-Polymer Electrolyte Xerogel Nanocomposites. Chem Mater. 1996;4756(29):2418–20.

102. Zhang X, Zhu J, Haldolaarachchige N, Ryu J, Young DP, Wei S, et al. Synthetic process engineered polyaniline nanostructures with tunable morphology and physical properties. Polymer (Guildf) [Internet]. 2012;53(10):2109–20. Available from: http://dx.doi.org/10.1016/j.polymer.2012.02.042

103. Cheng S, Hwang H, Maciel GE. Synthesis and pillaring of a layered vanadium oxide from V2O5 at ambient temperature. J Mol Struct [Internet]. 1998;470(1–2):135–49. Available from: http://www.sciencedirect.com/science/article/pii/S0022286098004761

104. Liu YJ, DeGroot DC, Schindler JL, Kannewurf CR, Kanatzidis MG. Intercalation of poly(ethylene oxide) in vanadium pentoxide (V2O5) xerogel. Chem Mater [Internet]. 1991;3(6):992–4. Available from: http://pubs.acs.org/doi/abs/10.1021/cm00018a004

105. Liu Y, Schindler JL, Degroot DC, Kannewurf CR, Hirpo W, Kanatzidis MG. Synthesis , Structure , and Reactions of Poly (ethylene oxide)/V2O5 Intercalative Nanocomposites. Chem Mater. 1996;(8):525–34.

106. Posudievsky OY, Biskulova SA, Pokhodenko VD. New hybrid guest-host nanocomposites based on polyaniline, poly(ethylene oxide) and V2O5. J Mater Chem. 2004;14(9):1419–23.

107. Jiang S, Li Z, Huang S, Lu S, Yu Y, Mou G, et al. Synthesis and Electrochromic Characterization of the Graphene/Poly(ethylene oxide)/V2O5.nH2O Ternary Nanocomposite Films. J Electrochem Soc [Internet]. 2014;161(10):H684–8. Available from: http://jes.ecsdl.org/cgi/doi/10.1149/2.0991410jes

108. Subba Reddy C V., Jin AP, Han X, Zhu QY, Mai LQ, Chen W. Preparation and characterization of (PVP + V2O5) cathode for battery applications. Electrochem commun. 2006;8(2):279–83.

109. Chun-Guey W, Jiunn-Yih H, Shui-Sheng H. Synthesis and characterization of processible conducting polyaniline/V2O5 nanocomposites. J Mater Chem. 2001;11(8):2061–6.

110. Wu CG, Chung MH. Water-soluble poly(2-(3thienyloxy)ethanesulfonic acid)/V2O5nanocomposites: Synthesis and electrochromic properties. J Solid State Chem. 2004;177(7):2285–94.

111. Nakajima H, Matsubayashi GE. Intercalation and polymerization of 4-anilinoaniline and 4-anilinoanilinium iodide in the VOPO4and V2O5interlayer spaces. J Mater Chem. 1995;5(1):105–8.

112. Yuan-hong W, Heng LIU, Ding ZHU, Zai-ping GUO, Hua-kun LIU, Shi-xue DOU. Preparation and electrochemical performance of hollow-spherical polypyrrole / V 2 O 5 composite. Trans Nonferrous Met Soc China [Internet]. 2010;21(6):1303–8. Available from: http://dx.doi.org/10.1016/S1003-6326(11)60857-1

113. Oliveira HP, Graeff CFO, Brunello CA, Guerra EM. Electrochromic and conductivity properties: A comparative study between melanin-like/V2O5· nH2O and polyaniline/V2O5· nH2O hybrid materials. J Non Cryst Solids. 2000;273(1–3):193–7.

114. Paulo Ä, Preto Ä. Synthesis, characterization and properties of a melanin-like/ vanadium pentoxide hybrid compound. J Mater Chem. 2000;(4):0–4.

115. Yatabe T, Matsubayashi G. Intercalation of 2-, 4=sulfanyIpyridine, 2,2’- and 4,4’-dithiobispyridine into VOP04 and gel-V2O5 interlayer spaces. J Mater Chem. 1996;5(11):1849–52.

116. Kanatzidis MG, Wu CG, Marcy HO, Kannewurf CR. Conductive Polymer Bronzes. Intercalated Polyaniline in V2O5Xerogels. J Am Chem Soc. 1989;111(11):4139–41.

117. Wu CG, DeGroot DC, Marcy HO, Schindler JL, Kannewurf CR, Liu YJ, et al. Redox intercalative polymerization of aniline in V2O5xerogel. The postintercalative intralamellar polymer growth in polyaniline/metal oxide nanocomposites is facilitated by molecular oxygen. Chem Mater. 1996;8(8):1992–2004.

118. Li ZF, Ruckenstein E. Intercalation of conductive polyaniline in the mesostructured V2O5. Langmuir. 2002;18(18):6956–61.

119. Huguenin F, Torresi RM. Investigation of the Electrical and Electrochemical Properties of Nanocomposites from V2O5, Polypyrrole, and Polyaniline. J Phys Chem C [Internet]. 2008;112:2202–9. Available from: http://pubs.acs.org/doi/abs/10.1021/cm702979k

120. Huguenin F, Torresi RM, Buttry DA. Lithium Electroinsertion into an Inorganic-Organic Hybrid Material Composed from V[sub 2]O[sub 5] and Polyaniline. J Electrochem Soc [Internet]. 2002;149(5):A546. Available from: http://jes.ecsdl.org/cgi/doi/10.1149/1.1464134

121. Petkov V, Parvanov V, Trikalitis P, Malliakas C, Vogt T, Kanatzidis MG. Three-dimensional structure of nanocomposites from atomic pair distribution function analysis: study of polyaniline and (polyaniline)(0.5)V(2)O(5) x 1.0 H(2)O. J Am Chem Soc. 2005;127(24):8805–12.

122. Kang SG, Kim KM, Park NG, Ryu KS, Chang SH. Factors affecting the electrochemical performance of organic/V 2O5 hybrid cathode materials. J Power Sources. 2004;133(2):263–7.

123. Guerra EM, Brunello CA, Graeff CFO, Oliveira HP. Synthesis, characterization, and conductivity studies of poly-o-methoxyaniline intercalated into V2O5 xerogel. J Solid State Chem. 2002;168(1):134–9.

124. Zhao J, Wang C, Li X, Li C. Intercalation of Conducting Poly(N-propane sulfonic acid aniline) in V2O5 Xerogel. J Appl Polym Sci. 2007;103:2569–74.

125. Wang G, Zhao J, Li X, Li C, Yuan W. Synthesis and characterization of electrically conductive and fluorescent poly(N-[5-(8-hydroxyquinoline)methyl]aniline)/V2O5xerogel hybrids. Synth Met. 2009;159(5–6):366–71.

126. Demets GJF, Anaissi FJ, Toma HE, Fontes MBA. Preparation and properties of polypyrrole/bentonite/vanadium (V) oxide ternary composites. Mater Res Bull. 2002;37(4):683–95.

127. Boyano I, Bengoechea M, de Meatza I, Miguel O, Cantero I, Ochoteco E, et al. Influence of acids in the Ppy/V2O5hybrid synthesis and performance as a cathode material. J Power Sources. 2007;174(2):1206–11.

128. Boyano I, Bengoechea M, de Meatza I, Miguel O, Cantero I, Ochoteco E, et al. Improvement in the Ppy/V2O5 hybrid as a cathode material for Li ion batteries using PSA as an organic additive. J Power Sources. 2007;166(2):471–7.

129. Kanatzidis M, Marcy H, Degroot DC, Kannewurfi CR. Conductive Polymer/Oxide Bronze Nanocomposites. Intercalated Polythiophene in V2O5 Xerogels. Chem Mater. 1990;2(3):222–4.

130. Murugan AV, Kale BB, Kwon C, Campet G, Vijayamohanan K. Synthesis and characterization of a new organo-inorganic poly(3,4-ethylene dioxythiophene) PEDOT/V2O5 nanocomposite by intercalation. J Mater Chem. 2001;11(10):2470–5.

131. Murugan AV, Kwon CW, Campet G, Kale BB, Mandale AB, Sainker SR, et al. A novel approach to prepare poly(3,4-ethylenedioxythiophene) nanoribbons between V2O5 layers by microwave irradiation. J Phys Chem B. 2004;108(30):10736–42.

132. Murugan AV, Kwon C, Campet G, Kale B., Maddanimath T, Vijayamohanan K. Electrochemical lithium insertion into a poly(3,4-ethylenedioxythiophene)PEDOT/V2O5 nanocomposite. J Power Sources [Internet]. 2002;105(1):1–5. Available from: http://linkinghub.elsevier.com/retrieve/pii/S0378775301009922

133. Kwon C-W, Murugan AV, Campet G. Preparation, Characterization and Electrochemical Lithium Insertion into the new Organic-Inorganic PEDOT/V2O5. Act Passiv Electron

Components. 2003;26(September):171–83.

134. Vadivel Murugan a. Novel organic-inorganic poly (3,4-ethylenedioxythiophene) based nanohybrid materials for rechargeable lithium batteries and supercapacitors. J Power Sources. 2006;159(1 SPEC. ISS.):312–8.

135. Maiyalagan T, Viswanathan B. Synthesis , characterization and electrocatalytic activity of Pt supported on poly (3 , 4-ethylenedioxythiophene)– V 2 O 5 nanocomposites electrodes for methanol oxidation. Mater Chem Phys [Internet]. 2010;121(1–2):165–71. Available from: http://dx.doi.org/10.1016/j.matchemphys.2010.01.003

136. Posudievsky OY, Biskulova SA, Pokhodenko VD. Cathode performance of new hybrid guest-host nanocomposites based on poly(2,5-dimercaptothiophene). Electrochem commun. 2005;7(5):477–82.

137. Park NG, Ryu KS, Park YJ, Kang MG, Kim DK, Kang SG, et al. Synthesis and electrochemical properties of V2O5 intercalated with binary polymers. J Power Sources. 2002;103(2):273–9.

138. Ferreira M, Zucolotto V, Constantino CJL, A Temperini ML, Torresi RM, Oliveira ON. Layer-by-layer hybrid films of polyaniline and vanadium oxide. Synth Met. 2003;137(1–3):969–70.

139. Huguenin F, Ferreira M, Zucolotto V, Nart FC, Torresi RM, Oliveira ON. Molecular-level manipulation of V2O5/polyaniline layer-by-layer films to control electrochromogenic and electrochemical properties. Chem Mater. 2004;16(11):2293–9.

140. Ferreira M, Huguenin F, Zucolotto V, Pereira da Silva JE, Córdoba de Torresi SI, Temperini MLA, et al. Electroactive Multilayer Films of Polyaniline and Vanadium Pentoxide. J Phys Chem B [Internet]. 2003;107(33):8351–4. Available from: http://dx.doi.org/10.1021/jp034465y

141. Rao MC, Ravindranadh K, Kasturi A, Shekhawat MS. Structural Stoichiometry and Phase Transitions of MoO 3 Thin Films for Solid State Microbatteries. Res J Recent Sci Res J Recent Sci. 2013;2(4):67–73.

142. Xiao X, Zhang C, Lin S, Huang L, Hu Z, Cheng Y, et al. Intercalation of cations into partially reduced molybdenum oxide for high-rate pseudocapacitors. Energy Storage Mater [Internet]. 2015;1:1–8. Available from: http://dx.doi.org/10.1016/j.ensm.2015.05.001

143. Guzman G, Yebka B, Livage J, Julien C. Lithium intercalation studies in hydrated molybdenum oxides. Solid State Ionics. 1996;86–88(1):407–13.

144. Światowska-Mrowiecka J, De Diesbach S, Maurice V, Zanna S, Klein L, Briand E, et al. Li-ion intercalation in thermal oxide thin films of MoO3as studied by XPS, RBS, and NRA. J Phys Chem C. 2008;112(29):11050–8.

145. M. Whittingham S. Intercalation Chemistry. 1st ed. Elsevier; 1982. 541 p.

146. Rao CNR, Biswas K. Essentials of Inorganic Materials Synthesis. 1st ed. John Wiley & Sons; 2015. 65-68 p.

147. Scanlon DO, Watson GW, Payne DJ, Atkinson GR, Egdell RG, Law DSL. Theoretical and Experimental Study of the Electronic Structures of MoO 3 and MoO 2. 2010;(010):4636–45.

148. Julien C, Mauger A, Vijh A, Zaghib K. Lithium Batteries: Science and Technology. 1st ed. Springer; 2015. 81 p.

149. Heinonen M, Henrich VE, Werfel F. Journal of Physics C : Solid State Physics Related content Photoemission study of the electronic structure of Mo and Mo oxides Photoemission study of the electronic structure of Mo and MO oxides. 1983;

150. Mehandru SP, Anderson AB. HxMoO3 Bronzes: Structures, Stabilities, and Electronic Properties. J Am Chem Soc. 1988;110(7):2061–5.

151. Eda K, Sotani N, Kunitomo M, Kaburagi M. Reexamination of Protonic Locations in Hydrogen Molybdenum Bronze, HxMoO3. J Solid State Chem. 1998;141(1):255–61.

152. Adams S. CDW superstructures in hydrogen molybdenum bronzes H(x)MoO3. J Solid State Chem. 2000;149(1):75–87.

153. Tagaya H, Ara K, Kadokawa J, Karasu M, Chiba K. Intercalation of Organic Compounds in the Layered Host Lattice MOO,. J Mater Chem. 1994;4(4):551–5.

154. Leroux F, F. Nazar L. Uptake of lithium by layered molybdenum oxide and its tin exchanged

derivatives: high volumetric capacity materials. Solid State Ionics. 2000;133:403–9.

155. Sian TS, Reddy GB. Infrared spectroscopic studies on Mg intercalated crystalline MoO 3 thin films. Appl Surf Sci. 2004;236(1):1–5.

156. Sian TS, Reddy GB. Infrared and electrochemical studies on Mg intercalated a-MoO3 thin films. Solid State Ionics. 2004;167(3–4):399–405.

157. Motter JP, Koski KJ, Cui Y. General strategy for zero-valent intercalation into two-dimensional layered nanomaterials. Chem Mater. 2014;26(7):2313–7.

158. Wang M, Koski KJ. Reversible chemochromic MoO3 nanoribbons through zerovalent metal intercalation. ACS Nano. 2015;9(3):3226–33.

159. Lerf A, Lalik E, Kolodziejski W, Klinowski J. Intercalation of Polyoxycation Species Into Conducting Layered Host Lattices of Moo3 and Tas2. J Phys Chem. 1992;96(18):7389–93.

160. Nazar LF, Zhang Z, Zinkweg D. Insertion of Poly (p-phenylenevinylene) in Layered MoO3. Journal of the American Chemical Society. 1992;114(15):6239–40.

161. Nazar LF, Wu H, Power WP. Synthesis and properties of a new (PEO)x[Na(H2O)]0.25MoO3nanocomposite. J Mater Chem. 1995;5(11):1985–93.

162. Chen W, Xu Q, Hu YS, Mai LQ, Zhu QY. Effect of modification by poly (ethylene oxide) on the reversibility of insertion / extraction of Li 1 ion in V 2 O 5 xerogel films. Microelectron Eng. 2002;66:1926–9.

163. Wang J, Matsubara I, Itoh T, Murayama N, Shin W, Izu N. Preparation of Polystyrene and Surfactant Co-intercalated MoO3 Nano Hybrids and their VOC Gas Sensing Properties. ieej Trans sensors micromachines. 2006;126(10):548–52.

164. Janauer GG, Dobley A, Guo J, Zavalij P, Whittingham MS. Novel tungsten, molybdenum, and vanadium oxides containing surfactant ions. Chem Mater. 1996;8(8):2096–101.

165. Hosono K, Matsubara I, Murayama N, Woosuck S, Izu N. Synthesis of polypyrrole/MoO3hybrid thin films and their volatile organic compound gas-sensing properties. Chem Mater. 2005;17(2):349–54.

166. Itoh T, Wang J, Matsubara I, Shin W, Izu N, Nishibori M, et al. VOCs sensing properties of

layered organic-inorganic hybrid thin films: MoO3with various interlayer organic components. Mater Lett. 2008;62(17–18):3021–3.

167. Matsubara I. Thin film processing of MoO 3 based hybrid materials. J Ceram Soc Japan. 2010;118(12):1124–30.

168. Kerr TA, Wu H, Nazar LF. Concurrent Polymerization and Insertion of Aniline in Molybdenum Trioxide: Formation and Properties of a [Poly(aniline)] 0.24 MoO 3 Nanocomposite. Chem Mater [Internet]. 1996;8(8):2005–15. Available from: http://pubs.acs.org/doi/abs/10.1021/cm960071q

169. Wang J, Matsubara I, Murayama N, Woosuck S, Izu N. The preparation of polyaniline intercalated MoO3thin film and its sensitivity to volatile organic compounds. Thin Solid Films. 2006;514(1–2):329–33.

170. Itoh T, Matsubara I, Shin W, Izu N, Nishibori M. Characterizations of interlayer organic-inorganic nanohybrid of molybdenum trioxide with polyaniline and poly(o-anisidine). Mater Chem Phys. 2008;110(1):115–9.

171. Goward GR, Kerr TA, Power WP, Nazar LF. Solid-state2H NMR determination of poly(aniline) conformation within a MoO3nanocomposite. Adv Mater. 1998;10(6):449–52.

172. Itoh T, Matsubara I, Shin W, Izu N, Nishibori M. Highly Aldehyde gas-sensing responsiveness and selectivity of layered organic-guest/MoO3-host hybrid sensor. J Ceram Soc Japan. 2007;115(11):742–4.

173. ITOH T, MATSUBARA I, SHIN W, IZU N, NISHIBORI M. XPS study of organic/MoO3 hybrid thin films for aldehyde gas sensors: correlation between average Mo valence and sensitivity. J Ceram Soc Japan. 2010;118(1375):171–4.

174. Chatakondu K, Green MLH, Qin J, Thompson ME, Wiseman PJ. Intercalation of Redox-active Organometallic Cubane Clusters into Layered Metal Oxides and Related Solids. J Chem Soc Chem Commun. 1988;4:223–5.

175. Hider RN, Wilkins CJ. Polymeric complexes from molybdenum trioxide, with notes on derivatives and related compounds. J Chem Soc Dalt Trans. 1984;1984(4):495–500.

176. Jing Y, Pan Q, Cheng Z, Dong X, Xiang Y. Direct thermal intercalation of amine into layered MoO3. Mater Sci Eng B Solid-State Mater Adv Technol. 2007;138(1):55–9.

177. De Farias RF, Airoldi C. Some structural features of MoO3-1,10-phenanthroline intercalation compounds. J Phys Chem Solids. 2003;64(11):2199–204.

178. De Farias RF. Synthesis and characterization of a MoO3-pyrrolidinedithiocarbamate hybrid. Int J Inorg Mater. 2001;3(7):931–5.

179. Afsharpour M, Mahjoub AR, Amini MM, Khodadadi AA. Organization of Molybdenum Oxide Nanohybrids by Intercalation of Aminohydroxy Ligands into Layered Molybdic Acid : Efficient Catalysts in Oxidation of Alcohols. Curr Nanosci. 2010;6:82–8.

180. Bissessur R. Inclusion of Poly(aniline) into MoO3. J Chem Soc Chem Commun. 1993;687–9.

181. Ke S, Ying M, Ya-An C, Zhao-Hui C, Xue-Hai J, Jian-Nian Y. Inclusion of poly(tetramethyl-p-phenylenediamine dihydrochloride) into MoO3: A cooperative formation route to construct a polymer/MoO3 layered structure. Chem Mater. 2001;13(2):250–2.

182. Tagaya H, Takeshi K, Kadokawa J, Karasu M, Chiba K. Preparation of new organic-inorganic nanocmposite by intercalation of organic compounds into MoO3 by ultrasound. Mater Rssearcb Bull. 1995;30(9):1161–71.

183. O.Oriakhi C, L. Nafshun R, Lerner MM. Preparation of Nanocomposites of Linear poly(eythyleneimine) with layered hosts. Mater Res Bull. 1996;31(12):1513–20.

184. Kerr TA, Leroux F, Nazar LF. Surfactant-Mediated Incorporation of Poly(p-phenylene) into MoO3. Chem Mater. 1998;10(11):2588–91.

185. Zapf PJ, Haushalter RC, Zubieta J. Hydrothermal Synthesis and Structural Characterization of a Series of One-Dimensional Organic/Inorganic Hybrid Materials of the [(MoO 3) n (2,2‘-bipy) m] Family: [MoO 3 (2,2‘-bipy)], [Mo 2 O 6 (2,2‘-bipy)], and [Mo 3 O 9 (2,2‘-bipy) 2]. Chem Mater [Internet]. 1997;9(9):2019–24. Available from: http://pubs.acs.org/doi/abs/10.1021/cm970260o

186. Abrantes M, Amarante TR, Antunes MM, Gago S, Almeida Paz FA, Margiolaki I, et al. Synthesis, structure, and catalytic performance in cyclooctene epoxidation of a

molybdenum oxide/bipyridine hybrid material: {[MoO3(bipy)] [MoO3(H2O)]}n. Inorg Chem. 2010;49(15):6865–73.

187. Hagrman PJ, LaDuca RL, Koo HJ, Rarig R, Haushalter RC, Whangbo MH, et al. Ligand influences on the structures of molybdenum oxide networks. Inorg Chem. 2000;39(19):4311–7.

188. Wei XM, Zeng HC. Large-scale organizations of MoO3 nanoplatelets with single-crystalline MoO3(4,4'-bipyridyl)0.5. J Phys Chem B. 2003;107(12):2619–22.

189. Wei XM, Zeng HC. Sulfidation of single molecular sheets of MoO3 pillared by bipyridine in nanohybrid MoO3(4,4'-bipyridyl)0.5. Chem Mater. 2003;15(2):433–42.

190. Rajagopal S, Nataraj D, Yu. Khyzhun O, Djaoued Y, Robichaud J, Senthil K, et al. Systematic synthesis and analysis of change in morphology, electronic structure and photoluminescence properties of pyrazine intercalated MoO3 hybrid nanostructures. Crystengcomm. 2011;13:2358–68.

191. Quites FJ, Bisio C, Marchese L, Pastore HO. The polyelectrolyte-MoO3 hybrids: Bottom up building of a layered anionic exchanger. Mater Res Bull [Internet]. 2013;48(9):3342–50. Available from: http://dx.doi.org/10.1016/j.materresbull.2013.05.024

192. Qi Y, Chen W, Mai L, Zhu Q, Jin A. Synthesis and electrochemical performance of PEO doped molybdenum trioxide nanobelts. Int J Electrochem Sci. 2006;1(6):317–23.

193. Wang F, Shifa TA, Yu P, He P, Liu Y, Wang F, et al. New Frontiers on van der Waals Layered Metal Phosphorous Trichalcogenides. Vol. 28, Advanced Functional Materials. 2018. p. 1–24.

194. Hulliger F. Structural Chemistry of Layer Type Phases. F L, editor. D. Reidel Publishing Company; 1976.

195. Levy FA. Intercalated Layered Materials. London: D.Reidel Publishing Company; 1979. 533-558 p.

196. Foot PJS, Nevett B a. Properties of NiPS3 and ZnPS3 prepared at ambient temperature. J Chem Soc Chem Commun. 1987;3(5):380.

197. Brec R, Schleich DM, Ouvrard G, Louisy A, Rouxel J. Physical properties of lithium intercalation compounds of the layered transition-metal chalcogenophosphites. Inorg Chem [Internet]. 1979;18(7):1814–8. Available from: http://pubs.acs.org/doi/abs/10.1021/ic50197a018

198. Clement R. Intercalation of Potentially Reactive Transition-Metal Complexes in the Lamellar MnPS3 Host Lattice. J Am Chem Soc. 1981;103(23):6998–7000.

199. Arun N, Jeevanandam P, Vasudevan S, Ramanathan K V. Motion of interlamellar hydrated sodium ions in layered Cd0.75PS3Na0.5(H2O)2. J Chem Phys. 1999;111(3):1231–9.

200. Du KZ, Wang XZ, Liu Y, Hu P, Utama MIB, Gan CK, et al. Weak Van der Waals Stacking, Wide-Range Band Gap, and Raman Study on Ultrathin Layers of Metal Phosphorus Trichalcogenides. ACS Nano. 2016;10(2):1738–43.

201. Cleary DA, Francis AH, Lifshitz E. Photoluminescence studies of layered transition metal phosphorus chalcogenides and their pyridine intercalation compounds. J Lumin. 1986;35(3):163–70.

202. Mercier H, Mathey Y, Canadell E. On the electronic Structure of MPS3 Phases. Inorg Chem. 1987;26:963–5.

203. Arbor A, Lifshitz E, Francis a H. Electronic Spectroscopy of Nearly Octahedrally Coordinated Manganese. Inorg Chem. 1981;2852(1980):3019–23.

204. Zhukov V, Boucher F, Alemany P, Evain M, Alvarez S. Electronic Structure, Chemical Bonding, and Jahn-Teller Distortions in CdPS3. Inorg Chem. 1995;34(5):1159–63.

205. Hefni MA, Nagasundaram N, Kreszowski D, Francis AH. ESR studies of inter- and intra-lamellar cation exchange processes in Cd2P2S6. J Phys Chem Solids. 1990;51(12):1405–11.

206. Mathey Y, Clement R, Sourisseau C, Lucazeau G. Vibrational Study of Layered MPX3 Compounds and of Some Intercalates with Co(η5-C5H5)2+ or Cr(η6-C6H6)2+. Inorg Chem. 1980;19(9):2773–9.

207. Evans JSO, O'Hare D, Clement R. The Structure of Co(η-C5H5)2 and NMe4+Intercalates of MnPS3: An X-ray, Neutron-Diffraction, and Solid-State NMR Study. J Am Chem Soc.

1995;117(16):4595–606.

208. Yang K, Su X, Zhang X, Chen X, Fu E, Qin J, et al. Synthesis, structural characterization and ferrimagnetic property of MnPS3 intercalated with nickel(II) cyclopolyamine complex cations. J Solid State Chem. 2004;177(11):4300–4.

209. Valencia P, Manzur J, Garcia AM, Paredes-Garcia V, Cardoso-Gil R, Schnelle W, et al. Magnetic behavior of lamellar MnPS3 and CdPS3 composites with a paramagnetic manganese(III) macrocyclic guest. J Chil Chem Soc. 2013;58(4):1952–6.

210. Glueck DS, Brough AR, Mountford P, Green MLH. Synthesis and Properties of Crown Ether-Alkali Metal Cation Intercalation Compounds of MPS3 (M = Mn, Cd, Zn). Inorg Chem. 1993;3(4):1893–902.

211. Leung C, Ma D. Phosphorus Vacancies and Intercalation in Lamellar NiPS3. J Chem Soc Chem Commun. 1988;49(50):629–30.

212. Schöllhorn R. Intercalation chemistry of Layered FePS3 An Approach toward Insulating Magnets below 90 K. Chem Mater. 1990;99(1–4):89–99.

213. Joy PA, Vasudevan S. The Intercalation Reaction of Pyridine with Manganese Thiophosphate, MnPS3. J Am Chem Soc. 1992;114(14):7792–801.

214. El-Meligi AA, Al-Saie AM, Al-Buflasa H, Bououdina M. Formation of composite nanomaterial MnPS3 layered structure intercalated with pyridine. J Alloys Compd. 2009;488(1):284–90.

215. Zhang X, Chen X, Su X, Yang C, Qin J, Inokuchi M. The intercalation reaction of 2,2'-bipyridine with layered compound MnPS3. J Solid State Chem. 2004;177(6):2014–22.

216. Chen X, Zou L, Zhang X, Qin J, Inokuchi M, Kinoshita M. The Intercalation of 4-Aminopyridine into Layered FePS3. J Incl Phenom. 2003;46(1–2):105–10.

217. Lacroix PG, Lemarinier VV, Clement R, Nakatanib K, Delaireb JA. Synthesis and Non-linear Optical Properties of Substituted Styrylpyridinium-MPS , Intercalation Compounds (M=Mn ,Cd). J Mater Chem. 1993;3(5):499–503.

218. Schmedt auf der Günne J, Eckert H, Léaustic A, Babonneau F. Vacancy ordering and host–

guest interactions in CdPS3 intercalates: Results from multidimensional solid state NMR. Phys Chem Chem Phys. 2003;5(6):1306.

219. Lacroix PG, Clément R, Nakatani K, Zyss J, Ledoux I. Stilbazolium-MPS3 nanocomposites with large second-order optical nonlinearity and permanent magnetization. Science (80-). 1994;263(5147):658–60.

220. Lagadic I, Lacroix PG, Clément R. Layered MPS 3 (M = Mn, Cd) Thin Films as Host Matrixes for Nonlinear Optical Material Processing. Chem Mater [Internet]. 1997;9(9):2004–12. Available from: http://pubs.acs.org/doi/abs/10.1021/cm970155e

221. Chen X, Yang C, Qin J, Inokuchi M, Fujii Y, Kinoshita M, et al. The Characterization and Magnetic Properties of Inorganic-Organic Hybrid Nanocomposites , Stilbazoliums Inserted into Layered FePS 3. J Incl Phenom Macrocycl Chem. 2002;42:71–5.

222. Léaustic A, Rivière E, Clément R. Photoinduced Modifications of the Magnetization of a Stilbazolium-MnPS3 Layered Intercalate. Chem Mater. 2003;15(25):4784–9.

223. Yi T, Tancrez N, Clément R, Ledoux-Rak I, Zyss J. Organic-MPS3 nanocomposites with large second-order nonlinear optical response. In: Journal of Luminescence. 2004. p. 389–95.

224. Yi T, Clément R, Haut C, Catala L, Gacoin T, Tancrez N, et al. J-aggregated dye-MnPS3 hybrid nanoparticles with giant quadratic optical nonlinearity. Adv Mater. 2005;17(3):335–8.

225. Liu Q, Zhou W, Gao C, Hu T, Zhao X. Synthesis and second-order optical nonlinearity of DAMS/Mn2P2S6 intercalated materials by ion exchange method. Chem Phys Lett [Internet]. 2009;477(4–6):388–91. Available from: http://dx.doi.org/10.1016/j.cplett.2009.07.019

226. Coradin T, Clément R, Lacroix PG, Nakatani K. From Intercalation to Aggregation: Nonlinear Optical Properties of Stilbazolium Chromophores−MPS3 Layered Hybrid Materials. Chem Mater [Internet]. 1996;8(8):2153–8. Available from: http://pubs.acs.org/doi/abs/10.1021/cm960060x

227. Coradin T, Veber M, Francis AH, Clément R. The MnPS3 layered phase as a substrate for

aggregate formation: The example of triarylpyrylium cations. J Mater Chem. 1998;8(6):1471–5.

228. Bénard S, Léaustic A, Rivière E, Yu R, Clément P. Interplay between magnetism and photochromism in spiropyran-MnPS3 intercalation compounds. Chem Mater. 2001;13(10):3709–16.

229. Léaustic A, Sour A, Rivière É, Clément R. Photoisomerisation of a conjugated chromophore intercalated into thin films of MPS3 layered compounds (M = Mn, Cd). A search for photomagnetic effects. Comptes Rendus l'Academie des Sci - Ser IIC Chem. 2001;4(2):91–5.

230. Lacroix P, Audiere JP, Clement R. Novel Tetrathiafulvalene-MPS3 (M = Mn , Cd) Layered Composite Materials. J Chem Soc Chem Commun. 1989;(536):536–7.

231. Lomas L, Lacroix P, Audiere JP, Clement R. Tetrathiafulvalene FePS3 layered intercalation compound: a new type of organic inorganic metal. J Mater Chem. 1991;1(3):475.

232. Chtioui-Gay I, Faulmann C, De Caro D, Jacob K, Valade L, De Caro P, et al. Synthesis, characterization, and thermoelectric properties of superconducting (BEDT-TTF)2I3 nanoparticles. J Mater Chem C. 2016;4(31):7449–54.

233. Demiralp E, A. Goddard III W. Conduction properties of the organic superconductor k-(BEDT-TTF)2Cu(NCS)2 based on Hubbard-unrestricted-Hartree-Fock band calculations. Phys Rev B. 1997;56(18):907–19.

234. Laukhina E, Tkacheva V, Chekhlov A, Yagubskii E, Wojciechowski R, Ulanski J, et al. Polymorphism of a new bis(ethylenedithio)tetrathiafulvalene (BEDT-TTF) based molecular conductor; Novel transformations in metallic BEDT-TTF layers. Chem Mater. 2004;16(12):2471–9.

235. Yang C, Qin J, Yakushi K, Nakazawa Y, Ichimura K. BEDT-TTF being inserted into a layered MnPS3. Synth Met. 1999;102(1–3):1482.

236. Zhou H, Zou L, Chen X, Yang C, Inokuchi M, Qin J. An inorganic-organic intercalated nanocomposite, BEDT-TTF into layered MnPS3. J Incl Phenom Macrocycl Chem. 2008;62(3–

4):293–6.

237. Köseoglu Y, Yildiz F, Yakhmi J V., Qin J, Chen X, Aktaş B. EPR studies on BEDT-TTF intercalated MnPS3 molecular magnet. J Magn Magn Mater. 2003;258–259:416–8.

238. Chen X, Zhou H, Zou L, Yang C, Qin J, Inokuchi M. A new organic-inorganic hybrid nanocomposite, BEDT-TTF intercalated into layered FePS3. J Incl Phenom. 2005;53(3):205–9.

239. Lagadic I, Leaustic A, Clement R. Intercalation of polyethers into the MPS3 (M = Mn, Cd) Host Lattice. J Chem Soc Chem Commun. 1992;3:9–10.

240. Manova E, Severac C, Andreev A, Clément R. NiPS3 intercalates as catalysts for the oxidation of sulfide ions: Synthesis, catalytic activity, and XPS study. J Catal. 1997;169(2):503–9.

241. Manríquez V, Barahona P, Ruiz D, Avila RE. Intercalation of polyethylene oxide PEO in layered MPS3(M = Ni, Fe) materials. Mater Res Bull. 2005;40(3):475–83.

242. Jeevanandam P, Vasudevan S. Intercalation of Alkali Metal−Polyethylene Oxide Polymer Electrolytes in Layered CdPS 3. Chem Mater [Internet]. 1998;10(5):1276–85. Available from: http://pubs.acs.org/doi/abs/10.1021/cm9706006

243. Manríquez V, Galdámez A, Ponce J, Brito I, Kasaneva J. Intercalation of polyaniline in the layered materials MPS3, M = Mn, Cd. Mater Res Bull. 1999;34(1):123–30.

244. Zhang D, Qin J, Yakushi K, Nakazawa Y, Ichimura K. Preparation of a new nanocomposite of conducting polyaniline into layered MnPS3. Mater Sci Eng A. 2000;286(1):183–7.

245. Yamanaka S, Kobayashi H, Tanaka M. NEW INTERCALATED COMPLEXES OF MPS 3 (M=Mg, Zn, Mn) WITH n -ALKYLAMINES. Chem Lett [Internet]. 1976;5(4):329–32. Available from: http://www.journal.csj.jp/doi/10.1246/cl.1976.329

246. Clement R, Green MLH. Organometallic Intercalates of some Lamellar Metal Phosphorus Trisulphides. JCS Dalt. 1979;1566–8.

247. Kim K, Liddle DJ, Cleary DA. A quantitative ESR study of cadmium phosphorus chalcogenide (Cd2P2S6) intercalated with cobaltocene. J Phys Chem [Internet]. 1990;94(7):3205–10.

Available from: http://pubs.acs.org/doi/abs/10.1021/j100370a083

248. Stanislaw R, Juliana B-G. Nonisothermal Calorimetric Studies of Pyridine Intercalation in CdPS3. J Phys Chem. 1987;(91):2201–6.

249. Kim K, Cleary DA. ESR study of the magnetic behavior of manganese thiophosphate (Mn2P2S6) intercalation compounds. J Phys Chem [Internet]. 1990;94(9):3816–9. Available from: http://pubs.acs.org/doi/abs/10.1021/j100372a086

250. Hill PG, Foot PJS, Davis R. Novel inorganic / conjugated polymer nano-composites. Synth Met. 1996;76:289–92.

251. Silipigni L, De Luca G, Quattrone T, Scolaro LM, Salvato G, Grasso V. An XPS analysis of the interaction of meso-tetrakis(N-methylpyridinium-4- yl)porphyrin with exfoliated manganese thiophosphate. J Phys Condens Matter. 2006;18(24):5759–72.

252. Oriakhi CO, Lerner MM. Rapid and Quantitative Displacement of Poly(ethylene oxide) from MnPS3 and Other Layered Hosts. Chem Mater. 1996;8(17):2016–22.

253. Sukpirom N, Oriakhi CO, Lerner MM. Preparation of layered nanocomposites of PEO with MnPS3, CdPS3 and MoO3 by melt intercalation. Mater Res Bull. 2000;35:325–31.

254. Liyanage AU, Lerner MM. Template preparation of NiPS3 polymer nanocomposites. RSC Adv. 2012;2(2):474.

255. Zhang H, Yi T, Li F, Delahaye E, Yu P, Clement R. Photochromic response of nanoparticles of spiropyran-MnPS3 intercalate: A search for optically bistable nanocomponents. J Photochem Photobiol A Chem. 2007;186(2–3):173–7.

256. Klingen VW, Otto R, H H. Uber die Darstellung und Eigenschaften von Hexathiound Hexaselenohyodiphosphaten. Z anorg allg Chem. 1973;(396):1973.

257. Van der Pauw LJ. A method of Measuring the Resistivity and Hall Coefficient on Lamellae of Arbitrary Shape. Philips Tech Rev. 1958;20:220–4.

258. Chakrabarti A, Hermann K, Druzinic R, Witko M, Wagner F, Petersen M. Geometric and electronic structure of vanadium pentoxide : and surface study A density functional bulk. Phys Rev B. 1999;59(16):583–90.

259. Fierro LJ., Arrua LA, Nieto JM., Kremenic G. Surface properties of Co-precipitated VTiO catalysts and their relation to the selectiveoxidation of isobutene. Appl Catal. 1988;37:323–38.

260. Bond GC, Flamerz S. Structure and reactivity of titania-supported oxides: IV. Characterisation of dried vanadia/titania catalyst precursors. Appl Catal. 1989;46(1):89–102.

261. Takagi-Kawai M, Soma M, Onishi T, Tamaru K. The adsorption and the reaction of NH 3 and NO x on supported V 2 O 5 catalysts: effect of supporting materials. Can J Chem. 1980;58:2132–7.

262. Cornaglia LM, Lombardo EA. XPS studies of the surface oxidation states on vanadium-phosphorus-oxygen (VPO) equilibrated catalysts. Appl Catal. 1995;127(1–2):125–38.

263. Kasperkiewicz J, Kovacich JA, Litchman D. XPS studies of vanadium and vanadium oxides. J Electron Spectros Relat Phenomena. 1990;32(2):123–32.

264. Kang ET, Neoh KG, Khor SH, Tan KL, Tan BT. X.p.s. studies of charge transfer interactions in some polyaniline complexes. Polymer (Guildf). 1990;31(2):202–7.

265. Kumar SN, Bouyssoux G, Gaillard F. Electronic and structural characterization of electrochemically snthesized conducting polyaniline from XPS studies. Surf Interface Anal. 1990;15(9):531–6.

266. Wagner CD, Zatko DA, Raymond RH. Use of the Oxygen KLL Auger Lines in Identification of Surface Chemical States by Electron Spectroscopy for Chemical Analysis. Anal Chem. 1980;52(9):1445–51.

267. Mitraka E, Jafari MJ, Vagin M, Liu X, Fahlman M, Ederth T, et al. Oxygen-induced doping on reduced PEDOT. J Mater Chem A. 2017;5(9):4404–12.

268. López GP, Castner DG, Ratner BD. XPS O 1s binding energies for polymers containing hydroxyl, ether, ketone and ester groups. Surf Interface Anal. 1991;17(5):267–72.

269. Stallworth PE, Johnson FS, Greenbaum SG, Passerini S, Flowers J, Smyrl W, et al. Magnetic resonance studies of chemically intercalated LixV2O5 (x = 1.16 and 1.48). Solid State Ionics.

2002;146(1–2):43–54.

270. Plachy T, Sedlacik M, Pavlinek V, Stejskal J. The observation of a conductivity threshold on the electrorheological effect of p-phenylenediamine oxidized with p-benzoquinone. J Mater Chem C [Internet]. 2015;3(38):9973–80. Available from: http://dx.doi.org/10.1039/c5tc02119g

271. Search H, Journals C, Contact A, Iopscience M, Address IP. Preparation of MoO3 nanostructures and their optical. J Phys Condens Matter. 2003;15.

272. Inzani K, Nematollahi M, Vullum-Bruer F, Grande T, Reenaas TW, Selbach SM. Electronic properties of reduced molybdenum oxides. Phys Chem Chem Phys. 2017;19(13):9232–45.

273. Al-Shihry SS, Halawy SA. Unsupported MoO3-Fe2O3 catalysts: Characterization and activity during 2-propanol decomposition. J Mol Catal A Chem. 1996;113(3):479–87.

274. Zou J, Schrader GL. Multicomponent thin film molybdate catalysts for the selective oxidation of 1,3-butadiene. J Catal. 1996;161(2):667–86.

275. Uchida K, Ayame A. Dynamic XPS measurements on bismuth molybdate surfaces. Surf Sci. 1996;357–358:170–5.

276. Brox B, Olefjord I. ESCA Studies of MoO2 and MoO3. Surf Interface Anal. 1988;13(1):3–6.

277. Persson I. Hydrated metal ions in aqueous solution: How regular are their structures? Pure Appl Chem. 2010;82(10):1901–17.

278. Batsanov SS. Van der Waals radii of elements. Inorg Mater. 2001;37(9):871–85.

279. Piacentini M, Khumalo FS, Leveque G, Olson CG, Lynch DW. X-ray photoemission and optical spectra of NiPS3, FePS3 and ZnPS3. Chem Phys. 1982;72(1–2):61–71.

280. Kang M, Jung J, Lee SY, Ryu JW, Kim SW. Conductivity, carrier density, mobility, Seebeck coefficient, and power factor in V2O5. Thermochim Acta [Internet]. 2014;576:71–4. Available from: http://dx.doi.org/10.1016/j.tca.2013.11.026

281. J. Littlefair P. The luminous effacacy of daylight: a review. Light Res Technol. 1985;17(5):162–82.

282. Agrawal DC, Leff HS, Menon VJ. Efficiency and efficacy of incandescent lamps. Am J Phys.

1996;64(5):649–54.

283. Elvidge CD, Keith DM, Tuttle BT, Baugh KE. Spectral identification of lighting type and character. Sensors. 2010;10(4):3961–88.

284. Wen X, Feng Y, Huang S, Huang F, Cheng YB, Green M, et al. Defect trapping states and charge carrier recombination in organic-inorganic halide perovskites. J Mater Chem C. 2015;4(4):793–800.

285. Ebenhoch B, Thomson SAJ, Genevičius K, Juška G, Samuel IDW. Charge carrier mobility of the organic photovoltaic materials PTB7 and PC71BM and its influence on device performance. Org Electron physics, Mater Appl. 2015;22:62–8.

286. Goodenough JB, Hamnett A, Leib M, Ramasesha SK, Werheit H. Physics of Non-Tetrahedrally Bonded Binary Compounds III. 1st ed. O M, editor. Springer; 1984. 579 p.

287. Byrne FP, Jin S, Paggiola G, Petchey THM, Clark JH, Farmer TJ, et al. Tools and techniques for solvent selection: green solvent selection guides. Sustain Chem Process. 2016;4(1).

Appendicies

Appendix A – V_2O_5 Characterisation and Electrical Measurements

A.1 V_2O_5 Nanocomposite IR

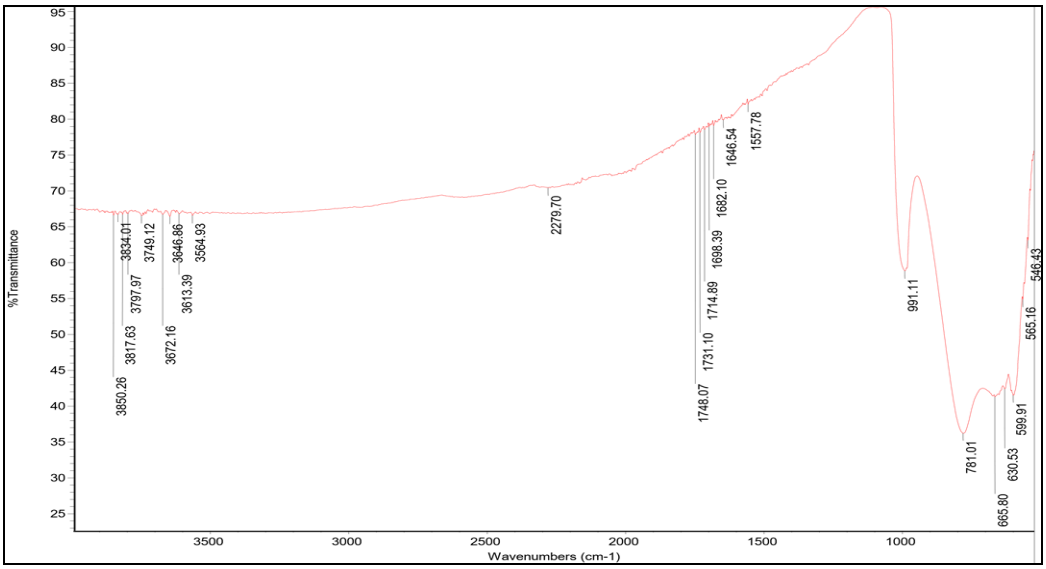

Figure A.1.1– V_2O_5 IR spectrum

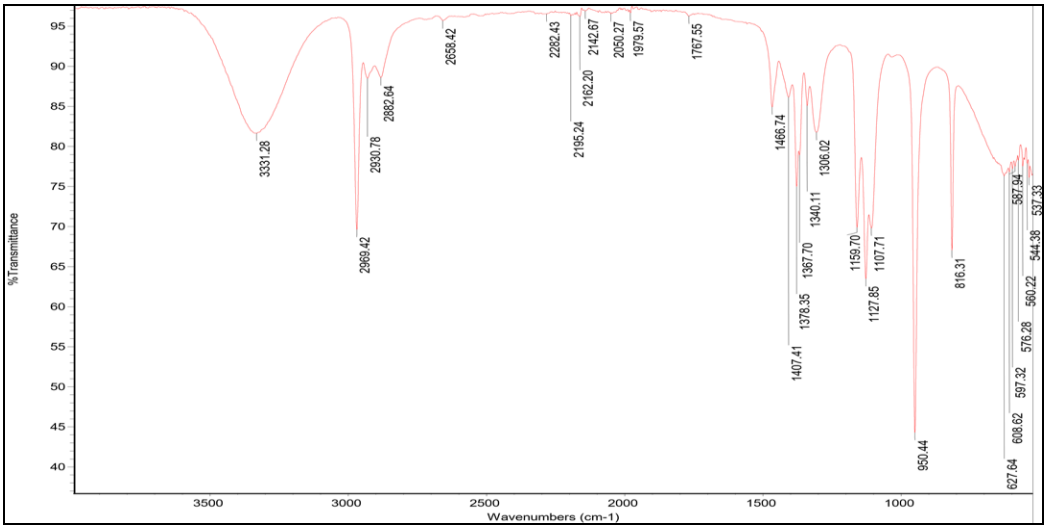

Figure A.1.2 – V_2O_5/AnAn$^+$ IR spectrum

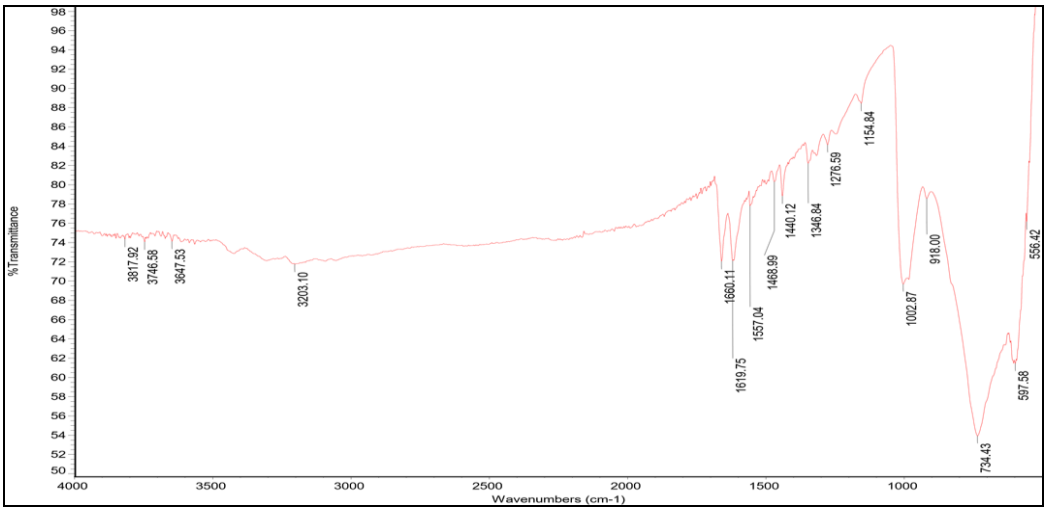

Figure A.1.3 – V_2O_5/2A5PhPyr IR spectrum

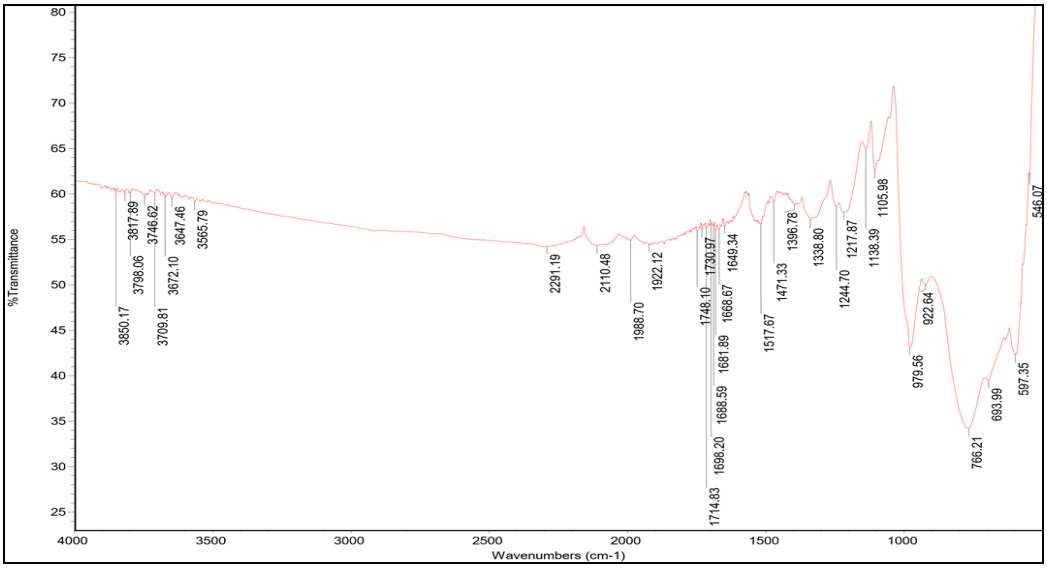

Figure A.1.4 – V_2O_5/EDOT IR spectrum

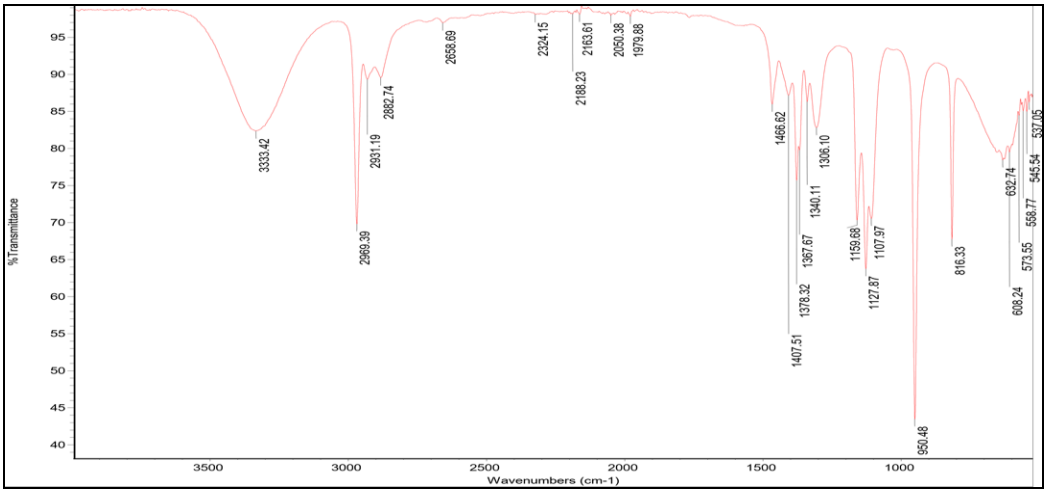

Figure A.1.5 – V_2O_5/PDA IR spectrum

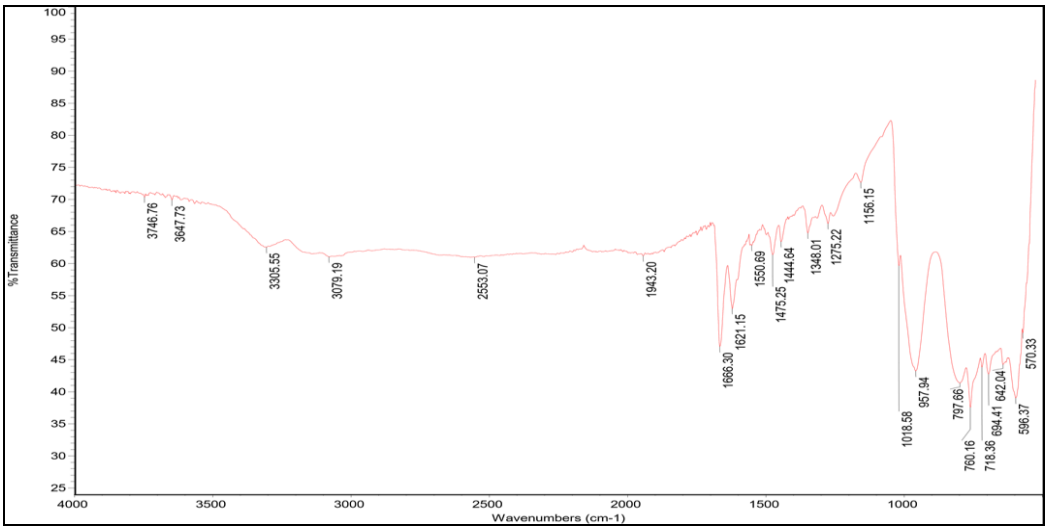

Figure A.1.6 – LiV_2O_5/2A5PhPyr IR spectrum

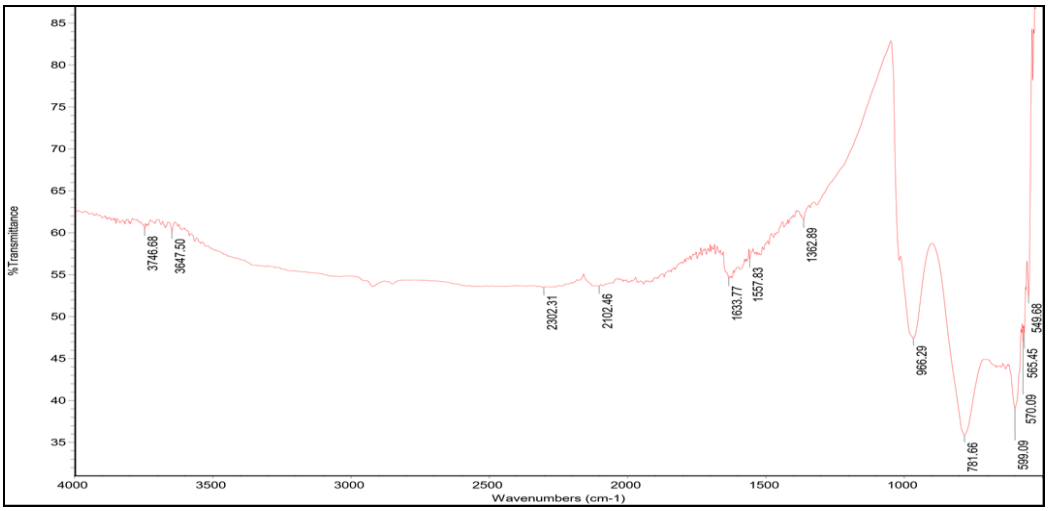

Figure A.1.7 – V_2O_5/5AQ IR spectrum

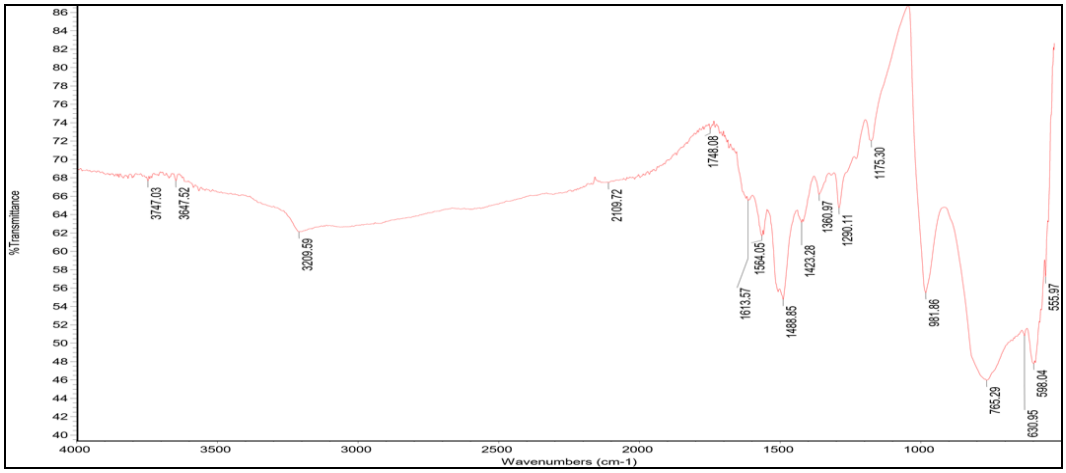

Figure A.1.8 – V_2O_5/1,4PDA-HQ IR spectrum

A.2 V_2O_5 Nanocomposite Raman Spectra

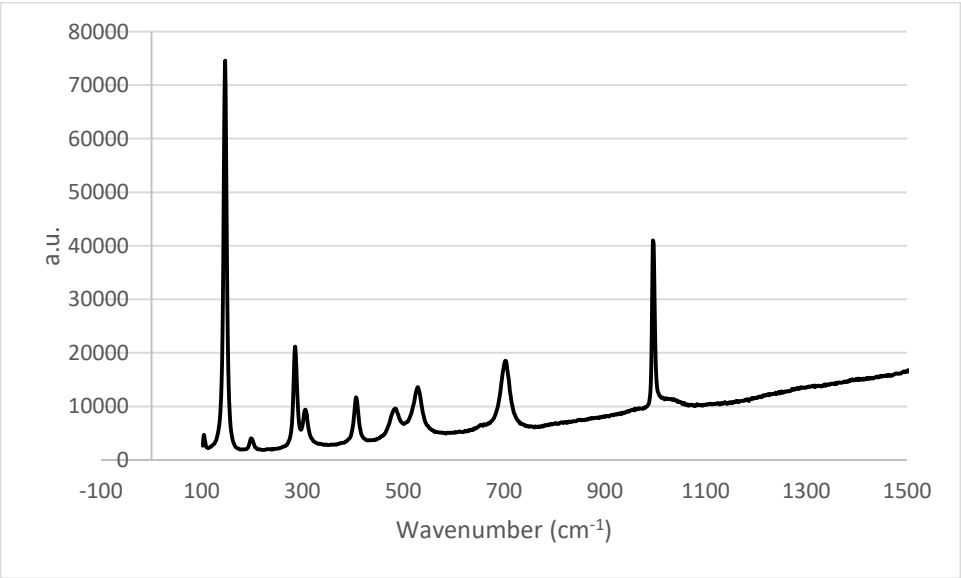

Figure A.2.1 - V_2O_5 Raman spectrum

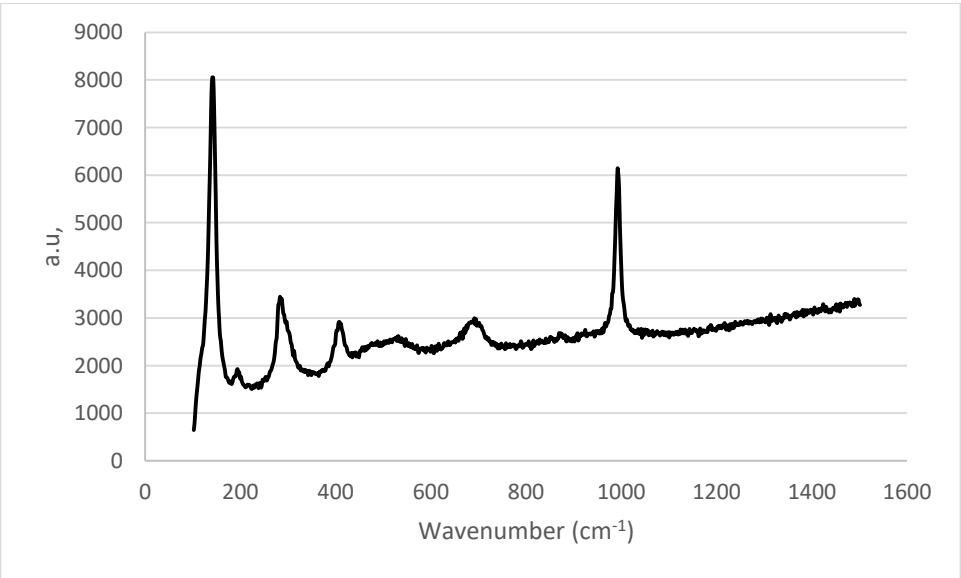

Figure A.2.2 – V_2O_5/AnAn$^+$ Raman spectrum

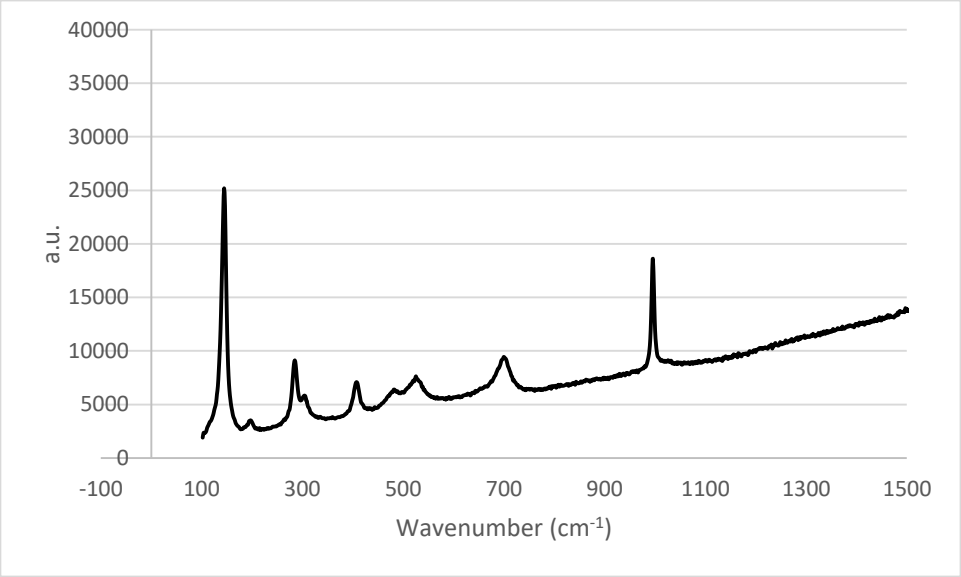

Figure A.2.3 – V_2O_5/2A5PhPyr (AB) Raman spectrum

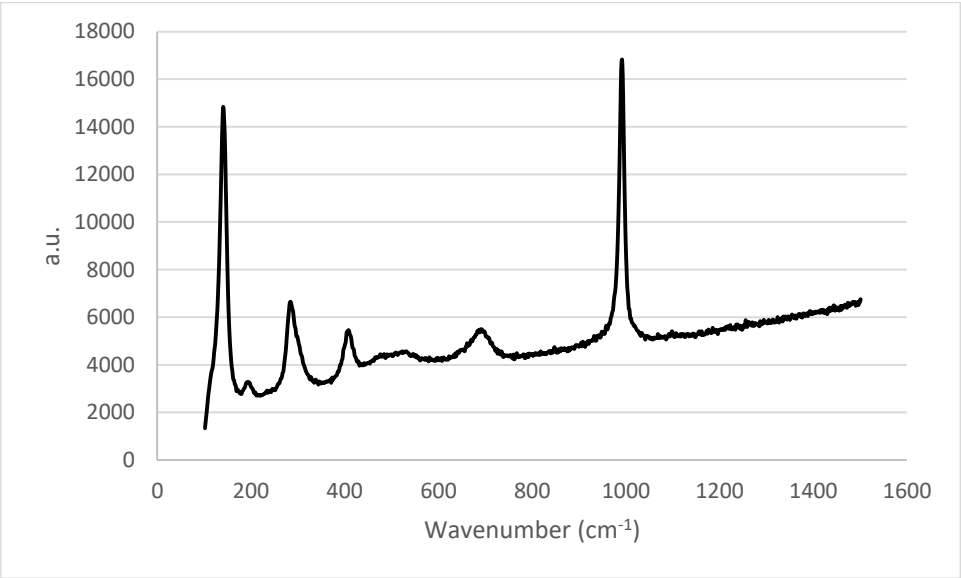

Figure A.2.4 – V_2O_5/EDOT Raman spectrum

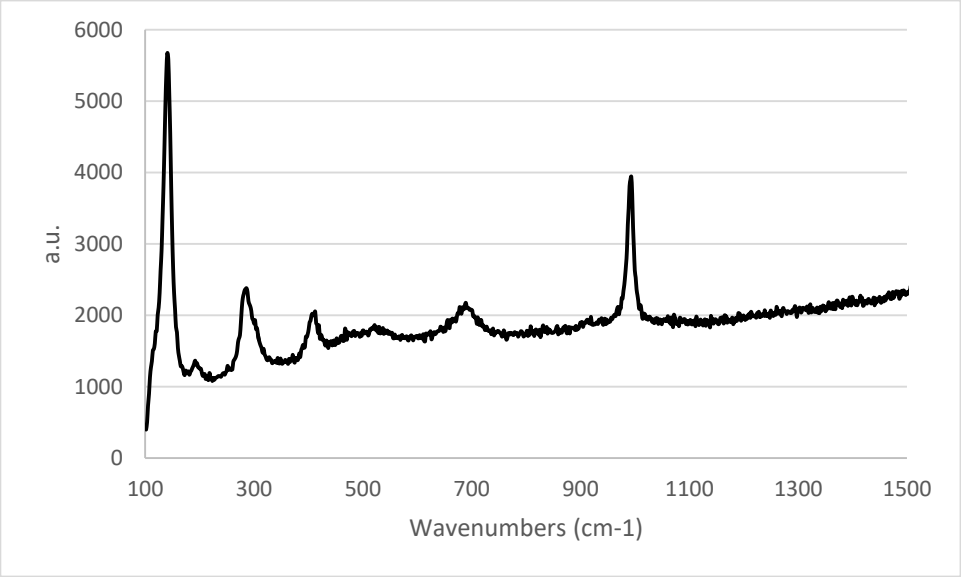

Figure A.2.5 – V_2O_5/PDA Raman spectrum

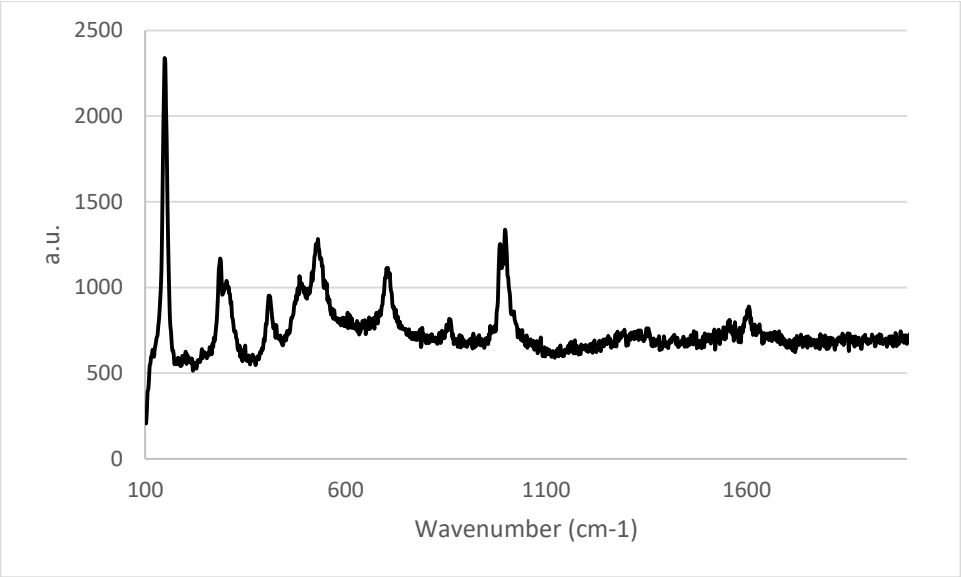

Figure A.2.6 – V_2O_5/PDA Raman spectrum

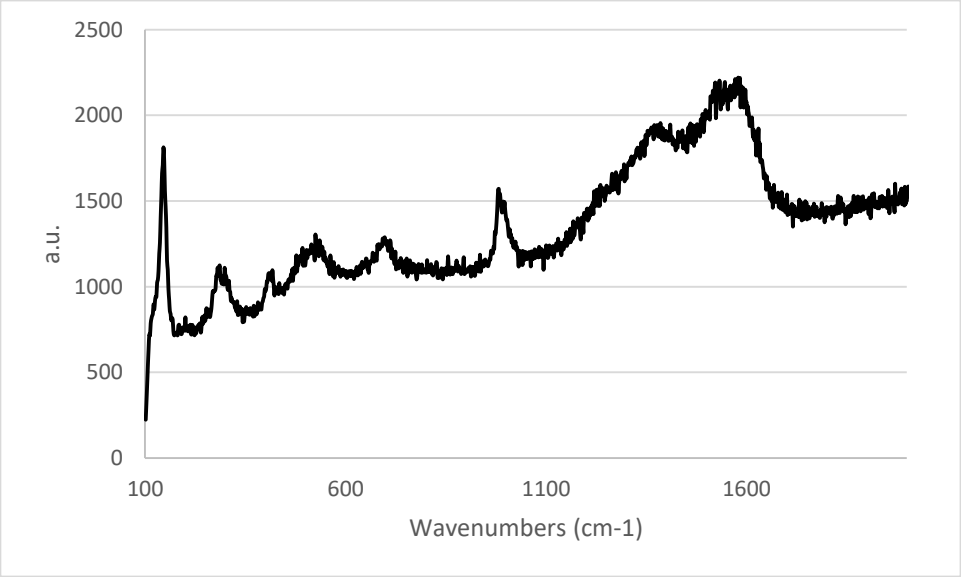

Figure A.2.7 – V_2O_5/PDA Raman spectrum

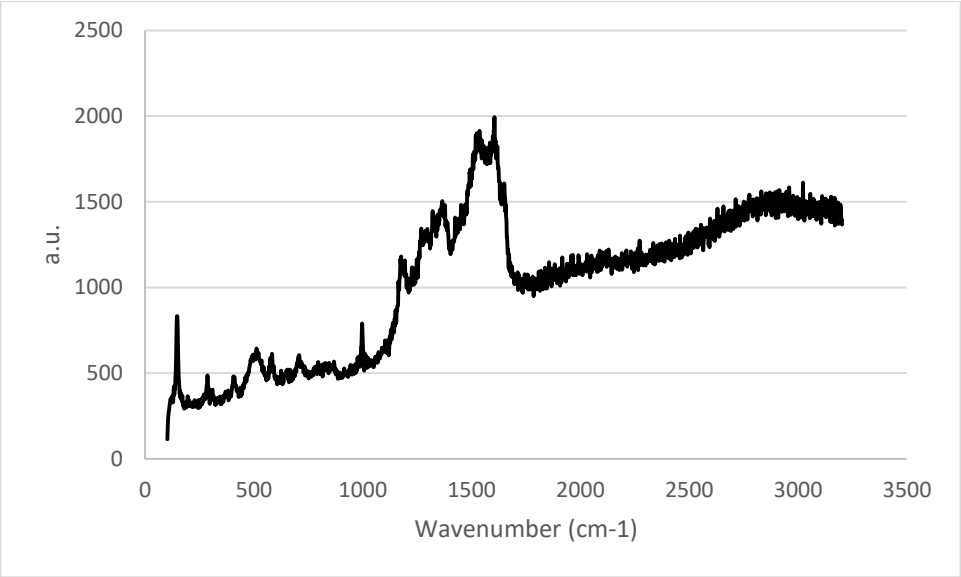

Figure A.2.8 – V_2O_5/1,4PDA-HQ Raman spectrum

A.3 V_2O_5 Nanocomposite TGA

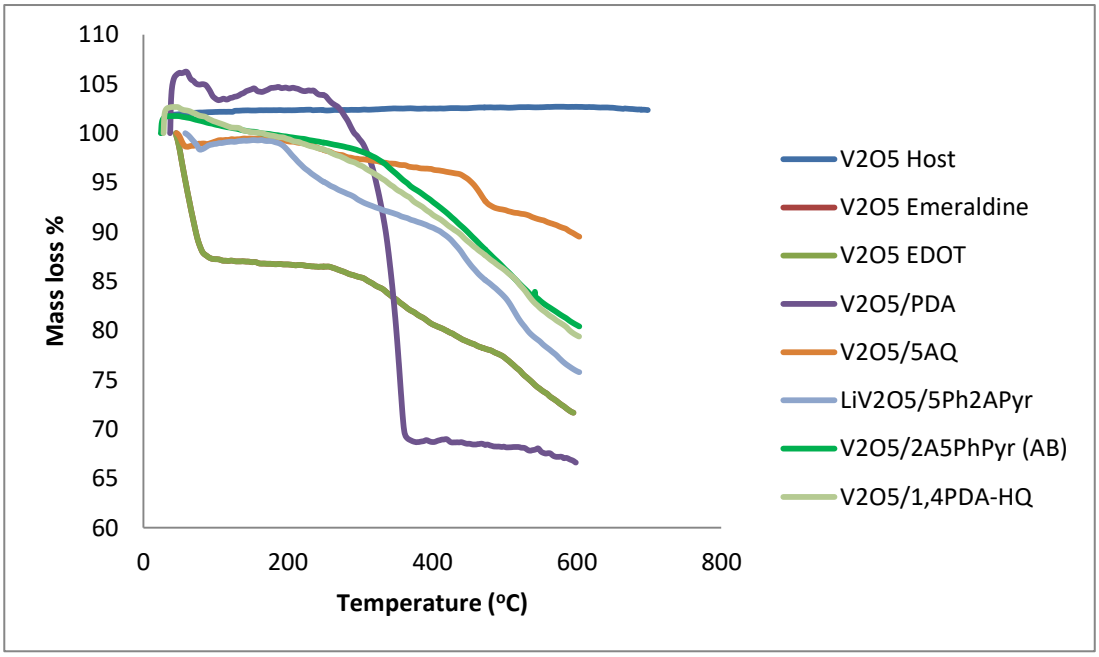

Figure A.3.1 - V_2O_5 nanocomposite Thermogravimetric Analysis (TGA)

A.4 V_2O_5 Nanocomposite Optical Spectroscopy and Tauc Plots

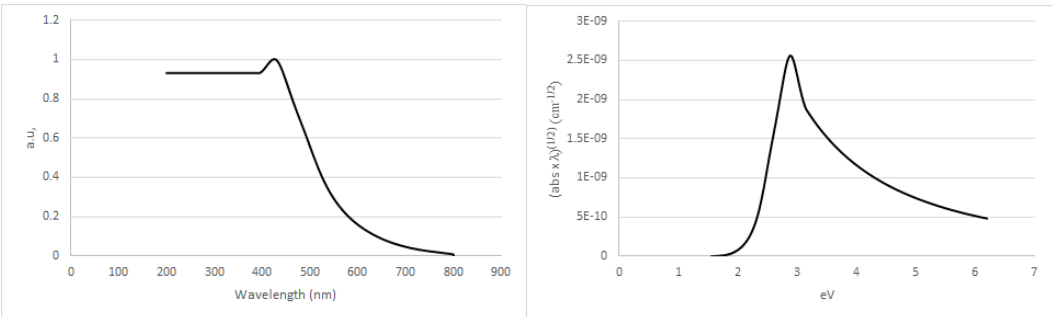

Figure A.4.1 – Left: V_2O_5 UV-Vis spectrum, Right: V_2O_5 Tauc plot

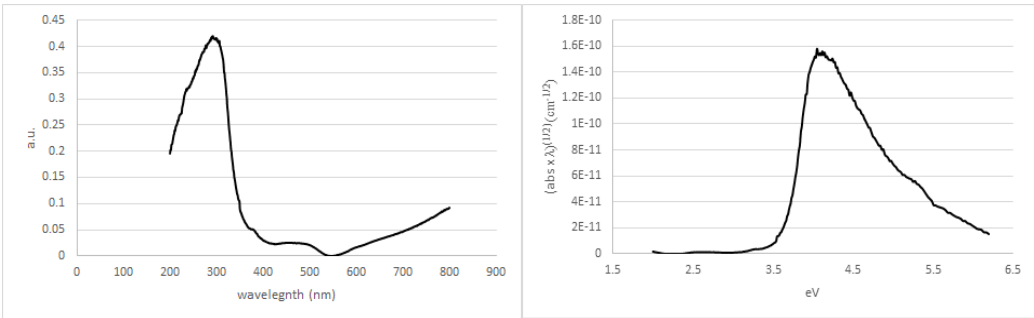

Figure A.4.2 – Left: $V_2O_5/AnAn^+$ UV-Vis spectrum, Right: $V_2O_5/AnAn^+$ Tauc plot

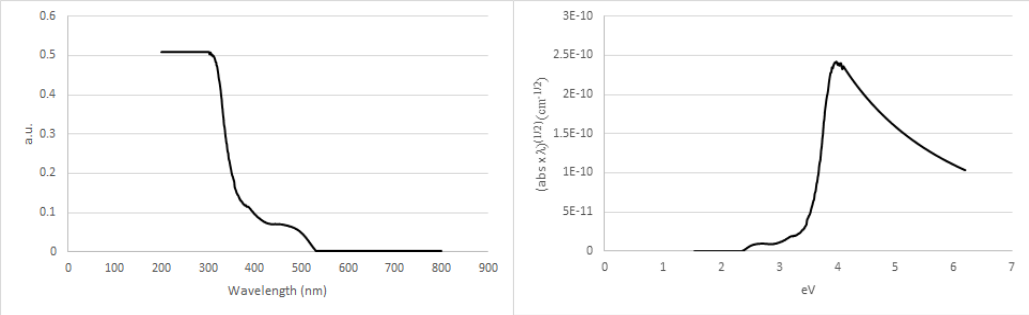

Figure A.4.3 – Left: V_2O_5/2A5PhPyr (AB) UV-Vis spectrum, Right: V_2O_5/2A5PhPyr (AB) Tauc plot

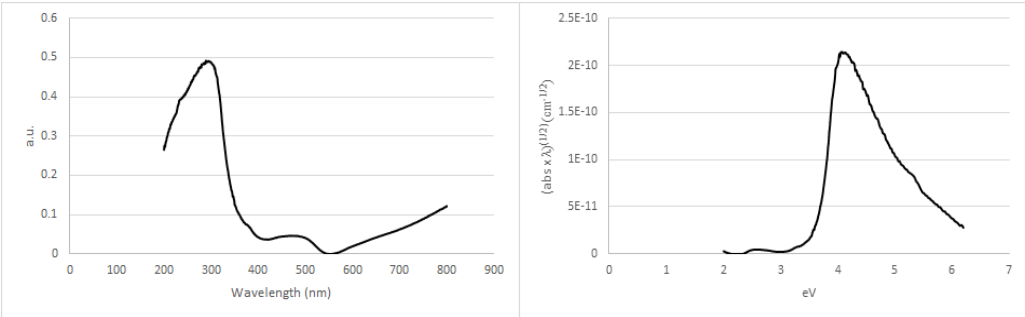

Figure A.4.4 – Left: V_2O_5/EDOT UV-Vis spectrum, Right: V_2O_5/EDOT Tauc plot

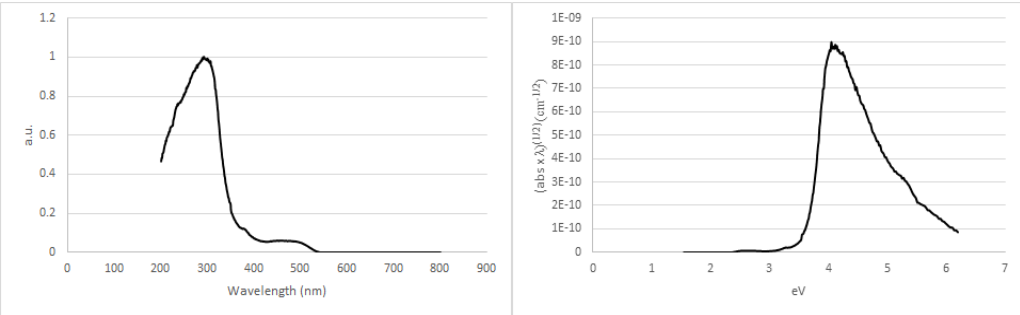

Figure A.4.5 – Left: V_2O_5/PDA UV-Vis spectrum, Right: V_2O_5/PDA Tauc plot

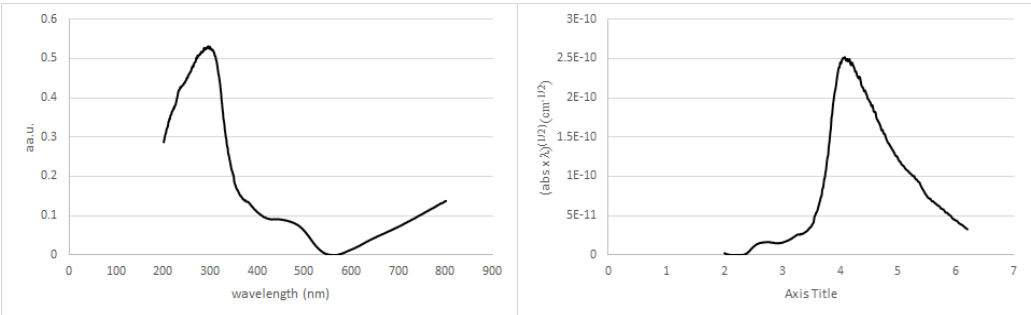

Figure A.4.6 – Left: (Li)V_2O_5/2A5PhPyr UV-Vis spectrum, Right: (Li)V_2O_5/2A5PhPyr Tauc plot

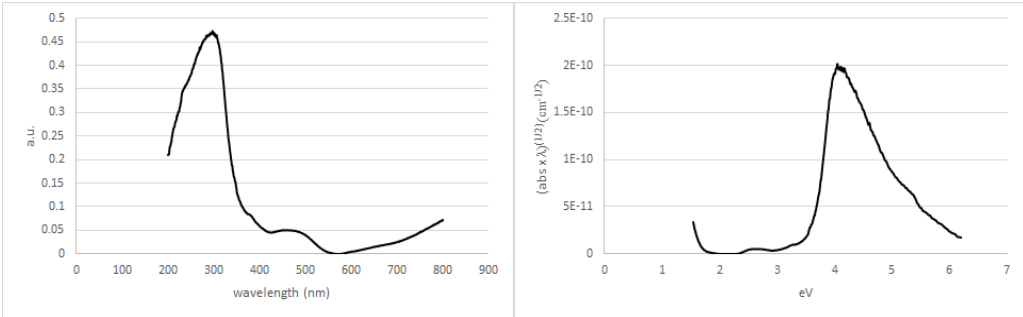

Figure A.4.7 – Left: V_2O_5/5AQ UV-Vis spectrum, Right: V_2O_5/5AQ Tauc plot

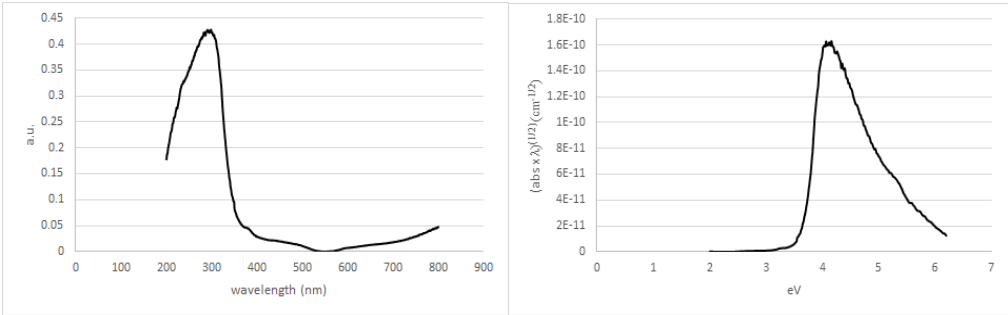

Figure A.4.8 – Left: V_2O_5/1,4PDA-HQ UV-Vis spectrum, Right: V_2O_5/1,4PDA-HQ Tauc plot

A.5 V_2O_5 Nanocomposite Seebeck coefficient plots

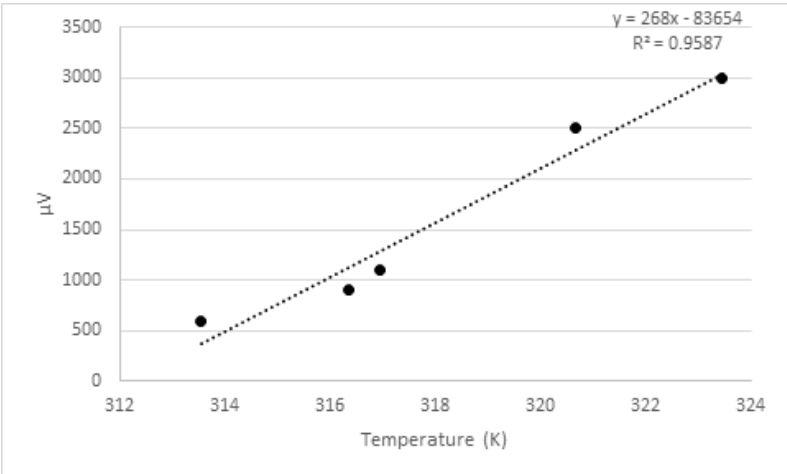

Figure A.5.1 – Seebeck coefficient plot for V_2O_5/AnAn$^+$

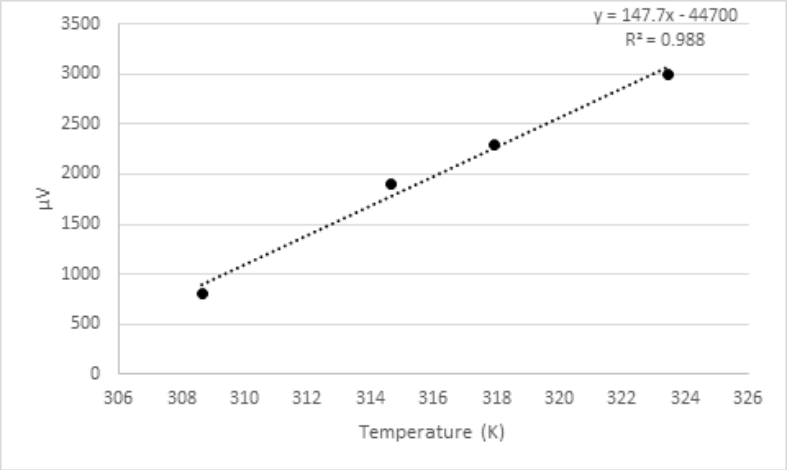

Figure A.5.2 – Seebeck coefficient plot for V_2O_5/2A5PhPyr (AB)

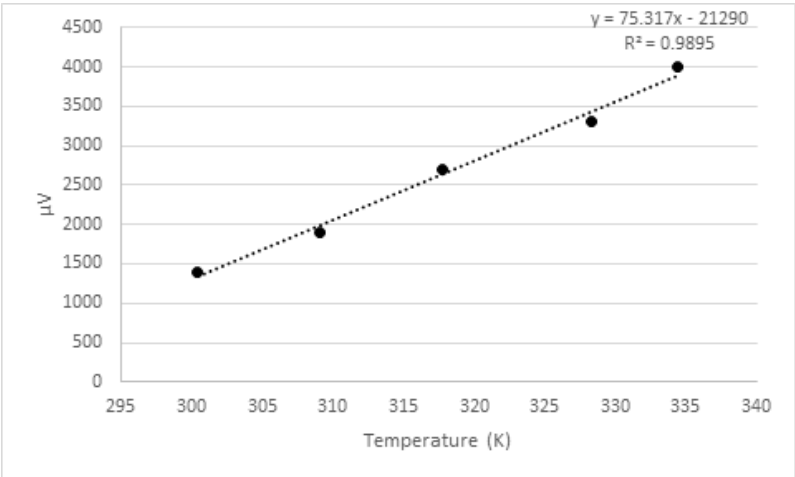

Figure A.5.3 – Seebeck coefficient plot for V_2O_5/EDOT

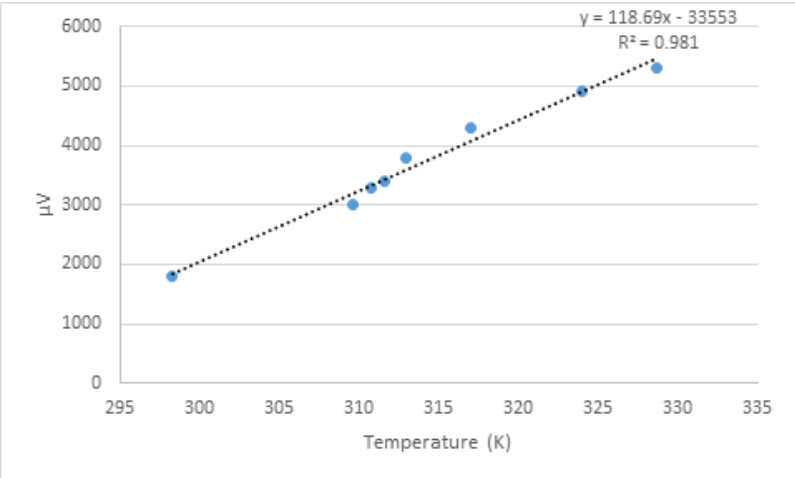

Figure A.5.4 – Seebeck coefficient plot for V_2O_5/1,4PDA-HQ

A.6 V_2O_5 Nanocomposite Capacitance vs Voltage (C-V) plots

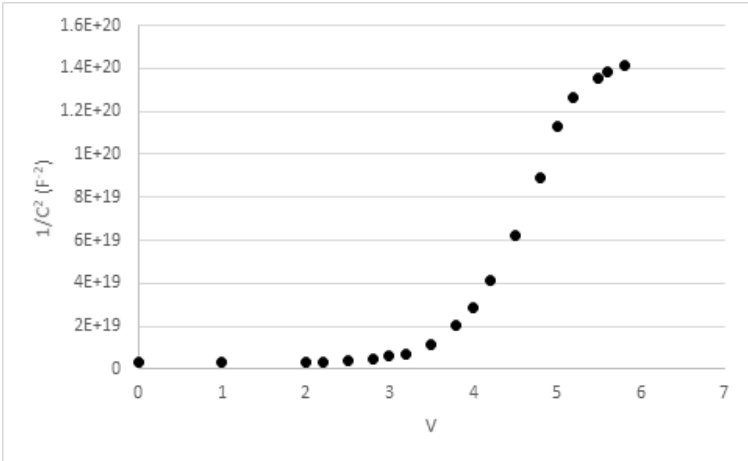

Figure A.6.1 – Capacitance vs Voltage plot for V_2O_5/AnAn$^+$ pressed Schottky device with Zn contact

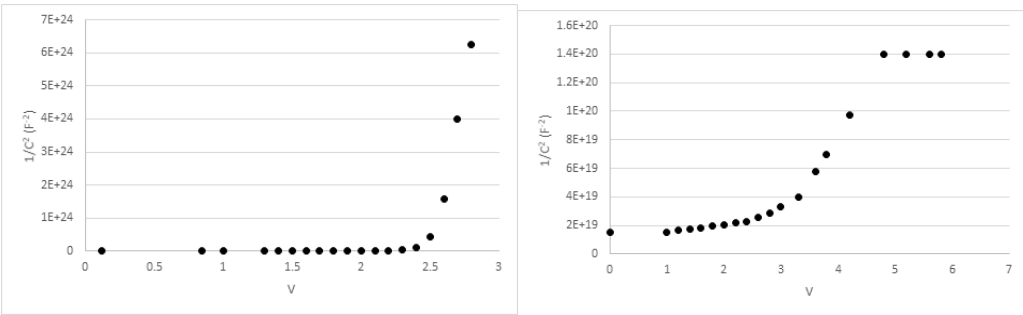

Figure A.6.2 – Capacitance vs Voltage plot for V_2O_5/AnAn$^+$ Schottky devices with Al contact where left: pressed pellet device and right: evaporated contact device

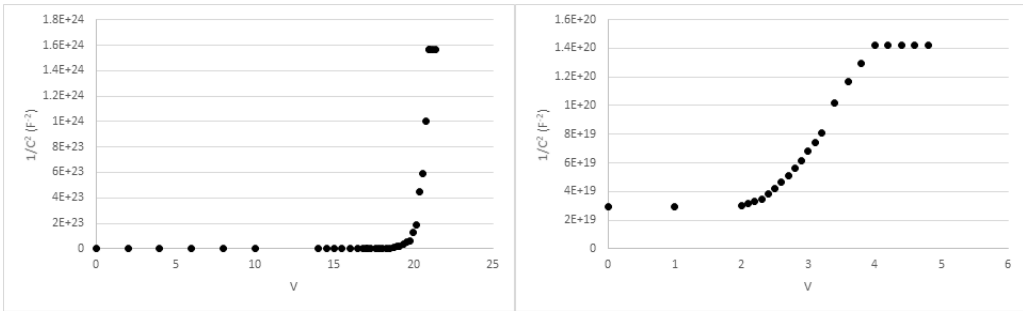

Figure A.6.3 – Capacitance vs Voltage plot for V_2O_5/AnAn$^+$ Schottky devices with Cu contact where left: pressed pellet device and right: evaporated contact device

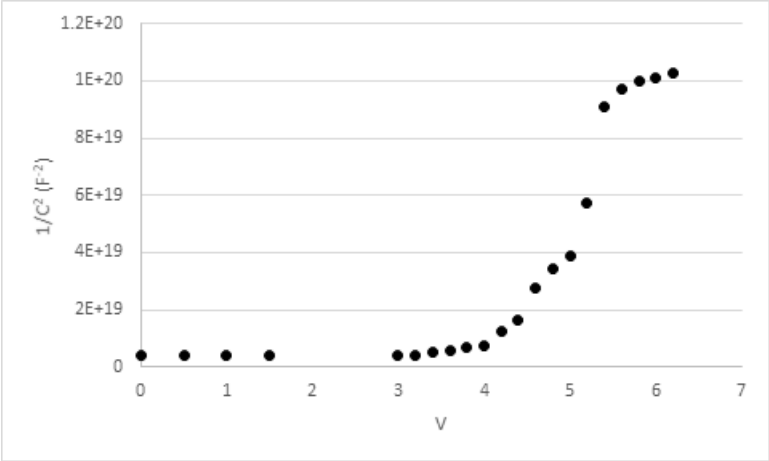

Figure A.6.4 – Capacitance vs Voltage plot for V_2O_5/AnAn$^+$ pressed Schottky devices with Sn contact

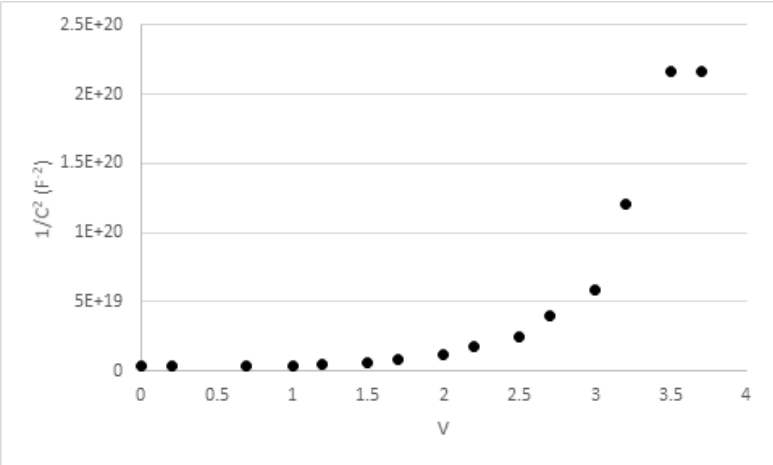

Figure A.6.5 – Capacitance vs Voltage plot for V_2O_5/AnAn$^+$ Schottky devices with $FePS_3$ contact

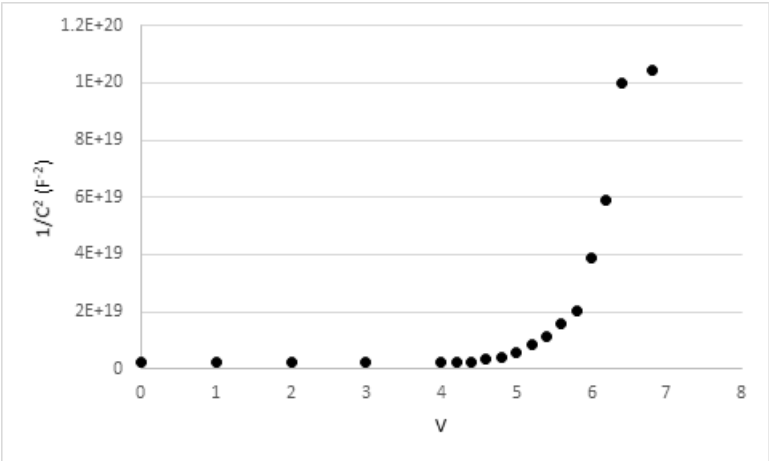

Figure A.6.6 – Capacitance vs Voltage plot for V_2O_5/2A5PhPyr pressed Schottky devices with Zn contact

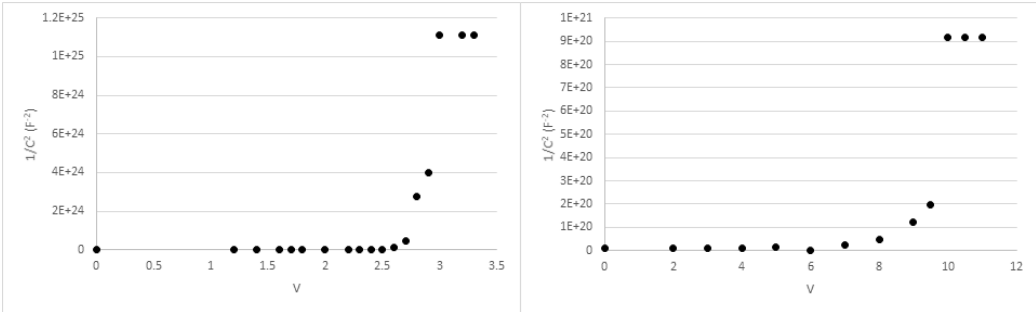

Figure A.6.7 – Capacitance vs Voltage plot for V_2O_5/2A5PhPyr pressed Schottky devices with Al contact where left: pressed pellet device and right: evaporated contact device

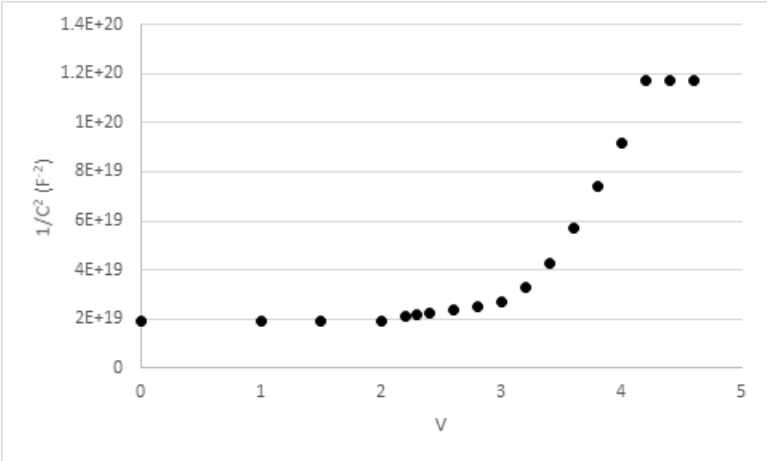

Figure A.6.8 – Capacitance vs Voltage plot for V_2O_5/EDOT pressed Schottky devices with Zn contact

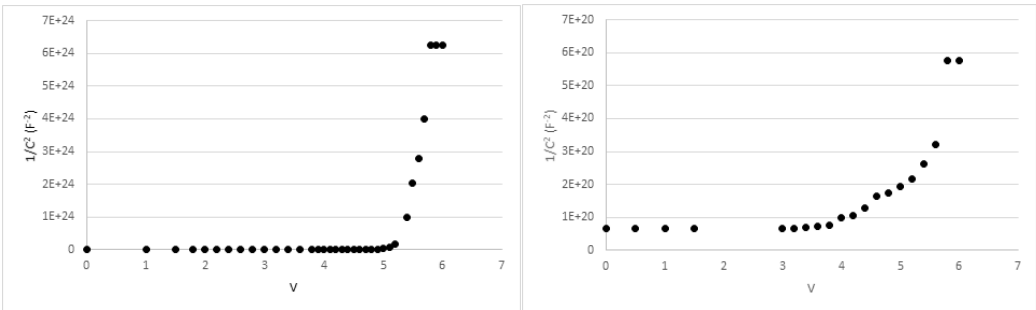

Figure A.6.9 – Capacitance vs Voltage plot for V_2O_5/EDOT pressed Schottky devices with Al contact where left: pressed pellet device and right: evaporated contact device

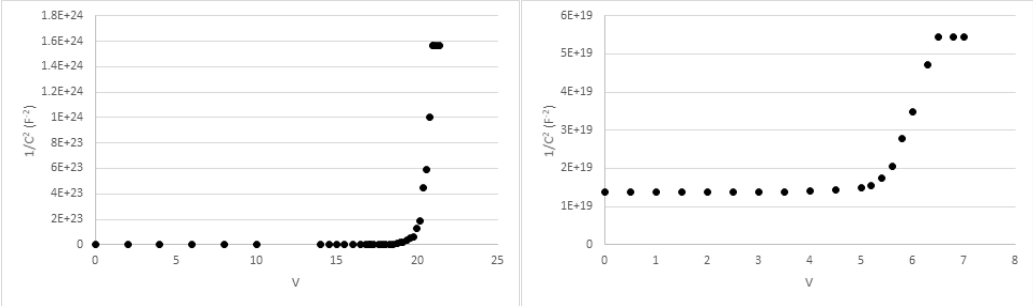

Figure A.6.10 – Capacitance vs Voltage plot for V_2O_5/EDOT pressed Schottky devices with Cu contact where left: pressed pellet device and right: evaporated contact device

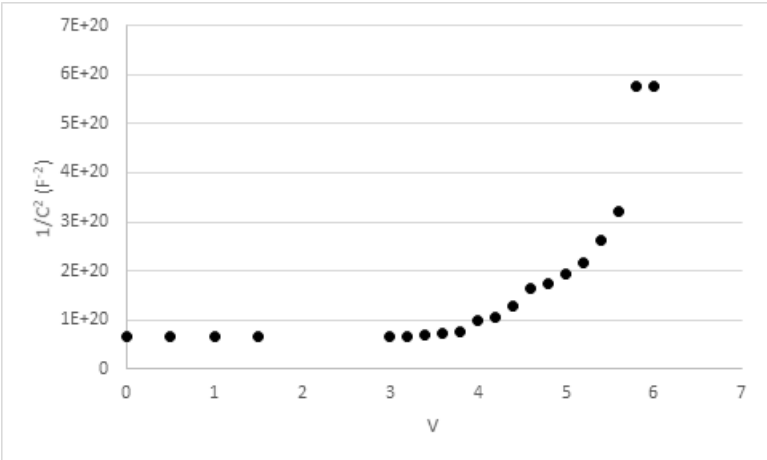

Figure A.6.11 – Capacitance vs Voltage plot for V_2O_5/EDOT pressed Schottky devices with Sn

Appendix B – MoO_3 Characterisation and Electrical Measurements

B.1 MoO_3 Nanocomposite IR

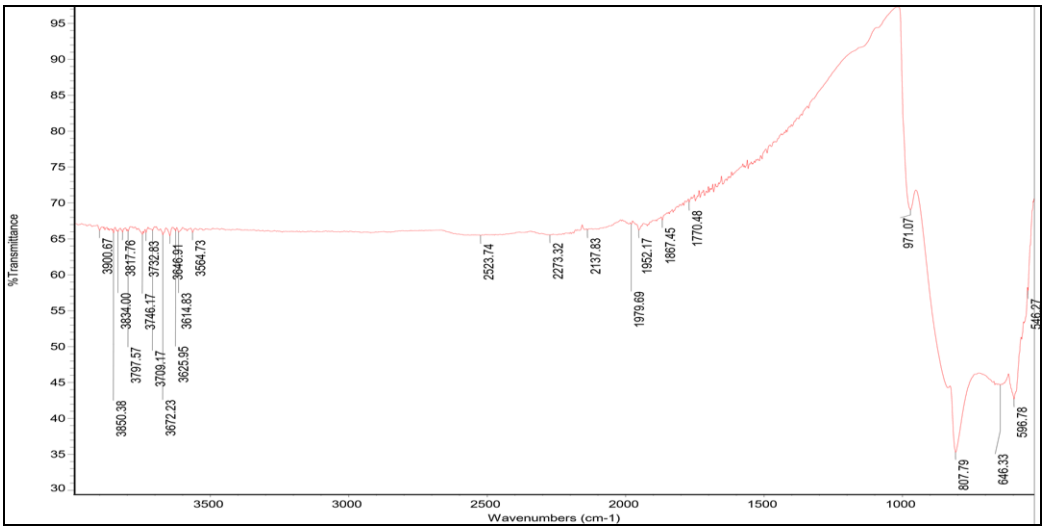

Figure B.1.1 – MoO_3 host IR spectrum

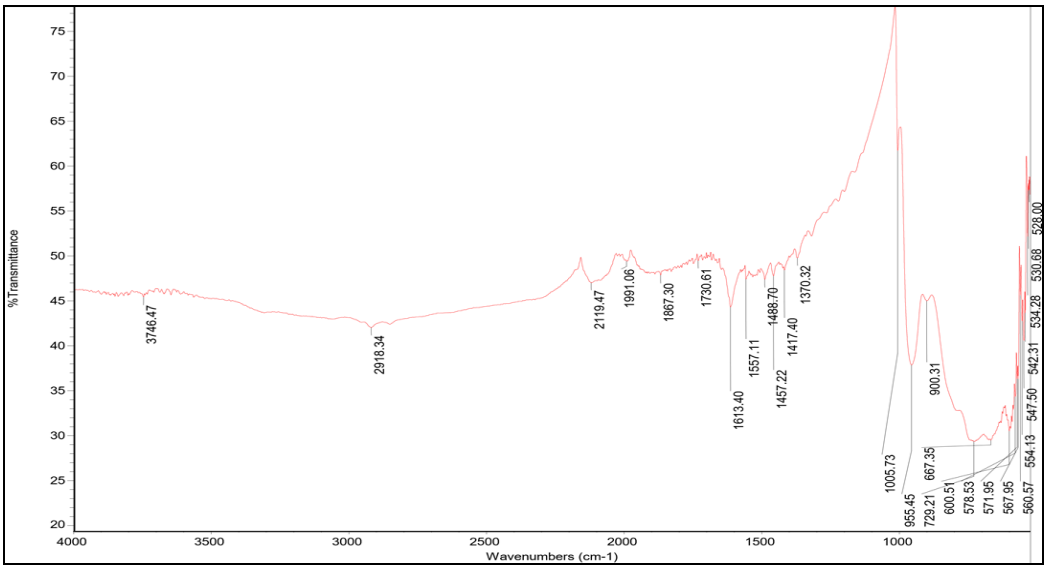

Figure B.1.2 – MoO_3/PDA IR spectrum

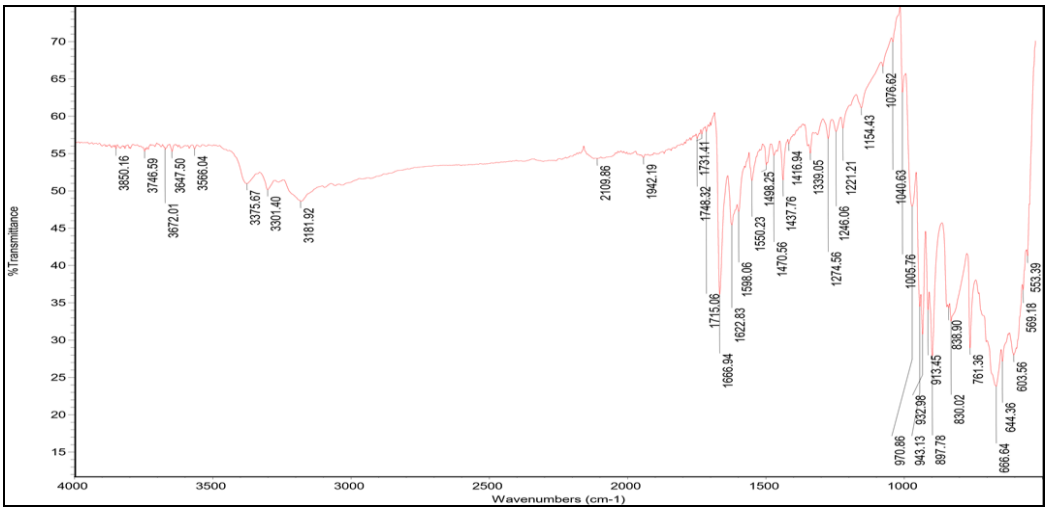

Figure B.1.3 – MoO_3/2A5PhPyr IR spectrum

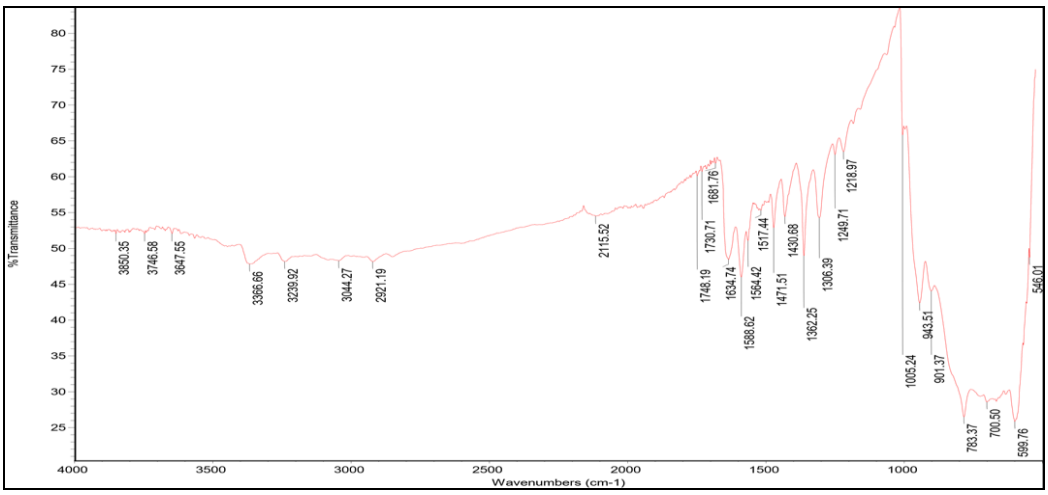

Figure B.1.4 – MoO_3/5AQ IR spectrum

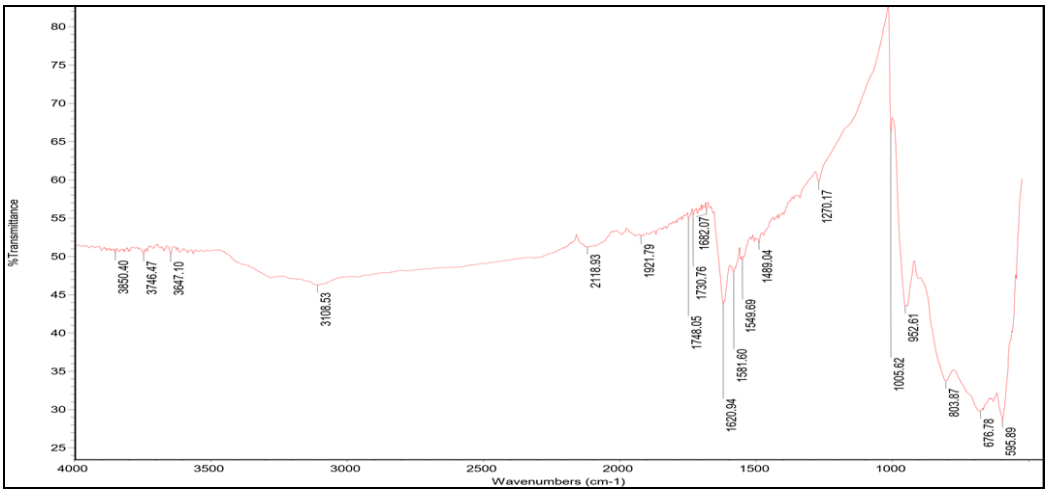

Figure B.1.5 – MoO_3/2AmThia IR spectrum

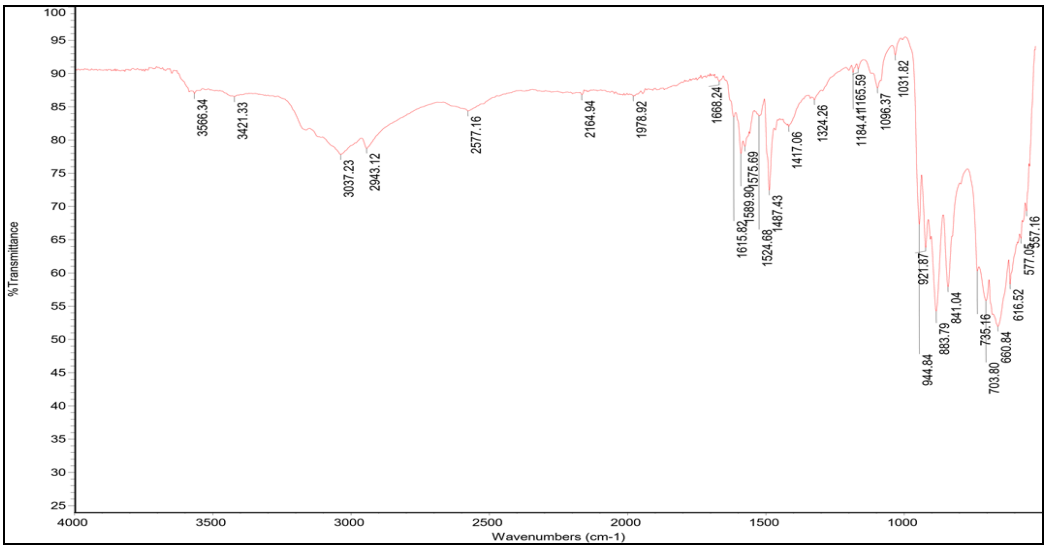

Figure B.1.6 – MoO_3/An IR spectrum

B.2 MoO_3 Raman Spectra

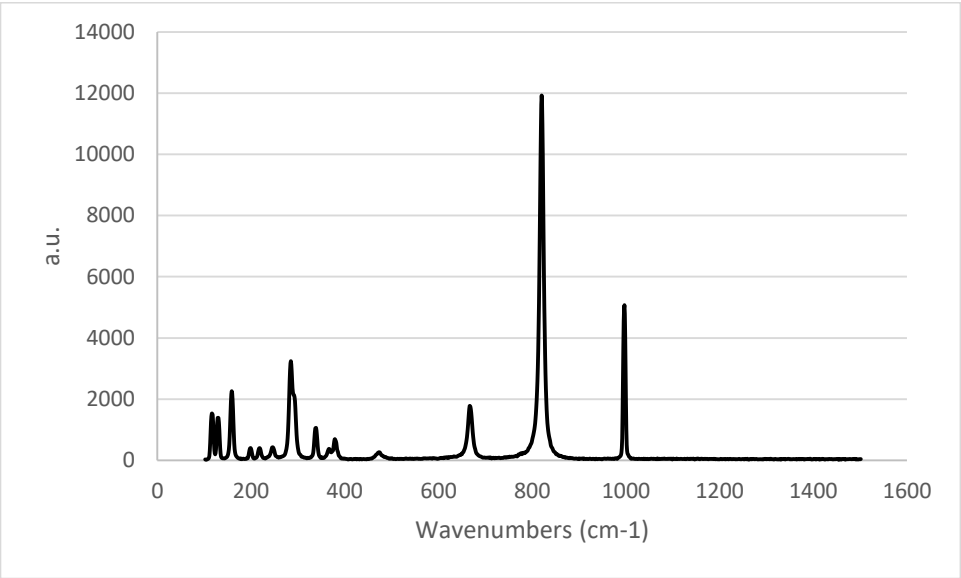

Figure B.2.1 – MoO_3 Raman spectrum

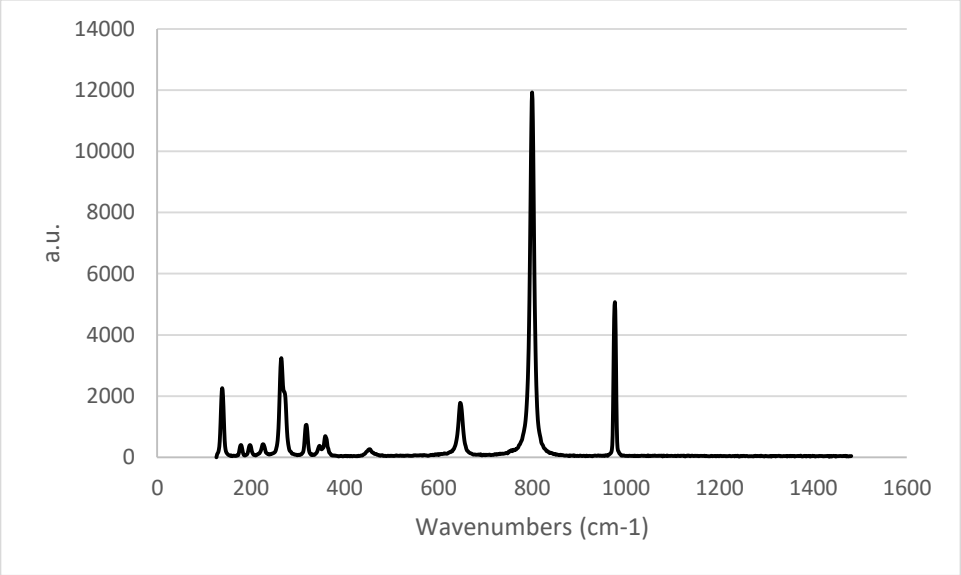

Figure B.2.2 – MoO_3/PDA Raman spectrum

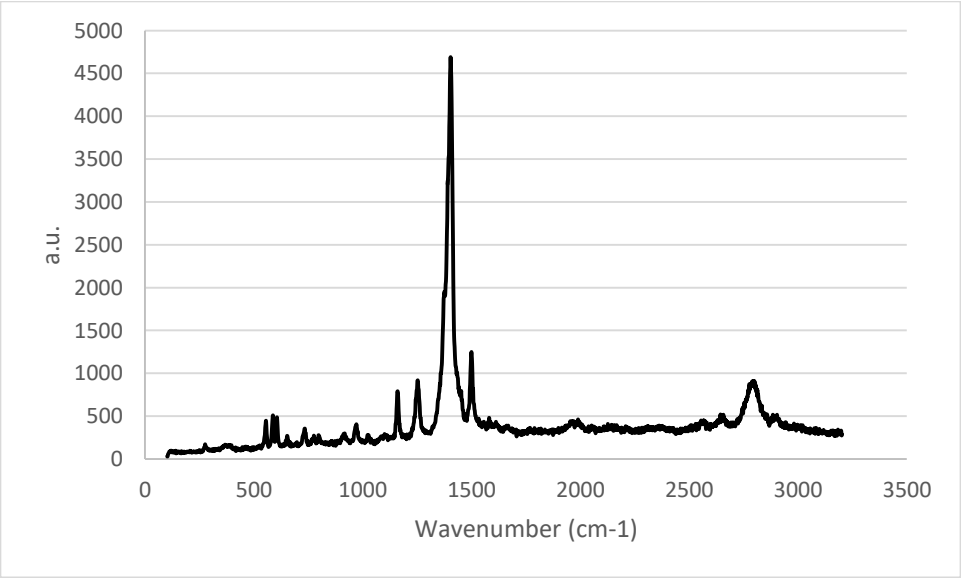

Figure B.2.3 – MoO_3/PDA Raman spectrum

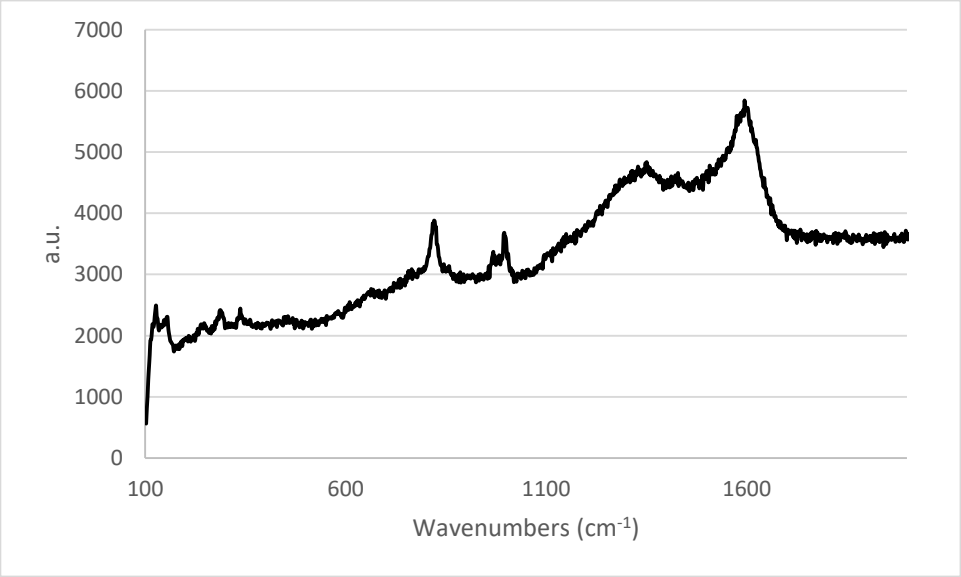

Figure B.2.4 – MoO_3/2A5PhPyr Raman spectrum

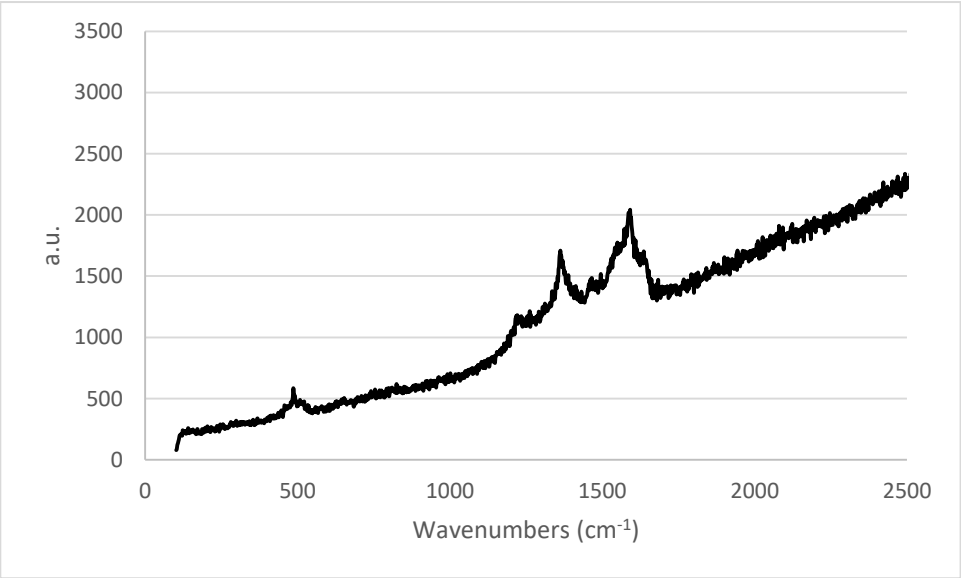

Figure B.2.5 – MoO_3/5AQ Raman spectrum

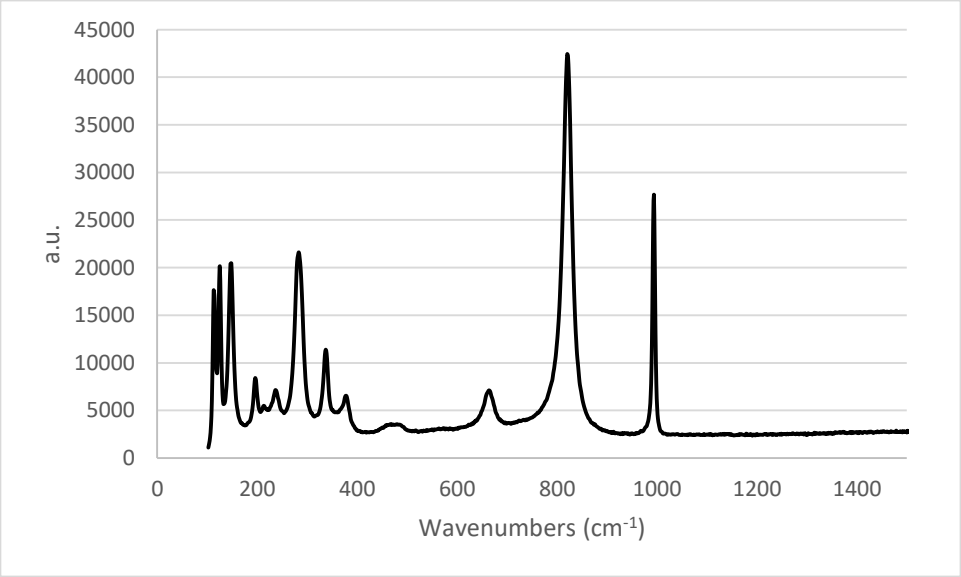

Figure B.2.6 – MoO_3/2AmThia Raman spectrum

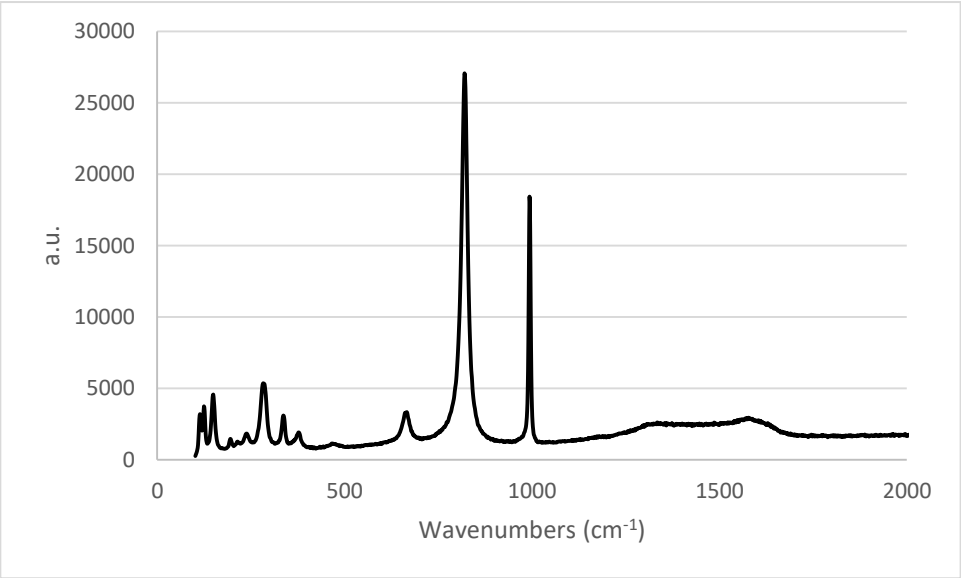

Figure B.2.7 – MoO_3/An Raman spectrum

B.3 MoO_3 Nanocomposite TGA

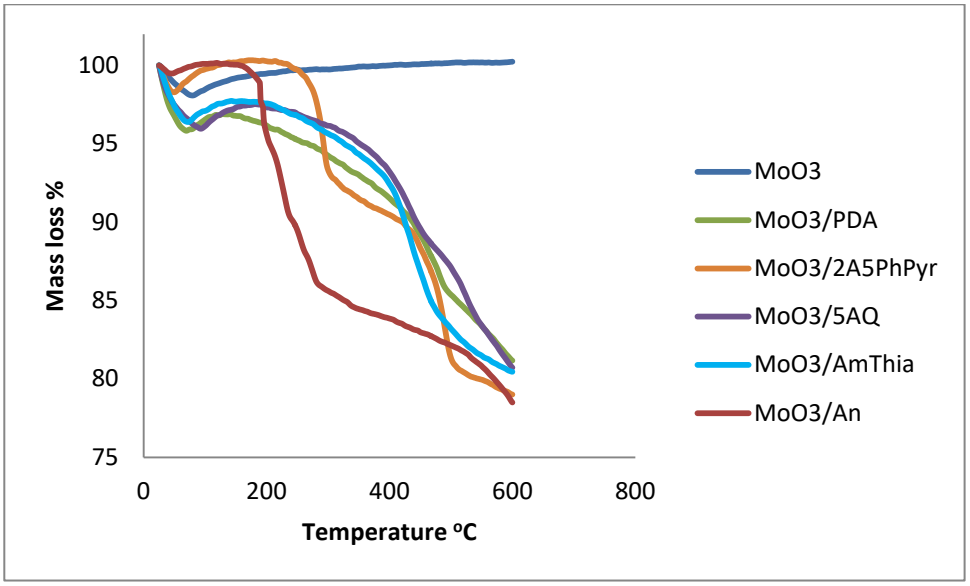

Figure B.3.1 – MoO_3 nanocomposite thermogravimetric analysis (TGA)

B.4 MoO_3 Nanocomposite Optical spectroscopy and Tauc plots

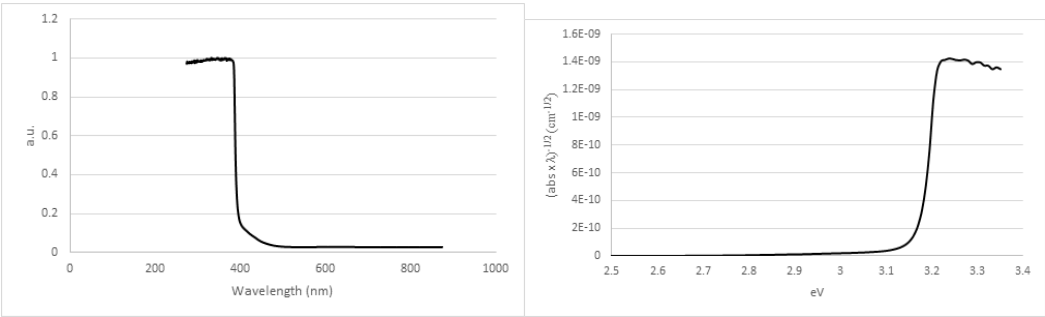

Figure B.4.1 – Left: MoO_3 UV-Vis spectrum, Right: MoO_3 Tauc plot

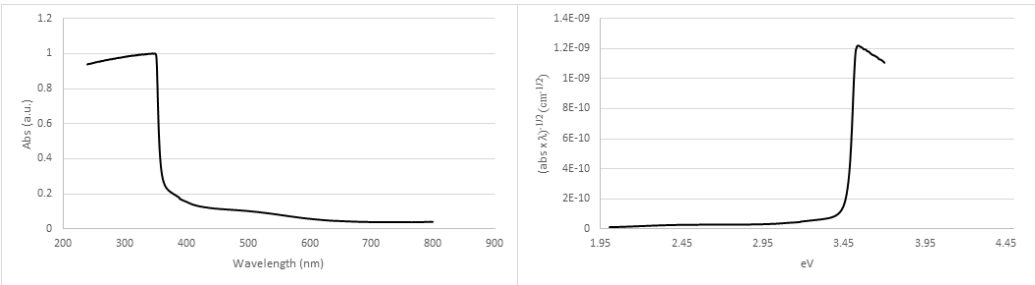

Figure B.4.2 – Left: MoO_3/PDA UV-Vis spectrum, Right: MoO_3/PDA Tauc plot

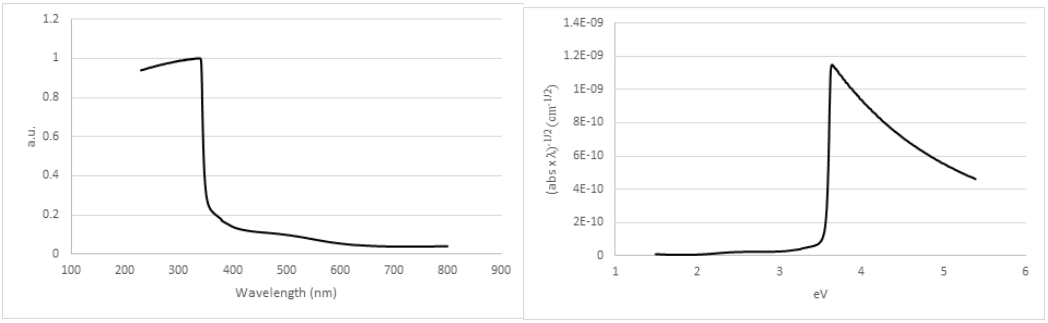

Figure B.4.3 – Left: MoO_3/2A5PhPyr UV-Vis spectrum, Right: MoO_3/2A5PhPyr Tauc plot

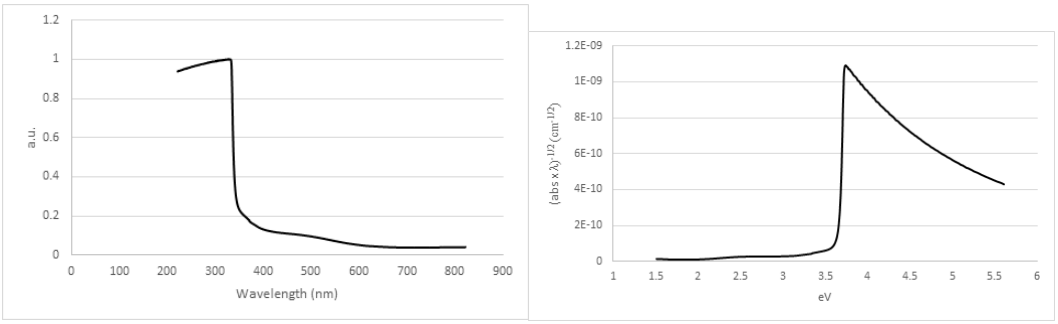

Figure B.4.4 – Left: MoO_3/5AQ UV-Vis spectrum, Right: MoO_3/5AQ Tauc plot

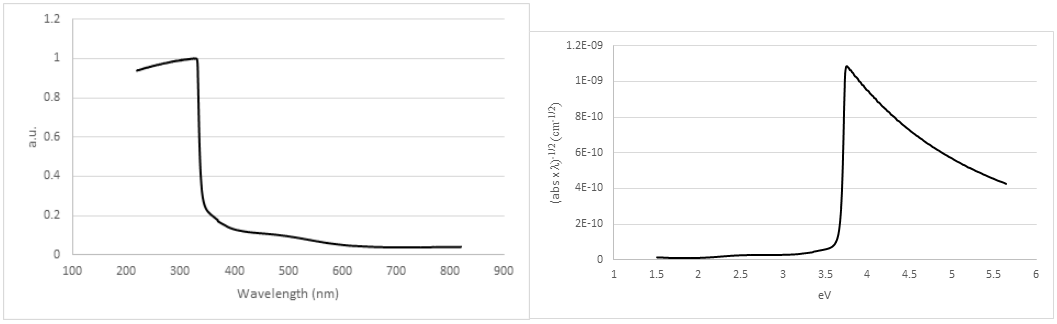

Figure B.4.5 – Left: MoO_3/2AmThia UV-Vis spectrum, Right: MoO_3/2AmThia Tauc plot

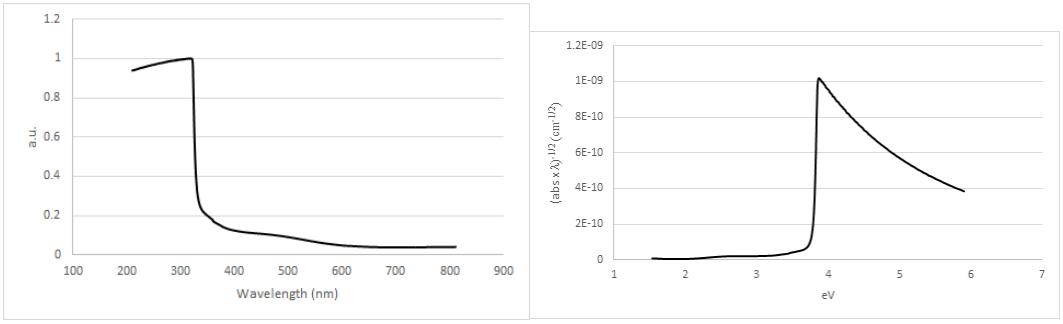

Figure B.4.6 – Left: MoO_3/2AmThia UV-Vis spectrum, Right: MoO_3/2AmThia Tauc plot

B.5 MoO_3 Nanocomposite Seebeck Coefficient Plots

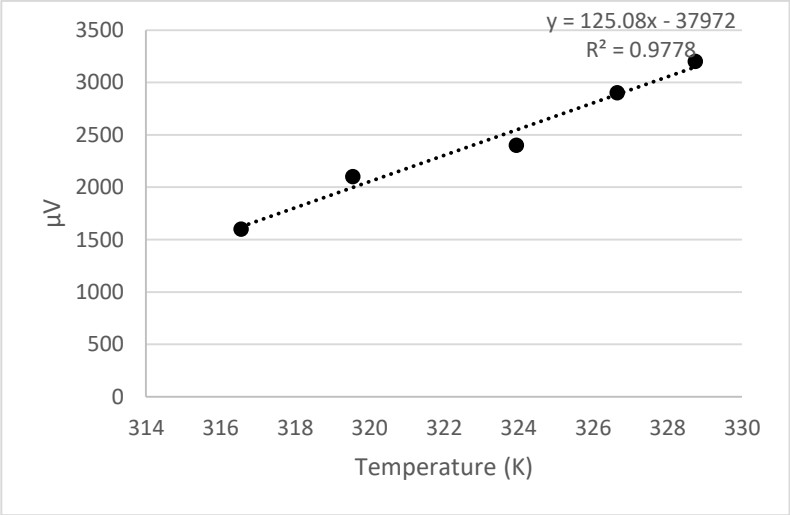

Figure B.5.1 – Seebeck coeffiecient plot for MoO_3/PDA

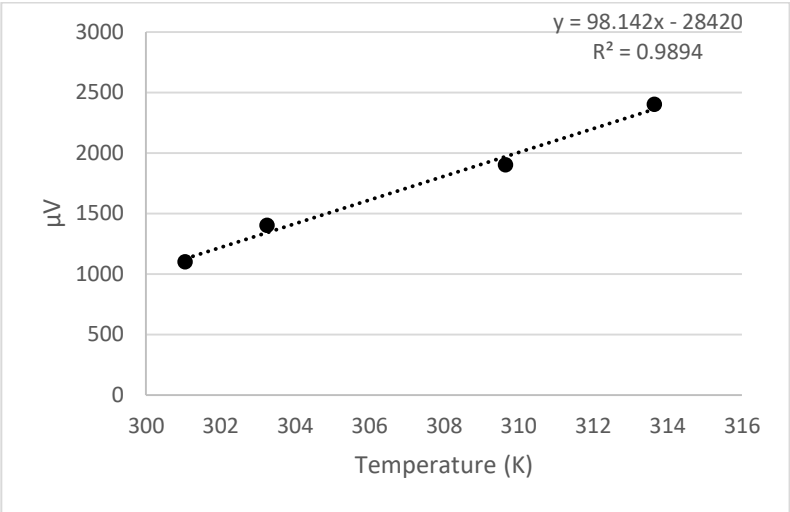

Figure B.5.2 – Seebeck coeffiecient plot for MoO_3/PDA

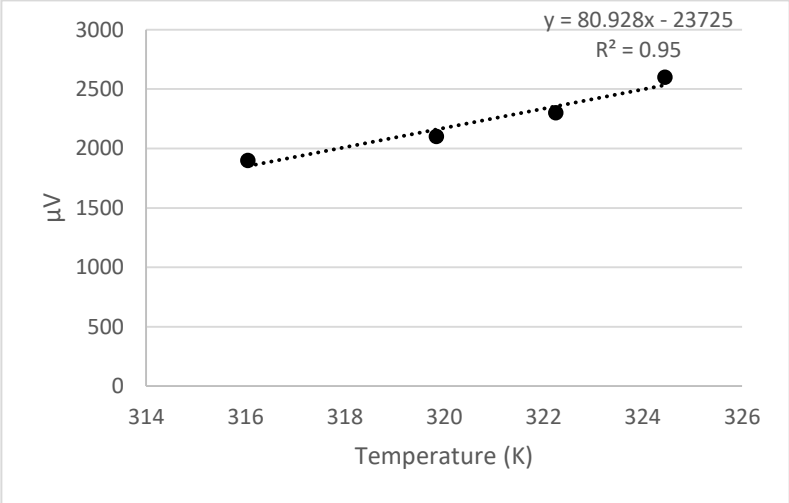

Figure B.5.3 – Seebeck coeffiecient plot for MoO_3/PDA

B.6 MoO_3 Nanocomposite Capacitance vs Voltage (C-V) Plots

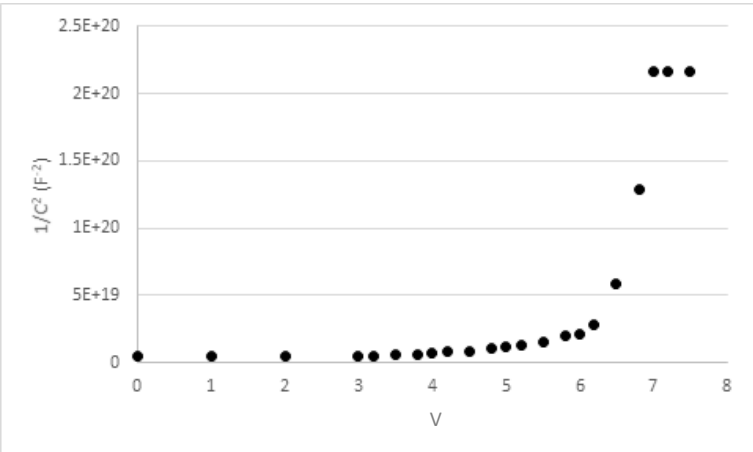

Figure B.6.1 – Capacitance vs Voltage plot for MoO_3/PDA pressed pellet device with Zn contact

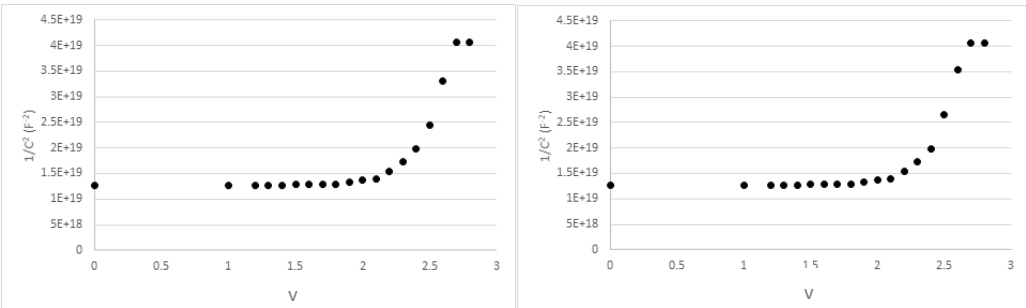

Figure B.6.2 – Capacitance vs Voltage plot for MoO_3/PDA device with Al contact where Left: pressed pellet device and Right: evaporated contact device

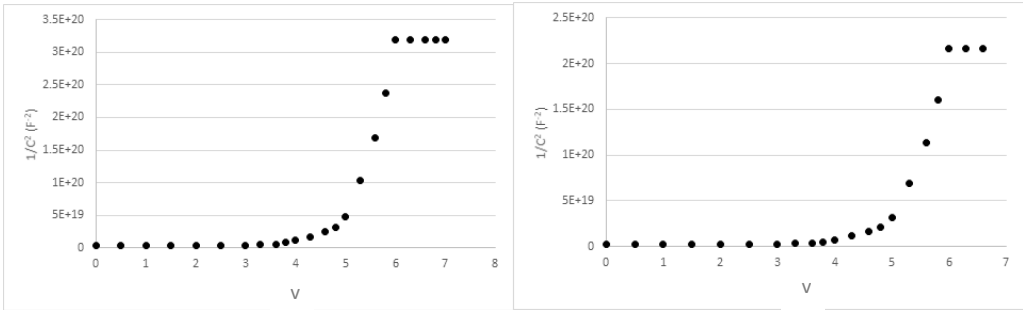

Figure B.6.3 – Capacitance vs Voltage plot for MoO_3/PDA device with Cu contact where Left: pressed pellet device and Right: evaporated contact device

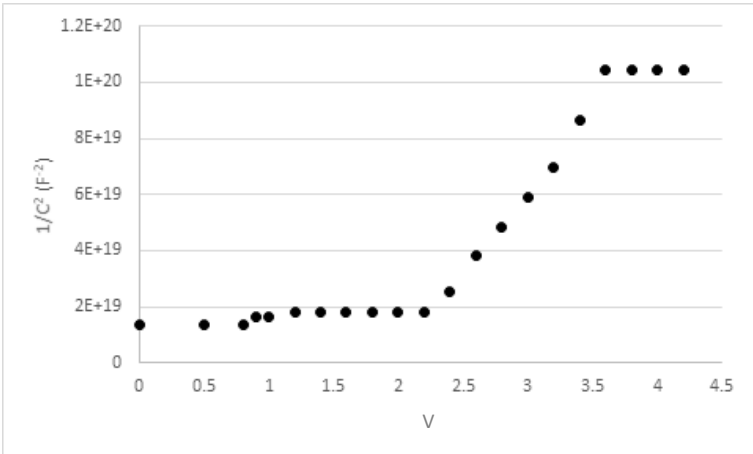

Figure B.6.4 – Capacitance vs Voltage plot for MoO_3/PDA pressed pellet device with Ni contact

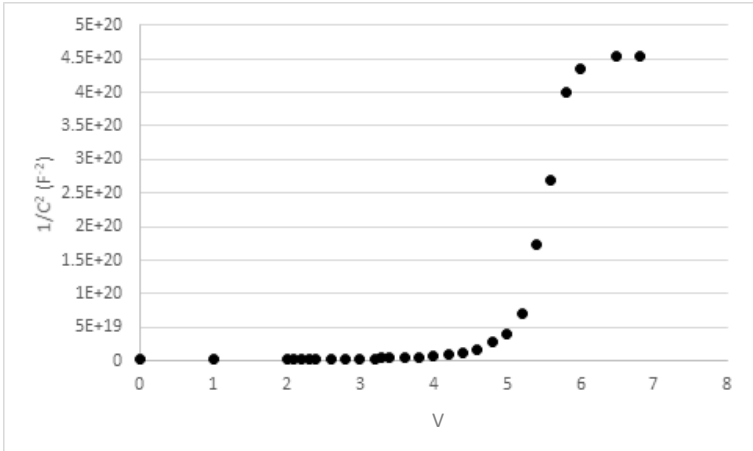

Figure B.6.5 – Capacitance vs Voltage plot for MoO_3/2A5PhPyr pressed pellet device with Zn contact

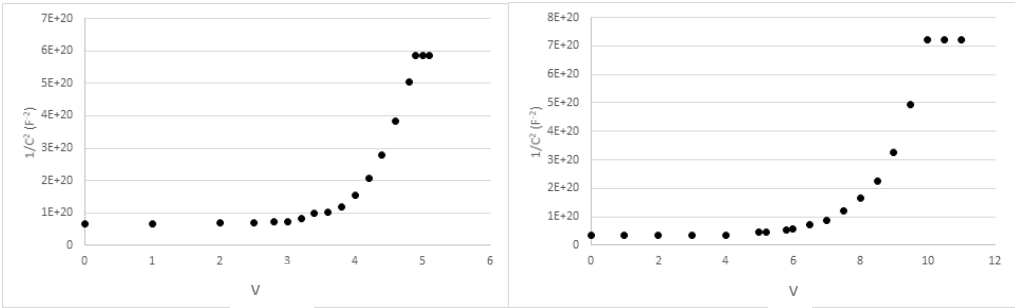

Figure B.6.6 – Capacitance vs Voltage plot for MoO_3/2A5PhPyr device with Al contact where Left: pressed pellet device and Right: evaporated contact device

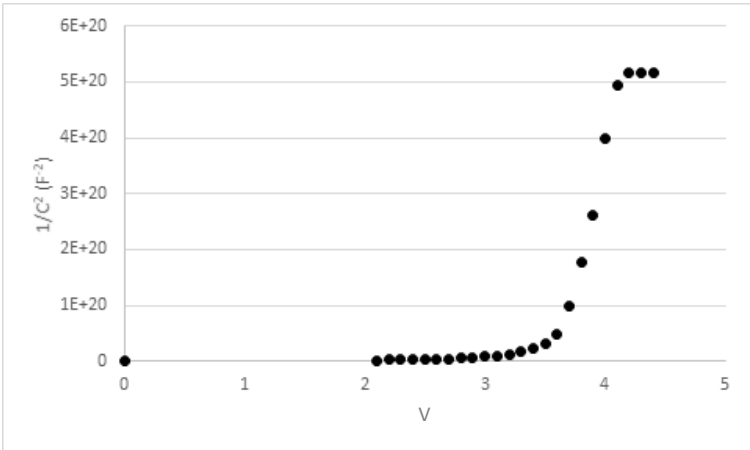

Figure B.6.7 – Capacitance vs Voltage plot for MoO_3/5AQ pressed pellet device with Zn contact

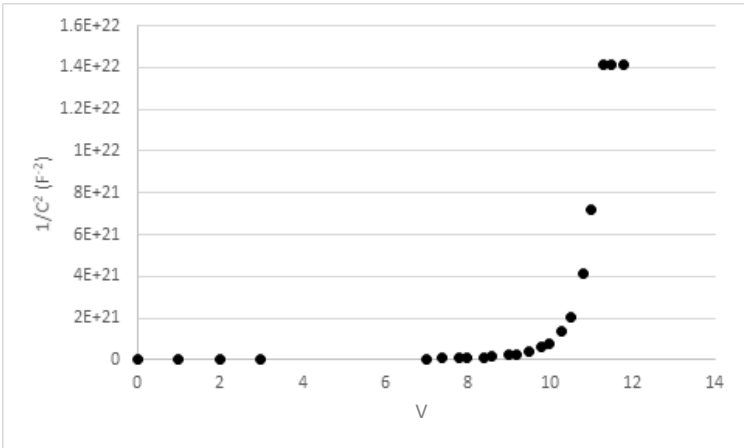

Figure B.6.8 – Capacitance vs Voltage plot for MoO_3/5AQ pressed pellet device with Al contact

Appendix C – $ZnPS_3$ Characterisation and Electrical Measurements

C.1 $ZnPS_3$ Nanocomposite IR Spectra

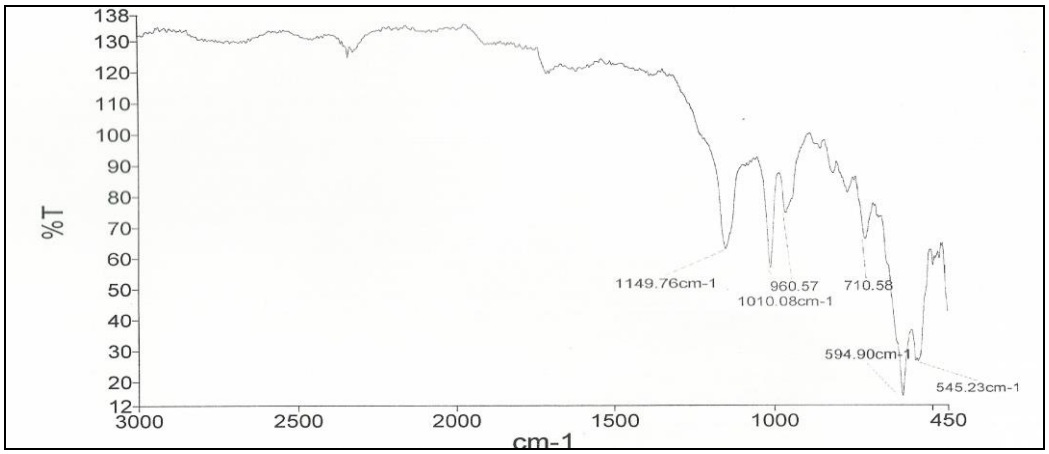

Figure C.1.1 – $ZnPS_3$ host IR spectrum

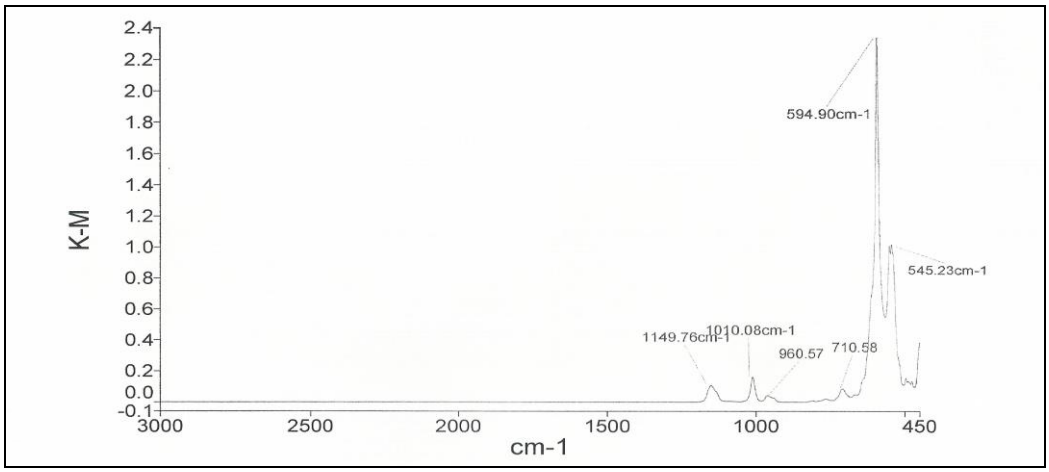

Figure C.1.2 – $ZnPS_3$ host IR spectrum, Kulbelka-Munk transformation

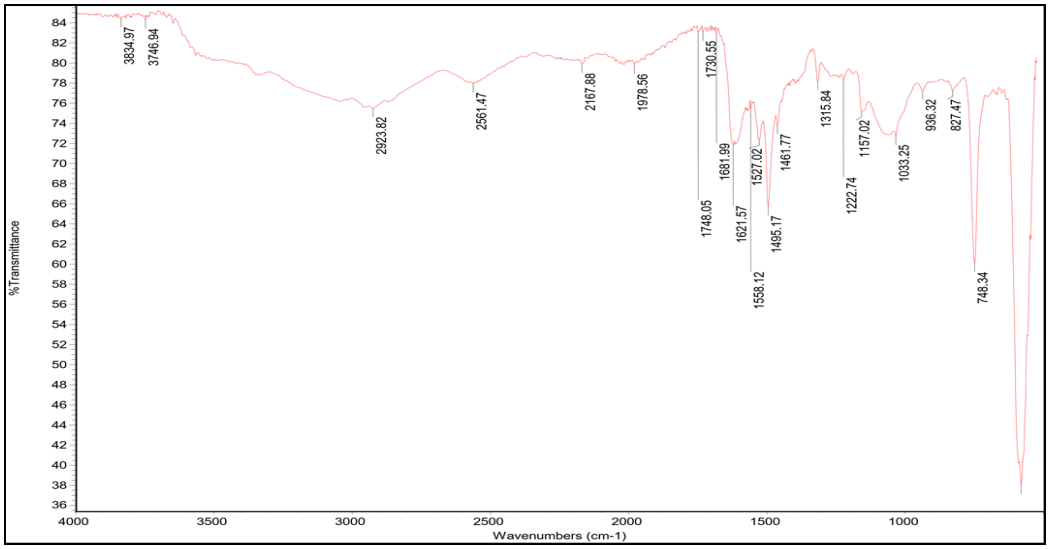

Figure C.1.3 – Mg_xZnPS_3 IR spectrum

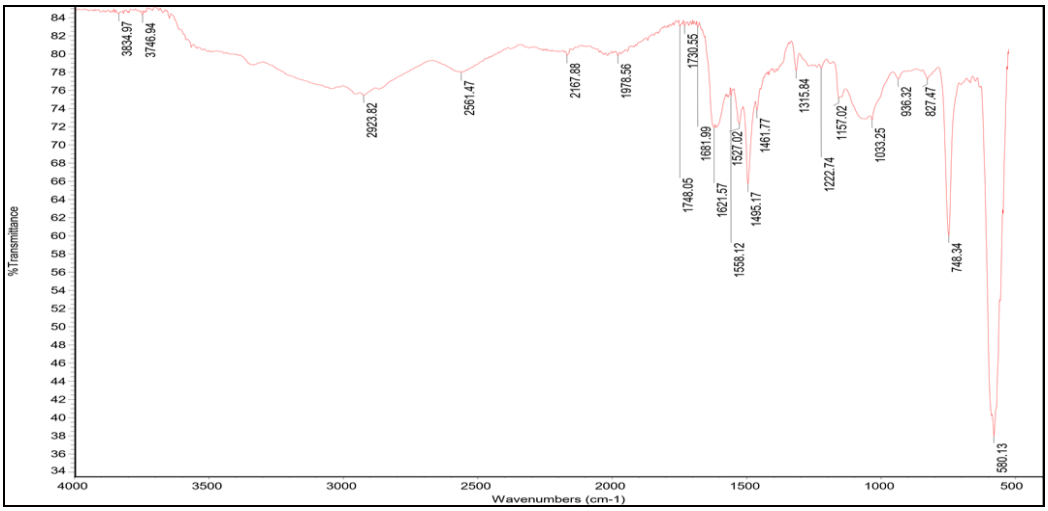

Figure C.1.4 – $ZnPS_3$/PDA IR spectrum

C.2 $ZnPS_3$ Nanocomposite Raman Spectra

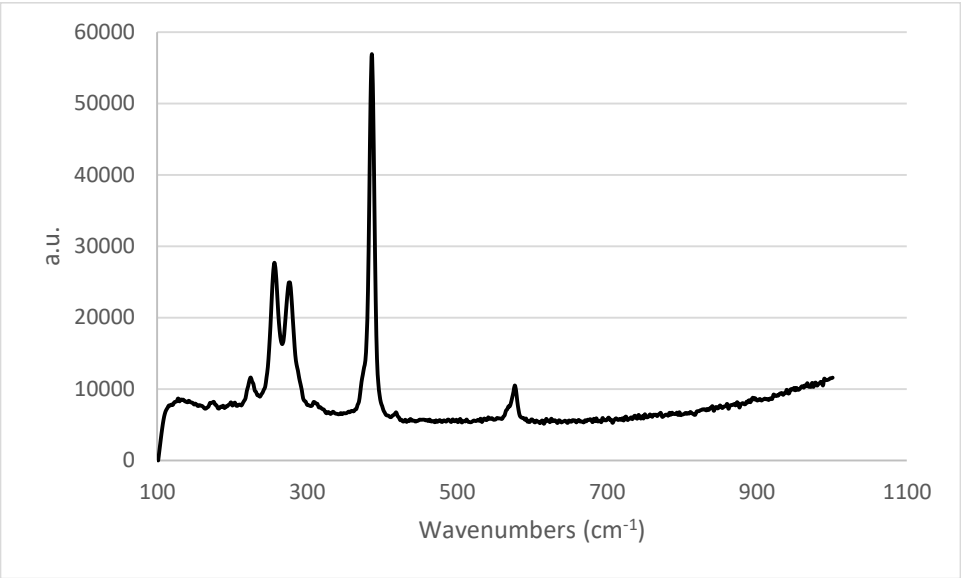

Figure C.2.1 – $ZnPS_3$ host Raman spectrum

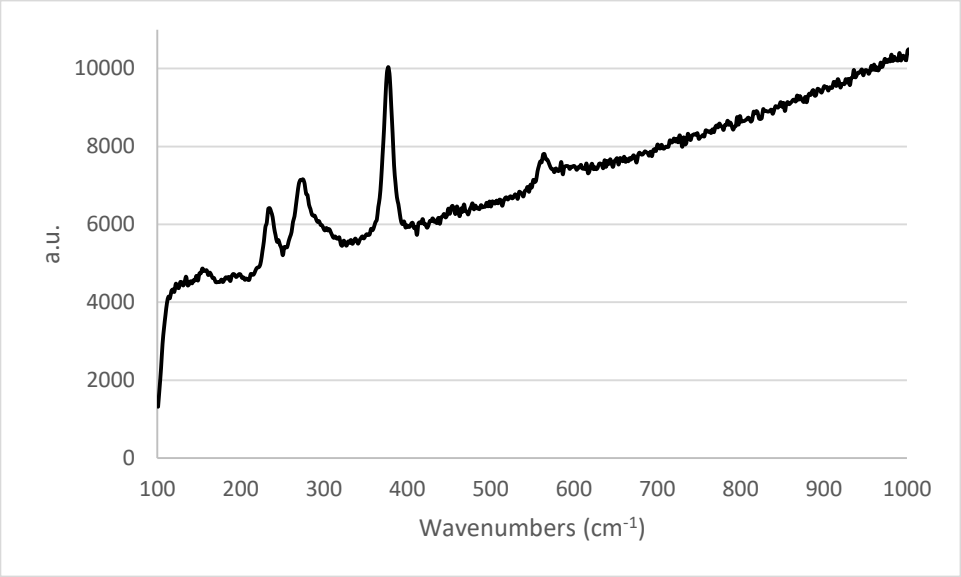

Figure C.2.2 – Mg_xZnPS_3 Raman spectrum

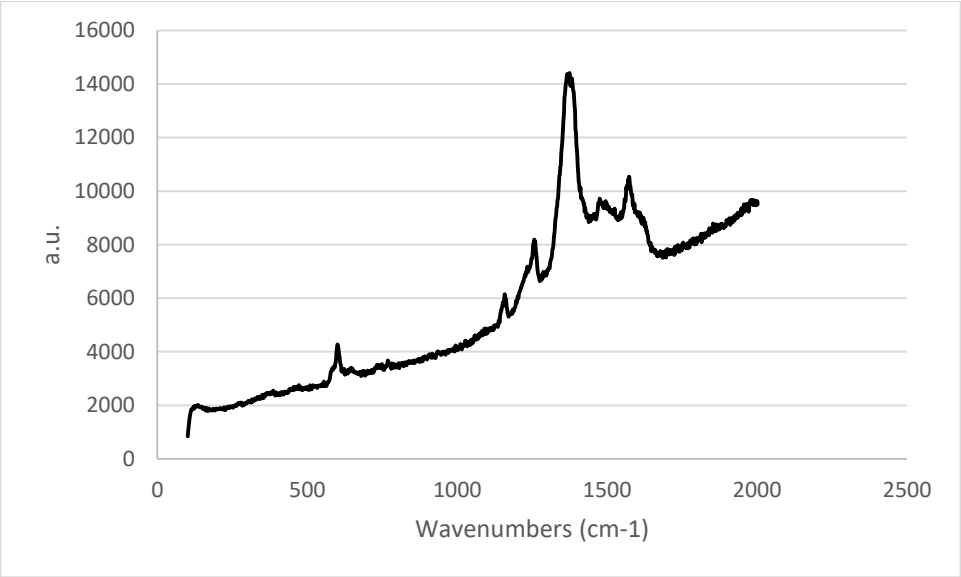

Figure C.2.3 – $ZnPS_3$/PDA Raman spectrum

C.3 $ZnPS_3$ Nanocomposite TGA

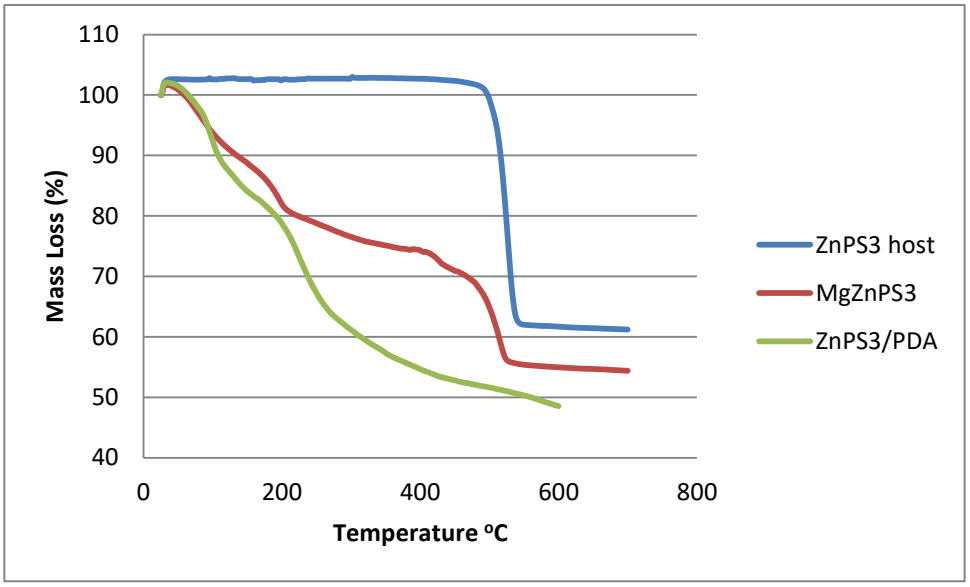

Figure C.3.1 – $ZnPS_3$ nanocomposite thermogravimetric analysis

C.4 $ZnPS_3$ Nanocomposite Capacitance vs Voltage (C-V) Plots

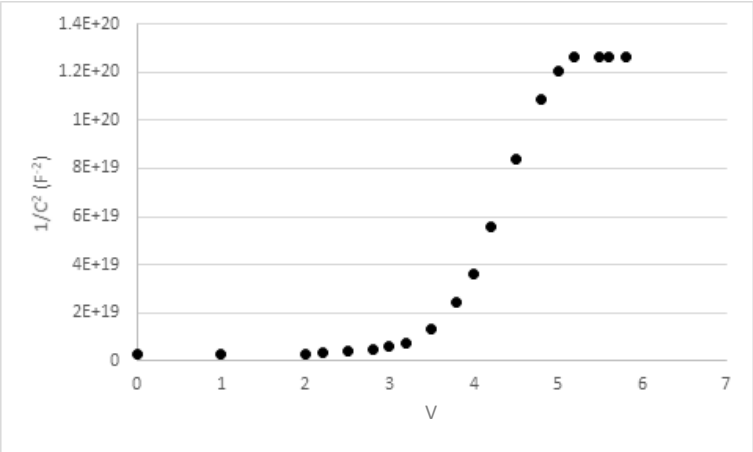

Figure C.4.1 – Capacitance vs Voltage plot for $ZnPS_3$/PDA pressed pellet Schottky device with a Cu contact